Theoretical Studies of the Nature of Actinide Bonds

by

Xiaobin Zhang

A Thesis submitted to the Faculty of Graduate Studies of

The University of Manitoba

in partial fulfilment of the requirements of the degree of

DOCTOR OF PHILOSOPHY

Department of Chemistry

University of Manitoba

Winnipeg

Abstract

In this Ph.D. thesis, the nature of actinide bonds has been investigated mainly using density functional theory (DFT). Various theoretical tools for bonding analysis are examined in this work.

The first chapter is an introduction to the chemical properties of actinides as well as the basic concepts of theories and tools that are used in the studies of this thesis. In Chapter 2, the chemistry of uranyl "Pacman" complexes have been investigated theoretically and compared to experimental work from collaborators. The theoretical methods from these projects are the foundation of the theoretical predictions in the rest of the chapters. In Chapter 3, a series of extractants of the polypyridyl family were studied, using DFT, to identify the electronic properties that preferentially influence actinide/lanthanide separations. Various theoretical tools are used to investigate the covalency of actinide bonds. The subsequent experiments by our collaborators confirmed the theoretical predictions. Because the π interactions between extractions and actinides are proved to be important, Chapter 4 further extended the investigation on the π systems of the extractants. In Chapter 5, the solvation effect at high temperature and pressure has been investigated using the change of dielectric constants as a function of temperature and pressure. The results agree well with the experimental data. This provides a convenient model to simulate the actinide aqueous system under extreme conditions that lack experimental data. Chapter 6 investigated the uranyl reduction on the TiO_2 surface. We propose that photoreduction can also be triggered by radiation from uranium decay. A new TiO_2 cluster was introduced because it is more crystal-like and provides both edges and surfaces. The calculations show that the reduction to uranium IV is more likely to occur on the cluster's edges. Finally, Chapter 7 summarizes the work in this thesis and provides an outlook on potential future projects. This thesis provides valuable information for understanding the nature of actinide bonds computationally.

Acknowledgments

First and foremost, I would like to thank my supervisor, Dr. Georg Schreckenbach, for his invaluable advice, continuous support, and patience during my Ph.D. study. It is very lucky for me to have the opportunity to work under his supervision toward this degree in the past few years. In the same vein, I would like to thank the members of my advisory committee, Dr. Rebecca Davis, Dr. Mario Bieringer, and Dr. Mostafa Fayek, for their help, advice, criticism, and support during the work toward to my degree. I must express my gratitude to Dr. Ping Yang and Dr. Enrique R. Batista for their guidance and training when I was working in their group at Los Alamos National Lab.

I would like to express my sincere thanks to the Bert and Lee Friesen Graduate Scholarship in Chemistry for the continuous generous financial support during my Ph.D. program.

Those people, all the present and former members of the Schreckenbach group, the professors and staff in the Chemistry Department, and Compute Canada staff, also deserve thanks for helping me in every aspect.

Lastly, I would like to thank my parents, Yingui Zhang and Liqin Zhang. Without their unfailing support and continuous encouragement, it would be impossible to complete this thesis. Thanks should also go to all my friends in Winnipeg for accompanying me along this journey.

Table of Contents

List of Figures

List of Tables

List of Abbreviations

AdNDP	Adaptive natural density partitioning
ADF	Amsterdam Density Functional, a computational chemistry program
AIMD	*ab initio* molecular dynamics
AONAO	Natural Atomic Orbital basis set
B3LYP	Becke, 3-parameter, Lee–Yang–Parr, exchange-correlation functional
BCP	Bond critical point
BTPs	Bistriazinyl-pyridine (2,6-bis(triazinyl)pyridines
C-PCM	Conductor-like PCM
CCP	Cage critical point
COSMO	Conductor -like screening model
CP	Critical point
CS	Closed-shell
D-PCM	Dielectric PCM.
D3BJ	D3 version of Grimme's dispersion correction with Becke-Johnson damping
DFT	Density functional theory
DKH	Douglas-Kroll-Hess method for relativistic calculations
DLPNO-CCSD(T)	Domain-based local pair natural orbital coupled-cluster theory
DMNAO	The first-order reduced density matrix in the basis of Natural Atomic Orbitals
Double Hybrid GGA	A GGA includes a certain amount of Hartree–Fock exchange and the second order perturbation theory correlation.
DZP	Double- ζ -plus-polarization
ECP	Effective core potential
EDA	Energy decomposition analysis
ELF	Electron Localization Function
ESP	Electrostatic potential
ETS	Extended Transition State scheme
ETS-NOCV	The combination of Extended Transition State (ETS) method and Natural Orbitals for Chemical Valence (NOCV) scheme

EXAFS	Extended X-ray absorption fine structure
FC	Frozen core approximation
GGA	Generalized gradient approximation
GTOs	Gaussian-type orbitals
HF	Hartree-Fock
HR-XANES	High energy resolution X-ray absorption near edge structure
Hybrid GGA	A GGA incorporate a portion of exact exchange from Hartree–Fock theory with the rest of the exchange–correlation energy from *ab initio* or empirical sources.
Hyper-GGA	A GGA involves occupied Kohn-Sham orbitals as additional non-local which usually refers to hybrid functionals.
IR	Infrared
KS-DFT	Kohn-Sham Density-Functional Theory
LC-ECP	'Large-Core' ECP
LDA	Local density approximation
LOL	localized orbital locator
LP	Lone-pairs (LP)
LSDA	Local spin density approximation
MAs	Minor actinides
MBPT	Many-body perturbation theory
Meta-GGA	A GGA includes second derivative of the electron density (the Laplacian). Nowadays a meta-GGA functional is referred more typically to one that includes a dependence on the kinetic energy density
MOs	Molecular orbitals
MP2	Second-order Møller-Plesset perturbation theory
NBO	Natural Bond Orbitals
NCP	Nuclear critical point
NMR	Nuclear magnetic resonance
NOCV	Natural Orbitals for Chemical Valence scheme
PBE	Perdew–Burke-Ernzerhof functional
PBE0	A hybrid GGA functional mixes the Perdew–Burke-Ernzerhof (PBE) exchange energy and Hartree–Fock exchange energy in a set 3:1 ratio, along with the full PBE correlation energy
PCM	Polarized continuum model, an implicit solvation model
PT2	The second order perturbation theory
PUREX	Plutonium uranium reduction extraction process

QTAIM	Quantum theory of atoms-in-molecules
RCP	Ring critical point
RPA	Random phase approximation
SC-ECP	“Small-Core” ECP
SCF	Self-consistent field
SOMO	Singly occupied molecular orbital
STOs	Slater-type orbitals
TALSPEAK	Trivalent Actinide–Lanthanide Separation by Phosphorus reagent Extraction from Aqueous Komplexes process
TZ2P	Triple-ζ plus two polarization function
UV	Ultraviolet
VDD	Voronoi Deformation Density
VWN	Local correlation functional by Vosko, Wilk and Nusair
X2C	Exact 2-component Hamiltonian for relativistic calculations
XAS	X-ray absorption spectra.
XC	Exchange-correlation
ZORA	The zeroth-order regular approximation

Chapter 1 : Introduction

1.1. Actinides and Their Usage

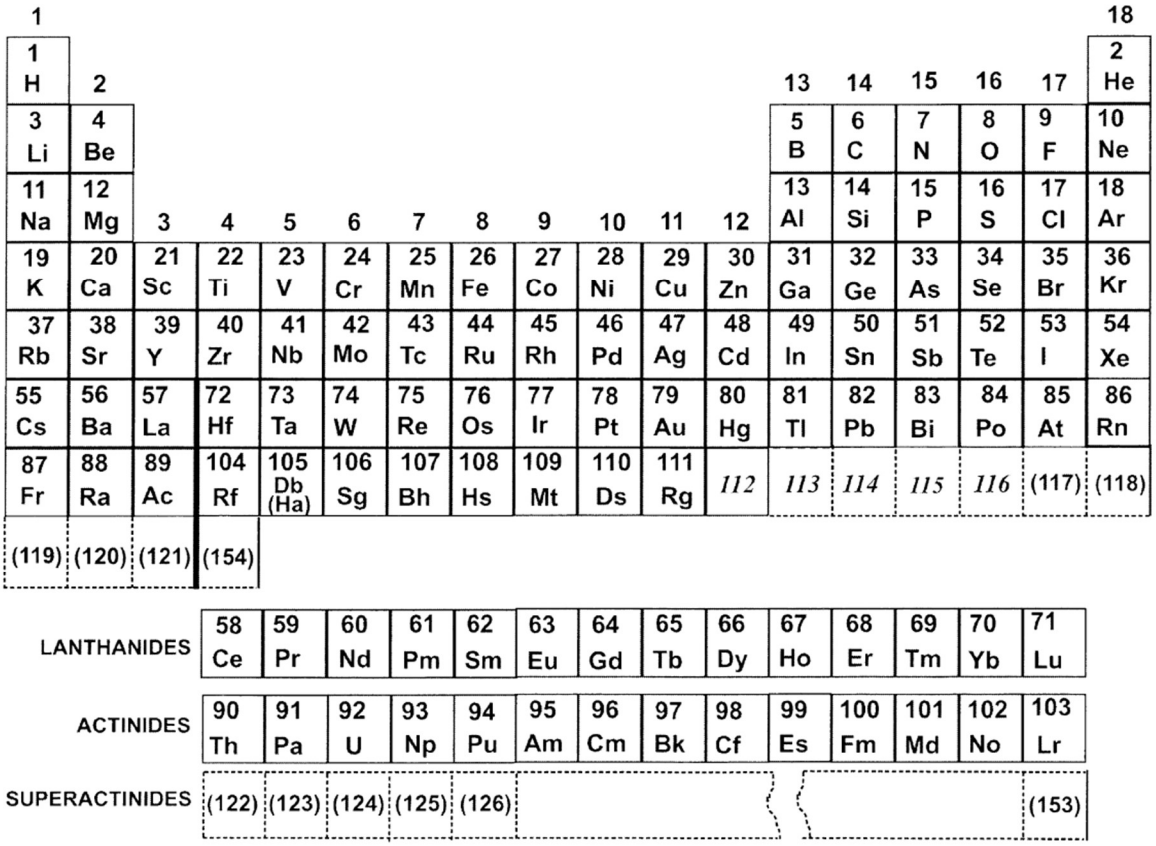

Figure 1.1 The periodic table of the elements, showing the placement of the actinides. (Figure reproduced from reference 1)

As Figure 1.1 shows, actinides are the chemical elements from atomic number 89 to 103. They are all radioactive metals. The atomic and ionic radii of actinides are very large. There are five actinides that can be found in the natural environment: thorium, protoactinium, uranium, neptunium, and plutonium.[2] Uranium and thorium are the only two actinides that exist in appreciable quantities in Earth's crust. By contrast, persisting natural plutonium has merely been identified in small quantities. Trace amounts of protactinium and neptunium are found naturally

as the products of the uranium radioactive decay and transmutation reactions in uranium ores. The rest of the actinides are all synthetic elements.

The usage of actinide compounds can be traced back to Roman times using uranium as colorants.[3] However, uranium was the first actinide discovered as a new chemical element, in 1789 by German chemist Martin Heinrich Klaproth.[4-6] This new element was named after the planet Uranus. Until Henri Becquerel discovered in 1896 that uranium emitted penetrating rays[5, 7], uranium had only been used as a colorant for ceramics and glasses for a century after its first discovery. Becquerel then proved that these penetrating rays could discharge an electroscope. Just shortly after this discovery, Marie Curie and her husband Pierre discovered two new elements with the same property in the uranium ore at trace levels and named them polonium and radium.[8] This new property was then described as radioactivity. In late 1938, nuclear fission[9] was discovered by Otto Hahn and Fritz Strassmann, and then its theory was explained by Lise Meitner and Otto Frisch. As a result, the first nuclear weapons were made in the Manhattan Project in the 1940s[10]. Since then, uranium has played a crucial role in the nuclear energy area until now. ^{235}U is the most important isotope of uranium because it is a lighter isotope of uranium that can absorb slow neutrons to induce a chain reaction, known as an "thermal neutron" reaction,.[9, 11] An advantage of using ^{235}U as fission fuel is that not only can it generate considerable power, but it can also generate other important actinide elements by radioactive decay or transmutation. Additionally, a breeder reactor can produce other valuable actinide elements, such as ^{239}Pu, through the neutron bombardment and subsequent beta decay of ^{238}U. This process, where ^{238}U captures a neutron to become ^{239}U, which then decays into ^{239}Np and finally into ^{239}Pu, is integral to the operation of breeder reactors. The superconductivity of thorium and uranium was also discovered.[12] The transactinide elements also have some applications. For example, Am is used in the ionization

chamber of smoke detectors as an alpha emission source. ^{238}Pu can be used as an energy source in heart pacemakers and deep-sea diving suits. Even in the Apollo space missions, ^{238}Pu was used as a heating source for the astronauts.[13] Besides being extensively used in the nuclear weapons industry, ^{239}Pu also has been employed in the nuclear industry as a nuclear fuel in fast-breeder reactors. Due to the various oxidation states and the unique *f* orbitals, the ability of actinide elements and their compounds as efficient reaction catalysts is also under continuing investigation.[5]

To peacefully use nuclear energy and to face the challenge of climate change, nuclear power provides a critical tool for meeting the demand of increasing energy supply while at the same time reducing greenhouse gas emissions. Yankee Rowe, the first commercial nuclear power plant in the world, was operational in the USA from 1960 to 1992.[14] According to data from the World Nuclear Association,[15] as of September 2022, there are about 440 commercial nuclear power reactors operable scattered across 31 countries and about 55 more are under construction in 15 countries. Meanwhile, over 160 ships and submarines are using nuclear power. As the world's second-largest source (28%) of low-carbon power, these nuclear power stations generated about 10.3% of the world's electricity in 2019. To study the properties of uranium and other actinides, produce medical and industrial isotopes, as well as train future workers and scientists, there are 220 research reactors in over 50 countries. For decades Canada has been a leader in nuclear research and technology. Per August 2022, approximately 15% of Canada's electricity was generated from nuclear power.[16] There are 19 reactors in Ontario that can provide 13.5 GWe of power capacity. Furthermore, Canada is globally renowned for its abundant uranium resources, boasting known reserves of 606,600 tons of U_3O_8 (514,400 tU) as of May 2022.[17] Additionally, in Northern Saskatchewan, the McArthur River and Cigar Lake mines are recognized as having the

highest-grade uranium deposits worldwide. 85% of Canada's uranium production is exported which is worth about $2 billion annually. Canada held the position of the world's leading uranium supplier, contributing approximately 22% of global production until 2009, when it was surpassed by Kazakhstan. As of now, Canada ranks as the third-largest uranium producer, accounting for 17% of the world's total production. Canada will continue to play a significant role in meeting future demands of uranium to respond to the worsening energy crisis. The fundamental study of uranium and related actinide elements will absolutely help Canada to keep its leading advantage.

The debate over nuclear power has intensified in the wake of major incidents such as the Chernobyl disaster in 1986 and the Fukushima Daiichi crisis in 2011. Despite ongoing efforts to transition away from fossil fuels, many countries, particularly in the developing world, continue to rely heavily on coal, oil, and natural gas for their energy needs. The 2022 conflict in Ukraine highlighted the vulnerabilities of even developed nations to fluctuations in the fossil fuel market. This reliance on fossil fuels not only affects energy security but also has broader economic implications, as these resources are essential for the production of industrial goods. For example, reducing the use of natural gas in energy generation could lead to more available and affordable supplies for the production of fertilizers, which is crucial for addressing the global food crisis. In this context, nuclear energy emerges as a viable transitional solution toward sustainable green energy. It's clear that ceasing the development and use of nuclear power will not immediately resolve challenges such as long-term radioactive waste management and actinide contamination; because of these issues, it becomes imperative to understand the fundamental nature of the elements involved.

1.2. Chemical Properties of Actinides

1.2.1. Minor Actinides Separation

In the nuclear industry, the plutonium uranium reduction extraction (PUREX) process removes the uranium and plutonium from spent nuclear fuel for subsequent refabrication into nuclear fuel.[18] The dominated elements in remaining post-PUREX nuclear wastes needing further processing are ^{137}Cs, ^{90}Sr, and the lanthanide elements from nuclear fission. However, there are actinides, such as americium and curium, in it, which are known as "minor actinides" (MAs). The MA isotopes and their daughters have several hundred years or even longer half-lives. Besides, they are α emitters, which make them even more dangerous. The removal of the MAs from post-PUREX nuclear wastes will be greatly helpful for nuclear waste storage. Therefore, it is highly desirable and is a hot topic in the actinide chemistry community. There are two possible technical routes for removing the MAs from post-PUREX nuclear wastes.[19] The first one is molten salt processing. Another one is liquid extraction.

One of the most pervasive challenges encountered in chemical processes is the separation of constituents from a homogeneous mixture.[20] Overcoming this challenge often involves the introduction of a second phase that is either immiscible or partially miscible, facilitating the separation based on distinct distribution coefficients of the components. These differences arise either from physical properties, such as polarity, or from chemical interactions, where solvents and constituents form complexes. Liquid-liquid extraction stands out as a prevalent method for isolating metal ions, wherein an aqueous phase containing the ions is mixed with an organic phase containing extractants.[21-23] The efficacy of this separation pivots on two critical factors: the varying affinity of metal ions towards the extractants and the differential solubility of the resulting

complexes in the aqueous and organic phases. This thesis predominantly explores the former, delving into the intricate metal ion affinity and extractant interactions.

There are many successful applications of liquid-liquid extractions in MA separation. The TALSPEAK (Trivalent Actinide–Lanthanide Separation by Phosphorus reagent Extraction from Aqueous Komplexes) process developed in the United States selectively extract lanthanides over actinides.[24, 25] The lanthanide and actinide ions are hard Lewis acids.[6] The separation of them is one of the most challenging task in actinide chemistry. It is believed that the 5*f*/6*d* covalency is the key for post-PUREX MA-extractant ligand designs.[26] Compared to traditional oxygen based hard-donor ligands, which show little selectivity for An^{3+} over Ln^{3+}, the interaction of soft-donor ligands with An^{3+} is stronger than with Ln^{3+}.[27] Thus, a considerable amount of research focusses on the development of soft-donor extractants for An^{3+}/Ln^{3+} separations.[28-34] Ideally, the ligand design would follow the so called "CHON" principle, which means the ligand only contains carbon, hydrogen, oxygen, and nitrogen atoms. In this way, their combustion products would be environmentally friendly. Therefore, in Europe, the design of nitrogen-donor ligands for MA extractants is favored over the sulfur-based ligands. Because of the special requirements of the nuclear industry, the extractant molecules most survive in low-pH environments and have resistance to radiation damage. Bistriazinyl-pyridine (2,6-bis(triazinyl)pyridines (BTPs)) derivatives are the most extensively studied soft-donor extractants in the European advanced fuel cycle research program, see Scheme 1.[30, 34] However, as Girnt et al. commented: “the level of understanding of BTPs’ selectivity on a molecular level is insufficient to target the design of new, more efficient and selective partitioning reagents or fine-tune partitioning process conditions. Such advances are presently empirical, on a trial and error basis”[35] Thus, the research of extractant ligand design still has a long way to go. Unlike early actinides such as uranium, because of the

strong radiation, the experimental research of MAs is only possible at a few specialist facilities with severe limits. Computational calculations thus play a very important role in this field. In Chapter 4 and Chapter 5, intense investigations were carried out for the ligand design of BTP ligands and their derivatives. It is worth noting that there are a lot of important factors, such as the solubility, complexation kinetics, thermodynamic formation constants, outer-sphere solvent effects, etc., that will affect separations. In this thesis, the metal–ligand covalency is the main focus.

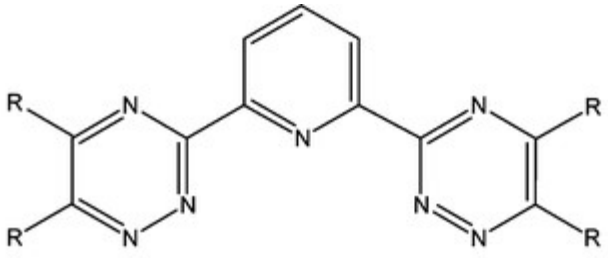

Scheme 1.1 Structure of BTPs. Typical R groups are R= CH_3, C_2H_5, n-C_3H_7, i-C_3H_7, n-C_4H_9, i-C_4H_9, $CyMe_4$ (one per triazin-3-yl ring)

1.2.2. Relativistic Effects

Unlike light elements, for heavy elements such as the actinides, the chemical consequences of relativity are very significant. The relativistic contributions can be divided into two parts: (1) The modification of electronic properties; (2) the spin-orbit effect. First, the relativistic mass correction of core electrons is huge. For example, the mass increase for the uranium 1s electron is 1.35 m_e (the mass of a stationary electron).[5] This effect results in the contraction and energetic stabilization of the 1s electrons. The *s* orbitals in higher primary quantum shells must be orthogonal to the 1s function. Also, all the *s* orbitals have a finite probability of being close to the nucleus where they are affected by the full force of the nuclear attraction. Thus, the relativistic stabilization of the 1s orbitals also stabilizes all the s orbitals. Which is the so-called *direct relativistic orbital contraction*. On the contrary, comparing to the non-relativistic analogues, because of the better shielding of the nucleus from the outer contracted core *s* and *p* electrons, the actinide valence *d* and *f* electrons are destabilized. This is known as the *indirect relativistic orbital expansion*. The spin–orbit coupling is the interaction between the electron's spin and the orbital motion of this electron around the nucleus. The spin-orbit coupling for actinides is much greater than for lanthanides. The electronic spectroscopy and magnetism are strongly affected by spin-orbit effects. For example, the photochemistry and photophysics processes involving a change in spin state are formally forbidden in non-relativistic quantum theory. However, by invoking spin–orbit coupling, the intersystem crossing allows the nonradiative transition between two electronic states of different multiplicity to happen.

1.2.3. Electronic Structure and Oxidation States

Table 1.1: Electronic ground state configurations of each actinide element. The noble gas core structure of radon, [Rn], is used to depict the electronic configurations. The various oxidation states, the symbol, and atomic number, Z, of each element are also given.[6]

Element	Symbol	Z	Configuration	Common oxidation states[a,b]
Actinium	Ac	89	$[Rn]6d^17s^2$	**+3**
Thorium	Th	90	$[Rn]6d^27s^2$	+3 +**4**
Protactinium	Pa	91	$[Rn]5f^26d^17s^2$	+<u>3</u> +4 +**5**
Uranium	U	92	$[Rn]5f^36d^17s^2$	+2 +3 +4[c] +5 +**6**
Neptunium	Np	93	$[Rn]5f^46d^17s^2$	+3 +4 +**5** +6 +7
Plutonium	Pu	94	$[Rn]5f^67s^2$	+3 +**4** +5 +6 +7
Americium	Am	95	$[Rn]5f^77s^2$	+<u>2</u> +**3** +4 +5 +6
Curium	Cm	96	$[Rn]5f^76d^17s^2$	+**3** +4
Berkelium	Bk	97	$[Rn]5f^97s^2$	+**3** +4
Californium	Cf	98	$[Rn]5f^{10}7s^2$	+<u>2</u> +**3** +<u>4</u>
Einsteinium	Es	99	$[Rn]5f^{11}7s^2$	+<u>2</u> +**3**
Fermium	Fm	100	$[Rn]5f^{12}7s^2$	+2 +**3**
Mendelevium	Md	101	$[Rn]5f^{13}7s^2$	+2 +**3**
Nobelium	No	102	$[Rn]5f^{14}7s^2$	+**2** +3
Lawrencium	Lr	103	$[Rn]5f^{14}6d^17s^2$	+**3**

[a] The most stable oxidation state of each element in aqueous solution is bolded.
[b] The oxidation states that are found only in solids are underlined.
[c] The most stable oxidation state in an aqueous solution with low dissolved oxygen.

As Table 1.1 shows, both 5*f* and 6*d* orbitals can be occupied in the ground states of the early actinides. The electron configurations for actinium and thorium show that the 6*d* orbitals have a lower energy than the 5*f* orbitals in the ground state, which is due to the near degeneracy of the 5*f* and 6*d* orbitals in early actinides. Thus, early actinides have various oxidation states, which are also given in Table 1.1. When the atomic numbers increase, these orbital energies invert and the gap between the 5*f* and 6*d* orbital energies begins to increase, see Figure 1.2. The reason is the imperfect screening of the increasing nuclear charge with continual addition of electrons in 5*f* orbitals.[36] The various oxidation states for these elements result in a rich redox chemistry, which

will be further investigated in Chapter 2. On the other hand, the late actinides all have ground-state electronic configurations of $5f^n\,7s^2$, where $n = 6–14$. This is completely analogous to the lanthanides. Thus, the later actinides are in favor of the +3 oxidation state like the lanthanides. As an exception, nobelium prefers the +2 oxidation state because of the fully filled 5*f* orbitals. Analogous to lanthanides, the effects of the actinide contraction decrease the size of atoms with the increase of atomic number due to imperfect shielding of the nuclear charge by 5*f* electrons. Both the effects of oxidation state and actinide contraction make later actinide very difficult to be separated from each other and from lanthanides.

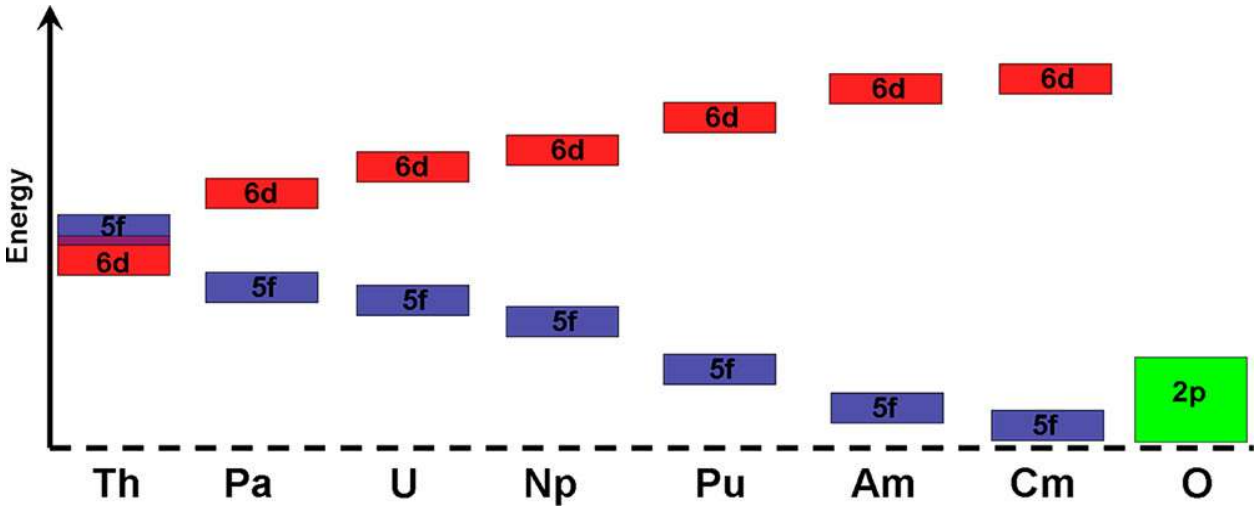

Figure 1.2 Qualitative schematic of the 5*f* and 6*d* atomic orbital energy levels for AnO_2 (Th–Cm) relative to the O–2*p* band in AnO_2 (Figure reproduced from reference 37)

The primary factor of the mobility of actinides in the environment is their oxidation state. [6, 38] Some actinides only exist in one oxidation state in common groundwater, such as Th^{4+}, Am^{3+}, and Cm^{3+}, while uranium, neptunium, and plutonium have a wide range of oxidation state values depending on environmental redox conditions. The most common species are An^{3+}, An^{4+}, AnO_2^+, and AnO_2^{2+}. The actinide complexes containing these ions generally have the bonding strength following in the order as $An^{4+} > AnO_2^{2+} \geq An^{3+} > AnO_2^+$. The complexes of the early actinides in a higher oxidation state usually have high solubilities and hence mobilities. These highly mobile

complexes are the primary concern as environmental contaminants accompanying human activities, such as, for example, mining and milling of uranium ores, nuclear energy, nuclear waste storage, and even nuclear weapons tests. For uranium, in natural environments, the most common oxidation states are +4 and +6.[4, 39] The +5 oxidation state of uranium is generally unstable. It disproportionates to the +4 and +6 oxidation states easily. The tetravalent uranium compounds tend to form insoluble precipitates from mildly acidic to alkaline conditions. The 6+ uranium compounds, on the other hand, usually containing the linear uranyl moiety [UO_2^{2+} or $(O=U=O)^{2+}$], are highly soluble and mobile. Thus, it is a very important uranium species. In solution, UO_2^{2+} not only forms soluble complexes with inorganic ligands such as carbonate, oxalate and hydroxide etc., but also can react with organic matter.[2] When an effective reductant is present, U(VI) can be reduced to U(IV). The reductants can be H_2S, Fe redox, fossil plants, methane, microbial activity or transported humic material. Hydrolysis reactions can occur under certain conditions.[40] The radiation from actinides in solution can also produce highly reactive species that can affect the oxidation state of the actinide, like e^-_{aq}, $H^\bullet$, $OH^\bullet$, and H_2O_2.

Plutonium has the most complex redox chemistry of the actinides.[39] There are multiple stable valence states that can exist in certain environmental conditions. The predominant oxidation states for plutonium are +5 and +6 under oxic conditions. However, at neutral pH and mildly reducing conditions, Pu(IV) is the most common plutonium ion. On the other hand, Pu(III) has much lower solubility. In contrast to uranium and plutonium, +5 is the stable oxidation state for neptunium, such as the NpO_2^+ cation from oxic to moderately suboxic conditions, or as neptunylcarbonato complexes at high pH. Neptunium-237 has a half-life of 2.1×10^6 years and will remain highly radioactive longer in the waster forms, thus is the greatest concern for nuclear waste storage. Better understanding of these actinide complexes not only results in novel chemistry,

but also helps us to control nuclear pollution in natural environments. Chapters 2-6 in this thesis are related to this quest.

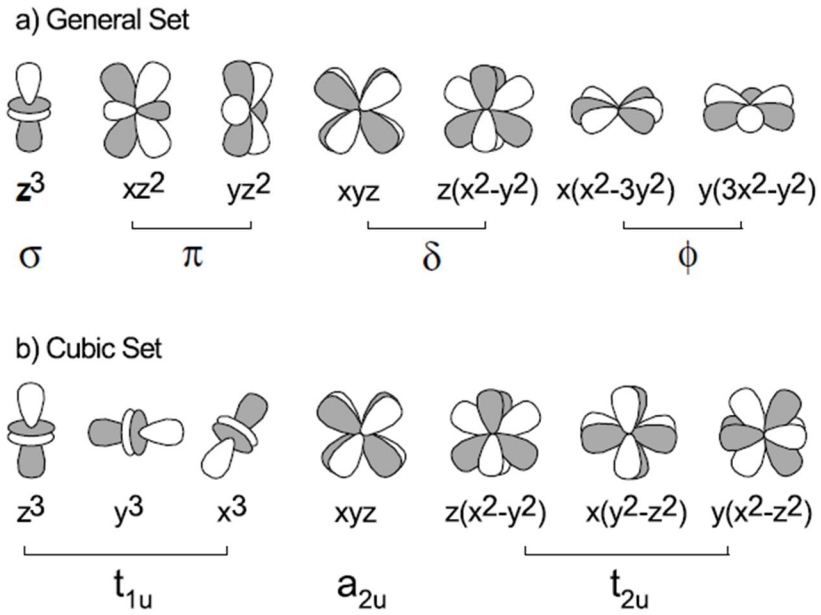

Figure 1.3 Qualitative representations of the general (a) set and cubic (b) set of valence *f* orbitals. (Figure reproduced from reference 1)

1.2.4. Bonding in Actinyl Ions

The *f* orbitals are one of the most important features of the lanthanides and actinides. However, there is no unique way to represent the *f* orbitals. Figure 1.3 shows the most common sets for f orbitals, the general set and cubic set, respectively. The unique shapes of the *f* orbitals enable them to form σ, π, δ, and ϕ bonds. This offers a great opportunity to explore new chemistry. The 5*f* orbitals of the actinides are more extend than the 4*f* orbitals in lanthanides. Thus, the actinides can have some covalent interactions using 5*f* orbitals. On the other hand, the 4*f* electrons in lanthanides are mostly behaving like core electrons. This is especially true when the +3 oxidation state is achieved. As the calculation results in Figure 1.4 show, the 4*f* electrons of lanthanide elements do not extend out far enough to participate in chemical bonding. It is believed

that the difference between the lanthanide 4*f* and the actinide 5*f* orbitals in covalent bonding is the key to separate them. However, the capability of covalent bonding of 5*f* orbitals decreases with increasing atomic number.

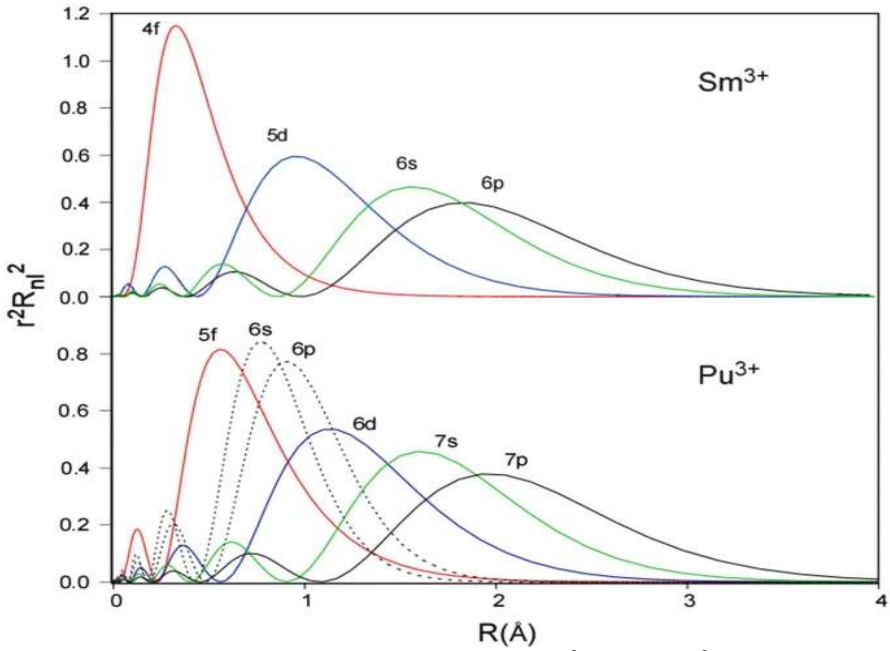

Figure 1.4 Relativistic radial distribution functions for Pu^{3+} and Sm^{3+}. Dashed lines indicate the orbitals normally considered as part of the [Rn] core.[41, 42] (Figure reproduced from reference 42)

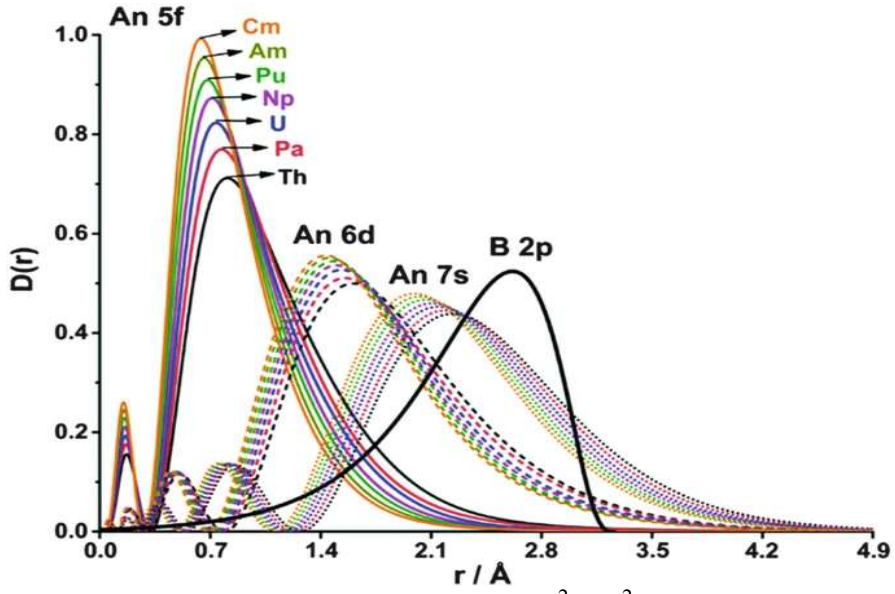

Figure 1.5 Atomic valence-orbital radial densities $D(r) = r^2R(r)^2$ of 5*f* (solid line), 6*d* (dash line), and 7*s* (dotted line) orbitals of the atoms Th through Cm and the overlap of the radial orbital densities of B-2*p* (black solid line) as obtained from B3LYP density functional calculations. (Figure reproduced from reference 43)

Figure 1.5 shows the contraction of the 5*f* orbital radial distribution from Th to Cm. The 5*f* orbital extension decreases with the increase of atomic number Z. This and the similar oxidation state makes the later actinide ions behave more like the lanthanides. Also, the corresponding 6*d* and 7*s* orbitals radially expand with the contraction of the 5*f* orbitals.

The actinyl ions, AnO_2^{n+} (n = 1, 2), and their complexes are probably the most studied compounds in actinide chemistry because of their importance in nuclear industry, especially in nuclear fuel reprocessing and in nuclear waste management. In most of the chapters in this thesis, they are used as models to study the chemistry of actinides. The *d* block transition metal dioxo complexes are usually bent. By contrast, the actinyl ions have linear structures.

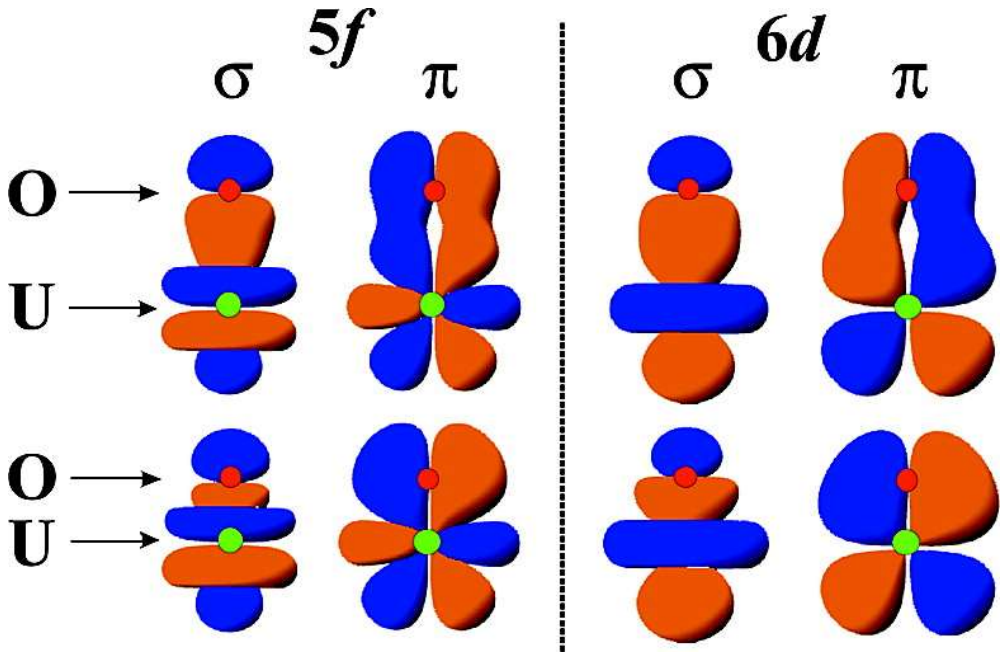

Figure 1.6 Examples of An-O bonding using uranyl as an example. (Figure adapted from reference 44)

Take uranyl for example, there are six symmetry-allowed bonds. Figures 1.6 shows two types of π bond using either 6*d* or 5*f* actinide orbitals. The σ bonds are also given in Figure 1.6 using the f_{z^3} orbital as an example. Interestingly, as Figure 1.7 shows, the σ bonding in U-O bonds has higher energy than π bonding. This may be due to the antibonding overlap between z^3 orbitals and oxygen $2p_z$ orbitals in the short U-O bond, see Figure 1.6. Thus, the U-O triple bonds in uranyl can be illustrated as in Figure 1.6.

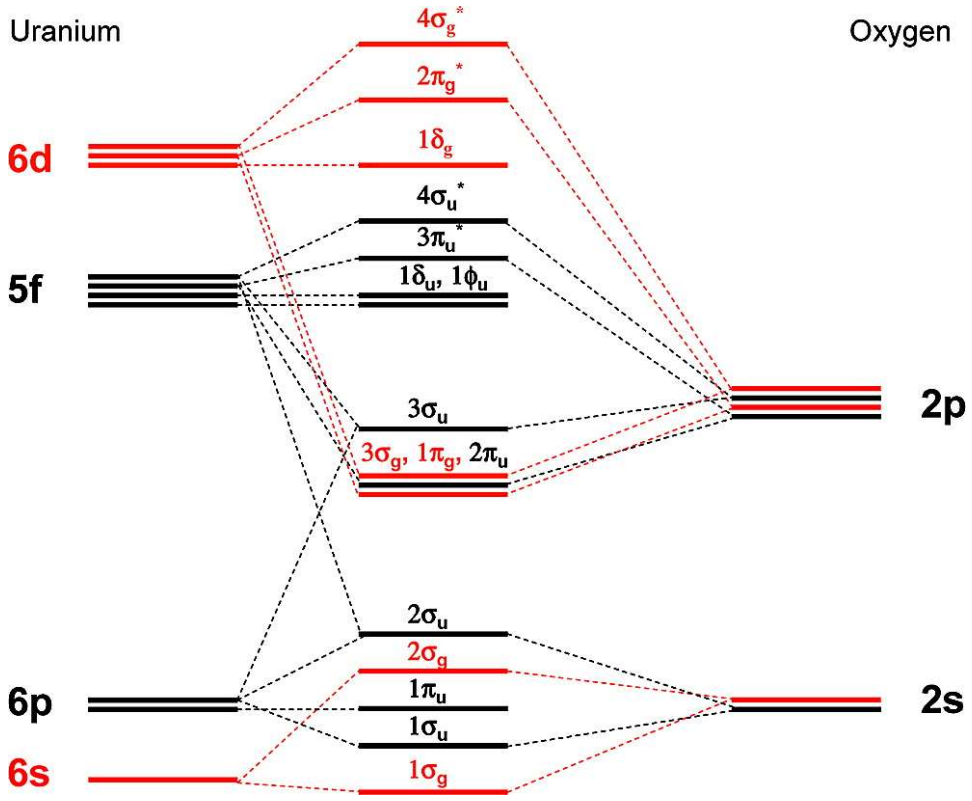

Figure 1.7 Molecular orbital energy level diagram for the uranyl(VI) ion. (Figure reproduced from reference 44)

Because of the symmetry, not all the *f* and *d* orbitals participate in bonding. Those orbitals remain non-bonding, for example, the δ and ϕ orbitals in Figure 1.3. Thus, NpO_2^{2+}, PuO_2^{2+}, and AmO_2^{2+} have one, two and three electrons in non-bonding 5*f* orbitals. UO_2^{2+}, NpO_2^{2+}, PuO_2^{2+}, and AmO_2^{2+} are all linear, which is due to the participation of 5*f* orbitals in bonding. Without the

special symmetry of the 5*f* orbitals, the ions would adopt to the symmetry of *d* orbitals to form bent structures. The ThO_2 molecule is a good example of this effect. It has a bent structure because the thorium 5*f* orbitals have much higher energy than in uranium, see Figure 1.2. The stability with respect to lower oxidation state species of those linear ions follows the order of U > Np > Pu > Am, which shows the increase of lanthanide-like behavior when the atomic number is increasing; recall the actinide contraction in Figure 1.4. The early actinides, namely uranium, neptunium, and plutonium, exhibit higher 5*f* covalency. Therefore, they will be good model compounds to distinguish the capability of extractants for lanthanide–actinide separation. The linear structure also offers a relatively simple first shell of solvation molecules in the equatorial plane and specific orientations of the *f* and *d* orbitals of the actinides. Thus, in Chapter 3, UO_2^{2+}, NpO_2^{2+}, and PuO_2^{2+} are used as a simplified model to study the capability of different extractants to separate lanthanides and later actinides.

1.2.5. The *f* Orbital Covalency

105 years after the discovery of dimethylzinc by Frankland, the first organoactinide compounds were prepared.[45] Actinide sandwich complexes, the cyclopentadienyluranium compounds, reported by Reynolds and Wilkinson in 1956, are among the first f element organometallics.[46] In 1968, uranocene was discovered by Andrew Streitwieser Jr. and Ulrich Mueller-Westerhoff, which was a milestone in organouranium chemistry.[47] Those compounds have played a central role for developing organoactinide chemistry electronic structure models. [47-50]

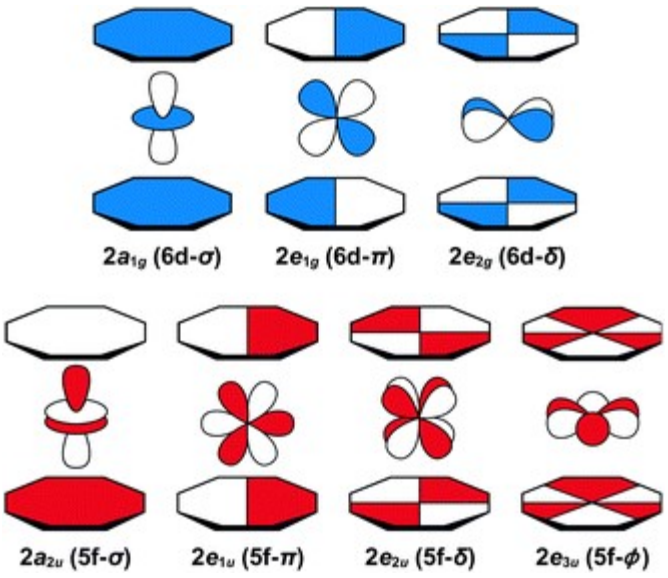

Figure 1.8 Representations of the 5*f*- and 6*d*-antibonding interactions in actinocenes.[51, 52] (Figure reproduced from reference 51)

Cyclopentadienyl's π orbitals form π bonding with metal *d* orbitals. The idea of synthesis of uranocene is extending this to uranium f orbitals and δ symmetry π orbitals of cyclooctatetraene. These δ bonds are represented in Figure 1.8. The synthesis of uranocene suggested a new type of bonding with two nodal planes coincident with the bond axis which are δ bonds. On the other hand, among lanthanide elements, only Ce can form a natural sandwich compound like the actinocenes. All the actinides with a stable tetravalent state can form analogous compounds like uranocene. They have the same bonding model as suggested by their magnetic properties. [6] Comparing to the actinidocenes, the bondings between lanthanides and cyclooctatetraene are essentially ionic. The lanthanide cyclooctatetraene complexes will react immediately with UCl_4 to form uranocene.[6] This is a good example to demonstrate that 5f orbitals are more extended than the 4f orbitals for covalent bonding. As Kenneth N. Raymond pointed out about 40 years ago: "A dominant question concerning organometallic compounds of the *f* metals is the degree to which 'covalency' is important in the bonding."[53] The combination of X-ray absorption spectra, such as K-edge X-ray

absorption spectra (XAS) and M_4 edge High Energy Resolution X-ray Absorption Near Edge Structure(HR-XANES), and theoretical calculations provides a unique way to probe the electronic structures and investigate the covalency of *f* metal bonding. The study and discussion of covalency in actinide bonding are one of the main topics of this thesis. Recently, the research of actinocenes has been extended by Minasian et al.[51] They provided the first experimental evidence for extensive ϕ-orbital interactions of thorocene by the C K-edge XAS analysis. On the contrary, both experimental and calculations-based pre-edge analysis showed that ϕ-type covalency in uranocene was negligible. The ϕ-type Kohn-Sham molecular orbitals for $(C_8H_8)_2Th$ and $(C_8H_8)_2U$ are showed in Figure 1.9. The calculated C 2p and Th 5f orbital mixings are significantly larger than the corresponding C 2p and U 5f orbital mixing. The latter is almost entirely metal based. In the early studies, orbital mixing has been proposed to increase with late actinides.[42, 54, 55] The unusual behavior of $(C_8H_8)_2Th$ is due to a near perfect energy match between the Th 5f and $(C_8H_8)_2^{4-}$ e_{3u} orbitals.[51, 56-58] This is consistent with the bent structure of ThO_2 mentioned above.

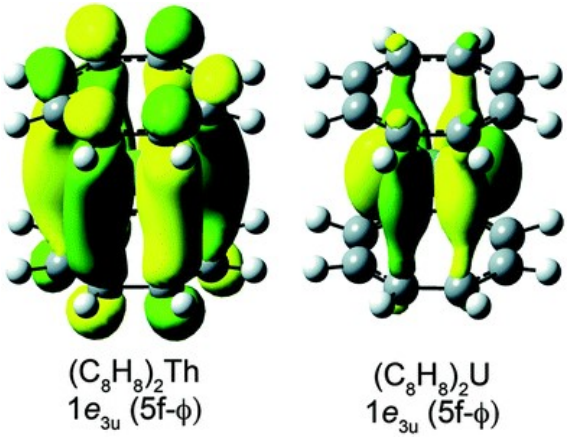

Figure 1.9 Representations of the bonding $1e_{3u}$ Kohn–Sham molecular orbitals for $(C_8H_8)_2Th$ (left) and $(C_8H_8)_2U$ (right). (Figure reproduced from reference 53)

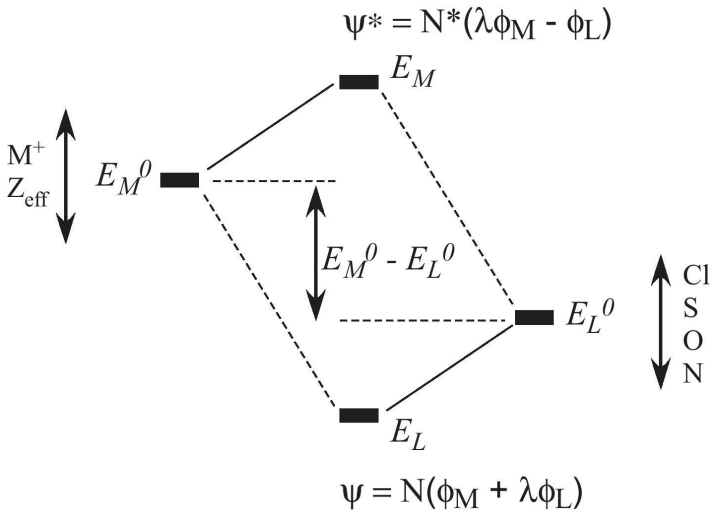

Figure 1.10 Molecular orbital interaction diagram illustrating the factors that can affect E_M^0 and E_L^0, influencing covalency. (Figure reproduced from reference 42)

The ligand-metal orbital mixing can be described by perturbation theory[59, 60]

$$\Psi = \frac{(\Phi_M + \lambda\Phi_L)}{\sqrt{1+2\lambda S_{ML}+\lambda^2}} \tag{1.1}$$

where Φ_M and Φ_L are metal and ligand orbitals, S_{ML} is the overlap integral, and λ is the mixing coefficient which is given to first order by

$$\lambda = \frac{H_{ML}}{E_M^0 - E_L^0} \tag{1.2}$$

where H_{ML} is the off-diagonal matrix element, which can have various forms depending on the different electronic structure models. H_{ML} is proportional to S_{ML} for the two fragment orbitals in Extended Hückel theory. E_M and E_L are the orbital energies for metal and ligand respectively, which are illustrated in Figure 1.10. λ is directly related to S_{ML}. Furthermore, the intensity of the pre-edge transitions in ligand K-edge XAS mentioned above is directly related to the mixing coefficient λ. This is how covalency can be measured experimentally by XAS. The mixing coefficient λ plays an important role in the investigation of covalent interactions. From equation 1.2, a covalent interaction can be divided into two ways: The overlap driven covalency (H_{ML}) and

near degeneracy driven covalency or energy driven covalency ($E_M^0 - E_L^0$). To increase λ one can either increase the overlap (H_{ML}) or make the denominator ($E_M^0 - E_L^0$) small. It has been pointed out that covalent interactions from orbital mixing are not always accompanied by a large orbital energy stabilization or stronger bonds.[60, 61] The energy associated with covalent mixing is given by second-order perturbation theory

$$\Delta E = \frac{|H_{ML}|^2}{E_M^0 - E_L^0} = \lambda H_{ML} \quad (1.3)$$

Equation 1.3 means, depending on the Hamiltonian matrix elements (H_{ML}), bonds with the same orbital mixing parameters (λ) may have different covalent contributions to the bond energies. Thus, it is usually only meaningful to compare bonding properties of the same type of bonds.

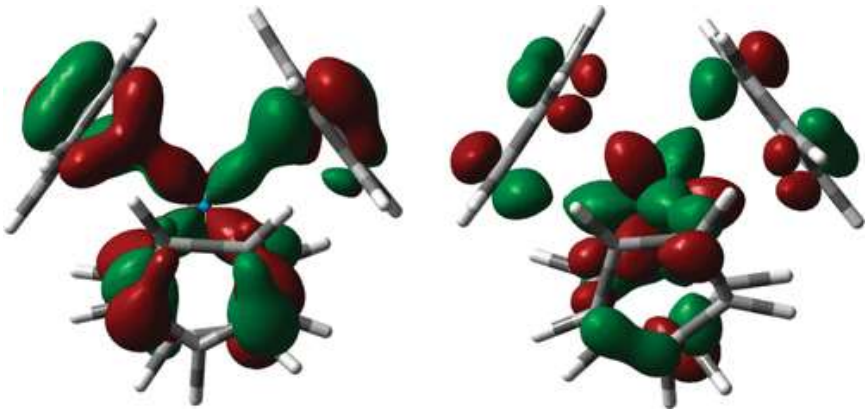

Figure 1.11 Three-dimensional representations of one component of the "t1" MOs of UCp_4 (left) and $AmCp_4$ (right). The contribution (%, Mulliken) of the actinide 5f orbitals to the $AmCp_4$ MO is ca. 30%, approximately twice that in UCp_4. (Figure adapted from reference 62)

However, whether orbital mixing is really covalency is still arguable in the actinide chemistry community. By the classical definition of covalency, a buildup of the electron density in the internuclear region due to overlapping atomic orbitals is required. Nikolas Kaltsoyannis in his review pointed out that, in 5*f* block complexes, significant valence orbital mixing does not

necessary lead to internuclear charge buildup.[59] His review discusses the analyses of the bonding in $AnCp_3$ and $AnCp_4$ (An = Th–Cm; Cp = η^5-C_5H_5) using both the traditional tools and topological analysis via the quantum theory of atoms-in-molecules (QTAIM; see also section 1.6). The two approaches given rather different conclusions. As Figure 1.11 illustrates, the 5f contribution to the americium orbital is much larger than that in the uranium compound. However, the metal–ligand overlap in the latter is better. The author further pointed out that there are not well-defined orbital energy levels for all quantum-chemical methodologies. For example, in the multiconfigurational approach, orbital energy levels lose their meaning.[63, 64] In such circumstances, measures of covalency that depend on orbital energy differences are inappropriate. The QTAIM analysis of $AnCp_4$[62] and $AnCp_3$[55] also suggested that the uranium bond is more covalent. Thus, when using quantum chemistry to investigate metal–ligand covalency in 5*f* block, extra care must be taken. In this thesis, the overlap driven covalency is focused on via both traditional computational tools and new methods such as topological analysis.

1.3. The Schrödinger Equation and Approximation Methods

1.3.1. Schrödinger Equation.

Solving the Schrödinger Equation is the fundamental goal of quantum chemistry.[65] Wave functions are the solutions to the Schrödinger Equation. They describe the quantum states of a given system in quantum mechanics.

The non-relativistic wave function evolves in time, for example in an excited state, according to the time-dependent Schrödinger Equation

$$\hat{H}\psi(x,t) = i\hbar\frac{\partial\psi}{\partial t} \qquad (1.4)$$

where i is the imaginary unit, $\hbar$ is the Planck constant divided by 2π, the symbol ∂/∂t indicates a partial derivative with respect to time t, Ψ is the wave function of the quantum system, and $\hat{\mathrm{H}}$ is the Hamiltonian operator.

The wave functions can form standing waves, which are known as stationary states. They can be determined by the time-independent Schrödinger Equation.

$$\hat{\mathrm{H}}\psi = E\psi \qquad (1.5)$$

where $\hat{H}$ is Hamiltonian operator, Ψ is a certain wave function, and E is the energy of the state Ψ.

For a molecular system in chemistry, there are five contributions to the Hamiltonian

$$\hat{\mathrm{H}} = -\sum\frac{\hbar^2}{2m_e}\nabla_i^2 - \sum_k\frac{\hbar^2}{2m_k}\nabla_k^2 - \sum_i\sum_k\frac{e^2Z_k}{r_{ik}} + \sum_{i<j}\frac{e^2}{r_{ij}} + \sum_{k<l}\frac{e^2Z_kZ_l}{r_{kl}} \qquad (1.6)$$

Where all units are atomic units except for m_e, which is the mass of a stationary electron. i and j run over electrons, k and l run over nuclei, m_k is the mass of nucleus k, ∇^2 is the Laplacian operator, e is the charge on the electron, Z is an atomic number, and r_{ab} is the distance between particles a and b. In Eq. 1.6, the first term is the kinetic energy operator for each electron in the system. The second term is the kinetic energy operator for each nucleus in the system. The third term is the total electron-nucleus Coulombic attraction in the molecule. The fourth term is the potential energy from Coulombic electron-electron repulsions. And the last term is the potential energy of Coulombic nuclear-nuclear repulsions.

1.3.2. Relativistic Effects

The time-independent Schrödinger equation is only valid for non-relativistic systems. As mentioned in section 1.2.1, the relativistic effects for heavy elements such as actinides are very important. The Dirac equation[66] has been derived by British physicist Paul Dirac in 1929, which is usually considered to give the good description for relativistic effects on the electronic structure in chemistry, especially with Breit and finite nucleus corrections for many-body effects. However, in Dirac theory, the particles can have positive or negative energies. The negative solutions of the Dirac equation relate to the discovery of antimatter, such as positrons. In this thesis, only the positive states of the electrons are considered.

The four-component Dirac equation is given by:

$$\widehat{H}_d\psi = E\psi \tag{1.7}$$

where:

$$\widehat{H}_d = c(\alpha \cdot p) + \beta c^2 + V \tag{1.8}$$

where c is the speed of light, p is the momentum, V is the external potential, and α (x, y, z-components) and β are the 4 × 4 Dirac matrices:

$$\alpha = \begin{bmatrix} 0 & \sigma \\ \sigma & 0 \end{bmatrix} \tag{1.9}$$

$$\sigma_x = \begin{bmatrix} 0 & 1 \\ 1 & 0 \end{bmatrix}, \sigma_y = \begin{bmatrix} 0 & -i \\ i & 0 \end{bmatrix}, \sigma_z = \begin{bmatrix} 1 & 0 \\ 0 & -1 \end{bmatrix} \tag{1.10}$$

$$\beta = \begin{bmatrix} I & 0 \\ 0 & I \end{bmatrix} \tag{1.11}$$

where I is the two-dimensional identity matrix and σ represents the 2 × 2 Pauli spin matrices.

There are the large component ψ_L and the small component ψ_s in the equation: ψ_L is much larger than ψ_s for positive energy states.

$$\psi = \begin{bmatrix} \psi_L \\ \psi_S \end{bmatrix} = \begin{bmatrix} \psi_L \uparrow \\ \psi_L \uparrow \\ \psi_S \downarrow \\ \psi_S \downarrow \end{bmatrix} \tag{1.12}$$

However, the regular four-component eigenvalue equation is not only computationally expensive but also has problems such as variational collapse. Even the non-regular two-component eigenvalue equation, obtained by a transformation from the regular four-component eigenvalue equation, turns out to be difficult to solve.

To solve these problems, many different approximations have been developed. One of the most popular approximations is the zeroth-order regular approximation (ZORA)[67, 68]. For solving the Dirac equation approximately, ZORA as a two-component spinor approach is based upon regularizing the wave equation by ignoring the energy dependence of the effective mass of the electron.[69] Thus, as a two-component method, only the large components will be calculated in the ZORA approximation.

The two-component ZORA equation is given by

$$\left[\frac{1}{2}(\sigma \cdot \hat{p})\kappa(\sigma \cdot \hat{p}) + V\right]\psi_n = \varepsilon_n^Z \psi_n \tag{1.13}$$

where

$$\kappa = \frac{2c^2}{2c^2 - V} \tag{1.14}$$

ε_n^Z in Equation 1.13 can be improved by scaling the ZORA energy.[70, 71]

$$\varepsilon_i^{scaled} = \frac{\varepsilon_i^Z}{1 + \langle \varphi_i | \sigma \cdot \hat{p} \frac{\kappa^2}{4c^2} \sigma \cdot \hat{p} | \varphi_i \rangle} \tag{1.15}$$

In this way, the total scaled ZORA energy at the density functional theory (DFT, see section 1.3.7) level can be written as

$$E_n^{scaled} = \sum_{i=1}^{N} [\langle \varphi_i \left| \sigma \cdot \hat{p} \frac{\kappa}{2} \sigma \cdot \hat{p} \right| \varphi_i \rangle - \varepsilon_i^{scaled} \langle \varphi_i \left| \sigma \cdot \hat{p} \frac{\kappa^2}{4c^2} \sigma \cdot \hat{p} \right| \varphi_i \rangle]$$

$$+E_{ne} + E_H + E_{xc} + E_{nn} \quad (1.16)$$

Where the summation adds up all the occupied orbitals. Equation 1.16 is identical to the non-relativistic total energy functional (also see section 1.3.7) except for the kinetic energy contribution, which includes the ZORA correction. For ordinary chemical purposes, such as geometry, scaled ZORA calculations are usually sufficient. Many other methods such as Douglas-Kroll-Hess[72, 73] and X2C[74] are also widely used.

Even if the approximations above are used, calculating systems with large numbers of electrons with significant correlation and relativistic effects is still a challenge in heavy-elements studies. Because usually only the valence electrons are typically correlated to chemical properties, one possible solutions of these difficulties is using the effective core potential (ECP) approach or so-called pseudopotentials. The effective core potentials (ECPs) replace electrons in the inner shells by a suitably parametrized one-electron operator. This approximation not only reduces the number of electrons in the calculations but also can include relativistic effects.[75-77] The 'large-core' ECPs (LC-ECPs) for actinides include everything but the valence shell. The "small-core" ECP (SC-ECP) on the other hand, only parameterize 60 electrons as core. Recent studies showed that SC-ECP had good agreement with experimental data and 4-component relativistic calculations such as geometries[78, 79] , frequencies[78, 79], ligand NMR chemical shifts[80-82] and dissociation energies[83]. Shamov et al. [84] and Odoh et al. [85] proved that the current SC-ECP is clearly superior to the older "large core" ECP (LC-ECP) for the chemical properties such as geometries, frequencies, and reduction potentials. When ECPs are not supported, another choice is the so-called the frozen core (FC) approximation. It neglects correlation effects and/ or core polarization for electrons in the low-lying core orbitals.

1.3.3. Born-Oppenheimer Approximation

Due to the correlated motions of particles, for many-particle molecular systems, it is extremely difficult to solve the Schrödinger Equation (Equations 1.4 and 1.5 in section 1.3.1) to determine the accurate wave functions. To simplify this problem, the Born-Oppenheimer approximation[86] was introduced. Because the movement of nuclei in the molecular systems is much slower than that of the electrons, the approximation assumes that the motion of atomic nuclei and electrons in a molecule can be separated. This assumption results in a new electronic Schrödinger Equation:

$$\left(\hat{H}_{el} + \hat{V}_N\right)\psi_{el}(q_i; q_k) = E_{el}\psi_{el}(q_i; q_k) \qquad (1.17)$$

where the subscript '*el*' emphasizes the invocation of the Born-Oppenheimer approximation. H_{el} includes the first, third, and fourth terms from Equation 1.6; V_N is the nuclear-nuclear repulsion energy which is the last term in Equation 1.6, q_i are independent variables (electronic coordinates), and q_k are parameters (nuclear coordinates). Obviously, in the Born-Oppenheimer approximation, V_N is a constant that represent a given set of fixed nuclear coordinates q_k. Thus, the V_N term can always be ignored during solving Equation 1.17. Generally speaking, the Born-Oppenheimer approximation can be very accurate in most cases in computational chemistry and significantly improve computational efficiency. However, the Born-Oppenheimer Approximation becomes problematic near Level Crossings.[87] Moreover, in the class of reactions known as Woodward-Hoffmann forbidden reactions, Waschewsky et al. proved that the Born-Oppenheimer approximation fails and can result in a marked reduction in the reaction rate.[88] In the regular quantum chemistry calculations, because of the Born–Oppenheimer approximation, temperature has no effect on the optimized structures. However, for actinides, good force field parameters are rare to yield reasonable molecular dynamics calculation results. On the other hand, ab initio

molecular dynamics (AIMD) are way too expensive for actinides. In Chapter 5, dielectric constants, which change as a function of pressure and temperature, were used to successfully predict the properties of the aqueous AnO_2-Cl system at high pressure and temperature.

The Schrödinger Equation cannot be solved exactly except for a hydrogen atom and H_2^+ cation. Thus, there are two principal approximation methods to solve Equation 1.17 in quantum chemistry: variational method and perturbation theory.

1.3.4. Variational Method

To put it simply, the variational principle[65] states that, if there are two (approximate) wavefunctions for a system, the one that produces the lower energy better represents the ground state wavefunction of the system. The true ground state wavefunction will of course yield the lowest energy (E_0). Assuming that we are solving for a ground-state wave function ψ_{el} and energy E_{el} which satisfy the electronic Schrödinger Equation including Born-Oppenheimer approximation:

$$\hat{H}_{el}\psi_{el} = E_{el}\psi_{el} \qquad (1.18)$$

Then multiply Equation 1.18 from the left by ψ_{el}^* and integrate over all space:

$$E_{el} = \frac{\int \psi_{el}^* \hat{H}_{el}\psi_{el} d\tau}{\int \psi_{el}^* \psi_{el} d\tau} = \frac{<\psi_{el}|\hat{H}_{el}|\psi_{el}>}{<\psi_{el}|\psi_{el}>} \qquad (1.19)$$

where $d\tau$ is the appropriate volume element.

If we substitute any other function ϕ instead of ψ_{el}:

$$E_{\varphi} = \frac{\int \phi^* \hat{H} \phi d\tau}{\int \phi^* \phi d\tau} = \frac{<\phi|\hat{H}|\phi>}{<\phi|\phi>} \qquad (1.20)$$

Because of the variational principle, the ground-state energy E_{el} will be smaller than or equal to E_ϕ:

$$E_{el} \leq E_\phi \qquad (1.21)$$

Thus, any trial function that obeys the proper boundary conditions can be used to calculate an upper bound to E_0. If a trial function is chosen with some arbitrary variational parameters, such as α, β, γ …:

$$E_{el} \leq E_{\phi}(\alpha, \beta, \gamma, \dots) \qquad (1.22)$$

the exact ground-state energy E_0 can be approached by optimizing these parameters.

1.3.5. Perturbation Theory

To solve the Schrödinger Equation using perturbation theory[65], the Hamiltonian operator can be written as the sum of the unperturbed Hamiltonian operator and a perturbation:

$$\hat{H} = \hat{H}^{(0)} + \hat{H}^{(1)} \qquad (1.23)$$

The perturbation approximation is that the description of a complex system can start with a simple system which is known ($\hat{H}^{(0)}$); then add an additional perturbation Hamiltonian for the weak disturbances if these disturbances are not too large.

Take the one-dimensional anharmonic oscillator for example

$$\hat{H} = -\frac{\hbar^2}{2m}\frac{d^2}{dx^2} + \frac{1}{2}kx^2 + cx^3 + dx^4 \qquad (1.24)$$

The Hamiltonian 1.24 is related to the Hamiltonian of the harmonic oscillator

$$\hat{H}^0 = -\frac{\hbar^2}{2m}\frac{d^2}{dx^2} + \frac{1}{2}kx^2 \qquad (1.25)$$

If the constants *c* and *d* in Hamiltonian 1.24 are all very small, then the eigenfunctions and eigenvalues of the anharmonic oscillator are expected to be closely related to those of the harmonic oscillator. Thus, the system with $\hat{H}^0$ and $\hat{H}$ are the unperturbed system and perturbed system,

respectively. Thus, the perturbation $\widehat{H}^{(1)}$ is the difference between these two Hamiltonians. Therefore, in Equation 1.23 $\widehat{H}^{(1)} = cx^3 + dx^4$.

For a nondegenerate system, the first-order energy correction is given by

$$E_n^{(1)} = \left\langle \psi_n^{(0)} \middle| \widehat{H}^{(1)} \middle| \psi_n^{(0)} \right\rangle = \int \psi_n^{(0)*} \widehat{H}^{(1)} \psi_n^{(0)} d\tau \qquad (1.26)$$

The ground state wave function for the harmonic oscillator is

$$\psi_0^{(0)} = \left(\frac{\alpha}{\pi}\right)^{\frac{1}{4}} e^{-\frac{\alpha x^2}{2}} \qquad (1.27)$$

Thus, the first-order energy correction for the ground state of anharmonic oscillator is

$$E_0^{(1)} = \left\langle \psi_0^{(0)} \middle| cx^3 + dx^4 \middle| \psi_0^{(0)} \right\rangle = \left(\frac{\alpha}{\pi}\right)^{\frac{1}{2}} \int_{-\infty}^{+\infty} e^{-\alpha x^2} (cx^3 + dx^4) dx = \frac{3d}{4\alpha^2} = \frac{3dh^2}{64\pi^4 \nu^2 m^2} \qquad (1.28)$$

where $\alpha \equiv 2\pi\nu m/\hbar = 4\pi^2 \nu m/h$ for the oscillator. Higher orders can be calculated in a similar fashion.

1.3.6. The Hartree-Fock Method and Post Hartree-Fock Approaches

The Hartree-Fock (HF) method[89, 90] is the first approximation for all atomic and molecular calculations. It is a milestone in modern quantum chemistry. In the Hartree-Fock method, MOs can be determined as eigenfunctions of a set of one-electron operators individually. Each electron, however, is treated as moving in the static field of all the other electrons which includes exchange effects on the Coulomb repulsion.

After applying the Born-Oppenheimer approximation, for a system with 2N electrons and M nuclei, Equation 1.6 can be written in atomic units as

$$\widehat{H}_{el} = -\frac{1}{2}\sum_{i=1}^{2N} \nabla_i^2 - \sum_{i=1}^{2N} \sum_{A=1}^{M} \frac{Z_A}{r_{iA}} + \sum_{i=1}^{2N} \sum_{j>i} \frac{1}{r_{ij}} + \sum_{A}^{M} \sum_{B<A}^{M} \frac{Z_A Z_B}{R_{AB}} \qquad (1.29)$$

where the four terms represent the kinetic energy of the electrons, the interaction of each electron with each nucleus, electron-electron interactions, and inter-nuclear interactions, respectively. It is worth noting that now Equation 1.29 uses atomic units.

The Hartree-Fock wave function can be descripted by the Slater determinant

$$\psi(1,2,\dots,2\mathrm{N}) = \frac{1}{\sqrt{(2N)!}}\begin{vmatrix} \psi_1\alpha(1) & \psi_1\beta(1) & \cdots & \psi_N\alpha(1) & \psi_N\beta(1) \\ \psi_1\alpha(2) & \psi_1\beta(2) & \cdots & \psi_N\alpha(2) & \psi_N\beta(2) \\ \vdots & \vdots & \ddots & \vdots & \vdots \\ \psi_1\alpha(2\mathrm{N}) & \psi_1\beta(2\mathrm{N}) & \cdots & \psi_N\alpha(2\mathrm{N}) & \psi_N\beta(2\mathrm{N}) \end{vmatrix} \quad (1.30)$$

The electron energy is

$$E_{el} = \left\langle \psi^*(1,2,\dots,2\mathrm{N}) \middle| \widehat{H} \middle| \psi(1,2,\dots,2\mathrm{N}) \right\rangle \quad (1.31)$$

The Equation 1.31 can be rewritten as

$$E_{el} = 2\sum_{j=1}^{N} I_j + \sum_{i=1}^{N}\sum_{j=1}^{N}(2J_{ij} - K_{ij}) \quad (1.32)$$

where

$$I_j = \int d\, r_j \psi_j^*(r_j)\left(-\frac{1}{2}\nabla_j^2 - \sum_N^M \frac{Z_A}{r_{jA}}\right)\psi_j(r_j) \quad (1.33)$$

$$J_{ij} = \int\int d\, r_1 d\, r_2 \psi_i^*(r_1)\psi_j^*(r_2)\frac{1}{r_{12}}\psi_i(r_1)\psi_j(r_2) \quad (1.34)$$

$$K_{ij} = \int\int d\, r_1 d\, r_2 \psi_i^*(r_1)\psi_j^*(r_2)\frac{1}{r_{12}}\psi_i(r_2)\psi_j(r_1) \quad (1.35)$$

Applying the variational principle to Equation 1.32, the spatial orbitals that minimize the energy E satisfy the equations

$$\hat{F}(r_1)\psi_i(r_1) = \varepsilon_i\psi_i(r_1) \qquad i = 1,2,\dots,N \quad (1.36)$$

where $\hat{\mathrm{F}}(r_1)$is the Fock operator

$$\hat{F}(r_1) = \hat{f}(r_1) + \sum_{j=1}^{N}[2\hat{J}_j(r_1) - \hat{K}_j(r_1)] \quad (1.37)$$

where

$$\hat{f}(r_1) = -\frac{1}{2}\nabla_1^2 - \sum_A \frac{Z_A}{r_{1A}} \quad (1.38)$$

$\hat{J}_j(r_1)$ is the Coulomb operator

$$\hat{J}_j(r_1)\psi_i(r_1) = \psi_i(r_1)\int d\, r_2 \psi_j^*(r_2)\frac{1}{r_{12}}\psi_j(r_2) \quad (1.39)$$

$\widehat{K}_j(r_1)$ is the exchange operator

$$\widehat{K}_j(r_1)\psi_i(r_1) = \psi_j(r_1)\int d\, r_2 \psi_j^*(r_2)\frac{1}{r_{12}}\psi_i(r_2) \quad (1.40)$$

An expression for the energy of the i^{th} molecular orbital can be obtain by multiplying Equation 1.40 from the left by $\psi_i^*(r_1)$ and integrating over r_1

$$\varepsilon_i = \int dr_1\, \psi_i^*(r_1)\hat{F}(r_1)\psi_i(r_1) \quad (1.41)$$

Applying the Fock operator to Equation 1.41, it becomes

$$\varepsilon_i = I_j \sum_{j=1}^{N}(2J_{ij} - K_{ij}) \quad (1.42)$$

Comparing with 1.32, we get

$$E = \sum_{i=1}^{N}(I_i + \varepsilon_i) \quad (1.43)$$

Clemens Roothaan suggested that the molecular orbitals can be expressed as linear combinations of basis functions

$$\psi = \sum_{v=1}^{K} c_v \phi_v \quad (1.44)$$

Thus, the Hartree-Fock-Roothaan Equations are

$$\sum_v F_{\mu v} c_v = \varepsilon \sum_v S_{\mu v} c_v \qquad \mu = 1,2,\ldots,K \quad (1.45)$$

where $F_{\mu v}$ is the Fock matrix Clements

$$F_{\mu v} = \int dr_1 \phi_{\mu}^{*}(r_1)\hat{F}(r_1)\phi_v(r_1) \quad (1.46)$$

and $S_{\mu v}$ is the overlap matrix elements

$$S_{\mu v} = \int dr_1 \phi_{\mu}^{*}(r_1)\phi_v(r_1) \quad (1.47)$$

The set of algebraic equations for the c_v in Equation 1.45 are the Hartree–Fock–Roothaan equations. They can be further written in matrix notation

$$\mathrm{Fc} = \varepsilon \mathrm{Sc} \quad (1.48)$$

where F and S are K × K matrices and c is a K × 1 column vector. This equation can be solved through a self-consistent procedure known as the self-consistent field (SCF) method.

Because HF uses a single Slater determinant to describe the system, as given in Equation 1.30, despite many successes of the HF method, there are two deficiencies of it. These deficiencies are the so-called non-dynamical and dynamical electron correlation, respectively.

$$E_{correlation} = E_0 - E_{HF} = E_{non-dynamical\ correlation} + E_{dnynamical\ correlation} \quad (1.49)$$

Where $E_{correlation}$ is the correlation energy as the difference between the ground state electronic energy and the HF energy, $E_{non-dynamica\ \ correlation}$ is the non-dynamical correlation, and $E_{dnynamical\ correlation}$ is the dynamical correlation.

The non-dynamical correlation relates to the use of a single Slater determinant to describe the system, which is particularly large for systems with near-degenerate energy levels. Such systems require several coefficient-weighted Slater determinants to describe. The dynamical correction relates to the difference between the instantaneous electron-electron interaction of the real system and the interaction of each electron in the mean field approximation of HF theory. The

sum of the two correlation terms is called correlation energy, which is defined as the difference between the ground state electronic energy and the HF energy.

The contributions of electron correlation energy are relatively small (~1%) compared to the total energy. However, large errors will be induced in properties calculations and reaction energies, if the correlation energy is not treated appropriately. Various approaches are developed to improve upon the HF method, which are the so-called post Hartree-Fock approaches.

In coupled cluster theory, an exponential ansatz of cluster operators is used for the many-electron wavefunction

$$|\Psi^{cc}\rangle = e^{\hat{T}}|\Phi^{HF}\rangle \quad (1.50)$$

where Φ^{HF} is a single Slater determinant, which is constructed from the HF one-electron orbitals. These orbitals best approximate the ground state energy of a many-electron system. Furthermore, $\hat{T}$ is the cluster operator, which is defined by

$$\hat{T} = \hat{T}_1 + \hat{T}_2 + \hat{T}_3 + \cdots \quad (1.51)$$

where $\hat{T}_1$ is the operator of all single excitations, $\hat{T}_2$ is the operator of all double excitations, and so on. In coupled cluster singles and doubles theory, the approximated cluster operator is truncated as

$$\hat{T} \approx \hat{T}_1 + \hat{T}_2 \quad (1.52)$$

Thus, the exponential operator $e^{\hat{T}}$ in equation 1.50 can be expanded as a Taylor series

$$e^{\hat{T}} = 1 + \hat{T}_1 + \hat{T}_2 + \frac{1}{2}\hat{T}_1^2 + \frac{1}{2}\hat{T}_1\hat{T}_2 + \frac{1}{2}\hat{T}_2\hat{T}_1 + \frac{1}{2}\hat{T}_2^2 + \cdots \quad (1.53)$$

The coupled cluster singles and doubles theory usually is not very accurate. Some forms of triples are needed for better accuracy. The triples in a perturbative manner with coupled cluster singles and doubles theory is referred to the coupled cluster singles and doubles and perturbatively included triples CCSD(T)[91] method. The CCSD(T) method is usually referred to as the golden

standard in quantum chemistry due to the error cancellations from perturbative triples. It can yield highly accurate reaction energies, transition state barriers and structures.[91] However, the scaling of CCSD is $O(N^6)$ and CCSD(T) is $O(N^7)$, where N is a relative measure of the size of the system. Which is too expensive for many of the systems in this thesis. In 2013, a new method called DLPNO-CCSD(T) method (domain based local pair natural orbital) was introduced.[92] In short, the DLPNO approximation employs localized occupied orbitals and obtains the correlation energy as a sum over electron pair correlation energies. The electron pairs with significant contributions are identified by the method and subsequently included in the correlation treatment. On the other hand, the pairs remaining enter the correlation energy are at the MP2 level or are just neglected. This strategy significantly reduces the cost of CCSD(T) calculations that is now comparable to some of the density functional theory (DFT) methods but with similar accuracy as the original CCSD(T).[93] In many cases of this thesis, DLPNO-CCSD(T) was used for getting better electronic energies, because the energy difference between extraction reactions of different ligands is usually very small.

1.3.7. Density Functional Theory

In this thesis, most of the calculations were carried out using density functional theory (DFT). It is the most popular method both in quantum chemistry and condensed matter physics, not only because of its accuracy, but also its efficiency. The many-body problem of N electrons depends on 3N spatial coordinates. In contrast, an electron density only depending on 3 spatial coordinates. Thus, DFT is much faster than the wavefunction methods such as HF and especially post-HF methods.

The Thomas-Fermi model[94] and Slater's X_α exchange functional[95, 96] are the predecessors of modern Density Functional Theory. The two fundamental Hohenberg-Kohn theorems[97] are the foundation stones of modern density functional theory. The first Hohenberg-Kohn theorem states that the external potential V(r) is a unique functional of the electron density ρ(r). The second one states that the ground state energy can be obtained variationally, which means that the density that minimizes the total energy is the exact ground state density. The Kohn-Sham (KS) equations are given by:

$$\widehat{H}_{ks}\phi_i \equiv \left[-\frac{1}{2}\nabla^2 + V_{\text{eff}}(r)\right]\phi_i(r) = \varepsilon_i\phi_i(r) \qquad (1.54)$$

where ϕ_i are the Kohn-Sham one-electron orbitals. Then the electron density can be written as

$$\rho(r) = \sum_{i=1}^{N}|\phi_i|^2 \qquad (1.55)$$

The $V_{\text{eff}}(r)$ in equation 1.54 is the effective potential

$$V_{\text{eff}}(r) = V(r) + \int \frac{\rho(r\prime)}{|r-r\prime|}dr' + V_{xc}(r) \qquad (1.56)$$

where $V(r)$ is external potential, $\rho(r')$ is the electron density, and $V_{xc}(r)$ is the exchange-correlation potential defined as

$$V_{xc}(r) = \frac{\delta E_{xc}[\rho]}{\delta\rho(r)} \qquad (1.57)$$

The exchange-correlation energy, E_{xc}, accounts for the difference between the true functional and the remaining terms. It contributes a small fraction to a system's total energy, but it is extremely crucial for accurate description of bonding. However, the exact exchange-correlation energy functional of DFT is unknown. Thus, different approximations have been developed to overcome this problem, see Figure 1.12. These include:

The local density approximation (LDA) indicates that the value of E_{xc} at some position r could be computed exclusively from the value of ρ at that position, i.e., the 'local' value of ρ. Systems including spin polarization, such as open-shell systems, must use the spin-polarized formalism, which is the local spin-density approximation (LSDA)

$$E_{xc}^{LSD}[n_{\uparrow}, n_{\downarrow}] = \int d^3r \; n \; \varepsilon_{xc}^{unif}(n_{\uparrow}, n_{\downarrow}) \tag{1.58}$$

Where $\varepsilon_{xc}^{unif}(n_{\uparrow}, n_{\downarrow})$ is the exchange-correlation energy per particle of an electron gas with uniform spin densities $n_{\uparrow}$ and $n_{\downarrow}$.

Generalized gradient approximation (GGA):

$$E_{xc}^{GGA}[n_{\uparrow}, n_{\downarrow}] = \int d^3r \; n \; \varepsilon_{xc}^{GGA}(n_{\uparrow}, n_{\downarrow}, \nabla n_{\uparrow}, \nabla n_{\downarrow}) \tag{1.59}$$

which introduces the density gradients $\nabla n_{\uparrow}$ and $\nabla n_{\downarrow}$.

Meta-GGA:

$$E_{xc}^{MGGA}[n_{\uparrow}, n_{\downarrow}] = \int d^3r \; n \; \varepsilon_{xc}^{MGGA}(n_{\uparrow}, n_{\downarrow}, \nabla n_{\uparrow}, \nabla n_{\downarrow}, \nabla^2 n_{\uparrow}, \nabla^2 n_{\downarrow}, \tau_{\uparrow}, \tau_{\downarrow}) \tag{1.60}$$

where $\nabla^2 n$ is the Laplacian of the density, and τ is the so-called kinetic energy density:

$$\tau_{\sigma}(r) = \frac{1}{2}\sum_{u}^{occ.} |\nabla \varphi_{i\sigma}(r)|^2 \tag{1.61}$$

Hyper-GGA:

$$E_{xc}^{HGGA}[n_{\uparrow}, n_{\downarrow}] = \int d^3r \; n \; \varepsilon_{xc}^{HGGA}(n_{\uparrow}, n_{\downarrow}, \nabla n_{\uparrow}, \nabla n_{\downarrow}, \nabla^2 n_{\uparrow}, \nabla^2 n_{\downarrow}, \tau_{\uparrow}, \tau_{\downarrow}, \varepsilon_{x\uparrow}, \varepsilon_{x\downarrow}) \tag{1.62}$$

where ε_x is the exact exchange energy density

$$\varepsilon_{x\sigma}(r) = \frac{1}{2}\int d^3r' \frac{n_x^{\sigma}(r,r')}{|r'-r|} = -\frac{1}{2n_{\sigma}(r)}\int d^3r' \frac{\left|\sum_i^{occ.} \phi_{i\sigma}^*(r)\phi_{i\sigma}(r')\right|^2}{|r'-r|} \tag{1.63}$$

The functionals including Hartree-Fock exchange are called hybrid GGA. For example, the most popular B3LYP functional is

$$E_{xc}^{B3LYP} = (1-a)E_x^{LSDA} + aE_x^{HF} + b\Delta E_x^{B} + (1-c)E_C^{LSDA} + cE_c^{LYP} \tag{1.64}$$

where a =0.20, b = 0.72, and c = 0.81. E_x^{LSDA} is the VWN local spin density approximation to the exchange and correlation.[98] E_x^{HF} is the Hartree–Fock exact exchange functional. E_x^B is the Becke 88 exchange functional.[99] E_c^{LYP} is the correlation functional of Lee, Yang and Parr. [100]

While the PBE0 functional is

$$E_{xc}^{PBE0} = \frac{1}{4}E_x^{HF} + \frac{3}{4}E_x^{PBE} + E_x^{PBE} \quad (1.65)$$

Recently, a novel class of 'double-hybrid' GGA functionals were suggested by Grimme,[101] which contain a fraction of nonlocal, orbital dependent correlation estimated at the level of second-order many-body perturbation theory (MBPT). MBPT is the usual second-order Møller-Plesset-type expression for the correlation energy. A simpler ansatz for double-hybrid GGA is

$$E_{xc}^{B2-P} = (1 - a_x)E_x^{GGA} + a_x E_x^{HF} + bE_c^{GGA} + cE_c^{PT2} \quad (1.66)$$

where a_x is the HF-exchange mixing parameter and b and c scale the contributions of GGA and perturbative correlation contributions, respectively. The term GGA denotes local exchange and correlation functionals consisting as usual of the LDA term with additional gradient corrections. The term E_c^{PT2} is the second-order Møller-Plesset-type expression which is evaluated with the Kohn-Sham orbitals with corresponding eigenvalues ϵ

$$E_c^{PT2} = \frac{1}{4}\sum_{ia}\sum_{jb}\frac{[(ia|jb) - (ib|ja)]^2}{\epsilon_i + \epsilon_j - \epsilon_a - \epsilon_b} \quad (1.67)$$

where the indices *ia* and *jb* represent single occupied-virtual replacements and the terms in brackets denote regular two-electron integrals over the KS orbitals.

The fifth rung of the ladder contains all the Kohn-Sham orbitals, both unoccupied and occupied (Figure 1.12). At this level, the adiabatic connection

$$E_{xc}[n_\uparrow, n_\downarrow] = \frac{1}{2}\int d^3r n(\boldsymbol{r}) \int d^3r' \int_0^1 d\lambda \frac{n_{xc}^{\lambda}([n_\uparrow, n_\downarrow]; \boldsymbol{r}, \boldsymbol{r'})}{|\boldsymbol{r'} - \boldsymbol{r}|} \quad (1.68)$$

leads to generalizations of the random phase approximation (RPA). Where $n(\boldsymbol{r})$ is the ground state density, $\lambda/|\mathbf{r'}-\mathbf{r}|$ is the strength of the electron-electron repulsions ($0 \leq \lambda \leq 1$), and $n_{xc}^{\lambda}([n_{\uparrow}, n_{\downarrow}]; \boldsymbol{r}, \boldsymbol{r'})$ is the density at **r'** of the exchange-correlation hole surrounding an electron at **r**,

$$n_{xc}^{\lambda} = n_x + n_c^{\lambda} \qquad (1.69)$$

where n_c is the correlation hole density and n_x is the exchange hole density which is independent of λ.

Jacob's ladder of DFT approximations is illustrated in Figure 1.12.[102-104] Each rung in Figure 1.12 incorporates the design elements from lower rungs. For example, PBE[105, 106] and BLYP[100, 107] belong to the family of GGA functionals, TPSS[108] and M06L[109] are meta-GGAs, and PBE0[110-112] and B3LYP[99, 100] are hybrid functionals belonging to the class of hyper-GGA. The lower rungs usually are not as accurate as the higher ones. On the other hand, they are easier to understand and are not as expensive as the methods on the higher rungs. Thus, the considerations of balancing accuracy and efficiency are needed for choosing the appropriate approximation.

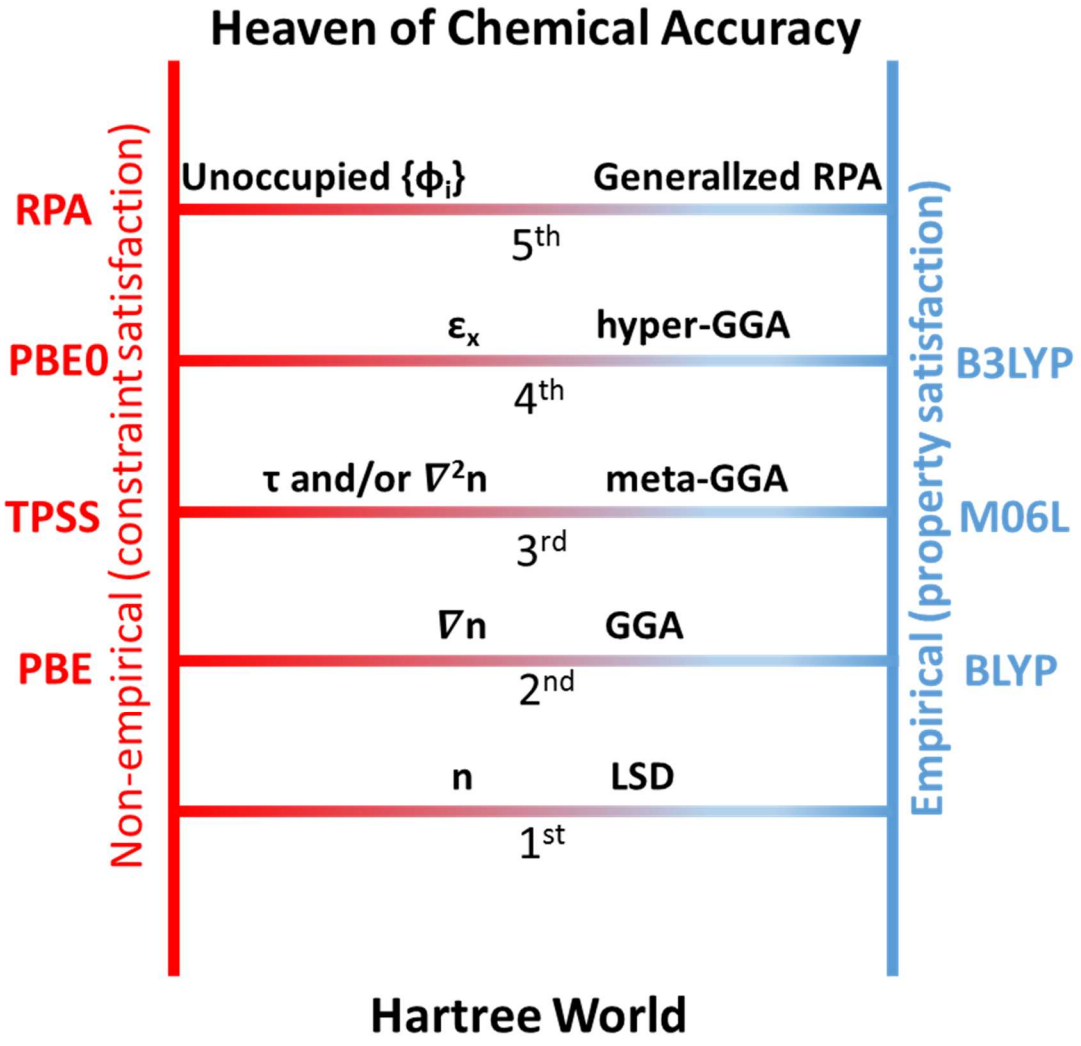

Figure 1.12 Jacob's ladder of density functional approximations to the exchange-correlation energy proposed by J. P. Perdew.[103] Some examples of actual approximate XC functionals are included.

1.3.8. Electronic Basis Sets

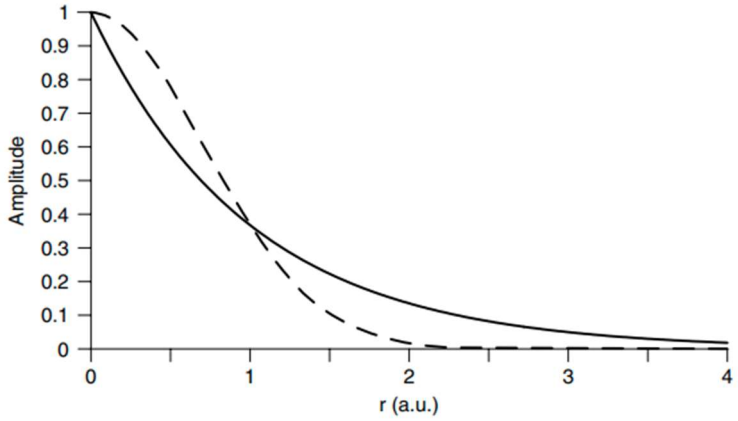

Figure 1.13 Behavior of e^x where x = r (solid line, STO) and $x = r^2$ (dashed line, GTO) (Figure adapted from reference 65)

A basis set in quantum chemistry, by definition, is the set of mathematical functions which are used to construct a wave function. In the HF theory, a linear combination of basis set functions is used to express the molecular orbitals. The HF limit has been reached when a complete basis set is used. However, it is impossible to use an infinite basis set in real applications. Thus, balancing the efficiency and accuracy when choosing a basis set is very important.

The Slater-type orbitals (STOs) and Gaussian-type orbitals (GTOs) are two principal types of basis functions that are used in modern quantum chemistry.

For the hydrogen atom, STOs use the exponentially decaying electronic distribution ($e^{-\xi r}$):

$$\varphi(r,\theta,\varphi;\ \xi,n,l,m) = \frac{(2\xi)^{n+\frac{1}{2}}}{[(2n)!]^{\frac{1}{2}}} r^{n-1} e^{-\xi r} Y_l^m(\theta,\varphi) \qquad (1.70)$$

where ξ is an exponent that can be chosen according to a simple set of rules developed by Slater,[113] n is the principal quantum number for the orbital, Y^l_m (θ,φ) is a spherical harmonic function where l and m are angular momentum quantum numbers.

The advantage of STOs is that they can describe the cusp at the nucleus correctly as Figure 1.13 shows. On the other hand, the integrals of the STOs needed in the SCF procedure have to be calculated numerically, which reduces the speed of computations. To address this problem, Boys, in 1950, suggested to change the radial decay e^{-r} of the STOs in equation 1.70 to e^{-r^2}. [114] Thus, the Atomic-Orbital-like basis function can be rewritten in the form of a Gaussian function:

$$\varphi(\mathrm{x,y,z};\alpha,\mathrm{i,j,k}) = (\frac{2\alpha}{\pi})^{3/4}[\frac{(8\alpha)^{i+j+k}i!j!k!}{(2i)!(2j)!(2k)!}]^{1/2}x^i y^j z^k e^{-\alpha(x^2+y^2+z^2)} \qquad (1.71)$$

where α is an exponent controlling the width of the GTO; i, j and k are non-negative integers which define the nature of the orbital in a Cartesian sense.

The so-called 'Gaussian Product Theorem' states that the product of two GTOs centered on two different atoms can be presented as a finite sum of Gaussians centered on a point along the line across these two atoms. Thus, a finite sum of two-center integrals can be used to reduce four-center integrals. In a similar way, these two-center integrals can be further reduced to one-center integrals. Thus, calculations using GTOs will be much faster than using STOs. However, as Figure 1.13 shows, GTOs decay much faster than STOs in the long range and give the wrong cusp, which brings some errors.

To combine the computational efficiency of GTO$_S$ and the proper shape of STOs, the so-called contracted Gaussian functions were developed.[115] Contracted Gaussian functions use several GTOs within one basis function to approximate STOs:

$$\Phi(x,y,z;\{\alpha\},I,j,k) = \sum_{a=1}^{M} c_a \phi(x,y,z;\alpha_a,i,j,k) \qquad (1.72)$$

where M is the number of Gaussians in the linear combination. The shape of the basis function is controlled by the coefficients c_α.

Most quantum chemistry programs nowadays are using GTOs for efficiency, just a few are still using STOs, such as ADF,[116] which was frequently used in this thesis.

1.4. Solvation Effects

The effect of solvent can be significant for actinide complexes. As mentioned before, the oxidation state of the predominant compounds depending on the redox conditions in solution. For example, the meta-stable U(V) complexes can be oxidized thus obstructing the isolation and characterization of them in aqueous solution.[39, 117-120] Also, chemical reactions are usually in solvent, which has significant effects on reaction energies and geometrical structures in some cases.

There are two choices for describing the effect of the solvent environment computationally, which are explicit and implicit/continuum solvation models. The explicit solvation model adds a number of solvent molecules around the solute molecule of interest. However, when a huge number of solvent molecules is included, the computational cost of the explicit approach will become extremely high due to the size of the (super-)molecule. On the other hand, the interactions between those solvent and solute molecules are complicated. Thus, after adding solvent molecules, the search for global minima becomes very difficult. Instead, an implicit/continuum model uses a number of the degrees of freedom of the constituent particles to simulate solvation effects in a continuous way by a distribution function.[121] These models were originally developed by Born,[122] Onsager,[123] and Kirkwood[124] over 90 years ago. There are two widely used implicit models: the polarized continuum model (PCM)[121, 125] and the conductor -like screening model (COSMO).[126-129] There are two types of PCMs: (1) The dielectric PCM (D-PCM), which uses a polarizable continuum. (2) Another is the conductor-like PCM (C-PCM) which is similar to COSMO in that the continuum is conductor-like. COSMO assumes that the surrounding medium can be well descripted as a conductor. The problem for continuum models is that the specific interactions

between solute and solvent molecules have been neglected.[130] However, when solvent molecules are around the solute, their performances are different from the bulk, which is known as cybotactic behavior. This problem can be fixed by including a number of explicit solvent molecules in the first solvation shell. Previous experimental and theoretical studies suggest that, for the actinyl ions, the first solvation shell is crucial.[131] Thus, the actinyl ions in this thesis include the first solvation shell in addition to the COSMO solvation model.[132]

There are several challenges in computationally studying the effects of temperature and pressure without dynamic simulations. The atomic nuclei are considered to be fixed by the Born–Oppenheimer approximation. Thus, the optimized structures are not affected by temperature in the calculation. In gas-phase, temperature only affects the average structure of compounds. The average structure will be the same as the structure of the local minimum on the potential energy surface under the harmonic oscillator approximation. However, solvation has a strong effect on molecular structures. The dependence of the static dielectric constant of water on temperature and pressure was measured in previous studies. [133, 134] Thus, the change of dielectric constant can be used for investigating the behavior of the aqueous AnO_2-Cl system under high temperature and pressure in Chapter 5.

The standard-state free energy of solvation, that is the standard-state free energy of transfer from the gas phase to the condensed phase, can be written as

$$\Delta G_S^o = \Delta G_{ENP} + G_{CDS} + \Delta G_{conc}^o \qquad (1.73)$$

The ENP subscript in equation 1.73 denotes the electronic (E), nuclear (N), and polarization (P) components of the free energy. The CDS subscript is the corresponding term in the free energy change associated with solvent cavitation(C), changes in dispersion (D) energy, and possible

changes in local solvent structure (S). The final term ΔG^{o}_{conc} is the energy from the concentration change between the gas-phase standard state and the liquid-phase standard state.

The solvation free energy is the free energy for molecules that are solvated by going from gas phase to solution. Because the standard states are different, another standard state correction per net change in the number of molecules needs to be considered when calculating the reactions in solvent:

$$\Delta G^{*}_{gas\rightarrow liq} = \Delta G^{o}_{gas\rightarrow liq} + \Delta G^{o\rightarrow *} \qquad (1.74)$$

where the superscripts "*" and "o" denote that the quantities are at a standard state of 1 mol/L and 1 atm, respectively, which are corresponding to the liquid-phase standard state and the gas-phase standard state. $\Delta G^{o\rightarrow *}$ is ΔG^{o}_{conc} in equation 1.73, where $\Delta G^{o\rightarrow *}$ = RTln(24.46). This would be 1.89 kcal/mol at room temperature.

1.5. Calculating Thermochemical Properties

The vibrational frequencies predict by quantum-chemical programs usually apply the harmonic approximation. Contributions to the thermodynamic properties are from translational, electronic, rotational, and vibrational degrees of freedom. One of the most important approximations is to assume that all the particles are non-interacting particles or a so-called ideal gas. Thus, the contributes from pressure are only applied to the translational entropy and because of the Born-Oppenheimer approximation there is no effect on geometry structures.

A pressure correction[135] was introduced in the solvent environment to remove the extra freedom the models introduce in the molecules prior to complexation, which is not the case in solution. However, the solvation model is wildly used in the calculation in this thesis. A

hypothetical ideal gas at concentrations corresponding to pressure at 1 atm at standard state is used even when the solvation model is applied. This is inappropriate in solution. Thus, the molecules written as reactants in the reaction equation have more freedom. To obtain applicable results, the concentration of liquid water must be calculated. The pressure parameter can be determined by

$$p=\rho_w RT/M \quad (1.75)$$

where ρ_w is the density of water at different conditions, R is gas constant, T is temperature, and M is the molar mass of water. The experimental density of liquid water is 997.02 kg/m^3 at standard state, which required $p = 1354$ atm. This method has previously been successfully applied to actinide systems.[136-139] In Chapter 5, the densities of liquid water at the standard state (1atm/25℃), 200atm/350℃ and 250atm/500℃ are 997 kg/m^3, 572.8 kg/m^3, and 300 kg/m^3, respectively. Thus, the pressure corrections for each condition are 1354 atm, 1626 atm and 1056 atm, respectively.

1.6. Bonding Analysis

Chemical bonding theory can be traced back to the work by Lewis from 1916. [140] In the Lewis picture, the electrons from atoms are grouped into lone pairs and bonding pairs that form molecules. This picture has been expanded over time especially after quantum mechanics was developed, for example, valence bond theory[141, 142] and molecular orbital theory[52, 143]. The foundation of chemistry is quantum physics; however, comparing to the traditional chemical concepts, quantum mechanics offers a very different picture for electrons, atoms and molecules. The traditional concepts for chemical bonding are not reconciled with quantum mechanical models easily.[144] The wavefunction yielded from solving the Schrödinger Equation contains all the

information of the system. The success of an investigation of a certain chemical problem is often not just in the calculations but lies in the analysis of wavefunction to extract useful information. There are many useful schemes that were developed for analyses of the chemical bonds. These methods can be roughly divided into three categories.[145]

The first group focuses on the charge rearrangement from the pairing of electron when chemical bonds are formed from atoms. Some of the schemes and concepts under this definition are Bond Order Orbitals,[146, 147] Natural Bond Orbitals (NBO), [148-152] Quantum Theory of Atoms in Molecules (QTAIM), [153, 154] the Electron Localization Function (ELF), [155] the Laplacian of the electron density ($\nabla^2\rho$),[153, 156] the deformation density ($\Delta\rho$), [157] and population schemes.[158, 159]

The second category focusses on chemically meaningful contributions by decomposition of the bond energy. The most popular decomposition schemes include the Kitaura−Morokuma method,[160] and the Extended Transition State (ETS) scheme.[70, 161-166]

The third group describes the chemical bond in terms of bond-orders or bond multiplicity indices. Examples include the Wiberg [167] and Mayer [168] bond orders, as well as those of Nalewajski, Köster, and Mrozek. [169-175]

The combination of Extended Transition State (ETS) method and Natural Orbitals for Chemical Valence (NOCV) scheme, ETS-NOCV,[145] links the concepts of bond-order, bond-orbitals, and charge rearrangement with the deformation density and energy decomposition together. This ETS-NOCV method was found to be very useful in this thesis.

The Multiwfn code [176], as a free, open-source and high-efficient program, is a powerful tool for wavefunction analysis, which is widely used in this thesis for bonding analysis.

1.6.1. Topological Analysis

The topology analysis technique in quantum chemistry was first proposed by Richard F.W. Bader and his colleagues. They developed the QTAIM in the 1990s. [153, 154] By applying a topological analysis to the electron density distribution, QTAIM offers a unique approach to define and think about chemical bonding. QTAIM relies on the theory of gradient dynamical systems. The 3D molecular space is partitioned into topological basins via the properties of the electron density gradient field.[177] In topology analysis, points in space where the first derivatives of the density vanish are called critical points (CPs)

$$\nabla\rho = i\frac{dp}{dx} + j\frac{dp}{dy} + k\frac{dp}{dz} \longrightarrow \begin{cases} = \vec{0} & (at\ critical\ points\ or\ \infty) \\ Generally\ \neq \vec{0} & (at\ all\ other\ points) \end{cases} \quad (1.76)$$

CPs are classified according to their rank ω and signature σ and are symbolized by (ω,σ). The rank ω is the number of non-zero curvatures of ρ at the critical point via Hessian matrix. The signature is the algebraic sum of the signs of the curvatures. Thus, CPs can be classified into four types: [153, 154]

1. (3,-3): Three negative curvatures, which means ρ is a local maximum. (3,-3) is also called nuclear critical point (NCP) because the positions of (3,-3) are nearly identical to nuclear positions,
2. (3,-1): Two negative curvatures, which is the second-order saddle point. The (3,-1) are usually locals between atomic pairs, thus (3,-1) is called bond critical point (BCP).
3. (3,+1): Only one negative curvature, which is a first-order saddle point. (3,+1) is referred to as ring critical point (RCP) because it often appears in the center of ring system.

4. (3,+3): None of the curvatures is negative, ρ is a local minimum. (3,+3) generally appears in the center of a cage system, hence is named as cage critical point (CCP).

The BCPs are of interest for bonding analysis because they are closely related to the nature of interactions between atoms. The properties of real space functions at BCPs are very important to analyze the chemical bonds. For example, the value of ρ at BCP is related to bonding strength,[178] while the sign of $\nabla^2\rho(r)$ at BCP is used for identifying bonding types for analogous bonds.[179] A rough criterion is that when ρ at BCP is larger than 0.20 e $Bohr^{-3}$, it is shared-shell interactions. In other words, it is a covalent bond. When ρ at BCP is smaller than 0.10 e $Bohr^{-3}$, it belongs to closed-shell interactions, for example, ionic interaction, van der Waals interaction, and hydrogen bonding. By applying indicators that rely on the local expression of the virial theorem, a sharper classification can be achieved: [153]

$$\frac{1}{4}\nabla^2\rho(r) = 2G(r) + V(r) \tag{1.77}$$

where $\nabla^2\rho(r)$ is the Laplacian of the density, $G(r)$ is the positive definite kinetic energy density and $V(r)$ is the potential energy density having a negative value. Thus, the sign of $\nabla^2\rho(r)$ depends on the relative magnitude of $G(r)$ and $V(r)$. Therefore, the ratio $|V_b|/2G_b$ can be set. When the ratio is smaller than 1, the kinetic energy density $G(r)$ is the leading term, and no covalency is expected. This type of interactions is defined as *pure* closed-shell (CS) interactions, for example, pure ionic or van der Waals bonding. When $|V_b|/G_b > 1$, there is some sharing of electrons. This case can be classified as *regular* CS. [180] The bonding schemes are illustrated in Scheme 2.[181]

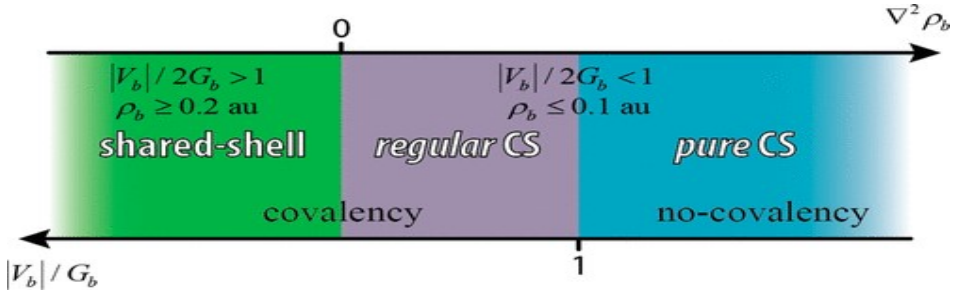

Scheme 2. Typical QTAIM Classification of Interactions (Figure reproduced from reference 181)

However, this criterion does not always work. For example, the BCP can be in a wrong position for certain bonds. [182] Moreover, this criterion is not sufficient for heavy atoms[183, 184] and multiple bonds.[185] The Laplacian of the electron density is always positive at the BCP for multiple bonds.[185, 186] Thus, other indicators for covalency must be used instead. The delocalization index, DI(A,B) or the energy density H_b can be used as quantitative indicators for comparing the degree of covalency of bonds. For example, the more negative the value of H_b the more covalent the bond. Corresponding discussions can be found in Chapters 2 and 3. After all, it is very difficult to describe the whole picture of chemical bonding just using a single point in space, for multiple bonds for example. It would be a wise choice to examine the properties like the Laplacian of the electron density in 3d space. What is more, the relationship between chemistry concepts with topological basins of the electron density is still arguable.

This topological technique has also been extended to other real space functions, for example, the electron localization function (ELF). In a certain region, the larger the electron localization, the more likely the electron motion is to be confined within it. When the electrons are completely localized, they can't be found outside. Thus, the electrons and electron pairs are fixed. Bader found that large electron localization in the regions must have large magnitudes of Fermi hole integration.[153] [187] However, this is difficult to be studied visually in the three-dimensional

world due to it being a six-dimension function. Becke and Edgecombe suggested ELF in 1990 after they found that there is a direct correlation between spherically averaged like-spin conditional pair probability and the Fermi hole.[155]

$\rho_{2,cond}^{\sigma\sigma}$ in HF can be spherically averaged and then expanded as a Taylor series [188]

$$\rho_{2,cond}^{\sigma\sigma}(r,s) = \frac{1}{3}\left[\sum_{i\in\sigma}^{occ}|\nabla\Psi_i(r)|^2 - \frac{1}{4}\frac{|\nabla\rho_\sigma(r)|^2}{\rho_\sigma(r)}\right]s^2 + \cdots \quad (1.78)$$

where the *r* is reference position, *s* is a spherical radius, Ψ is a spin orbital, and the *occ* superscript means that only occupied orbitals are included. The zeroth order term is 0 because of the Pauli exclusion principle. The first order term depends on the gradient of the Fermi hole at *r*. It is eliminated because the Fermi hole at *r* is a maximum point. Thus, only second and higher orders are left. The term in square brackets corresponds the curvature of $\rho_{2,cond}^{\sigma\sigma}$ at *r* and can be written as D_σ. Thus, the real space function D_σ is an indicator to measure the localization of electrons. The larger the value of D_σ, the lower the amount of electron localization, and vice versa.

The generalized ELF can be defined as

$$ELF = \frac{1}{1+\chi^2} \quad (1.79)$$

where

$$\chi = \frac{\left(\frac{1}{2}\right)(D_\alpha + D_\beta)}{\left(\frac{1}{2}\right)\left(D_\alpha^0 + D_\beta^0\right)} \quad (1.80)$$

where D^o is the D with the same density at *r* in the non-interacting homogeneous electron gas model. Because this definition only works for HF, Savin et al. extend it to KS-DFT.[189, 190] The difference is in the χ term

$$\chi = \frac{\tau_r - \tau_w}{\tau_h} \tag{1.81}$$

where

$$\tau_r = \frac{1}{2}\sum_i^{occ}|\nabla\Psi_i|^2 = \frac{1}{8}\sum_i|\nabla\rho_i|^2/\rho_i \tag{1.82}$$

$$\tau_w = \frac{1}{8}|\nabla\rho_i|^2/\rho_i \tag{1.83}$$

$$\tau_h = \frac{3}{10}(3\pi^2)^{2/3}\rho^{5/3} \tag{1.84}$$

where the τ_r is positive-definite kinetic energy density, the τ_w is the kinetic energy density in the Thomas-Fermi non-interacting homogeneous electron gas model, and the τ_h is the Von Weizsäcker kinetic energy density.

The first topology analysis application of ELF for small molecules was given by Silvi and Savin.[189] Since then, the method has been widely used in different fields of quantum chemistry research. The electron localization function (ELF) is a useful tool for studying the electronic structure, such as the covalency in chemical bonding.

1.6.2. ETS-NOCV Analysis

Assuming that a molecule was formed from fragments, the interactions that constitute a chemical bond between fragments can be defined as

$$\Delta E_{bond} = \Delta E_{strain} + \Delta E_{int} \tag{1.85}$$

where ΔE_{bond} is the total bonding energy. ΔE_{strain} is the strain or preparation energy. It represents the energy required for distorting separated fragments from their isolated equilibrium

geometry to the geometry structure they will take up in the final product. ΔE_{int} is the interaction energy between the fragments in the combined complex.

ΔE_{int} can be further decomposed into a number of chemically meaningful components

$$\Delta E_{int} = \Delta E_{elstat} + \Delta E_{Pauli} + \Delta E_{oi} + \Delta E_{disp} \quad (1.86)$$

where ΔE_{elstat} corresponds to the classical electrostatic interaction between the distorted fragments in the final molecule. ΔE_{Pauli} refer to the repulsive Pauli interaction between occupied orbitals on the fragments in the combined molecule, which is positive and destabilizing. The ΔE_{elstat} and ΔE_{Pauli} usually combine into the steric interaction ΔE_{steric}.[162, 163] The ΔE_{steric} corresponds to the total interaction energy between the fragments alone by their occupied orbitals according to the wavefunction of the final molecule without any involvement of virtual orbitals. On the other hand, ΔE_{oi} accounts for the interactions between the occupied molecular orbitals of one fragment and the unoccupied molecular orbitals of the other fragment, as well as mixing of occupied and virtual orbitals within the same fragment, which is the so-called inner-fragment polarization. The last term ΔE_{disp} represents the dispersion interaction between fragments, which is usually obtained from Grimme's dispersion correction[191] in DFT calculations.

The NOCV approach has been derived from the Nalewajski-Mrozek valence theory that diagonalizes the deformation density matrix.[173, 175] Each NOCV ψ_i is defined as an eigenvector of the deformation density matrix in the basis of the fragment orbitals

$$\Delta P \Psi_i = v_i \Psi_i \quad (1.87)$$

Thus, in the NOCV representation, the deformation density $\Delta\rho$ can be expressed as a sum of pairs of complementary eigenfunctions (Ψ_{-k}, Ψ_k) corresponding to eigenvalues ν_k and $-\nu_k$ with the same absolute value but opposite signs:[145, 173-175]

$$\Delta P(r) = \sum \Delta\rho_k(r) = \sum \nu_k[-\Psi_{-k}^2(r) + \Psi_k^2(r)] \quad (1.88)$$

where *k* goes over the NOCV pairs.

However, the NOCV scheme does not provide information about the energetics related to the charge rearrangement, while ETS does. Combine these two methods provides a compact analysis tool for the chemical bond. In this way, orbitals (NOCVs) can describe the charge rearrangement and the corresponding energy contributions from the orbitals to the chemical bond. The orbital interaction term ΔE_{oi} in equation 1.86 is expressed in terms of NOCVs as

$$\Delta E_{oi} = \sum \Delta E_k^{oi} = \sum \nu_k(-F_{-k}^{TS} + F_k^{TS}) \quad (1.89)$$

where the diagonal transition-state Kohn-Sham matrix elements $-F_{-k}^{TS}$ and F_k^{TS} are corresponding to NOCVs with eigenvalues $-\nu_k$ and ν_k, respectively. There are two advantages of this expression. First, usually, only a few complementary NOCV pairs have significant contributions to the total ΔE_{oi}. Second, not only can each $\Delta\rho_k(r)$ be visualized but also there is a well-defined corresponding bonding energy contribution ΔE_{oi} to it.

Figure 1.14 visualizes the ETS-NOCV analysis of ΔE_{oi} in equations 1.86 and 1.89 for C-C σ bonding of C_2H_6 from $H_3C\uparrow$ and $\downarrow CH_3$ radical fragments. The two complementary NOCVs responsible for the σ-transfer of density from A to B are shown as $(\psi_{-1}^{\alpha}, \psi_1^{\alpha})$ in Figure 1.14(a). They correspond to donation from the occupied SOMO of A to the empty orbital of B. Similarly, Figure 1.14(b) shows the NOCVs for the σ-transfer of density from B to A. The σ-deformation

density is shown in Figure 1.14(c). The corresponding orbital stabilization energy ΔE_{oi} is −86.7 kcal/mol. Finally, in Figure 1.14(d), the σ-orbital interaction energy associated with the formation of the σ-bond is clearly represented for the term $\Delta E_{oi}$of σ bond.

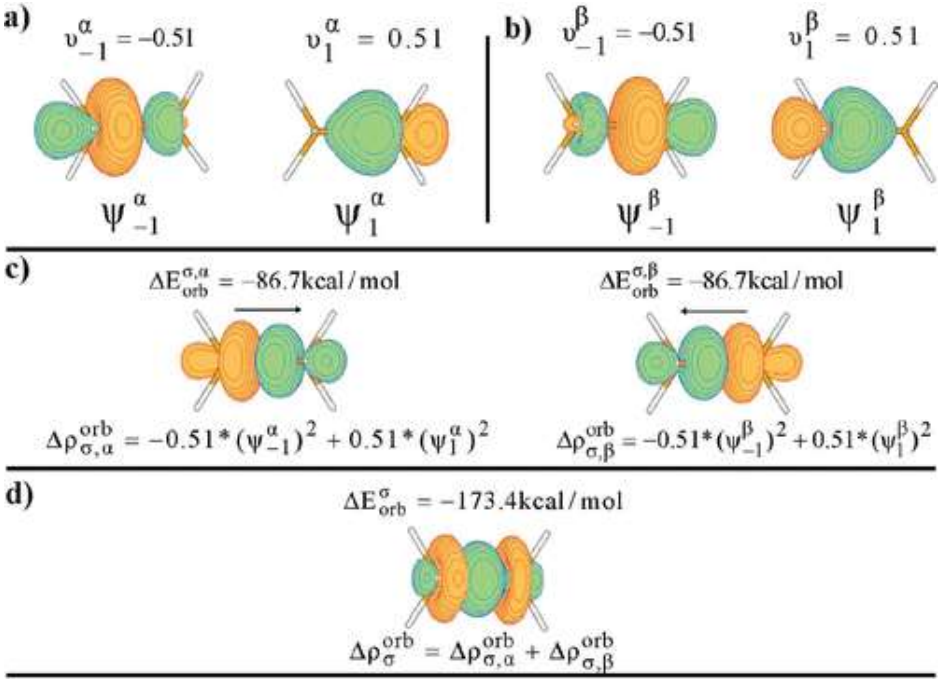

Figure 1.14. (a) Contours of complementary NOVCs ($\psi_{-1}^{\alpha},\psi_{+1}^{\alpha}$) representing donation from Me_A (left) to Me_B (right) and corresponding eigenvalues ($\upsilon_{-1}^{\alpha},\upsilon_{+1}^{\alpha}$) in C_2H_6. The numerically smallest contour values are ±0.1 a.u. (b) Contours of complementary NOVC's ($\psi_{-1}^{\beta},\psi_{+1}^{\beta}$) representing donation from Me_B (right) to Me_A (left) and corresponding eigenvalues ($\upsilon_{-1}^{\beta},\upsilon_{+1}^{\beta}$) in C_2H_6. The numerically smallest contour values are ±0.1 a.u. (c) Contours of sigma donation ($\Delta\rho_{\sigma,\alpha}^{oi}$) from Me_A to Me_B (left) and sigma donation ($\Delta\rho_{\sigma,\beta}^{oi}$) from Me_B to Me_A (right). The smallest contour values are ±0.0 a.u. The corresponding orbital stabilization energies are $\Delta E_{oi}^{\sigma,\alpha} = \Delta E_{oi}^{\sigma,\beta} =$ −86.7 kcal/mol. (d) Total sigma donation $\Delta\rho_{\sigma}^{oi} = \Delta,\rho_{\sigma,\alpha}^{oi} + \Delta\rho_{\sigma,\beta}^{oi}$ and corresponding stabilization energies $\Delta E_{oi}^{\sigma} = \Delta E_{oi}^{\sigma,\alpha} + \Delta E_{oi}^{\sigma,\beta} = -173.4$ kcal/mol. The smallest contour values are ±0.01 a.u. (Figure and figure caption taken from reference 145)

1.6.3. Adaptive Natural Density Partitioning (AdNDP) Analysis

The Lewis approach of the localized bonding was extended to three-center two-electron (3c-2e) bonds in addition to lone-pairs (LP) and two-center two-electron (2c-2e) bonds with the development of the chemical bonding theory for boron hydrides.[192] This description can consistently be extend to larger localized and delocalized system for multi-center bonds. The procedure of obtaining such a description of chemical bonding is defined as adaptive natural density partitioning (AdNDP), as introduced by Boldyrev et al. [193] The AdNDP can be treated as a generalization of the NBO analysis by Weinhold[152] NBO analysis is able to recover up to 3-centers 2-electrons (3c-2e) orbitals from the density matrix, while the AdNDP can generate multi-center orbitals. The basic idea of AdNDP is very similar to NBO analysis, that is, constructing then diagonalizing a proper sub-block of the density matrix in a natural atomic orbital (NAO) basis. The density matrix P is represented in block form as

$$\boldsymbol{P} = \begin{vmatrix} \boldsymbol{P}_{11} & \boldsymbol{P}_{12} & \cdots & \boldsymbol{P}_{1N} \\ \boldsymbol{P}_{21} & \boldsymbol{P}_{22} & \cdots & \boldsymbol{P}_{2N} \\ \cdots & \cdots & \cdots & \cdots \\ \boldsymbol{P}_{i1} & \boldsymbol{P}_{i2} & \cdots & \boldsymbol{P}_{iN} \\ \cdots & \cdots & \cdots & \cdots \\ \boldsymbol{P}_{N1} & \boldsymbol{P}_{N2} & \cdots & \boldsymbol{P}_{NN} \end{vmatrix} \tag{1.90}$$

where block $\boldsymbol{P}_{jj}$ corresponds to the jth atomic center.

After diagonalizing the density matrix sub-blocks, if one or more eigenvalues exceeds the predefined threshold, which is commonly set to close to 2.0 for a closed shell system, then the corresponding orbitals will be candidate n-centers 2-electrons (nc-2e) bonds.

For example, 2×2 sub-blocks of the form

$$P^{(ij)} = \begin{bmatrix} P_{ii} & P_{ij} \\ P_{ji} & P_{jj} \end{bmatrix} \tag{1.91}$$

can reveal 2c-2e bonds between centers *i* and *j*, when the eigenvectors have eigenvalues close to 2.0. And so on for higher numbers of centers. Thus, the AdNDP achieves a seamless description of systems featuring both localized and delocalized bonding without needing to invoke the concept of resonance.

However, the "Natural Orbital"-based methods intrinsically depend on the threshold values. Unlike NBO that can operate in a "black-box" manner that allows for changing thresholds without the user's participation, AdNDP requires explicit specification of the thresholds from the user's chemical intuition. Inappropriate thresholds will lead to an amount of accepted bonds exceeding the amount of valence electron pairs. The analysis cannot be successfully accomplished in this case. This also means that different AdNDP patterns can be obtained from the search process carried out by different people. The general recommendations for the AdNDP analysis search process given by Lu are: [176, 194]

1. The final remaining electron density should be as less as possible.
2. The occupation numbers of each AdNDP orbital should be as close to 2.0 (or 1.0 for open shell system) as possible.
3. The number of atom centers of each AdNDP orbital should be as low as possible.
4. The AdNDP orbitals generated should be consistent with molecular symmetry.

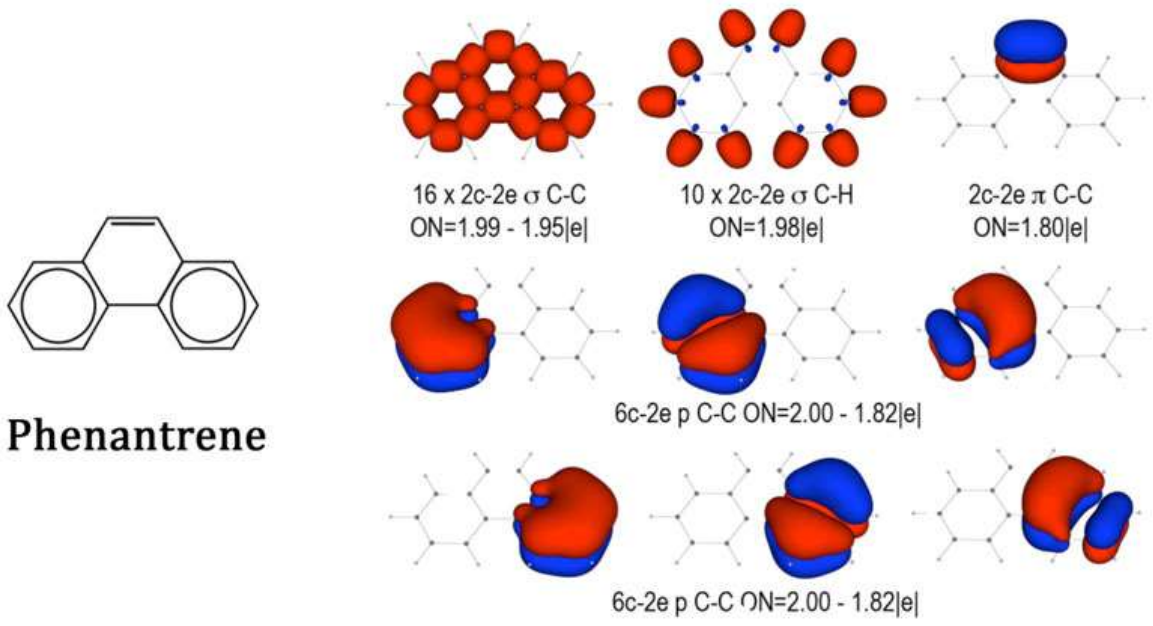

Figure 1.15. AdNDP analysis for phenanthrene ($C_{14}H_{10}$) (Figure reproduced from reference 195)

The AdNDP analysis has had many successes in different systems, for example, all-boron clusters,[193] CB_6^{2-} and C_2B^{5-} clusters,[196] a set of typical aromatic organic,[195] and gold clusters.[163] Figure 1.15 shows the AdNDP analysis for phenanthrene. As a classic π-aromatic compound phenanthrene has 14 π electrons. The bonding picture revealed in Figure 1.15 is consistent with generally accepted Clar's structure, and also consistent with nuclear independent chemical shifts representation. There are 16 C-C σ bonds and 10 2c-2e C-H σ bonds. One 2c-2e C-C π bond with contributions from the two upper carbon atoms of the central six-atomic ring is found, which revealed the difference in the aromaticity of the three rings. Finally, for the two peripheral six membered rings, there are six 6c-2e C-C π bonds for each ring. In chapter 4, the AdNDP analysis is carried out for investigating the BTP ligand and its derivatives, which are also aromatic systems.

1.7. Organization of this Thesis

This thesis is written in a sandwich style agglomeration of several manuscripts published or submitted in peer-reviewed scientific journals as well as manuscripts that are in preparation during the course of the doctoral program. The overall aim of this thesis is further understanding of the bonding in actinide chemistry by using computational methods. In each chapter, particular questions regarding the structure and properties of actinide complexes are answered. John People [65, 197] has introduced the concept of the "model chemistry", Figure 1.16a. It gives an approximate quantum-chemical method on one axis and the basis set on the other. Schreckenbach and Shamov[198] proposed to add two new axes, one for "relativity" and another for "solvation". The former one is the approximate relativistic method, and the later one is the model used to account for the bulk solvent or, more generally, for condensed-phase effects. This is shown schematically in Figure 1.16. The research in this work is basically following the arrows in the schematic representation in Figure 1.16. For "relativity", we are sticking to the ZORA method as, from the previous experience, the structural and electronic properties as well as the chemistry of actinide species are predicted by using ZORA at a sufficiently accurate level. On the other hand, a lot of tools are not implemented for higher levels of relativity calculations yet, such as spin-orbit ZORA. For the "solvation" axis, the actinides species are calculated from gas phase (Chapter 2) to aqueous phase (Chapters 3 and 4) and even to aqueous phase at high pressure and temperature (Chapter 5). In Chapter 6, due to the difficulty of the calculations, continuum solvation models were not used, but explicit water molecules were included for the first solvation shell of uranyl ions. For the "model chemistry", various methods at different levels of theory were applied throughout the projects, which range from pure GGA to Hybrid GGA and even post-HF methods such as CCSD(T). The high-accuracy calculations are needed as the energies in exchange reaction usually

are just a couple of kcals per mol. Also, a lot of bonding analysis methods introduced in Chapter 1 are tested in this thesis to understand and explain the actinide chemistry. The logic behind these projects is that: The theoretical tools were tested and verified by experiment in Chapter 2. Then the tested theoretical tools guided the theoretically led projects in the later chapters. Meanwhile, some new tools are also examined both theoretically and experimentally.

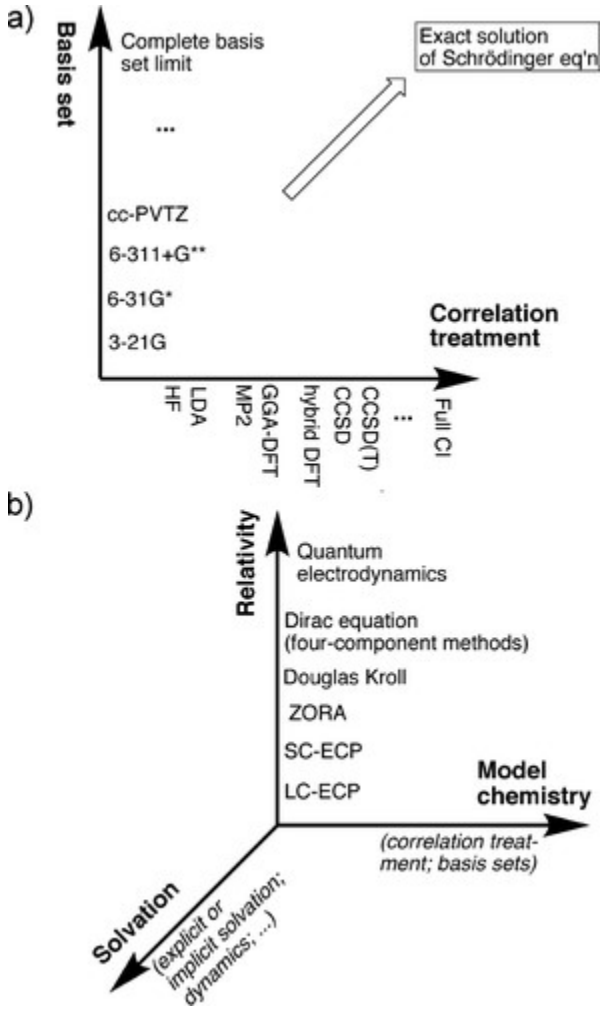

Figure 1.16. Schematic representation of (a) model chemistries according to Pople and (b) three levels of approximation required in computational actinide chemistry (Figure reproduced from reference 198)

In Chapter 1, a brief introduction to the background of actinide chemistry, target complexes, and the computational methods and tools used in this thesis are presented. The projects in this thesis are usually carried out both theoretically and experimentally. The theoretical calculations and analysis were performed exclusively by me. Chapter 2 contain the investigation of actinide chemistry in a "Pacman" Schiff-base polypyrrolic macrocycle, for the topics such as actinide element reduction and the covalency in actinide bonds. Chapters 3 and 4 are about the ligand design of the BTP ligand and its derivatives for actinides/lanthanides separation. In Chapters 5, DFT calculations were used to explore the behavior of aqueous AnO_2-Cl coordination chemistry at high pressure and temperature via changing dielectric constants. In the next chapter, Chapter 6 the reduction of uranium(VI) on the surface of TiO_2 under dark environment was studied, with a particular focus on the role of edges and corners. Finally, in Chapter 7, a summary and linkages between the different chapters in this thesis are presented. Then, future directions for the works compiled in this thesis are discussed. I hope that this thesis will make a contribution to actinide chemistry and help to reach the goal of peaceful use of nuclear power.

1.8. References

1. Morss, L. R.; Edelstein, N. M.; Fuger, J.; Katz, J. J.; Morss, L., *The chemistry of the actinide and transactinide elements*. Springer: 2006; Vol. 1.
2. Runde, W., The chemical interactions of actinides in the environment. *Los Alamos Science* **2000,** *26*, 392-411.
3. Caley, E. R., The earliest known use of a material containing uranium. *Isis* **1948,** *38* (3/4), 190-193.
4. Weigel, F., Uranium. In *The chemistry of the actinide elements. 2. ed*, 1986.
5. Nikolas, K.; Stephen , T. L., Catalyst: Nuclear Power in the 21st Century. *Chem* **2016,** *1* (5), 659-662.
6. Kaltsoyannis, N.; Scott, P. R., *The F Elements*. Oxford University Press: 2007.
7. Allisy, A., Henri Becquerel: the discovery of radioactivity. *Radiation protection dosimetry* **1996,** *68* (1-2), 3-10.
8. Fröman, N., Marie and Pierre Curie and the discovery of polonium and radium. *Palestra na royal swedish academy of sciences, em Estocolmo, Suécia* **1996**.
9. Vandenbosch, R., *Nuclear fission*. Elsevier: 2012.
10. Reed, B. C., *The history and science of the Manhattan Project*. Springer: 2014.
11. Wagemans, C., The nuclear fission process. **1991**.
12. Gordon, J.; Montgomery, H.; Noer, R.; Pickett, G.; Tobón, R., Superconductivity of thorium and uranium. *Physical Review* **1966,** *152* (1), 432.
13. Plutonium-238 Production for Space Exploration. https://www.acs.org/content/acs/en/education/whatischemistry/landmarks/plutonium-238-production.html (accessed 18th September).
14. Outline History of Nuclear Energy. https://world-nuclear.org/information-library/current-and-future-generation/outline-history-of-nuclear-energy.aspx (accessed 18th September).
15. Nuclear Power in the World Today. https://world-nuclear.org/information-library/current-and-future-generation/nuclear-power-in-the-world-today.aspx (accessed 18th September).
16. Nuclear Power in Canada. https://world-nuclear.org/information-library/country-profiles/countries-a-f/canada-nuclear-power.aspx (accessed 18th September).
17. Uranium in Canada. https://world-nuclear.org/information-library/country-profiles/countries-a-f/canada-uranium.aspx (accessed 18th September).
18. *The Nuclear Fuel Cycle: From Ore to Waste*. 1996.
19. Organisation for Economic, C.-o.; Development, *Actinide and Fission Product Partitioning and Transmutation Eleventh Information Exchange Meeting, San Francisco, California, USA, 1-4 November 2010*. OECD Publishing: 2000.
20. Hanson, C., Recent advances in liquid-liquid extraction. **2013**.
21. Starý, J., *The solvent extraction of metal chelates*. Elsevier: 2013.
22. Kislik, V. S., *Solvent extraction: classical and novel approaches*. Elsevier: 2011.
23. Vander Hoogerstraete, T.; Wellens, S.; Verachtert, K.; Binnemans, K., Removal of transition metals from rare earths by solvent extraction with an undiluted phosphonium ionic liquid: separations relevant to rare-earth magnet recycling. *Green Chemistry* **2013,** *15* (4), 919-927.
24. Braley, J. C.; Grimes, T. S.; Nash, K. L., Alternatives to HDEHP and DTPA for Simplified TALSPEAK Separations. *Industrial & Engineering Chemistry Research* **2012,** *51* (2), 629-638.
25. Nilsson, M.; Nash, K. L., Review Article: A Review of the Development and Operational Characteristics of the TALSPEAK Process. *Solvent extraction and ion exchange* **2007,** *25* (6).

26. Diamond, R. M.; Street, K.; Seaborg, G. T., An Ion-exchange Study of Possible Hybridized 5f Bonding in the Actinides1. *Journal of the American Chemical Society* **1954,** *76* (6), 1461-1469.
27. Jensen, M. P.; Bond, A. H., Comparison of Covalency in the Complexes of Trivalent Actinide and Lanthanide Cations. *Journal of the American Chemical Society* **2002,** *124* (33), 9870-9877.
28. Jensen, M. P.; Bond, A. H., Influence of aggregation on the extraction of trivalent lanthanide and actinide cations by purified Cyanex 272, Cyanex 301, and Cyanex 302. *Radiochimica acta* **2002,** *90* (4), 205-209.
29. Actinide separation science. *Radiochim. Acta* **1995,** *70/71*.
30. Ekberg, C.; Fermvik, A.; Retegan, T.; Skarnemark, G.; Foreman, M. R. S.; Hudson, M. J.; Englund, S.; Nilsson, M., An overview and historical look back at the solvent extraction using nitrogen donor ligands to extract and separate An(III) from Ln(III). *Radiochimica Acta* **2008,** *96* (4-5), 225.
31. Actinide Partitioning – A Review. *Solvent Extr. Ion Exch.* **2001,** *19*.
32. Modolo, G.; Kluxen, P.; Geist, A., Demonstration of the LUCA process for the separation of americium(III) from curium(III), californium(III), and lanthanides(III) in acidic solution using a synergistic mixture of bis(chlorophenyl)dithiophosphinic acid and tris(2-ethylhexyl)phosphate. *Radiochimica acta* **2010,** *98* (4).
33. Peterman, D. R.; Martin, L. R.; Klaehn, J. R.; Harrup, M. K.; Greenhalgh, M. R.; Luther, T. A., Selective separation of minor actinides and lanthanides using aromatic dithiophosphinic and phosphinic acid derivatives. *Journal of radioanalytical and nuclear chemistry.* **2009,** *282* (2).
34. Sanex-BTP process development studies. *Journal of nuclear science and technology.* **2002,** (Suppl. 3).
35. Girnt, D.; Roesky, P. W.; Geist, A.; Ruff, C. M.; Panak, P. J.; Denecke, M. A., 6-(3,5-Dimethyl-1 H -pyrazol-1-yl)-2,2′-bipyridine as Ligand for Actinide(III)/Lanthanide(III) Separation. *Inorganic chemistry.* **2010,** *49* (20).
36. Clark, D. L.; Hobart, D. E., Discovery of the Transuranium Elements Inspired Rearrangement of the Periodic Table and the Approach for Finding New Elements. In *The Periodic Table I: Historical Development and Essential Features*, Mingos, D. M. P., Ed. Springer International Publishing: Cham, 2019; pp 225-259.
37. Wen, X.-D.; Martin, R. L.; Henderson, T. M.; Scuseria, G. E., Density Functional Theory Studies of the Electronic Structure of Solid State Actinide Oxides. *Chemical Reviews* **2013,** *113* (2), 1063-1096.
38. Maher, K.; Bargar, J. R.; Brown, G. E., Environmental Speciation of Actinides. *Inorganic Chemistry* **2013,** *52* (7), 3510-3532.
39. Graves, C. R.; Kiplinger, J. L., Pentavalent uranium chemistry—synthetic pursuit of a rare oxidation state. *Chemical Communications* **2009,** (26), 3831-3853.
40. Zanonato, P.; Di Bernardo, P.; Bismondo, A.; Liu, G.; Chen, X.; Rao, L., Hydrolysis of uranium (VI) at variable temperatures (10− 85 C). *Journal of the American Chemical Society* **2004,** *126* (17), 5515-5522.
41. Schreckenbach, G.; Hay, P. J.; Martin, R. L., Density functional calculations on actinide compounds: Survey of recent progress and application to [UO2X4]2− (X=F, Cl, OH) and AnF6 (An=U, Np, Pu). *Journal of Computational Chemistry* **1999,** *20* (1), 70-90.
42. Neidig, M. L.; Clark, D. L.; Martin, R. L., Covalency in f-element complexes. *Coordination Chemistry Reviews* **2013,** *257* (2), 394-406.

43. Hu, S.-X.; Chen, M.; Ao, B., Theoretical studies on the oxidation states and electronic structures of actinide-borides: AnB 12 (An= Th–Cm) clusters. *Physical Chemistry Chemical Physics* **2018,** *20* (37), 23856-23863.
44. Denning, R. G., Electronic Structure and Bonding in Actinyl Ions and their Analogs. *The Journal of Physical Chemistry A* **2007,** *111* (20), 4125-4143.
45. Seyferth, D., Uranocene. The First Member of a New Class of Organometallic Derivatives of the f Elements. *Organometallics* **2004,** *23* (15), 3562-3583.
46. Reynolds, L. T.; Wilkinson, G., π-cyclopentadienyl compounds of uranium-IV and thorium-IV. *Journal of Inorganic and Nuclear Chemistry* **1956,** *2* (4), 246-253.
47. Streitwieser, A.; Mueller-Westerhoff, U., Bis(cyclooctatetraenyl)uranium (uranocene). A new class of sandwich complexes that utilize atomic f orbitals. *Journal of the American Chemical Society* **1968,** *90* (26), 7364-7364.
48. Streitwieser, A.; Yoshida, N., Di-.pi.-cyclooctatetraenethorium. *Journal of the American Chemical Society* **1969,** *91* (26), 7528-7528.
49. Karraker, D. G.; Stone, J. A.; Jones, E. R.; Edelstein, N., Bis(cyclooctatetraenyl)neptunium(IV) and bis(cyclooctatetraenyl)plutonium(IV). *Journal of the American Chemical Society* **1970,** *92* (16), 4841-4845.
50. Starks, D. F.; Parsons, T. C.; Streitwieser, A.; Edelstein, N., Bis(.pi.-cyclooctatetraene)protactinium. *Inorganic Chemistry* **1974,** *13* (6), 1307-1308.
51. Minasian, S. G.; Keith, J. M.; Batista, E. R.; Boland, K. S.; Clark, D. L.; Kozimor, S. A.; Martin, R. L.; Shuh, D. K.; Tyliszczak, T., New evidence for 5f covalency in actinocenes determined from carbon K-edge XAS and electronic structure theory. *Chemical Science* **2014,** *5* (1), 351-359.
52. Hückel, E., Theory of free radicals of organic chemistry. *Transactions of the Faraday Society* **1934,** *30*, 40-52.
53. Raymond, K. N., The structure determination of uranocene and the first COT lanthanide complexes. *New Journal of Chemistry* **2015,** *39* (10), 7540-7543.
54. Prodan, I. D.; Scuseria, G. E.; Martin, R. L., Covalency in the actinide dioxides: Systematic study of the electronic properties using screened hybrid density functional theory. *Physical Review B* **2007,** *76* (3), 033101.
55. Kirker, I.; Kaltsoyannis, N., Does covalency really increase across the 5f series? A comparison of molecular orbital, natural population, spin and electron density analyses of AnCp3 (An = Th–Cm; Cp = η5-C5H5). *Dalton Transactions* **2011,** *40* (1), 124-131.
56. Warren, K. D. In *Ligand field theory of f-orbital sandwich complexes*, New Concepts, Berlin, Heidelberg, 1977//; Wallace, W. E.; Sankar, S. G.; Rao, V. U. S.; Hoffman, D. K.; Ruedenberg, R.; Verkade, J. G.; Warren, K. D.; Schubert, K.; Linarès, C.; Louat, A.; Blanchard, M., Eds. Springer Berlin Heidelberg: Berlin, Heidelberg, 1977; pp 97-138.
57. Kerridge, A.; Kaltsoyannis, N., Are the Ground States of the Later Actinocenes Multiconfigurational? All-Electron Spin−Orbit Coupled CASPT2 Calculations on An(η8-C8H8)2 (An = Th, U, Pu, Cm). *The Journal of Physical Chemistry A* **2009,** *113* (30), 8737-8745.
58. Hayes, R. G.; Edelstein, N., Elementary molecular orbital calculation on U(C8H8)2 and its application to the electronic structures of U(C8H8)2, NP(C8H8)2, and Pu(C8H8)2. *Journal of the American Chemical Society* **1972,** *94* (25), 8688-8691.
59. Kaltsoyannis, N., Does Covalency Increase or Decrease across the Actinide Series? Implications for Minor Actinide Partitioning. *Inorganic Chemistry* **2013,** *52* (7), 3407-3413.

60. Minasian, S. G.; Keith, J. M.; Batista, E. R.; Boland, K. S.; Clark, D. L.; Conradson, S. D.; Kozimor, S. A.; Martin, R. L.; Schwarz, D. E.; Shuh, D. K.; Wagner, G. L.; Wilkerson, M. P.; Wolfsberg, L. E.; Yang, P., Determining Relative f and d Orbital Contributions to M–Cl Covalency in MCl62– (M = Ti, Zr, Hf, U) and UOCl5– Using Cl K-Edge X-ray Absorption Spectroscopy and Time-Dependent Density Functional Theory. *Journal of the American Chemical Society* **2012,** *134* (12), 5586-5597.
61. Barros, N.; Maynau, D.; Maron, L.; Eisenstein, O.; Zi, G.; Andersen, R. A., Single but Stronger UO, Double but Weaker UNMe Bonds: The Tale Told by Cp2UO and Cp2UNR. *Organometallics* **2007,** *26* (20), 5059-5065.
62. Tassell, M. J.; Kaltsoyannis, N., Covalency in AnCp4 (An = Th–Cm): a comparison of molecular orbital, natural population and atoms-in-molecules analyses. *Dalton Transactions* **2010,** *39* (29), 6719-6725.
63. Malmqvist, P. Å.; Roos, B. O.; Schimmelpfennig, B., The restricted active space (RAS) state interaction approach with spin–orbit coupling. *Chemical Physics Letters* **2002,** *357* (3), 230-240.
64. Roos, B. O.; Taylor, P. R.; Sigbahn, P. E. M., A complete active space SCF method (CASSCF) using a density matrix formulated super-CI approach. *Chemical Physics* **1980,** *48* (2), 157-173.
65. Cramer, C. J., *Essentials of computational chemistry: theories and models*. John Wiley & Sons: 2013.
66. Dirac, P. A. M., *The principles of quantum mechanics*. Oxford university press: 1981.
67. Lenthe, E. v.; Ehlers, A.; Baerends, E.-J., Geometry optimizations in the zero order regular approximation for relativistic effects. *The Journal of Chemical Physics* **1999,** *110* (18), 8943-8953.
68. Dyall, K. G.; van Lenthe, E., Relativistic regular approximations revisited: An infinite-order relativistic approximation. *The Journal of chemical physics* **1999,** *111* (4), 1366-1372.
69. Autschbach, J.; Govind, N.; Atta-Fynn, R.; Bylaska, E. J.; Weare, J. W.; de Jong, W. A., Computational tools for predictive modeling of properties in complex actinide systems. *Computational methods in lanthanide and actinide chemistry* **2015**, 299-342.
70. Lenthe, E. v.; Baerends, E. J.; Snijders, J. G., Relativistic total energy using regular approximations. *The Journal of Chemical Physics* **1994,** *101* (11), 9783-9792.
71. Van Lenthe, E. v.; Snijders, J.; Baerends, E., The zero-order regular approximation for relativistic effects: The effect of spin–orbit coupling in closed shell molecules. *The Journal of chemical physics* **1996,** *105* (15), 6505-6516.
72. Reiher, M.; Wolf, A., Exact decoupling of the Dirac Hamiltonian. I. General theory. *The Journal of chemical physics* **2004,** *121* (5), 2037-2047.
73. Wolf, A.; Reiher, M.; Hess, B. A., The generalized Douglas–Kroll transformation. *The Journal of chemical physics* **2002,** *117* (20), 9215-9226.
74. Cheng, L.; Gauss, J., Analytic energy gradients for the spin-free exact two-component theory using an exact block diagonalization for the one-electron Dirac Hamiltonian. *The Journal of chemical physics* **2011,** *135* (8), 084114.
75. Cao, X.; Weigand, A., Relativistic pseudopotentials and their applications. *Computational Methods in Lanthanide and Actinide Chemistry* **2015**, 147-179.
76. Dolg, M.; Cao, X., Relativistic pseudopotentials: their development and scope of applications. *Chemical reviews* **2012,** *112* (1), 403-480.
77. Cao, X.; Dolg, M., Relativistic pseudopotentials. In *Relativistic methods for chemists*, Springer: 2010; pp 215-277.

78. Han, Y.-K.; Hirao, K., Density functional studies of UO 2 2+ and AnF 6 (An= U, Np, and Pu) using scalar-relativistic effective core potentials. *The Journal of Chemical Physics* **2000,** *113* (17), 7345-7350.
79. Han, Y. K., Density functional studies of AnF6 (An= U, Np, and Pu) and UF6− nCln (n= 1–6) using hybrid functionals: geometries and vibrational frequencies. *Journal of Computational Chemistry* **2001,** *22* (16), 2010-2017.
80. Schreckenbach, G.; Wolff, S. K.; Ziegler, T., NMR shielding calculations across the Periodic Table: Diamagnetic Uranium compounds. 1. Methods and issues. *The Journal of Physical Chemistry A* **2000,** *104* (35), 8244-8255.
81. Schreckenbach, G., Density functional calculations of 19F and 235U NMR chemical shifts in uranium (VI) chloride fluorides UF6− nCln: Influence of the relativistic approximation and role of the exchange-correlation functional. *International journal of quantum chemistry* **2005,** *101* (4), 372-380.
82. Straka, M.; Kaupp, M., Calculation of 19F NMR chemical shifts in uranium complexes using density functional theory and pseudopotentials. *Chemical physics* **2005,** *311* (1-2), 45-56.
83. Batista, E. R.; Martin, R. L.; Hay, P. J.; Peralta, J. E.; Scuseria, G. E., Density functional investigations of the properties and thermochemistry of UF 6 and UF 5 using valence-electron and all-electron approaches. *The Journal of chemical physics* **2004,** *121* (5), 2144-2150.
84. Shamov, G. A.; Schreckenbach, G., Density Functional Studies of Actinyl Aquo Complexes Studied Using Small-Core Effective Core Potentials and a Scalar Four-Component Relativistic Method. *The Journal of Physical Chemistry A* **2006,** *110* (43), 12072-12072.
85. Odoh, S. O.; Schreckenbach, G., Performance of relativistic effective core potentials in DFT calculations on Actinide compounds. *The Journal of Physical Chemistry A* **2010,** *114* (4), 1957-1963.
86. Born, M.; Oppenheimer, R., Zur Quantentheorie der Molekeln. *Annalen der Physik* **1927,** *389* (20), 457-484.
87. Gordon, A.; Avron, J., Born-Oppenheimer approximation near level crossing. *Physical Review Letters* **2000,** *85* (1), 34.
88. Gabriela, C., What Woodward and Hoffmann didn't tell us: the failure of the Born–Oppenheimer approximation in competing reaction pathways. *Journal of the Chemical Society, Faraday Transactions* **1994,** *90* (12), 1581-1598.
89. Hartree, D. R., The Wave Mechanics of an Atom with a Non-Coulomb Central Field. Part I. Theory and Methods. *Mathematical Proceedings of the Cambridge Philosophical Society* **1928,** *24* (1), 89-110.
90. Hartree, D. R. In *The wave mechanics of an atom with a non-coulomb central field. Part II. Some results and discussion*, Mathematical Proceedings of the Cambridge Philosophical Society, Cambridge University Press: 1928; pp 111-132.
91. Purvis III, G. D.; Bartlett, R. J., A full coupled-cluster singles and doubles model: The inclusion of disconnected triples. *The Journal of Chemical Physics* **1982,** *76* (4), 1910-1918.
92. Riplinger, C.; Neese, F., An efficient and near linear scaling pair natural orbital based local coupled cluster method. *The Journal of chemical physics* **2013,** *138* (3), 034106.
93. Sandler, I.; Chen, J.; Taylor, M.; Sharma, S.; Ho, J., Accuracy of DLPNO-CCSD(T): Effect of Basis Set and System Size. *The Journal of Physical Chemistry A* **2021,** *125* (7), 1553-1563.
94. Thomas, L. H. In *The calculation of atomic fields*, Mathematical proceedings of the Cambridge philosophical society, Cambridge University Press: 1927; pp 542-548.

95. Slater, J. C., A simplification of the Hartree-Fock method. *Physical review* **1951,** *81* (3), 385.
96. Slater, J. C., Statistical Exchange-Correlation in the Self-Consistent Field. In *Advances in Quantum Chemistry*, Löwdin, P.-O., Ed. Academic Press: 1972; Vol. 6, pp 1-92.
97. Hohenberg, P.; Kohn, W., Inhomogeneous electron gas. *Physical review* **1964,** *136* (3B), B864.
98. Vosko, S. H.; Wilk, L.; Nusair, M., Accurate spin-dependent electron liquid correlation energies for local spin density calculations: a critical analysis. *Canadian Journal of Physics* **1980,** *58* (8), 1200-1211.
99. Becke, A. D., A new mixing of Hartree–Fock and local density-functional theories. *The Journal of Chemical Physics* **1993,** *98* (2), 1372-1377.
100. Lee, C.; Yang, W.; Parr, R. G., Development of the Colle-Salvetti correlation-energy formula into a functional of the electron density. *Physical Review B* **1988,** *37* (2), 785-789.
101. Grimme, S., Semiempirical hybrid density functional with perturbative second-order correlation. *The Journal of chemical physics* **2006,** *124* (3), 034108.
102. Perdew, J. P.; Ruzsinszky, A.; Tao, J.; Staroverov, V. N.; Scuseria, G. E.; Csonka, G. I., Prescription for the design and selection of density functional approximations: More constraint satisfaction with fewer fits. *The Journal of chemical physics* **2005,** *123* (6), 062201.
103. Perdew, J. P.; Schmidt, K. In *Jacob's ladder of density functional approximations for the exchange-correlation energy*, AIP Conference Proceedings, American Institute of Physics: 2001; pp 1-20.
104. Sabbe, M. K.; Reyniers, M.-F.; Reuter, K., First-principles kinetic modeling in heterogeneous catalysis: an industrial perspective on best-practice, gaps and needs. *Catalysis Science & Technology* **2012,** *2* (10), 2010-2024.
105. Perdew, J. P.; Burke, K.; Ernzerhof, M., Generalized Gradient Approximation Made Simple. *Physical Review Letters* **1996,** *77* (18), 3865-3868.
106. Perdew, J. P.; Burke, K.; Ernzerhof, M., Generalized Gradient Approximation Made Simple [Phys. Rev. Lett. 77, 3865 (1996)]. *Physical Review Letters* **1997,** *78* (7), 1396-1396.
107. Becke, A. D., Density-functional exchange-energy approximation with correct asymptotic behavior. *Physical review A* **1988,** *38* (6), 3098.
108. Tao, J.; Perdew, J. P.; Staroverov, V. N.; Scuseria, G. E., Climbing the density functional ladder: Nonempirical meta–generalized gradient approximation designed for molecules and solids. *Physical Review Letters* **2003,** *91* (14), 146401.
109. Zhao, Y.; Truhlar, D. G., A new local density functional for main-group thermochemistry, transition metal bonding, thermochemical kinetics, and noncovalent interactions. *The Journal of chemical physics* **2006,** *125* (19), 194101.
110. Perdew, J. P.; Chevary, J. A.; Vosko, S. H.; Jackson, K. A.; Pederson, M. R.; Singh, D. J.; Fiolhais, C., Atoms, molecules, solids, and surfaces: Applications of the generalized gradient approximation for exchange and correlation. *Physical Review B* **1992,** *46* (11), 6671-6687.
111. Perdew, J. P.; Wang, Y., Accurate and simple analytic representation of the electron-gas correlation energy. *Physical Review B* **1992,** *45* (23), 13244-13249.
112. Adamo, C.; Barone, V., Toward reliable density functional methods without adjustable parameters: The PBE0 model. *The Journal of chemical physics* **1999,** *110* (13), 6158-6170.
113. Slater, J. C., Atomic shielding constants. *Physical Review* **1930,** *36* (1), 57.

114. Boys, S. F., Electronic wave functions-I. A general method of calculation for the stationary states of any molecular system. *Proceedings of the Royal Society of London. Series A. Mathematical and Physical Sciences* **1950,** *200* (1063), 542-554.
115. Hehre, W. J.; Stewart, R. F.; Pople, J. A., Self-Consistent Molecular-Orbital Methods. I. Use of Gaussian Expansions of Slater-Type Atomic Orbitals. *The Journal of Chemical Physics* **1969,** *51* (6), 2657-2664.
116. te Velde, G.; Bickelhaupt, F. M.; Baerends, E. J.; Fonseca Guerra, C.; van Gisbergen, S. J. A.; Snijders, J. G.; Ziegler, T., Chemistry with ADF. *Journal of Computational Chemistry* **2001,** *22* (9), 931-967.
117. Arnold, P. L.; Pécharman, A. F.; Love, J. B., Oxo group protonation and silylation of pentavalent uranyl pacman complexes. *Angewandte Chemie* **2011,** *123* (40), 9628-9630.
118. Fortier, S.; Hayton, T. W., Oxo ligand functionalization in the uranyl ion (UO22+). *Coordination Chemistry Reviews* **2010,** *254* (3-4), 197-214.
119. Ikeda, A.; Hennig, C.; Tsushima, S.; Takao, K.; Ikeda, Y.; Scheinost, A. C.; Bernhard, G., Comparative study of uranyl (VI) and-(V) carbonato complexes in an aqueous solution. *Inorganic chemistry* **2007,** *46* (10), 4212-4219.
120. Mizuoka, K.; Grenthe, I.; Ikeda, Y., Structural and kinetic studies on uranyl (V) carbonate complex using 13C NMR spectroscopy. *Inorganic chemistry* **2005,** *44* (13), 4472-4474.
121. Tomasi, J.; Mennucci, B.; Cammi, R., Quantum mechanical continuum solvation models. *Chemical reviews* **2005,** *105* (8), 2999-3094.
122. Born, M., Volumen und hydratationswärme der ionen. *Zeitschrift für physik* **1920,** *1* (1), 45-48.
123. Onsager, L., Electric moments of molecules in liquids. *Journal of the American Chemical Society* **1936,** *58* (8), 1486-1493.
124. Kirkwood, J. G., The dielectric polarization of polar liquids. *The Journal of Chemical Physics* **1939,** *7* (10), 911-919.
125. Cossi, M.; Rega, N.; Scalmani, G.; Barone, V., Energies, structures, and electronic properties of molecules in solution with the C-PCM solvation model. *Journal of computational chemistry* **2003,** *24* (6), 669-681.
126. Klamt, A.; Schüürmann, G., COSMO: a new approach to dielectric screening in solvents with explicit expressions for the screening energy and its gradient. *Journal of the Chemical Society, Perkin Transactions 2* **1993,** (5), 799-805.
127. Klamt, A., Conductor-like screening model for real solvents: a new approach to the quantitative calculation of solvation phenomena. *The Journal of Physical Chemistry* **1995,** *99* (7), 2224-2235.
128. Andzelm, J.; Kölmel, C.; Klamt, A., Incorporation of solvent effects into density functional calculations of molecular energies and geometries. *The Journal of chemical physics* **1995,** *103* (21), 9312-9320.
129. Klamt, A.; Jonas, V., Treatment of the outlying charge in continuum solvation models. *The Journal of chemical physics* **1996,** *105* (22), 9972-9981.
130. Cramer, C. J.; Truhlar, D. G., Implicit solvation models: equilibria, structure, spectra, and dynamics. *Chemical Reviews* **1999,** *99* (8), 2161-2200.
131. Spencer, S.; Gagliardi, L.; Handy, N. C.; Ioannou, A. G.; Skylaris, C.-K.; Willetts, A.; Simper, A. M., Hydration of UO22+ and PuO22+. *The Journal of Physical Chemistry A* **1999,** *103* (12), 1831-1837.

132. Wang, C.-Z.; Lan, J.-H.; Zhao, Y.-L.; Chai, Z.-F.; Wei, Y.-Z.; Shi, W.-Q., Density Functional Theory Studies of UO22+ and NpO2+ Complexes with Carbamoylmethylphosphine Oxide Ligands. *Inorganic Chemistry* **2013,** *52* (1), 196-203.
133. Uematsu, M.; Frank, E. U., Static Dielectric Constant of Water and Steam. *Journal of Physical and Chemical Reference Data* **1980,** *9* (4), 1291-1306.
134. Hamelin, J.; Mehl, J. B.; Moldover, M. R., The Static Dielectric Constant of Liquid Water Between 274 and 418 K Near the Saturated Vapor Pressure. *International Journal of Thermophysics* **1998,** *19* (5), 1359-1380.
135. Martin, R. L.; Hay, P. J.; Pratt, L. R., Hydrolysis of Ferric Ion in Water and Conformational Equilibrium. *The Journal of Physical Chemistry A* **1998,** *102* (20), 3565-3573.
136. Kelley, M. P.; Su, J.; Urban, M.; Luckey, M.; Batista, E. R.; Yang, P.; Shafer, J. C., On the Origin of Covalent Bonding in Heavy Actinides. *Journal of the American Chemical Society* **2017,** *139* (29), 9901-9908.
137. Deblonde, G. J.-P.; Kelley, M. P.; Su, J.; Batista, E. R.; Yang, P.; Booth, C. H.; Abergel, R. J., Spectroscopic and Computational Characterization of Diethylenetriaminepentaacetic Acid/Transplutonium Chelates: Evidencing Heterogeneity in the Heavy Actinide(III) Series. *Angewandte Chemie International Edition* **2018,** *57* (17), 4521-4526.
138. Kelley, M. P.; Deblonde, G. J. P.; Su, J.; Booth, C. H.; Abergel, R. J.; Batista, E. R.; Yang, P., Bond Covalency and Oxidation State of Actinide Ions Complexed with Therapeutic Chelating Agent 3,4,3-LI(1,2-HOPO). *Inorganic Chemistry* **2018,** *57* (9), 5352-5363.
139. Zhang, X.; Adelman, S.; Arko, B.; De Silva, C.; Su, J.; Kozimor, S.; Mocko, V.; Shafer, J.; Stein, B.; Schreckenbach, G., Advancing the Am Extractant Design through the Interplay among Planarity, Preorganization, and Substitution Effects. *Inorganic Chemistry* **2022,** *61* (30), 11556-11570.
140. Lewis, G. N., THE ATOM AND THE MOLECULE. *Journal of the American Chemical Society* **1916,** *38* (4), 762-785.
141. Heitler, W.; London, F., Wechselwirkung neutraler Atome und hom$\diamond$opolare Bindung nach der Quantenmechanik. *The European physical journal.* **1927,** *44* (6-7).
142. Shaik, S.; Hiberty, P. C.; Lipkowitz, K. B.; Larter, R.; Cundari, T. R., *Valence Bond Theory, Its History, Fundamentals, and Applications: A Primer*. Wiley-VCH: 2004; Vol. 20.
143. Mulliken, R. S., Electronic structures of polyatomic molecules and valence. *Physical Review* **1932,** *40* (1), 55.
144. Esser, S., QTAIM and the Interactive Conception of Chemical Bonding. *Philosophy of Science* **2019,** *86* (5), 1307-1317.
145. Mitoraj, M. P.; Michalak, A.; Ziegler, T., A Combined Charge and Energy Decomposition Scheme for Bond Analysis. *Journal of Chemical Theory and Computation* **2009,** *5* (4), 962-975.
146. Jug, K., A maximum bond order principle. *Journal of the American Chemical Society* **1977,** *99* (24), 7800-7805.
147. Jug, K., Bond order orbitals and eigenvalues. *Journal of the American Chemical Society* **1978,** *100* (21), 6581-6586.
148. Foster, J. P.; Weinhold, F., Natural hybrid orbitals. *Journal of the American Chemical Society* **1980,** *102* (24), 7211-7218.
149. Reed, A. E.; Weinhold, F., Natural localized molecular orbitals. *The Journal of chemical physics* **1985,** *83* (4), 1736-1740.
150. Reed, A. E.; Weinhold, F., Natural bond orbital analysis of near-Hartree–Fock water dimer. *The Journal of chemical physics* **1983,** *78* (6), 4066-4073.

151. Reed, A. E.; Weinhold, F.; Curtiss, L. A.; Pochatko, D. J., Natural bond orbital analysis of molecular interactions: Theoretical studies of binary complexes of HF, H2O, NH3, N2, O2, F2, CO, and CO2 with HF, H2O, and NH3. *The Journal of Chemical Physics* **1986,** *84* (10), 5687-5705.
152. Reed, A. E.; Curtiss, L. A.; Weinhold, F., Intermolecular interactions from a natural bond orbital, donor-acceptor viewpoint. *Chemical Reviews* **1988,** *88* (6), 899-926.
153. Bader, R. F. W.; Bader, R. F., *Atoms in Molecules: A Quantum Theory*. Clarendon Press: 1990.
154. Matta, C. F.; Massa, L.; Keith, T. A., Richard F. W. Bader: A True Pioneer. *The Journal of Physical Chemistry A* **2011,** *115* (45), 12427-12431.
155. Becke, A. D.; Edgecombe, K. E., A simple measure of electron localization in atomic and molecular systems. *The Journal of chemical physics* **1990,** *92* (9), 5397-5403.
156. Esterhuysen, C.; Frenking, G., The nature of the chemical bond revisited. An energy partitioning analysis of diatomic molecules E2 (E=N–Bi, F–I), CO and BF. *Theoretical Chemistry Accounts* **2004,** *111* (2), 381-389.
157. Coppens, P.; Hall, M. B., *Electron distributions and the chemical bond*. Springer Science & Business Media: 2012.
158. Löwdin, P. O., On the non-orthogonality problem connected with the use of atomic wave functions in the theory of molecules and crystals. *The Journal of Chemical Physics* **1950,** *18* (3), 365-375.
159. Mulliken, R. S., Electronic population analysis on LCAO–MO molecular wave functions. I. *The Journal of Chemical Physics* **1955,** *23* (10), 1833-1840.
160. Kitaura, K.; Morokuma, K., A new energy decomposition scheme for molecular interactions within the Hartree-Fock approximation. *International Journal of Quantum Chemistry* **1976,** *10* (2), 325-340.
161. Ziegler, T.; Rauk, A., On the calculation of bonding energies by the Hartree Fock Slater method. *Theoretica chimica acta* **1977,** *46* (1), 1-10.
162. Ziegler, T.; Rauk, A., Carbon monoxide, carbon monosulfide, molecular nitrogen, phosphorus trifluoride, and methyl isocyanide as .sigma. donors and .pi. acceptors. A theoretical study by the Hartree-Fock-Slater transition-state method. *Inorganic Chemistry* **1979,** *18* (7), 1755-1759.
163. Ziegler, T.; Rauk, A., A theoretical study of the ethylene-metal bond in complexes between copper(1+), silver(1+), gold(1+), platinum(0) or platinum(2+) and ethylene, based on the Hartree-Fock-Slater transition-state method. *Inorganic Chemistry* **1979,** *18* (6), 1558-1565.
164. Van Lenthe, E.; Van Leeuwen, R.; Baerends, E.; Snijders, J., Relativistic regular two-component Hamiltonians. *International Journal of Quantum Chemistry* **1996,** *57* (3), 281-293.
165. Jacobsen, H.; Ziegler, T., Nonclassical double bonds in ethylene analogs: influence of Pauli repulsion on trans bending and .pi.-bond strength. A density functional study. *Journal of the American Chemical Society* **1994,** *116* (9), 3667-3679.
166. Bickelhaupt, F. M.; Baerends, E. J., Kohn-Sham Density Functional Theory: Predicting and Understanding Chemistry. In *Reviews in Computational Chemistry*, 2000; pp 1-86.
167. Wiberg, K. B., Application of the pople-santry-segal CNDO method to the cyclopropylcarbinyl and cyclobutyl cation and to bicyclobutane. *Tetrahedron* **1968,** *24* (3), 1083-1096.
168. Mayer, I., Charge, bond order and valence in the AB initio SCF theory. *Chemical Physics Letters* **1983,** *97* (3), 270-274.

169. Nalewajski, R. F.; Köster, A. M.; Jug, K., Chemical valence from the two-particle density matrix. *Theoretica chimica acta* **1993,** *85* (6), 463-484.
170. Nalewajski, R. F.; Mrozek, J., Modified valence indices from the two-particle density matrix. *International journal of quantum chemistry* **1994,** *51* (4), 187-200.
171. Nalewajski, R. F.; Formosinho, S. J.; Varandas, A. J.; Mrozek, J., Quantum mechanical valence study of a bond-breaking–bond-forming process in triatomic systems. *International journal of quantum chemistry* **1994,** *52* (5), 1153-1176.
172. Nalewajski, R. F.; Mrozek, J.; Mazur, G., Quantum chemical valence indices from the one-determinantal difference approach. *Canadian journal of chemistry* **1996,** *74* (6), 1121-1130.
173. Nalewajski, R. F.; Mrozek, J.; Michalak, A., Two-electron valence indices from the Kohn-Sham orbitals. *International Journal of Quantum Chemistry* **1997,** *61* (3), 589-601.
174. Mrozek, J.; Nalewajski, R. F.; Michalak, A., Exploring bonding patterns of molecular systems using quantum mechanical bond multiplicities. *Polish Journal of Chemistry* **1998,** *72* (7S), 1779-1791.
175. Michalak, A.; DeKock, R. L.; Ziegler, T., Bond Multiplicity in Transition-Metal Complexes: Applications of Two-Electron Valence Indices. *The Journal of Physical Chemistry A* **2008,** *112* (31), 7256-7263.
176. Lu, T.; Chen, F., Multiwfn: A multifunctional wavefunction analyzer. *Journal of Computational Chemistry* **2012,** *33* (5), 580-592.
177. Bader, R., Atoms in molecules: a quantum theory. Inter Ser Monogr Chem. Clarendon Press, Oxford: 1994.
178. Emamian, S.; Lu, T.; Kruse, H.; Emamian, H., Exploring nature and predicting strength of hydrogen bonds: A correlation analysis between atoms-in-molecules descriptors, binding energies, and energy components of symmetry-adapted perturbation theory. *Journal of computational chemistry* **2019,** *40* (32), 2868-2881.
179. Becke, A., *The quantum theory of atoms in molecules: from solid state to DNA and drug design*. John Wiley & Sons: 2007.
180. Nakanishi, W.; Hayashi, S., Role of dG/dw and dV/dw in AIM Analysis: An Approach to the Nature of Weak to Strong Interactions. *The Journal of Physical Chemistry A* **2013,** *117* (8), 1795-1803.
181. Pilmé, J.; Renault, E.; Bassal, F.; Amaouch, M.; Montavon, G.; Galland, N., QTAIM Analysis in the Context of Quasirelativistic Quantum Calculations. *Journal of Chemical Theory and Computation* **2014,** *10* (11), 4830-4841.
182. Cremer, D.; Kraka, E., Chemical bonds without bonding electron density—does the difference electron-density analysis suffice for a description of the chemical bond? *Angewandte Chemie International Edition in English* **1984,** *23* (8), 627-628.
183. Farrugia, L. J.; Senn, H. M., Metal−Metal and Metal−Ligand Bonding at a QTAIM Catastrophe: A Combined Experimental and Theoretical Charge Density Study on the Alkylidyne Cluster Fe3(μ-H)(μ-COMe)(CO)10. *The Journal of Physical Chemistry A* **2010,** *114* (51), 13418-13433.
184. Du, J.; Sun, X.; Jiang, G., Exploring the interaction natures in plutonyl (VI) complexes with topological analyses of electron density. *International Journal of Molecular Sciences* **2016,** *17* (4), 414.
185. Vallet, V.; Wahlgren, U.; Grenthe, I., Probing the Nature of Chemical Bonding in Uranyl(VI) Complexes with Quantum Chemical Methods. *The Journal of Physical Chemistry A* **2012,** *116* (50), 12373-12380.

186. Michelini, M. d. C.; Russo, N.; Sicilia, E., Gas-Phase Chemistry of Actinides Ions: New Insights into the Reaction of UO+ and UO2+ with Water. *Journal of the American Chemical Society* **2007,** *129* (14), 4229-4239.
187. Bader, R. F.; Stephens, M. E., Spatial localization of the electronic pair and number distributions in molecules. *Journal of the American Chemical Society* **1975,** *97* (26), 7391-7399.
188. Becke, A. D., Local exchange-correlation approximations and first-row molecular dissociation energies. *International Journal of Quantum Chemistry* **1985,** *27* (5), 585-594.
189. Silvi, B.; Savin, A., Classification of chemical bonds based on topological analysis of electron localization functions. *Nature* **1994,** *371* (6499), 683-686.
190. Savin, A.; Jepsen, O.; Flad, J.; Andersen, O. K.; Preuss, H.; von Schnering, H. G., Electron localization in solid-state structures of the elements: the diamond structure. *Angewandte Chemie International Edition in English* **1992,** *31* (2), 187-188.
191. Grimme, S.; Antony, J.; Ehrlich, S.; Krieg, H., A consistent and accurate ab initio parametrization of density functional dispersion correction (DFT-D) for the 94 elements H-Pu. *The Journal of Chemical Physics* **2010,** *132* (15), 154104.
192. Lipscomb, W. N., *Boron hydrides*. Courier Corporation: 2012.
193. Zubarev, D. Y.; Boldyrev, A. I., " Developing paradigms of chemical bonding: adaptive natural density partitioning. *Physical chemistry chemical physics* **2008,** *10* (34), 5207-5217.
194. Multiwfn Software Manual http://sobereva.com/multiwfn/Multiwfn_manual.html (accessed September 10th).
195. Zubarev, D. Y.; Boldyrev, A. I., Revealing Intuitively Assessable Chemical Bonding Patterns in Organic Aromatic Molecules via Adaptive Natural Density Partitioning. *The Journal of Organic Chemistry* **2008,** *73* (23), 9251-9258.
196. Averkiev, B. B.; Zubarev, D. Y.; Wang, L.-M.; Huang, W.; Wang, L.-S.; Boldyrev, A. I., Carbon avoids hypercoordination in CB6−, CB62−, and C2B5− planar carbon− boron clusters. *Journal of the American Chemical Society* **2008,** *130* (29), 9248-9250.
197. Pople, J., Two-dimensional chart of quantum chemistry. *The Journal of Chemical Physics* **1965,** *43* (10), S229-S230.
198. Schreckenbach, G.; Shamov, G. A., Theoretical Actinide Molecular Science. *Accounts of Chemical Research* **2010,** *43* (1), 19-29.

Preface to Chapter 2

This chapter is based on a manuscript that was published in the journal "*Angewandte Chemie*". The full citation of the paper is as follows:

> P. L. Arnold, M. S. Dutkiewicz, M. Zegke, O. Walter, C. Apostolidis, E. Hollis, A.-F. Pécharman, N. Magnani, J.-C. Griveau, E. Colineau, R. Caciuffo, X. Zhang, G. Schreckenbach, J. B. Love, Subtle Interactions and Electron Transfer between U^{III}, Np^{III}, or Pu^{III} and Uranyl Mediated by the Oxo Group *Angew. Chem. Int. Ed.* **2016**, *55*, 12797.

and on a manuscript that was published in the journal "*Chemical Science*". The full citation of the paper is as follows:

> Zegke, M., Zhang, X., Pidchenko, I., Hlina, J.A., Lord, R.M., Purkis, J., Nichol, G.S., Magnani, N., Schreckenbach, G., Vitova, T. Love, J.B. and Arnold P.L. Differential uranyl (v) oxo-group bonding between the uranium and metal cations from groups 1, 2, 4, and 12; a high energy resolution X-ray absorption, computational, and synthetic study. *Chemical science*, *10*(42), pp.9740-9751.

All the DFT calculations and theoretical analysis in this chapter were carried out by Xiaobin Zhang. The manuscripts were prepared together with the other authors.

Copyright permissions have been obtained from the publishers of the first article and all the other authors. P. L. Arnold, M. Zegke, E. Hollis, A.-F. Pécharman, J. B. Love are affiliated with School of Chemistry, University of Edinburgh, United Kingdom. M. S. Dutkiewicz, O. Walter, C. Apostolidis, N. Magnani, J.-C. Griveau, E. Colineau, R. Caciuffo are affiliated with the European Commission, Joint research centre, Institute for Transuranium Elements, Karlsruhe, Germany.

Copyright permissions have also been obtained from the publishers of the second article and all the other authors. Zegke, M., Hlina, J.A., Lord, R.M., Purkis, J., Nichol, G.S., Love, J.B. and Arnold P.L. are affiliated with School of Chemistry, The University of Edinburgh, David Brewster Road, Edinburgh, United Kingdom. Pidchenko, I. and Vitova, T. are affiliated with Institute for Nuclear Waste Disposal (INE), Karlsruhe Institute of Technology (KIT), Karlsruhe, Germany. Magnani, N. is affiliated with Institute for Transuranium Elements, Joint Research Centre, European Commission, Karlsruhe, Germany

Chapter 2. Theoretical Study of Subtle Interactions and Bonding between Uranyl and Metal Cations by Oxo Group.

2.1. Introduction

The uranyl(VI) dication $U^{VI}O_2^{2+}$ is the most common form of uranium in the environment,[1] and is usually very inert to chemical modification due to its strong U=O bonds with a nominal bond order of three.[2] In contrast, the uranyl(V) monocation, $U^{V}O_2^{+}$, obtained by single-electron reduction, is unstable in aqueous systems and likely disproportionates to uranyl(VI) and uranium(IV),[3] through U-O bonding between adjacent uranyl centres, traditionally known as cation-cation interactions (CCIs).[4] One of the notable features of the $5f^1$ uranyl(V) ion is its tendency to coordinate to other metal cations through the oxo group, behavior more reminiscent of the heavier f^1 and f^2 neptunyl and plutonyl cations, which form a variety of oxo-bridged CCIs that interfere with nuclear waste manipulations.[5] Reduction of U^{VI} uranyl to the more Lewis basic U^{V} uranyl ion dramatically increases CCI interactions, providing good models for the behavior of the Np and Pu ions, which are significantly more radioactive than the uranyl ion. Along with the actinyl ions, civil nuclear waste also contains a large number of 5*f* metal cations from fuel additives and cladding bombardment.[6, 7] Thus, understanding the interaction of uranyl, which represents about 98 % of spent fuel, with other 5*f* metal ions is important.

Uranyl(V) complexes can be isolated and studied under anaerobic conditions,[1, 6, 8] and judicious choice of ligands such as Pacman,[9] aza-β-diketiminate[10] or β-ketoiminate[11] can lead to chemically inert dinuclear uranium(V) dioxo complexes through selective oxo-functionalisation reactions such as reductive silylation or borylation.[12, 13] The reduction of uranium(VI) to uranium(V) in the uranyl ion is thermodynamically accessible,[14, 15] and recent work by us and

others has shown that reduction can be accompanied by oxo-group functionalization with either main group[12, 16, 17] or magnetically more interesting 3*d*- and 4*f*- metal cations.[9, 18-21] The strong anisotropy of the *f*-block ions has enabled recent breakthroughs in the design of molecular magnets with slow relaxation times that could have applications in spintronic devices, for example.[22] Actinides have been favored over lanthanides in this area due to the relatively greater proportion of covalency (and therefore potential for magnetic communication) in their bonding interactions. Furthermore, the axial symmetry of the uranyl ion offers a design element to control the orientation of the magnetic vector of the single 5*f* electron in U^{V} uranyl complexes and has been used to construct mixed, oxo-bridged uranyl–transition-metal single molecule magnets (SMMs).[21]

Simple U^{III} complexes can reduce and activate inert small molecules,[23] but no such reactivity has been reported for transuranic An^{III} complexes in which the An^{IV} formal oxidation state is less thermodynamically favored compared to U^{IV}. The difference in preferred coordination geometries of actinyl and actinide cations has been used successfully to make coordination network materials that combine uranium as U^{VI} uranyl and the transuranic neptunium(IV) cation in a phosphate structure,[24] but to the best of our knowledge no reaction to form a heterobimetallic actinide complex through an inner-sphere redox reaction has been reported. We envisaged that the binding and redox-reaction of the uranyl oxo group with potentially reducing *f*-block metal cations could provide fundamental information on the behavior of actinyl cations in solution, and a versatile and powerful design principle for the synthesis of electronically coupled, redox-active, 5*f* elements.[9] Herein, we present a study that integrates computational calculations with experimental spectroscopy, focusing on the first actinide-functionalized uranyl(V) complexes and their 5*f*-5*f* magnetic coupling.

The enhanced oxo-basicity of the [Rn] $5f^1$-electron configuration of uranyl(V) also facilitates the formation of complexes that combine uranyl(V) with the late 3*d* elements Mn(II), Fe(II), Ni(II) and Co(II). This feature can result in uranium-metal communication, for example in a trinuclear [Co-O=U=O-Co] complex that exhibits a magnetic exchange and a slow relaxation at a reversal barrier temperature of 30.5 ± 0.9 K, resulting in 5*f*-3*d* single molecule magnetism.[18, 21, 25-27] Our collaborators have also reported the exclusively group(I) mono-oxo metalated uranyl(V) complexes $[(py)_3LiOUO(py)(H_2L)]$, $[(py)_3NaOUO(py)(H_2L)]$**,** and $[(py)_3KOUO(py)(H_2L)]$**B**, and their catalytic synthesis *via* the oxo-aluminated uranyl(V) complexes $[(py)(R_2AlOUO)(py)(H_2L)]$ (R = Me or ^{i}Bu)**D**.[28] It is shown that uranyl(VI) to uranyl(V) reduction is possible by both homolytic bond cleavage[14] and sterically induced reduction[19] as well as *via* a direct reductive metalation.[17, 29] Importantly, uranyl(VI) complexes in which one oxo group is coordinated by a Lewis acid group, such as a borane or metal complex, are activated towards single-electron reduction by as much as 0.6 V.[11, 12, 15, 16, 30] This has been used to direct the functionalisation of the oxo group by d- and p-block reagents. For example, coordination of uranyl Pacman complexes by $[Zn[N(SiMe_3)_2]Cl]$ results in reductive oxo-silylation whereas with $Mg[N(SiMe_3)_2]_2$ the reduced oxo-metalated complex is formed.[14] It has also been used to control the abstraction of a single oxo atom by boranes and silanes.[31] Borane coordination has also been used to shift the redox couple of the uranyl ion so far that the U^{VI} to U^{IV} reduction can be achieved by dihydrogen, a simple reducing agent of greater relevance to real-world uranyl chemistry; H_2 is formed from radiolysis of water in spent nuclear fuel storage ($E_{1/2}$ (H_2) = −0.54 V vs Fc/Fc^+).[32]

The electronic structures of the actinyl ions in different formal oxidation states can be probed by various experimental and computational techniques. Experimentally, High Energy Resolution X-ray Absorption Near Edge Structure (HR-XANES) and Resonant Inelastic X-ray

Scattering (RIXS) have recently emerged as very sensitive tools for characterisation of oxidation states and electronic structures of actinide elements.[33-43] In particular, since they directly probe the An 5*f* valence unoccupied orbitals, they can distinguish small variations in the chemical bonding at the metal for uranyl(VI) and uranyl(V) compounds. These experimental spectroscopic techniques are most readily interpreted in combination with computational analyses.[38, 42] Recently, we, as well as others, have applied the quantum theory of atoms-in-molecules (QTAIM)[44, 45] and energy decomposition analysis (EDA)[46, 47] to analyse chemical bonding in *f*-element organometallic complexes.[48-56]

The hexameric ring structures formed with the most strongly reducing alkali metals Rb and Cs are interesting in the context of nuclear waste behaviour as the highly radiotoxic ^{137}Cs is generated in nuclear reactors and has a half-life of 30.1 years.[57] Herein, in order to better understand the bonding nature of the oxo-bridged complexes, we also present a set of mono-metalated uranyl(V) complexes that incorporate a variety of *s*- and *d*-block metal cations metal cations from groups 1, 2, 4, and 12 and adopt very similar structural motifs. One synthetic route to these compounds includes the unique combination of group 2 or group 12 metals with their respective halide salts for reduction and metalation has been achieved by experimental collaborators. We and our experimental collaborators have analysed the complexes using a combination of various of computational techniques and spectroscopic, including EDA, molecular orbital (MO) analysis, QTAIM, and HR-XANES to validate the uranyl(V) oxidation state and the metal-oxo interactions, in order to better understand the effect that different reductants have on the bonding and covalency on the uranyl electronic structure.

2.2. Computational Details

The computational study of reduced uranium complexes is difficult, not only because of the large size of the calculation for an open-shell actinide but also because of spin-orbit and multiplet effects arising from the unpaired f electrons that result in a large number of close-lying states.[19] However, a single-configurational method is still valid for the specific structural, energetic and topological questions addressed here.[58, 59]

All geometries were fully optimized at the DFT level using the PBE functional[60] with correlation-consistent all electron Gaussian basis sets of double- ζ -plus-polarization (DZP) quality for the large component and corresponding kinetically balanced basis sets for the small component,[61] using the Priroda code,[62] version 2013. Priroda applies the full Dirac equation but with spin-orbit projected out and neglected.[61, 63] Vibrational frequency calculations were performed at the same level of theory in order to verify that the geometries are real minima on the potential energy surfaces and to calculate free energies.

Topology analysis such as QTAIM, Orbital composition analysis with Ros-Schuit (SCPA) partition[46, 64] and Orbital composition analysis of localized orbitals with Hirshfeld partition were performed with the MultiWFN code.[65] Energy decomposition analysis (EDA) [46, 47] was interfaced with the Amsterdam Density Functional (ADF)[66] program. ADF calculations were performed using the PBE functional and the scalar zeroth order regular approximation (ZORA) method[67-71] with corresponding double zeta polarised (DZP) basis set for light elements and triple zeta polarised (TZP) for uranium. [72]

2.3. Results and Discussion

2.3.1. Bonding between U^{III}, Np^{III}, or Pu^{III} and Uranyl Mediated by the Oxo Group

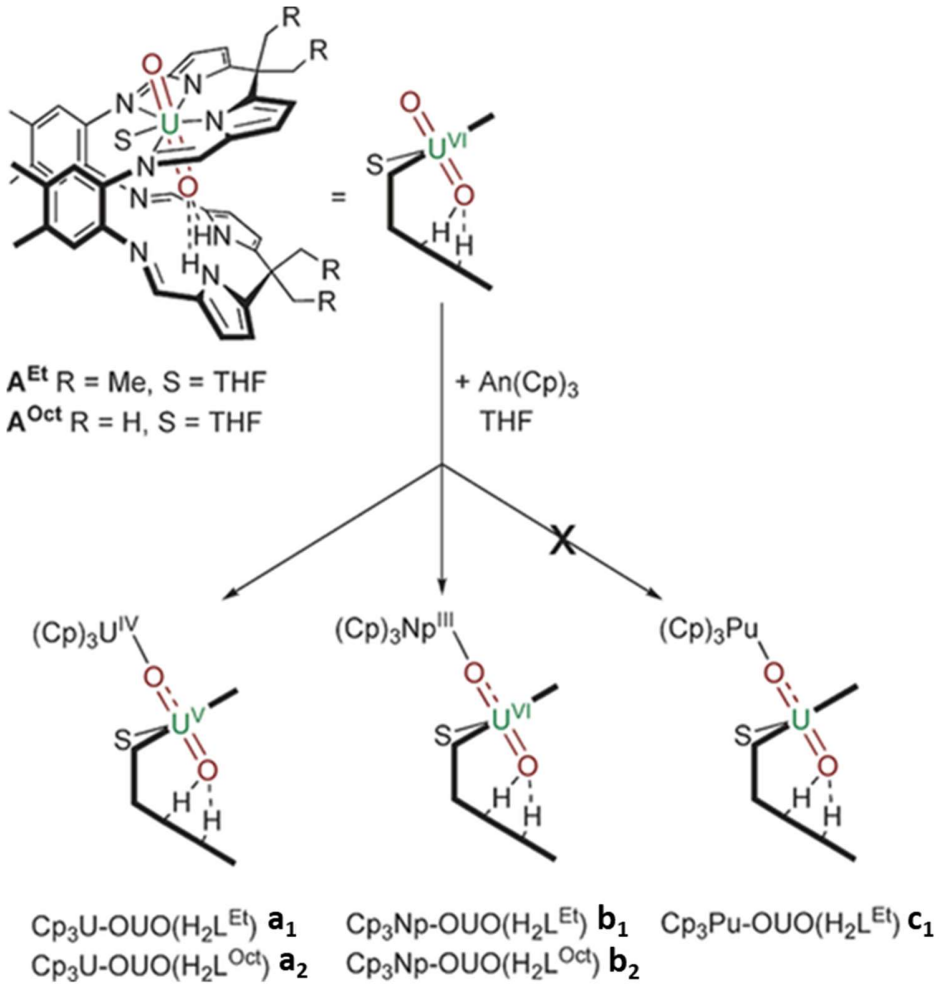

Scheme 2.1. Reductive oxo-metalation of uranyl complexes by $AnCp_3$ (An = U, Np, Pu).

Our experimental collaborators found that the reaction between THF solutions of $[(UO_2)(THF)(H_2L)]$ (**A**) and Cp_3An (An=U, Np, Pu, $Cp=C_5H_5$) results in a color change of the greenish solution of **A** to brown or red-brown for U and Np, but no observable reaction for the Pu analogue; presumably the Pu cation is insufficiently Lewis acidic and the THF donor solvent thus becomes competitive with Pu-oxo coordination (Scheme 2.1).

However, all of the experimental characterization data agree on the extent of electron transfer from the organometallic actinide to the uranyl group:

- NMR: The paramagnetic shifting of the resonances in the macrocyclic ligand in both **a** and **b** is suggestive of singly reduced uranyl(V) in both. The paramagnetic chemical shifts of the Cp ring protons are less diagnostic; in the U–U complexes **a** the chemical shift of the Cp protons is similar to most U^{IV} complexes, whereas those in the Np–U complexes **b** are comparable with those of some Np^{III} cyclopentadienyl complexes.
- NIR–UV/Vis–IR: The vibrational data support U^{IV}–U^{V} oxidation states for **a** and Np^{IV}–U^{V} oxidation states for **b**.
- XRD: The crystal structures of both the Cp_3An–(OUO) systems are isostructural, and present convincing evidence for single electron transfer in **a** but less so in **b**. The data show characteristic elongation of the U−(μ-O)−An distances and to smaller extent also U−O(*endo*), suggestive of the uranyl(V) ion in both but the An−O_{exo} uranyl distances are more in line with U^{IV} and Np^{III} formal oxidation state assignments.
- SQUID magnetometry: For $\mathbf{a_2}$ the data are consistent with full electron transfer to form a U^{IV}–U^{V} complex. However, for $\mathbf{b_2}$ the magnetic ground state saturation values closely match those of the isolated Np^{III} ion, suggesting a donor–acceptor oxo bridged Np^{III}–U^{VI} product.

DFT calculations on models of $\mathbf{a_2}$ to $\mathbf{c_2}$ (where $\mathbf{c_2}$ is the Pu analogue to $\mathbf{a_2}$ and $\mathbf{b_2}$) help with the bond type assignments and support the proposed decreasing level of electron transfer from Cp_3U through Cp_3Pu.

Table 2.1 Gas phase Gibbs free energies for the reactions Cp_3An^{III} + $[OU^{VI}O(THF)(H_2L^{oct})]$→ $[Cp_3An(UO_2)(THF)(H_2L^{oct})]$ (An = U, Np, Pu) at Priroda DZP scalar four-component PBE level. (Numbers in kcal/mol)

Cp_3U^{III}	$[OU^{VI}O(THF)(H_2L^{oct})]$	$[Cp_3U(UO_2)(THF)(H_2L^{oct})]$	ΔG_{298} gas phase
-17937565.85	-19107828.16	-37045408.92	-14.91
Cp_3Np^{III}	$[OU^{VI}O(THF)(H_2L^{oct})]$	$[Cp_3Np(UO_2)(THF)(H_2L^{oct})]$	ΔG_{298} gas phase
-18433034.22	-19107828.16	-37540868.70	-6.31
Cp_3Pu^{III}	$[OU^{VI}O(THF)(H_2L^{oct})]$	$[Cp_3Pu(UO_2)(THF)(H_2L^{oct})]$	ΔG_{298} gas phase
-18937970.87	-19107828.16	-38045796.23	2.81

The Gibbs free energies for each reaction in Scheme 2.1 were calculated, and the result are presented in in Table 2.1. The positive gas-phase value (2.81kcal mol^{-1}) for Cp_3Pu suggests that the reaction to form **C2** is unfavorable, which agrees with the experimental observation shown in Scheme 2.1.

Table 2.2 Calculated uncorrected[a] An^{IV}/An^{III} Reduction potentials at Priroda DZP Four-Component PBE level (Numbers in eV)

	Half-reaction (gas phase)	Potential vs ferrocene[b] (gas phase)
Cp_3U^{IV+}/Cp_3U^{III}	-5.50	-1.21
$Cp_3Np^{IV+}/Cp_3Np^{III}$	-5.90	-0.81
$Cp_3Pu^{IV+}/Cp_3Pu^{III}$	-6.29	-0.41

[a] Multiplet, Spin-orbit effects as well as solvent corrections are in principle very important for reduction potential calculations at the DFT level. [73] However, there are no empirical corrections available for multiplet and spin-orbit effects for these low oxidation state actinide elements. Thus, we can only obtain a qualitative comparison of these reduction potentials rather than exact results. Solvent effects can be neglected for a qualitative comparison, since the An^{IV}/An^{III} complexes have similar structures and charges and hence relatively similar free energies of solvation.

[b] The gas phase Fc^+/Fc reduction potential in this work is -6.71 eV at the Priroda DZP four-component PBE level.

The calculated uncorrected, gas-phase Cp_3An^{IV}/Cp_3An^{III} reduction potentials vs. ferrocene shown in Table 2.2 are −1.21eV for U, −0.81eV for Np, and −0.41eV for Pu and follow the same trend as the experimental data, that is, the reduction of Cp_3AnCl is −1.80V for U^{IV} and −1.29V for Np^{IV} in THF vs. ferrocene.[74] Our collaborators previously measured the relatively facile reduction of the uranyl complex $\mathbf{A^{Oct}}$ as −1.18V vs. ferrocene in THF solution[75] and so comparison of these reduction potentials predicts that it will be more difficult to transfer an electron from Cp_3Np^{III} than Cp_3U^{III}. The calculated charges and spin densities on the An and uranium centers are given in Tables 2.3 and 2.4. They agree with the oxidation states assigned by SQUID magnetometry, with the spin density on the U^V centers decreasing in the order **a**>**b**>**c** because all the unpaired electrons in these systems are very localized (see Figures 2.1–2.3). Figure 2.1 shows that all the SOMOs are strongly localized in $\mathbf{a_2}$. The contributions from the U in the Cp_3 fragment is only about 6%. These data indicate the full transfer of one electron to form $U^{IV}U^V$. In contrast, the highest SOMOs in $\mathbf{b_2}$ and $\mathbf{c_2}$, shown in Figure 2.2 and Figure 2.3 are very delocalized between the An and uranyl U. Thus, as Table 2.4 shows, the extent of electron transfer can be deduced by comparing the separated fragments Cp_3An^{III} and $U^{VI}O_2(H_2L^{Oct})$ to the final products $\mathbf{a_2}/\mathbf{b_2}/\mathbf{c_2}$. The spin density analyses indicate that the U–U system (**a**) has complete one-electron transfer but in contrast Np–U(**b**) and Pu–U(**c**) have just half.

Table 2.3 Calculated Hirshfeld charges in complexes **a2**, **b2** and **c2** in Scheme 2.1

Cp_3An	U^{III}	0.4514	Np^{III}	0.4145	Pu^{III}	0.3771
complex b	U	0.4649	Np	0.4078	Pu	0.3596
Difference	Δ	0.0135	Δ	-0.0067	Δ	-0.0175
A^{oct}	U^{VI}	0.5243	U^{VI}	0.5243	U^{VI}	0.5243
complex b	U	0.4862	U	0.4969	U	0.5021
Difference	Δ	-0.0381	Δ	-0.0274	Δ	-0.0222

Table 2.4 Calculated spin densities for reactions of complexes **a2**, **b2** and **c2** in Scheme 2.1

Cp_3An	U^{III}	2.7372	Np^{III}	3.8902	Pu^{III}	4.9970
complex b	U	2.0392	Np	3.3900	Pu	4.6396
Difference	Δ	-0.6980	Δ	-0.5002	Δ	-0.3574
A^{oct}	U^{VI}	0.0000	U^{VI}	0.0000	U^{VI}	0.0000
complex b	U	1.0131	U	0.7434	U	0.6327
Difference	Δ	1.0131	Δ	0.7434	Δ	0.6327

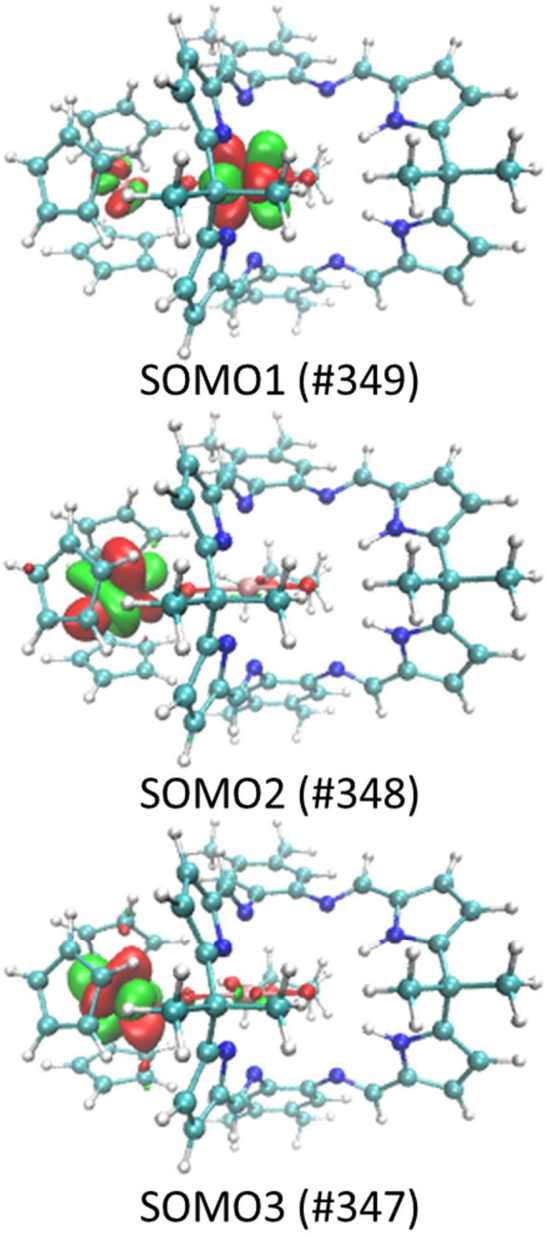

Figure 2.1 SOMOs of complex **a2** [$Cp_3U(UO_2)(THF)(H_2L^{oct})$]

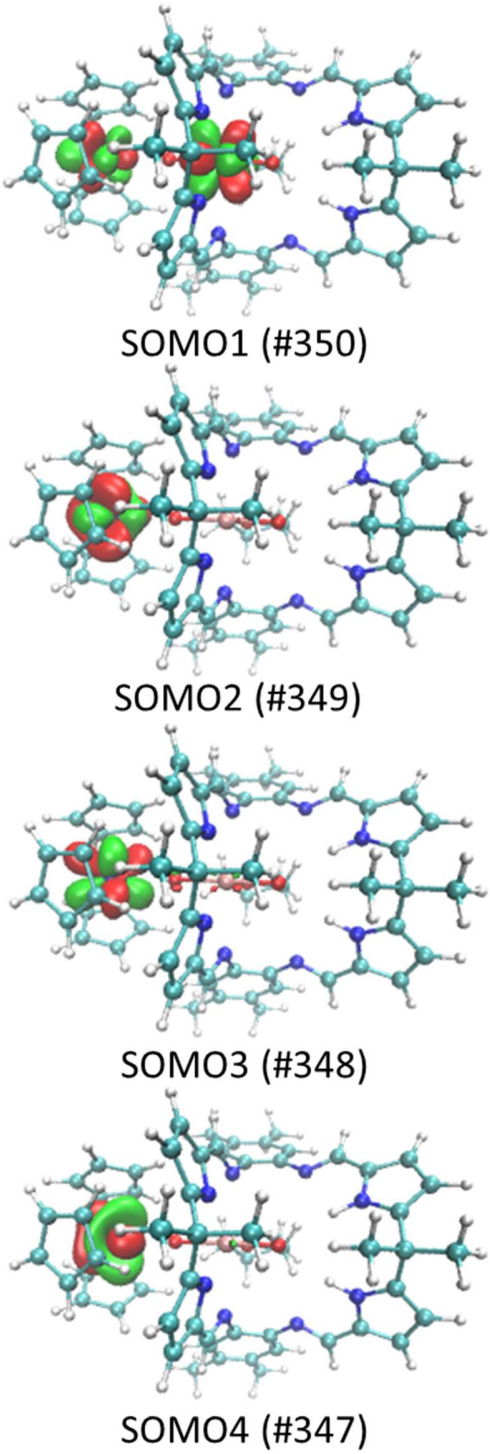

Figure 2.2 SOMOs of complex **b2** [$Cp_3Np(UO_2)(THF)(H_2L^{oct})$]

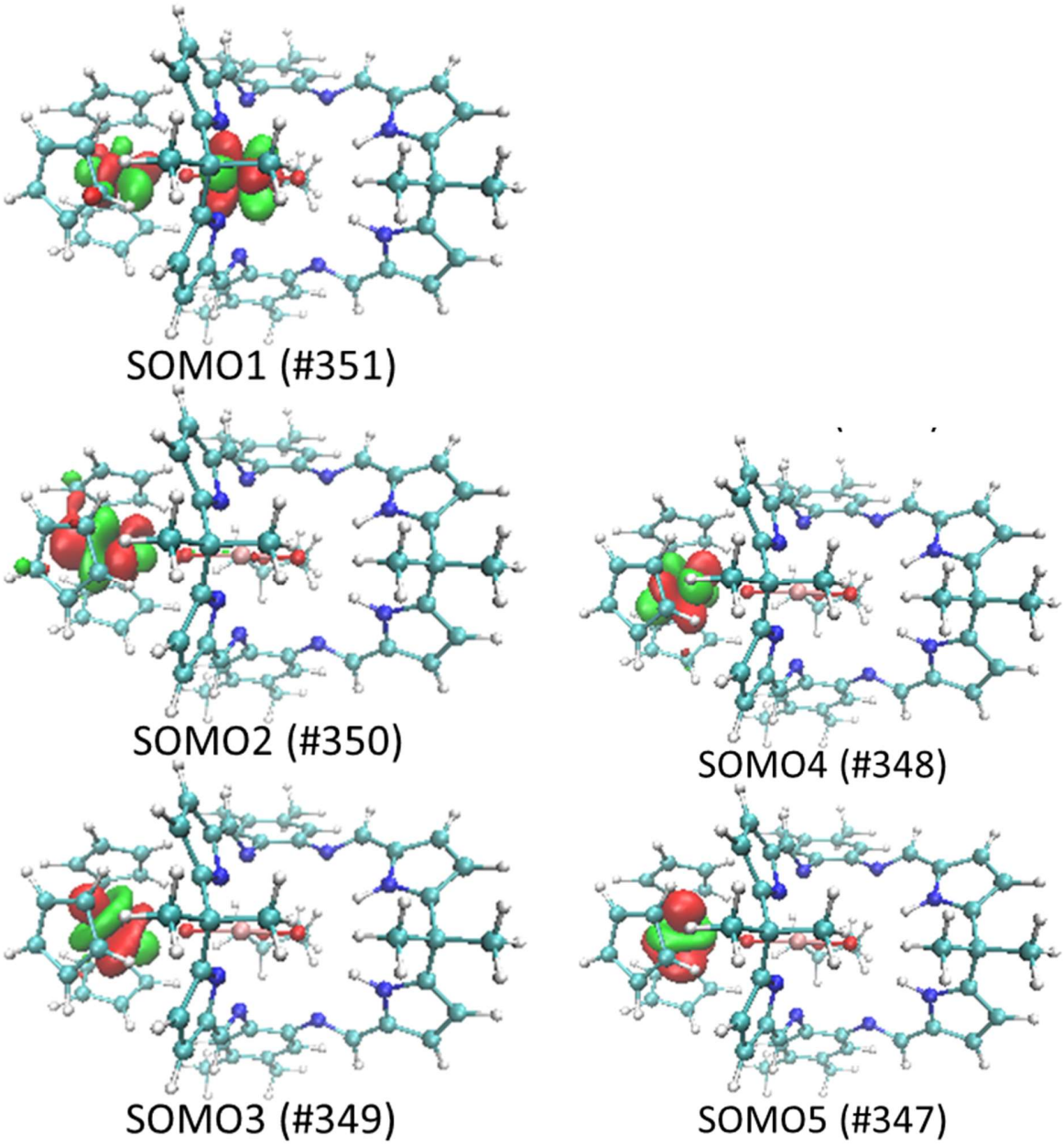

Figure 2.3 SOMOs of complex **c2** [$Cp_3Pu(UO_2)(THF)(H_2L^{oct})$]

An orbital composition analysis, Table 2.5, shows that the three SOMOs in the U–U complex **a₂** have *f* with minor *d* contributions. The Np–U system (**b₂**) is similar but has non-negligible *s* character in a singly occupied orbital which may contribute to the observed paramagnetically shifted ^{1}H NMR spectrum. More importantly in this respect, the spin density on the Cp hydrogen atoms in Table 2.6 is on average twice that of the U system.[76] DFT calculated spin density analyses explain the strongly shifted NMR spectra by spin density contributions at the hydrogen nuclei.

Table 2.5 Orbital composition analysis for SOMOs of complexes **a2**, **b2** and **c2**.[a]

Complex **a2** (U-U)		
Orbital		347
U(139)	5F	93.56%
U(139)	6D	0.50%
Orbital		348
U(139)	5F	92.78%
U(139)	6D	0.78%
Orbital		349
U(138)	5F	91.50%
U(139)	5F	5.98%
Complex **b2** (Np-U)		
Orbital		347
Np(1)	5F	96.06%
Orbital		348
Np(1)	5F	95.81%
Orbital		349
Np(1)	5F	94.67%
Np(1)	6S	2.21%
Orbital		350
Np(1)	5F	31.11%
Np(1)	6D	1.39%
U(2)	5F	63.30%
Complex **c2** (Pu-U)		
Orbital		347
Pu(1)	5F	96.01%
Pu(1)	6S	0.70%
Orbital		348
Pu(1)	5F	96.74%
Orbital		349
Pu(1)	5F	95.88%
Orbital		350
Pu(1)	5F	93.92%
C(138)	2P	0.61%
Orbital		351
Pu(1)	5F	37.84%
Pu(1)	6D	0.54%
U(2)	5F	56.58%
C(112)	2P	0.56%

[a] The atom number corresponds to the optimized gas phase structures in SI of original paper.[77]

Table 2.6 Spin density on nucleus of complexes **a_2**, **b_2** and **c_2**.[a]

Spin density on nuclei pairs of **a_2** (U-U)		
#C,#H	C	H
95,96	-0.00069	0.00054
97,98	-0.00009	0.00042
99,100	-0.00049	0.00028
101,102	-0.00038	0.00060
103,104	-0.00021	0.00033
105,106	-0.00024	0.00034
107,108	-0.00052	0.00044
109,110	-0.00022	0.00039
111,112	-0.00054	0.00036
113,114	-0.00016	0.00024
115,116	-0.00030	0.00044
117,118	-0.00026	0.00060
119,120	-0.00004	0.00027
121,122	-0.00066	0.00037
123,124	-0.00038	0.00032
avg.	-0.00034	0.00040
Spin density on nuclei pairs of **b_2** (Np-U)		
#C,#H	C	H
110,111	-0.00082	0.00099
112,113	-0.00022	0.00066
114,115	-0.00110	0.00087
116,117	-0.00044	0.00073
118,119	-0.00092	0.00079
120,121	-0.00086	0.00072
122,123	-0.00087	0.00090

124,125	-0.00016	0.00057
126,127	-0.00111	0.00080
128,129	-0.00049	0.00064
130,131	-0.00108	0.00074
132,133	-0.00022	0.00058
134,135	-0.00080	0.00097
136,137	-0.00084	0.00071
138,139	-0.00043	0.00063
avg.	-0.00069	0.00075

Spin density on nuclei pairs of **C_2** (Pu-U)

#C,#H	C	H
110,111	-0.00140	0.00124
112,113	-0.00015	0.00102
114,115	-0.00232	0.00121
116,117	-0.00024	0.00075
118,119	-0.00133	0.00097
120,121	-0.00139	0.00091
122,123	-0.00089	0.00095
124,125	-0.00032	0.00085
126,127	-0.00170	0.00100
128,129	-0.00028	0.00071
130,131	-0.00209	0.00103
132,133	-0.00025	0.00078
134,135	-0.00094	0.00108
136,137	-0.00157	0.00088
138,139	-0.00019	0.00069
avg.	-0.00100	0.00094

[a] The atom number corresponds to the optimized gas phase structures in SI of original paper. [77]

2.3.2. Bonding between uranyl(v) and metal cations from groups 1, 2, 4, and 12 Mediated by the Oxo Group

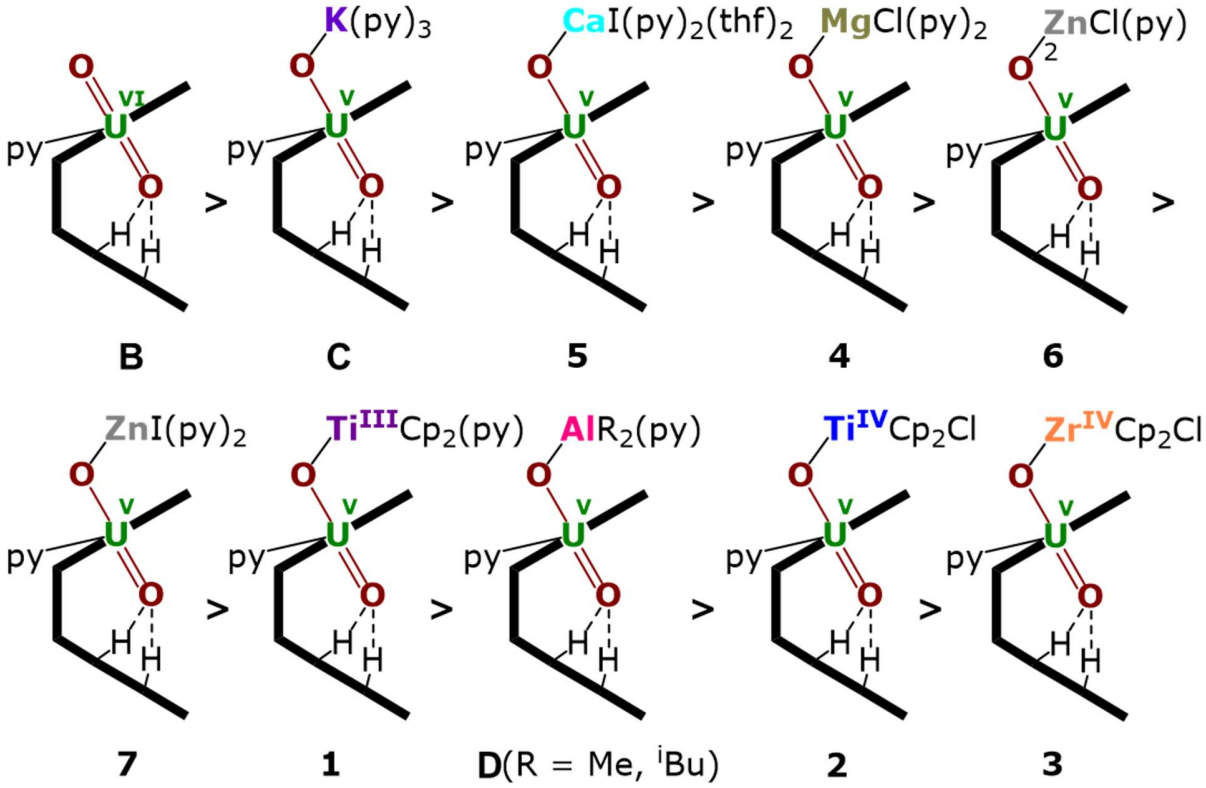

Figure 2.4 Uranyl Pacman complexes in order of decreasing bond strength of the exogenous uranyl-oxygen bond.

Gas phase geometry optimizations were carried on for the complexes which were synthesised experimentally (see Figure 2.4). The calculated structures are in good agreement with the experimental X-ray data in each case. Formal charges, spin densities and the bond orders were calculated on the basis of these gas-phase electronic structure calculations. QTAIM can be a very useful tool to evaluate, at least in a comparative manner, ionicity and covalency of bonds in *f*-element organometallic complexes. Further investigation using QTAIM allows the Bond Critical Points (BCPs) of the metalated uranyl to be determined, with the contour line diagrams of the Laplacian of the electron density ($\nabla^2\rho$) (Figure 2.5, right) giving more general information about the chemical bonds. One should however bear in mind that QTAIM can fail by placing the BCP

in the wrong position.[78] As the $\nabla^2\rho$ diagram shows, all BCPs are in reasonable positions and the values of the Laplacian in the areas between U, O, and Zn atoms are all positive. The positive $\nabla^2\rho$ values of the BCPs in the QTAIM indicate that all of the M-O bonds are largely ionic. However, this criterion is not sufficient for heavy atoms[79, 80] and multiple bonds.[81] In this case, the Laplacian of ρ is not a good indicator for the covalent or ionic character of U-O bonds. However, we can conclude from the positive $\nabla^2\rho$ values that the M-O bonds are very ionic.

The energy density (H) at the BCP suggests that U-O is a covalent bond (H < 0) and M-O is an ionic bond (H > 0). The degree of covalency of the U-O bonds can be characterised by the electron density (ρ) and energy density (H) at the BCP. Higher (absolute) values of ρ and H indicate greater covalency. The absolute values of ρ and H in the O_{exo}-M bond for M = Mg, Ca, ZnCl and ZnI are collated in Tables 2.7. These, and the computed values for the other complexes (see Tables A2.1 – A2.4) suggest a tendency of decreasing strength of the U-O_{exo} bonding in the order **B** > **C** (K) > **5** (Ca) > **4** (Mg) > **6** (ZnCl) > **7** (ZnI) > **1** (Ti^{III}) > **D** (Al) > **2** (Ti^{IV}) > **3** (Zr) (Figure 2.4).

Table 2.7 Computed properties of selected bonds in compounds **4 – 7**

Metric	**4** (Mg)	**5** (Ca)	**6** (ZnCl)	**7** (ZnI)
U-O_{exo} bond length (Å)	1.941	1.925	1.944	1.949
O_{exo}-M bond length (Å)	1.940	2.324	1.918	1.924
U-O_{exo} bond order	1.642	1.750	1.704	1.699
O_{exo}-M bond order	0.643	0.540	0.599	0.599
ρ of U-O_{exo} bond	0.190	0.201	0.183	0.180
ρ of O_{exo}-M bond	0.050	0.036	0.090	0.089
Hirshfeld charge on U	0.450	0.455	0.439	0.438
EDA of U-O bond, eV	**4** (Mg)	**5** (Ca)	**6** (ZnCl)	**7** (ZnI)
Orbital interaction	-11.87	-13.56	-11.50	-11.30
Electrostatic interaction	-12.08	-13.23	-11.43	-11.29

Likewise, the smallest bond order for the U-O_{exo} bond is calculated for **3** (Zr) at 1.382 and is largest for **C** (K) with a value of 2.224 (Table 3.1). The Mayer and Mulliken bond order analyses (Table 2.7 and Table A2.3) further confirm the reduction in the uranyl UO bond order for all the uranyl(V) complexes compared to uranyl(VI) **B**, while the calculated charges and spin densities (Table A2.4) further support the correct assignment of the uranyl(V) oxidation state.

The Electron Localisation Function (ELF)[82-84] is a complementary tool that indicates the ionic character of the bonds in 3D space and demonstrates clearly that there is almost no electron density between the O and Zn atoms as well as O and U atoms (Figure 2.5, left). For comparison, a very high electron density is visible between the C and N atoms in the coordinated pyridine, which shows typical dative covalent bonds. The QTAIM and ELF diagrams do not show electron density between U-O because uranium is very heavy and has a large radius; as such the bonding area will cover a large region and is "diluted". However, these maps show very clear ionic character for the M-O bond. The electron density difference graphs (for example, Figure A2.5) shows clear electron density increases during formation of the U-O bonds. Furthermore, the electron density difference graph indicates that the formation of the Ca-O bond greatly weakens the electron density between U-O_{exo} which reduces the overlap – or, in other words, the covalency. This supports the above conclusions drawn from electron density (ρ) and energy density (H) at the BCP.

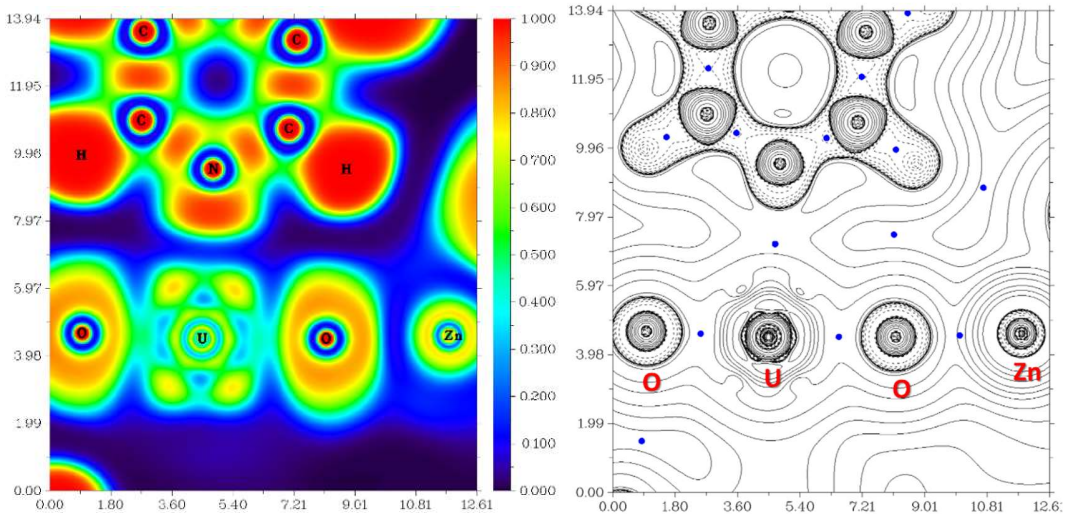

Figure 2.5 Electron Localisation Function (ELF) diagram (left) and $\nabla^2\rho$ contour line diagram (right) of the (py)OUO-Zn fragment in complex **6** (ZnCl) (Length unit: Bohr) The value of ELF is given by the colour scale. For the$\nabla^2\rho$ diagram, blue points are BCPs, solid lines and dotted lines represent positive and negative values of the Laplacian of the electron density.

The formal charges of the uranium atom in **1** to **7** were calculated in Table A2.4, which agree well with HR-XANES data (see below). However, usually, a higher calculated partial atomic charge on the U atom is indicative of an increased ionic contribution to the bonding. The highest value is seen for the Ca complex **5**, with lower values for the alkaline earth compound **4** (Mg) and for the zinc compounds **6** (ZnCl) and **7** (ZnI). This suggests that the ionic interactions of U-O_{exo} bond in these compounds follow the order of **5** > **4** > **6** ≥ **7**. The bond lengths of U-O_{exo} suggest stronger bonds in the Ca (**5**) and Mg (**4**) adducts than in the Zn adducts (**6** and **7**) in Table 2.7. The spin densities in Table A2.4 show that the uranium has the same oxidation state in all of these compounds. Thus, the ionic interaction becomes weaker when the bond becomes longer, which are dominated by the reduced U-O_{exo} covalency. The QTAIM values show that the covalent contribution to the U-O_{exo} bonding is also greater in the alkaline earth (Ae) than the Zn complexes. However, the QTAIM values show there is more covalent character in the O_{exo}-Zn bonding than the O_{exo}-Ae bonding.

Additionally, the DFT calculated interatomic interaction energies in the U^{V}-O_{exo} bonds have been analysed using EDA,[47, 85, 86] in which the orbital interaction terms can be interpreted as covalent contributions. Both EDA (Table 2.7, see computational procedures in Appendix 2 for more details) and orbital mixing (Table A2.6) directly support the QTAIM results. This indicates that ionic character and covalent contributions are correlated: Stronger ionic character shortens bond lengths leading to improved orbital overlap, and vice versa. Although the absolute values of the ionic interactions show the same tendency as the covalency, the orbital contribution of U-O bonding (Tables A2.4-A2.6) suggest that the total polarization increases as follows: **5** (Ca) = **4** (Mg) < **6** (ZnCl) = **7** (ZnI), which means the overall covalency follows the trend **5** (Ca) > **4** (Mg) > **6** (ZnCl) = **7** (ZnI).

The computational methods also allow a study of the nature of the hydrogen bonding between the *endo*-uranyl oxo atom and the two lower pocket pyrrole N-H atoms, and whether this is affected by the increased oxo basicity of the uranyl(V).[87, 88] Hydrogen bonds can be categorised as "strong" or "strongly covalent" (D···A 2.2 – 2.5 Å), "moderate" or "mostly electrostatic" (D···A 2.5 – 3.2 Å) and "weak" or electrostatic/ dispersion (D···A 3.2 – 4.0 Å)[89] The properties of the BCPs of these bonds for both the uranyl(VI) complex **B** and the uranyl(V) complexes **C**, and **1** to **7** were determined in the gas-phase using QTAIM (Table A2.2 and Figure A2.3).

The presence of hydrogen bonding for the pyrrole N-H···O1, as well as of the methyl C-H···O1, is supported by the values of the electron density ρ and the Laplacian $\nabla^2\rho$ which lie within characteristic ranges;[89] the electron density of N-H···O1 is about one order of magnitude smaller than that seen for a covalent bond. While both the N-H···O1 and C-H···O1 interactions can be classified as hydrogen bonds, no significant difference is seen between uranyl(VI) and uranyl(V) complexes so their relative strength cannot be determined computationally.[90] However, according

to the computed and experimental bond distances, the hydrogen bonds of the pyrrole rings to the uranyl oxygen (N-H···O1) can be classified as moderate strength hydrogen bonds. The interaction between the methyl hydrogen atoms (C-H···O1) is classified as weak. (Table A2.7) Thus, both hydrogen bonds "protect" the endogenous uranyl oxygen and presumably attenuate any uranyl oxo-functionalisation in the lower macrocyclic pocket.

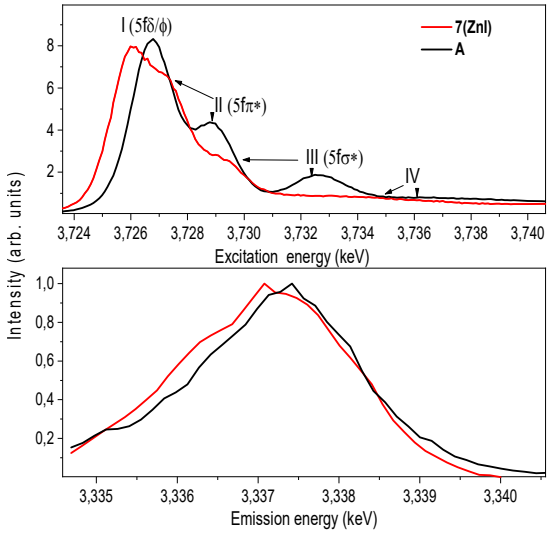

Figure 2.6 Experimental uranium M_4 edge HR-XANES (top) and resonant X-ray emission (RXES) (bottom) spectra of complexes **7** (ZnI) and **B**. The RXES are measured at excitation energies corresponding to the maximum intensity of the first peak (I) of the respective HR-XANES spectrum.

The U M_4 edge HR-XANES spectrum (Figure 2.6) describes the U 5*f* unoccupied density of states in the presence of a $3d_{3/2}$ core-hole. Due to the dipole selection rule $\Delta l = \pm 1$, $\Delta s = 0$, absorption is seen when electrons are excited from the $3d_{3/2}$ orbitals of U to lowest unoccupied valence orbitals that have substantial U *f* contributions. The energy position of the absorption edge is therefore sensitive to the level of screening of the $3d_{3/2}$ core-hole by the electron density in the vicinity of the uranium atom. The linear structure of uranyl(VI) leads to the U valence orbitals being most usefully described in terms of their δ, ϕ, π^* or σ^* character with respect to rotation

about the U−O *z*-axis. The δ and ϕ are the lowest unoccupied orbitals, and are essentially non-bonding orbitals, whereas the π^*, σ^* are anti-bonding orbitals with predominant U 5*f* character. The U M_4 edge HR-XANES spectra of the uranyl(VI) complex **B** and the uranyl(V) complex **7** (ZnI) were recorded by our collaborators and the peaks marked with I, II, III were assigned previously to electronic transitions to the $5f\delta/\phi$, $5f\pi^*$, and $5f\sigma^*$ orbitals, respectively, for uranyl(VI) by DFT calculations. This assignment of the spectral peaks is valid also for the uranyl(V) and uranyl(VI) complexes investigated here (Figure A2.2). DFT ground-state calculations were also undertaken to determine which atomic orbital and unoccupied molecular orbitals contain appreciable U 5*f* character for **B** and **7** (ZnI) using the Priroda code (Figure A2.2). The Mulliken and Ros-Schuit (SCPA) orbital population analyses report differences of less than 5% for the low energy orbitals, which increases for orbitals with energies higher than -1 eV. Nevertheless, the results are consistent.

The HR-XANES spectra provide insights into the covalency of the uranyl bond driven by orbital overlap; the classical definition of this bond covalency is the accumulation of charge in the midpoint of the bond.[40] The strong filled-filled interaction due to the large overlap of O 2*p* with U 6*p* orbitals, which are hybridised with U 5*f* in the σ bonding orbital, leads to a vertical shift of the σ^* orbital compared to the δ/ϕ non-bonding orbitals.[91] The effect has been described as "pushing from below".[2, 91-96] The energy shift of the II (π^*) and III peaks (σ^*) with respect to the I (δ/ϕ) peak is much smaller for **7** (ZnI) (I-II ≈ 1.4 eV, I-III ≈ 3.6 eV) compared to **B** (I-II ≈ 2.2 eV, II-III ≈ 5.7 eV) (cf. Figure 2.6 and Table A2.2), which indicates a weaker filled-filled interaction and therefore a reduction of the U-O bond covalency for **7** (ZnI).[39, 42, 44] Based on all experimental and theoretical evidence we conclude that there is an orbital overlap driven reduction of U-O_{exo} covalency for **7** (ZnI) compared to **B**.

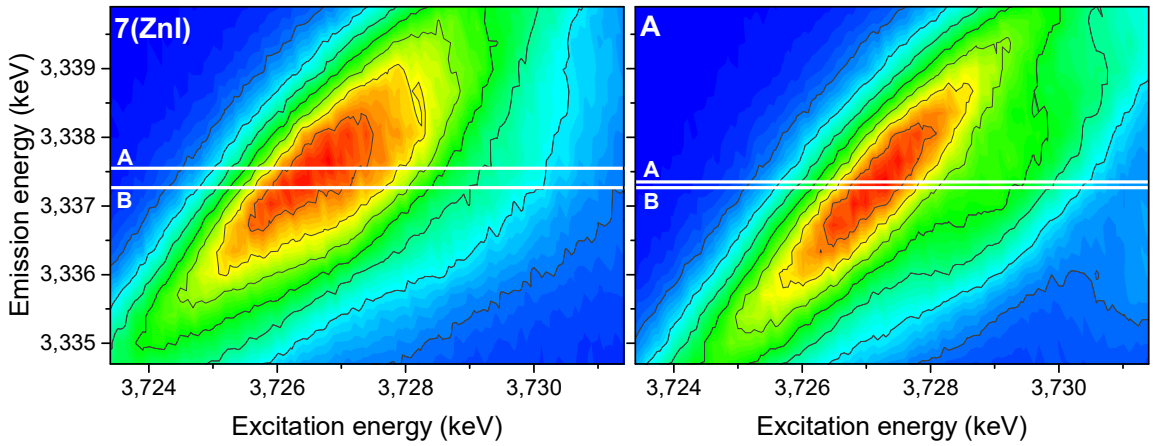

Figure 2.7 U 3d4f RIXS spectra of complexes **7** (ZnI) and **B**. Lines A and B mark the energy positions of the maximum intensity of the resonant and normal emission, respectively.

The analyses of the experimental U 3*d*4*f* RIXS maps for **7** (ZnI) and **B** provide additional insights (Figure 2.7). The energy shift between the resonant and normal emission maxima is approximately 0.28 ± 0.02 eV for **7**, and 0.08 ± 0.02 eV for **B** (energy shift between lines A and B in Figure 3.11). As previously illustrated,[97] this energy shift can be used as a relative measure of the level of localisation of the U 5*f* orbitals and suggests that the U 5*f* orbitals are more contracted in the uranyl(V) compound **7** compared to the uranyl(VI) compound **B**. Calculations for U(V)-yl and U(VI)-yl considering only the axial U-O bond also indicate a slight contraction of the sigma bonding orbital for uranyl(V) compared to uranyl(VI) (See Figure A2.4: Normally, reducing the uranyl from oxidation state VI to V leads to a greater delocalisation of the 5*f* orbitals.[91])The RIXS results for the 5*f* orbitals appears to offer a new tool for estimating the energy-degeneracy driven covalency of the actinide-oxygen bond.[40, 91] As a consequence of the lowering in energy of the 5*f* orbitals to closer alignment with the oxygen AOs, the energy-degeneracy driven covalency of the U-O bond appears to have a stronger contribution for the uranyl(V) complex compared to the uranyl(VI) complex **B**. This notion needs to be further verified in the future by comparing experimental and computational results for suitable U systems.

2.4. Conclusions

The first reduction of the uranyl dication by another actinide complex, and the first use of a redox reaction to generate a heterobimetallic transuranic complex were reported in the first paper.[77] For the more reducing An^{III} ions the oxo group provides a capable bridge between the two actinide cations. To conclude, in this chapter, although there is some disagreement between techniques as to the formal oxidation states, in combination they and theoretical calculations show that the extent of electron transfer to the uranyl is U>Np>Pu. A strong donor–acceptor interaction, or perhaps even non-integral formal oxidation states for Np and U, are probably most appropriate for **b**. Somewhat surprisingly, any interaction between the Pu^{III} and U^{VI} is too weak to be observed in the presence of coordinating THF solvent, and calculated free energies suggest that the reaction is unlikely to happen. Characterizing paramagnetic actinide complexes with complicated electronic structures is very challenging even with modern techniques, and at first glance the classical interpretations of the data give contradictory pictures. However, we have shown how a satisfying electronic structure can be defined by a combined experimental and computational analysis. This new synthetic route should provide opportunities for new uranyl functionalization with other *f*-block metal cations to form other unusual and potentially interesting *f*-electron behaviors.

Then, we have further theoretically investigated the systems of mono-oxo-metallated uranyl(V) complexes, which were reduced from uranyl(VI) successfully by group 1, group 2, group 4, and group 12 metals and organometallic reagents by our experimental collaborators. The experimental results show that single electron reduction with a Ti(II) synthon leads to a f^1-d^1 system, and the reduction using an unusual procedure involving a combination of a group 2 or 12 metal and its respective metal halide allows the straightforward synthesis of Mg, Ca, and Zn -

uranyl(V) complexes **4** to **7**. The experimental work from our collaborators shows it is possible to incorporate Cs^+ cations into a uranyl framework under reducing conditions, and that strikingly different coordination modes are possible for these most polarisable group 1 cations compared with the lighter group 1 congeners. Theoretical calculations in this chapter using QTAIM and other methods verify the assignment of the uranyl(V) oxidation state and help classify the strength of hydrogen bonding in the lower macrocyclic pocket as moderate, which is supported by the strong paramagnetic effect on the chemical shifts of the two pyrrolic NH hydrogens.

The covalency of the U-O bond in uranyl(V) complexes can be manipulated experimentally by varying the identity of the metal that binds to the uranyl *exo*-oxo group. The U M_4 edge HR-XANES are used for the first time by our experimental collaborators to provide insight into the covalency of the uranyl(V) bonding driven by orbital overlap. Combined with our quantum chemical studies, the results show there is an orbital overlap driven reduction of U-O covalency for **7** (ZnI) compared to **B**. The parent uranyl(VI) complex **B** has more delocalized 5*f* orbitals than for the U(V) complex **7** as suggested by 3*d*4*f* RIXS and computations. The BCP analyses show greater electron density between the U and O_{exo} for Ae complexes **4**/**5** and more covalent O-Zn bonding for the Zn complexes **6** and **7**. Thus, the O_{exo}-M bonds follow the opposite trend to the U-O_{exo} bond, and the O_{exo}-Zn bonds have a larger covalent contribution compared to the Mg-O_{exo}/Ca-O_{exo} bonds. The U M_4 edge HR-XANES and RIXS have high potential for detailed investigations of the uranium valence orbitals with *f* character and their interaction with ligand valence orbitals. The results contribute fundamentally to our understanding and tailoring of the reduction mechanisms of uranyl on an electronic and structural level.

To conclude, in this chapter, the synergy of experimental spectroscopies and theoretical calculations has proven to be a powerful tool for understanding the bonding nature of actinide

complexes. However, it also underscores the necessity for ongoing verification of these findings through the comparison of enhanced experimental data and more advanced computational results in the future.

2.5. References

1. Polly, L. A.; Jason, B. L.; Dipti, P., Pentavalent uranyl complexes. *Coordination Chemistry Reviews* **2009,** *253* (15), 1973-1978.
2. Denning, R. G., Electronic Structure and Bonding in Actinyl Ions and their Analogs. *The Journal of Physical Chemistry A* **2007,** *111* (20), 4125-4143.
3. Wander, M. C. F.; Shuford, K. L., A theoretical study of the qualitative reaction mechanism for the homogeneous disproportionation of pentavalent uranyl ions. *Geochimica et Cosmochimica Acta* **2012,** *84*, 177-185.
4. Steele, H.; Taylor, R. J., A Theoretical Study of the Inner-Sphere Disproportionation Reaction Mechanism of the Pentavalent Actinyl Ions. *Inorganic Chemistry* **2007,** *46* (16), 6311-6318.
5. Vlaisavljevich, B.; Miró, P.; Ma, D.; Sigmon, G. E.; Burns, P. C.; Cramer, C. J.; Gagliardi, L., Synthesis and Characterization of the First 2 D Neptunyl Structure Stabilized by Side-on Cation–Cation Interactions. *Chemistry – A European Journal* **2013,** *19* (9), 2937-2941.
6. Natrajan, L.; Burdet, F.; Pécaut, J.; Mazzanti, M., Synthesis and Structure of a Stable Pentavalent-Uranyl Coordination Polymer. *Journal of the American Chemical Society* **2006,** *128* (22), 7152-7153.
7. Nocton, G.; Horeglad, P.; Pécaut, J.; Mazzanti, M., Polynuclear Cation−Cation Complexes of Pentavalent Uranyl: Relating Stability and Magnetic Properties to Structure. *Journal of the American Chemical Society* **2008,** *130* (49), 16633-16645.
8. Berthet, J.-C.; Nierlich, M.; Ephritikhine, M., Isolation of a Uranyl [UO2]+ Species: Crystallographic Comparison of the Dioxouranium(V) and (VI) Compounds [UO2(OPPh3)4](OTf)n (n=1, 2). *Angewandte Chemie International Edition* **2003,** *42* (17), 1952-1954.
9. Arnold, P. L.; Hollis, E.; White, F. J.; Magnani, N.; Caciuffo, R.; Love, J. B., Single-Electron Uranyl Reduction by a Rare-Earth Cation. *Angewandte Chemie International Edition* **2011,** *50* (4), 887-890.
10. Chatelain, L.; Mougel, V.; Pécaut, J.; Mazzanti, M., Magnetic communication and reactivity of a stable homometallic cation–cation trimer of pentavalent uranyl. *Chemical Science* **2012,** *3* (4), 1075-1079.
11. Brown, J. L.; Wu, G.; Hayton, T. W., Oxo Ligand Silylation in a Uranyl β-Ketoiminate Complex. *Journal of the American Chemical Society* **2010,** *132* (21), 7248-7249.
12. Schnaars, D. D.; Wu, G.; Hayton, T. W., Borane-Mediated Silylation of a Metal–Oxo Ligand. *Inorganic Chemistry* **2011,** *50* (11), 4695-4697.
13. Arnold, P. L.; Jones, G. M.; Odoh, S. O.; Schreckenbach, G.; Magnani, N.; Love, J. B., Strongly coupled binuclear uranium–oxo complexes from uranyl oxo rearrangement and reductive silylation. *Nature Chemistry* **2012,** *4* (3), 221-227.

14. Arnold, P. L.; Pécharman, A.-F.; Lord, R. M.; Jones, G. M.; Hollis, E.; Nichol, G. S.; Maron, L.; Fang, J.; Davin, T.; Love, J. B., Control of Oxo-Group Functionalization and Reduction of the Uranyl Ion. *Inorganic Chemistry* **2015,** *54* (7), 3702-3710.
15. Arnold, P. L.; Pécharman, A.-F.; Hollis, E.; Yahia, A.; Maron, L.; Parsons, S.; Love, J. B., Uranyl oxo activation and functionalization by metal cation coordination. *Nature Chemistry* **2010,** *2* (12), 1056-1061.
16. Pedrick, E. A.; Wu, G.; Hayton, T. W., Reductive Silylation of the Uranyl Ion with Ph3SiOTf. *Inorganic Chemistry* **2014,** *53* (23), 12237-12239.
17. Jones, G. M.; Arnold, P. L.; Love, J. B., Oxo–Group-14-Element Bond Formation in Binuclear Uranium(V) Pacman Complexes. *Chemistry – A European Journal* **2013,** *19* (31), 10287-10294.
18. Chatelain, L.; Walsh, J. P. S.; Pécaut, J.; Tuna, F.; Mazzanti, M., Self-Assembly of a 3d–5f Trinuclear Single-Molecule Magnet from a Pentavalent Uranyl Complex. *Angewandte Chemie International Edition* **2014,** *53* (49), 13434-13438.
19. Arnold, P. L.; Hollis, E.; Nichol, G. S.; Love, J. B.; Griveau, J.-C.; Caciuffo, R.; Magnani, N.; Maron, L.; Castro, L.; Yahia, A.; Odoh, S. O.; Schreckenbach, G., Oxo-Functionalization and Reduction of the Uranyl Ion through Lanthanide-Element Bond Homolysis: Synthetic, Structural, and Bonding Analysis of a Series of Singly Reduced Uranyl–Rare Earth 5f1-4fn Complexes. *Journal of the American Chemical Society* **2013,** *135* (10), 3841-3854.
20. Chatelain, L.; Walsh, J. P.; Pécaut, J.; Tuna, F.; Mazzanti, M., Self‐Assembly of a 3d–5f Trinuclear Single‐Molecule Magnet from a Pentavalent Uranyl Complex. *Angewandte Chemie* **2014,** *126* (49), 13652-13656.
21. Mougel, V.; Chatelain, L.; Pécaut, J.; Caciuffo, R.; Colineau, E.; Griveau, J.-C.; Mazzanti, M., Uranium and manganese assembled in a wheel-shaped nanoscale single-molecule magnet with high spin-reversal barrier. *Nature Chemistry* **2012,** *4* (12), 1011-1017.
22. Rinehart, J. D.; Long, J. R., Exploiting single-ion anisotropy in the design of f-element single-molecule magnets. *Chemical Science* **2011,** *2* (11), 2078-2085.
23. Arnold, P. L., Uranium-mediated activation of small molecules. *Chemical Communications* **2011,** *47* (32), 9005-9010.
24. Nelson, A.-G. D.; Bray, T. H.; Albrecht-Schmitt, T. E., Capitalizing on Differing Coordination Environments and Redox Potentials to Prepare an Ordered Heterobimetallic UVI/NpIV Diphosphonate. *Angewandte Chemie International Edition* **2008,** *47* (33), 6252-6254.
25. Camp, C.; Toniolo, D.; Andrez, J.; Pécaut, J.; Mazzanti, M., A versatile route to homo- and hetero-bimetallic 5f–5f and 3d–5f complexes supported by a redox active ligand framework. *Dalton Transactions* **2017,** *46* (34), 11145-11148.
26. Chatelain, L.; Tuna, F.; Pécaut, J.; Mazzanti, M., Synthesis and SMM behaviour of trinuclear versus dinuclear 3d–5f uranyl(v)–cobalt(ii) cation–cation complexes. *Dalton Transactions* **2017,** *46* (17), 5498-5502.
27. Chatelain, L.; Pécaut, J.; Tuna, F.; Mazzanti, M., Heterometallic Fe2II–UV and Ni2II–UV Exchange-Coupled Single-Molecule Magnets: Effect of the 3 d Ion on the Magnetic Properties. *Chemistry – A European Journal* **2015,** *21* (50), 18038-18042.
28. Zegke, M.; Nichol, G. S.; Arnold, P. L.; Love, J. B., Catalytic one-electron reduction of uranyl (VI) to Group 1 uranyl (V) complexes via Al (III) coordination. *Chemical Communications* **2015,** *51* (27), 5876-5879.
29. Arnold, P. L.; Cowie, B. E.; Suvova, M.; Zegke, M.; Magnani, N.; Colineau, E.; Griveau, J.-C.; Caciuffo, R.; Love, J. B., Axially Symmetric U−O−Ln- and U−O−U-Containing Molecules

from the Control of Uranyl Reduction with Simple f-Block Halides. *Angewandte Chemie International Edition* **2017,** *56* (36), 10775-10779.
30. Hayton, T. W.; Wu, G., Exploring the Effects of Reduction or Lewis Acid Coordination on the U═O Bond of the Uranyl Moiety. *Inorganic Chemistry* **2009,** *48* (7), 3065-3072.
31. Cowie, B. E.; Nichol, G. S.; Love, J. B.; Arnold, P. L., Double uranium oxo cations derived from uranyl by borane or silane reduction. *Chemical Communications* **2018,** *54* (31), 3839-3842.
32. Bell, N. L.; Shaw, B.; Arnold, P. L.; Love, J. B., Uranyl to Uranium(IV) Conversion through Manipulation of Axial and Equatorial Ligands. *Journal of the American Chemical Society* **2018,** *140* (9), 3378-3384.
33. Vitova, T.; Kvashnina, K. O.; Nocton, G.; Sukharina, G.; Denecke, M. A.; Butorin, S. M.; Mazzanti, M.; Caciuffo, R.; Soldatov, A.; Behrends, T.; Geckeis, H., High energy resolution x-ray absorption spectroscopy study of uranium in varying valence states. *Physical Review B* **2010,** *82* (23), 235118.
34. Kvashnina, K. O.; Butorin, S. M.; Martin, P.; Glatzel, P., Chemical State of Complex Uranium Oxides. *Physical Review Letters* **2013,** *111* (25), 253002.
35. Vitova, T.; Denecke, M. A.; Göttlicher, J.; Jorissen, K.; Kas, J. J.; Kvashnina, K.; Prüßmann, T.; Rehr, J. J.; Rothe, J., Actinide and lanthanide speciation with high-energy resolution X-ray techniques. *Journal of Physics: Conference Series* **2013,** *430* (1), 012117.
36. Vitova, T.; Green, J. C.; Denning, R. G.; Löble, M.; Kvashnina, K.; Kas, J. J.; Jorissen, K.; Rehr, J. J.; Malcherek, T.; Denecke, M. A., Polarization Dependent High Energy Resolution X-ray Absorption Study of Dicesium Uranyl Tetrachloride. *Inorganic Chemistry* **2015,** *54* (1), 174-182.
37. Y. Podkovyrna , I. P., T. Pruessmann , S. Bahl , J. Göttlicher , A. Soldatov and T. Vitova, Probing Covalency in the UO3 Polymorphs by U M4 edge HR-XANES. In *16th International Conference on X-ray Absorption Fine Structure*, Karlsruhe, 2015.
38. Pidchenko, I.; Heberling, F.; Kvashnina, K. O.; Finck, N.; Schild, D.; Bohnert, E.; Schäfer, T.; Rothe, J.; Geckeis, H.; Vitova, T., Aqueous U(VI) interaction with magnetite nanoparticles in a mixed flow reactor system: HR-XANES study. *Journal of Physics: Conference Series* **2016,** *712* (1), 012086.
39. Bahl, S.; Peuget, S.; Pidchenko, I.; Pruessmann, T.; Rothe, J.; Dardenne, K.; Delrieu, J.; Fellhauer, D.; Jégou, C.; Geckeis, H.; Vitova, T., Pu Coexists in Three Oxidation States in a Borosilicate Glass: Implications for Pu Solubility. *Inorganic Chemistry* **2017,** *56* (22), 13982-13990.
40. Vitova, T.; Pidchenko, I.; Fellhauer, D.; Bagus, P. S.; Joly, Y.; Pruessmann, T.; Bahl, S.; Gonzalez-Robles, E.; Rothe, J.; Altmaier, M.; Denecke, M. A.; Geckeis, H., The role of the 5f valence orbitals of early actinides in chemical bonding. *Nature Communications* **2017,** *8* (1), 16053.
41. Pidchenko, I.; Kvashnina, K. O.; Yokosawa, T.; Finck, N.; Bahl, S.; Schild, D.; Polly, R.; Bohnert, E.; Rossberg, A.; Göttlicher, J.; Dardenne, K.; Rothe, J.; Schäfer, T.; Geckeis, H.; Vitova, T., Uranium Redox Transformations after U(VI) Coprecipitation with Magnetite Nanoparticles. *Environmental Science & Technology* **2017,** *51* (4), 2217-2225.
42. Vitova, T.; Pidchenko, I.; Biswas, S.; Beridze, G.; Dunne, P. W.; Schild, D.; Wang, Z.; Kowalski, P. M.; Baker, R. J., Dehydration of the Uranyl Peroxide Studtite, [UO2(η2-O2)(H2O)2]·2H2O, Affords a Drastic Change in the Electronic Structure: A Combined X-ray Spectroscopic and Theoretical Analysis. *Inorganic Chemistry* **2018,** *57* (4), 1735-1743.

43. Popa, K.; Prieur, D.; Manara, D.; Naji, M.; Vigier, J.-F.; Martin, P. M.; Dieste Blanco, O.; Scheinost, A. C.; Prüßmann, T.; Vitova, T.; Raison, P. E.; Somers, J.; Konings, R. J. M., Further insights into the chemistry of the Bi–U–O system. *Dalton Transactions* **2016,** *45* (18), 7847-7855.
44. Bader, R. F. W.; Bader, R. F., *Atoms in Molecules: A Quantum Theory*. Clarendon Press: 1990.
45. Bader, R. F. W., A Bond Path: A Universal Indicator of Bonded Interactions. *The Journal of Physical Chemistry A* **1998,** *102* (37), 7314-7323.
46. Ziegler, T.; Rauk, A., On the calculation of bonding energies by the Hartree Fock Slater method: I. The transition state method. *Theoretica chimica acta* **1977,** *46*, 1-10.
47. Morokuma, K., Molecular orbital studies of hydrogen bonds. III. C= O··· H–O hydrogen bond in H2CO··· H2O and H2CO··· 2H2O. *The Journal of Chemical Physics* **1971,** *55* (3), 1236-1244.
48. Arnold, P. L.; Farnaby, J. H.; White, R. C.; Kaltsoyannis, N.; Gardiner, M. G.; Love, J. B., Switchable π-coordination and C–H metallation in small-cavity macrocyclic uranium and thorium complexes. *Chemical Science* **2014,** *5* (2), 756-765.
49. Arnold, P. L.; Turner, Z. R.; Kaltsoyannis, N.; Pelekanaki, P.; Bellabarba, R. M.; Tooze, R. P., Covalency in CeIV and UIV Halide and N-Heterocyclic Carbene Bonds. *Chemistry – A European Journal* **2010,** *16* (31), 9623-9629.
50. King, D. M.; Tuna, F.; McInnes, E. J. L.; McMaster, J.; Lewis, W.; Blake, A. J.; Liddle, S. T., Isolation and characterization of a uranium(VI)–nitride triple bond. *Nature Chemistry* **2013,** *5* (6), 482-488.
51. Tassell, M. J.; Kaltsoyannis, N., Covalency in AnCp4 (An = Th–Cm): a comparison of molecular orbital, natural population and atoms-in-molecules analyses. *Dalton Transactions* **2010,** *39* (29), 6719-6725.
52. Kirker, I.; Kaltsoyannis, N., Does covalency really increase across the 5f series? A comparison of molecular orbital, natural population, spin and electron density analyses of AnCp3 (An = Th–Cm; Cp = η5-C5H5). *Dalton Transactions* **2011,** *40* (1), 124-131.
53. Saleh, L. M. A.; Birjkumar, K. H.; Protchenko, A. V.; Schwarz, A. D.; Aldridge, S.; Jones, C.; Kaltsoyannis, N.; Mountford, P., Group 3 and Lanthanide Boryl Compounds: Syntheses, Structures, and Bonding Analyses of Sc−B, Y−B, and Lu−B σ-Coordinated NHC Analogues. *Journal of the American Chemical Society* **2011,** *133* (11), 3836-3839.
54. Brown, J. L.; Fortier, S.; Wu, G.; Kaltsoyannis, N.; Hayton, T. W., Synthesis and Spectroscopic and Computational Characterization of the Chalcogenido-Substituted Analogues of the Uranyl Ion, [OUE]2+ (E = S, Se). *Journal of the American Chemical Society* **2013,** *135* (14), 5352-5355.
55. Jones, M. B.; Gaunt, A. J.; Gordon, J. C.; Kaltsoyannis, N.; Neu, M. P.; Scott, B. L., Uncovering f-element bonding differences and electronic structure in a series of 1 : 3 and 1 : 4 complexes with a diselenophosphinate ligand. *Chemical Science* **2013,** *4* (3), 1189-1203.
56. Mountain, A. R. E.; Kaltsoyannis, N., Do QTAIM metrics correlate with the strength of heavy element–ligand bonds? *Dalton Transactions* **2013,** *42* (37), 13477-13486.
57. Unterweger, M. P., Half-life measurements at the National Institute of Standards and Technology. *Applied Radiation and Isotopes* **2002,** *56* (1-2), 125-130.
58. Clavaguéra-Sarrio, C.; Vallet, V.; Maynau, D.; Marsden, C. J., Can density functional methods be used for open-shell actinide molecules? Comparison with multiconfigurational spin-orbit studies. *The Journal of Chemical Physics* **2004,** *121* (11), 5312-5321.

59. Shamov, G. A.; Schreckenbach, G., Density Functional Studies of Actinyl Aquo Complexes Studied Using Small-Core Effective Core Potentials and a Scalar Four-Component Relativistic Method. *The Journal of Physical Chemistry A* **2006,** *110* (43), 12072-12072.
60. Perdew, J. P.; Burke, K.; Ernzerhof, M., Generalized gradient approximation made simple. *Phys. Rev. Lett.* **1996,** *77* (18), 3865-3868.
61. Laikov, D. N., Fast evaluation of density functional exchange-correlation terms using the expansion of the electron density in auxiliary basis sets. *Chemical Physics Letters* **1997,** *281* (1-3), 151-156.
62. Laikov, D. N.; Ustynyuk, Y. A., PRIRODA-04: a quantum-chemical program suite. New possibilities in the study of molecular systems with the application of parallel computing. *Russian chemical bulletin* **2005,** *54*, 820-826.
63. Dyall, K. G., An exact separation of the spin-free and spin-dependent terms of the Dirac–Coulomb–Breit Hamiltonian. *The Journal of chemical physics* **1994,** *100* (3), 2118-2127.
64. Lu, T.; CHEN, F.-W., Calculation of molecular orbital composition. *Acta Chimica Sinica* **2011,** *69* (20), 2393.
65. Lu, T.; Chen, F., *J. Comp. Chem.* **2012,** *33*, 580.
66. Te Velde, G. t.; Bickelhaupt, F. M.; Baerends, E. J.; Fonseca Guerra, C.; van Gisbergen, S. J.; Snijders, J. G.; Ziegler, T., Chemistry with ADF. *Journal of Computational Chemistry* **2001,** *22* (9), 931-967.
67. Lenthe, E. v.; Ehlers, A.; Baerends, E.-J., Geometry optimizations in the zero order regular approximation for relativistic effects. *The Journal of Chemical Physics* **1999,** *110* (18), 8943-8953.
68. Lenthe, E. v.; Baerends, E. J.; Snijders, J. G., Relativistic regular two-component Hamiltonians. *The Journal of Chemical Physics* **1993,** *99* (6), 4597-4610.
69. Van Lenthe, E.; Van Leeuwen, R.; Baerends, E.; Snijders, J., Relativistic regular two-component Hamiltonians. *International Journal of Quantum Chemistry* **1996,** *57* (3), 281-293.
70. Lenthe, E. v.; Baerends, E. J.; Snijders, J. G., Relativistic total energy using regular approximations. *The Journal of Chemical Physics* **1994,** *101* (11), 9783-9792.
71. Van Lenthe, E. v.; Snijders, J.; Baerends, E., The zero-order regular approximation for relativistic effects: The effect of spin–orbit coupling in closed shell molecules. *The Journal of chemical physics* **1996,** *105* (15), 6505-6516.
72. Van Lenthe, E.; Baerends, E. J., Optimized Slater-type basis sets for the elements 1–118. *Journal of Computational Chemistry* **2003,** *24* (9), 1142-1156.
73. Hay, P. J.; Martin, R. L.; Schreckenbach, G., *J. Phys. Chem.* **2000,** *104*, 6259.
74. Sonnenberger, D. C.; Gaudiello, J. G., Cyclic voltammetric study of organoactinide compounds of uranium(IV) and neptunium(IV). Ligand effects on the M(IV)/M(III) couple. *Inorganic Chemistry* **1988,** *27* (15), 2747-2748.
75. Berard, J. J.; Schreckenbach, G.; Arnold, P. L.; Patel, D.; Love, J. B., Computational Density Functional Study of Polypyrrolic Macrocycles: Analysis of Actinyl-Oxo to 3d Transition Metal Bonding. *Inorganic Chemistry* **2008,** *47* (24), 11583-11592.
76. J. Autschbach in Annual Reports in Computational Chemistry, Vol. 11 (Ed.:), Elsevier, Dordrecht, 2015, p. 3.
77. Arnold, P. L.; Dutkiewicz, M. S.; Zegke, M.; Walter, O.; Apostolidis, C.; Hollis, E.; Pécharman, A. F.; Magnani, N.; Griveau, J. C.; Colineau, E., Subtle interactions and electron transfer between UIII, NpIII, or PuIII and uranyl mediated by the oxo group. *Angewandte Chemie* **2016,** *128* (41), 12989-12993.

78. Cremer, D.; Kraka, E., Chemical bonds without bonding electron density—does the difference electron-density analysis suffice for a description of the chemical bond? *Angewandte Chemie International Edition in English* **1984,** *23* (8), 627-628.
79. Farrugia, L. J.; Senn, H. M., Metal− metal and metal− ligand bonding at a QTAIM catastrophe: a combined experimental and theoretical charge density study on the alkylidyne cluster Fe3 (μ-H)(μ-COMe)(CO) 10. *The Journal of Physical Chemistry A* **2010,** *114* (51), 13418-13433.
80. Du, J.; Sun, X.; Jiang, G., Exploring the interaction natures in plutonyl (VI) complexes with topological analyses of electron density. *International Journal of Molecular Sciences* **2016,** *17* (4), 414.
81. Vallet, V.; Wahlgren, U.; Grenthe, I., Probing the nature of chemical bonding in uranyl (VI) complexes with quantum chemical methods. *The Journal of Physical Chemistry A* **2012,** *116* (50), 12373-12380.
82. Becke, A. D.; Edgecombe, K. E., A simple measure of electron localization in atomic and molecular systems. *The Journal of chemical physics* **1990,** *92* (9), 5397-5403.
83. Savin, A.; Jepsen, O.; Flad, J.; Andersen, O. K.; Preuss, H.; von Schnering, H. G., Electron Localization in Solid-State Structures of the Elements: the Diamond Structure. *Angewandte Chemie International Edition in English* **1992,** *31* (2), 187-188.
84. Savin, A., The electron localization function (ELF) and its relatives: interpretations and difficulties. *Journal of Molecular Structure: THEOCHEM* **2005,** *727* (1), 127-131.
85. Kitaura, K.; Morokuma, K., A new energy decomposition scheme for molecular interactions within the Hartree-Fock approximation. *International Journal of Quantum Chemistry* **1976,** *10* (2), 325-340.
86. Ziegler, T.; Rauk, A., On the calculation of bonding energies by the Hartree Fock Slater method. *Theoretica chimica acta* **1977,** *46* (1), 1-10.
87. Vallet, V.; Privalov, T.; Wahlgren, U.; Grenthe, I., The mechanism of water exchange in AmO2 (H2O) 52+ and in the isoelectronic UO2 (H2O) 5+ and NpO2 (H2O) 52+ complexes as studied by quantum chemical methods. *Journal of the American Chemical Society* **2004,** *126* (25), 7766-7767.
88. Steiner, T., The hydrogen bond in the solid state. *Angewandte Chemie International Edition* **2002,** *41* (1), 48-76.
89. Popelier, P., Characterization of a dihydrogen bond on the basis of the electron density. *The Journal of Physical Chemistry A* **1998,** *102* (10), 1873-1878.
90. Koch, U.; Popelier, P. L., Characterization of CHO hydrogen bonds on the basis of the charge density. *The Journal of Physical Chemistry* **1995,** *99* (24), 9747-9754.
91. Neidig, M. L.; Clark, D. L.; Martin, R. L., Covalency in f-element complexes. *Coordination Chemistry Reviews* **2013,** *257* (2), 394-406.
92. Dyall, K. G., Bonding and bending in the actinyls. *Molecular Physics* **1999,** *96* (4), 511-518.
93. Pepper, M.; Bursten, B. E., The electronic structure of actinide-containing molecules: a challenge to applied quantum chemistry. *Chemical Reviews* **1991,** *91* (5), 719-741.
94. Tatsumi, K.; Hoffmann, R., Bent cis d0 MoO22+ vs. linear trans d0f0 UO22+: a significant role for nonvalence 6p orbitals in uranyl. *Inorganic Chemistry* **1980,** *19* (9), 2656-2658.
95. Kaltsoyannis, N., Computational Study of Analogues of the Uranyl Ion Containing the −NUN− Unit: Density Functional Theory Calculations on UO22+, UON+, UN2, UO(NPH3)3+,

U(NPH3)24+, [UCl4{NPR3}2] (R = H, Me), and [UOCl4{NP(C6H5)3}]. *Inorganic Chemistry* **2000,** *39* (26), 6009-6017.
96. Kaltsoyannis, N., Covalency hinders AnO2(H2O)+ → AnO(OH)2+ isomerisation (An = Pa–Pu). *Dalton Transactions* **2016,** *45* (7), 3158-3162.
97. Bahl, S.; Peuget, S.; Pidchenko, I.; Pruessmann, T.; Rothe, J. r.; Dardenne, K.; Delrieu, J.; Fellhauer, D.; Jégou, C.; Geckeis, H., Pu coexists in three oxidation states in a borosilicate glass: implications for Pu solubility. *Inorganic Chemistry* **2017,** *56* (22), 13982-13990.

Appendix 2.

A 2.1. Computational procedures and results

Due to the technical requirement of closed-shell fragments imposed by the ADF program, the fragments of [M-O↑↑] and [U-O↓↓] cannot converge properly, and only charged fragments converged, which means that the two fragments are [M-O]2- and [U-O]2+(Figure A3.1). Considering the large ionic character of the bonds, this approach is still reasonable. However, as a consequence these results have qualitative meaning only.

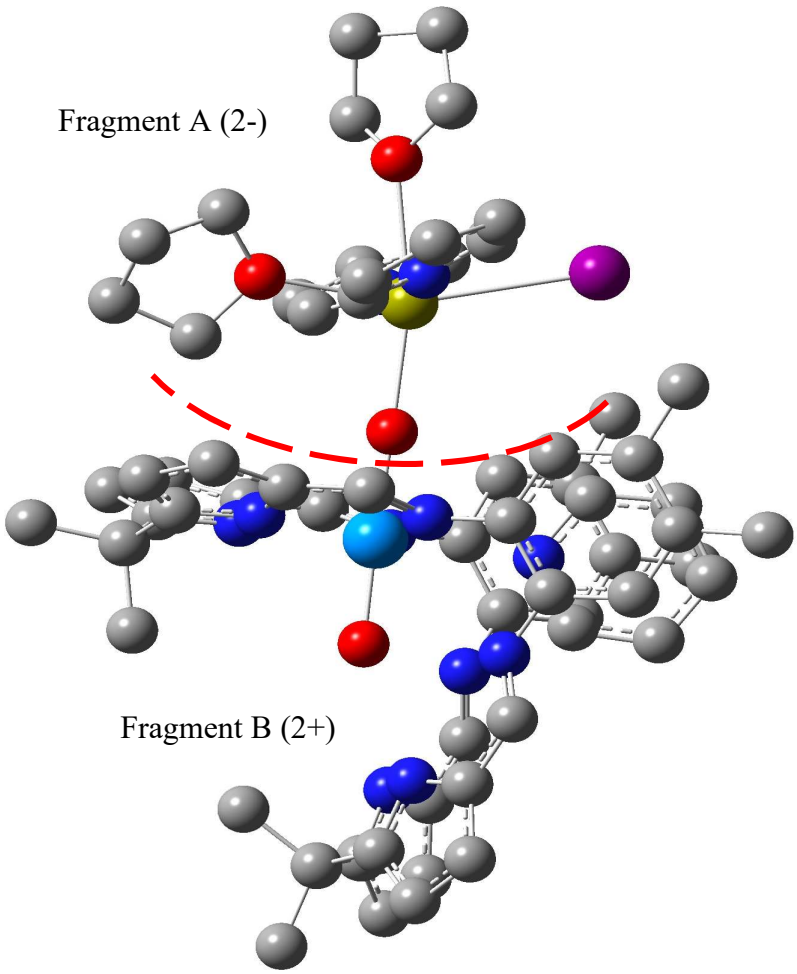

Figure A 2.1 An example of fragments used for EDA. Hydrogen atoms are hidden.

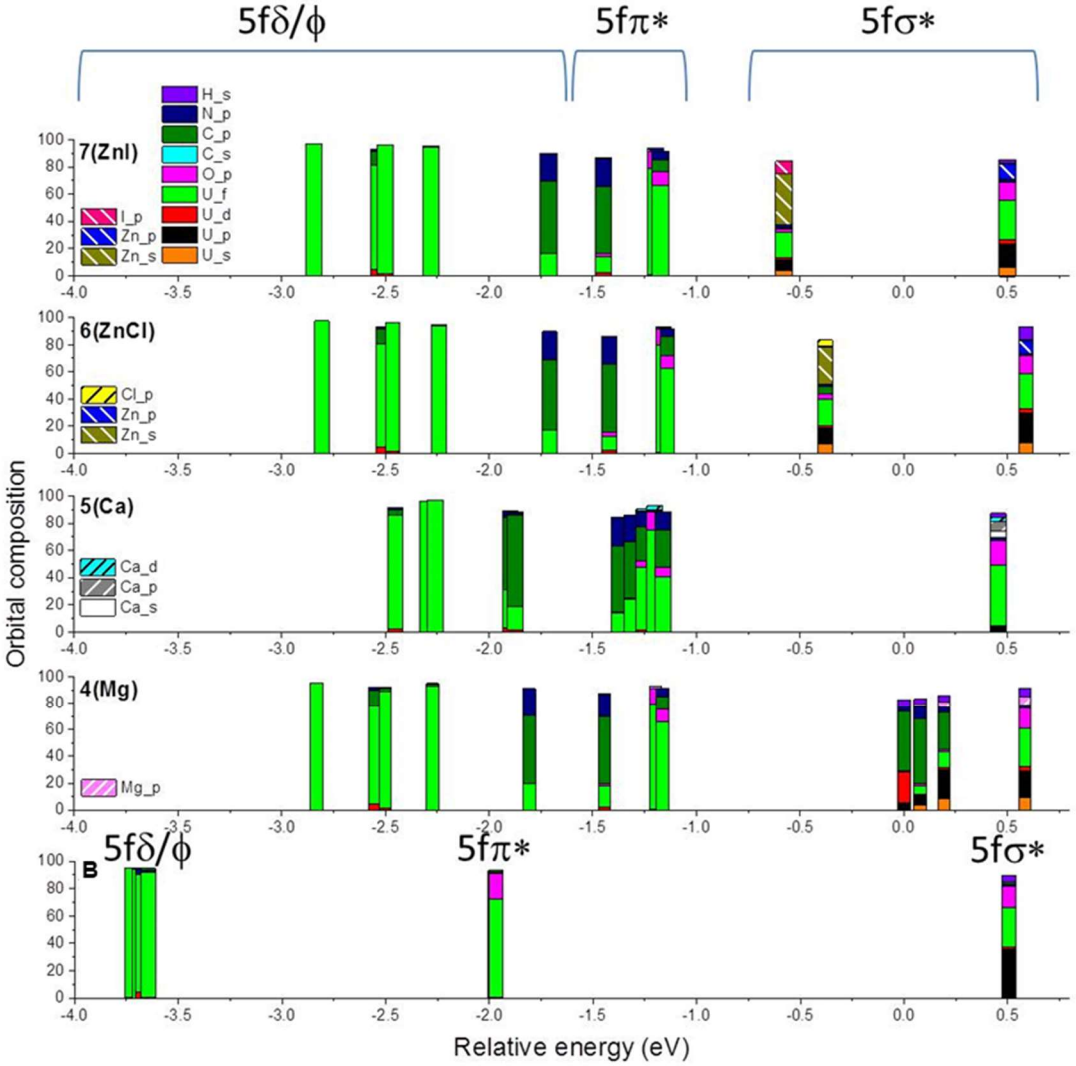

Figure A 2.2 From bottom to top: relative energies and orbital compositions obtained by Mulliken population analyses for unoccupied valence orbitals with U 5*f* content for **B**, **4** (Mg), **5** (Ca), **6** (ZnCl) and **7** (ZnI) compounds. Contributions smaller than 2 % contributions of atomic orbitals are not included.

Table A 2.1 Selected calculated bond distances (Å)

Complex	M-O2	O2-U	U=O1
D[Al]	1.818	1.984	1.870
C[K]	2.808	1.870	1.882
1[Ti(III)]	2.101	1.967	1.867
2[Ti(IV)]	1.938	2.016	1.858
3[Zr]	2.026	2.039	1.860
4[Mg]	1.940	1.941	1.872
5[Ca]	2.324	1.925	1.877
6[ZnCl]	1.918	1.944	1.872
7[ZnI]	1.924	1.949	1.872
B[U(VI)]	-	1.801	1.837

Table A 2.2 Properties of selected bond critical points.

Complex	Parameter	$\nabla^2 \rho$	ρ	H
D[Al]	Al-O1	0.529	0.072	0.003
	O1-U	0.180	0.166	-0.074
	U=O2	0.419	0.230	-0.143
C[K]	K-O1	0.067	0.013	0.004
	O1-U	0.433	0.233	-0.146
	U=O2	0.431	0.225	-0.137
1[Ti(III)]	Ti(3)-O1	0.306	0.066	-0.003
	O1-U	0.431	0.174	-0.082
	U=O2	0.427	0.231	-0.145
2[Ti(IV)]	Ti(4)-O1	0.446	0.104	-0.016
	O1-U	0.410	0.154	-0.063
	U=O2	0.431	0.237	-0.152
3[Zr]	Zr-O1	0.404	0.110	-0.025
	O1-U	0.381	0.147	-0.058
	U=O2	0.431	0.236	-0.150
4[Mg]	Mg-O2	0.391	0.050	0.011
	O2-U	0.414	0.190	-0.098
	U=O1	0.415	0.229	-0.142
5[Ca]	Ca-O2	0.203	0.036	0.006
	O2-U	0.433	0.201	-0.109
	U=O1	0.438	0.228	-0.140
6[ZnCl]	Zn-O2	0.472	0.090	-0.017
	O2-U	0.454	0.183	-0.090
	U=O1	0.417	0.229	-0.142
7[ZnI]	Zn-O2	0.460	0.089	-0.017
	O2-U	0.451	0.180	-0.087
	U=O1	0.418	0.229	-0.142
B[U(VI)]	O1=U	0.439	0.277	-0.207
	U=O2	0.450	0.252	-0.171

Table A 2.3 Selected calculated bond orders.

Complex	Parameter	Mayer	Mulliken
D[Al]	Al-O1	0.829	0.653
	O1-U	1.465	0.605
	U=O2	2.159	0.850
C[K]	K-O1	0.083	0.043
	O1-U	2.224	0.937
	U=O2	2.091	0.837
1[Ti(III)]	Ti(III)-O1	0.655	0.441
	O1-U	1.668	0.729
	U=O2	2.197	0.885
2[Ti(IV)]	Ti(IV)-O1	0.883	0.507
	O1-U	1.424	0.643
	U=O2	2.230	0.875
3[Zr]	Zr-O1	0.897	0.493
	O1-U	1.382	0.649
	U=O2	2.220	0.871
4[Mg]	Mg-O1	0.643	0.524
	O1-U	1.642	0.651
	U=O2	2.134	0.852
5[Ca]	Ca-O1	0.540	0.371
	O1-U	1.750	0.678
	U=O2	2.157	0.851
6[ZnCl]	Zn-O1	0.599	0.427
	O1-U	1.704	0.745
	U=O2	2.149	0.860
7[ZnI]	Zn-O1	0.599	0.423
	O1-U	1.699	0.749
	U=O2	2.155	0.862
B[U(VI)]	O1=U	2.455	0.846
	U=O2	2.188	0.942

Table A 2.4 Partial Atomic Charge of Uranium atoms

	Hirshfeld	Spin density
1[Ti(III)]	0.441	1.08
2[Ti(IV)]	0.481	1.01
3[Zr]	0.484	1.06
4[Mg]	0.450	1.03
5[Ca]	0.455	0.93
6[ZnCl]	0.439	1.05
7[ZnI]	0.438	1.05
[U(VI)]	0.520	-
B[U(V)]	0.415	0.76

Table A 2.5 Uranium atomic orbital contribution of selected molecular orbitals related to U-O_{exo} Bonds

	4[Mg]		**5**[Ca]		**6**[ZnCl]		**7**[ZnI]	
	orbital#	contribution	orbital#	contribution	orbital#	contribution	orbital#	contribution
U-O_{exo} σ bond	294	4.92%	355	41.88%	304	7.09%	318	9.12%
	293	8.90%	353	14.74%	302	9.34%	317	38.40%
	291	38.72%	301	29.07%				
U-O_{exo} π bond	282	12.60%	346	8.89%	290	5.64%	311	14.47%
	280	6.58%	343	4.83%	291	8.52%	307	6.42%
	277	6.98%	341	3.66%	289	4.98%		
			340	4.58%				

Table A2.5 contains the uranium atomic orbital contributions to the O_{exo} dominant π and σ U-O bonding MOs of **4, 5, 6** and **7**. The π bonding orbitals are more stable then σ bonding orbitals, which may be due to a "pushing from below" effect.[1-7] Although there are some arguments that orbital mixing and covalency should be separated in compounds of elements toward the middle of the actinide series, however, in uranium chemistry, they can be treated as synonymous.[8] One can see clearly the tendency in the sum of uranium atomic orbital contributions for σ bonds that are about as follows: **5** (Ca) (56%) ⩾ **4** (Mg) (52%) > **6** (ZnI) (47%) ⩾ **7** (ZnCl) (44%), which suggests a decrease of covalency. This agrees with QTAIM and EDA results. For π bonds, the contributions are about as follows: **4** (Mg) (26%) > **5** (Ca) (22%) ⩾ **6** (ZnI) (21%) ⩾ **7** (ZnCl) (19%). This may due to π bonds not being affected too much for symmetry reasons.

Table A 2.6 Uranium atomic orbital contributions of localized U-O_{exo} bonding orbitals

	5[Ca]	**4**[Mg]	**6**[ZnCl]	**7**[ZnI]
σ	28.50%	26.70%	21.60%	22.80%
π	20.00%	17.10%	16.60%	18.20%
π	20.10%	17.70%	16.90%	18.70%

Due to the large number of split bonding MOs, we also localized those orbitals. Table A3.6 shows the U atomic orbital contributions to localized U-O_{exo} bonding orbitals. Increased U character can be taken as indicative of increased covalent character. Thus, we find an order of **5** (Ca) ⩾ **4** (Mg) > **6** (ZnI) ⩾ **7** (ZnCl)

Table A 2.7 Properties of BCPs of hydrogen bonds

Complex	Parameter	$\nabla^2 \rho$	ρ	H	Bond length H⋯A cal.	Bond length D⋯A cal.
D[Al]	C1-H⋯O	0.0217	0.0064	0.0014	2.670	3.736
	C2-H⋯O	0.0361	0.0093	0.0022	2.435	3.475
	N1-H⋯O	0.0773	0.0218	0.0021	1.986	3.010
	N2-H⋯O	0.0806	0.0230	0.0019	1.964	2.991
C[K]	C1-H⋯O	0.0227	0.0067	0.0015	2.646	3.727
	C2-H⋯O	0.0360	0.0092	0.0022	2.440	3.470
	N1-H⋯O	0.0856	0.0249	0.0015	1.906	2.935
	N2-H⋯O	0.0905	0.0268	0.0011	1.935	2.962
1[Ti(III)]	C1-H⋯O	-	-	-	3.224	4.210
	C2-H⋯O	0.0342	0.0089	0.0021	2.450	3.510
	N1-H⋯O	0.0645	0.0176	0.0025	2.069	3.095
	N2-H⋯O	0.0685	0.0189	0.0024	2.041	3.066
2[Ti(IV)]	C1-H⋯O	0.0138	0.0044	0.0009	2.884	3.922
	C2-H⋯O	0.0282	0.0074	0.0018	2.542	3.591
	N1-H⋯O	0.0604	0.0158	0.0027	2.044	3.073
	N2-H⋯O	0.0682	0.0185	0.0025	2.107	3.128
3[Zr]	C1-H⋯O	0.0155	0.0040	0.0010	2.827	3.872
	C2-H⋯O	0.0297	0.0077	0.0019	2.521	3.567
	N1-H⋯O	0.0640	0.0170	0.0026	2.080	3.101
	N2-H⋯O	0.0710	0.0194	0.0024	2.025	3.054
4[Mg]	C1-H⋯O	0.0236	0.0069	0.0015	2.631	3.706
	C2-H⋯O	0.0366	0.0094	0.0022	2.431	3.467
	N1-H⋯O	0.0833	0.0241	0.0016	1.946	2.974
	N2-H⋯O	0.0820	0.0235	0.0018	1.956	2.982

5[Ca]	C1-H···O	0.0214	0.0062	0.0014	2.676	3.744
	C2-H···O	0.0308	0.0080	0.0020	2.508	3.548
	N1-H···O	0.0621	0.0125	0.0025	2.016	3.043
	N2-H···O	0.0724	0.0201	0.0023	2.010	3.035
6[ZnCl]	C1-H···O	0.0156	0.0049	0.0010	2.821	3.874
	C2-H···O	0.0389	0.0100	0.0023	2.400	3.443
	N1-H···O	0.0786	0.0224	0.0019	1.976	3.001
	N2-H···O	0.0791	0.0226	0.0019	1.973	2.997
7[ZnI]	C1-H···O	0.0153	0.0048	0.0010	2.832	3.880
	C2-H···O	0.0385	0.0099	0.0023	2.404	3.448
	N1-H···O	0.0781	0.0222	0.0020	1.979	3.004
	N2-H···O	0.0772	0.0219	0.0020	1.986	3.010
B[U(VI)]	C1-H···O	0.0176	0.0052	0.0011	2.767	3.818
	C2-H···O	0.0313	0.0079	0.0020	2.497	3.545
	N1-H···O	0.0669	0.0173	0.0027	2.065	3.086
	N2-H···O	0.0666	0.0172	0.0027	2.068	3.088

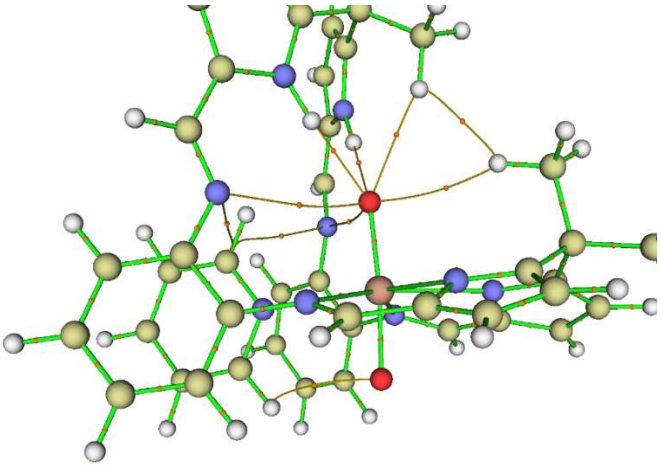

Figure A 2.3 BCPs near O2 in complex **B**.

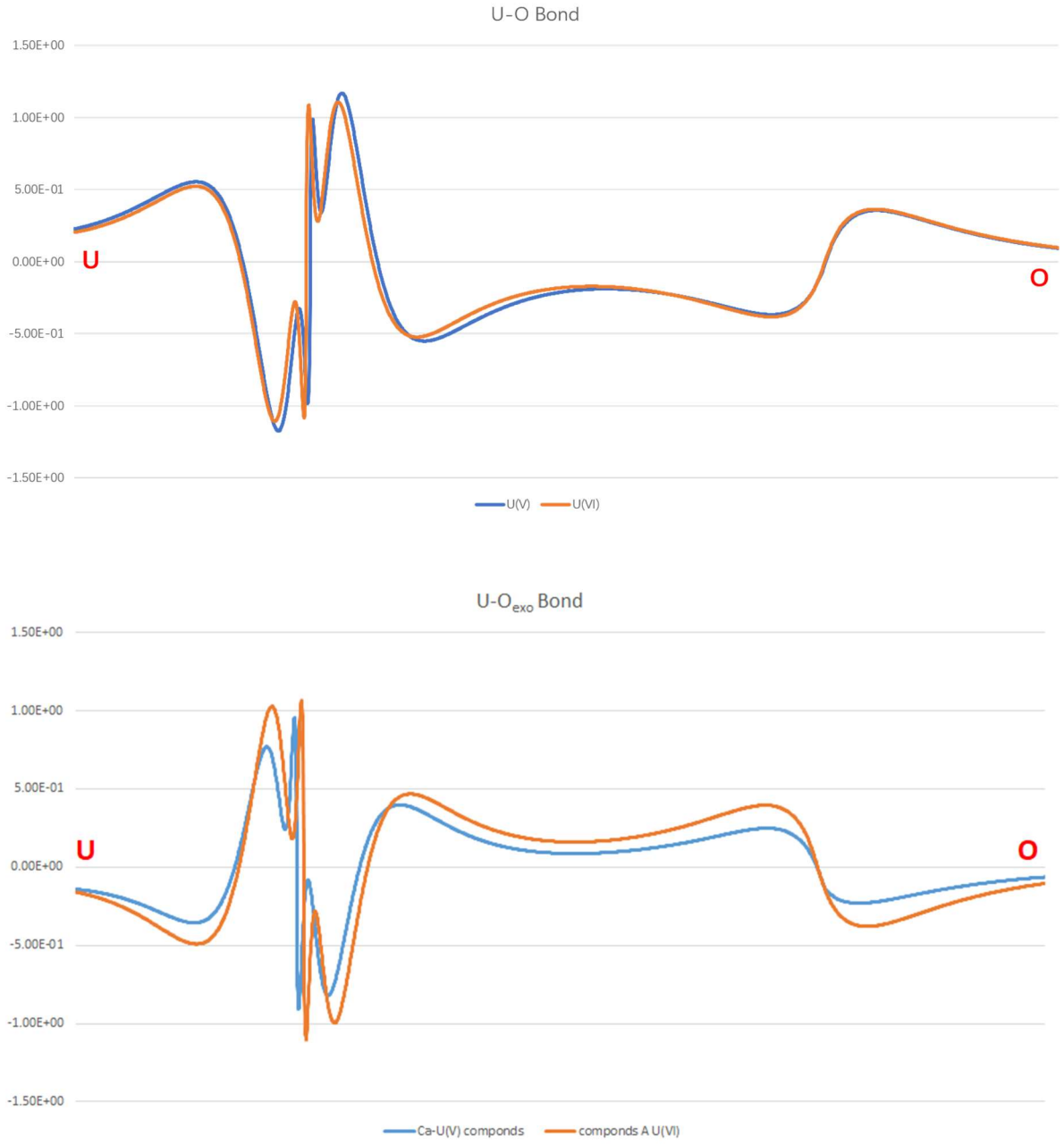

Figure A 2.4 Bond contraction of the U-O_{yl} bond in uranyl(V) compared to uranyl(VI), traced along the U–O direction. **Top**: Bonding orbital (U($5f_{z3}$)–O($2p_z$) of UO_2^{2+} (orange) and UO_2^{+} (blue). **Bottom:** Bonding orbital (U($5f_{z3}$)–O_{exo}($2p_z$) of the U(VI) complex (**B**), orange, vs. the U(V) Ca complex (**5**), blue.

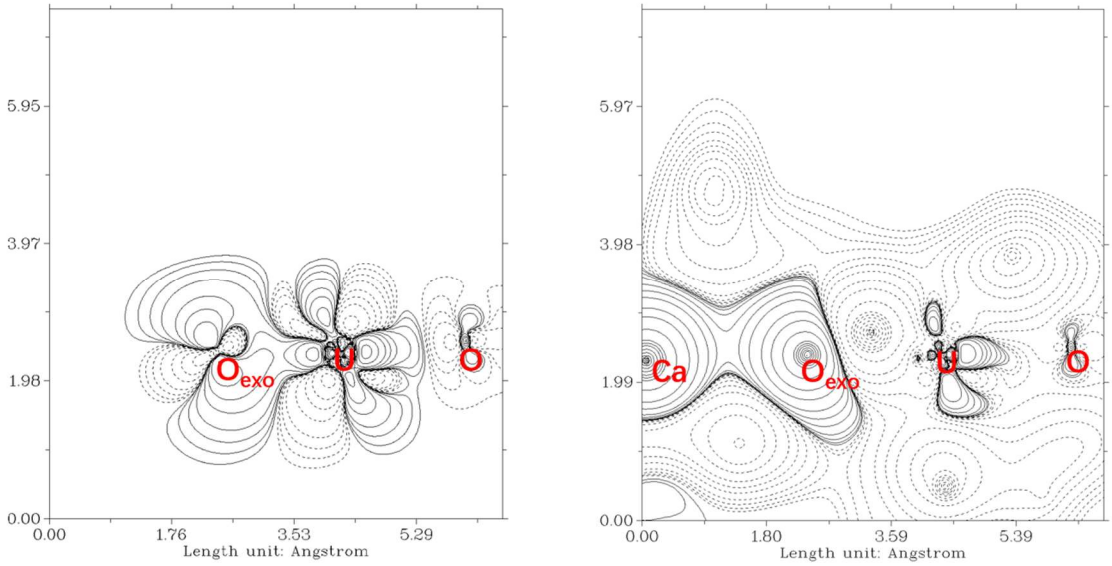

Figure A 2.5 Electron density difference graph. In the graph, solid lines and dashed lines correspond to the regions having increased electron density and decreased electron density during formation of the U-O bonds of compound **B** and **5[Ca]**, respectively. Unrelated atoms and corresponding densities are omitted.

A 2.2. References

1. R. G. Denning, *The Journal of Physical Chemistry A*, 2007, **111**, 4125-4143.
2. M. L. Neidig, D. L. Clark and R. L. Martin, *Coordination Chemistry Reviews*, 2013, **257**, 394-406.
3. K. G. Dyall, *Molecular Physics*, 1999, **96**, 511-518.
4. M. Pepper and B. E. Bursten, *Chemical Reviews*, 1991, **91**, 719-741.
5. K. Tatsumi and R. Hoffmann, *Inorganic Chemistry*, 1980, **19**, 2656-2658.
6. N. Kaltsoyannis, *Inorganic Chemistry*, 2000, **39**, 6009-6017.
7. N. Kaltsoyannis, *Dalton Transactions*, 2016, **45**, 3158-3162.
8. P. L. Arnold, J. H. Farnaby, R. C. White, N. Kaltsoyannis, M. G. Gardiner and J. B. Love, *Chemical Science*, 2014, **5**, 756-765.

Preface to Chapter 3

This chapter is based on a manuscript that was submitted for publication in the journal "*Inorganic Chemistry*". The full citation of the paper is as follows:

> Zhang, X., Adelman, S.L., Arko, B.T., De Silva, C.R., Su, J., Kozimor, S.A., Mocko, V., Shafer, J.C., Stein, B.W., Schreckenbach, G., Batista, E.R., and Yang, P. Advancing the Am Extractant Design through the Interplay among Planarity, Preorganization, and Substitution Effects. *Inorganic Chemistry*, **2022** *61*(30), pp.11556-11570.

All the theoretical calculations and analysis in this chapter were carried out by Xiaobin Zhang. The manuscript was prepared together with the other authors.

 Adelman, S.L., Arko, B.T., Kozimor, S.A., Mocko, V., Stein, B.W., are affiliated with Chemistry Division, Los Alamos National Laboratory, Los Alamos, New Mexico, United States. De Silva, C.R., are affiliated with Department of Chemistry & Physics, Western Carolina University, Cullowhee, North Carolina, United States. Shafer, J.C., are affiliated with Department of Chemistry, Colorado School of Mines, Golden, Colorado 80401, United States. Su, J., Batista, E.R., and Yang, P. are affiliated with Theoretical Division, Los Alamos National Laboratory, Los Alamos, New Mexico, United States.

Chapter 3. Advancing Am Extractant Design through the Interplay among Planarity, Preorganization and Substitution Effects

3.1. Abstract

Advancing the field of chemical separations is important for nearly every area of science and technology. Some of the most challenging separations are associated with the americium ion, Am(III), for its extraction in the nuclear fuel cycle, ^{241}Am production for industrial usage, and environmental cleanup efforts,. Herein, a series of extractants were studied, using first-principle calculations, to identify the electronic properties that preferentially influence Am(III) binding in separations. As the most used extractant family and because it affords a high degree of functionalization, the polypyridyl family of extractants was chosen to study the effects of the planarity of the structure, preorganization of coordinating atoms, and substitution of various functional groups. The actinyl ions are used as a structurally simplified surrogate model to quickly screen the most promising candidates that can separate these metal ions. The down selected extractants are then tested for the Am(III)/Eu(III) system. Our results showed that π interactions, especially those between the central terpyridine ring and Am(III), played a crucial role for separation. Adding an electron donating group onto the terpyridine backbone increased the binding energies to Am(III) and stabilized Am(terpyridine) coordination. Increasing the planarity of the extractant increased the binding strength as well, although this effect was found to be rather weak. Pre-organizing the coordinating atoms of an extractant to their binding configuration as in the bound metal-complex speeds up the binding process and significantly improves the kinetics of the separation process. This conclusion is validated by the synthesized 1,2-dihydrodipyrido[4,3-*b*;5,6-*b*]acridine (**13**) extractant, a preorganized derivative of the terpyridine extractant, which we

experimentally showed was four times more effective at separating Am^{3+} from Eu^{3+} ($SF_{Am/Eu} \sim 23 \pm 1$).

3.2. Introduction

Advancing separation science is of wide-ranging importance because this field impacts nearly every area of modern society and technology. Separation science plays a critical role in energy production, is essential for ensuring inventories of strategic national resources, and central for the development of specialty chemicals ranging from pharmaceuticals, polymers, and critical materials.[1] Through the field of separation science will emerge solutions to some of the most daunting problems facing today's society; e.g. preserving clean water, reducing anthropogenic greenhouse gasses in the atmosphere, and rehabilitating contaminated superfund sites. From this perspective, it is critical to advance the field of separation science and provide fundamental insight that enables researchers to solve important challenges regarding energy, environment, and public health.

One area of separations in desperate need of attention is associated with element of americium (Am).[2] Advancing americium separation science supports nuclear waste cleanup, storage, and advancement of nuclear power generation because the Am radioisotope is a major constituent in spent nuclear fuel. The special nuclear properties associated with ^{241}Am also find broad application in industry. For instance, the soft γ-radiation emitted from ^{241}Am finds application in determination of thicknesses of metal sheets, glass, etc.[3-5] It also finds usage in compaction tests for soils.[6-8] The americium-beryllium (Am-Be) neutron sources are also deployed by the petroleum industry in neutron activation analyses for oil-well logging and drilling

exploration.[9-11] Hence, identifying ways to improve americium separations can significantly impact americium processing effort for ^{241}Am industrial usage.

^{241}Am is obtained as a fission product from the decay of ^{241}Pu, according to the decay chain. The separation of americium(III), Am(III), from lanthanides(III), Ln(III), cations represents a major chemical challenge standing over seven decades.[12-16] This class of separations is one of the most difficult in inorganic chemistry because the Am(III) and Ln(III) cations share many chemical properties; similar atomic radii, similar stability of the +3 oxidation state, similar oxophilicity, and similar speciation and reactivity in aqueous solutions.[17] Despite the seemingly insurmountable challenge associated with Am(III)/Ln(III) separation problems, seminal advances have provided a basis upon which liquid-liquid extraction methods have been developed that separate Am(III) from Ln(III) on a large scale and under conditions that are compatible with industrial needs. Typically the approach consists in dissolving the mixture of Am(III) and Ln(III) feedstock and using an extractant to selectively pull Am(III) from acidic aqueous media into an organic diluent.[18]

The polypyridyl family of extractants is the most used extractant family for Am(III)/Ln(III) separations because it affords a high degree of functionalization.[16] For reasons not well understood, certain polypyridyl extractants are particularly effective for Am(III)/Ln(III) separations displaying exceptional separation factors, meanwhile other chemically related polypyridyl extractants are completely ineffective.[16] When designing a new extractant it is difficult to predict, *a priori*, what type of properties the extractant will have, e.g. effective and selective vs incompetent and indiscriminate. Often, only slight modification at the periphery of the polypyridyl scaffolding imparts substantial changes in extractant properties.[19] Additionally, developing a synthetic route and purification method for a range of potential extractants can be a time-consuming and costly process. Advancing our understanding of the correlations between

polypyridyl features and Am(III) extraction ability will improve predictive capabilities in extractant designs and support advancement of americium processing and technologies. Within this context, and capitalizing on the faster speed of computation versus actual synthesis, we set out to develop a computational method to guide synthetic efforts in extractant design. As a proof-of-principle, we limited the design space to a sub-class of polypyridyl extractants to those that contain three *N*-heterocyclic rings, specifically terpyridyl based extractants that is the most used category for Am separations.[13] Using density functional theory calculations, we were able to rapidly vary the number of nitrogen atoms within the ring structure, the substituents bound to the terpyridyl backbone, and the linkages between the three-membered ring system. Terpyridine (**1**) and fourteen derivative extractants were evaluated (see Scheme 3.1). Note, an analogous experimental campaign that required synthesis of all fifteen compounds shown in Scheme 3.1 would require substantial investment in human power, budget, and time. In contrast, using our computational methods we evaluated how extractant planarity and preorganization for metal binding varied as a

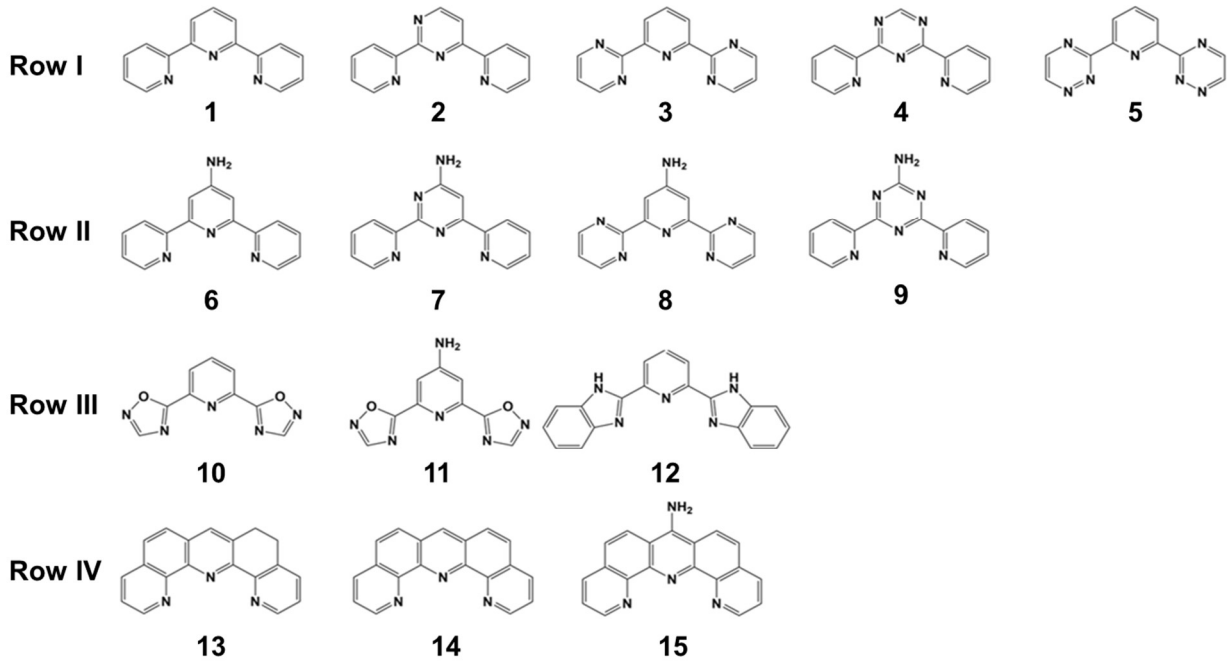

Scheme 3.1. Structures of the Selected Extractants

function of the ancillary substituents bound to the terpyridyl backbone (e.g. the -NH_2 group in *Row II*) as well as the number of heterocyclic nitrogen atoms (e.g. three in extractant **1** and four in extractant **2**).

Admittedly, at the onset of this study it was unclear if any of the fifteen terpyridine derivatives would outperform extractant **1**. There are also many factors that influence a separation that cannot be captured computationally, e.g., solubility, binding kinetics, surface transfer effects, impact from secondary and tertiary solution structure formation, etc. However, upon computationally screening against metrics that could be modeled, some promising candidates were identified, potential extractants that may not be obvious *a priori*. Two of these candidates were subsequently synthesized and evaluated. This experimental effort provided confidence and credibility for our computational methodology and validated our predictions.

There are many extractant properties that impact Am(III)/Ln(III) separations that can be computationally evaluated. These include electronic impact from electron-donating or -withdrawing groups, the electronic conjugation, and level of delocalization of the electronic states. Other extractant parameters that can be discreetly evaluated using DFT are softness vs hardness of the coordinating atoms, structural impacts associated with the number of metal binding atoms from the extractant, and extractant flexibility/rigidity. It is also straight forward to computationally test structural reorganization energies needed for metal coordination. From this perspective, the high level of functionalization afforded by terpyridyl based extractants distinguish this class of compounds as being exceptionally-suited as a computational test bed for a number of variables that influence the Am(III)/Ln(III) separation process.

It is important to consider the possible effects of tuning these various parameters. For instance, the planarity of the extractant will be strongly codependent with the conjugation of the π orbital system and with the electronic nature of the substitution functional groups. Substituent groups will affect the reactivity of the extractant not only by the electronic effects they induce but also by introducing steric effects that can limit the flexibility of the extractant conformations. It has been shown that steric effects result from the repulsion between nearby H-atoms in coordinated pyridyl groups, see Figure 3.1. One approach to minimize this repulsion is to replace the C-H in the six-member rings by a nitrogen atom, which increases the planarity of the multi-ring system. This change also impacts the electron donating property of the ring by serving as an electron-withdrawing group. For example, experimental thermodynamic data [20] compared the formation constants of lanthanides complexes with a variety of terpyridyl extractants and showed that the 2,6-bis(124ispel124d-2-yl)pyrimidine (**2** in Scheme 3.1) did not improve upon the binding affinity of 2,2':6',2''-terpyridine (**1** in Scheme 3.1), while the 2,6-bis(1,2,4-triazin-3-yl)pyridine (**5** in Scheme 3.1) performed even worse.

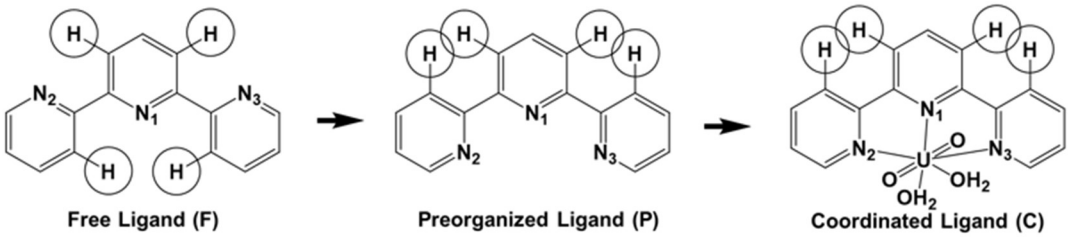

Figure 3.1 Most stable trans-configuration **1** of a free extractant (F), the optimized cis-configuration of an extractant preorganized for bonding (P) and coordinated configuration (C) of extractant in a metal complex. The H-H repulsions occur in (P) and (C) configurations.

Another avenue that has been to explored to limit steric repulsion between extractants and the metals to which they bind was to use five-membered rings instead of six-membered rings to increase the H-H distance. However, the 2,6-bis(124ispel124dazole-2-yl)pyridine (**12** in Scheme

3.1) also gave lower affinity for lanthanides as compared those observed with **1**.[20] Replacing pairs of sterically interacting H atoms with bridging phenyl groups is an alternative strategy to limit steric repulsion between the flanking and the central ring systems. For example, dipyridoacridine (**14** in Scheme 3.1) showed higher affinity to Ln(III) ions than **1**. [19] 2-amino-4,6-di-(pyridine-2-yl)-1,3,5-triazine (**9** in Scheme 3.1) is an extractant with a higher stability constant than **1** for An(III) over Ln(III) and it has been proposed that the selectivity displayed by this extractant might come from decreasing the steric effects shown in Figure 3.1. Consistently, it has been reported that substitution with electron-donating groups on the center ring leads to improved extraction performance, whereas electron-withdrawing groups have the opposite effect. [21-23] This can be explained by the basicity of the extractants, essentially, the electron negativity of the coordinating N atoms. Adding more complexity to the challenge, Ionova et al. reported the thermodynamic stability of Ln(III)-extractant increases when both the increase of donor ability of the central ring and the acceptor ability of the lateral ones.[20] Beyond the stability, how the interplay of center and lateral rings impacts the separation factors (the difference between the stability of two metal ions) is still unsettled.

Scheme 3.1 shows the structures of the extractants studied in this work. In *Row I*, five extractants with different degrees of steric repulsion were chosen by modifying the numbers of nitrogen atoms and their positions in the six member rings starting from terpyridine (extractant **1**). The extractants in *Row II* include the electron donating group -NH_2 attached to the extractants **1**-**4** from *Row I*. The extractants in *Row III* replace the external six-membered rings with five-membered rings, as well as include the introduction of an electron donating group to extractant **10** to yield extractant **11**. Finally, *Row IV* features highly rigid extractants **13**, **14** and **15**, derivatized

from extractant **1** by the addition of one or two bridging phenyl groups with or without an electron donating group -NH_2, to study the effects of preorganization.

To start from a structurally simplified, surrogate model for the single ion coordination, we studied the coordination of the extractants in Scheme 3.1 to the actinyl ions (UO_2^{2+}, NpO_2^{2+} and PuO_2^{2+}) by limiting the coordination in the equatorial plane to one extractant. The actinyl units, with [Rn] $5f^0$, $5f^1$ and $5f^2$ electron configurations respectively, provide geometrically simplified models to study the selectivity of the different extractants. It is also well established that binding within the actinyl equatorial plane is largely dominated by ionic interactions.[24, 25] From this perspective, bonding in the actinyl equatorial plane may be quite similar to that associated with the ionic bonding interactions that seem to dominate lanthanides and minor actinides (like Am) chemistry. Calculations were carried out for the best candidate extractants to evaluate how the conclusions from the AnO_2^{2+} series transfer to predictions for binding of Am(III) vs Eu(III). Since the set of extractants was now smaller, higher levels of theory was afforded for more complex models, and some were synthesized and experimentally tested for the solvent extraction process. To isolate the different electronic and mechanical properties that affect the selective metal coordination of extractants, the structural, thermodynamic, and electronic properties of selected nitrogen-donor extractants and their actinyl complexes have been systematically investigated by relativistic quantum chemical calculations.

The following aspects are discussed in the first section of the paper: (1) the thermodynamic properties of these extractants for separating actinyls, (2) the impact from structural modifications on separations, such as planarity, preorganization, electrostatic potential (ESP), and (3) the electronic effects on actinyl and extractant bonding. In the second section of the paper, the

transferability of the lessons learned from the study of coordination to actinyl to the separation of trivalent An(III) from Ln(III) is evaluated by both theoretical and experimental means.

3.3. Computational Details

Unless otherwise noted, all the electronic structure calculations presented in this work were carried out with Density Functional Theory (DFT) using the ADF 2019 software package.[26-28] The choice of DFT functional for actinide calculations has been extensively tested in previous studies.[29-32] Within ADF, the GGA functionals such as PBE[33] give the best predictions for bond lengths and vibrational frequencies, as well as correct trends of reaction energies compared to hybrid functionals such as B3LYP. [34-37] All geometry optimizations were carried out with the PBE functional, relativistic scalar ZORA Hamiltonian, [38-40] and all-electron TZ2P basis set [41] in conjunction with the COSMO[42] implicit solvation model. The radii values of the atomic spheres in the COSMO solvation model for atoms in this study are the corresponding Van der Waals radii from the MM3 method by Allinger [43] divided by 1.2. Although the radii values for atoms heavier than uranium are not ideal, these heavy metals are well buried inside of the first solvation shell and do not have direct contact with the solvation cavity. Hence, the radii settings for them do not affect the results of the geometry optimization. In order to limit the numerical noise from the solvation model, vibrational frequencies below 100 cm^{-1} including suspicious imaginary frequencies were scanned by the ADF program with higher precision. The spin-orbit coupling effect was not considered in this work as, for the types of compounds studied here, it has a minor effect in molecular structures, vibrational frequencies, and reaction energies – provided that the oxidation state of the heavy atom does not change. Grimme's dispersion[44] correction with Becke-Johnson damping (D3BJ)[45] was used for actinyl systems, however this model has not been parameterized beyond Pu and could not be invoked in the Am calculations. Further discussion of

dispersion correction can be found in the section A3.7 in Appendix 3. Consequently, it was not used for the Eu calculations or in the calculations of the separation of trivalent An(III) from Ln(III) on an equal footing. Frequency calculations were performed to ensure optimization convergence to local minima on the potential energy surface. These frequencies were also used to compute the entropy term in the Gibbs free energy at the harmonic approximation. A standard state correction of 1354 atm was applied to the enthalpy to model the restrictions imposed by the liquid phase. [46] This method has successfully been applied to actinide systems previously.[30, 47-50] To further validate the binding energies for Am^{3+} and Eu^{3+} systems, single point calculations were carried out at the coupled-cluster level, namely DLPNO-CCSD(T),[50] on the DFT optimized structures with the scalar ZORA Hamiltonian using the ORCA program.[51] The SARC-ZORA-TZVP basis sets [52, 53] were used for Am and Eu, and the ZORA-def2-TZVP basis sets [54] were used for other light atoms.

To understand the fundamental factors that drive the bonding and separation, various bonding analysis methods were used to analyze the bonding nature of the molecules. In particular, Hirshfeld charge analysis [55] and electrostatic potential (ESP) give good representations of the charge rearrangement and distribution for ionic interactions. Hirshfeld charges are defined relative to the deformation density, which is the difference between the molecular and unrelaxed atomic charge densities. The atomic charges from Hirshfeld method agree well with conventional chemical intuition and generally more interpretable than Mulliken charge that distribute electron density equally to the two atoms. As thus, the Hirshfeld charges were used in the previous studies and explained experimental results well.[56, 57] The analysis of lone pair electrons of electronic donating group in extractants was carried on with the NBO6[58] and MultiWFN package.[59] While energy decomposition analysis (EDA) [60, 61] and its extension, the extended transition state method

for energy decomposition analysis combined with the natural orbitals for chemical valence theory (ETS-NOCV)[62], and quantum theory of atoms in molecules (QTAIM)[63, 64] provided rationalization of the extractant-metal interactions, especially for covalent interactions. The details of ETS-NOCV analysis can be found in section A3.5 of the Appendix 3.

3.4. Experimental Details

3.4.1. General.

Extractants **13** and **14** were synthesized and purified according to the literature procedure.[65] The nuclear magnetic resonance (NMR) spectra were collected on a Bruker 400 MHz Ascend instrument in deuterated chloroform ($CDCl_3$; Cambridge Isotope Laboratories). Terpyridine (97%, Alfa Aesar), 6,7-dihydro-5H-quinoline-8-one (98%, AmBeed), 8-aminoquinoline-7-carbaldehyde (95%, AmBeed), 2-bromohexanoic acid (97%, Sigma Aldrich), *n*-octanol (>99%, Sigma Aldrich), and nitric acid [$HNO_{3(aq)}$, optima grade, Fisher Scientific] were obtained commercially and used as received. Water used was deionized and purified in a two-step process. First it was passed through a Thermo Fisher Scientific Barnstead MicroPure UV system to achieve a resistivity of 18.2 MΩ•cm. Second, the 18.2 MΩ•cm water was distilled in a Savillex Teflon distillation apparatus (DST-1000). This Teflon distilled and high resistivity (> 18.2 MΩ•cm) water will be referred to hereafter as TDMQ. Radioisotopes ^{155}Eu and ^{241}Am were obtained from Eckert and Ziegler in dilute hydrochloric acid.

¡CAUTION! ^{241}Am [$t_{½}$ = 432.2(6) years][66], ^{155} Eu [$t_{½}$ = 4.753(14) years][66] , and the daughter products from these two radionuclides constitute serious health threats because of radioactive decay. Hence, all studies that involved manipulation of these radionuclides were conducted in a radiation laboratory equipped with HEPA filtered hoods, continuous air monitors,

negative pressure gloveboxes, and monitoring equipment appropriate for detecting α-, β-, and γ-radiation. Entrance to the laboratory space was controlled with a hand and foot monitoring instrument for α-, β-, and γ-emitting radioisotopes and a full body personal contamination monitoring station.

3.4.2. Gamma Spectroscopy.

All γ-spectroscopy measurements were made using a high purity germanium detector (ORTEC GEM30P4-70 HPGe) that was equipped with an ORTEC DSPEC-50 multichannel analyzer (operated at 2500 V) and with a MOBIUS cryostat system (ORTEC 805709). The detector was housed in pre-World War II) shielding. The detector diameter was 50.0 mm and the detector length was 53.5 mm. The detector had a Be window (thickness = 0.5 mm and outer dead-layer thickness = 0.3 μm). The detector components included a p-type Al-windowed high-purity germanium (HPGe) detector with a measured FWHM at 1333 keV of approximately 2.2 keV and was relatively efficient (about 10%). Relative total source activity uncertainties ranged from 2.6% to 3.3%. All spectra were analyzed using the Gamma Vision software package (Model A66-B32, version 6.07). A detector response function was established and its accuracy monitored using a standard that contained a mixture of radionuclides, (^{241}Am, ^{109}Cd, ^{57}Co, ^{139}Ce, ^{203}Hg, ^{113}Sn, ^{137}Cs, ^{88}Y, and ^{60}Co). This standard was traceable to the National Institute of Standards and Technology (NIST) and supplied by Eckert & Ziegler. Performance was evaluated daily with an Eu-152 calibration standard (Eckert & Ziegler). Quantification of ^{155}Eu and ^{241}Am was achieved by monitoring the 86.5 keV (0.37) and 59.5 keV (0.359) lines, respectively.[67]

3.4.3. Solvent Extraction.

In a fume hood and with no exclusion of air and moisture, radioisotope stock solutions that contained either $^{155}Eu_{(aq)}$ (3.6 μCi/mL) and $^{241}Am_{(aq)}$ (20 μCi/mL) were prepared by evaporating to dryness an aliquot of the commercially available solution, consequently in dilute $HCl_{(aq)}$. The resulting residue was dissolved in nitric acid (8 M) and this process was repeated three times to ensure the matrix changed from $HCl_{(aq)}$ to $HNO_{3(aq)}$. Meanwhile, the organic solutions were prepared by dissolving a given extractant (20 mM) with 2-bromohexanoic acid (1.95 g, 1 M) in *n*-octanol (10 mL). These solutions were pre-equilibrated (for 1 h) with $HNO_{3(aq)}$ (10 mL, 0.01 M), centrifuged, and phase separated. For each trial, the aqueous solutions were prepared by adding ^{155}Eu (0.15 μCi) and ^{241}Am (0.2 μCi) to a 2 mL polystyrene conical vial that contained $HNO_{3(aq)}$ (100 μL, 0.01 M). The volume of the organic fraction (V_{org}) was equal to the volume of the aqueous fraction (V_{aq}); $V_{org} = V_{aq} = 300$ μL. After shaking each trial in a ThermoScientific shaker (800 rpm at 25°C), the samples were allowed to settle, and the organic and aqueous phases separated. The organic layer was pipetted off of the aqueous layer. Aliquots were then taken from each layer and the relative concentrations of ^{155}Eu and ^{241}Am quantified by γ-spectroscopy. The distribution ratio (D_{Am} and D_{Eu}) for each radioisotope was then determined and is defined as being the concertation of the analyte in the organic fraction, $[M]_{org}$ (M = ^{241}Am or ^{155}Eu), divided by the concentration of the analyte in the aqueous fraction, $[M]_{aq}$; $D_M = [M]_{org} \div [M]_{aq}$. Separation factors ($SF_{Am/Eu}$) of ^{241}Am from ^{155}Eu were subsequently calculated by dividing the D_{Am} by D_{Eu}; $SF_{Am/Eu} = [D_{Am}] \div [D_{Eu}]$.[68] Measurements were performed in triplicate and the uncertainty reported as the standard deviation of the mean (at 1σ).

3.5. Results and Discussion

3.5.1. Thermodynamics of extractants binding to actinyl ions.

The affinity of all the proposed extractants towards actinide coordination was evaluated via the Gibbs free energy of the solvent displacement reaction (3.1):

$$AnO_2(H_2O)_5^{2+} + L \rightarrow AnO_2(H_2O)_2L^{2+} + 3H_2O \quad (3.1)$$

where L represents the extractants shown in Scheme 3.1.

Previous experimental and theoretical studies suggest that for the three actinyl ions, UO_2^{2+}, NpO_2^{2+}, and PuO_2^{2+}, the most prevalent form in liquid water is in the form of the penta-aquo complex, $AnO_2(H_2O)_5^{2+}$.[69-80] Figure 3.2 shows selected optimized structures of representative UO_2^{2+} compounds. The structures of $NpO_2^{2+}$and PuO_2^{2+}compounds are very similar to the analogous UO_2^{2+}compounds.

Figure 3.3 and Table A3.4.1 show the reaction Gibbs free energy for all fifteen extractants reacting with UO_2^{2+}, NpO_2^{2+}, and PuO_2^{2+}. All of the proposed extractants preferentially bind to NpO_2^{2+} and PuO_2^{2+} relative to UO_2^{2+}. Extractant **15** displays the highest affinity towards actinyl binding, with ΔG values of -32.06, -37.27, and -40.92 kcal/mol for UO_2^{2+}, NpO_2^{2+}, and PuO_2^{2+}, respectively. The ΔG of extractants in *Row I* show that, the replacement of C-H by nitrogen although this substitution reduces the H-H steric repulsion it weakens the binding affinity in comparison to the parent **1** extractant because this substitution also introduces an electron-withdrawing modification as a competing effect. Note that the extractant **5** shows more negative ΔG due to the forming of the intra-molecule hydrogen bonds between N atoms and water. The following ETS-NOCV and QTAIM analyses show that the bonding between the extractant **5** and

actinyl ions is weaker than the extractant **4.** Which is consistent with the conclusion that increase the number of N atoms will decrease the bonding. However, the addition of an electron donating group, such as the amine added in the extractants of *Row II*, results in more favorable ΔG values for AnO_2^{2+} complexation for the corresponding extractants: ΔG(**6**) < ΔG(**1**), ΔG(**7**) < ΔG(**2**), ΔG(**8**) < ΔG(**3**), and ΔG(**9**) < ΔG(**4**).

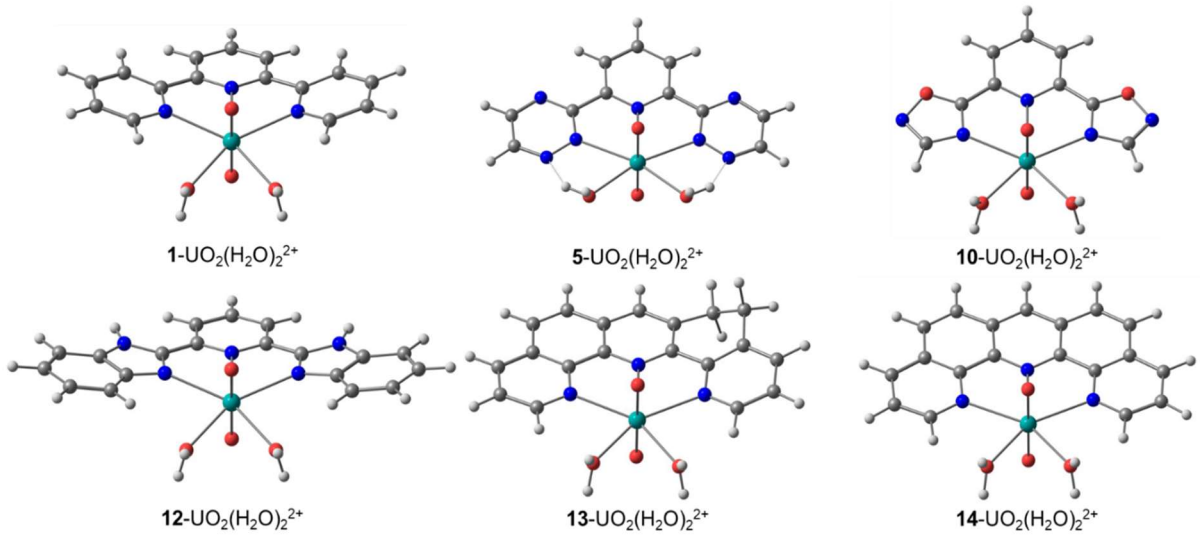

Figure 3.2 Selected optimized structures of L-$UO_2(H_2O)_2$ $^{2+}$ complexes (Red = Oxygen, White = Hydrogen, Grey =Carbon, Dark Blue = Nitrogen, Light Blue = Uranium). The side view structures are shown in Figure A3.1.1.1

The difference between the ΔG values for two different metal centers with the same extractant, $\Delta\Delta G_{Np\text{-}U}$ and $\Delta\Delta G_{Pu\text{-}Np}$, is directly associated to the separation efficiency of that extractant. The larger ΔΔG values for a given pair of metals indicate larger thermodynamic difference and consequently the greater potential for better separations. Extractant **15** had the largest $\Delta\Delta G_{Np\text{-}U}$ and $\Delta\Delta G_{Pu\text{-}Np}$ (shown in Table A3.4.1) followed by **14** and are, therefore, a good candidate for separating UO_2^{2+}, NpO_2^{2+}, and PuO_2^{2+} ions. Several factors were evaluated to analyze the differences in the thermodynamic behavior. These include reorganization energy, planarity of extractants, and substitution effects and are discussed in the following sections.

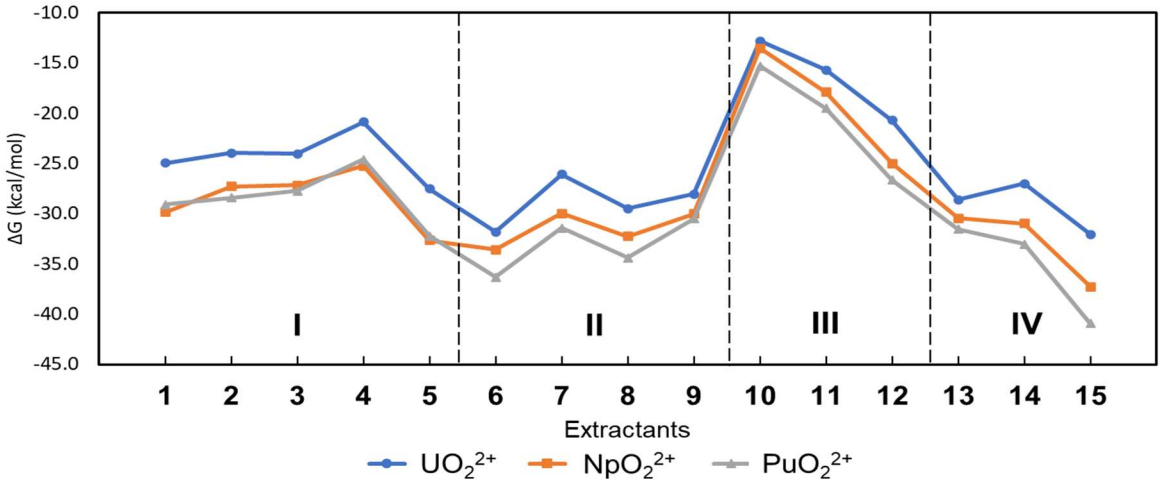

Figure 3.3 Gibbs Free Energies (ΔG, kcal/mol) for reaction (3.1) in water. Roman numerals represent the row which the extractants belong to in Scheme 3.1. The lines are only show to help guide the eye.

3.5.2. Reorganization energy.

For the extractants with the side rings that can freely rotate, the nitrogen atoms tend to be in *trans*-configuration in the uncoordinated state (see Figure 3.1). This configuration minimizes the steric repulsion between the H atoms, maintains the conjugation of the rings, and minimizes the Coulombic repulsion between the more negatively charged nitrogen. Thus, there is an extra energetic cost required to reorganize the extractants to the *cis*-configuration, which is the optimal structure for the hypothetical actinyl complexes. Table 3.1 shows the reorganization energies of extractants, computed as the energy differences between the extractant molecule in its configuration in the metal complex (upon removing the AnO_2^{2+} motif and water molecules) and its global minimum as a free extractant. Some of the extractants, **1**, **6**, and **12**, have high reorganization energies compared to the available thermal energy at room temperature ($k_BT = 0.59$ kcal/mol at 298 K) which likely adversely affect the reaction kinetics. This effect was previously observed in the calculated the reorganization energies of various polyazine extractants.[81] Hence,

minimizing the barrier between the *cis*- and *trans*-configurations of the extractants should improve the kinetics for extractants to bind metal centers.

Table 3.1 Reorganization energies of extractants in Scheme 3.1 (kcal/mol). $\Delta E_{P\text{-}F}$: The energy difference between the trans-configuration of free extractant (F) and extractant in its preorganized cis-configuration (P). $\Delta E_{C\text{-}P}$: Energy cost to deform the extractant molecule from P to the coordinated configuration (C) in complexes. $\Delta E_{C\text{-}F}$: Total reorganization energy cost for the extractant from F to C, where $\Delta E_{C\text{-}F} = \Delta E_{P\text{-}F} + \Delta E_{C\text{-}P}$

Extractant	1	2	3	4	5	6	7	8	9	10	11	12	13	14	15
$\Delta E_{P\text{-}F}$	3.2	1.8	0.0	0.0	0.0	3.2	2.0	0.0	0.7	0.1	0.0	5.7	0.0	0.0	0.0
$\Delta E_{C\text{-}P}$	3.0	2.1	1.5	1.9	1.6	3.7	2.7	1.9	2.0	4.5	5.0	4.3	1.9	1.5	1.6
$\Delta E_{C\text{-}F}$	6.2	3.9	1.5	1.9	1.6	7.0	4.6	1.9	2.7	4.6	5.0	10.0	1.9	1.5	1.6

There are several ways to reduce the energy cost associated with the extractants' *trans*-to-*cis* geometry rearrangement. For example, replacing C-H in pyridyl rings with a N-atom, making the side ring smaller, or replacing the two repelling H atoms with bridging groups. Extractants **13, 14** and **15** take the latter approach and have very low reorganization energies. Reducing the size of the side rings to five-member rings, as in **10**, **11**, and **12**, yields the opposite effect with a large reorganization energy (see Table 3.1). Finally, the extractants in *Row IV* were locked in the binding configuration, therefore, having minimal reorganization energies.

3.5.3. Planarity.

The planarity of the extractants was defined as the angle formed between the planes of the flanking rings and the plane of the center ring (See Figure A3.3.2.1). Table 3.2 shows the calculated angles for the extractants coordinated to UO_2^{2+}. The corresponding quantities for NpO_2^{2+} and PuO_2^{2+} complexes are presented in Tables A3.3.2.1 and A3.3.2.2. The extractants with H-H repulsions, such as **1**, **6** and **12**, display the largest angles, which indicates a warped or non-planar molecule. As hypothesized, when H-H repulsions are reduced by substituting C-H in the

pyridyl rings with nitrogen atoms, the optimized configurations are closer to planar. Introduction of an electron-donating group (-NH_2) onto the central pyridine ring generated more planar extractants, as illustrated by **4** that have slightly smaller angles than **3**, similarly **9** has smaller angles than **6**. Reduction of the H-H repulsion using five-membered rings containing N-H, **12**, is not as effective because the final coordinated extractant is still a warped structure. Extractants **10** and **11** are the most planar structures because they completely lack H-H repulsions. In comparison, fusing the two adjacent rings with phenyl linkages provide another way to achieve high planarity, as seen in **14**, and **15**. For **13**, due to the coexistence of -CH=CH- and the -CH_2-CH_2- bridging, it exhibits an asymmetric structure.

Table 3.2 Angles of planes between the center and the flanking rings for extractants in Scheme 3.1 coordinated to UO_2^{2+}. Two numbers for each extractant are reported, one for each flanking ring.

Extractants	**1**	**2**	**3**	**4**	**5**	**6**	**7**	**8**	**9**	**10**	**11**	**12**	**13**	**14**	**15**
Angles (°)	11.4	6.2	5.9	2.3	3.7	14.1	5.7	5.4	1.5	0.0	0.1	7.8	1.7	0.3	0.2
	11.5	10.9	6.0	2.3	3.7	14.2	6.2	5.4	1.5	0.1	0.1	8.0	11.3	0.4	0.4

The correlation between planarity and binding affinity is weak and sometimes reversed, for example, the the ΔG values (Figure 3.3 and Table A3.4.1) for extractants in *Row I* (Scheme 3.1) decreases in the order **1** < **2** < **3** < **4**. Meanwhile planarity for those same extractants decreases in the reverse order (**4** < **3** < **2** < **1**) listed in Table 3.2. Another example of this lack of correlation is from extractant **10**, which has a nearly perfect planar structure and exhibits the least favorable ΔG value. In light of the finding that the planarity is not a determining factor of the binding affinity, it is natural to draw the conclusion that that electronic effects induced from the terpyridine substituents has stronger impact than extractant planarity.

3.5.4. Substitution effects.

The general trend of extractant binding energy is essentially the same for all three actinyl ions (Figure 3.3). To simplify the discussion, we focus the analysis on the UO_2^{2+} system. As mentioned above, two competing factors are at play when the C-H in pyridyl rings are replaced by N atoms; (*1*) there is reduction of H-H steric repulsion, which facilitates preorganization for metal complexation and (*2*) the extractant becomes more electron deficient, which reduces the interaction between the metal and the extractant. For example, in the *Row I* series, despite the decreasing trend of reorganization energies the complexation with UO_2^{2+} becomes less favorable; the values of ΔG monotonically decrease from -26.4 kcal/mol for **1** to -20.9 kcal/mol for **4**. Another example is from extractant **10**. This completely planar extractant has the worst ΔG value for UO_2^{2+} binding, which can be attributed to the multiple electron-withdrawing atoms in the side rings and the high reorganization energy associated with the flanking ring flip required to bind UO_2^{2+}. The addition of electron donating groups strengthens the binding energies, as illustrated by comparing extractant **6** and **1**, **7** and **2**, **8** and **3**, and **9** and **4**.

To further delve into the extractant-metal interactions, we consider how the charge changes as a function of extractant derivative. The U-N bond lengths, Hirshfeld charges of N atoms, and electrostatic potentials (ESP) values are shown in Tables A3.2.2, S3.1.1, and A3.3.1.2, respectively. The U-N bond lengths shows a strong correlation between Hirshfeld charge and bond strength with the strongest bonds being the shorter ones. A more negative charge for a N atom suggests stronger interactions between the extractant and the metal. This is consistent with the observation that **10** has the weakest interaction while **15** has the strongest. ESP and Hirshfeld charges demonstrate that increasing the number of N atoms in the ring reduces the overall electronegativity of the extractant. For example, the absolute values of the charge and ESP of extractant fragments

after coordination follow the order of **1** > **2** > **4**, **1** > **3** > **5**, and **6** > **7** > **9**. This means that the replacement of C-H in the pyridyl rings by N atoms to reduce hydrogen-hydrogen repulsion also weakens the ionic interactions between the extractant and the metal. With more nitrogen atoms added into the side rings, the charge density will continuously reduce on the coordinating N-atoms, N2 and N3, and make them less donating than that of the central ring. Furthermore, the position of these N-atoms is important. For example, comparing $\Delta\Delta G_{Pu\text{-}Np}$ for extractant **8** (-2.2 kcal/mol) with that for **9** (-0.5 kcal/mol), shows that the addition of N atoms in the central ring gives an unfavorable effect to the PuO_2^{2+}-NpO_2^{2+} separation. In comparison, adding bridging groups (-CH=CH- or -CH_2-CH_2-) has little impact on the charge density of coordinating N-atoms.

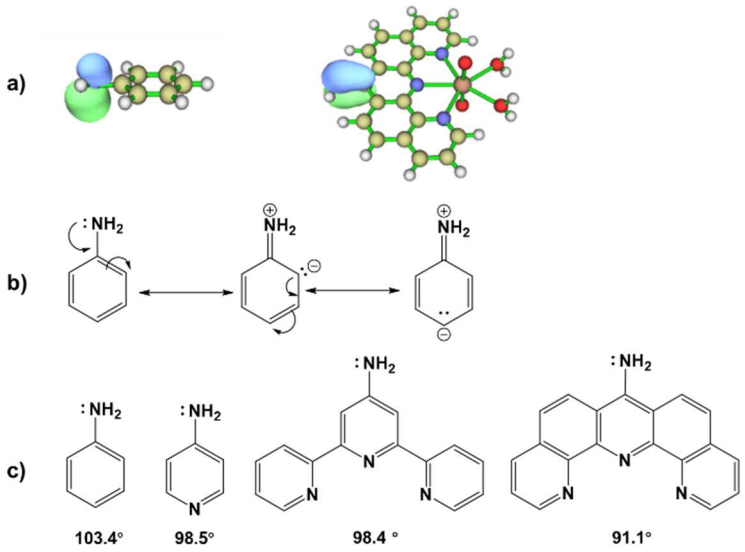

Figure 3.4 a) Lone pair of aniline and extractant **15** from NBO analysis. b) Resonance Structures of aniline. c) The angle between the N lone pair and C-N bond of -NH_2 groups of different extractants.

Introducing oxygen in the side rings, which has stronger electron withdrawing ability than nitrogen, results in the weakest extractant-actinide bond for **10**. On the other hand, introducing an electron donating group (-NH_2) onto the central ring has a strong effect towards enhancing the coordination reaction. This effect is clear in Figure 3.3, comparing extractants in *Row I* against

those in *Row II*, as well as extractants **11** against **10** and **15** against **14**, respectively. The electron-withdrawing substitution, $-NO_2$, is also investigated, see section A3.4 in the Appendix 3. The substitution of H for the $-NH_2$ group introduces a lone pair of electrons and the formation of a partial double bond character N-C π-bond through resonance, as illustrated in Figure 3.4 for extractant **15**. This substituted six-membered ring in **15** has a resonant structure that places more negative charge on the *para* amino group. The low reorganization energy, high planarity, and electron-donating effects all indicate that **15** should be a potential good candidate extractant for actinyl separation.

3.5.5. Bonding nature.

Interactions between extractant and metal ions were analyzed on the basis of the energy decomposition analysis method which decomposes the total energy of the coordinated complex into dispersion term, Pauli repulsion, ionic interaction, and orbital interactions between the fragments: AnO_2^{2+} and extractants in the coordinated geometry (see Figure A3.5.1). The dispersion correction terms are consistent at about -8 kcal/mol. The ionic component in the energy decomposition is systematically stronger than the covalent component (orbital) although by only 10 to 20%. However, when Pauli repulsion and electrostatic interaction are considered together, the steric interactions between fragments are much smaller than the orbital interactions. (Tables A3.5.1.1-A3.5.1.3) This highlights the effect of the orbital component on the bond formation. When the number of nitrogen atoms increases, the extractant-AnO_2^{2+} interaction becomes weaker in both, steric and covalent terms, leading to a longer extractant-AnO_2^{2+} distance. For example, the order of electrostatic and orbital interactions of extractants in *Row II* is **6** > **7** > **9** for the central ring modification and **6** > **8** for the modification on the side rings. Note that the extractants **8** and **9** have the same number of nitrogen atoms and hence similar electrostatic and orbital interactions.

The total bonding energies from EDA shows good correlation with the calculated reaction free energies shown in Figure 3.3 and Table A3.4.1, see Figure A3.5.1.1. The reaction free energies (ΔG) of reaction (1) do not only contain the bonding energy but also the energy of pre-organization and release of water molecules. However, the pre-organization energies are quite small compared to the bonding energies and the energy of releasing three water molecules is consistent for all extractants, see equation (1). Thus, the ΔG will mainly reflect the actual bonding strength between the metal and extractant. Therefore, the ΔΔG could be useful for comparing the bonding between different extractants.

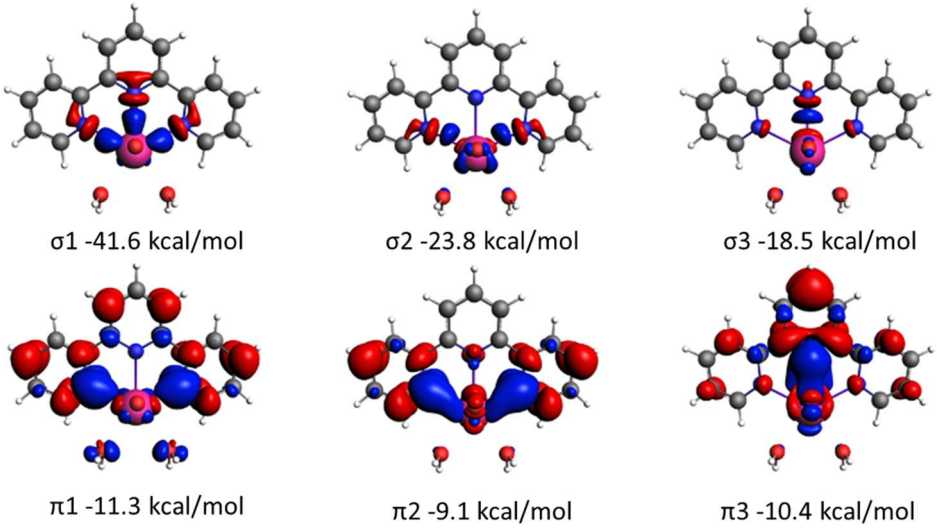

Figure 3.5 ETS-NOCV deformation density (isocontour 0.003 a.u. for σ and isocontour 0.0003 a.u. for π) of the most important interactions between extractant **1** and UO_2 $(H_2O)_2^{2+}$ motif. Electron density flows from red to blue.

ETS-NOCV analysis are performed to further investigate the details of the orbital interactions from EDA. Figure 3.5 and Table A3.5.3.1 illustrate the most important orbital interactions for extractant **1**-UO_2^{2+} compounds based on ETS-NOCV analysis. Even though there is about 50% 5*f* character contribution in the σ1 interaction, overall, all three σ interactions mainly

correspond to the nitrogen lone pair donating into the unoccupied actinyl 6*d* orbitals. Meanwhile, π interactions from the heterocyclic ring π electrons donated to the unoccupied actinyl 5*f* orbitals (Figures A3.5.3.2-A3.5.3.7). The extractant **14** can participate to a larger extent in π bonding than **1**, owing to the planar structure adopted after coordination (Figure A5.3.8). This indicates that the π-bonding interactions likely make an important contribution to the selectivity based on subtle differences in the behavior of the 4*f* and 5*f* electrons. The localized singly occupied 5*f* orbitals are of 99% 5*f* character in Np(VI) and Pu(VI) complexes, which agrees with the calculations of Pu, Am, and Cm complexes with the ADPTZ extractant (extractant **9** in this work) reported by Miguirditchian et al.[82] The additional *f* electrons occupy previously empty *f* orbitals that can be donated to as well as increase the repulsion with the extractants' electron density and reduce complex stability in the order PuO_2^{2+} < NpO_2^{2+} < UO_2^{2+} (See Tables A3.5.3.1-A3.5.3.4; Table A3.5.3.2 contains the contributions of the UO_2^{2+} compounds from Tables A3.5.3.1 divided by 2 to match the β spin open-shell results for the $NpO_2^{2+}$and PuO_2^{2+} compounds).

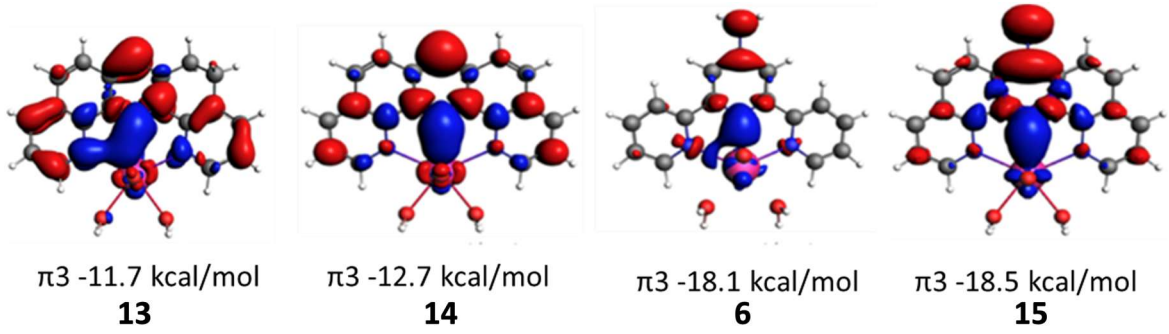

Figure 3.6 Selected ETS-NOCV deformation density (iso-contour 0.0003 a.u.) of π3 interactions between extractants **6**, **13**, **14**, **15** and UO_2 $(H_2O)_2^{2+}$. Electron density flows from red to blue.

As discussed above, extractants **1** and **14** have very similar interaction strength, while extractant **14** has better selectivity for separating $NpO_2^{2+}$and PuO_2^{2+}compounds. ETS-NOCV results in Table A3.5.3.1 indicate that the selectivity might result from overall better π interactions,

especially from better π3 interactions. Figure 3.6, Table A3.5.1.1, and Table A3.5.3.1 show that the electron donating -NH_2 group improves the overall interactions including the π3 interaction energies that are significantly increased. At the same time, the selectivity for separating NpO_2^{2+} and PuO_2^{2+} compounds is significantly increased.

On the basis of these observations and previous reports of Am(III)-ligand bonding, [83-85] we hypothesize that the more extended π system in extractants will lead to higher selectivity, such as extractants **13**, **14**, **15**. However comparing the π interactions of **1** vs. **14**, and **6** vs **15,** the results show that the conjugated π system in the extractant only marginally improved the bonding strength on the order of 0.4 to 2.3 kcal/mol. In contrast the addition of an electron donation group at the center ring (**1** vs. **6**) shows more prominent impact by increasing 7.7 kcal/mol. Therefore, combining all the effects, extractant **15** will be a very promising candidate to separate UO_2^{2+}, NpO_2^{2+} and PuO_2^{2+} from each other, outperforming extractant **1**. From Figure 3.3 and Table A3.4.1, the expected trend in separation ability from $\Delta\Delta G_{Pu\text{-}Np}$ is **15** > **14** > **13** > **1** (-3.7 kcal/mol > -2.0 kcal/mol > -1.1 kcal/mol > 0.8 kcal/mol)

The QTAIM gives another point of view of the orbital interactions. The density (ρ(r)) of the bond critical points (BCPs) can be a probe overall bonding interactions while ETS-NOCV method is based on conventional molecular orbitals. Hence, the ρ(r) can be an indication of the overall bond strength of any atom pairs. For example, for extractant **1**, the orbital interaction between metal and center ring is weaker than the lateral rings. The sum of the ρ(r) shows very good correlation against the orbital interactions from EDA and the sum of σ and π interactions from ETS-NOCV (Figures A3.5.2.1 and A3.5.2.2). The good correlation also confirms that ETS-NOCV results capture most of important covalent interactions.

3.6. Separation of trivalent Am(III) from Eu(III)

3.6.1. Theoretical Predictions

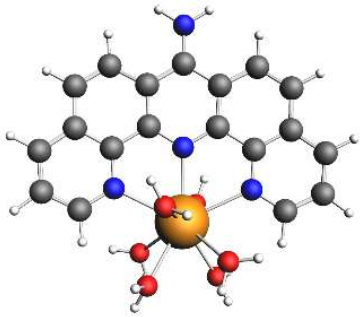

Figure 3.7 Optimized structure of **15**-Am$(H_2O)_6^{3+}$ complex (Red = Oxygen, White = Hydrogen, Grey =Carbon, Dark Blue = Nitrogen, Orange = Americium)

With insight in hand from the simplified AnO_2^{2+} complexation models, we sought to expand our methodology to the more electronically complicated ($5f^6$) and structurally diverse Am(III) and Eu(III) terpyridine systems. Extractants **1**, **13**, **14**, and **15** were selected based on the propensity for binding the AnO_2^{2+} ions. The trend of bond lengths of trivalent Am and Eu complexes (Table A3.6.2) is similar to that of the actinyl-ion compounds in Table A3.2.2-A3.2.4.

Additional down selection was carried out based on the following ion exchange reaction, where we calculated the ΔΔG as previously described.[21, 82, 86]

$$Am(H_2O)_9^{3+} + EuL(H_2O)_6^{3+} \leftrightharpoons Eu(H_2O)_9^{3+} + AmL(H_2O)_6^{3+} \quad (3.2)$$

The model used the coordination number of nine, as reported from experimental data for Eu(III) and Am(III).[87, 88] With this smaller set of molecules we used the more accurate – and also more expensive – DLPNO-CCSD(T) methodology for DFT optimized geometries. The optimized structure of Am is depicted in Figure 3.7 and the ΔΔG are tabulated in Table 3.3. The predicted trend of the absolute ΔΔG values for reaction (3.2) follows the order, **15** > **14** > **13** > **1**. However, the PBE functional predicts the wrong sign of ΔΔG between Am and Eu, the order of separation

selectivity is consistent with **15** having the largest absolute ΔΔG value using both methods. This might come from that PBE tends to overestimate the bond energy for Eu(III) with respect to Am(III).[89, 90] Using the BP86 functional with ZORA approximation and all electron calculations, the authors observed the same overestimation of Eu bonding for gas-phase structures. The authors reported that the double hybrid B2PLYP functional is needed to reproduce the experimental selectivity. Therefore, we evaluated hybrid PBE0, double hybrid B2PLYP, and the gold-standard DLPN-CCSD(T) method for further validation. All these calculations were carried out with single-point energy calculations with the same PBE optimized geometries. The DLPNO-CCSD(T) and B2PLYP give consistent results with the binding preference between Am and Eu as **15** > **14** > **13** > **1.** We conclude that PBE can be used for pre-screening a large set of extractants given its computational efficiency, however, the final results should be carefully benchmarked against more accurate methods. It is important to cross validate multiple methods when comparing between actinide series and lanthanide series instead of within the same series. Ultimately, we concluded that extractants **1**, **13**, **14**, and **15** were viable candidates.

Table 3.3 Gibbs Free Energies (ΔΔG, kcal/mol) for Reaction (3.2) in Water

Extractants	**1**	**13**	**14**	**15**
DLPNO-CCSD(T)//PBE	-1.0	-2.6	-6.2	-6.9

Experimentally, extractant **1** is a mediocre extractant, with reported Am(III)/Eu(III) separation factors ($SF_{Am/Eu}$) that range 7-10,[5] and **9** has slightly higher $SF_{Am/Eu}$ of ~18, [82, 91]. Reiterating, the extractants selected for the Am(III)/Eu(III) separation computational study were selected from the original group on the basis of their selectivity for AnO_2^{2+}, which is a simpler calculation to run for screening. The consistency of the calculated ΔΔG for Am(III)/Eu(III)

separation with experiment gives us hope that the predicted **14** and **15** extractants will lead to improved separation factors. Seeking experimental validation for the theoretical predictions, an effort was launched to synthesize extractant **14** and **15** as the best candidate identified. Although our computational results indicated that extractant **15** was the most promising candidate for Am/Eu separations, its preparation proved to be synthetically challenging. Hence, we pivoted and prepared the closely-related extractants **13** and **14** because calculations on both of these extractants also looked promising for Am/Eu separations.

5.2 Experimental Separation Factors

Compounds **13** and **14** were experimentally evaluated as ^{241}Am selective extractants to test our prediction that preorganization increases $SF_{Am/Eu}$ in liquid/liquid extractions. These extractants were prepared using well-established synthetic protocols and isolated in high-purity and reasonable chemical yield. Although predicted to be an excellent extractant, **14** was sparingly soluble in most common solvents used as the organic phases for liquid/liquid separations. This unfortunate characteristic rendered **14** poorly suited for liquid/liquid separations and $SF_{Am/Eu}$ values were inconclusive. Pivoting our attention to the closely related **13** provided more satisfying results. This extractant is structurally similar to **14**, differing only in the degree of unsaturation associated with one six-membered ring in the ancillary terpyridine backbone.

To establish confidence and credibility in our separation method, we first characterized the $SF_{Am/Eu}$ values using the well-known extractant **1.** Our findings show that **1** is a mediocre ^{241}Am extractant and that its selectivity for removing ^{241}Am from ^{155}Eu is underwhelming; $SF_{Am/Eu} = 5.2 \pm 0.2$ at equilibrium (Figure 3.8). These results agree well with values reported previously; 7-12 depending on experimental conditions.[13] In contrast, when **13** was used as the extractant, the $SF_{Am/Eu}$ at earlier times (5-15 min) was four times higher, 23 ± 1, than observed with **1** (Figure 3.9).

In addition, the time dependence of $SF_{Am/Eu}$ with **13** was opposite of that observed with extractant **1**: instead of gradually increasing as a function of time, $SF_{Am/Eu}$ decreased with time. This divergent trend is a result of the marginal increase in D_{Am} and substantial increase in D_{Eu} upon approaching equilibrium. Even with this decrease in $SF_{Am/Eu}$ over time, it is clear that the preorganized extractant **13** outperformed **1** by a factor of two. We additionally speculate that the rapid binding of ^{241}Am, manifested in the two orders of magnitude higher value of D_{Am} obtained with **13** versus with **1**, was a direct result of extractant preorganization, which enabled rapid and fast binding of ^{241}Am.

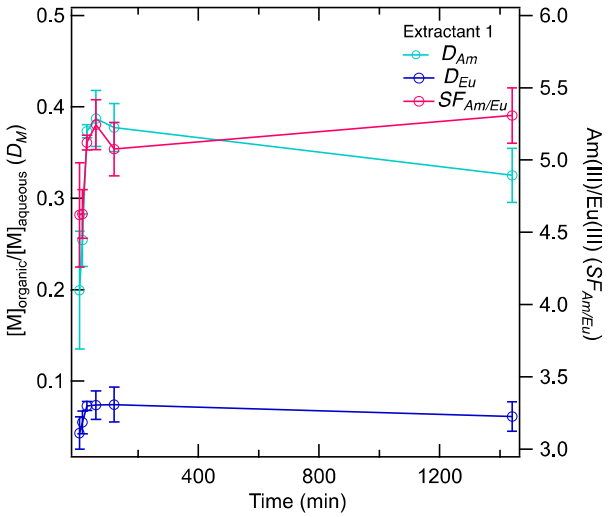

Figure 3.8 A plot showing how distribution coefficients from ^{241}Am and ^{155}Eu changes as a function of time (1 to 24 h) during a liquid/liquid separation facilitated by extractant **1**. The ingoing aqueous phase contained ^{241}Am (0.2 mCi) and ^{155}Eu (0.15 mCi) dissolved in $HNO_{3(aq)}$ (0.01 M) and the ingoing organic phase contained extractant **1** (20 mM) dissolved in a mixture of n-octanol and 2-bromohexanoic acid (1 M). Error bars have been obtained by the propagation of error over a triplicate set of each time trial.

Although the $SF_{Am/Eu}$ and D_{Am} values from **13** are dwarfed by many of the specialty extractants that have been developed previously (and/or discovered recently), the results herein are exciting within the context of our aforementioned computational results. Consider that with short contact times (<15 min) we measured $SF_{Am/Eu}$ from **13** to be four times higher than that from **1** (Figure 3.9). It is quite satisfying to compare these values with the calculated $\Delta\Delta G_{Eu\text{-}Am}$ from

reaction (3.2), which for **13** is 1.6 kcal/mol more favorable than that calculated with **1**. These results serve as proof-of-principle in our computational methodology as we would not have predicted *a priori* superiority of **13** over **1** without the in-depth electronic structure analyses. Although we acknowledge a need for more experimental data to test the generality of our predictive capabilities, we are excited by this experimental validation of our computational results and its implications regarding extraction design. Emboldened by these results, we are modifying substituents on **13**, and consequently extractant **14** as well, to provide more desirable solubility properties.

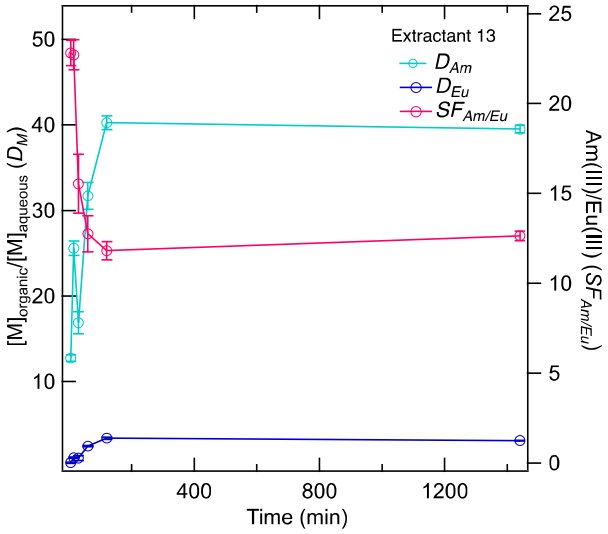

Figure 3.9 A plot showing how distribution coefficients from ^{241}Am and ^{155}Eu changes as a function of time (<1 h) during a liquid/liquid separation facilitated by extractant **13**. The ingoing aqueous phase contained ^{241}Am (0.2 mCi) and ^{155}Eu (0.15 mCi) dissolved in $HNO_{3(aq)}$ (0.01 M) and the ingoing organic phase contained extractant **13** (20 mM) dissolved in a mixture of n-octanol that contained 2-bromohexanoic acid (1 M). Error bars have been obtained by the propagation of error over a triplicate set of each time trial.

3.7. Conclusion

In this study, the An(III)/Ln(III) separation performance from terpyridine-based extractants has been evaluated systematically as a function of substituents that impact the extractants' structure and electronics using relativistic quantum chemical calculations. The results identified design principles that seem to be important for effective An(III)/Ln(III) separations and revolve around several aspects of the extractant-ion interactions. Using a simplified model based on AnO_2^{2+} complexation, we interrogated a set of variables associated with binding of 5f-elements. These variables include how planarity and reorganization of an extractant for metal complexation varied as a function of the ancillary substituents bound to the terpyridyl backbone and the number of nitrogen atoms contained within the aromatic ring system. Extractant planarity appears, at first glance, to be an obviously important variable. However, it was found that planarity had only a minor effect on metal coordination for the family of extractants studied herein. Often, and unexpectedly, modifying the terpyridine backbone to achieve extractant planarity decreased aptitude for AnO_2^{2+} complexation. Instead, we learned that the reorganization of the extractant to be in a configuration favorable for metal coordination was more influential than just terpyridine planarity. For example, methodic introduction of substituents on the terpyridine backbone that preorganized the terpyridine for metal binding was found to systematically and substantial impact AnO_2^{2+} binding. Results from these extractant–actinyl interactions provided a clean and simplified model, upon which we built more sophisticated calculations that included Am(III) and Eu(III). To gain highly accurate binding energies of an extractant to an f-element metal center, it is critical to pay special attention to include all potential factors such as solvation effects, entropy of lower frequencies, and the electronic theory that is sufficient to describe complex open-shell f-systems. Noteworthy, our results show that to obtain correct reaction energies for Am(III)/Eu(III) separation,

high-level of theory single-point calculations at the CCSD level are needed in order to reproduce experimental results on the selectivity for Am(III)/Eu(III) separation. This demonstrates that actinyl ions as a simple model can be used to screen huge amounts of newly designed extractants in the future without calculating the trivalent actinide and lanthanide compounds which are computationally much more difficult and costly. To screen large volumes of extractant candidates aiming for searching the highest selectivity of ligands to metals, it is important to use a computationally economic method. We can take advantage of error cancellation that is embedded in the calculation of the ΔΔΔG. While taking the difference between systems, we will be able to reduce the systematic errors induced by the computational methods and result in more reliable output.[92-94] Overall, we found that substituting the C–H motif with a nitrogen atom in the pyridine rings reduced steric repulsions between adjacent N-heterocyclic rings. Unfortunately, this substitution also weakened the bonding between the extractant and Am(III). Note that the BTP ligand (extractant **5**) in this study actually is different from the BTP extractants in the previous experimental study.[95-101] Ligand **5** only contains the core but without any modifications, such as extra carbon chains. Those modifications usually help BTP extractants to better move into different solvents in the extraction process. However, in this study, we only focus the effects from bonding itself. The effects of those modifications will be investigated in a future paper. In contrast, replacing pairs of clashing H atoms with alkyl bridging groups (see extractant in *Row IV* of Scheme 3.1) was shown to pre-organize extractants into geometric configurations poised for metal binding. The impact from this modification has enhanced the reaction rate and only marginally negative impact on the electronegativity associated with the terpyridyl binding unit. We also observed computationally that adding electron donating groups (e.g. $–NH_2$) improved ionic interactions as well as orbital interactions between the terpyridyl extractants and the bound metal +3 cation.

Considering that the Pauli repulsion cancels part of the ionic interaction, the orbital interactions would become more important. After further investigating the orbital interactions by the ETS-NOCV method, our results indicate that terpyridine–An(III) π-bonding interactions play an important role toward binding selectivity. These results led us to postulate the preorganized extractant **13** would favor selective binding of Am(III) over Eu(III). Consistent with that prediction were experimental studies, which provided confidence and credibility with our interpretation of the theoretical results. The connection between theory and experiment demonstrates how a well-defined computational framework can be used to guide extractant design and tune extractant properties from modifications at the periphery of a the extractant backbones. The discovery rate is faster than would be possible if each and every extractant permutation were to be synthesized and experimentally tested. Our results also highlight the need for reliable predictive capabilities to screen the effects of extractant modifications on liquid/liquid separations processes that are currently not easily modeled using electronic structure approaches (e.g. solubility of the extractant and the extracted species). We hope this work, alongside impactful separation studies published previously,[16, 91, 102] will stimulate discussion and modeling efforts that advance extractant design principles. The impact of improving predictive capability within this context pf An(III)/Ln(III) separations would be profound and provide economically viable and time efficient methods that support separation science beyond the Am(III)/Ln(III) problem, potentially touching on other important and emerging liquid/liquid separation problems.

3.8. References

1. Chu, S. *Critical Materials Strategy*; U.S. Department of Energy: 2011.
2. Madic, C.; Ouvrier, N., Introduction EUROPART : EUROpean research program for the PARTitioning of minor actinides from high active wastes arising from. *Radiochimica Acta* **2009,** *4-5*, 183-185.
3. Yin, H. M.; Luo, Z., Investigation of the Nuclear Gauge Density Calibration Method. *Road Materials and Pavement Design* **2009,** *10* (3), 625-645.
4. Artemyev, I. B.; Artemiev, B. V.; Vladimirov, Y. L.; Vladimirov, L. V., Modernization of radiation detectors thickness gauge. *Journal of Physics: Conference Series* **2017,** *808*, 012012.
5. Dutta, D., Measurement of Material Thickness using X-Ray Attenuation. *Masters Thesis, Mississippi State University: Starkville, MI,* **2017**.
6. LeVert, F.; Helminski, E., Literature review and commercial source evaluation of americium-241. Final report, March 1, 1972--May 31, 1973. **1973**.
7. Seaborg, G. T., The synthetic actinides-from discovery to manufacture. *Nuclear Applications and Technology* **1970,** *9* (6), 830-850.
8. Wasterlund, I., *Soil and Root Damage in Forestry: Reducing the Impact of Forest Mechanization*. Elsevier: 2020.
9. Mangeng, C. A.; Thayer, G. R., Beneficial uses of sup 241/Am. **1984**.
10. Guinn, V. P.; Wagner, C. D., Instrumental Neutron Activation Analysis. *Analytical Chemistry* **1960,** *32* (3), 317-323.
11. Ozden, B.; Brennan, C.; Landsberger, S., Environmental assessment of red mud by determining natural radionuclides using neutron activation analysis. *Environmental Earth Sciences* **2019,** *78* (4), 114.
12. Hudson, M. J.; Harwood, L. M.; Laventine, D. M.; Lewis, F. W., Use of Soft Heterocyclic N-Donor Ligands To Separate Actinides and Lanthanides. *Inorganic Chemistry* **2013,** *52* (7), 3414-3428.
13. Kolarik, Z., Complexation and Separation of Lanthanides(III) and Actinides(III) by Heterocyclic N-Donors in Solutions. *Chemical Reviews* **2008,** *108* (10), 4208-4252.
14. Lewis, F. W.; Hudson, M. J.; Harwood, L. M., Development of Highly Selective Ligands for Separations of Actinides from Lanthanides in the Nuclear Fuel Cycle. *Synlett* **2011,** *2011* (18), 2609-2632.
15. Panak, P. J.; Geist, A., Complexation and Extraction of Trivalent Actinides and Lanthanides by Triazinylpyridine N-Donor Ligands. *Chemical Reviews* **2013,** *113* (2), 1199-1236.
16. Ekberg, C.; Fermvik, A.; Retegan, T.; Skarnemark, G.; Foreman, M. R. S.; Hudson, M. J.; Englund, S.; Nilsson, M., An overview and historical look back at the solvent extraction using nitrogen donor ligands to extract and separate An(III) from Ln(III). *Radiochimica Acta* **2008,** *96* (4-5), 225-233.
17. Cotton, S., *Lanthanide and actinide chemistry*. John Wiley & Sons: Chichester, 2009.
18. Veliscek-Carolan, J., Separation of actinides from spent nuclear fuel: A review. *Journal of Hazardous Materials* **2016,** *318*, 266-281.
19. Hancock, R. D., The pyridyl group in ligand design for selective metal ion complexation and sensing. *Chemical Society Reviews* **2013,** *42* (4), 1500-1524.

20. Ionova, G.; Rabbe, C.; Guillaumont, R.; Ionov, S.; Madic, C.; Krupa, J.-C.; Guillaneux, D., A donor–acceptor model of Ln(III) complexation with terdentate nitrogen planar ligands. *New Journal of Chemistry* **2002,** *26* (2), 234-242.
21. Chen, Y.-M.; Wang, C.-Z.; Wu, Q.-Y.; Lan, J.-H.; Chai, Z.-F.; Nie, C.-M.; Shi, W.-Q., Theoretical Insights into Modification of Nitrogen-Donor Ligands to Improve Performance on Am(III)/Eu(III) Separation. *Inorganic Chemistry* **2020,** *59* (5), 3221-3231.
22. Trumm, S.; Wipff, G.; Geist, A.; Panak, P. J.; Fanghänel, T., Optimising BTP ligands by tuning their basicity. *Radiochimica Acta* **2011,** *99* (1), 13-16.
23. Benay, G.; Schurhammer, R.; Desaphy, J.; Wipff, G., Substituent effects on BTP's basicity and complexation properties with LnIII lanthanide ions. *New Journal of Chemistry* **2011,** *35* (1), 184-189.
24. Spencer, L. P.; Yang, P.; Minasian, S. G.; Jilek, R. E.; Batista, E. R.; Boland, K. S.; Boncella, J. M.; Conradson, S. D.; Clark, D. L.; Hayton, T. W.; Kozimor, S. A.; Martin, R. L.; MacInnes, M. M.; Olson, A. C.; Scott, B. L.; Shuh, D. K.; Wilkerson, M. P., Tetrahalide Complexes of the [U(NR)2]2+ Ion: Synthesis, Theory, and Chlorine K-Edge X-ray Absorption Spectroscopy. *Journal of the American Chemical Society* **2013,** *135*, 2279-2290.
25. Bejger, C.; Tian, Y.-H.; Baker, B. J.; Boland, K. S.; Scott, B. L.; Batista, E. R.; Kozimor, S. A.; Sessler, J. L., Synthesis and characterization of tetrathiafulvalene-salphen actinide complex. *Dalton Transactions* **2013,** *42*, 6716-6719.
26. Fonseca Guerra, C.; Snijders, J. G.; te Velde, G.; Baerends, E. J., Towards an order-N DFT method. *Theoretical Chemistry Accounts* **1998,** *99* (6), 391-403.
27. te Velde, G.; Bickelhaupt, F. M.; Baerends, E. J.; Fonseca Guerra, C.; van Gisbergen, S. J. A.; Snijders, J. G.; Ziegler, T., Chemistry with ADF. *Journal of Computational Chemistry* **2001,** *22* (9), 931-967.
28. Baerends, E. J.; Ziegler, T.; Atkins, A. J.; Autschbach, J.; Bashford, D.; Baseggio, O.; Brces, A.; Bickelhaupt, F. M.; Bo, C.; Boerritger, P. M.; Cavallo, L.; Daul, C.; Chong, D. P.; Chulhai, D. V.; Deng, L.; Dickson, R. M.; Dieterich, J. M.; Ellis, D. E.; van Faassen, M.; Ghysels, A.; Giammona, A.; van Gisbergen, S. J. A.; Goez, A.; Gtz, A. W.; Gusarov, S.; Harris, F. E.; van den Hoek, P.; Hu, Z.; Jacob, C. R.; Jacobsen, H.; Jensen, L.; Joubert, L.; Kaminski, J. W.; van Kessel, G.; Knig, C.; Kootstra, F.; Kovalenko, A.; Krykunov, M.; van Lenthe, E.; McCormack, D. A.; Michalak, A.; Mitoraj, M.; Morton, S. M.; Neugebauer, J.; Nicu, V. P.; Noodleman, L.; Osinga, V. P.; Patchkovskii, S.; Pavanello, M.; Peeples, C. A.; Philipsen, P. H. T.; Post, D.; Pye, C. C.; Ramanantoanina, H.; Ramos, P.; Ravenek, W.; Rodrguez, J. I.; Ros, P.; Rger, R.; Schipper, P. R. T.; Schlns, D.; van Schoot, H.; Schreckenbach, G.; Seldenthuis, J. S.; Seth, M.; Snijders, J. G.; Sol, ADF2019, SCM, Theoretical Chemistry, Vrije Universiteit, Amsterdam, The Netherlands, https://www.scm.com.
29. Shamov, G. A.; Schreckenbach, G., Density Functional Studies of Actinyl Aquo Complexes Studied Using Small-Core Effective Core Potentials and a Scalar Four-Component Relativistic Method. *The Journal of Physical Chemistry A* **2006,** *110* (43), 12072-12072.
30. Shamov, G. A.; Schreckenbach, G., Density Functional Studies of Actinyl Aquo Complexes Studied Using Small-Core Effective Core Potentials and a Scalar Four-Component Relativistic Method. *The Journal of Physical Chemistry A* **2005,** *109* (48), 10961-10974.
31. Shamov, G. A.; Schreckenbach, G.; Vo, T. N., A Comparative Relativistic DFT and Ab Initio Study on the Structure and Thermodynamics of the Oxofluorides of Uranium(IV), (V) and (VI). *Chemistry – A European Journal* **2007,** *13* (17), 4932-4947.

32. Shamov, G. A.; Schreckenbach, G.; Martin, R. L.; Hay, P. J., Crown Ether Inclusion Complexes of the Early Actinide Elements, [AnO2(18-crown-6)]n+, An = U, Np, Pu and n = 1, 2: A Relativistic Density Functional Study. *Inorganic Chemistry* **2008,** *47* (5), 1465-1475.
33. Perdew, J. P.; Burke, K.; Ernzerhof, M., Generalized Gradient Approximation Made Simple. *Physical Review Letters* **1996,** *77* (18), 3865-3868.
34. Becke, A. D., Density-functional thermochemistry. III. The role of exact exchange. *The Journal of Chemical Physics* **1993,** *98* (7), 5648-5652.
35. Lee, C.; Yang, W.; Parr, R. G., Development of the Colle-Salvetti correlation-energy formula into a functional of the electron density. *Physical Review B* **1988,** *37* (2), 785-789.
36. Vosko, S. H.; Wilk, L.; Nusair, M., Accurate spin-dependent electron liquid correlation energies for local spin density calculations: a critical analysis. *Canadian Journal of Physics* **1980,** *58* (8), 1200-1211.
37. Stephens, P. J.; Devlin, F. J.; Chabalowski, C. F.; Frisch, M. J., Ab Initio Calculation of Vibrational Absorption and Circular Dichroism Spectra Using Density Functional Force Fields. *The Journal of Physical Chemistry* **1994,** *98* (45), 11623-11627.
38. Lenthe, E. v.; Baerends, E. J.; Snijders, J. G., Relativistic regular two-component Hamiltonians. *The Journal of Chemical Physics* **1993,** *99* (6), 4597-4610.
39. Lenthe, E. v.; Baerends, E. J.; Snijders, J. G., Relativistic total energy using regular approximations. *The Journal of Chemical Physics* **1994,** *101* (11), 9783-9792.
40. Lenthe, E. v.; Ehlers, A.; Baerends, E.-J., Geometry optimizations in the zero order regular approximation for relativistic effects. *The Journal of Chemical Physics* **1999,** *110* (18), 8943-8953.
41. Van Lenthe, E.; Baerends, E. J., Optimized Slater-type basis sets for the elements 1–118. *Journal of Computational Chemistry* **2003,** *24* (9), 1142-1156.
42. Pye, C. C.; Ziegler, T., An implementation of the conductor-like screening model of solvation within the Amsterdam density functional package. *Theoretical Chemistry Accounts* **1999,** *101* (6), 396-408.
43. Allinger, N. L.; Zhou, X.; Bergsma, J., Molecular mechanics parameters. *Journal of Molecular Structure: THEOCHEM* **1994,** *312* (1), 69-83.
44. Grimme, S.; Antony, J.; Ehrlich, S.; Krieg, H., A consistent and accurate ab initio parametrization of density functional dispersion correction (DFT-D) for the 94 elements H-Pu. *The Journal of Chemical Physics* **2010,** *132* (15), 154104.
45. Grimme, S.; Ehrlich, S.; Goerigk, L., Effect of the damping function in dispersion corrected density functional theory. *Journal of Computational Chemistry* **2011,** *32* (7), 1456-1465.
46. Martin, R. L.; Hay, P. J.; Pratt, L. R., Hydrolysis of Ferric Ion in Water and Conformational Equilibrium. *The Journal of Physical Chemistry A* **1998,** *102* (20), 3565-3573.
47. Deblonde, G. J.-P.; Kelley, M. P.; Su, J.; Batista, E. R.; Yang, P.; Booth, C. H.; Abergel, R. J., Spectroscopic and Computational Characterization of Diethylenetriaminepentaacetic Acid/Transplutonium Chelates: Evidencing Heterogeneity in the Heavy Actinide(III) Series. *Angewandte Chemie International Edition* **2018,** *57* (17), 4521-4526.
48. Kelley, M. P.; Deblonde, G. J. P.; Su, J.; Booth, C. H.; Abergel, R. J.; Batista, E. R.; Yang, P., Bond Covalency and Oxidation State of Actinide Ions Complexed with Therapeutic Chelating Agent 3,4,3-LI(1,2-HOPO). *Inorganic Chemistry* **2018,** *57* (9), 5352-5363.
49. Kelley, M. P.; Su, J.; Urban, M.; Luckey, M.; Batista, E. R.; Yang, P.; Shafer, J. C., On the Origin of Covalent Bonding in Heavy Actinides. *Journal of the American Chemical Society* **2017,** *139* (29), 9901-9908.

50. Paulechka, E.; Kazakov, A., Efficient DLPNO–CCSD(T)-Based Estimation of Formation Enthalpies for C-, H-, O-, and N-Containing Closed-Shell Compounds Validated Against Critically Evaluated Experimental Data. *The Journal of Physical Chemistry A* **2017,** *121* (22), 4379-4387.
51. Neese, F., Software update: the ORCA program system, version 4.0. *WIREs Computational Molecular Science* **2018,** *8* (1), e1327.
52. Pantazis, D. A.; Neese, F., All-Electron Scalar Relativistic Basis Sets for the Actinides. *Journal of Chemical Theory and Computation* **2011,** *7* (3), 677-684.
53. Pantazis, D. A.; Neese, F., All-Electron Scalar Relativistic Basis Sets for the Lanthanides. *Journal of Chemical Theory and Computation* **2009,** *5* (9), 2229-2238.
54. Weigend, F.; Ahlrichs, R., Balanced basis sets of split valence, triple zeta valence and quadruple zeta valence quality for H to Rn: Design and assessment of accuracy. *Physical Chemistry Chemical Physics* **2005,** *7* (18), 3297-3305.
55. Hirshfeld, F. L., Bonded-atom fragments for describing molecular charge densities. *Theoretica chimica acta* **1977,** *44* (2), 129-138.
56. Zegke, M.; Zhang, X.; Pidchenko, I.; Hlina, J. A.; Lord, R. M.; Purkis, J.; Nichol, G. S.; Magnani, N.; Schreckenbach, G.; Vitova, T.; Love, J. B.; Arnold, P. L., Differential uranyl(v) oxo-group bonding between the uranium and metal cations from groups 1, 2, 4, and 12; a high energy resolution X-ray absorption, computational, and synthetic study. *Chemical Science* **2019,** *10* (42), 9740-9751.
57. Arnold, P. L.; Dutkiewicz, M. S.; Zegke, M.; Walter, O.; Apostolidis, C.; Hollis, E.; Pécharman, A. F.; Magnani, N.; Griveau, J. C.; Colineau, E., Subtle interactions and electron transfer between UIII, NpIII, or PuIII and uranyl mediated by the oxo group. *Angewandte Chemie* **2016,** *128* (41), 12989-12993.
58. Glendening, E. D.; Landis, C. R.; Weinhold, F., NBO 6.0: Natural bond orbital analysis program. *Journal of Computational Chemistry* **2013,** *34* (16), 1429-1437.
59. Lu, T.; Chen, F., Multiwfn: A multifunctional wavefunction analyzer. *Journal of Computational Chemistry* **2012,** *33* (5), 580-592.
60. Ziegler, T.; Rauk, A., A theoretical study of the ethylene-metal bond in complexes between copper(1+), silver(1+), gold(1+), platinum(0) or platinum(2+) and ethylene, based on the Hartree-Fock-Slater transition-state method. *Inorganic Chemistry* **1979,** *18* (6), 1558-1565.
61. Ziegler, T.; Rauk, A., Carbon monoxide, carbon monosulfide, molecular nitrogen, phosphorus trifluoride, and methyl isocyanide as .sigma. donors and .pi. acceptors. A theoretical study by the Hartree-Fock-Slater transition-state method. *Inorganic Chemistry* **1979,** *18* (7), 1755-1759.
62. Mitoraj, M. P.; Michalak, A.; Ziegler, T., A Combined Charge and Energy Decomposition Scheme for Bond Analysis. *Journal of Chemical Theory and Computation* **2009,** *5* (4), 962-975.
63. Rodríguez, J. I., An efficient method for computing the QTAIM topology of a scalar field: The electron density case. *Journal of Computational Chemistry* **2013,** *34* (8), 681-686.
64. Rodríguez, J. I.; Bader, R. F. W.; Ayers, P. W.; Michel, C.; Götz, A. W.; Bo, C., A high performance grid-based algorithm for computing QTAIM properties. *Chemical Physics Letters* **2009,** *472* (1), 149-152.
65. Hung, C.-Y.; Wang, T.-L.; Jang, Y.; Kim, W. Y.; Schmehl, R. H.; Thummel, R. P., Dipyrido[4,3-b;5,6-b]acridine Derivatives and Their Ruthenium(II) Complexes. *Inorganic Chemistry* **1996,** *35* (20), 5953-5956.
66. National Nuclear Data Center. https://www.nndc.bnl.gov/nudat2/ (accessed Oct 21).
67. The National Isotope Development Center. https://www.isotopes.gov/ (accessed Oct. 21).

68. Horwitz, E. P.; McAlister, D. R.; Dietz, M. L., Extraction chromatography versus solvent extraction: How similar are they? *Separation Science and Technology* **2006,** *41* (10), 2163-2182.
69. Seaborg, G. T.; Katz, J. J.; Morss, L. R., *The Chemistry of the Actinide Elements: Volume 2*. Springer Science & Business Media: 2012; Vol. 2.
70. Bardin, N.; Rubini, P.; Madie, C., Hydration of Actinyl(VI), MO2+2aq (M = U, Np, Pu). An NMR Study. *Radiochimica Acta* **1998,** *83* (4), 189-194.
71. Antonio, R.; Soderholm, L.; Williams, C. W.; Blaudeau, J.-P.; Bursten, B. E., Neptunium redox speciation. *Radiochimica Acta* **2001,** *89* (1), 17-26.
72. Skanthakumar, S.; Antonio, M. R.; Soderholm, L., A Comparison of Neptunyl(V) and Neptunyl(VI) Solution Coordination: The Stability of Cation−Cation Interactions. *Inorganic Chemistry* **2008,** *47* (11), 4591-4595.
73. Allen, P. G.; Bucher, J. J.; Shuh, D. K.; Edelstein, N. M.; Reich, T., Investigation of Aquo and Chloro Complexes of UO(2)(2+), NpO(2)(+), Np(4+), and Pu(3+) by X-ray Absorption Fine Structure Spectroscopy. *Inorg Chem* **1997,** *36* (21), 4676-4683.
74. Hay, P. J.; Martin, R. L.; Schreckenbach, G., Theoretical Studies of the Properties and Solution Chemistry of AnO22+ and AnO2+ Aquo Complexes for An = U, Np, and Pu. *The Journal of Physical Chemistry A* **2000,** *104* (26), 6259-6270.
75. Wahlgren, U.; Moll, H.; Grenthe, I.; Schimmelpfennig, B.; Maron, L.; Vallet, V.; Gropen, O., Structure of Uranium(VI) in Strong Alkaline Solutions. A Combined Theoretical and Experimental Investigation. *The Journal of Physical Chemistry A* **1999,** *103* (41), 8257-8264.
76. Spencer, S.; Gagliardi, L.; Handy, N. C.; Ioannou, A. G.; Skylaris, C.-K.; Willetts, A.; Simper, A. M., Hydration of UO22+ and PuO22+. *The Journal of Physical Chemistry A* **1999,** *103* (12), 1831-1837.
77. Aaberg, M.; Ferri, D.; Glaser, J.; Grenthe, I., Structure of the hydrated dioxouranium(VI) ion in aqueous solution. An x-ray diffraction and proton NMR study. *Inorganic Chemistry* **1983,** *22* (26), 3986-3989.
78. Maerzke, K. A.; Goff, G. S.; Runde, W. H.; Schneider, W. F.; Maginn, E. J., Structure and Dynamics of Uranyl(VI) and Plutonyl(VI) Cations in Ionic Liquid/Water Mixtures via Molecular Dynamics Simulations. *The Journal of Physical Chemistry B* **2013,** *117* (37), 10852-10868.
79. Cao, Z.; Balasubramanian, K., Theoretical studies of UO2(H2O)n2+,NpO2(H2O)n+, and PuO2(H2O)n2+ complexes (n=4–6) in aqueous solution and gas phase. *The Journal of Chemical Physics* **2005,** *123* (11), 114309.
80. X-ray absorption spectroscopy and actinide electrochemistry: a setup dedicated to radioactive samples applied to neptunium chemistry. *Journal of Synchrotron Radiation* **2022,** *29* (1), 1--10.
81. de Sahb, C.; Watson, L. A.; Nadas, J.; Hay, B. P., Design Criteria for Polyazine Extractants To Separate AnIII from LnIII. *Inorganic Chemistry* **2013,** *52* (18), 10632-10642.
82. Miguirditchian, M.; Guillaneux, D.; Guillaumont, D.; Moisy, P.; Madic, C.; Jensen, M. P.; Nash, K. L., Thermodynamic Study of the Complexation of Trivalent Actinide and Lanthanide Cations by ADPTZ, a Tridentate N-Donor Ligand. *Inorganic Chemistry* **2005,** *44* (5), 1404-1412.
83. Adam, C.; Kaden, P.; Beele, B. B.; Müllich, U.; Trumm, S.; Geist, A.; Panak, P. J.; Denecke, M. A., Evidence for covalence in a N-donor complex of americium(iii). *Dalton Transactions* **2013,** *42* (39), 14068-14074.
84. Yu, X.; Sergentu, D.-C.; Feng, R.; Autschbach, J., Covalency of Trivalent Actinide Ions with Different Donor Ligands: Do Density Functional and Multiconfigurational Wavefunction

Calculations Corroborate the Observed "Breaks"? *Inorganic Chemistry* **2021,** *60* (23), 17744-17757.
85. Dan, D.; Celis-Barros, C.; White, F. D.; Sperling, J. M.; Albrecht-Schmitt, T. E., Origin of Selectivity of a Triazinyl Ligand for Americium(III) over Neodymium(III). *Chemistry – A European Journal* **2019,** *25* (13), 3248-3252.
86. Miguirditchian, M.; Guillaumont, D.; Saint-Maxent, A.; Moisy, P.; Guillaneux, D.; Madic, C., Thermodynamics of plutonium(iii) and curium(iii) complexation with a N-donor ligand. *Dalton Transactions* **2019,** *48* (3), 839-842.
87. Apostolidis, C.; Schimmelpfennig, B.; Magnani, N.; Lindqvist-Reis, P.; Walter, O.; Sykora, R.; Morgenstern, A.; Colineau, E.; Caciuffo, R.; Klenze, R.; Haire, R. G.; Rebizant, J.; Bruchertseifer, F.; Fanghänel, T., [An(H2O)9](CF3SO3)3 (An=U–Cm, Cf): Exploring Their Stability, Structural Chemistry, and Magnetic Behavior by Experiment and Theory. *Angewandte Chemie International Edition* **2010,** *49* (36), 6343-6347.
88. Choppin, G. R., Factors in Ln(III) complexation. *Journal of Alloys and Compounds* **1997,** *249* (1), 1-8.
89. Kaneko, M.; Miyashita, S.; Nakashima, S., Benchmark study of the Mössbauer isomer shifts of Eu and Np complexes by relativistic DFT calculations for understanding the bonding nature of f-block compounds. *Dalton Transactions* **2015,** *44* (17), 8080-8088.
90. Kaneko, M.; Miyashita, S.; Nakashima, S., Bonding Study on the Chemical Separation of Am(III) from Eu(III) by S-, N-, and O-Donor Ligands by Means of All-Electron ZORA-DFT Calculation. *Inorganic Chemistry* **2015,** *54* (14), 7103-7109.
91. Bryantsev, V. S.; Hay, B. P., Theoretical prediction of Am(iii)/Eu(iii) selectivity to aid the design of actinide-lanthanide separation agents. *Dalton Transactions* **2015,** *44* (17), 7935-7942.
92. Bessen, N. P.; Popov, I. A.; Heathman, C. R.; Grimes, T. S.; Zalupski, P. R.; Moreau, L. M.; Smith, K. F.; Booth, C. H.; Abergel, R. J.; Batista, E. R.; Yang, P.; Shafer, J. C., Complexation of Lanthanides and Heavy Actinides with Aqueous Sulfur-Donating Ligands. *Inorganic Chemistry* **2021,** *60* (9), 6125-6134.
93. Lehman-Andino, I.; Su, J.; Papathanasiou, K. E.; Eaton, T. M.; Jian, J.; Dan, D.; Albrecht-Schmitt, T. E.; Dares, C. J.; Batista, E. R.; Yang, P.; Gibson, J. K.; Kavallieratos, K., Soft-donor dipicolinamide derivatives for selective actinide(iii)/lanthanide(iii) separation: the role of S- vs. O-donor sites. *Chemical Communications* **2019,** *55* (17), 2441-2444.
94. Aurora E. Clark, M. J. S., Zhu Liu, Ernesto Martinez-Baez, Jing Su, Enrique R. Batista, Ping Yang, Andrew Wildman, Torin Stetina, Xiaosong Li, Ken Newcomb, Edward J. Maginn, Jochen Autschbach, David A. Dixon, Changing the Landscape in Solvent Extraction. In *Ion Exchange and Solvent Extraction*, 1st ed ed.; Moyer, B. A., Ed. CRC Press.: 2019; Vol. 23.
95. Berthet, J.-C.; Miquel, Y.; Iveson, P. B.; Nierlich, M.; Thuéry, P.; Madic, C.; Ephritikhine, M., The affinity and selectivity of terdentate nitrogen ligands towards trivalent lanthanide and uranium ions viewed from the crystal structures of the 1 ∶ 3 complexes. *Journal of the Chemical Society, Dalton Transactions* **2002,** (16), 3265-3272.
96. Rawat, N.; Bhattacharyya, A.; Ghosh, S.; Gadly, T.; Tomar, B., Thermodynamics of complexation of lanthanides with 2, 6-bis (5, 6-diethyl-1, 2, 4-triazin-3-yl) pyridine. *Radiochimica Acta* **2011,** *99* (11), 705-712.
97. Iveson, P. B.; Rivière, C.; Guillaneux, D.; Nierlich, M.; Thuéry, P.; Ephritikhine, M.; Madic, C., Selective complexation of uranium(iii) over cerium(iii) by 2,6-bis(5,6-dialkyl-1,2,4-triazin-3-yl)pyridines: 1H NMR and X-ray crystallography studies. *Chemical Communications* **2001,** (16), 1512-1513.

98. Miguirditchian, M.; Guillaneux, D.; Francois, N.; Airvault, S.; Ducros, S.; Thauvin, D.; Madic, C.; Illemassene, M.; Lagarde, G.; Krupa, J.-C., Complexation of lanthanide (III) and actinide (III) cations with tridentate nitrogen-donor ligands: A luminescence and spectrophotometric study. *Nuclear science and engineering* **2006,** *153* (3), 223-232.
99. Hudson, M. J.; Boucher, C. E.; Braekers, D.; Desreux, J. F.; Drew, M. G.; Foreman, M. R. S. J.; Harwood, L. M.; Hill, C.; Madic, C.; Marken, F., New bis (triazinyl) pyridines for selective extraction of americium (III). *New Journal of Chemistry* **2006,** *30* (8), 1171-1183.
100. Hudson, M. J.; Foreman, M. R. S. J.; Hill, C.; Huet, N.; Madic, C., Studies on the parallel synthesis and evaluation of new heterocyclic extractants for the partitioning of minor actinides. *Solvent extraction and ion exchange* **2003,** *21* (5), 637-652.
101. Trumm, S.; Geist, A.; Panak, P. J.; Fanghänel, T., An improved hydrolytically-stable bis-triazinyl-pyridine (BTP) for selective actinide extraction. *Solvent Extraction and Ion Exchange* **2011,** *29* (2), 213-229.
102. Cary, S. K.; Su, J.; Galley, S. S.; Albrecht-Schmitt, T. E.; Batista, E. R.; Ferrier, M. G.; Kozimor, S. A.; Mocko, V.; Scott, B. L.; Van Alstine, C. E.; White, F. D.; Yang, P., A series of dithiocarbamates for americium, curium, and californium. *Dalton Transactions* **2018,** *47*, 14452.

Appendix 3.

A 3.1. Structures

A 3.1.1. Structure of actinyl compounds.

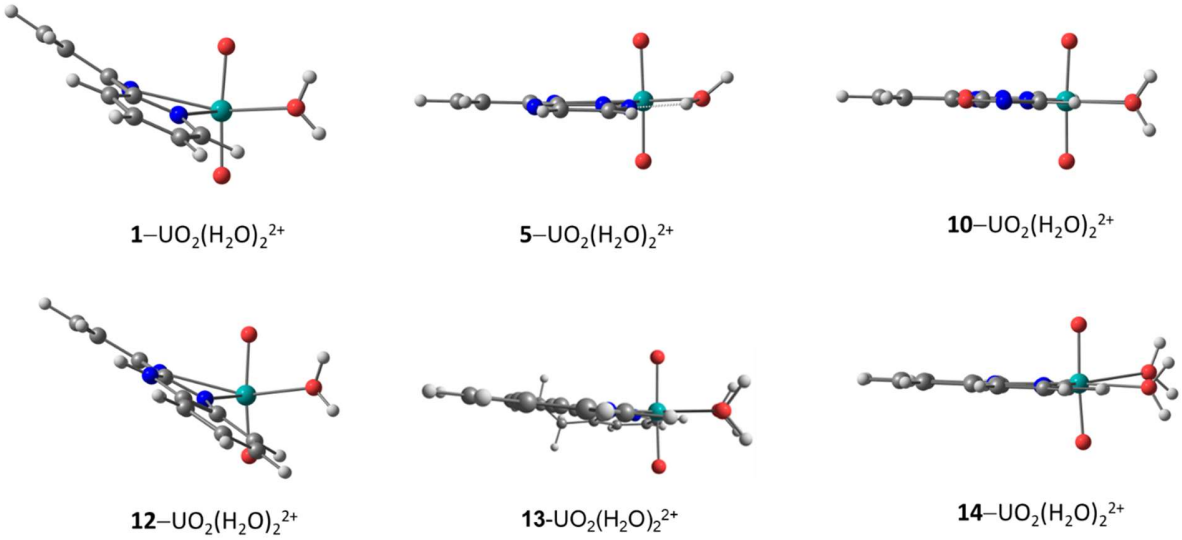

Figure A 3.1.1.1 The side view of optimized structures of selected L-$UO_2(H_2O)_2^{2+}$ (L=**1**, **5**, **10**, **12**, **13**, **14**) complexes (Red = Oxygen, White = Hydrogen, Grey =Carbon, Dark Blue = Nitrogen, Light Blue = Uranium)

A 3.2. Geometrical parameter for extractants

Table A 3.2.1 Distance (Å) of N2 and N3 atoms in the extractants (**1**-**15**)

Extractant	**1**	**2**	**3**	**4**	**5**
P [a]	4.779	4.834	4.739	4.609	4.693
C [b]	4.492	4.549	4.565	4.586	4.558
ΔD	-0.287	-0.285	-0.174	-0.023	-0.135
Extractant	**6**	**7**	**8**	**9**	**10**
P [a]	4.824	4.860	4.688	4.783	5.008
C [b]	4.492	4.560	4.585	4.601	4.527
ΔD	-0.332	-0.300	-0.103	-0.182	-0.481
Extractant	**11**	**12**	**13**	**14**	**15**
P [a]	5.022	4.869	4.780	4.743	4.686
C [b]	4.547	4.480	4.607	4.620	4.612
ΔD	-0.475	-0.389	-0.173	-0.123	-0.074

[a] Preorganized extractant

[b] Coordinated extractant in UO_2^{2+}(VI) compounds

Table A 3.2.2 U-N distances of $UO_2^{2+}(H_2O)_2L$ (L=**1**-**15**) compounds (Å)

Extractant	**1**	**2**	**3**	**4**	**5**
U-N1	2.545	2.539	2.544	2.528	2.580
U-N2	2.524	2.542	2.545	2.563	2.561
U-N3	2.524	2.544	2.545	2.563	2.561
Extractant	**6**	**7**	**8**	**9**	**10**
U-N1	2.500	2.501	2.499	2.495	2.618
U-N2	2.524	2.540	2.545	2.561	2.535
U-N3	2.524	2.543	2.546	2.561	2.535
Extractant	**11**	**12**	**13**	**14**	**15**
U-N1	2.566	2.570	2.528	2.523	2.492
U-N2	2.536	2.503	2.555	2.559	2.547
U-N3	2.536	2.503	2.554	2.559	2.547

Table A 3.2.3 Np-N distances of $NpO_2^{2+}(H_2O)_2L$ (L=**1**-**15**) compounds (Å)

Extractant	**1**	**2**	**3**	**4**	**5**
Np-N1	2.537	2.527	2.529	2.514	2.576
Np-N2	2.515	2.535	2.540	2.555	2.551
Np-N3	2.515	2.540	2.538	2.556	2.551
Extractant	**6**	**7**	**8**	**9**	**10**
Np-N1	2.493	2.489	2.482	2.479	2.603
Np-N2	2.521	2.535	2.543	2.552	2.524
Np-N3	2.521	2.540	2.542	2.552	2.524
Extractant	**11**	**12**	**13**	**14**	**15**
Np-N1	2.553	2.560	2.509	2.506	2.482
Np-N2	2.527	2.505	2.549	2.552	2.546
Np-N3	2.527	2.505	2.548	2.551	2.545

Table A 3.2.4 Pu-N distances of $PuO_2^{2+}(H_2O)_2L$ (L=**1**-**15**) compounds (Å)

Extractant	**1**	**2**	**3**	**4**	**5**
Pu-N1	2.541	2.529	2.532	2.513	2.559
Pu-N2	2.507	2.523	2.528	2.549	2.549
Pu-N3	2.507	2.524	2.531	2.548	2.549
Extractant	**6**	**7**	**8**	**9**	**10**
Pu-N1	2.492	2.487	2.492	2.476	2.601
Pu-N2	2.518	2.527	2.537	2.541	2.517
Pu-N3	2.519	2.527	2.537	2.543	2.517
Extractant	**11**	**12**	**13**	**14**	**15**
Pu-N1	2.559	2.574	2.518	2.506	2.502
Pu-N2	2.528	2.508	2.547	2.553	2.547
Pu-N3	2.528	2.507	2.541	2.556	2.551

A 3.3. Properties of the extractants

A 3.3.1. Charge analysis of extractants

Table A 3.3.1.1 Values for the ESP Surface Minima (a.u.) for the extractants (**1**-**15**)

a.u.	**1**	**2**	**3**	**4**	**5**
F [a]	-0.08	-0.13	-0.14	-0.12	-0.14
P [b]	-0.17	-0.15	-0.14 [d]	-0.12 [d]	-0.14 [d]
C [c]	-0.17	-0.16	-0.16	-0.14	-0.14
a.u.	**6**	**7**	**8**	**9**	**10**
F [a]	-0.09	-0.14	-0.17	-0.12	-0.09
P [b]	-0.18	-0.16	-0.18	-0.15	-0.09 [d]
C [c]	-0.21	-0.19	-0.18	-0.17	-0.10
a.u.	**11**	**12**	**13**	**14**	**15**
F [a]	-0.12	-0.09	-0.17	-0.16	-0.19
P [b]	-0.12 [d]	-0.16	-0.17 [d]	-0.16 [d]	-0.19 [d]
C [c]	-0.13	-0.17	-0.17	-0.17	-0.20

[a] F for free extractants

[b] P for preorganized extractants

[c] C for coordinated UO_2^{2+} extractants compounds

[d] The free extractant and preorganized extractant are identical

Table A 3.3.1.2 Hirshfeld charges of donating nitrogen atoms in the extractants (**1**-**15**) in their free extractant configuration (F), pre-organized cis-configuration (P), and coordinated configuration (C)

Extractant		**1**	**2**	**3**	**4**	**5**
	N1	-0.147	-0.141	-0.189	-0.134	-0.180
F[a]	N2	-0.176	-0.169	-0.193	-0.193	-0.145
	N3	-0.176	-0.201	-0.193	-0.193	-0.145
	N1	-0.199	-0.192	-0.189 [d]	-0.190 [d]	-0.180 [d]
P[b]	N2	-0.205	-0.198	-0.193 [d]	-0.193 [d]	-0.145 [d]
	N3	-0.205	-0.201	-0.193 [d]	-0.193 [d]	-0.145 [d]
	N1	-0.194	-0.190	-0.187	-0.185	-0.177
C[c]	N2	-0.204	-0.196	-0.194	-0.192	-0.145
	N3	-0.204	-0.200	-0.194	-0.192	-0.145
Extractant		**6**	**7**	**8**	**9**	**10**
	N1	-0.177	-0.174	-0.170	-0.223	-0.164
F[a]	N2	-0.177	-0.173	-0.197	-0.195	-0.212
	N3	-0.177	-0.204	-0.197	-0.195	-0.212
	N1	-0.233	-0.229	-0.224	-0.223 [d]	-0.164 [d]
P[b]	N2	-0.208	-0.203	-0.197	-0.195 [d]	-0.212 [d]
	N3	-0.208	-0.204	-0.197	-0.195 [d]	-0.212 [d]
	N1	-0.233	-0.232	-0.229	-0.229	-0.156
C[c]	N2	-0.207	-0.201	-0.196	-0.197	-0.219
	N3	-0.207	-0.203	-0.196	-0.197	-0.219
Extractant		**11**	**12**	**13**	**14**	**15**
	N1	-0.205	-0.149	-0.200	-0.193	-0.234
F[a]	N2	-0.217	-0.237	-0.206	-0.203	-0.206
	N3	-0.217	-0.237	-0.207	-0.203	-0.206
	N1	-0.205 [d]	-0.188	-0.200 [d]	-0.193 [d]	-0.234 [d]
P[b]	N2	-0.217 [d]	-0.257	-0.206 [d]	-0.203 [d]	-0.206 [d]
	N3	-0.217 [d]	-0.257	-0.207 [d]	-0.203 [d]	-0.206 [d]
	N1	-0.201	-0.181	-0.198	-0.195	-0.239
C[c]	N2	-0.224	-0.263	-0.207	-0.203	-0.207
	N3	-0.224	-0.263	-0.206	-0.203	-0.207

[a] F for free extractants

[b] P for preorganized extractants

[c] C for coordinated UO_2^{2+} extractants compounds

[d] The free extractant and preorganized extractant are identical

A 3.3.2. Planarity analysis of the extractants

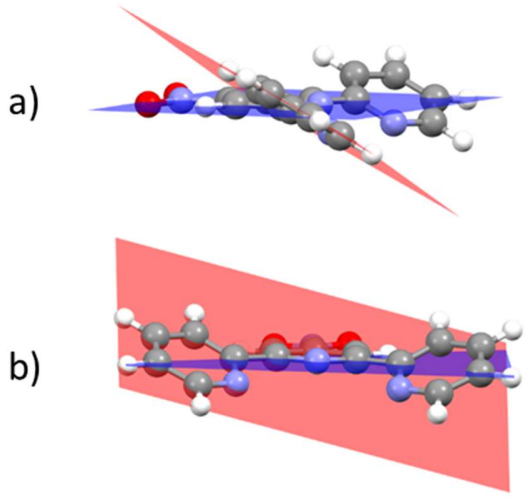

Figure A 3.3.2.1 a) and b) shows different side views of the definition of the angle between the normal to the planes of the flanking ring and the normal to the center ring for extractant 1. The measurements were carried on by CCDC Mercury 4.3.1.

Table A 3.3.2.1 Angles of planes between the center and the flanking rings of the for extractants (**1-15**) in Scheme 1 coordinated to NpO_2^{2+}. Two numbers for each extractant are reported, one for each flanking ring.

Extractants	**1**	**2**	**3**	**4**	**5**
Angles	12.0	5.4	5.6	2.9	3.9
	12.1	6.1	5.6	3.0	3.9
Extractants	**6**	**7**	**8**	**9**	**10**
Angles	13.7	5.9	0.7	1.7	0.0
	13.8	6.8	0.8	1.8	0.1
Extractants	**11**	**12**	**13**	**14**	**15**
Angles	0.1	8.6	2.6	1.2	1.3
	0.2	8.7	12.2	1.2	1.8

Table A 3.3.2.2 Angles of planes between the center and the flanking rings for extractants (1-15) in Scheme 1 coordinated to PuO_2^{2+}. Two numbers for each extractant are reported, one for each flanking ring.

Extractants	**1**	**2**	**3**	**4**	**5**
Angles	11.5	6.9	5.1	4.2	4.7
	11.6	8.0	6.6	4.6	4.8
Extractants	**6**	**7**	**8**	**9**	**10**
Angles	10.8	5.3	1.6	1.1	0.6
	13.2	6.5	2.7	1.8	0.7
Extractants	**11**	**12**	**13**	**14**	**15**
Angles	1.3	8.0	2.6	0.9	1.3
	1.4	8.2	13.0	0.9	1.6

A 3.4. Thermodynamics of extractants binding to actinyl ions.

Table A 3.4.1 Gibbs Free Energies (ΔG, kcal/mol) for Reaction (1) in Water at PBE level.

Extractant	**1**	**2**	**3**	**4**	**5**	**6**	**7**	**8**	**9**	**10**	**11**	**12**	**13**	**14**	**15**
UO_2^{2+}	-25.0	-23.9	-24.1	-20.9	-27.5	-31.8	-26.1	-29.5	-28.1	-12.8	-15.7	-20.7	-28.6	-27.0	-32.1
NpO_2^{2+}	-29.9	-27.3	-27.2	-25.3	-32.7	-33.6	-30.0	-32.3	-30.0	-13.5	-17.9	-25.0	-30.4	-31.0	-37.3
PuO_2^{2+}	-29.1	-28.4	-27.7	-24.6	-32.2	-36.3	-31.4	-34.4	-30.5	-15.3	-19.5	-26.7	-31.5	-33.0	-40.9
$\Delta\Delta G_{Np-U}$	-4.9	-3.4	-3.1	-4.4	-5.1	-1.8	-3.9	-2.7	-2.0	-0.7	-2.2	-4.3	-1.8	-4.0	-5.2
$\Delta\Delta G_{Pu-Np}$	0.8	-1.1	-0.6	0.7	0.4	-2.7	-1.5	-2.2	-0.5	-1.8	-1.6	-1.7	-1.1	-2.0	-3.7

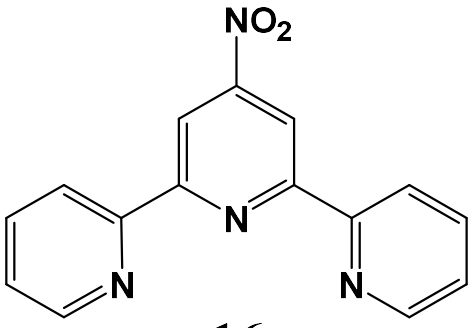

16

Figure A 3.4.1 Structure of extractant **16**

Table A 3.4.2 Gibbs Free Energies (ΔG, kcal/mol) for Reaction (1) in Water at PBE level.

Extractant	**1**	**6**	**16**
UO_2^{2+}	-25.0	-31.8	-22.1
NpO_2^{2+}	-29.9	-33.6	-20.2
PuO_2^{2+}	-29.1	-36.3	-24.0
$\Delta\Delta G_{Np-U}$	-4.9	-1.8	-3.1
$\Delta\Delta G_{Pu-Np}$	0.8	-2.7	-0.6

The electron-withdrawing substitution, $-NO_2$ for example in this case, weaken the bonding between extractant and metals with reduced π- interactions. This is consistent with previous reported studies. Thus, we focus on electron donating group, -NH2, in the main text.

A 3.5. Bonding analysis

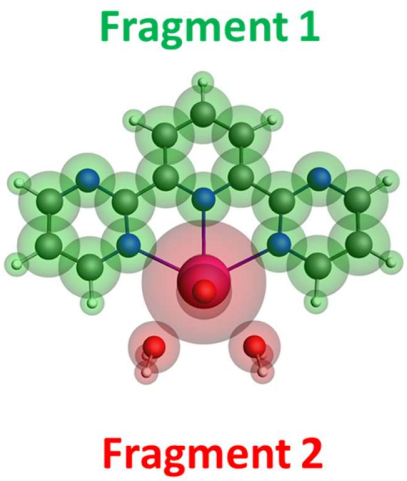

Figure A 3.5.1 Example of the fragments used in the Energy Decomposition Analysis (EDA) and Extended Transition State Method and the Natural Orbitals for Chemical Valence Scheme (ETS-NOCV). Two fragments were defined highlighted here in green, Extractant 1, and the second one in red, the AnO_2^{2+} and coordinating water molecules.

In order to investigate the bonding nature between AnO_2^{2+} and extractants, the two fragments can be defined as in Figure S5.1. Thus, the bond energies of $AnO_2(H_2O)_n^{2+}$ and extractants are:

$$\Delta E=\Delta E_{prep}+\Delta E_{int}$$

Where the preparation energy(ΔE_{prep}) is the amount of energy that is required to deform the $AnO_2(H_2O)_n^{2+}$ and extractants from their equilibrium structure to the geometry of fragments have in the complex. And the interaction energy(ΔE_{int}) is the change in energy when the prepared fragments (two gas phase fragments in the complex geometry as Figure S5.1 shows) are combined to form the complex in solvent (water). The energy decomposition analysis (EDA) depends on the fragments chosen. To represent dative bonding between $AnO_2(H_2O)_n^{2+}$ and extractants, the fragment 1 keeps all electrons of nitrogen lone pairs. In this way, a quantitative EDA divides the interaction energy in the electrostatic interaction (V_{elstat}), Pauli repulsion (E_{Pauli}), attractive orbital interactions (E_{oi}), solvation energies (E_{Sol}), and dispersion energies (E_{Disper}):

$$\Delta E_{int}=\Delta V_{elstat}+\Delta E_{Pauli}+\Delta E_{oi}+\Delta E_{Sol}+\Delta E_{Disper}$$

The electrostatic interaction is the energy between the unperturbed charge distributions of the prepared fragments, which can be used as probe for investigating ionic interactions between AnO_2^{2+} and extractants. The Pauli repulsion is steric repulsions from the destabilizing interactions between occupied orbitals of the fragments. Charge transfer and polarization is represented by the orbital interaction, which can be used as probe for investigating covalent interactions between AnO_2^{2+} and extractants. Solvation energies give the energy change associated with the transfer of a molecule between ideal gas and solvent by COSMO model. Dispersion energies between two fragments are gave from Grimme's D3 correction.

The energy decomposition analysis - natural orbitals for chemical valence (EDA-NOCV), also known as extended transition state - natural orbitals for chemical valence (ETS-NOCV), is used for the analyzation of the orbital interactions, E_{oi}, defined above. This method gives more details of the orbital interactions between AnO_2^{2+} and extractants than EDA (section S5.1) or quantum theory of atoms in molecules (QTAIM) (section S5.2) because the deformation density is decomposed into different components (σ and π in this work) of the chemical bond. See section S5.3.

A 3.5.1. EDA analysis for $AnO_2^{2+}(H_2O)_2L$ (An=U, Np, Pu; L=1-15) compounds

Table A 3.5.1.1EDA for $UO_2^{2+}(H_2O)_2L$ (L=**1-15**) compounds (kcal/mol).

Extractant	1	2	3	4	5	6	7	8	9	10	11	12	13	14	15
Pauli	146.2	140.9	139.0	135.4	164.4	152.1	147.1	145.6	141.5	120.8	126.2	139.9	140.2	139.2	148.1
Electrostatic	-174.8	-167.0	-160.6	-157.8	-191.2	-186.1	-180.1	-173.6	-172.0	-134.5	-147.8	-177.4	-174.0	-170.7	-184.6
Steric [a]	-28.6	-26.1	-21.6	-22.4	-26.8	-34.0	-33.0	-28.0	-30.5	-13.7	-21.6	-37.5	-33.8	-31.5	-36.5
Orbital	-151.5	-146.6	-143.0	-141.6	-162.1	-159.9	-155.4	-152.8	-150.5	-118.7	-127.9	-148.4	-151.1	-150.2	-160.1
Dispersion	-8.1	-8.0	-7.9	-7.9	-8.2	-8.2	-8.0	-7.9	-7.9	-7.0	-7.0	-8.8	-8.0	-7.9	-8.0
Total	-188.2	-180.7	-172.5	-171.9	-197.1	-202.1	-196.4	-188.7	-188.9	-139.4	-156.5	-194.7	-192.9	-189.6	-204.6

[a] Steric interaction is the sum of the Pauli repulsion and Electrostatic interaction.

Table A 3.5.1.2EDA for $NpO_2^{2+}(H_2O)_2L$ (L=**1-15**) compounds (kcal/mol).

Extractant	1	2	3	4	5	6	7	8	9	10	11	12	13	14	15
Pauli	147.8	142.3	141.2	137.7	160.3	152.0	148.1	148.2	144.8	124.9	129.7	143.0	142.6	142.2	147.6
Electrostatic	-173.5	-166.3	-160.6	-157.7	-188.6	-184.4	-179.1	-174.2	-172.4	-135.2	-148.1	-177.4	-173.8	-171.0	-183.0
Steric [a]	-25.7	-24.0	-19.4	-20.0	-28.3	-32.4	-31.0	-26.0	-27.6	-10.3	-18.4	-34.4	-31.2	-28.8	-35.4
Orbital	-151.2	-146.2	-143.3	-141.9	-156.6	-158.8	-154.6	-151.1	-150.9	-120.0	-129.2	-148.4	-151.2	-149.5	-158.5
Dispersion	-8.1	-7.9	-7.8	-7.7	-8.1	-8.0	-7.9	-7.8	-7.8	-7.0	-7.0	-8.7	-7.9	-7.8	-7.8
Total	-185.0	-178.1	-170.5	-169.6	-193.0	-199.2	-193.5	-184.9	-186.3	-137.3	-154.6	-191.5	-190.3	-186.1	-201.7

[a] Steric interaction is the sum of the Pauli repulsion and Electrostatic interaction.

Table A 3.5.1.3 EDA for $PuO_2^{2+}(H_2O)_2L$ (L=**1-15**) compounds (kcal/mol).

Extractant	1	2	3	4	5	6	7	8	9	10	11	12	13	14	15
Pauli	138.5	134.7	132.7	129.2	156.4	144.8	140	136.4	136.6	116.4	117.5	129.4	130.9	129.8	132.1
Electrostatic	-169.5	-162.5	-156.6	-153.7	-186.2	-181.5	-175.4	-168.1	-168.5	-131.7	-142.2	-170.8	-167.8	-164.8	-174.7
Steric	-31.0	-27.8	-23.9	-24.5	-29.8	-36.7	-35.4	-31.7	-31.9	-15.3	-24.7	-41.4	-36.9	-35.0	-42.6
Orbital	-145.4	-140.9	-137.9	-135.8	-154.3	-157.5	-150.4	-149.8	-145.4	-113.4	-123	-144.2	-146.6	-146.3	-156.8
Dispersion	-8.8	-8.6	-8.5	-8.5	-8.7	-8.7	-8.6	-8.4	-8.5	-7.5	-7.5	-9.4	-8.6	-8.5	-8.5
Total	-185.2	-177.3	-170.3	-168.8	-192.8	-202.9	-194.4	-189.9	-185.8	-136.2	-155.2	-195.0	-192.1	-189.8	-207.9

[a] Steric interaction is the sum of the Pauli repulsion and Electrostatic interaction.

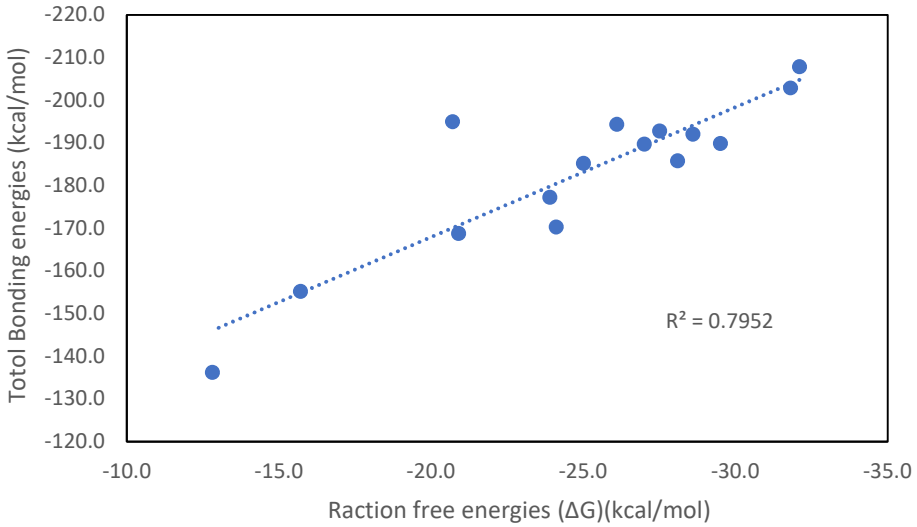

Figure A 3.5.1.1 Correlation between reaction free energies and total bonding energies for $UO_2^{2+}(H_2O)_2L$ (L=1-15) compounds (kcal/mol).

A 3.5.2. QTAIM analysis for $AnO_2^{2+}(H_2O)_2L$ (An=U, Np, Pu; L=1-15) compounds

Table A 3.5.2.1 Calculated topological properties (a.u.) of M-N in $UO_2^{2+}(H_2O)_2L$ (L=**1-15**) compounds

	Bonds	**1**	**2**	**3**	**4**	**5**
	N1-M	0.059	0.059	0.059	0.060	0.054
ρ(r)	N2-M	0.062	0.059	0.059	0.057	0.056
	N3-M	0.062	0.060	0.059	0.057	0.056
	Bonds	**6**	**7**	**8**	**9**	**10**
	N1-M	0.065	0.064	0.065	0.065	0.050
ρ(r)	N2-M	0.062	0.060	0.059	0.057	0.057
	N3-M	0.062	0.060	0.059	0.057	0.057
	Bonds	**11**	**12**	**13**	**14**	**15**
	N1-M	0.056	0.056	0.061	0.062	0.066
ρ(r)	N2-M	0.057	0.061	0.058	0.058	0.059
	N3-M	0.057	0.061	0.058	0.058	0.059

Table A 3.5.2.2 Calculated topological properties (a.u.) of M-N in $NpO_2^{2+}(H_2O)_2L$ (L=**1-15**) compounds

	Bonds	**1**	**2**	**3**	**4**	**5**
	N1-M	0.058	0.059	0.059	0.060	0.052
ρ(r)	N2-M	0.061	0.059	0.058	0.056	0.055
	N3-M	0.061	0.058	0.058	0.056	0.055
	Bonds	**6**	**7**	**8**	**9**	**10**
	N1-M	0.063	0.064	0.065	0.065	0.050
ρ(r)	N2-M	0.060	0.059	0.057	0.056	0.057
	N3-M	0.060	0.058	0.057	0.056	0.057
	Bonds	**11**	**12**	**13**	**14**	**15**
	N1-M	0.056	0.055	0.062	0.062	0.064
ρ(r)	N2-M	0.056	0.060	0.057	0.057	0.057
	N3-M	0.056	0.060	0.057	0.057	0.057

Table A 3.5.2.3 Calculated topological properties (a.u.) of M-N in $PuO_2^{2+}(H_2O)_2L$ (L=**1-15**) compounds

	Bonds	**1**	**2**	**3**	**4**	**5**
	N1-M	0.055	0.056	0.057	0.058	0.053
ρ(r)	N2-M	0.060	0.059	0.057	0.055	0.054
	N3-M	0.060	0.058	0.057	0.055	0.054
	Bonds	**6**	**7**	**8**	**9**	**10**
	N1-M	0.060	0.061	0.061	0.063	0.049
ρ(r)	N2-M	0.058	0.057	0.055	0.056	0.056
	N3-M	0.058	0.057	0.055	0.056	0.056
	Bonds	**11**	**12**	**13**	**14**	**15**
	N1-M	0.052	0.051	0.058	0.059	0.059
ρ(r)	N2-M	0.054	0.058	0.055	0.054	0.054
	N3-M	0.054	0.058	0.056	0.054	0.053

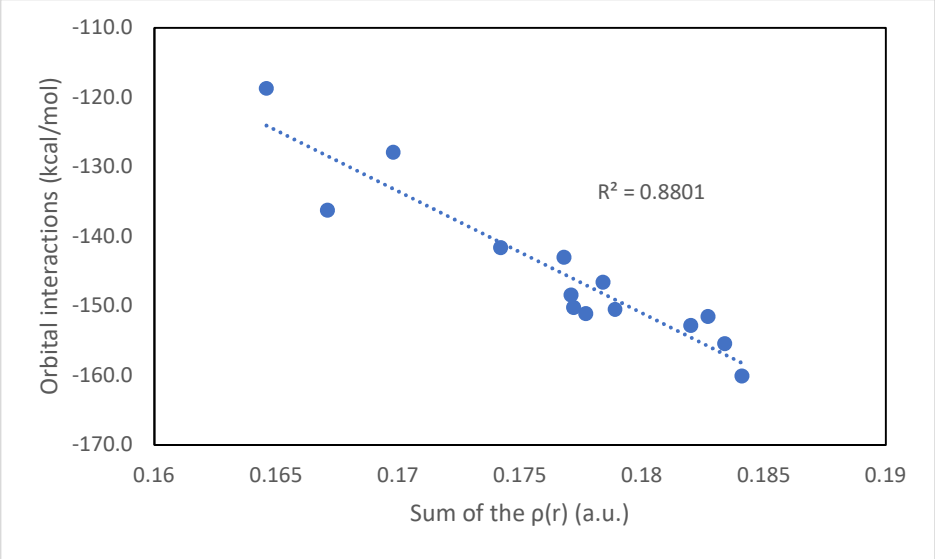

Figure A 3.5.2.1 Correlation between orbital interactions (kcal/mol) from EDA and the sum of the ρ(r) from QTAIM (a.u.). (The extractant 6 is not included due to the intra-molecule hydrogen bonds)

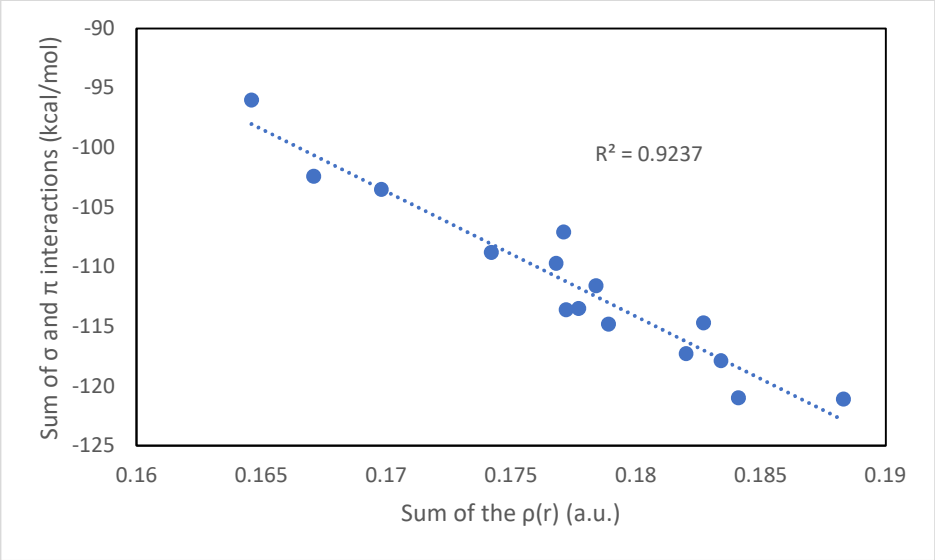

Figure A 3.5.2.2 Correlation between sum of σ and π orbital interactions (kcal/mol) from ETS-NOCV and the sum of the ρ(r) from QTAIM (a.u.).

A 3.5.3. ETS-NOCV analysis

Table A 3.5.3.1ETS-NOCV analysis for interactions between $UO_2^{2+}(H_2O)_2$ and L (L=**1**-**15**) (kcal/mol).

	1	**2**	**3**	**4**	**5**	**6**	**7**	**8**	**9**	**10**	**11**	**12**	**13**	**14**	**15**
σ 1	-41.6	-40.9	-41.3	-40.1	-36.3	-43.6	-42.7	-42.9	-41.7	-35.4	-37.1	-38.4	-41.7	-41.5	-43.0
σ 2	-23.8	-22.7	-21.4	-21.8	-19.3	-23.5	-22.4	-20.9	-21.6	-19.3	-18.9	-20.1	-21.7	-21.3	-21.4
σ 3	-18.5	-17.9	-18.0	-17.5	-15.3	-16.1	-17.2	-17.9	-17.6	-15.9	-16.6	-17.1	-18.4	-18.3	-18.7
π 1	-11.3	-11.0	-10.2	-10.0	-11.9	-10.8	-10.2	-9.8	-10.0	-10.3	-9.8	-16.2	-11.3	-11.5	-11.3
π 2	-9.1	-9.0	-8.4	-8.6	-10.7	-9.0	-9.0	-8.2	-8.9	-6.5	-6.4	-10.1	-8.7	-8.3	-8.2
π 3	-10.4	-10.1	-10.5	-10.8	-8.9	-18.1	-16.4	-17.6	-15.1	-8.7	-14.7	-9.2	-11.7	-12.7	-18.5
σ total	-83.9	-81.5	-80.7	-79.4	-70.9	-83.3	-82.3	-81.7	-80.9	-70.6	-72.6	-71.7	-81.8	-81.1	-83.0
π total	-30.8	-30.1	-29.1	-29.4	-31.5	-37.9	-35.6	-35.6	-33.9	-25.4	-30.9	-35.4	-31.7	-32.5	-38.0
Total	-114.7	-111.6	-109.7	-108.8	-102.4	-121.1	-117.9	-117.3	-114.8	-96.0	-103.5	-107.1	-113.5	-113.6	-121.0

Table A 3.5.3.2 β spin ETS-NOCV analysis for interactions between $UO_2^{2+}(H_2O)_2$ and L (L=**1**-**15**) (kcal/mol). The β spin results of UO_2^{2+} compound are shown for better comparing with open-shell NpO_2^{2+} and PuO_2^{2+} compounds by divided by 2 from close-shell calculation in Table A 3.5.3.1.

	1	**2**	**3**	**4**	**5**	**6**	**7**	**8**	**9**	**10**	**11**	**12**	**13**	**14**	**15**
σ 1	-20.8	-20.5	-20.7	-20.1	-18.2	-21.8	-21.4	-21.5	-20.9	-17.7	-18.6	-19.2	-20.9	-20.8	-21.5
σ 2	-11.9	-11.4	-10.7	-10.9	-9.7	-11.8	-11.2	-10.5	-10.8	-9.7	-9.5	-10.1	-10.9	-10.7	-10.7
σ 3	-9.3	-9.0	-9.0	-8.8	-7.7	-8.1	-8.6	-9.0	-8.8	-8.0	-8.3	-8.6	-9.2	-9.2	-9.4
π 1	-5.7	-5.5	-5.1	-5.0	-6.0	-5.4	-5.1	-4.9	-5.0	-5.2	-4.9	-8.1	-5.7	-5.8	-5.7
π 2	-4.6	-4.5	-4.2	-4.3	-5.4	-4.5	-4.5	-4.1	-4.5	-3.3	-3.2	-5.1	-4.4	-4.2	-4.1
π 3	-5.2	-5.1	-5.3	-5.4	-4.5	-9.1	-8.2	-8.8	-7.6	-4.4	-7.4	-4.6	-5.9	-6.4	-9.3
σ total	-42.0	-40.8	-40.4	-39.7	-35.5	-41.6	-41.2	-40.9	-40.5	-35.3	-36.3	-37.8	-40.9	-40.6	-41.6
π total	-15.4	-15.1	-14.6	-14.7	-15.8	-19.0	-17.8	-17.8	-17.0	-12.8	-15.5	-17.8	-15.9	-16.3	-19.0
Total	-57.4	-55.8	-54.9	-54.4	-51.2	-60.6	-59.0	-58.7	-57.5	-48.1	-51.8	-55.6	-56.8	-56.8	-60.6

Table A 3.5.3.3 β spin ETS-NOCV analysis for interactions between $NpO_2^{2+}(H_2O)_2$ and L (L=**1**-**15**) (kcal/mol).

	1	**2**	**3**	**4**	**5**	**6**	**7**	**8**	**9**	**10**	**11**	**12**	**13**	**14**	**15**
σ 1	-19.0	-18.7	-19.0	-18.5	-16.4	-19.7	-19.4	-20.0	-19.3	-16.4	-17.1	-17.4	-19.2	-19.2	-19.0
σ 2	-11.1	-10.4	-9.8	-10.0	-9.3	-10.7	-10.2	-9.6	-9.9	-9.2	-8.8	-10.2	-10.0	-10.0	-9.0
σ 3	-8.9	-8.6	-8.6	-8.5	-7.5	-7.8	-8.4	-9.0	-8.7	-7.8	-8.0	-8.3	-8.7	-8.9	-8.7
π 1	-5.5	-4.8	-4.7	-4.7	-6.4	-5.0	-4.7	-4.9	-4.6	-4.9	-4.5	-7.2	-5.2	-5.5	-5.1
π 2	-4.4	-4.4	-4.0	-4.2	-6.5	-4.3	-4.3	-3.9	-4.3	-3.0	-3.0	-4.9	-4.2	-3.9	-3.5
π 3	-5.0	-5.3	-5.2	-5.2	-4.2	-8.6	-7.9	-8.0	-7.2	-4.2	-7.2	-4.0	-6.0	-6.1	-8.5
σ total	-39.0	-37.8	-37.4	-37.0	-33.2	-38.2	-38.0	-38.6	-37.9	-33.3	-33.9	-35.9	-37.9	-38.1	-36.8
π total	-14.9	-14.5	-13.9	-14.1	-17.1	-17.9	-17.0	-16.8	-16.2	-12.1	-14.7	-16.1	-15.4	-15.6	-17.2
Total	-53.8	-52.2	-51.3	-51.1	-50.3	-56.1	-55.0	-55.3	-54.1	-45.4	-48.6	-52.0	-53.4	-53.6	-53.9

Table A 3.5.3.4 β spin ETS-NOCV analysis for interactions between $PuO_2^{2+}(H_2O)_2$ and L (L=**1**-**15**) (kcal/mol).

	1	**2**	**3**	**4**	**5**	**6**	**7**	**8**	**9**	**10**	**11**	**12**	**13**	**14**	**15**
σ 1	-18.2	-18.1	-18.3	-17.9	-16.0	-17.7	-18.3	-17.7	-18.6	-16.0	-15.4	-15.8	-17.7	-17.3	-16.2
σ 2	-10.7	-10.3	-9.5	-9.8	-8.9	-9.8	-9.7	-8.9	-9.6	-8.8	-8.0	-9.2	-9.5	-9.0	-8.3
σ 3	-8.7	-8.6	-8.5	-8.4	-7.3	-8.3	-7.9	-8.1	-8.3	-7.7	-7.4	-7.8	-8.5	-8.4	-7.6
π 1	-5.3	-5.0	-4.7	-4.5	-5.6	-3.9	-4.4	-3.8	-4.5	-4.7	-3.8	-6.2	-5.0	-4.7	-3.4
π 2	-4.0	-4.0	-3.9	-3.9	-4.3	-3.7	-4.1	-3.8	-4.2	-3.1	-2.3	-4.6	-3.7	-3.3	-2.8
π 3	-4.7	-4.7	-4.8	-5.0	-4.2	-6.3	-7.3	-6.8	-7.2	-4.0	-5.9	-3.2	-5.0	-5.6	-7.0
σ total	-37.7	-37.0	-36.3	-36.1	-32.3	-35.8	-35.9	-34.7	-36.4	-32.5	-30.9	-32.8	-35.6	-34.7	-32.1
π total	-13.9	-13.7	-13.3	-13.4	-14.0	-14.0	-15.8	-14.4	-15.9	-11.9	-12.0	-14.0	-13.7	-13.6	-13.2
Total	-51.6	-50.7	-49.6	-49.5	-46.3	-49.8	-51.7	-49.2	-52.4	-44.4	-42.9	-46.8	-49.3	-48.3	-45.3

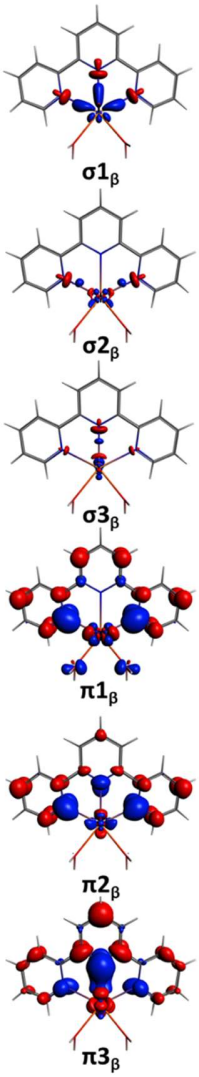

Figure A 3.5.3.1 Example of the β spin ETS-NOCV deformation density (iso-contour 0.003 a.u. for σ and iso-contour 0.0003 a.u. for π) of the most important interactions between extractant 1 and PuO_2^{2+}. Electron density flow from red to blue.

The the α spin analysis is interrupted by unpaired *f* electrons due to the difference of the occupied *f* orbitals on Pu between $PuO_2(H_2O)^{2+}$ fragment and final compound. Because of the degeneracy of 5*f* orbitals, it is very hard to keep the occupied f orbitals are the same for both $PuO_2(H_2O)^{2+}$ fragment and final compound. On the other hand, the β spin results are very similar to UO_2^{2+}. However, the β spin results might have less physical meaning than the α spin. Since α and β spins are in the different space in unrestricted calculation that β spins might not very good to represent the affect from unpaired *f* electrons. Thus, the β spin results below are only for reference.

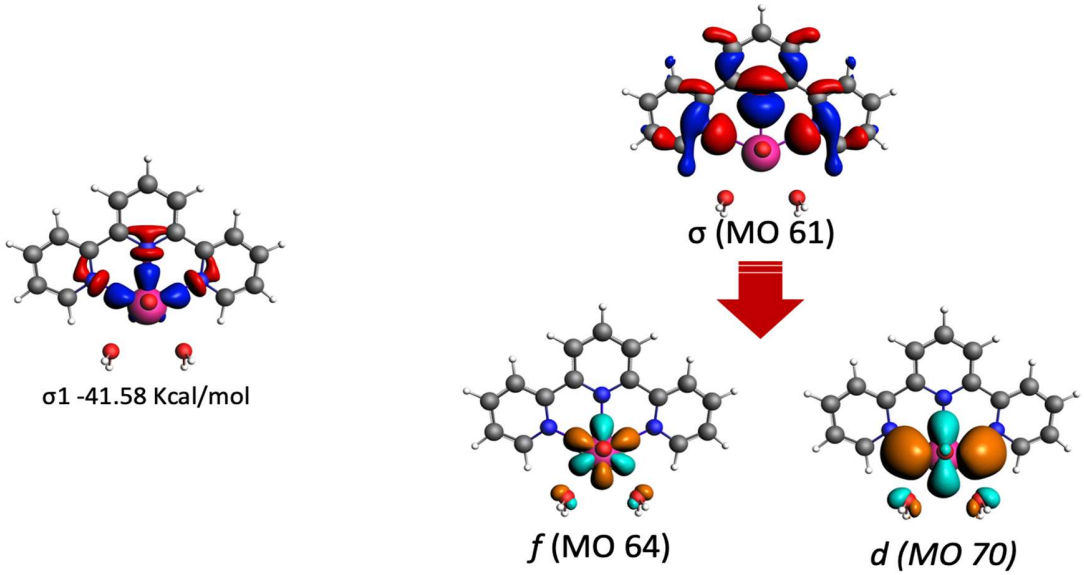

Figure A 3.5.3.2 Deformation densities Δρ (is-ocontour 0.003 a.u.) for σ1 in Table A 3.5.3.1 from ETS-NOCV calculations on neutral closed-shell singlet fragments of extractant **1** and UO_2^{2+} interaction (left). Electron density flows from red to blue. The corresponding frontier orbitals (iso-contour 0.03 a.u.) of the fragments for the σ1 deformation densities on the left are shown on the right. The frontier orbitals on the right represent the nitrogen lone pair electrons donating to the *f* and *d* empty orbitals.

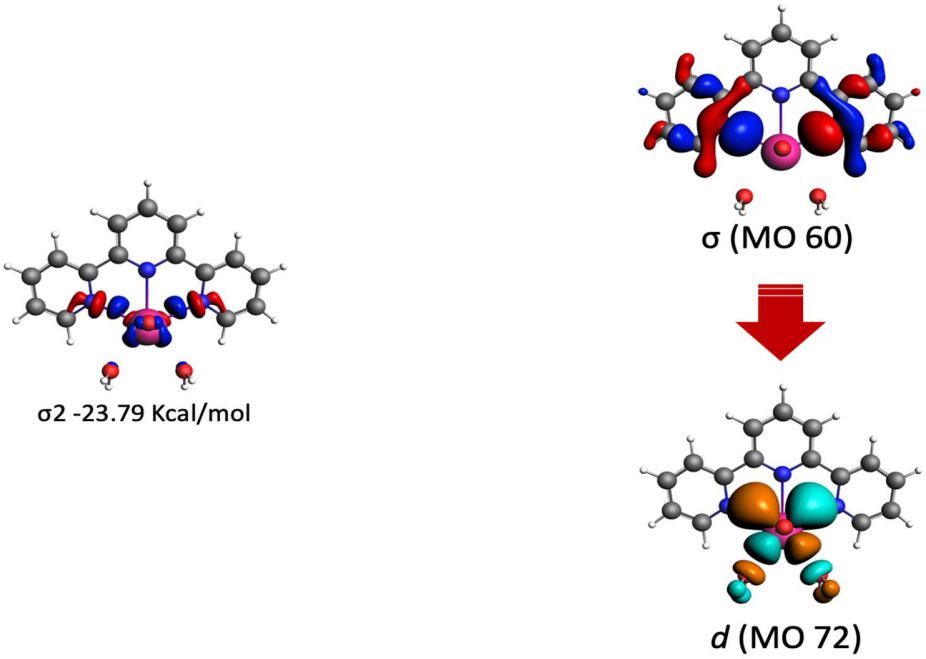

Figure A 3.5.3.3 Deformation densities Δρ (iso-contour 0.003 a.u.) for σ2 in Table A 3.5.3.1 from ETS-NOCV calculations on neutral closed-shell singlet fragments of extractant **1** and UO_2^{2+} interaction (left). Electron density flows from red to blue. The corresponding frontier orbitals (iso-contour 0.03 a.u.) of the fragments for the σ2 deformation densities on the left are shown on the right. The frontier orbitals on the right represent the nitrogen lone pair electrons donating to the *d* empty orbitals.

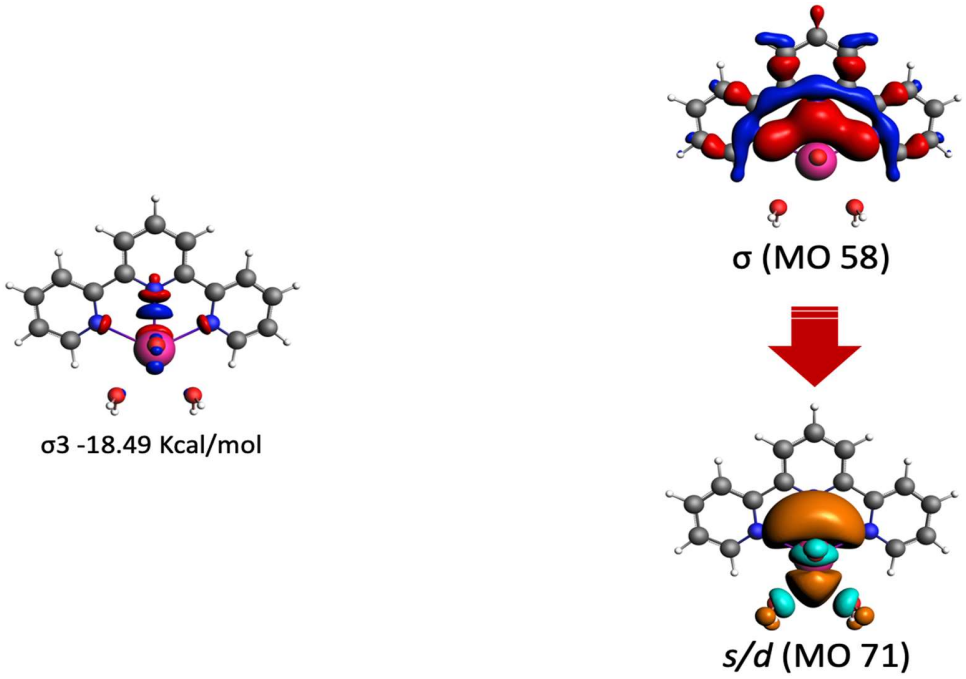

Figure A 3.5.3.4 Deformation densities Δρ (iso-contour 0.003 a.u.) for σ3 in Table A 3.5.3.1 from ETS-NOCV calculations on neutral closed-shell singlet fragments of extractant **1** and UO_2^{2+} interaction (left). Electron density flows from red to blue. The corresponding frontier orbitals (iso-contour 0.03 a.u.) of the fragments for the σ3 deformation densities on the left are shown on the right. The frontier orbitals on the right represent the nitrogen lone pair electrons donating to the *d* and *s* empty orbitals.

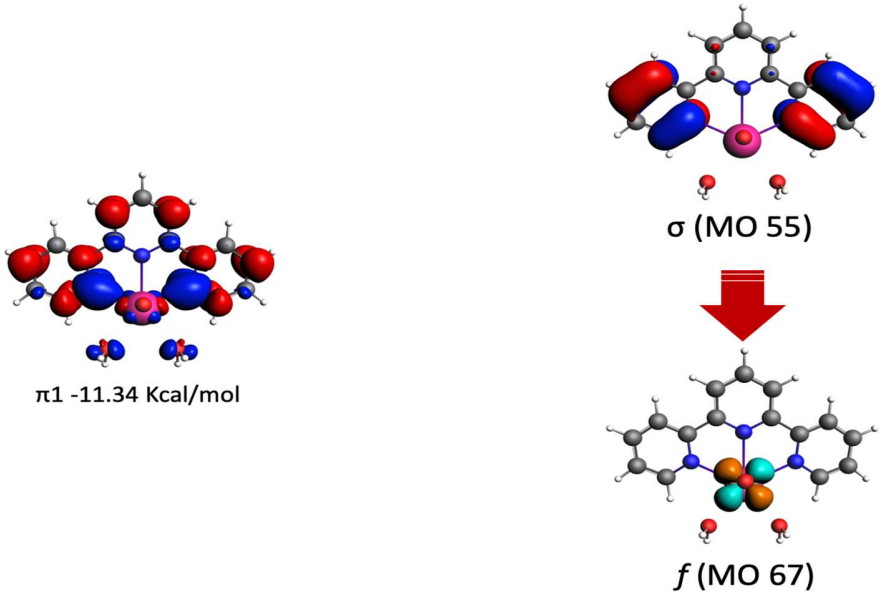

Figure A 3.5.3.5 Deformation densities Δρ (isocontour 0.003 a.u.) for π1 in Table A 3.5.3.1 from ETS-NOCV calculations on neutral closed-shell singlet fragments of extractant **1** and UO_2^{2+} interaction (left). Electron density flows from red to blue. The corresponding frontier orbitals (isocontour 0.03 a.u.) of the fragments for the π1 deformation densities on the left are shown on the right. The frontier orbitals on the right represent the nitrogen lone pair electrons donating to the *f* empty orbitals.

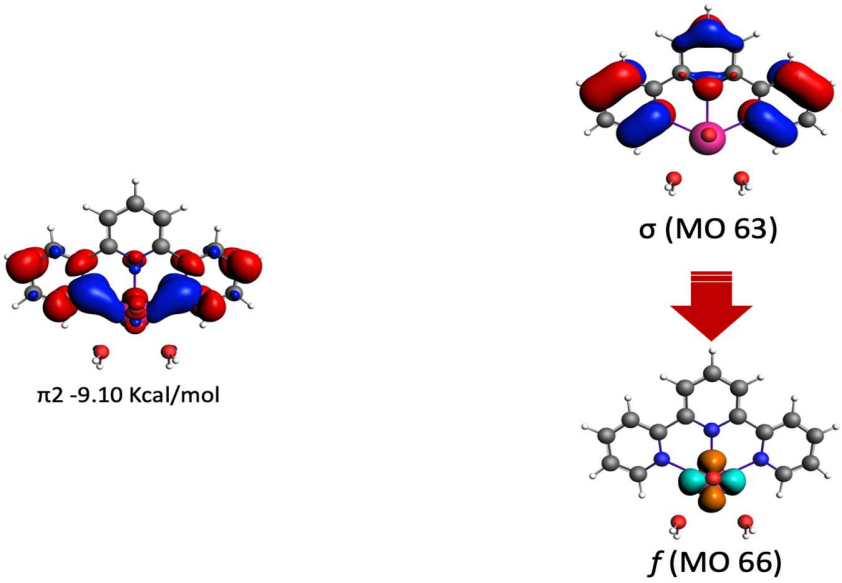

Figure A 3.5.3.6 Deformation densities Δρ (iso-contour 0.003 a.u.) for π2 in Table A 3.5.3.1 from ETS-NOCV calculations on neutral closed-shell singlet fragments of extractant **1** and UO_2^{2+} interaction (left). Electron density flows from red to blue. The corresponding frontier orbitals (iso-contour 0.03 a.u.) of the fragments for the π2 deformation densities on the left are shown on the right. The frontier orbitals on the right represent the nitrogen lone pair electrons donating to the *f* empty orbitals.

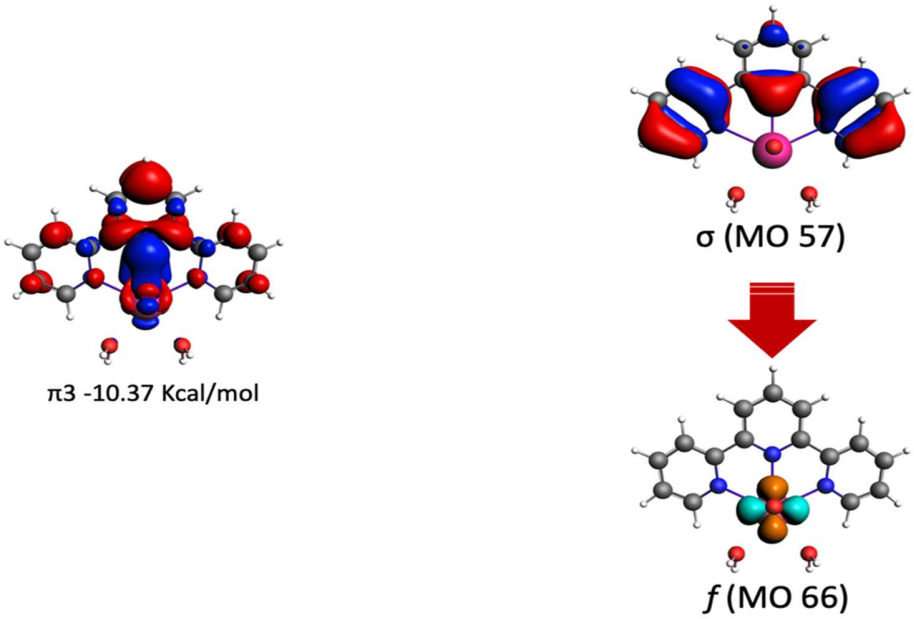

Figure A 3.5.3.7 Deformation densities Δρ (iso-contour 0.003 a.u.) for π3 in Table A 3.5.3.1 from ETS-NOCV calculations on neutral closed-shell singlet fragments of extractant **1** and UO_2^{2+} interaction (left). Electron density flows from red to blue. The corresponding frontier orbitals (iso-contour 0.03 a.u.) of the fragments for the π3 deformation densities on the left are shown on the right. The frontier orbitals on the right represent the nitrogen lone pair electrons donating to the *f* empty orbitals.

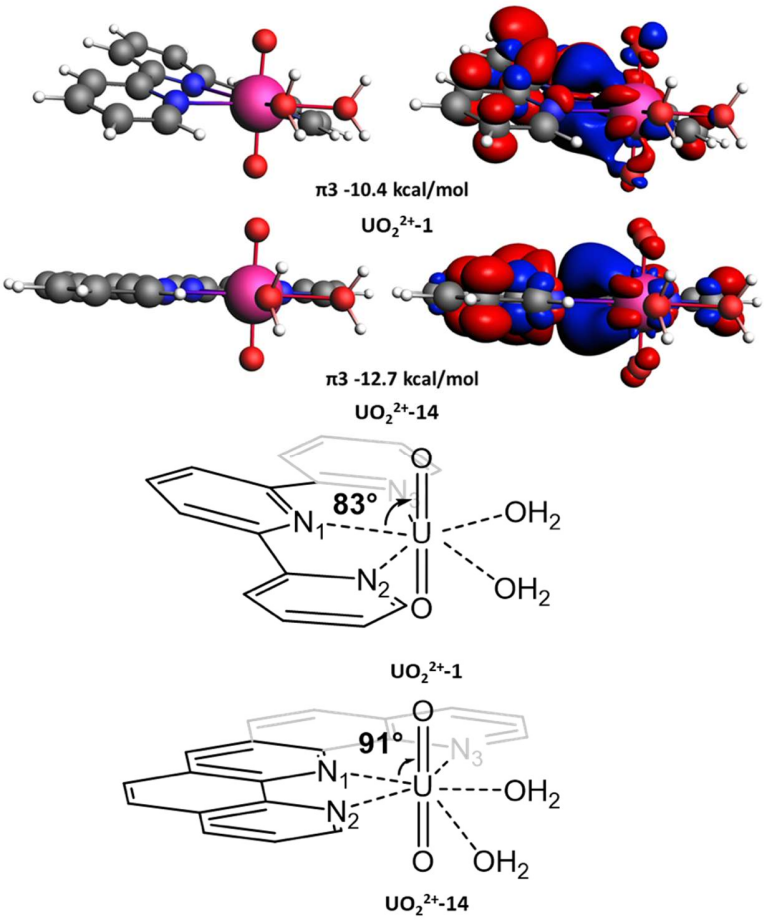

Figure A 3.5.3.8 Selected side view of ETS-NOCV deformation density (iso-contour 0.0003 a.u.) of π3 interactions between extractants **1**, **14** and motif $UO_2(H_2O)_2^{2+}$. Electron density flows from red to blue. The examples here show that a planar structure on the equatorial plane helps to form better π interactions.

A 3.6. Separation of trivalent Am(III) from Eu(III)

Table A 3.6.1 Gibbs Free Energies (ΔΔG, kcal/mol) at PBE level for Reaction (3.2) in Water

Extractants	**1**	**13**	**14**	**15**
PBE	6.7	6.8	8.5	11.7

Table 3.6.2 Am/Eu-N distances of $Am/Eu^{3+}(H_2O)6L$ (L=**1**, **13**, **14**, **15**) compounds (Å)

Extractant	**1**	**13**	**14**	**15**	Extractant	**1**	**13**	**14**	**15**
Am-N1	2.556	2.534	2.529	2.508	Eu-N1	2.602	2.562	2.559	2.550
Am-N2	2.521	2.543	2.549	2.537	Eu-N2	2.568	2.588	2.586	2.579
Am-N3	2.565	2.591	2.594	2.579	Eu-N3	2.580	2.603	2.583	2.580

A 3.7. Effect of dispersion correction

The dispersion correction usually helps DFT method to improve the description of weak non-covalent interactions. The improvement for strong covalent σ and π interaction discussed in this study is usually negligible. Thus, the lack of dispersion corrections should have little impact. To further verify this point, we calculated the complexes of actinyl with ligand **1** as an example and compared the results with and without dispersion from both 1) structural and 2) bonding (EDA and ETS-NOCV) perspectives.

The geometrical parameters and bonding analysis results are tabulated in below in Table A 3.7.1-A 3.7.3. The dispersion correction makes M-N1 and M-N2/N3 bond slightly shorter for about 0.002 Å and 0.004 Å, respectively, shown in Table A 3.7.1. Slightly shorter bonds lead to slightly stronger interaction energies, but both are marginal, as shown by the EDA analysis in Table A 3.7.2. The dispersion correction term in EDA is small compared to rest of the terms, on the order of -8 kcal/mol for all complexes (Table A 3.5.1.1-A 3.5.1.3). When consider the difference of these interaction energies (ΔΔG) between different ligands, this term cancels out and leaving no impact on the conclusions.

Table A 3.7.1 M-N distances of $MO_2^{2+}(H_2O)_2L$ (M=U/Np/Pu, L=**1**) compounds (Å) without and with dispersion correction.

Extractant **1**	U		Np		Pu	
	without	with	without	with	without	with
M-N1	2.547	2.545	2.539	2.537	2.543	2.541
M-N2	2.529	2.524	2.519	2.515	2.511	2.507
M-N3	2.529	2.524	2.519	2.515	2.511	2.507

Table A 3.7.2 EDA for $MO_2^{2+}(H_2O)_2L$ (M=U/Np/Pu, L=**1**) compounds (kcal/mol) without and with dispersion correction.

Extractant **1**	U		Np		Pu	
	without	with	without	with	without	with
Pauli	143.8	146.2	145.8	147.8	136.6	138.5
Electrostatic	-173.5	-174.8	-172.4	-173.5	-168.4	-169.5
Steric [a]	-29.7	-28.6	-26.7	-25.7	-31.8	-31.0
Orbital	-150.6	-151.5	-150.4	-151.2	-144.7	-145.4
Dispersion	-	-8.1	-	-8.1	-	-8.8
Total	-180.2	-188.2	-177.0	-185.0	-176.5	-185.2

[a] Steric interaction is the sum of the Pauli repulsion and Electrostatic interaction.

Table A 3.7.3 ETS-NOCV for $MO_2^{2+}(H_2O)_2L$ (M=U/Np/Pu, L=1) compounds (kcal/mol) without and with dispersion correction. The second column is divided by 2 because the first column contains both α and β contributions for fair comparison with the β spin results of open-shell NpO_2^{2+} and PuO_2^{2+} compounds.

Extractant **1**	U		U(β)		Np(β)		Pu(β)	
	without	with	without	with	without	with	without	with
σ 1	-41.6	-41.4	-20.8	-20.7	-19.0	-18.9	-18.2	-18.1
σ 2	-23.8	-23.7	-11.9	-11.8	-11.1	-11.0	-10.7	-10.7
σ 3	-18.5	-18.5	-9.3	-9.3	-8.9	-9.0	-8.7	-8.8
π 1	-11.3	-11.2	-5.7	-5.6	-5.5	-5.4	-5.3	-5.2
π 2	-9.1	-9.0	-4.6	-4.5	-4.4	-4.4	-4.0	-3.9
π 3	-10.4	-10.3	-5.2	-5.1	-5.0	-4.9	-4.7	-4.7
σ total	-83.9	-83.7	-42.0	-41.8	-39.0	-38.9	-37.7	-37.6
π total	-30.8	-30.4	-15.4	-15.2	-14.9	-14.7	-13.9	-13.8
Total	-114.7	-114.1	-57.4	-57.0	-53.8	-53.6	-51.6	-51.4

Chapter 4 . Theoretical Study of Modifications of Terpyridine-type Ligands for Actinide Separation

4.1 Introduction

In the nuclear industry, the plutonium uranium reduction extraction (PUREX) process removes the uranium and plutonium from spent nuclear fuel for subsequent refabrication into nuclear fuel.[1] Lipophilic Bistriazinylpyridine (BTP) derivatives are the most extensively studied soft-donor extractants in the European advanced fuel cycle research program, see Scheme 4.1.[2, 3] Evolving from the BTP, lipophilic Bistriazinyl Bipyridines, 6,6'-bis(5,6-dialkyl-1,2,4-triazin-3-yl)-2,2'-bipyridines (BTBPs, Scheme 4.2) were synthesized at Reading University, UK[4, 5] $CyMe_4$-BTBP (Scheme 4.2, R = $CyMe_4$, one per triazin-3-yl ring) is the current reference molecule for developing actinide-(III) separation processes in Europe.[6] In Chapter 3, a series of extractants of the polypyridyl family, including barebone BTP, were studied using first-principle calculations with actinyl ions as a structurally simplified surrogate model to identify the electronic properties that preferentially influence Am(III) binding in separations. The results show that π interactions, especially between the central terpyridine ring and metal *f* orbitals, play a crucial role in separation. Adding an electron-donating group onto the terpyridine backbone increases the binding energies and the selectivity of Am(III) over Eu(III). By contrast, the electron-withdrawing group had an adverse effect. This agrees with experimental observations. For example, the separation factors for Am(III) over Eu(III) ($SF_{Am(III)/Eu(III)}$) of n-Pr-MeO-BTP, n-Pr-BTP, and n-Pr-Cl-BTP are 113, 90, and 29, respectively, where R = n-C_3H_7 and X = MeO, H, and Cl in Scheme 4.1. [7, 8] Also, changing the $CyMe_4$ side-groups to five-membered O- or S- heterocycles rings (Cy_5-O-Me_4-BTBP, Cy_5-S-Me_4-BTBP, see Scheme 4.2), that contain amore electron-withdrawing atom, had an adverse effect both on solubility and on extraction performance.[9]

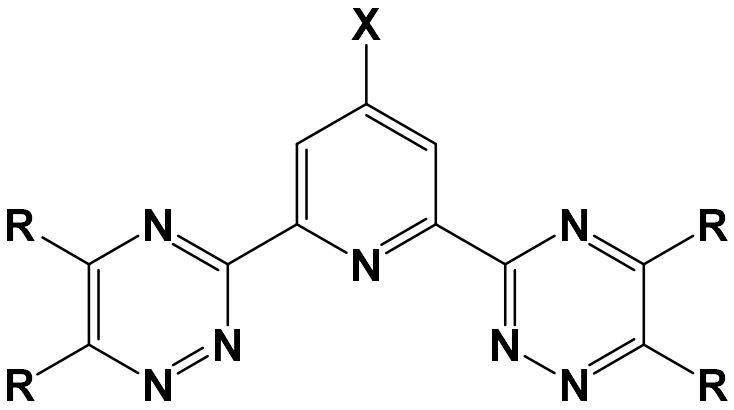

Scheme 4.1 Structure of BTPs. Typical R groups are R= CH_3, C_2H_5, *n*-C_3H_7, *i*-C_3H_7, *n*-C_4H_9, *i*-C_4H_9, $CyMe_4$ (one per triazin-3-yl ring), X = H, OMe and Cl

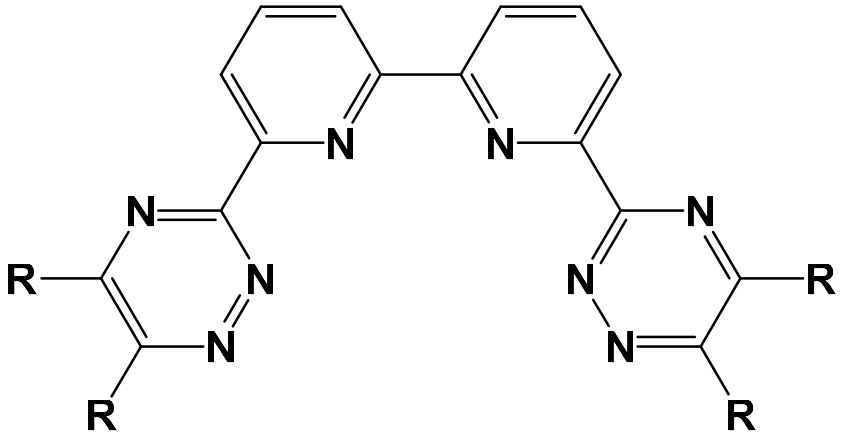

Scheme 4.2 Structure of BTBPs. Typical R groups are R= CH_3, C_2H_5, *n*-C_3H_7, *i*-C_3H_7, *n*-C_4H_9, *i*-C_4H_9, $CyMe_4$ (one per triazin-3-yl ring), Cy_5-O-Me_4 (one per triazin-3-yl ring) and Cy_5-S-Me_4 (one per triazin-3-yl ring)

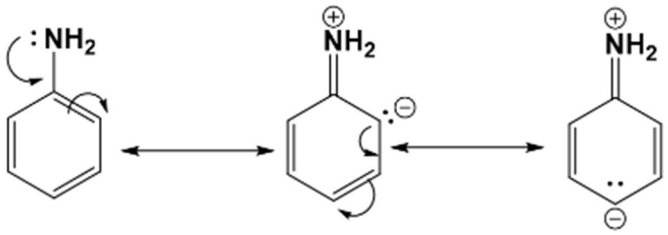

Scheme 4.3 Resonance structures of aniline.

Consequently, interesting questions are whether the central terpyridine ring is superior to other rings, and the mechanism behind it. The difference between the BTP derivatives used in experiment and the barebone BTP extractant **5** in Chapter 3 for bonding, where R = H in Scheme 4.1. In other words, how lipophilic chains affect bonding. Besides, the -NH_2 group as an electron-donating group is somehow experimentally unfavored because it is unstable. Thus, using -NMe_2 instead of -NH_2 and the resulting effects are also discussed in this chapter. Benay et al. [10] studied substituents on the BTP center ring computationally and reported the intrinsic basicity of the ligands, in the order of R = NMe_2 > NH_2 > OMe > C_6H5 > t-Butyl > Me > H > F > Cl. This order agrees with the experimental observations mentioned above that an electron-donating group on the terpyridine backbone increases the binding energies and the selectivity of Am(III) over Eu(III) and vice versa. However, unlike -NH_2, -NMe_2 group is rather bulky. The repulsion between the -NMe_2 group and the C-H units of extractant **18**, see Scheme 4.4, results in the lone pair of nitrogen not being perfectly in the same plane as the rest of the conjugate system. As Scheme 4.3 shows, this imperfect alignment will affect the electronegativity of the corresponding nitrogen atom for ionic bonding. Moreover, the study in Chapter 3 showed the importance of the π-system of the pyridine ring for separation. Thus, a modified extractant **19** was included in this chapter to reduce this repulsion. The additional extractants in Chapter 3 are used as a basis for those proposed in the current chapter. They are given in Schemes 4.4 and 4.5. In Chapter 3, energy decomposition analysis (EDA)[11, 12] and its extension, the extended transition state method for energy decomposition analysis combined with the natural orbitals for chemical valence theory (ETS-NOCV)[13] , provided rationalization of the ligand-metal interactions. However, because the ETS-NOCV method still based on molecular orbitals (MOs), for high-symmetry extractants, the ETS-NOCV patterns from degenerated MOs cannot give a pure description for a given bond. Hence, a

localized orbital method is required. Adaptive Natural Density Partitioning (AdNDP), introduced by Boldyrev et al.,[14] has had many successes in analyzing various typical aromatic organic molecules.[15] AdNDP can describe the multi-centers bonds in a localized way, which is more compatible with traditional chemistry concepts than MOs and MO-based methods. Thus, AdNDP analysis was carried on in this chapter for the π-systems in the polypyridyl family extractants and the bonding between metal ions and the π-system of the extractant. However, the AdNDP method, unlike Natural Bond Orbitals (NBO), cannot operate in a "black-box" manner without the user's participation. AdNDP requires explicit specification of the thresholds based on the the user's chemical intuition. So, different AdNDP patterns can be obtained from different search processes. Thus, many other methods such as the ETS-NOCV, [13] and multicenter bond order, were also used to validate the AdNDP results.

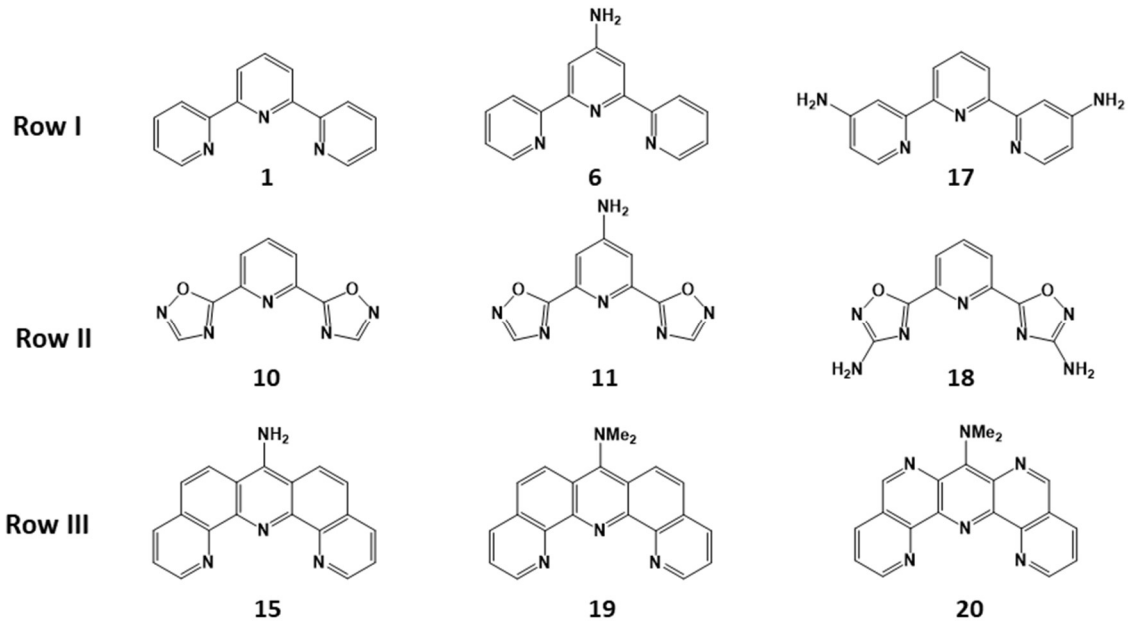

Scheme 4.4 Structures of selected extractants

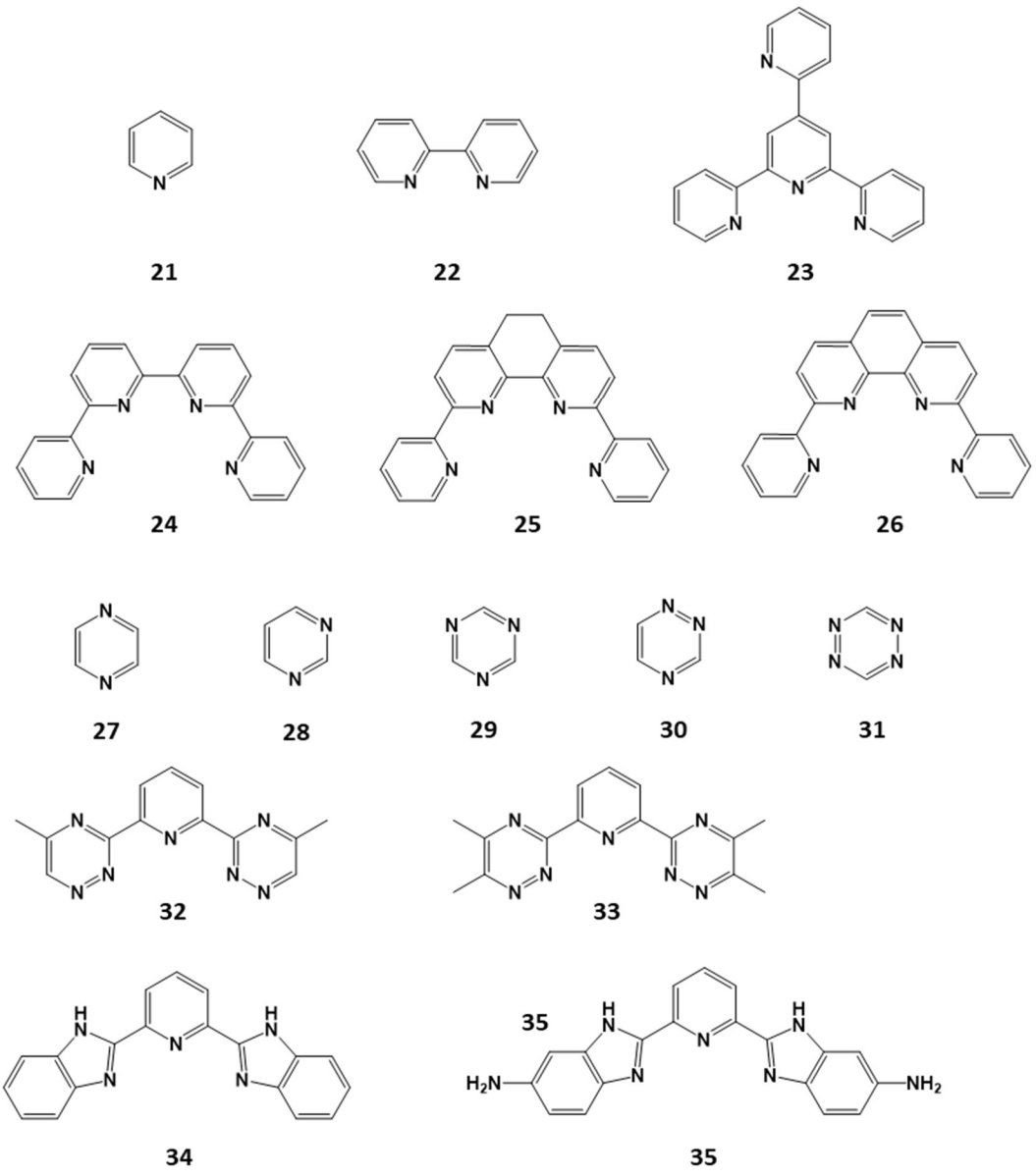

Scheme 4.5 Structures of selected extractants

4.2 Computational details

Unless otherwise noted, all the electronic structure calculations presented in this work were carried out with Density Functional Theory (DFT) using the ADF 2019 software package.[16-18] The choice of DFT functional and basis set for actinide calculations are the same as in Chapter 3, i.e. PBE[19] and all-electron TZ2P basis set.[20] All geometry optimizations were carried out with the scalar relativistic ZORA Hamiltonian,[21-23] and in conjunction with the COSMO[24] implicit solvation model. The radii values of the atomic spheres in the COSMO solvation model for atoms in this study are the corresponding Van der Waals radii from the MM3 method by Allinger [25] divided by 1.2. Although the radii values for atoms heavier than uranium are not ideal, as tested in Chapter 3, these heavy metals are well buried inside the first solvation shell and do not have direct contact with the solvation cavity. Hence, the radii settings for them do not affect the results of the geometry optimization. The vibrational frequencies below 100 cm^{-1} including suspicious imaginary frequencies were scanned by the ADF program with higher precision in order to limit the numerical noise from the solvation model. Because of the minor effect on molecular structures, vibrational frequencies, and reaction energies, provided that the oxidation state of the heavy atom does not change, the spin-orbit coupling effects were not considered in this work. Furthermore, many analysis tools are not yet implemented for the spin-orbital ZORA Hamiltonian. Grimme's D3 dispersion[26] correction with Becke-Johnson damping (D3BJ)[27] was used for the actinyl systems. However, this model has not been parameterized beyond Pu. Thus, the calculations invoking Am and Eu comparisons were carried on without this correction. The study in Chapter 3 showed that the dispersion contributions between extractants and metal ions are quite consistent and will not affect the trends of the results. Frequency calculations were performed to ensure optimization convergence to local minima on the potential energy surface. These frequencies were also used to compute the entropy term in the Gibbs free energy at the harmonic approximation. A standard state correction of 1354 atm was applied to the enthalpy to model the restrictions imposed by the liquid phase.[28] This method has successfully been applied to actinide systems previously.[29-32] The calculations in Chapter 3 and previous studies[33, 34] revealed that the pure GGAs, such as PBE or BP86, tend to overestimate the energy of bonding between Eu(III) and ligands. In addition, single-point

energy corrections from higher levels of theory, such as double hybrid GGA or DLPNO-CCSD(T)[35] greatly improved the reproducibility of the calculations for the experimental selectivity of S-, N- and O-donor ligands for Am(III)/Eu(III) separation. Thus, to gain more accurate energies, single-point calculations in gas-phase were carried out at the coupled-cluster level, namely DLPNO-CCSD(T),[35] on the DFT predicted structures with a scaler ZORA Hamiltonian using the ORCA program[36] for the trivalent Am(III)/Eu(III) systems. The SARC-ZORA-TZVP basis set[37, 38] was used for Am and Eu, and the ZORA-def2-TZVP basis set[39] was used for the other, light atoms.

To further understand the fundamental factors that drive the bonding and separation, various bonding analysis methods were used to analyze the bonding nature of the molecules. In particular, Hirshfeld charge analysis[40] was used to represent the charge rearrangement and distribution because it agrees well with conventional chemical intuition, and was thus used in previous studies where it explained experimental results.[41, 42] Energy decomposition analysis (EDA)[11, 12] and its extension, the extended transition state method for energy decomposition analysis combined with the natural orbitals for chemical valence theory (ETS-NOCV)[13], provided rationalization of the ligand-metal interactions. Adaptive Natural Density Partitioning (AdNDP)[15, 43, 44] analysis and various other types of analysis such as multicenter bond order and localized orbital locator (LOL) were carried out using the MultiWFN package.[45] The Natural Atomic Orbital basis set (AONAO) and the first-order reduced density matrix in the basis of Natural Atomic Orbitals (DMNAO) from NBO6[46] calculations for the AdNDP method were calculated using ADF. However, because Slater basis sets are not supported very well by many third-party programs, it is hard to visualize the AdNDP results from ADF. Thus, the wavefunctions of actinide/lanthanide compounds for the purpose of visualizing AdNDP were obtained from single-point energy calculations using the Gaussian 16 program[47] with the PBE functional[19] and NBO6[46]. The corresponding valence basis sets ECP60MWBSEG[48] and ECP28MWBSEG[49] were adopted for actinides and Eu, respectively. The def2-svp basis set[39] was used for other light atoms. Furthermore, the free extractants in Schemes 4.4 and 4.5 are also optimized using the def2-svp basis set[39] with PBE functional,[19] and then studied using AdNDP.

4.3 Results and discussion

4.3.1. Thermodynamics of extractants binding to actinyl ions

Previous experimental and theoretical studies suggest that, for the three actinyl ions UO_2^{2+}, NpO_2^{2+}, and PuO_2^{2+}, the most prevalent form in liquid water is in the form of the penta-aquo complex, $AnO_2(H_2O)_5^{2+}$.[50-61] Thus, firstly, the affinity of the proposed extractants towards actinide coordination was evaluated via the Gibbs free energy of the solvent displacement reaction (4.1):

$$AnO_2(H_2O)_5^{2+} + L \rightarrow AnO_2(H_2O)_2L^{2+} + 3H_2O \qquad (4.1)$$

where L represents the extractants shown in Scheme 4.4. The difference between the ΔG values for two different metal centers with the same extractant, $\Delta\Delta G_{Np\text{-}U}$ and $\Delta\Delta G_{Pu\text{-}Np}$, is directly associated to the separation efficiency of that extractant. A larger ΔΔG values for a given pair of metals indicates a larger thermodynamic difference and consequently a greater potential for better separations.

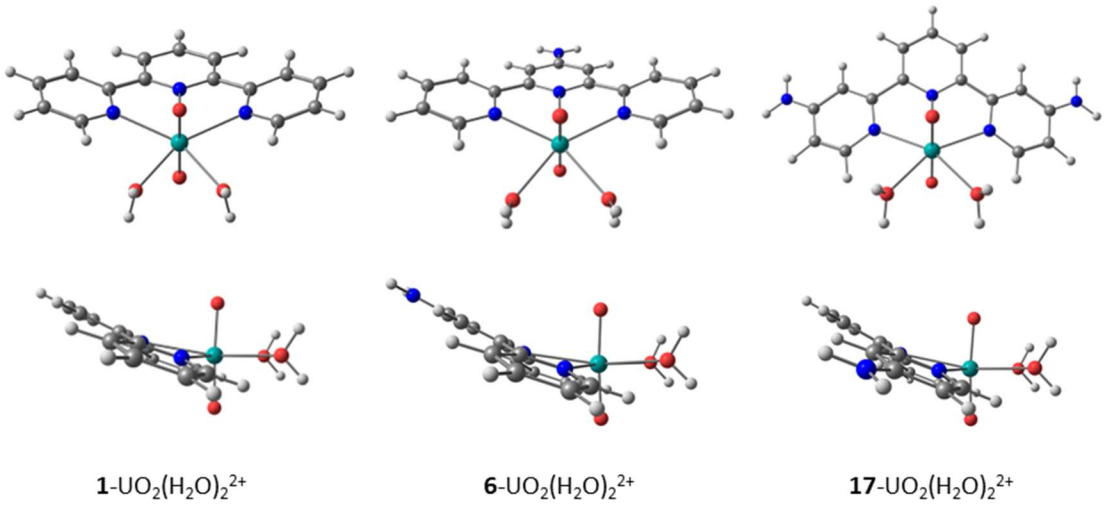

Figure 4.1 Front and side views of optimized structures of L-$UO_2(H_2O)_2^{2+}$ complexes, where L=**1**, **6**, and **17** in *Row I* of Scheme 4.4 (Red = Oxygen, White = Hydrogen, Grey =Carbon, Dark Blue = Nitrogen, Light Blue = Uranium).

Table 4.1 Gibbs Free Energies (ΔG, kcal/mol) for Reaction (4.1) of extractants in *Row I* of Scheme 4.4 in water at the PBE-D3BJ level.

Extractant	**1**	**6**	**17**
UO_2^{2+}	-25.0	-31.8	-35.2
NpO_2^{2+}	-29.9	-33.6	-37.2
PuO_2^{2+}	-29.1	-36.3	-38.9
$\Delta\Delta G_{Np-U}$	-4.9	-1.8	-2.0
$\Delta\Delta G_{Pu-Np}$	0.8	-2.7	-1.6

To investigate the difference between the center pyridine ring and lateral rings of terpy and its derivative, the extractant **17** is involved in addition to the extractants **1** and **6** in Chapter 3, which are illustrated in *Row I* of Scheme 4.4. The -NH_2 electron-donating group on the lateral rings of extractant **17** should give very similar electronegativity of the donating nitrogen atom as the center ring of extractant **6**; details will be discussed in section 4.3.2. If the extractants **6** and **17** have similar covalency for the bonding of the modified rings from extractant **1**, extractant **17** is expected to perform much better than extractant **6**. However, Table 4.1 shows the reaction Gibbs free energy for all three extractants in *Row I* of Scheme 4.4 reacting with UO_2^{2+}, NpO_2^{2+}, and PuO_2^{2+}, which tells quite a different story. All of the proposed extractants preferentially bind to NpO_2^{2+} and PuO_2^{2+} relative to UO_2^{2+}, see Figure 4.1. As expected, extractant **17**, which has one electron donating -NH_2 group on each lateral ring, displays the highest affinity towards actinyl binding, with ΔG values of -35.2, -37.2, and -38.9 kcal/mol for UO_2^{2+}, NpO_2^{2+}, and PuO_2^{2+}, respectively. However, compared to extractant **6**, which has only one -NH_2 group on center pyridine ring, extractant **17** does not show improvement in selectivity but only gives almost the same $\Delta\Delta G_{Np-U}$ value and a smaller $\Delta\Delta G_{Pu-Np}$ value. This indicates that the electronic structure of the center pyridine ring is different for bonding from those of the lateral pyridine rings. Since the σ bonds formed by the nitrogen lone pair are the same for each extractant, the origin of this difference might be in the different π systems of the rings.

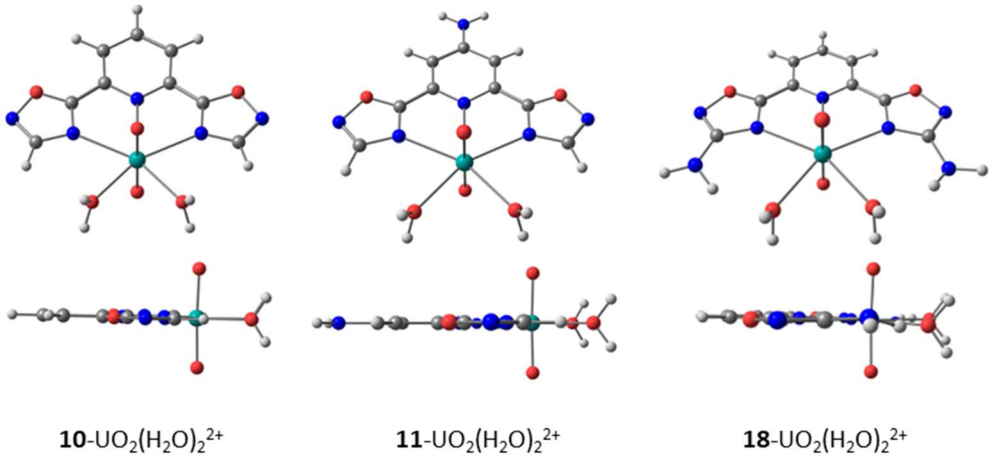

Figure 4.2 Front and side views of optimized structures of L-$UO_2(H_2O)_2$ $^{2+}$ complexes, where L=**10**, **11**, and **18** in *Row II* of Scheme 4.4 (Red = Oxygen, White = Hydrogen, Grey =Carbon, Dark Blue = Nitrogen, Light Blue = Uranium).

Table 4.2 Gibbs Free Energies (ΔG, kcal/mol) for Reaction (4.1) of extractants in *Row II* of Scheme 4.4 in water at PBE level.

Extractant	**10**	**11**	**18**
UO_2^{2+}	-12.8	-15.7	-10.8
NpO_2^{2+}	-13.5	-17.9	-13.2
PuO_2^{2+}	-15.3	-19.5	-17.2
$\Delta\Delta G_{Np-U}$	-0.7	-2.2	-2.4
$\Delta\Delta G_{Pu-Np}$	-1.8	-1.6	-3.9

The extractants in *Row II* of Scheme 4.4 are the extractant **10** and its derivatives. The extractant **10** has two five-member lateral rings. Unlike the extractant **1**, the lateral rings of the extractant **10** only have one hydrogen that can be replaced by an $-NH_2$ group, which is next to the donating nitrogen atom. Thus, the donating nitrogen atoms in the extractant **18** will not be as negative as in extractant **17** as illustrated in Scheme 4.3. This is confirmed by charge analysis in section 4.3.2. Therefore, the difference between the ΔΔG values for extractants **11** and **18** more reflects the difference of covalency between them as the result of the modification by adding $-NH_2$ groups. The reaction Gibbs free energy for the extractants **10** and its derivatives in *Row II* of Scheme 4.4 for reaction (4.1) are summarized in Table 4.2. Figure 4.2 shows the optimized structures. Unlike extractants in *Row I*, extractant **18** with one electron donating $-NH_2$ group

on each lateral ring gives larger $\Delta\Delta G_{Np\text{-}U}$ and $\Delta\Delta G_{Pu\text{-}Np}$ than extractant **11**, which has one -NH_2 group on the center ring, while extractant **11** does not show a large improvement compared to the original extractant **10** for $\Delta\Delta G_{Pu\text{-}Np}$. The thermodynamic calculations indicate that the π systems of the lateral rings of extractant **1** and its derivatives in *Row I* of Scheme 4.4 are different from extractant **10** and its derivatives in *Row II*, which form bonds with the actinides with a higher degree of covalency.

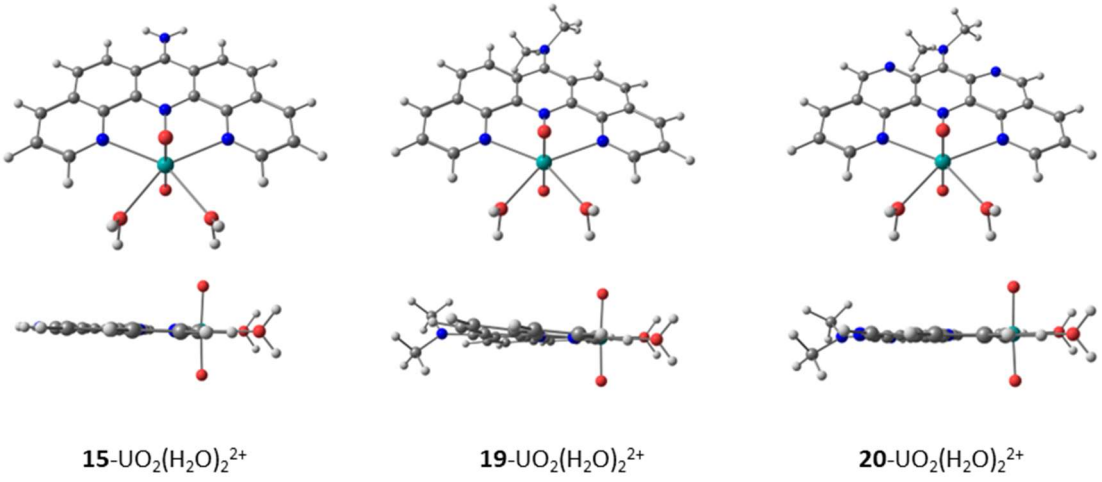

Figure 4.3 Front and side views of optimized structures of L-$UO_2(H_2O)_2^{2+}$ complexes, where L=**15**, **19**, and **20** in *Row II* of Scheme 4.4 (Red = Oxygen, White = Hydrogen, Grey =Carbon, Dark Blue = Nitrogen, Light Blue = Uranium).

Table 4.3 Gibbs Free Energies (ΔG, kcal/mol) for Reaction (4.1) of extractants in *Row III* of Scheme 4.4 in water at PBE level.

Extractant	**15**	**19**	**20**
UO_2^{2+}	-32.1	-32.1	-31.1
NpO_2^{2+}	-37.3	-37.1	-33.4
PuO_2^{2+}	-40.9	-43.1	-40.9
$\Delta\Delta G_{Np\text{-}U}$	-5.2	-5.0	-2.3
$\Delta\Delta G_{Pu\text{-}Np}$	-3.7	-6.0	-7.5

Figure 4.3 shows the optimized structures for the compounds of extractants **15**, **19** and **20** (*Row III* of Scheme 4.4). The additional nitrogen atoms in extractant **20** reduce the dihedral angle of -NMe_2 group and extractant ring from ~45° to ~35° . Table 4.3 shows the reaction Gibbs free energy for extractants in *Row III* of Scheme 4.4 reacting with UO_2^{2+}, NpO_2^{2+}, and PuO_2^{2+}. The extractant **15** was predicted to be the best extractant in Chapter 3. Although -NMe_2 is a stronger electron donating group than -NH_2, by replacing the -NH_2 electron donating group with an -NMe_2 group, extractant **19** shows the same affinity as extractant **15** for UO_2^{2+} and NpO_2^{2+}, and larger affinity for PuO_2^{2+} which leads to larger $\Delta\Delta G_{Pu\text{-}Np}$. Extractant **20** shows less affinity to UO_2^{2+} and NpO_2^{2+} due to the additional electron withdrawing nitrogen atoms. However, it also gives the largest $\Delta\Delta G_{Pu\text{-}Np}$ gap (-7.5 kcal/mol, Table 4.3) so far in the studies in this thesis.

4.3.2. Bonding analysis of uranyl compounds

Table 4.4 Hirshfeld charges of donating nitrogen atoms in extractants **1**, **6**, **17**, **10**, **11** and **18** in their pre-organized cis-configuration.

Extractant	**1**	**6**	**17**	**10**	**11**	**18**
N1	-0.199	-0.233	-0.204	-0.164	-0.205	-0.168
N2	-0.205	-0.208	-0.243	-0.212	-0.217	-0.224
N3	-0.205	-0.208	-0.243	-0.212	-0.217	-0.224

Table 4.5 Select bond length (Å) for L- $UO_2^{2+}(H_2O)_2$ (L = **1**, **6**, **17**, **10**, **11**, and **18**) complexes

Extractant	**1**	**6**	**17**	**10**	**11**	**18**
U–N1	2.545	2.500	2.547	2.618	2.566	2.574
U–N2	2.524	2.524	2.485	2.535	2.536	2.554
U–N3	2.524	2.524	2.485	2.535	2.536	2.554

As Table 4.4 shows, the Hirshfeld charges of unmodified donating nitrogen atoms are the same across extractants **1**, **6**, and **17**. On the other hand, the electron-donating -NH_2 group makes the donating nitrogen atom in either the center or lateral rings more electronegative. The Hirshfeld charges of the donating atoms in the lateral rings of extractant **17** are more negative than those of the center ring of extractant **6**. However, as discussed in section 4.3.1, extractant **17** did not show an advantage over extractant

6, although extractant **17** has two -NH_2 groups. This indicates that the differences in selectivity of extractant **6** and **17** are mainly due to covalent interactions rather than ionic interactions. The U-N bond lengths of extractants **1**, **6**, and **17** in Table 4.5 agree very well with the calculated atomic charges in Table 4.4. Extractant **10** has the longest center ring U-N1 bond length of all the extractants in Chapter 3 and this chapter, see Table 4.5 and Table A4.2.2. On the other hand, the U-N2/N3 bond lengths of extractant **10** indicate that it has similar lateral ring bonding strength as the rest of the tri-pyridine extractants. Upon adding an -NH_2 group to the center ring of extractant **10**, extractant **11** still has the longest center ring bond length among extractants with an -NH_2 group on the center ring. The lateral ring bond length of extractant **11** is still shorter than the center U-N1 bond. Thus, it is reasonable to expect that strengthening the lateral ring bonding will be more effective than for the center ring. The thermodynamics calculations in section 4.3.1 above confirm this expectation that extractant **18** gives larger $\Delta\Delta G_{Np\text{-}U}$ and $\Delta\Delta G_{Pu\text{-}Np}$ (-2.4 and -3.9 kcal/mol) than extractant **11** (-2.2 and -1.6 kcal/mol). As Figure 4.3 shows, the lateral ring only has one position where a -NH_2 group can be added, which is next to the bonding nitrogen atoms. Thus, the -NH_2 substitution only slightly increases the electronegativity of the nitrogen atoms in the lateral rings. The U-N2/N3 bond lengths are slightly longer than in extractant **10** and **11**, see Table 4.5 and Figure 4.3, which is due to the repulsion from the -NH_2 groups and coordinated water molecules. The π1 and π2 ETS-NOCV interactions in Table 4.6 relate to π interactions of the lateral rings. Although extractant **18** has a longer lateral bond length, the π1 and π2 energies are larger than for extractants **10** and **11**.

Table 4.6 ETS-NOCV analysis for interactions between $UO_2^{2+}(H_2O)_2$ and L (L=**10**, **11** and **18**) (kcal/mol).

Extractant	**10**	**11**	**18**
σ 1	-35.4	-37.1	-37.9
σ 2	-19.3	-18.9	-19.5
σ 3	-15.9	-16.6	-17.4
π 1	-10.3	-9.8	-10.8
π 2	-6.5	-6.4	-7.1
π 3	-8.7	-14.7	-9.9
σ total	-70.6	-72.6	-74.8
π total	-25.4	-30.9	-27.8
Total	-96	-103.5	-102.6

Table 4.7 Hirshfeld charges of donating nitrogen atoms in extractants **15**, **19** and **20**

Extractant	**15**	**19**	**20**
N1	-0.234	-0.222	-0.228
N2	-0.206	-0.206	-0.199
N3	-0.206	-0.206	-0.199

Table 4.8 Selected bond length (Å) for L- $UO_2^{2+}(H_2O)_2$ (L = **15**, **19**, and **20**) complexes

Extractant	**15**	**19**	**20**
U–N1	2.492	2.503	2.487
U–N2	2.547	2.542	2.569
U–N3	2.547	2.543	2.569

Table 4.7 shows the Hirshfeld charges of donating nitrogen atoms of extractants **15**, **19** and **20**. The atomic charges of the donating atoms in the extractants strongly relate to ionic interactions between extractants and metal ions. As expected, although $-NMe_2$ has stronger ability to donate electrons, because of the steric repulsion, the electronegativity of the nitrogen atom in the center ring of extractant **19**, N1, is more positive than for extractant **15**. For extractant **20**, the additional nitrogen atoms in the ring generally reduce the electronegativity of the donating nitrogens, thus the N2 and N3 are weakened. On the other hand, the better resonance effect of the $-NMe_2$ group for **20** offsets this negative effect for N1 in the center ring.

This makes metal-N2/N3 bonds longer and allows the metal to move closer to N1. Thus, the U-N1 bond length of extractant **20** is 2.487Å (Table 4.8), which is the shortest among all the extractants from **1** to **20**. To investigate the covalent interactions between extractants and uranyl, the results of ETS-NOCV analysis are summarised in Table 4.9. The σ interactions of extractants **15** and **19** are almost the same, even though the U-N1 bond length of extractant **19** is longer than that of **15**. This indicates that the σ bonds are not overly sensitive to the bond length changes, also see σ1 and π3 in Table 4.6 for extractant **11** for example. By contrast, extractant **19** has stronger a π3 interaction than **15** despite the longer U-N1 bond length. From Figure 4.4, this is clearly due to the electron donation from the Me groups. The σ2 and π2 interactions are mainly interactions between the lateral rings and uranyl ion. The extractant **20** has much weaker lateral bonds but stronger center bonds. Again, extractant **20** gives the strongest π3 interaction. This is accompanied by the largest $\Delta\Delta G_{Pu\text{-}Np}$ gap (-7.5 kcal/mol, Table 4.3) in this thesis.

The thermodynamics calculations, atomic charge analysis and ETS-NOCV analysis indicate that the modifications of the ring, such as adding electron-donating group to the ring or replacing the C-H in the ring to a nitrogen atom, has a strong effect on the covalent bonding between the extractant and uranyl, especially for π bonding. The following section will further investigate the π system of the different extractants in Schemes 4.4 and 4.5 using AdNDP.

Table 4.9 ETS-NOCV analysis for interactions between $UO_2^{2+}(H_2O)_2$ and L (L=**15**, **18** and **19**) (kcal/mol).

Extractant	**15**	**18**	**19**
σ 1	-43.0	-42.7	-42.3
σ 2	-21.4	-21.6	-20.0
σ 3	-18.7	-18.6	-18.1
π 1	-11.3	-11.4	-10.6
π 2	-8.2	-8.2	-7.6
π 3	-18.5	-20.0	-21.2
σ total	-83.0	-82.9	-80.4
π total	-38.0	-39.6	-39.4
Total	-121.0	-122.5	-119.8

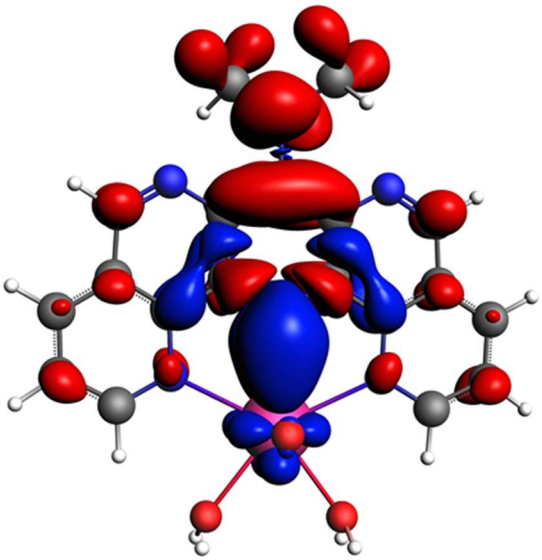

Figure 4.4 ETS-NOCV deformation density (iso-contour 0.0003 a.u.) of the π3 interactions between ligand **20** and $UO_2(H_2O)_2^{2+}$. Electron density flow is from red to blue.

4.3.3. Extractant π system analysis using AdNDP

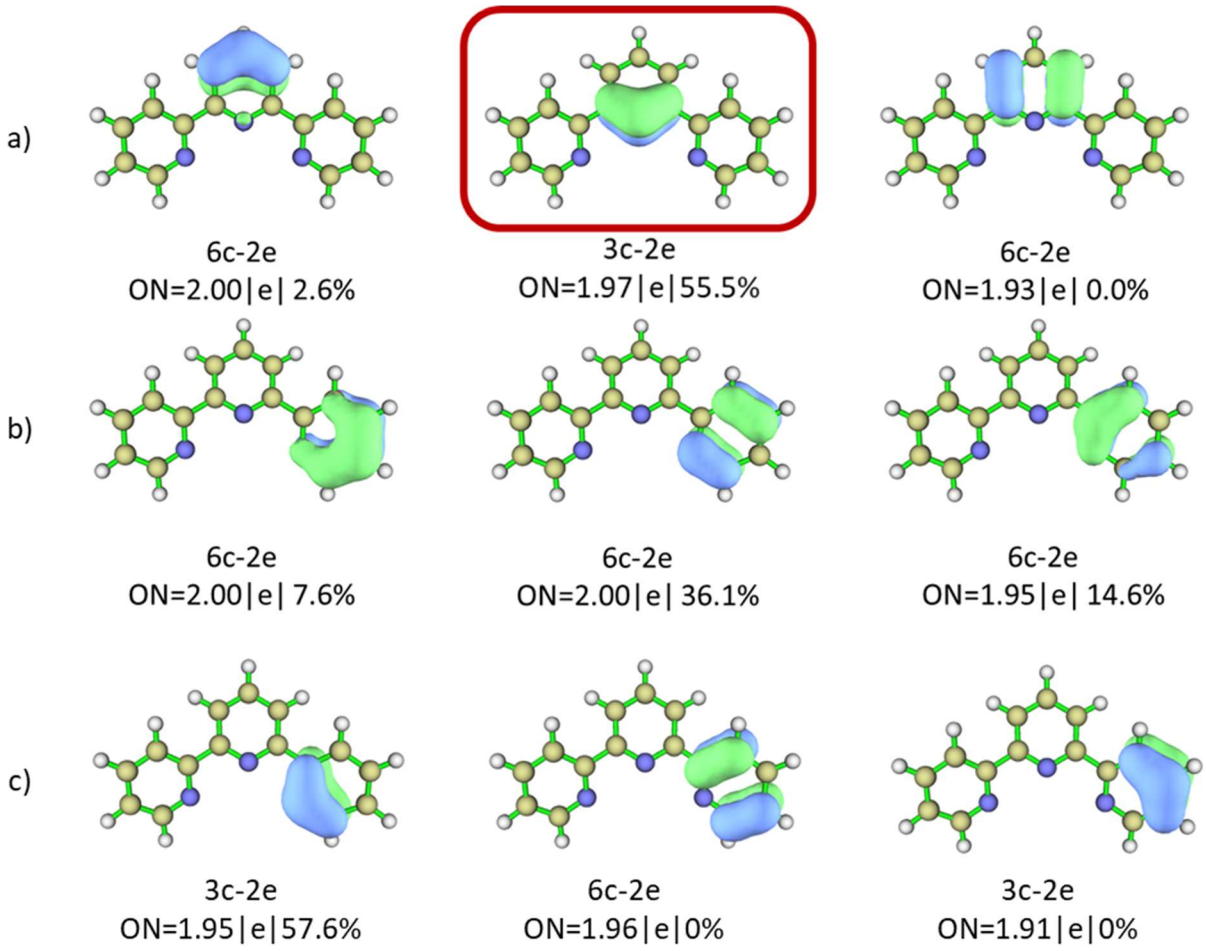

Figure 4.5 AdNDP orbitals and the contributions of donating nitrogen atom of extractant **1**, terpy. a) π-bonding pattern for center ring. b) First possible π-bonding pattern for lateral rings. c) Second possible π-bonding pattern for lateral rings. 6c-2e for six-center two-electrons and 3c-2e for three-center two-electrons. The iso-contour value is 0.05 a.u. ON stands for occupation number.

Because the π interactions play an important role in selectivity, as discussed in Chapter 3 and previous sections in this chapter, in order to better understand the bonding nature of these actinide compounds, AdNDP analysis was performed to investigate the details of the electronic structure of the ligands to reveal the nature of these π interactions. Figure 4.5 shows the AdNDP π-bonding patterns of the center and lateral heterocyclic rings of extractant **1**, terpy. In Figure 4.5a,

the first and second π-bonding patterns for the center pyridine ring of extractant **1** are different from those of the single pyridine ring **21** (Figure 4.6). These two π-bonding patterns are almost 3c-2e bonds, which means that the center pyridine ring of extractant **1** is less aromatic than a single pyridine ring. This is confirmed by the multicenter bond order. The normalized multicenter bond order for the center ring of extractant **1** is 0.646, while for a single pyridine ring and benzene ring, it is 0.658 and 0.660, respectively. The difference of π-bonding patterns between extractant **1** and pyridine **21** is likely due to the effect of the functional groups on the ring. Figure 4.5b and 5.5c show two possible π-bonding patterns for the lateral rings for extractant **1**. The π-bonding patterns in Figure 4.5b are supported by the MOs in Figure 4.7 which are also corresponding to the ETS-NOCV π-bonding patterns, see A4.5.3.5-7. On the other hand, the normalized multicenter bond order of the lateral rings are about 0.653 which is close to that of the pyridine ring, 0.658. If the lateral rings in extractant **1** would have the same bonding pattern as the center ring, the multicenter bond order should be smaller. The π-bonding patterns in Figure 4.5b for the lateral ring of extractant **1** is also very similar to that of the pyridine ring in Figure 4.6. The π-bonding patterns in Figure 4.5b have higher occupation numbers than the π-bonding patterns in Figure 4.5c as well. Therefore, the π-bonding patterns in Figure 4.5b are more reasonable and will be used for discussion. The marked π-bonding pattern at the center ring (red box in Figure 4.5a) is supposedly better than the other two π-bonding patterns (in Figure 4.5b) for donating π electrons, since it has an appropriate shape and the highest contribution from nitrogen. Thus, we hypothesize that it is more beneficial to add the $-NH_2$ donating group to the center ring rather than the side rings.

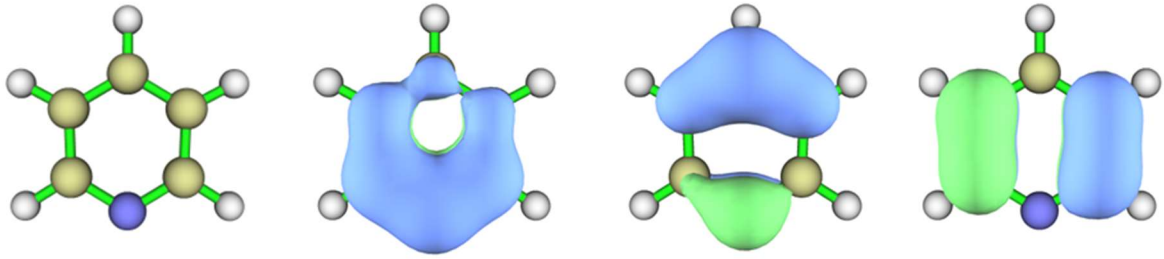

Figure 4.6 Selected six-center two-electrons (6c-2e) ADNDP orbitals π-bonding pattern for pyridine, **21**, according to AdNDP (iso-contour 0.05 a.u.).

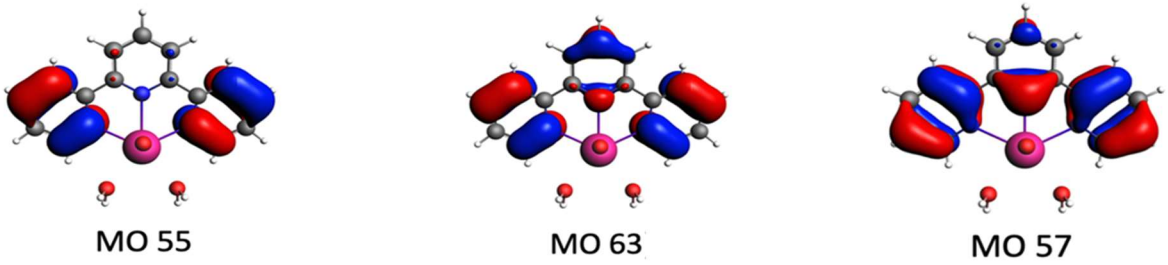

Figure 4.7 Frontier molecular orbitals (iso-contour 0.03 a.u.) of the extractant **1** fragment of **1**-$UO_2(H_2O)_2^{2+}$ corresponding to the π deformation densities in ETS-NOCV analysis, see Appendix 4, A4.5.3.5-7.

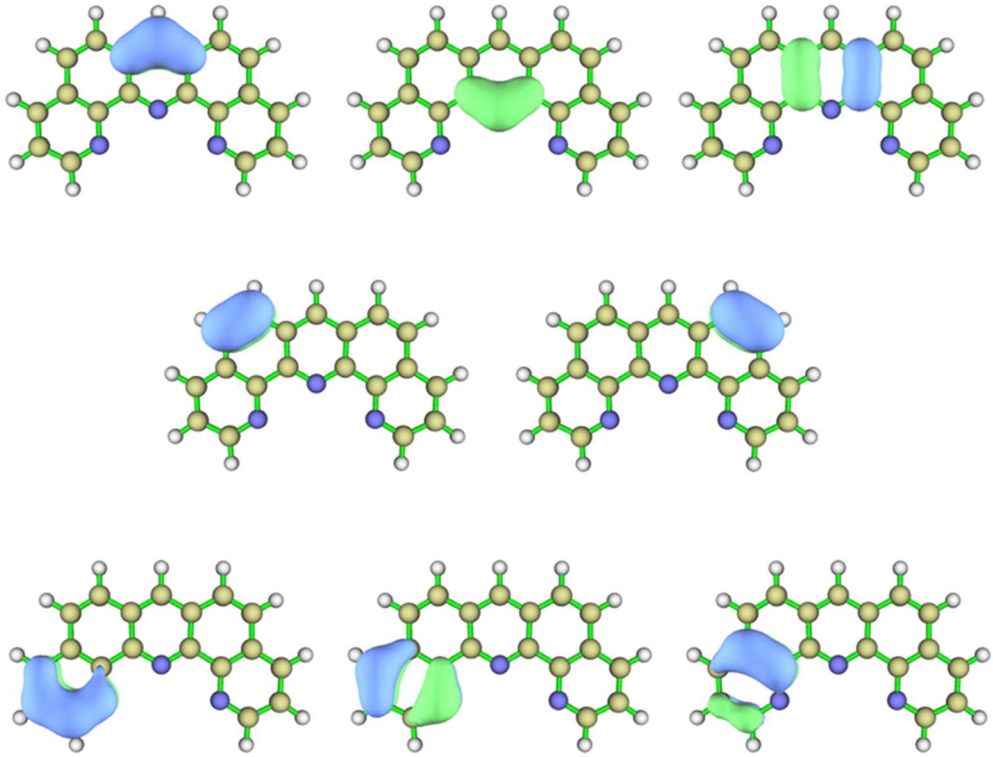

Figure 4.8 Selected six-center two-electrons (6c-2e) and three-center two-electrons (3c-2e) ADNDP orbitals π-bonding pattern for extractant **14** according to AdNDP (iso-contour 0.05 a.u.).

Figure 4.8 shows the AdNDP π-bonding patterns for extractant **14**. The π-bonding patterns of the center ring are the same as for extractant **1**. For the lateral rings, the AdNDP π-bonding patterns are exactly the same as in the analysis for phenantrene by Zubarev et al.[14] These patterns are also similar to those of extractant **1**, Figure 4.5. The π-bonding framework consists of two 2c-2e C-C π bonds with contributions from the two -C=C- substitutions of the central pyridine ring. These π-bonding patterns are supported by the π-electron LOL analysis, see Figure 4.9. Again, the center ring shows better potential for π bonding due to the symmetry and localization of the electron density.

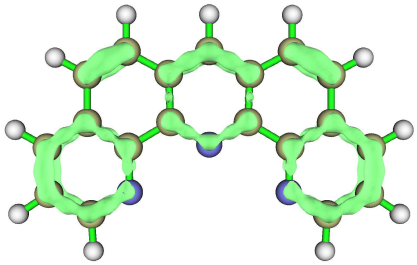

Figure 4.9 π-electron LOL analysis for extractant **14** (iso-contour 0.08 a.u.).

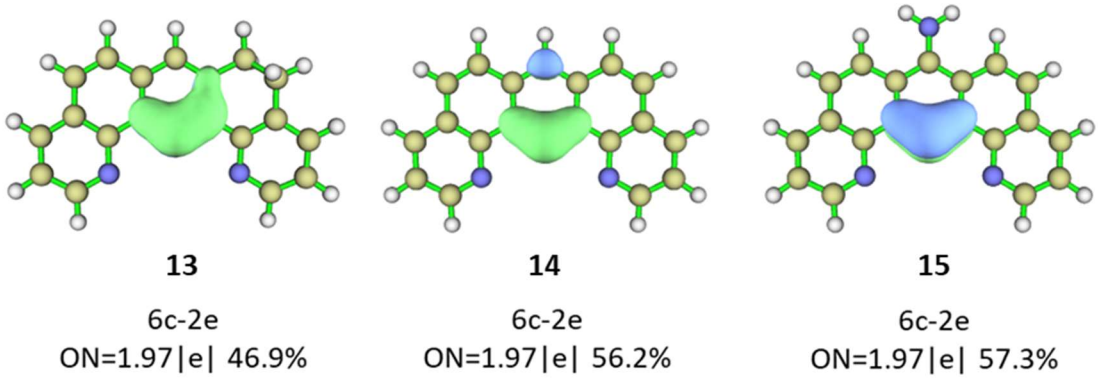

Figure 4.10 Selected six-center two-electron (6c-2e) π-bonding patterns for the center pyridine ring according to AdNDP, and the contributions of donating nitrogen atom for extractants **13**, **14**, and **15** (iso-contour 0.05 a.u.). ON for occupation number.

Figure 4.10 shows the AdNDP π-bonding patterns for different extractants. These patterns are analogous to the marked orbital in Figure 4.5 a). The AdNDP π-bonding patterns of **13** and **14** prove more clearly that the substitutions do disrupt the π conjugation in the backbone of the center ring in the extractant. The center of the orbital of extractant **13** has moved away from N1 compared to extractant **14**, and the contribution of the nitrogen of extractant **13** is about 9.3% lower than for extractant **14**. The ETS-NOCV analysis for extractant **13** in Chapter 3 showed a similar pattern as the ADNDP. The π orbital of ligand **13** in Figure 4.10 also becomes more delocalized with a larger normalized multicenter bond order value of 0.6112 compared to extractant **14**, 0.5978. This

explains why extractant **13** performs worse than extractant **14**. It further agrees with the reaction Gibbs free energy calculations in Chapter 3, that extractant **13** has less selectivity than extractant **14**. Comparing the AdNDP π-bonding patterns of **14** and **15**, the -NH_2 donating group also makes the orbital more localized around the N1 atom with normalized multicenter bond order value of 0.5722 and increases the nitrogen contribution by about 1% due to the C=N π bond. From Figure 4.11, when the -NH_2 donating group exists, it is better to count it is as part of the conjugate system. The existence of -NH_2 or -NMe_2 places the electron in the first π-bonding pattern in Figure 4.5a more toward the nitrogen atom, see Figures 4.11 and 4.12. More importantly, this π-bonding pattern will change the shape even more toward the metal upon coordination, see Figures 4.1.2 and 4.13, which forms an additional π bond in the center ring as compared to extractants without -NH_2 or -NMe_2.

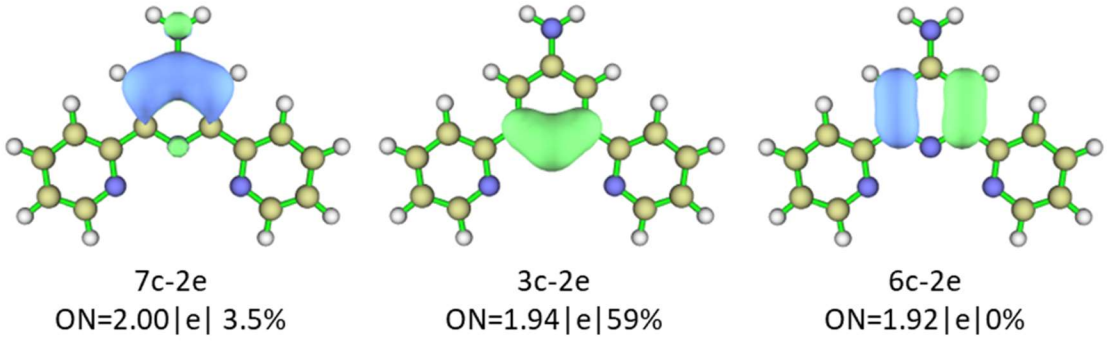

Figure 4.11 Selected π-bonding patterns for the center pyridine ring according to AdNDP, and the contributions of donating nitrogen atom for extractant **6** (iso-contour 0.05 a.u.). ON for occupation number.

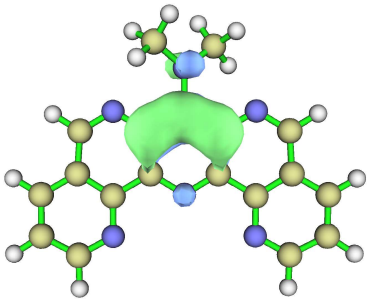

Figure 4.12 Selected seven-center two-electrons (7c-2e) ADNDP orbitals π-bonding pattern for extractant **20**

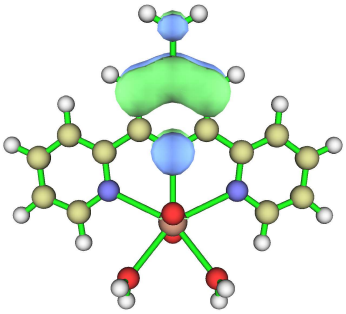

Figure 4.13 Selected seven-center two-electrons (7c-2e) ADNDP orbitals π-bonding pattern for compound **6**-UO_2^{2+}

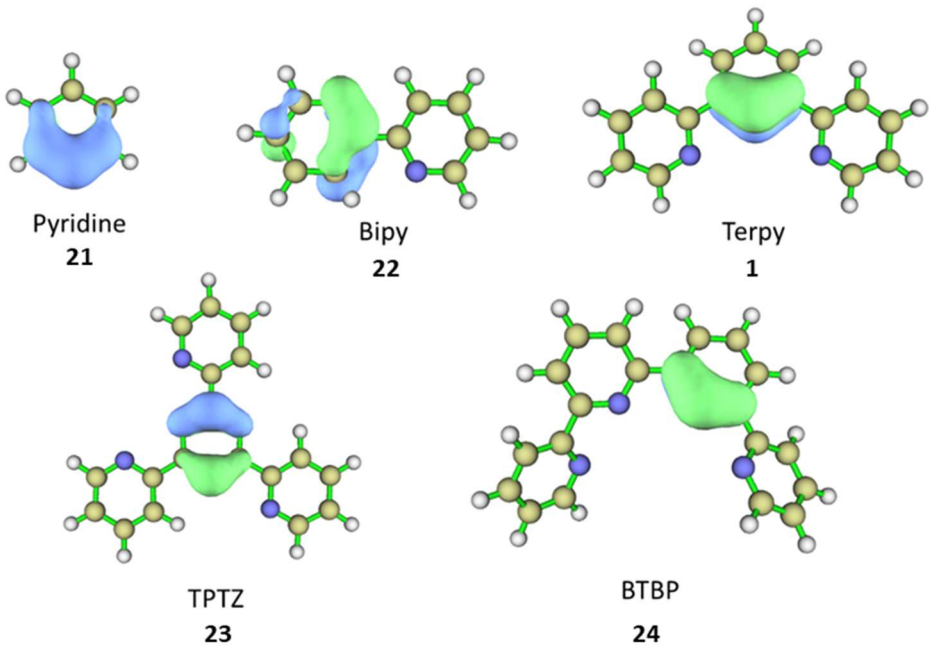

Figure 4.14 Selected six-center two-electron (6c-2e) AdNDP π-bonding patterns for various ligands (iso-contour 0.05 a.u.)

The AdNDP π-bonding patterns reveal the importance of the local symmetry of the ring. Further investigation shows that an approximate bilateral symmetry with the symmetry axis crossing the donating nitrogen is needed to yield an appropriate orbital shape for π interactions; see pyridine(**21**), Terpy(**1**), and BTBP(**24**) in Figure 4.14. However, TPTZ(**23**) with an approximate C3 symmetry yields a worse shape with a more delocalized π orbital. On the other hand, BTBP(**24**) has two rings with appropriate π orbital shape (one of which is shown in Figure 4.14). This can help to explain the general decrease of the selectivity of Am(III) over Eu(III) in the order BTBPs(**24**) > terpy(**1**) ≈ TPTZ(**23**) > bipy(**22**) ≈ pyridyl-substituted amines(**1**).[7, 62] Interestingly, it looks like the bridging benzo group will not change the π pattern for bonding, see BTBP(**24**) and BTPhen(**26**) in Figure 4.15 for example. The improved planarity helps BTPhens(**26**) to perform generally better than BTBPs.[7] Furthermore, if the nitrogen lone pairs are also counted

as part of the local symmetry of the ring, the AdNDP π-bonding patterns in Figure 4.16 shows similar results that the orientation of the π-bonding patterns follows the symmetry of the ring.

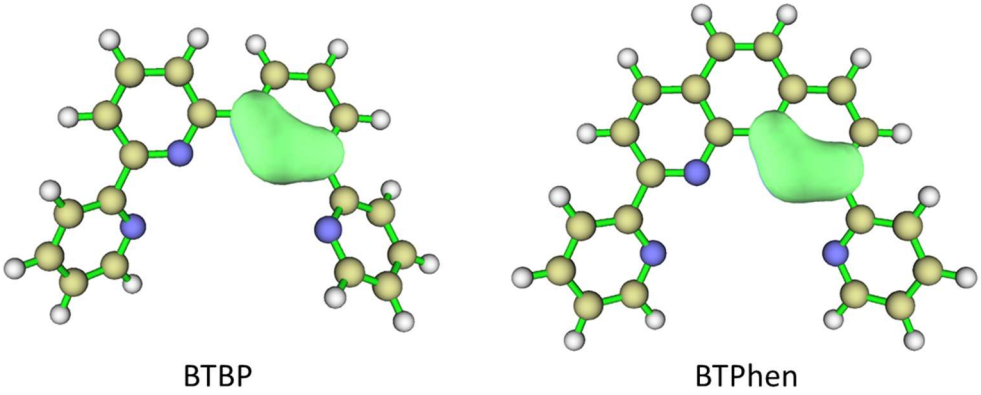

Figure 4.15 Selected six-center two-electrons (6c-2e) ADNDP orbitals (iso-contour 0.05 a.u.) of BTBP (**24**) and BTPhen(**26**).

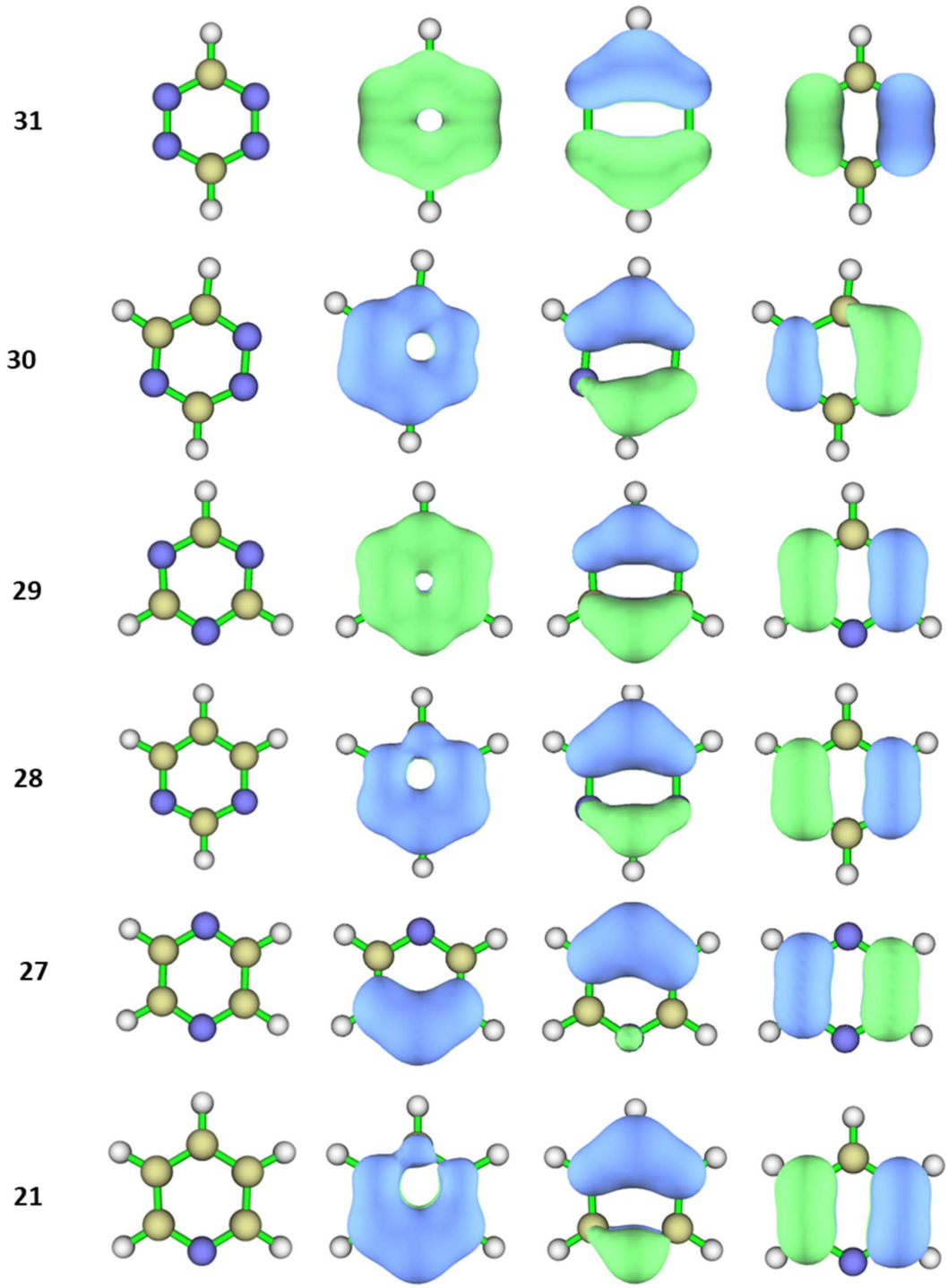

Figure 4.16 Selected six-center two-electrons (6c-2e) π-bonding patterns (iso-contour 0.05 a.u.) for extractants **21 and 27** – **31**.

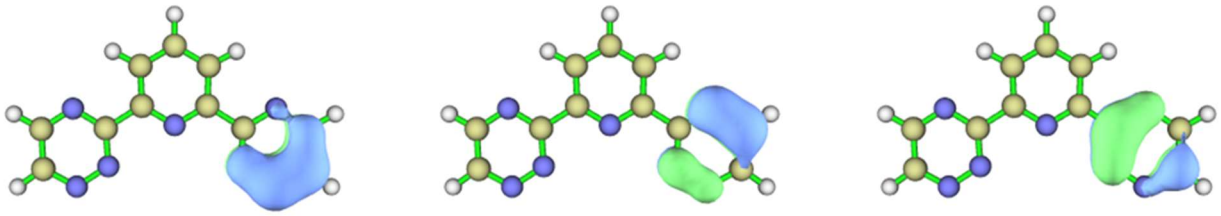

Figure 4.17 Selected six-center two-electrons (6c-2e) π-bonding patterns (iso-contour 0.05 a.u.) for extractant **5**, barebone BTP.

As Figure 4.17 shows, the lateral ring of extractant **5** behaves similar to **30** in Figure 4.16: when the substitution functional group and nitrogen lone pair exist at the same time, these two effects overlap. The substitution functional groups determine the overall shape of the π-bonding pattern, while the nitrogen changes the weight of the contribution of the atoms on the ring. This weighs the first and third patterns toward the nitrogen atoms; as a consequence, the second pattern is also rotated in the same direction. Lipophilic Bistriazinylpyridines (BTP) show high selectivity for Am(III) over Eu(III). The difference between extractant **5** and lipophilic BTPs used in experiments is that lipophilic BTPs usually contain carbon chains on the lateral rings to increase solubility and reaction kinetic. AdNDP analysis in Figure 4.18 clearly show that the lipophilic substitution groups on the lateral rings also change the shapes of the π-bonding patterns. After the first Me group is added to the lateral rings, because the local symmetry becomes C_{2v}-like, the corresponding π-bonding patterns of extractant **32** have the same shape as the marked AdNDP π-bonding pattern in Figure 4.5 a). Although the donating nitrogen atom is not on the symmetry axis, the contribution of it is increased to 28.8% from 24.8% in extractant **5**. The normalized multicenter bond order for the corresponding lateral ring is reduced from 0.6449 to 0.6257. The second Me group shows an accumulated effect on top of the first Me group; it changes the symmetry axis of

the lateral ring of extractant **33** and increases the contribution of the donating nitrogen to 36.1%. As a result of these changes, the π orbitals of the lateral rings become more appropriate for π bonding than those of extractant **5,** which might help to explain the selectivity of BTPs for Am(III) over Eu(III). The π-bonding patterns for the lateral ring of extractant **17** is shown in Figure 4.19. The normalized multicenter bond order for the lateral ring of extractant **17** is 0.6256 instead of 0.6459 in extractant **1**, which is close to that of the center ring of extractant **6**, 0.6154. This indicates that they have similar π-bonding patterns. The first π-bonding pattern shows the effect from the donating -NH_2 group, which is the same as for the π-bonding pattern in Figures 4.11 and 4.12, while the second π-bonding pattern represents the same effect as for extractant **32** in Figure 4.18. Compared to extractant **6**, the donating nitrogen atom of the lateral rings of **17** is not on the symmetry axis and has less electron density, which leads to weaker π bonding. Thus, the electron donating group on the lateral ring is not as effective as on the center ring. This agrees with the thermodynamic calculations in section 4.3.1.

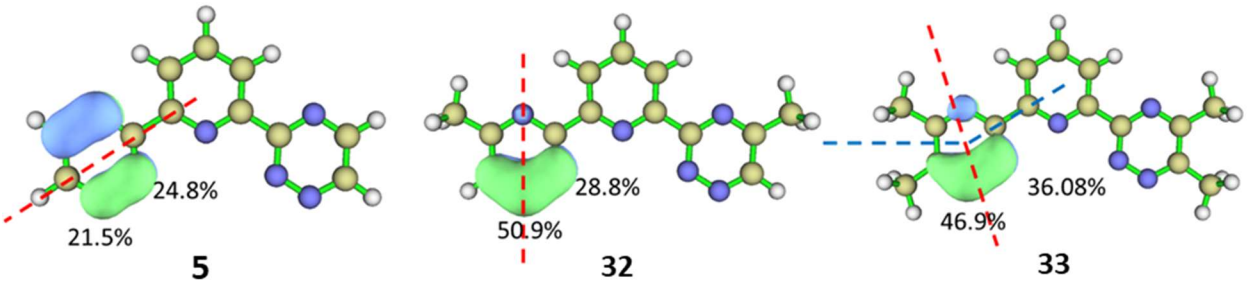

Figure 4.18 Selected six-center two-electrons (6c-2e) AdDNP π-bonding patterns and the contributions of nitrogen atoms for ligand **5** and its derivatives, extractants **32** and **33.** (iso-contour 0.05 a.u.) The red dashed line and the blue dashed line represent the symmetry axis and the total effect of substitution functional groups of each side of the symmetry axis, respectively.

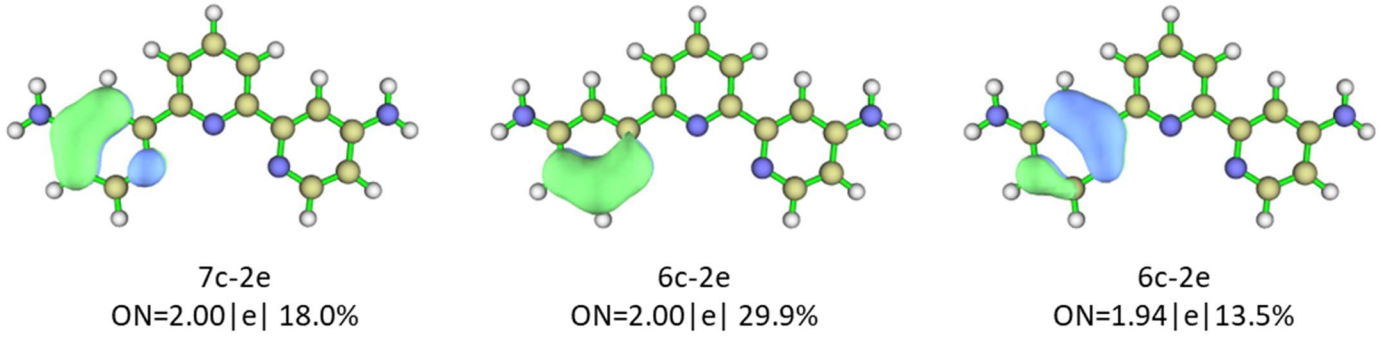

Figure 4.19 Selected seven-center two-electrons (7c-2e) and six-center two-electrons (6c-2e) AdDNP π-bonding patterns and the contributions of donating nitrogen atoms for the lateral ring of extractant **17** (iso-contour 0.05 a.u.) ON stands for occupation number.

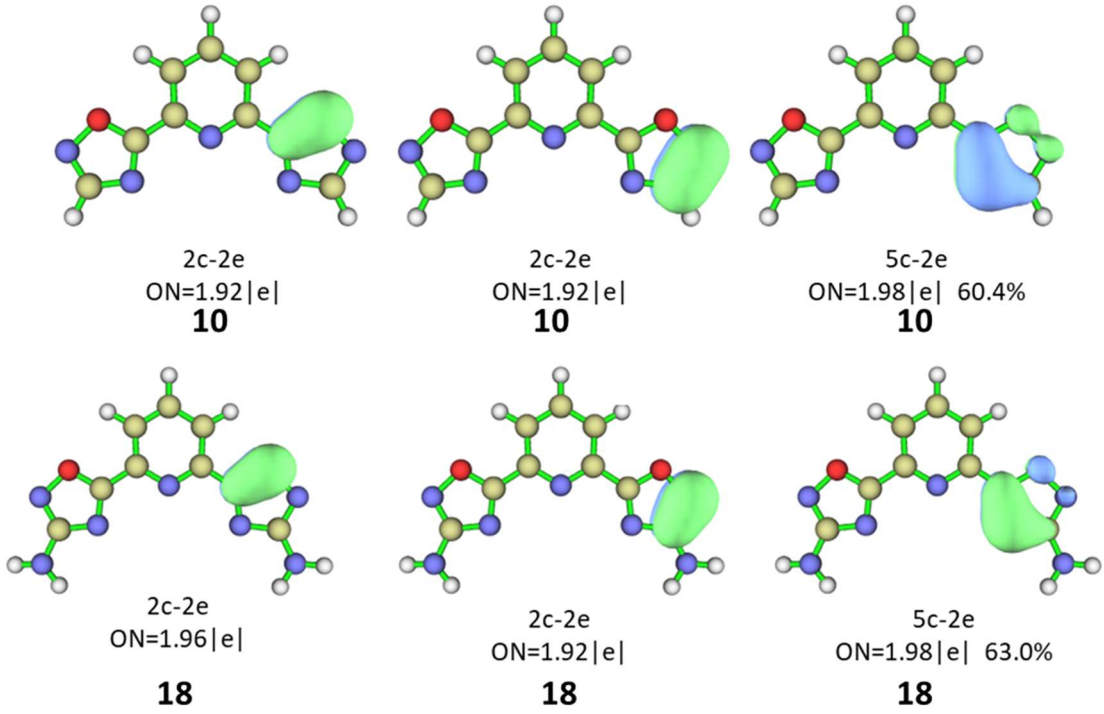

Figure 4.20 Selected five-center two-electrons (5c-2e) AdDNP π-bonding patterns and the contributions of donating nitrogen atoms for the lateral ring of extractants **10** and **18** (iso-contour 0.05 a.u.) ON stands for occupation number.

Considering the five-membered ring extractants, the center rings of extractants **10**, **11** and **18** are similar to those of ligand **1**. As discussed in Chapter 3 and sections above, extractant **11**

does not improve too much compared to extractant **10**. However, extractants **10** and **11** do show more selectivity than extractant **1**. For example, $\Delta\Delta G_{Pu\text{-}Np}$ are -1.8 kcal/mol and -1.6 kcal/mol for extractants **10** and **11**, respectively, compared to 0.8 kcal/mol for extractant **1**. Figure 4.20 shows that the π-bonding patterns of the lateral five-membered rings of extractant **10** are different from those of the six-member pyridine rings in Figure 4.5b and Figure 4.8. The third π-bonding pattern gives a similar shape as the marked pattern in Figure 4.5 a) with 60.4% contributions from the donating nitrogen. The substitution of $-NH_2$ on the lateral ring of extractant **18** does not change the shape of the π-bonding patterns but increases the contribution of the donating nitrogen by 2.6%. Because the lateral rings also have appropriate orbital shape for π-bonding and because of the long center-ring bond length, strengthening the lateral rings is more effective. Extractant **12**, on the other hand, has two appropriate π-bonding patterns shown in the first row in Figure 4.21. These AdNDP π-bonding patterns are supported by ETS-NOCV deformation density patterns, see Figure 4.22. These observations help explain the selectivity of extractants **10**, **11**, **12**, and **18**.

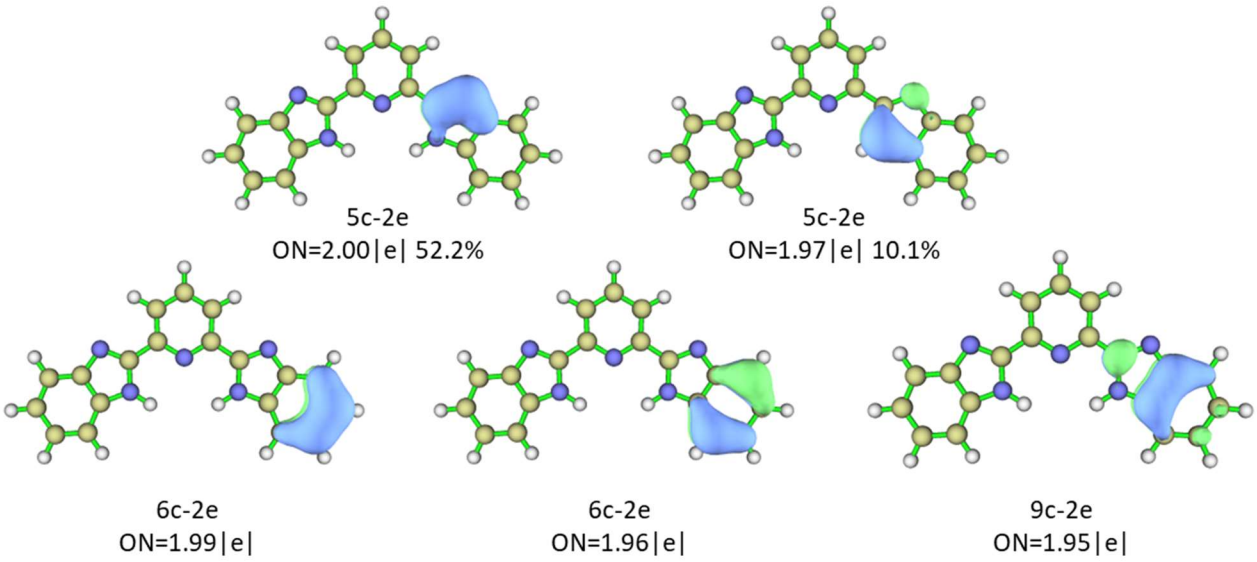

Figure 4.21 Selected AdNDP π-bonding patterns and the contributions of donating nitrogen atom for extractant **12.** (iso-contour 0.05 a.u.) ON stands for occupation number.

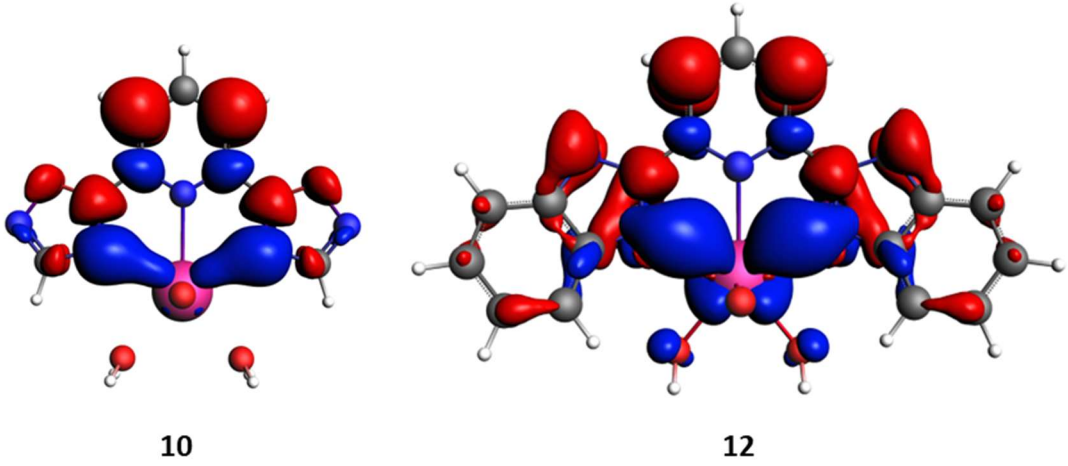

Figure 4.22 Corresponding frontier orbitals (iso-contour 0.03 a.u.) of extractants **10** and **12** for the lateral π deformation densities from ETS-NOCV analysis. Electron density flow is from red to blue.

4.3.4. Bonding analysis using AdNDP

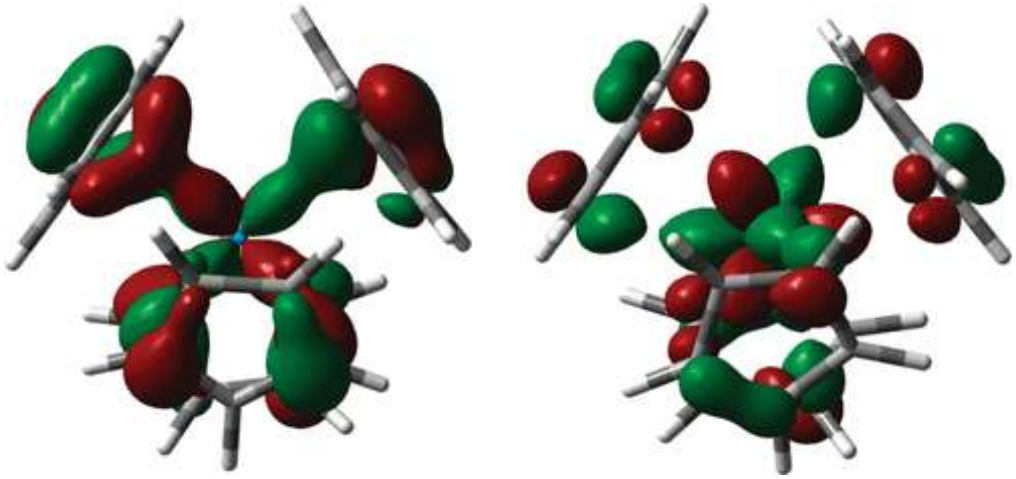

Figure 4.23 Three-dimensional representations of one component of the "t1" MOs of UCp_4 (left) and $AmCp_4$ (right). The contribution (%, Mulliken) of the actinide 5f orbitals to the $AmCp_4$ MO is ca. 30%, approximately twice that in UCp_4. (Figure adapted from reference 63)

Orbital mixing is an important factor to determine the degree of covalent interactions for the overlap-driven covalency. By the classical definition of covalency, a buildup of the electron density in the internuclear region due to overlapping atomic orbitals is required. As mentioned in Chapter 1, section 1.2.4, Nikolas Kaltsoyannis pointed out that, in 5*f* block complexes, significant valence orbital mixing does not necessary lead to internuclear charge buildup.[63, 64] In his review, the analyses of the bonding in $AnCp_3$ and $AnCp_4$ (An = Th–Cm; Cp = η^5-C_5H_5) use both the traditional tools and topological analysis via the quantum theory of atoms-in-molecules (QTAIM). The two approaches given rather different conclusions. As the MOs in Figure 4.23 illustrate, the 5*f* contribution to the americium orbital is much larger than that in the uranium compound. However, the metal–ligand overlap in the latter is better.

The ETS-NOCV and AdNDP methods could be useful to investigate the actinide bonds. Figure 4.24 shows the interactions between the Cp ligand and U^{4+}/Am^{4+} in ETS-NOCV. The ETS-NOCV results show that there is not a single η-5 bond between ligand and metal, but three types of bonds: η^4, η^3, and η^5. The η^4 and η^3 bonds correspond to the left and right MOs in Figure 4.23. Interestingly, the energies of the η^5 bonds (right) are only half those of η^4 and η^3. The bonding energies of the U-Cp bonds are stronger than those of the Am-Cp bonds. The spatial extend of the U-Cp bonds is also larger than that of the U-Am bonds. Although being a rather different approach, AdNDP gives very similar bonding patterns. The uranium and americium contributions of the AdNDP boding patterns are summarized in Figure 4.25. The results show that UCp_4 has higher orbital mixing than $AmCp_4$. This emphasizes that selecting a single or a few canonical MOs which might somehow appear to relate to the bonding could be misleading. On the other hand, the ETS-NOCV and AdNDP methods provide meaningful bonding patterns. The energies from ETS-

NOCV partly relate to energy-driven covalency, while orbital contributions or orbital mixing from the AdNDP method relate to overlap-driven covalency.

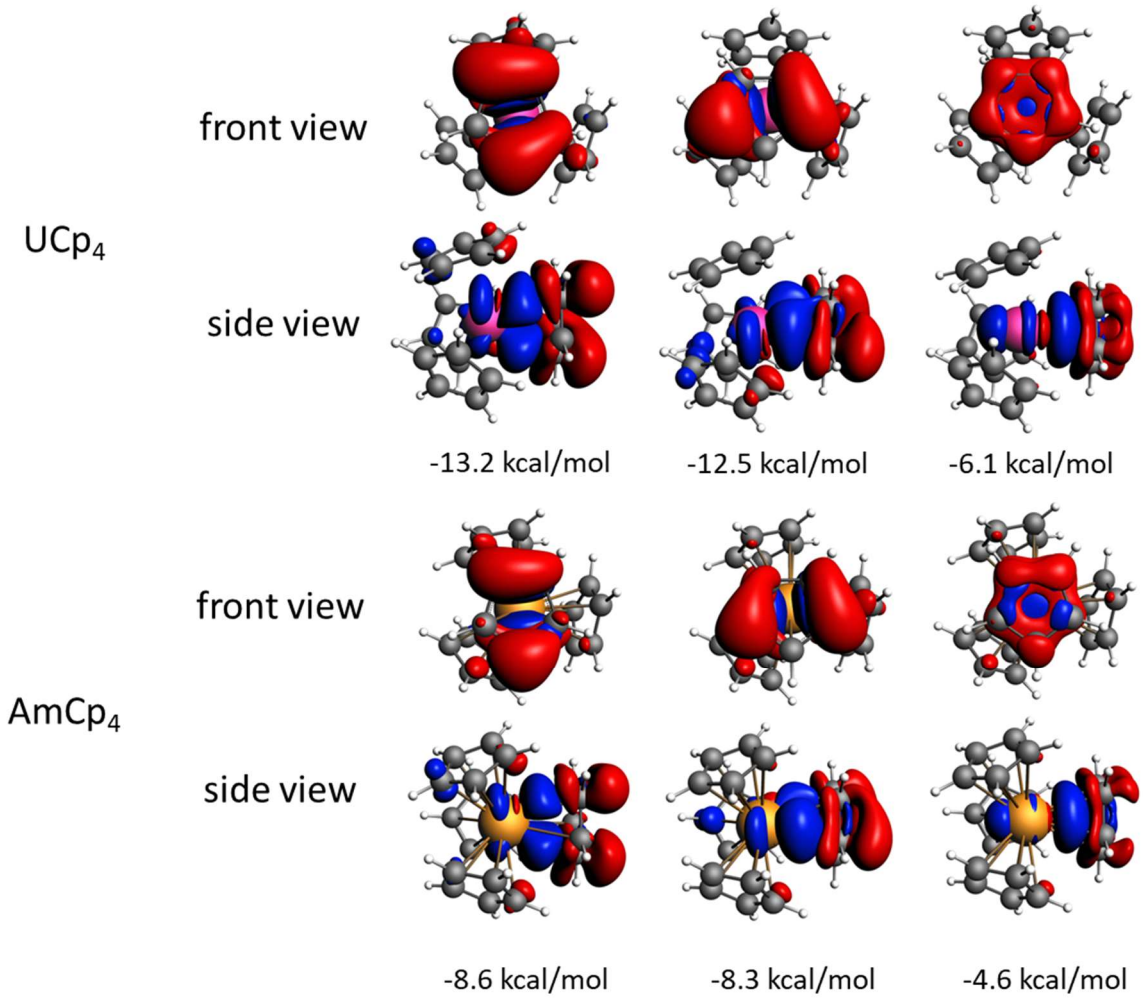

Figure 4.24 Selected ETS-NOCV deformation densities (iso-contour 0.0003 a.u.) of UCp_4 and $AmCp_4$ with corresponding bond energy contributions. Electron density flows from red to blue.

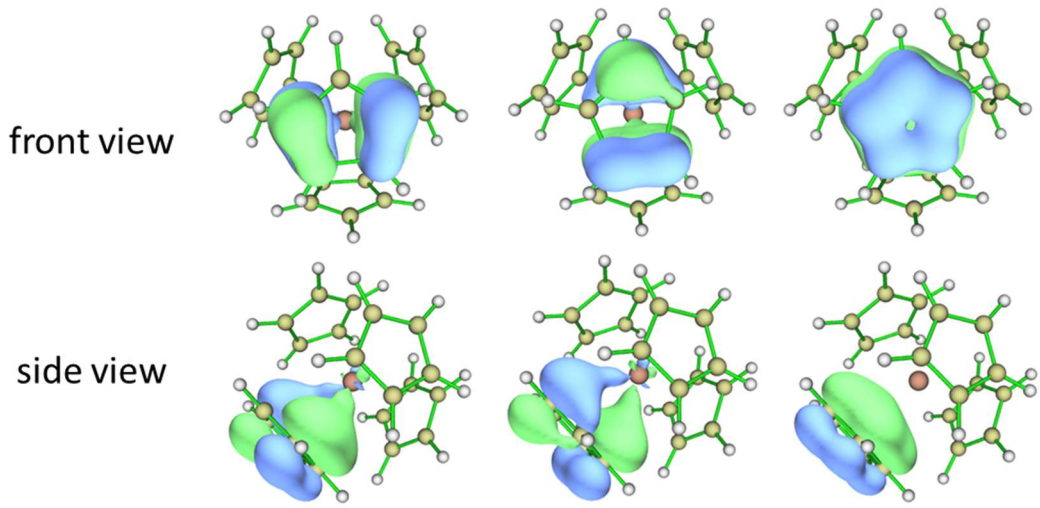

Figure 4.25 Selected AdNDP bonding patterns between Cp ligand and U^{4+}/Am^{4+}. (iso-contour 0.05 a.u.)

Table 4.10 Uranium and americium contributions (> 0.5%) and the composition of actinide metal contributions for U/AmCp$_4$ in AdNDP bonding patterns

Bonds		η^4	η^3	η^5
U contribution	Total	17.7%	16.5%	5.9%
	6*d*	9.4%	8.4%	
	5*f*	8.0%	7.8%	4.7%
Am contribution	Total	10.4%	10.1%	4.0%
	6*d*	6.8%	6.3%	
	5*f*	3.6%	3.7%	3.2%

Table 4.11 Uranium contributions (> 0.5%) and the composition of actinide metal contributions for L-$UO_2^{2+}(H_2O)_2$ compounds (L=**1**, **6**, and **17**) in AdNDP bonding patterns

Extractants		**1**		**6**			**17**		
Bond Type		σ	π	σ	π		σ	π	
Center	Total	11.68%	1.16%	13.56%	2.11%	1.58%	11.52%	1.14%	
	7s	1.19%		0.95%			1.18%		
	6d	6.19%	0.27%	7.24%	0.43%	0.16%	6.13%	0.28%	
	5f	4.05%	0.86%	5.11%	1.64%	1.36%	3.97%	0.83%	
Lateral	Total	13.27%	1.12%	12.58%	1.10%		13.89%	1.12%	2.12%
	7s	1.33%		1.45%			1.40%		
	6d	6.87%	0.31%	6.55%	0.30%		7.26%	0.28%	0.29%
	5f	4.84%	0.79%	4.37%	0.77%		4.99%	0.81%	1.80%

The discussions above for Cp_4 compounds, which were introduced in Chapter 1, show the capablility of AdNDP as a bonding analysis tool especially for multi-center bonds, for example, π bonding in this study. The uranium contributions for L-$UO_2^{2+}(H_2O)_2$ compounds, where L are extractants in Row 1 in Scheme 4.4, are summarized in Table 4.11. The results show that the σ bonds are 7*s*, 6*d*, and 5*f* hybrids. On the other hand, the π bonds are 6*d* and 5*f* hybrids. The uranium contributions to the σ bonds are higher than to the π bonds. This agrees with the previous ETS-NOCV study in Chapter 3. However, the uranium 5*f* contributions dominante the π bonds, while the 6d contributions dominante the σ bonds. These observations also agree very well with the conclusion form the previous ETS-NOCV study. The first column of π bonds for **6** and **17** in Table 4.11 correspond to the marked pattern in Figure 4.5a and the second column corresponds to Figures 4.12 and 4.13. (See also Figure 4.26 below.) For the center ring, the former has higher uranium contributions. While for the lateral rings, the latter has higher uranium contributions. This agrees with the conclusion from discussions above in section 4.3.3 for Figure 4.24. The electron donating -NH_2 group significantly increases the uranium 5*f* contributions in the π bonds. Because of the symmetry, the uranium 5*f* contributions in the first lateral ring π bonding of **17** is 0.8% compared to the center ring of **6** where it is 1.6%. The higher uranium *f* contributions might lead to better selectivity.

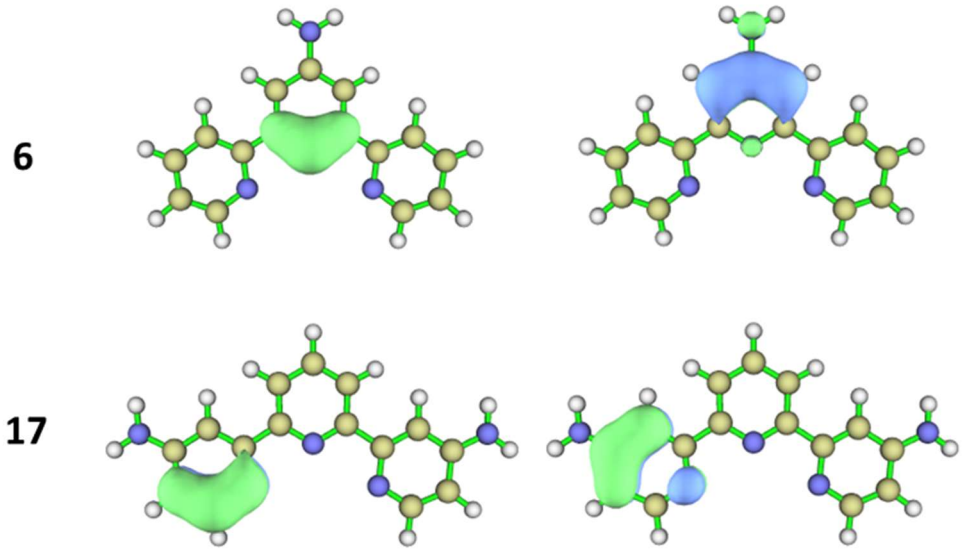

Figure 4.26 Selected AdNDP π-bonding patterns for extractant **6** and **17** (iso-contour 0.05 a.u.)

Table 4.12 Uranium contributions (> 0.5%) and the composition of uranium contributions for the **13**-$UO_2^{2+}(H_2O)_2$ complex in AdNDP bonding patterns

Extractants		**15**	
Bond Type		σ	π
Center	Total	13.11%	1.07%
	7s	0.97%	
	6d	6.99%	0.19%
	5f	4.91%	0.78%
Lateral 1	Total	12.20%	1.18%
	7s	1.48%	
	6d	6.38%	0.25%
	5f	4.14%	0.92%
Lateral 2	Total	12.16%	1.01%
	7s	1.49%	
	6d	6.40%	0.24%
	5f	4.05%	0.75%

Table 4.13 Uranium contributions (> 0.5%) and the composition of uranium contributions for L-$UO_2^{2+}(H_2O)_2$ complexes (L=**14**, **15**, **19**, and **20**) in AdNDP bonding patterns

Extractants		**14**		**15**			**19**			**20**		
Bond Type		σ	π	σ	π		σ	π		σ	π	
Center	Total	13.06%	1.23%	13.67%	2.20%	1.75%	13.48%	2.08%	1.79%	13.63%	2.21%	2.04%
	7s	0.99%		1.05%			1.01%			1.04%		
	6d	7.00%	0.24%	7.34%	0.34%	0.16%	7.26%	0.31%	0.14%	7.31%	0.34%	0.17%
	5f	4.83%	0.97%	5.03%	1.83%	1.53%	4.97%	1.74%	1.59%	5.04%	1.84%	1.80%
Lateral	Total	12.03%	1.07%	12.03%	1.02%		12.12%	1.05%		11.62%	0.93%	
	7s	1.49%		1.51%			1.49%			1.45%		
	6d	6.33%	0.24%	6.42%	0.26%		6.47%	0.26%		6.19%	0.24%	
	5f	4.00%	0.83%	3.88%	0.75%		3.95%	0.77%		3.76%	0.68%	

The uranium contributions in the **13**-$UO_2^{2+}(H_2O)_2$ complex for the asymmetric extractant **13** are summarized in Table 4.12, while the uranium contributions for symmetric extractants are summarized in Table 4.13. In Table 4.12, the lateral 1 bonding pattern corresponds to the lateral ring attached to the -C=C- group, whereas lateral 2 is for the lateral ring that is next to the -CH_2-CH_2- group. The latter ring is slightly off the extractant plane, which leads to lower 5*f* contribution of 0.75% compared to 0.92% for the former. The 6*d* contributions and σ bonds are almost unaffected, which shows the importance of the planarity. This is also supported by the π interactions of extractants **6** and **15**. Extractant **15** has prefect planarity parallel to the *f* orbitals with 5*f* contributions of 1.83% and 1.53%. While extractant **6** is not perfectly planar, and has lower 5*f* contributions of 1.64% and 1.36%, see the structures in Figure 4.1 as well. Extractant **19** shows similar uranium contributions to extract **15**. Extractant **20** gives higher uranium contributions for the center ring bonding and lower for the lateral ring bonding compared to extractant **19** as expected.

4.3.5. Theoretical Predictions of trivalent Am(III) from Eu(III) separation

To further examine the conclusions made in the previous section, extractants **19** and **20** were selected for trivalent Am(III) from Eu(III) separation and compared with extractants **1**, **13**, **14**, and **15** in Chapter 3. Additional calculations were carried out based on the following ion exchange reaction, where we calculated the ΔΔG as previously described.[65-67]

$$Am(H_2O)_9^{3+} + EuL(H_2O)_6^{3+} \leftrightharpoons Eu(H_2O)_9^{3+} + AmL(H_2O)_6^{3+} \qquad (4.2)$$

Table 4.14 Gibbs Free Energies (ΔΔG, kcal/mol) for Reaction (4.2) in Water

Extractants	**1**	**13**	**14**	**15**	**19**	**20**
DLPNO-CCSD(T)//PBE	-1.0	-2.6	-6.2	-6.9	-8.0	-8.8

In Table 4.14, the predicted trend of the absolute ΔΔG values for reaction (4.2) follows the order, **20** > **19** >**15** > **14** > **13** > **1**, which agrees very well with the predictions from thermodynamics calculations and bonding analysis of the actinyl complexes.

Table 4.15 Americium and europium β spin contributions (> 0.25%) and their composition of contributions for L-Am/$Eu^{3+}(H_2O)_6$ complexes (L=**15**, **19**, and **20**) in AdNDP bonding patterns

Extractants			**15**			**19**			**20**		
Bond Type			σ	π		σ	π		σ	Π	
Am contributions	Center	Total	8.06%	0.66%	0.42%	7.78%	0.56%	0.33%	7.88%	0.64%	0.42%
		7s	0.90%			0.85%			0.88%		
		6d	5.15%	0.32%	0.24%	5.04%	0.27%	0.19%	5.06%	0.31%	0.23%
		5f	1.96%	0.32%	0.18%	1.84%	0.28%	0.13%	1.89%	0.31%	0.18%
	Lateral 1	Total	7.59%	0.54%		7.51%	0.54%		7.26%	0.48%	
		7s	0.92%			0.92%			0.92%		
		6d	4.90%	0.31%		4.86%	0.31%		4.72%	0.28%	
		5f	1.73%	0.22%		1.69%	0.21%		1.58%	0.19%	
	Lateral 2	Total	7.34%	0.49%		7.27%	0.50%		7.05%	0.44%	
		7s	0.94%			0.93%			0.96%		
		6d	4.80%	0.29%		4.77%	0.30%		4.63%	0.26%	
		5f	1.57%	0.19%		1.53%	0.19%		1.43%	0.17%	
Eu contributions	Center	Total	4.93%			4.69%			4.81%		
		6s	0.67%			0.67%			0.68%		
		5d	3.81%			3.61%			3.69%		
		4f	0.40%			0.38%			0.39%		
	Lateral 1	Total	4.82%			4.82%			4.65%		
		6s	0.81%			0.77%			0.78%		
		5d	3.60%			3.63%			3.49%		
		4f	0.37%			0.38%			0.34%		
	Lateral 2	Total	4.81%			4.75%			4.59%		
		6s	0.80%			0.77%			0.78%		
		5d	3.61%			3.59%			3.46%		
		4f	0.37%			0.35%			0.32%		

Table 4.15 shows the Am and Eu β spin contributions, thus the numbers are about half of the total bond strength. The results clearly show that there are no significant π interactions between the extractants and Eu due to the core like *f* orbitals. The 4*f* contributions for the σ bonds are also very small. This again emphasizes the importance of the π interactions for Am/Eu separation. Because of the actinide and lanthanide contraction, the trivalent Am and Eu ions are situated toward one side of the extractant yielding a slightly asymmetric lateral bonding, see lateral 1 and

2 in Table 4.12. This indicates that strengthening the center ring is probably more effective than lateral rings. Extractant **15** shows stronger bonding to Am with higher 5f contributions than extractants **19** and **20**. However, this advantage is offset by stronger Eu interactions. Thus, extractant **15** is outperformed by extractant **20**. This also indicates that slightly weakening the lateral rings, such as in extractant **20**, might help to reduce the affinity for Eu(III).

4.4 Conclusion

In this study, various terpyridine-based extractants have been evaluated systematically via different approaches. The AdNDP method combined with other analysis tools, such as the ETS-NOCV method, gave us comprehensive insights into the bonding nature of actinide and lanthanide bonding. This is especially important as we demonstrated that the popular way to discuss the chemical bonding based on MOs can be misleading, as illustrated by investigating the $AnCp_4$ systems (An + U, Am, section 4.3.4). The AdNDP analysis for π systems of the extractants helped us to figure out the possible origins of the ligand selectivity. We have shown that the π systems of nitrogen heterocyclic rings are strongly affected by the chemical environment, specifically the local symmetry of the ring. With appropriate positions of the functional groups, the π orbital can be localized on the donating nitrogen atoms leading to better π interactions. For example, the center ring of terpy, **1**, has a better shape for π bonding than the lateral rings, and the lipophilic chains in BTP extractants not only improve the solubility and reaction kinetics, but also improve the bonding. The actinide/lanthanide contribution analysis in AdNDP bonding patterns confirmed the conclusions from the previous investigations in this chapter and in Chapter 3. The contribution analysis also emphasises the importance of π interactions between actinide/lanthanide and extractants since there are no π interactions observed for the Eu compounds. Extractant **20** is predicted to be the best candidate in this work. The success of extractant **20** also indicates that

strengthening the center ring and slightly weakening the lateral rings might help to improve the selectivity for Am(III) over Eu(III). We hope this work provides useful information and inspirations for advanced extractant design principles.

4.5 References

1. *The Nuclear Fuel Cycle: From Ore to Waste*. 1996.
2. Ekberg, C.; Fermvik, A.; Retegan, T.; Skarnemark, G.; Foreman, M. R. S.; Hudson, M. J.; Englund, S.; Nilsson, M., An overview and historical look back at the solvent extraction using nitrogen donor ligands to extract and separate An(III) from Ln(III). *Radiochimica Acta* **2008,** *96* (4-5), 225.
3. Sanex-BTP process development studies. *Journal of nuclear science and technology.* **2002,** (Suppl. 3).
4. Drew, M. G.; Foreman, M. R.; Hill, C.; Hudson, M. J.; Madic, C., 6, 6′-bis-(5, 6-diethyl-[1, 2, 4] triazin-3-yl)-2, 2′-bipyridyl the first example of a new class of quadridentate heterocyclic extraction reagents for the separation of americium (III) and europium (III). *Inorganic Chemistry Communications* **2005,** *8* (3), 239-241.
5. Foreman, M. R. S. J.; Hudson, M. J.; Geist, A.; Madic, C.; Weigl, M., An Investigation into the Extraction of Americium (III), Lanthanides and D-Block Metals by 6, 6′-Bis-(5, 6-dipentyl-[1, 2, 4] triazin-3-yl)-[2, 2′] bipyridinyl (C5-BTBP). *Solvent extraction and ion exchange* **2005,** *23* (5), 645-662.
6. Geist, A.; Hill, C.; Modolo, G.; Foreman, M. R. S. J.; Weigl, M.; Gompper, K.; Hudson, M. J., 6, 6′-Bis (5, 5, 8, 8-tetramethyl-5, 6, 7, 8-tetrahydro-benzo [1, 2, 4] triazin-3-yl)[2, 2′] bipyridine, an effective extracting agent for the separation of americium (III) and curium (III) from the lanthanides. *Solvent extraction and ion exchange* **2006,** *24* (4), 463-483.
7. Panak, P. J.; Geist, A., Complexation and Extraction of Trivalent Actinides and Lanthanides by Triazinylpyridine N-Donor Ligands. *Chemical Reviews* **2013,** *113* (2), 1199-1236.
8. Trumm, S.; Wipff, G.; Geist, A.; Panak, P. J.; Fanghänel, T., Optimising BTP ligands by tuning their basicity. *Radiochimica Acta* **2011,** *99* (1), 13-16.
9. Harwood, L. M.; Lewis, F. W.; Hudson, M. J.; John, J.; Distler, P., The separation of americium (III) from europium (III) by two new 6, 6'-bistriazinyl-2, 2'-bipyridines in different diluents. *Solvent Extraction and Ion Exchange* **2011,** *29* (4), 551-576.
10. Benay, G.; Schurhammer, R.; Desaphy, J.; Wipff, G., Substituent effects on BTP's basicity and complexation properties with LnIII lanthanide ions. *New Journal of Chemistry* **2011,** *35* (1), 184-189.
11. Ziegler, T.; Rauk, A., A theoretical study of the ethylene-metal bond in complexes between copper(1+), silver(1+), gold(1+), platinum(0) or platinum(2+) and ethylene, based on the Hartree-Fock-Slater transition-state method. *Inorganic Chemistry* **1979,** *18* (6), 1558-1565.
12. Ziegler, T.; Rauk, A., Carbon monoxide, carbon monosulfide, molecular nitrogen, phosphorus trifluoride, and methyl isocyanide as .sigma. donors and .pi. acceptors. A theoretical study by the Hartree-Fock-Slater transition-state method. *Inorganic Chemistry* **1979,** *18* (7), 1755-1759.
13. Mitoraj, M. P.; Michalak, A.; Ziegler, T., A Combined Charge and Energy Decomposition Scheme for Bond Analysis. *Journal of Chemical Theory and Computation* **2009,** *5* (4), 962-975.

14. Zubarev, D. Y.; Boldyrev, A. I., " Developing paradigms of chemical bonding: adaptive natural density partitioning. *Physical chemistry chemical physics* **2008,** *10* (34), 5207-5217.
15. Zubarev, D. Y.; Boldyrev, A. I., Revealing Intuitively Assessable Chemical Bonding Patterns in Organic Aromatic Molecules via Adaptive Natural Density Partitioning. *The Journal of Organic Chemistry* **2008,** *73* (23), 9251-9258.
16. Fonseca Guerra, C.; Snijders, J. G.; te Velde, G.; Baerends, E. J., Towards an order-N DFT method. *Theoretical Chemistry Accounts* **1998,** *99* (6), 391-403.
17. te Velde, G.; Bickelhaupt, F. M.; Baerends, E. J.; Fonseca Guerra, C.; van Gisbergen, S. J. A.; Snijders, J. G.; Ziegler, T., Chemistry with ADF. *Journal of Computational Chemistry* **2001,** *22* (9), 931-967.
18. Baerends, E. J.; Ziegler, T.; Atkins, A. J.; Autschbach, J.; Bashford, D.; Baseggio, O.; Brces, A.; Bickelhaupt, F. M.; Bo, C.; Boerritger, P. M.; Cavallo, L.; Daul, C.; Chong, D. P.; Chulhai, D. V.; Deng, L.; Dickson, R. M.; Dieterich, J. M.; Ellis, D. E.; van Faassen, M.; Ghysels, A.; Giammona, A.; van Gisbergen, S. J. A.; Goez, A.; Gtz, A. W.; Gusarov, S.; Harris, F. E.; van den Hoek, P.; Hu, Z.; Jacob, C. R.; Jacobsen, H.; Jensen, L.; Joubert, L.; Kaminski, J. W.; van Kessel, G.; Knig, C.; Kootstra, F.; Kovalenko, A.; Krykunov, M.; van Lenthe, E.; McCormack, D. A.; Michalak, A.; Mitoraj, M.; Morton, S. M.; Neugebauer, J.; Nicu, V. P.; Noodleman, L.; Osinga, V. P.; Patchkovskii, S.; Pavanello, M.; Peeples, C. A.; Philipsen, P. H. T.; Post, D.; Pye, C. C.; Ramanantoanina, H.; Ramos, P.; Ravenek, W.; Rodrguez, J. I.; Ros, P.; Rger, R.; Schipper, P. R. T.; Schlns, D.; van Schoot, H.; Schreckenbach, G.; Seldenthuis, J. S.; Seth, M.; Snijders, J. G.; Sol, ADF2017, SCM, Theoretical Chemistry, Vrije Universiteit, Amsterdam, The Netherlands, https://www.scm.com.
19. Perdew, J. P.; Burke, K.; Ernzerhof, M., Generalized Gradient Approximation Made Simple. *Physical Review Letters* **1996,** *77* (18), 3865-3868.
20. Van Lenthe, E.; Baerends, E. J., Optimized Slater-type basis sets for the elements 1–118. *Journal of Computational Chemistry* **2003,** *24* (9), 1142-1156.
21. Lenthe, E. v.; Baerends, E. J.; Snijders, J. G., Relativistic regular two-component Hamiltonians. *The Journal of Chemical Physics* **1993,** *99* (6), 4597-4610.
22. Lenthe, E. v.; Baerends, E. J.; Snijders, J. G., Relativistic total energy using regular approximations. *The Journal of Chemical Physics* **1994,** *101* (11), 9783-9792.
23. Lenthe, E. v.; Ehlers, A.; Baerends, E.-J., Geometry optimizations in the zero order regular approximation for relativistic effects. *The Journal of Chemical Physics* **1999,** *110* (18), 8943-8953.
24. Pye, C. C.; Ziegler, T., An implementation of the conductor-like screening model of solvation within the Amsterdam density functional package. *Theoretical Chemistry Accounts* **1999,** *101* (6), 396-408.
25. Allinger, N. L.; Zhou, X.; Bergsma, J., Molecular mechanics parameters. *Journal of Molecular Structure: THEOCHEM* **1994,** *312* (1), 69-83.
26. Grimme, S.; Antony, J.; Ehrlich, S.; Krieg, H., A consistent and accurate ab initio parametrization of density functional dispersion correction (DFT-D) for the 94 elements H-Pu. *The Journal of Chemical Physics* **2010,** *132* (15), 154104.
27. Grimme, S.; Ehrlich, S.; Goerigk, L., Effect of the damping function in dispersion corrected density functional theory. *Journal of Computational Chemistry* **2011,** *32* (7), 1456-1465.
28. Martin, R. L.; Hay, P. J.; Pratt, L. R., Hydrolysis of Ferric Ion in Water and Conformational Equilibrium. *The Journal of Physical Chemistry A* **1998,** *102* (20), 3565-3573.

29. Shamov, G. A.; Schreckenbach, G., Density Functional Studies of Actinyl Aquo Complexes Studied Using Small-Core Effective Core Potentials and a Scalar Four-Component Relativistic Method. *The Journal of Physical Chemistry A* **2005,** *109* (48), 10961-10974.
30. Deblonde, G. J.-P.; Kelley, M. P.; Su, J.; Batista, E. R.; Yang, P.; Booth, C. H.; Abergel, R. J., Spectroscopic and Computational Characterization of Diethylenetriaminepentaacetic Acid/Transplutonium Chelates: Evidencing Heterogeneity in the Heavy Actinide(III) Series. *Angewandte Chemie International Edition* **2018,** *57* (17), 4521-4526.
31. Kelley, M. P.; Deblonde, G. J. P.; Su, J.; Booth, C. H.; Abergel, R. J.; Batista, E. R.; Yang, P., Bond Covalency and Oxidation State of Actinide Ions Complexed with Therapeutic Chelating Agent 3,4,3-LI(1,2-HOPO). *Inorganic Chemistry* **2018,** *57* (9), 5352-5363.
32. Kelley, M. P.; Su, J.; Urban, M.; Luckey, M.; Batista, E. R.; Yang, P.; Shafer, J. C., On the Origin of Covalent Bonding in Heavy Actinides. *Journal of the American Chemical Society* **2017,** *139* (29), 9901-9908.
33. Kaneko, M.; Miyashita, S.; Nakashima, S., Benchmark study of the Mössbauer isomer shifts of Eu and Np complexes by relativistic DFT calculations for understanding the bonding nature of f-block compounds. *Dalton Transactions* **2015,** *44* (17), 8080-8088.
34. Kaneko, M.; Miyashita, S.; Nakashima, S., Bonding Study on the Chemical Separation of Am(III) from Eu(III) by S-, N-, and O-Donor Ligands by Means of All-Electron ZORA-DFT Calculation. *Inorganic Chemistry* **2015,** *54* (14), 7103-7109.
35. Paulechka, E.; Kazakov, A., Efficient DLPNO–CCSD(T)-Based Estimation of Formation Enthalpies for C-, H-, O-, and N-Containing Closed-Shell Compounds Validated Against Critically Evaluated Experimental Data. *The Journal of Physical Chemistry A* **2017,** *121* (22), 4379-4387.
36. Neese, F., Software update: the ORCA program system, version 4.0. *WIREs Computational Molecular Science* **2018,** *8* (1), e1327.
37. Pantazis, D. A.; Neese, F., All-Electron Scalar Relativistic Basis Sets for the Actinides. *Journal of Chemical Theory and Computation* **2011,** *7* (3), 677-684.
38. Pantazis, D. A.; Neese, F., All-Electron Scalar Relativistic Basis Sets for the Lanthanides. *Journal of Chemical Theory and Computation* **2009,** *5* (9), 2229-2238.
39. Weigend, F.; Ahlrichs, R., Balanced basis sets of split valence, triple zeta valence and quadruple zeta valence quality for H to Rn: Design and assessment of accuracy. *Physical Chemistry Chemical Physics* **2005,** *7* (18), 3297-3305.
40. Hirshfeld, F. L., Bonded-atom fragments for describing molecular charge densities. *Theoretica chimica acta* **1977,** *44* (2), 129-138.
41. Zegke, M.; Zhang, X.; Pidchenko, I.; Hlina, J. A.; Lord, R. M.; Purkis, J.; Nichol, G. S.; Magnani, N.; Schreckenbach, G.; Vitova, T.; Love, J. B.; Arnold, P. L., Differential uranyl(v) oxo-group bonding between the uranium and metal cations from groups 1, 2, 4, and 12; a high energy resolution X-ray absorption, computational, and synthetic study. *Chemical Science* **2019,** *10* (42), 9740-9751.
42. Arnold, P. L.; Dutkiewicz, M. S.; Zegke, M.; Walter, O.; Apostolidis, C.; Hollis, E.; Pécharman, A. F.; Magnani, N.; Griveau, J. C.; Colineau, E., Subtle interactions and electron transfer between UIII, NpIII, or PuIII and uranyl mediated by the oxo group. *Angewandte Chemie* **2016,** *128* (41), 12989-12993.
43. Galeev, T. R.; Chen, Q.; Guo, J. C.; Bai, H.; Miao, C. Q.; Lu, H. G.; Sergeeva, A. P.; Li, S. D.; Boldyrev, A. I., Deciphering the mystery of hexagon holes in an all-boron graphene α-sheet. *Phys Chem Chem Phys* **2011,** *13* (24), 11575-8.

44. Zubarev, D. Y.; Boldyrev, A. I., ”Developing paradigms of chemical bonding: adaptive natural density partitioning. *Physical Chemistry Chemical Physics* **2008,** *10* (34), 5207-5217.
45. Lu, T.; Chen, F., Multiwfn: A multifunctional wavefunction analyzer. *Journal of Computational Chemistry* **2012,** *33* (5), 580-592.
46. Glendening, E. D.; Landis, C. R.; Weinhold, F., NBO 6.0: Natural bond orbital analysis program. *Journal of Computational Chemistry* **2013,** *34* (16), 1429-1437.
47. Frisch, M. J.; Trucks, G. W.; Schlegel, H. B.; Scuseria, G. E.; Robb, M. A.; Cheeseman, J. R.; Scalmani, G.; Barone, V.; Petersson, G. A.; Nakatsuji, H.; Li, X.; Caricato, M.; Marenich, A. V.; Bloino, J.; Janesko, B. G.; Gomperts, R.; Mennucci, B.; Hratchian, H. P.; Ortiz, J. V.; Izmaylov, A. F.; Sonnenberg, J. L.; Williams; Ding, F.; Lipparini, F.; Egidi, F.; Goings, J.; Peng, B.; Petrone, A.; Henderson, T.; Ranasinghe, D.; Zakrzewski, V. G.; Gao, J.; Rega, N.; Zheng, G.; Liang, W.; Hada, M.; Ehara, M.; Toyota, K.; Fukuda, R.; Hasegawa, J.; Ishida, M.; Nakajima, T.; Honda, Y.; Kitao, O.; Nakai, H.; Vreven, T.; Throssell, K.; Montgomery Jr., J. A.; Peralta, J. E.; Ogliaro, F.; Bearpark, M. J.; Heyd, J. J.; Brothers, E. N.; Kudin, K. N.; Staroverov, V. N.; Keith, T. A.; Kobayashi, R.; Normand, J.; Raghavachari, K.; Rendell, A. P.; Burant, J. C.; Iyengar, S. S.; Tomasi, J.; Cossi, M.; Millam, J. M.; Klene, M.; Adamo, C.; Cammi, R.; Ochterski, J. W.; Martin, R. L.; Morokuma, K.; Farkas, O.; Foresman, J. B.; Fox, D. J. *Gaussian 16 Rev. B.01*, Wallingford, CT, 2016.
48. Cao, X.; Dolg, M., Segmented contraction scheme for small-core actinide pseudopotential basis sets. *Journal of Molecular Structure: THEOCHEM* **2004,** *673* (1), 203-209.
49. Cao, X.; Dolg, M., Segmented contraction scheme for small-core lanthanide pseudopotential basis sets. *Journal of Molecular Structure: THEOCHEM* **2002,** *581* (1), 139-147.
50. Seaborg, G. T.; Katz, J. J.; Morss, L. R., *The Chemistry of the Actinide Elements: Volume 2*. Springer Science & Business Media: 2012; Vol. 2.
51. Bardin, N.; Rubini, P.; Madie, C., Hydration of Actinyl(VI), MO2+2aq (M = U, Np, Pu). An NMR Study. *Radiochimica Acta* **1998,** *83* (4), 189-194.
52. Antonio, R.; Soderholm, L.; Williams, C. W.; Blaudeau, J.-P.; Bursten, B. E., Neptunium redox speciation. *Radiochimica Acta* **2001,** *89* (1), 17-26.
53. Skanthakumar, S.; Antonio, M. R.; Soderholm, L., A Comparison of Neptunyl(V) and Neptunyl(VI) Solution Coordination: The Stability of Cation−Cation Interactions. *Inorganic Chemistry* **2008,** *47* (11), 4591-4595.
54. Allen, P. G.; Bucher, J. J.; Shuh, D. K.; Edelstein, N. M.; Reich, T., Investigation of Aquo and Chloro Complexes of UO(2)(2+), NpO(2)(+), Np(4+), and Pu(3+) by X-ray Absorption Fine Structure Spectroscopy. *Inorg Chem* **1997,** *36* (21), 4676-4683.
55. Hay, P. J.; Martin, R. L.; Schreckenbach, G., Theoretical Studies of the Properties and Solution Chemistry of AnO22+ and AnO2+ Aquo Complexes for An = U, Np, and Pu. *The Journal of Physical Chemistry A* **2000,** *104* (26), 6259-6270.
56. Wahlgren, U.; Moll, H.; Grenthe, I.; Schimmelpfennig, B.; Maron, L.; Vallet, V.; Gropen, O., Structure of Uranium(VI) in Strong Alkaline Solutions. A Combined Theoretical and Experimental Investigation. *The Journal of Physical Chemistry A* **1999,** *103* (41), 8257-8264.
57. Spencer, S.; Gagliardi, L.; Handy, N. C.; Ioannou, A. G.; Skylaris, C.-K.; Willetts, A.; Simper, A. M., Hydration of UO22+ and PuO22+. *The Journal of Physical Chemistry A* **1999,** *103* (12), 1831-1837.
58. Aaberg, M.; Ferri, D.; Glaser, J.; Grenthe, I., Structure of the hydrated dioxouranium(VI) ion in aqueous solution. An x-ray diffraction and proton NMR study. *Inorganic Chemistry* **1983,** *22* (26), 3986-3989.

59. Maerzke, K. A.; Goff, G. S.; Runde, W. H.; Schneider, W. F.; Maginn, E. J., Structure and Dynamics of Uranyl(VI) and Plutonyl(VI) Cations in Ionic Liquid/Water Mixtures via Molecular Dynamics Simulations. *The Journal of Physical Chemistry B* **2013,** *117* (37), 10852-10868.
60. Cao, Z.; Balasubramanian, K., Theoretical studies of UO2(H2O)n2+,NpO2(H2O)n+, and PuO2(H2O)n2+ complexes (n=4–6) in aqueous solution and gas phase. *The Journal of Chemical Physics* **2005,** *123* (11), 114309.
61. X-ray absorption spectroscopy and actinide electrochemistry: a setup dedicated to radioactive samples applied to neptunium chemistry. *Journal of Synchrotron Radiation* **2022,** *29* (1), 1--10.
62. Kolarik, Z., Complexation and Separation of Lanthanides(III) and Actinides(III) by Heterocyclic N-Donors in Solutions. *Chemical Reviews* **2008,** *108* (10), 4208-4252.
63. Tassell, M. J.; Kaltsoyannis, N., Covalency in AnCp4 (An = Th–Cm): a comparison of molecular orbital, natural population and atoms-in-molecules analyses. *Dalton Transactions* **2010,** *39* (29), 6719-6725.
64. Kaltsoyannis, N., Does Covalency Increase or Decrease across the Actinide Series? Implications for Minor Actinide Partitioning. *Inorganic Chemistry* **2013,** *52* (7), 3407-3413.
65. Miguirditchian, M.; Guillaneux, D.; Guillaumont, D.; Moisy, P.; Madic, C.; Jensen, M. P.; Nash, K. L., Thermodynamic Study of the Complexation of Trivalent Actinide and Lanthanide Cations by ADPTZ, a Tridentate N-Donor Ligand. *Inorganic Chemistry* **2005,** *44* (5), 1404-1412.
66. Chen, Y.-M.; Wang, C.-Z.; Wu, Q.-Y.; Lan, J.-H.; Chai, Z.-F.; Nie, C.-M.; Shi, W.-Q., Theoretical Insights into Modification of Nitrogen-Donor Ligands to Improve Performance on Am(III)/Eu(III) Separation. *Inorganic Chemistry* **2020,** *59* (5), 3221-3231.
67. Miguirditchian, M.; Guillaumont, D.; Saint-Maxent, A.; Moisy, P.; Guillaneux, D.; Madic, C., Thermodynamics of plutonium(iii) and curium(iii) complexation with a N-donor ligand. *Dalton Transactions* **2019,** *48* (3), 839-842.

Preface to Chapter 5

This chapter is based on a manuscript is that to be submitted for publication soon.

All the theoretical calculations and analysis in this chapter were carried out by Xiaobin Zhang. The manuscript was prepared together with the other authors.

Copyright permissions have been obtained from all the other authors. Morgan P. Kelley, Enrique R. Batista and Ping Yang are affiliated with Theoretical Division, Los Alamos National Laboratory, Los Alamos, New Mexico, United States. Artaches Migdissov is affiliated with Earth and Environmental Sciences Division, Los Alamos National Laboratory, Los Alamos, New Mexico, United States. Andy Gaunt and Hongwu Xu are affiliated with Chemistry Division, Los Alamos National Laboratory, Los Alamos, New Mexico, United States.

Chapter 5. Aqueous AnO_2-Cl Coordination Chemistry at High Temperature and Pressure

5.1. Introduction

Nuclear waste storage and, additionally, unlikely but catastrophic incidents such as the disaster at the Fukushima Daiichi nuclear power plant, must account for not only elevated temperatures, but also elevated pressures. Despite the need to understand the aqueous chemistry of systems relevant to the nuclear fuel cycle under non-standard state conditions, most thermodynamic measurements of actinide systems have been performed at room temperature and atmospheric pressure.

The uranyl chloride system is a basic but relevant model system extensively studied at standard state conditions, including not only thermodynamic measurements but also aqueous structural determinations using techniques like high energy X-ray scattering and Extended X-Ray Absorption Fine Structure (EXAFS).[1-8] Only very recent work, however, has attempted to measure uranyl-chloride speciation at elevated temperatures. [9-11] These measurements show that the stability constants for the addition of the first two chloride ligands to the aqueous uranyl generally increase with temperature, though some measurements have high uncertainty. The addition of subsequent chloride ions is not as clearcut, with stability constants having no correlation with temperature. [9] As far as we are aware no study has been undertaken at elevated pressure.

The goal of this work is to use computational chemistry in the form of density functional theory (DFT) and coupled-cluster theory to gain a molecular picture of the uranyl-chloride system at high T/P. The thermodynamics of chloride addition to aqueous

uranyl are investigated experimentally, which is done separately by collaborators, and computationally, and the effects of elevating both temperature and pressure on the system are considered. However, there are several challenges in computationally studying the effects of temperature and pressure without dynamic simulations. First, the Born–Oppenheimer approximation assumes that the motion of atomic nuclei is so much slower than that of their associated electrons that they can be considered to be fixed. This results in temperature having no effect on the optimized structures. Furthermore, thermochemistry calculations use the ideal gas model, which means that the pressure only contributes to translational entropy and will have no effect on the optimized structure either. Finally, most implicit solvation models are optimized at standard temperature (298.15K) and pressure (1 atm). In order to overcome those challenges, in this work we demonstrate that we can use a rather simple approach of solvent dielectric constants that change as a function of pressure and temperature to study the aqueous AnO_2-Cl system.

5.2. Computational Methods

All geometry optimization and frequency calculations were performed using ADF 2017. [12, 13] Structures of the actinyl complexes and corresponding small molecules were optimized using density functional theory (DFT) with the hybrid B3LYP functional, [14, 15] relativistic scalar zeroth order regular approximation (ZORA) Hamiltonian[16-18], and all-electron triple-ζ plus two polarization function (TZ2P) basis sets.[19]

In gas-phase calculations, temperature only affects the average structure of compounds. The average structure will be the same as the structure of the local minimum on the potential energy surface under the harmonic oscillator approximation. When anharmonic effects are considered, the average structure will slightly deviate from the

structure of the minimal point. In this study, this direct temperature effect is minor. The pressure effects on the electronic structure or the geometry can be ignored. This is a reasonable assumption for pressures lower than ~1 GPa, based on experimental measurements. [20] However, the dielectric constant has a strong effect on solvent structure. The dependence of the static dielectric constant of water on temperature and pressure was measured in previous work. [21, 22] Thus, the change of dielectric constant could be a critical factor and be used for investigating the behavior of the aqueous AnO_2-Cl system under high temperature and pressure, including structures, spectra, and thermodynamics properties. The COSMO implicit solvation model[23-26] was used to model the complexes in aqueous environment. The radii values of the atomic spheres in the COSMO solvation model for atoms in this study are the corresponding van der Waals radii from the MM3 method by Allinger [27] divided by 1.2. Although the radii values for atoms heavier than uranium are not ideal, these heavy metals are well buried inside of the first solvation shell and do not have direct contact with the solvation cavity. Hence, the radii settings for them do not affect the results of the geometry optimization. To include pressure and temperature effects using an implicit solvation model, three experimental dielectric constants for water were used to simulate different pressures and temperatures: 78.39 (1atm/25°C), 14.07 (200atm/350°C), and 1.7 (250atm/500°C).[21, 22] The first two situations correspond to the experimental conditions in this work, and the last one, 250atm/500°C, represents an extrapolation introduced to predict the behaviour of this system under geothermal conditions.

Frequency calculations were performed to determine thermodynamic properties of each structure and to ensure each structure is at a local minimum on the potential energy surface. Thermodynamic properties, including heat capacity, internal energy, entropy, and

derived properties (i.e. free energy, G) were calculated at 25°C, 350°C, and 500°C. A pressure correction was introduced in the solvent environment to remove the extra freedom the models introduce in the molecules prior to complexation, which is not the case in solution. [28] In this approximation, the pressure p in the solution environment was determined from the density of liquid water at different conditions:

$$p=\rho RT/M \tag{5.1}$$

where ρ is the density of water at different conditions, R is gas constant, T is temperature, and M is the molar mass of water. The densities of liquid water at the standard state (1atm/25°C), 200atm/350°C and 250atm/500°C are 997 kg/m^3, 572.8 kg/m^3, and 300 kg/m^3, respectively. [21, 22] Thus, the pressure corrections for each condition are 1354 atm, 1626 atm and 1056 atm. This method has previously been successfully applied to actinide systems.[29-32] When molecules are solvated by going from gas phase to solution, another standard state correction per net change in the number of molecules needs to be considered:

$$\Delta G^*_{gas\rightarrow liq} = \Delta G^o_{gas\rightarrow liq} + \Delta G^{o\rightarrow *} \tag{5.2}$$

where $\Delta G^{o\rightarrow *} = RT\ln(24.46)$. As mentioned above, the pressure only contributes to the translational entropy in the partition function when calculating the statistical thermodynamics, resulting in the pressure correction of density for water per net change in the number of molecules.

In summary, the approach used in this work is:

$$\Delta G_{tot} = \Delta E_{elec} + \Delta G_{sol} + (\Delta G_{thermo} + \Delta G_{density} + \Delta G_{state}) \tag{5.3}$$

where E_{elec} is the electronic energy of the single point coupled cluster calculation, G_{sol} is the solvation energy from the DFT-COSMO calculations, G_{thermo} is the thermodynamic correction from the implicitly solvated DFT calculations, $G_{density}$ is the density correction from equation (5.1), and G_{state} is the standard state correction shown in equation (5.2). The sum of the latter three terms gives the overall thermodynamic correction term.

Finally, higher accuracy energies (E_{elec}) in gas-phase were obtained via coupled cluster methodology (DLPNO-CCSD(T))[33] as implemented in the ORCA code.[34] Scalar relativistic effects were included with the ZORA Hamiltonian and the corresponding basis set ZORA-def2-TZVP. [35] Because of the high computational cost of the coupled-clusters calculations, these calculations were performed on the DFT solution-optimized geometries.

The following aspects are discussed in the results and discussion sections of the chapter:

(1) The T/P effects, represented by dielectric constants, on the structures of aqueous AnO_2-Cl compounds; (2) The thermodynamic properties of those aqueous AnO_2-Cl compounds; (3) how (1) and (2) ultimately affect the vibrational spectra, and comparison with experimental data.

5.3. Results and Discussion

5.3.1. Structures

Fourteen distinct structures were considered, encompassing AnO_2 coordination numbers of both 4 and 5 and ranging from 0 to 5 chlorine atoms with the balance of the 1st solvation sphere occupied by water. Figure 5.1 shows examples of selected five and four coordinate aqueous uranyl-chloride structures. These structures, marked from S01 to S14, are described in the Appendix 5, Figure A5.1 and Table A5.1.

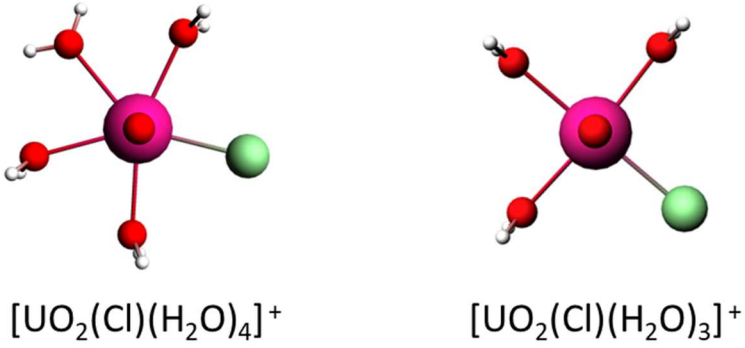

Figure 5.1 Selected five and four coordinate aqueous uranyl-chloride structures

The five-coordinated $[UO_2(H_2O)_5]^{2+}$ complex has all five of the coordinating water molecules in the equatorial plane of the uranyl, with a single water approximately in the equatorial plane and the other four aligned with their hydrogen atoms perpendicular to the plane. This configuration is similar to those reported by Bühl et al. [36] and Parmar et al., [37] who optimized the uranyl complex including a complete second solvation shell. This structure, as the most prevalent in low pH solution, and correlated uranyl-chloride structures are compared against available experimental data. The calculated bond lengths at room temperature for the axial U-O bond are within 0.01 Å of reported EXAFS values, [8] while the uranium-water and uranium-chlorine distances are also very close to reported EXAFS values. When the concentration of Cl- increased

in the experiment, the bond length of U-water and U-Cl bonds are also longer. This agrees well with the calculated trends in Table 5.3-5.6 and Figure 5.3.

For the uranyl system, two isomers were found for the five-coordinated structures when the number of Cl atoms is 2 or 3. The strong electrostatic repulsion between the Cl^- anions leads to the global minima when the separation among the coordinating Cl^- anions is maximized. Interestingly, for four coordinate uranyl structures, the structure with cis chlorines is lower in energy than the trans structure. Upon analyzing the terms in the total energy, it is found that the cis Cl^- ions polarize the molecule inducing an electric dipole moment that leads to a significant increase in the stabilizing solvation energy which overcomes the electrostatic repulsion. (See Appendix 5, Table A5.2.) Similar behavior can be found in the neptunyl and plutonyl systems as well. (See Appendix, Tables A5.3 and A5.4.) Furthermore, for the uranyl and neptunyl systems, the energy differences between the five-coordinated trans and cis isomers when the number of Cl is 2 or 3 at 1atm/25℃ and 200atm/350℃ are generally only about 1kcal/mol, which means that they can both exist at these temperatures. For the plutonyl system, the more polar structure, S05, is more stable than S06 by about 4.5 kcal/mol. The Hirshfeld charges (See Tables A5.5-A5.7) show that, although the plutonium bonds are much shorter, the Pu-Cl bonds are more polar. This can explain how the plutonyl compounds overcome the electrostatic repulsion at lower temperatures. When the temperature reaches 500℃, the dielectric constant of the solvent is close to zero. As a result, the polar structures become less favorable due to the absence of solvation stabilization.

Table 5.1 Calculated uranyl U=O bond lengths (Å) dependence on temperature for five-coordinated structures.

# of Cl-	0	1	2		3		4	5
	S01	S02	S03	S04	S05	S06	S07	S08
25℃	1.761	1.771	1.777	1.776	1.780	1.780	1.784	1.784
350℃	1.760	1.771	1.777	1.776	1.781	1.780	1.784	1.784
500℃	1.753	1.768	1.777	1.772	1.779	1.777	1.779	1.782

Table 5.2 Calculated uranyl U=O bond lengths (Å) dependence on temperature for four-coordinated structures.

# of Cl-	0	1	2		3	4
	S09	S10	S11	S12	S13	S14
25℃	1.757	1.768	1.777	1.776	1.782	1.787
350℃	1.757	1.769	1.778	1.776	1.783	1.787
500℃	1.751	1.767	1.778	1.776	1.777	1.784

Table 5.1, Table 5.2, and Figure 5.2 show that the changes of uranyl U=O distances are minimal in the range of dielectric constants studied from 78.39 (1atm/25℃) to 14.07 (200atm/350℃). At 1.7 (250atm/ 500℃), larger changes were observed. As T increases, the dielectric constant decreases. The stabilizing polarization energy of the solvent environment decreases favoring the ionic interaction between the U and Cl^- rather than the dipole, which leads to a shorter U=O and U-Cl bonds (see Tables 5.1-5.4 and Figures 5.2-5.3). Because of the ionic nature of the uranyl-Cl bond, the effects resulting from the changes of the dielectric constants (change in T/P) are more significant for U-Cl compared to U-O. Notice that, as Tables 5.3 and 5.4 and Figure 5.3 show, in the 3 and 4 Cl^- complexes there are two types of U-Cl bonds, short and long bonds. When the coordinated number of Cl^- is 3 and 4 (also see structures S06 and S07 in Figure A5.2), there are two short bonds and one long bond, and two short and long bonds,

respectively. For example, in structure S06, the U-Cl bond with two water molecules nearby is longer than the U-Cl bonds with only one water nearby. The ionic interactions between two water molecules make the former bond weaker than the latter. All U-Cl bonds lengths decrease when the dielectric constant decreases as a function of temperature.

Table 5.3 Calculated U-Cl Bond lengths (Å) for for five-coordinated structures at different temperatures.

# of Cl-	1	2		3		4	5
	S02	S03	S04	S05	S06	S07	S08
25℃	2.670	2.695*	2.718*	2.708	2.738*	2.765*	
				2.765*	2.785	2.827*	2.845**
350℃	2.656	2.690*	2.712*	2.700	2.729*	2.762*	
				2.768*	2.790	2.835*	2.847**
500℃	2.595	2.652*	2.693*	2.643	2.716*	2.731*	
				2.789*	2.832	2.923*	2.900**

*Average bond length of two nearly equivalent U-Cl bonds.
**Average bond length of four nearly equivalent U-Cl bonds.

The effect of the change in dielectric constant is less significant in the U=O bond (see Tables 5.1 and 5.2 and Figure 5.2), although a similar shortening trend, as discussed in the context of the U-Cl bond, is observed. The weaker effect is most likely due to this already being a very strong covalent bond. However, as the number of Cl^- increases, the U=O distance systematically increases. Two effects may contribute to this weakening of the U=O bond: the withdrawal of electrons from the U=O bond by the equatorial Cl or so-call "pi-competition",[38] and the repulsion between the formally Cl^- and O^{2-}. Tables 5.5 and 5.6 show that the U-water bonds become longer

when the temperature or the number of Cl^- increases due to the repulsion from Cl^- and stronger U=O bonds.

The neptunyl and plutonyl systems behave very similar to the uranyl systems, see Tables A5.8 to A5.19. However, the structures become more disturbed at higher temperatures. It is worth to notice that there are no five-coordinated structures when the 4 Cl^- coordinate to the metal at 500℃. Because of the strong repulsion from the shorter Cl bonds, the water will be pushed out to the second solvation shell.

Table 5.4 Calculated U-Cl bond lengths (Å) for for four-coordinated structures at different temperatures.

# of Cl-	1	2		3	4
	s10	s11	s12	s13	s14
25℃	2.633	2.659*	2.679*	2.633	
				2.702*	2.721**
350℃	2.618	2.650*	2.670*	2.677	
				2.699*	2.722**
500℃	2.553	2.613*	2.636*	2.658	
				2.687	
				2.728	2.746**

*Average bond length of two nearly equivalent U-Cl bonds.
**Average bond length of four nearly equivalent U-Cl bonds.

Table 5.5 Calculated average U-water bond lengths (Å) for five-coordinated structures at different temperatures.

# of Cl-	0	1	2		3		4
	S01	S02	S03	S04	S05	S06	S07
25℃	2.458	2.501	2.558	2.528	2.601	2.568	2.612
350℃	2.461	2.509	2.564	2.540	2.606	2.576	2.624
500℃	2.485	2.549	2.639	2.571	2.701	2.611	2.769

Table 5.6 Calculated average U-water bond lengths (Å) for four-coordinated structures at different temperatures.

# of Cl-	0	1	2		3
	S09	s10	s11	s12	s13
25℃	2.394	2.419	2.442	2.431	2.461
350℃	2.395	2.421	2.454	2.433	2.465
500℃	2.421	2.472	2.541	2.488	2.614

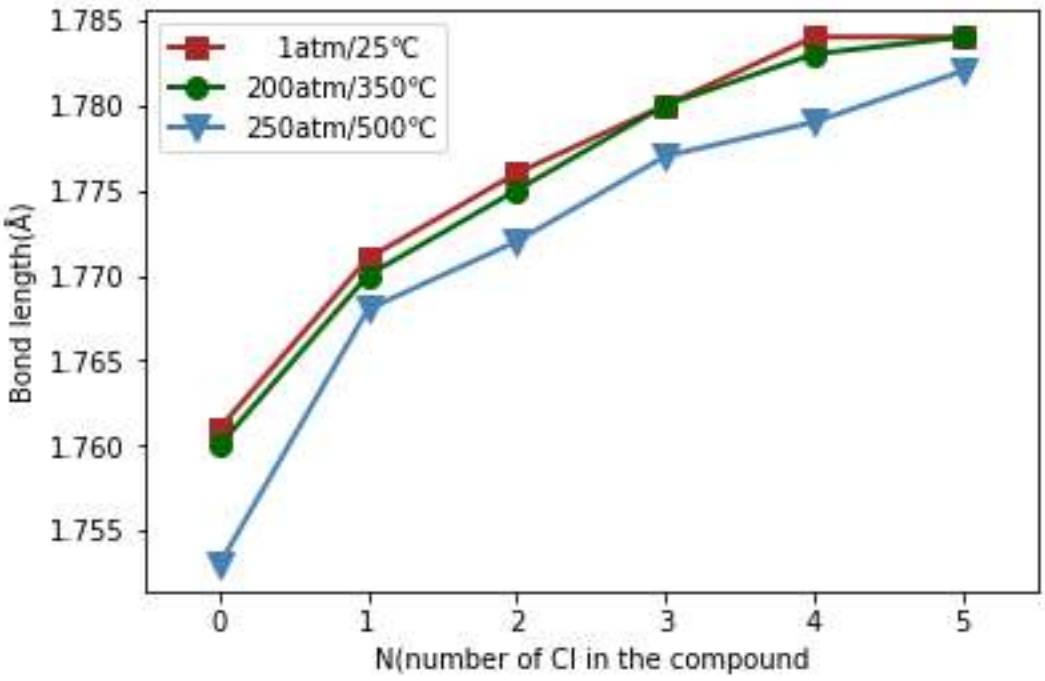

Figure 5.2 Calculated U=O bond lengths for five coordinate aqueous uranyl-chloride structures

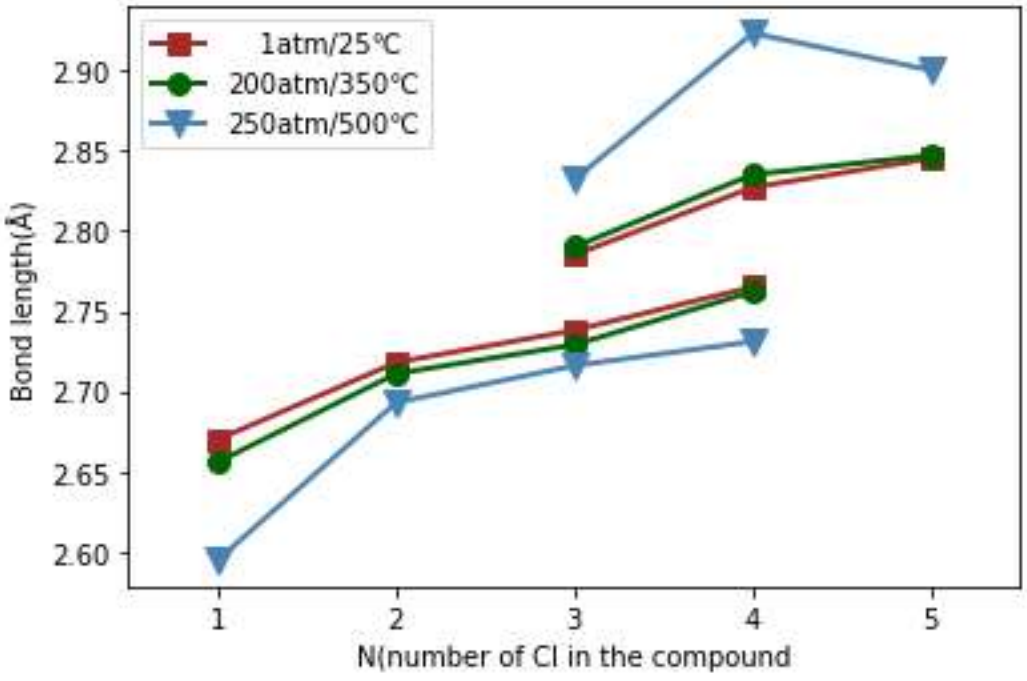

Figure 5.3 Calculated U-Cl bond lengths for five coordinate aqueous uranyl-chloride structures

5.3.2. Thermodynamics

The first solvation shell of actinyl ions needs to be computed explicitly to correctly describe the system. Therefore, the coordination numbers of uranyl ions with different numbers of Cl^- anions at different temperature and pressure were first investigated. The structures of complexes with different equatorial coordination numbers can be found in the Appendix 5 (Figures A6.1-A5.3 and Table A5.1).

The relative stability of the aqueous uranyl species with different coordination numbers as a function of the number of chlorine atoms in the first solvation shell were evaluated by calculating the free energies for water addition in the following reactions of water addition going from tetra- to penta- coordinate uranyl:

$$UO_2(H_2O)_{4-n}Cl_n^{2-n} + H_2O \rightarrow UO_2(H_2O)_{5-n}Cl_n^{2-n}$$

R1. $UO_2(H_2O)_4^{2+} + H_2O \rightarrow UO_2(H_2O)_5^{2+}$ (5.4)

R2. $UO_2(H_2O)_3Cl^{+} + H_2O \rightarrow UO_2(H_2O)_4Cl^{+}$ (5.5)

R3. $UO_2(H_2O)_2Cl_2 + H_2O \rightarrow UO_2(H_2O)_3Cl_2$ (5.6)

R4. $UO_2(H_2O)_1Cl_3^{-} + H_2O \rightarrow UO_2(H_2O)_2Cl_3^{-}$ (5.7)

R5. $UO_2Cl_4^{2-} + H_2O \rightarrow UO_2(H_2O)Cl_4^{2-}$ (5.8)

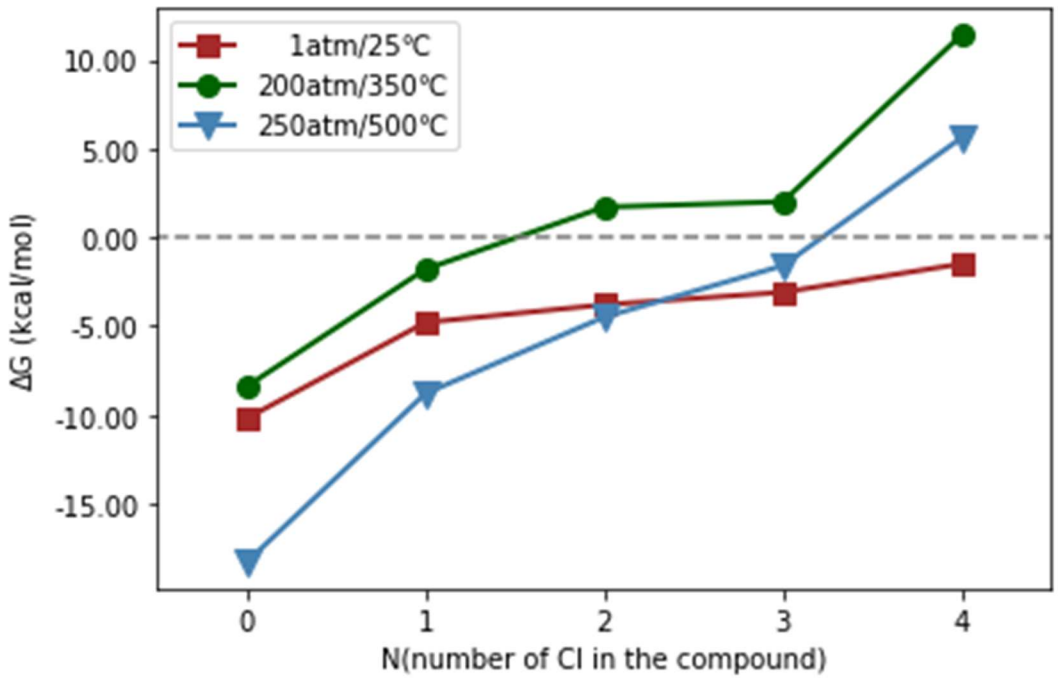

Figure 5.4 Calculated Gibbs free energy for the reaction of addition of a water molecule to the 4-coordinated uranyl-chloride species, yielding a 5-coordinated species, which are shown as R1-5 in equations 6.4-6.8.

The uranyl-chloride complexes at each coordination number are the lowest energy structures described in Figures S2 and S3. In the absence of chlorine and under standard conditions, the uranyl penta aqua complex, $UO_2(H_2O)_5^{2+}$, was found to be the most stable configuration favored by roughly 8 kcal/mol over the four-coordinate structure. This is consistent with previous DFT calculations, [39-41] as well as EXAFS experiments showing a coordination number of five, [42] serving as validation for our methodology. The addition of Cl^- to the first solvation shell leads to the displacement of water molecules. As Figure 5.4 shows, at 25 ℃/1atm the red line is always negative indicating that the most stable configuration for all compounds is the penta-coordinated one. However, at 350℃/200atm, for the first three chlorine additions (1, 2 and 3 Cl atoms), four- and five-coordinated species should coexist in equilibrium, as evidenced by the Gibbs free energy being very close to 0. For the four-chlorine species the addition of a water molecule is endergonic indicating that only the four-coordinated species is stable. Although this molecule can be calculated, it is very high in energy and not present in experiment. At 500℃, the first two chlorine additions are stabilized in five-coordinated structures, while two water molecules will be lost in subsequent additions, reducing the coordination number to four. In all situations, as the number of Cl^- increases, eventually the repulsion among the Cl^- anions overcomes the attractive interactions

towards the uranium center and the coordination number reduces to four, which allows for the Cl^- ions to be farther apart. This is particularly noticeable at high temperature and pressure conditions.

In order to investigate the impact of the effect of temperature and pressure, take R2 for example, the total free energy can be broken down into terms, according to equation (3). ΔG_{thermo} and $\Delta G_{density}$ are combined here, as they both contribute only to the translational entropy.

Table 5.7 Energy terms for R2 at different temperatures.

Kcal/mol	ΔG_{tot}	ΔE_{elec}	$\Delta G_{thermo}+\Delta G_{density}$	ΔG_{sol}	ΔG_{state}
25℃	-4.06	-21.96	9.05	10.74	-1.89
350℃	-1.83	-22.08	13.96	10.25	-3.96
500℃	-8.78	-22.21	14.85	3.50	-4.91

As Table 5.7 shows, there are two competing factors affecting the ΔG_{tot} term: $\Delta G_{thermo}+\Delta G_{density}$ and ΔG_{sol}. The former increases with temperature while the latter decreases as temperature increases and the dielectric constants becomes smaller at high temperature. In our model, the main determining factor of the solvation energy is the dielectric constant, which follows a non-linear relation with temperature in this range. A very small effect in the solvation energy, of only 0.5 kcal/mol, can be observed when increasing the temperature from 25℃ to 350℃. However, when the temperature increases from 350℃ to 500℃, as the dielectric constant drops from 14.1 to 1.7, the solvation energy dramatically changes from 10.25 kcal/mol to 3.50 kcal/mol. These changes initially make ΔG_{tot} more positive from 25℃ to 350℃, and then more negative from 350℃ to 500℃.

The stepwise addition of chloride to the 1st solvation shell of uranyl, replacing a water molecule, is shown according to the reactions below, where N gives the number of chlorides in the product (see Figure 5.5).

At 1atm/25°C:

R6. $UO_2(H_2O)_5^{2+} + Cl^- \rightarrow UO_2(H_2O)_4Cl^+ + H_2O$ (5.9)

R7. $UO_2(H_2O)_4Cl^+ + Cl^- \rightarrow UO_2(H_2O)_3Cl_2 + H_2O$ (5.10)

R8. $UO_2(H_2O)_3Cl_2 + Cl^- \rightarrow UO_2(H_2O)_2Cl_3^- + H_2O$ (5.11)

R9. $UO_2(H_2O)_2Cl_3^- + Cl^- \rightarrow UO_2(H_2O)Cl_4^{2-} + H_2O$ (5.12)

At 200atm/350°C:

R10. $UO_2(H_2O)_5^{2+} + Cl^- \rightarrow UO_2(H_2O)_4Cl^+ + H_2O$ (5.13)

R11. $UO_2(H_2O)_4Cl^+ + Cl^- \rightarrow UO_2(H_2O)_2Cl_2 + 2H_2O$ (5.14)

R12. $UO_2(H_2O)_2Cl_2 + Cl^- \rightarrow UO_2(H_2O)_1Cl_3^- + H_2O$ (5.15)

R13. $UO_2(H_2O)Cl_3^- + Cl^- \rightarrow UO_2Cl_4^{2-} + H_2O$ (5.16)

At 250atm/500°C

R14. $UO_2(H_2O)_5^{2+} + Cl^- \rightarrow UO_2(H_2O)_4Cl^+ + H_2O$ (5.17)

R15. $UO_2(H_2O)_4Cl^+ + Cl^- \rightarrow UO_2(H_2O)_3Cl_2 + H_2O$ (5.18)

R16. $UO_2(H_2O)_3Cl_2 + Cl^- \rightarrow UO_2(H_2O)_2Cl_3^- + H_2O$ (5.19)

R17. $UO_2(H_2O)_2Cl_3^- + Cl^- \rightarrow UO_2Cl_4^{2-} + 2H_2O$ (5.20)

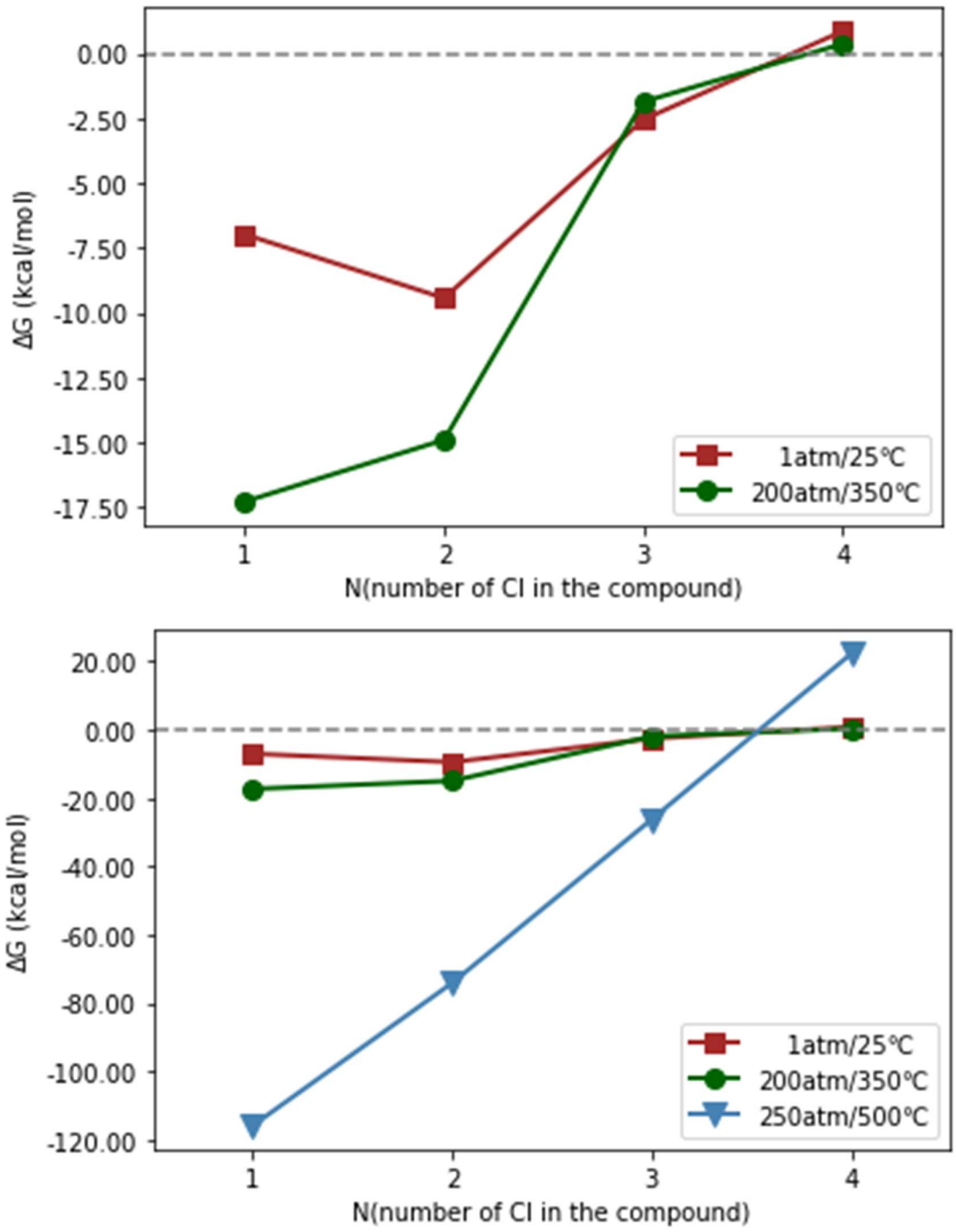

Figure 5.5 Calculated Gibbs free energy for the reaction of the stepwise addition of Cl^- to aqueous uranyl-chloride. The top figure shows the details of reaction energy change for 1atm/25°C and 200atm/350°C, which are hard to distinguish in lower figure containing reaction at 250atm/350°C with large order of magnitude. The lines are only showed to help guide the eye.

As shown in Figure 5.5, the addition of the first, second, and third Cl^- to the first solvation shell of the uranyl is thermodynamically favorable. The second Cl^- addition gains extra energy from the intramolecular hydrogen bonds at room temperature. This effect becomes weaker when the temperature is increased because the structure cannot maintain some of the hydrogen bonds. Adding a fourth or fifth Cl^- is not thermodynamically favorable. This is consistent with the EXAFS experiments of Allen et al.,[8] who found that, even at very high chloride concentrations (14 M), the average number of Cl^- in the 1st solvation shell of uranyl was between two and three. These trends remain similar as the temperature is increased up to 500 °C. On the other hand, the absolute values of Gibbs free energies for the first three additions are in the order of 500°C>350°C>25°C evidencing that the addition of the Cl^- becomes even more favorable when the temperature is increased. Because the solvation effect is weaker at high temperature, the U-Cl bonding becomes stronger. The favored number of coordinated chloride ions remains three as the temperature increases, with the addition of the fourth Cl^- to the uranyl ion being even less likely at higher T than at standard state conditions. This is due to the repulsions from neighboring Cl^- that rises quickly when the number of Cl^- is increased. This is consistent with experimental studies measuring the impact of temperature on aqueous uranyl-chloride thermodynamics, which show an increase in the stability constant of the first two chloride additions with increasing temperature. [9-11]

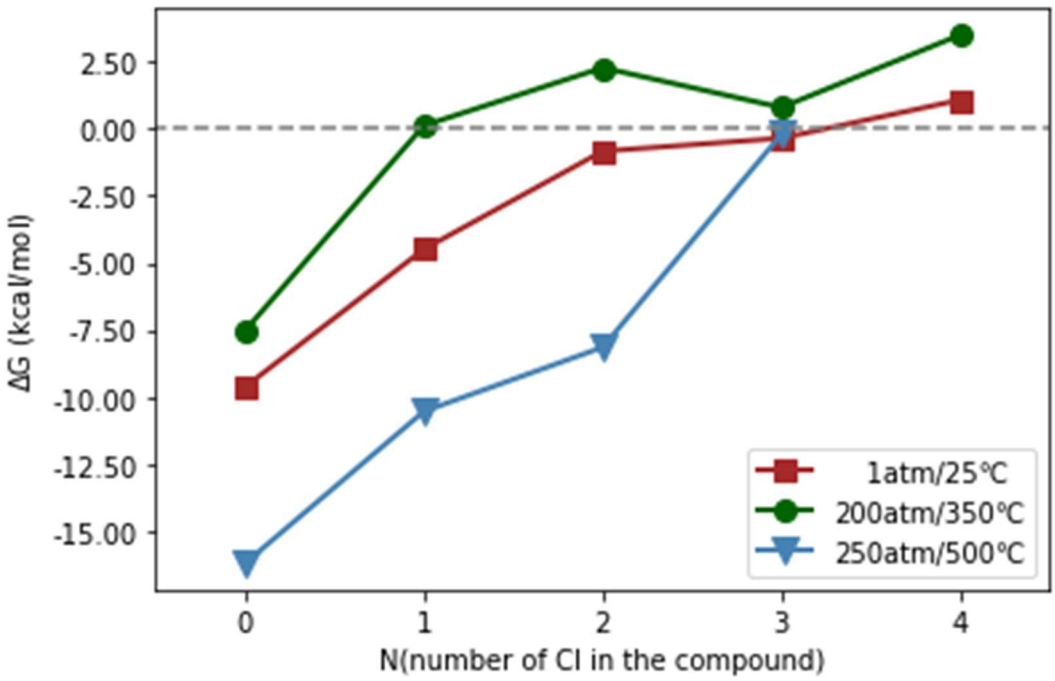

Figure 5.6 Calculated Gibbs free energy for the reaction of addition of a water molecule to the 4-coordinated neptunyl-chloride species, yielding a 5-coordinated species.

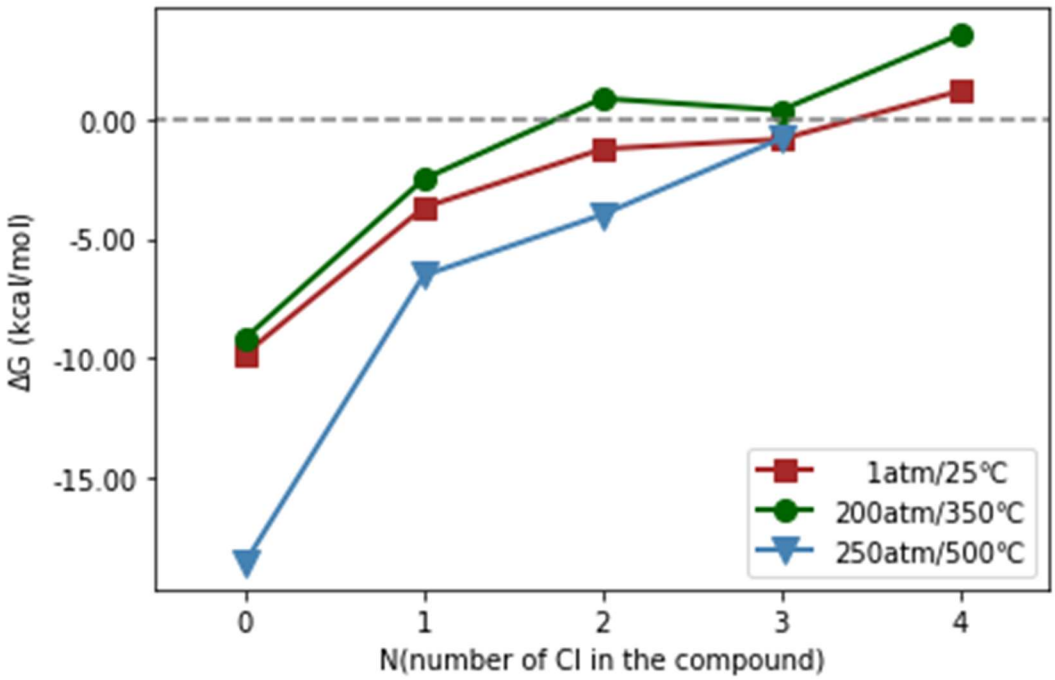

Figure 5.7 Calculated Gibbs free energy for the reaction of addition of a water molecule to the 4-coordinated plutonyl-chloride species, yielding a 5-coordinated species.

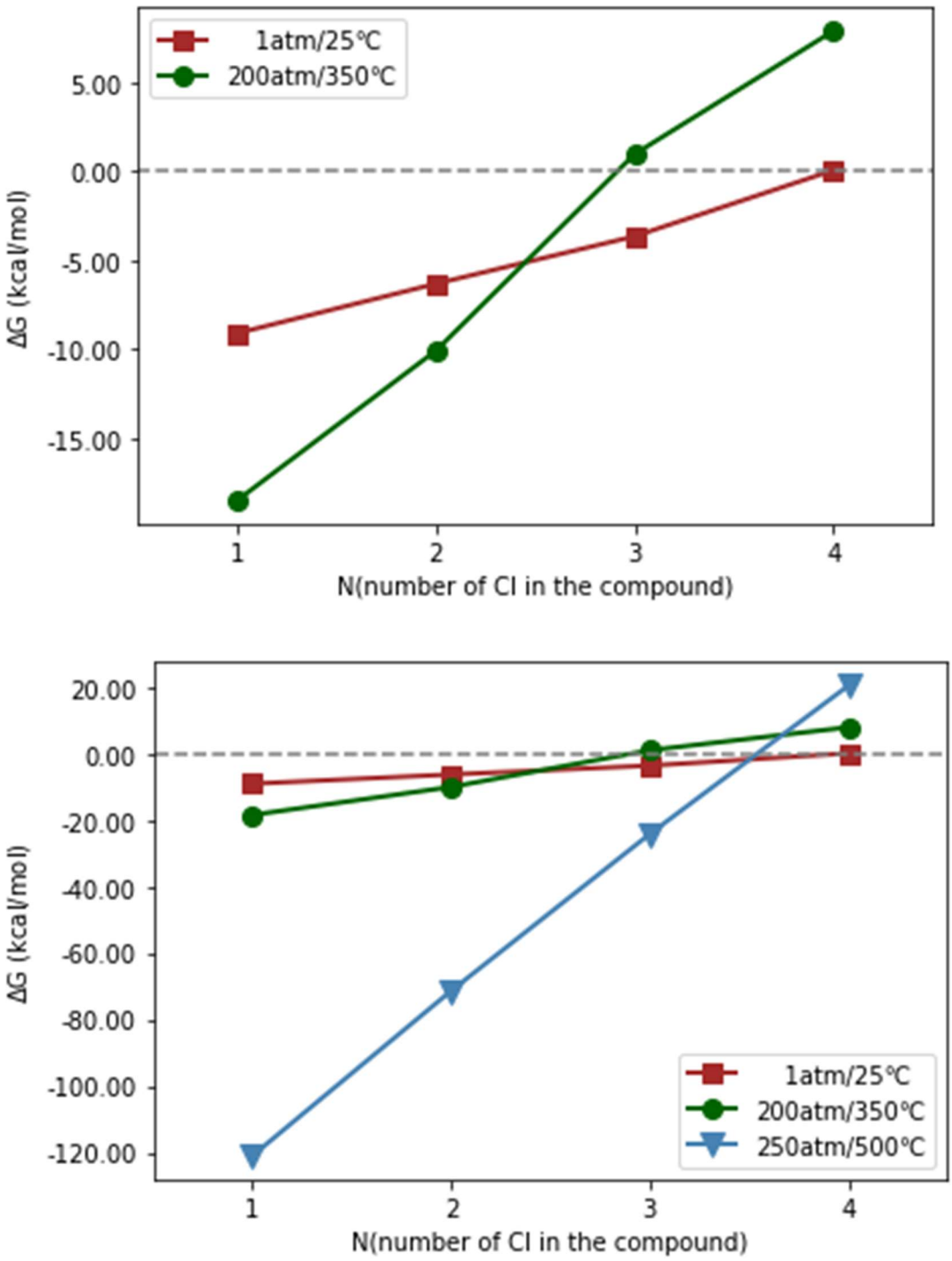

Figure 5.8 Calculated free energy change for the stepwise addition of Cl^- to aqueous neptunyl-chloride. The top figure shows the details of reaction energy change for 1atm/25℃ and 200atm/350℃, which are hard to distinguish in lower figure containing reaction at 250atm/350℃ with large order of magnitude. The lines are only showed to help guide the eye.

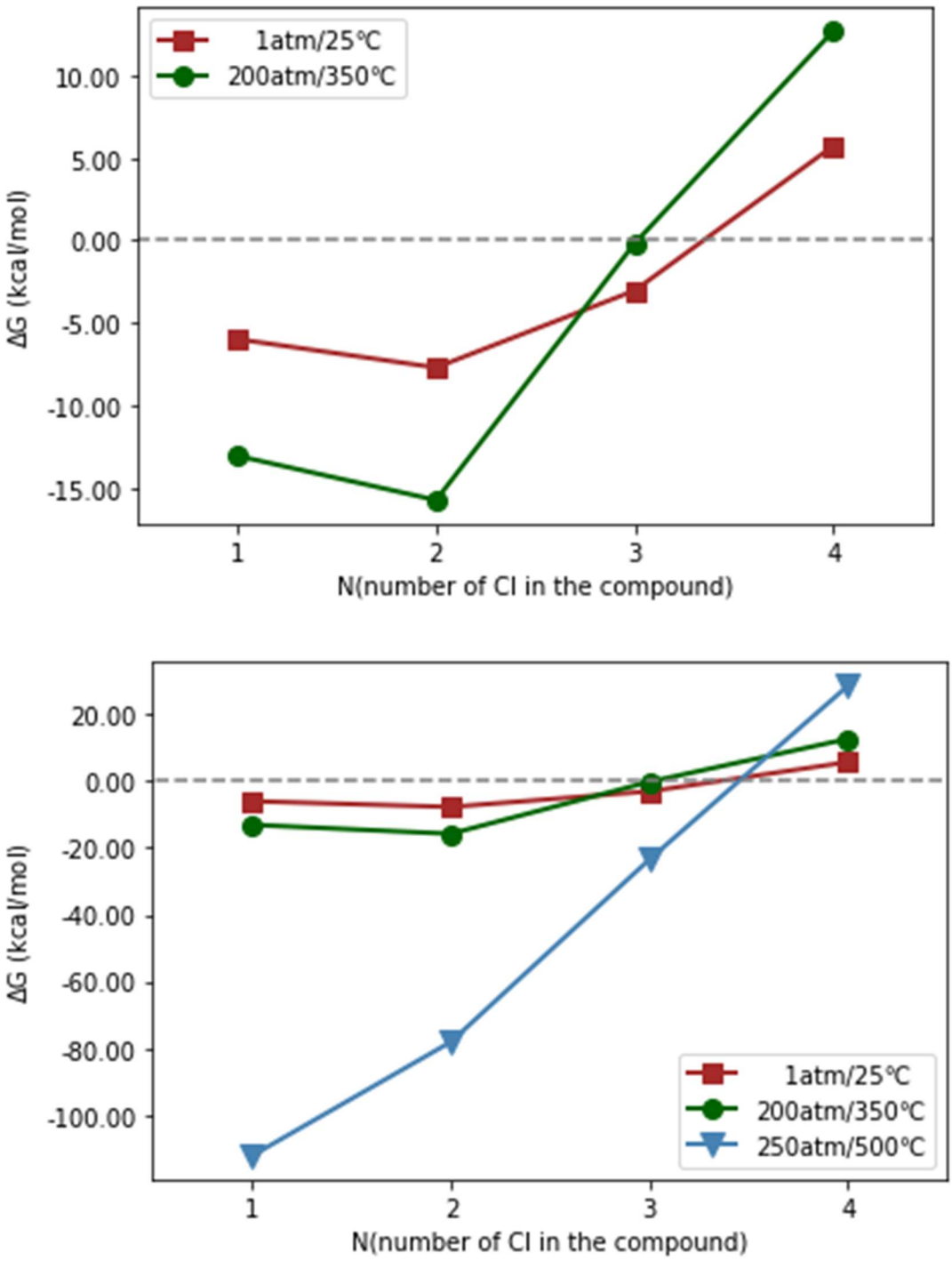

Figure 5.9 Calculated free energy change for the stepwise addition of Cl^- to aqueous plutonyl-chloride. The top figure shows the details of reaction energy change for 1atm/25°C and 200atm/350°C, which are hard to distinguish in lower figure containing reaction at 250atm/350°C with large order of magnitude. The lines are only showed to help guide the eye.

As Figures 5.6 and 5.7 show, the water additions for the neptunyl and plutonyl systems from 4-coordinated species to 5-coordinated species give very similar trends to the uranyl system. However, the reaction Gibbs free energies of neptunyl and plutonyl are generally less negative than for the uranyl system. Due to shorter Cl bonds, the five-coordinate structures with four Cl^- become thermodynamically unfavorable. As mentioned above, five-coordinated structures do not exist when the 4 Cl^- coordinate to the metal at 500℃ for the same reason. The Cl^- coordination for the neptunyl and plutonyl systems are only favorable for the first two additions at 350℃, see Figures 5.8 and 5.9. In almost all cases, the fourth coordination of Cl^- becomes thermodynamically unfavorable. However, at 500℃, their behaviors are very similar to the uranyl system. The behavior of first two Cl- additions is slightly different for water molecule orientations between uranyl, neptunyl, and plutonyl. This is due to the different structure configurations between uranyl, neptunyl, and plutonyl, see Figure 5.10.

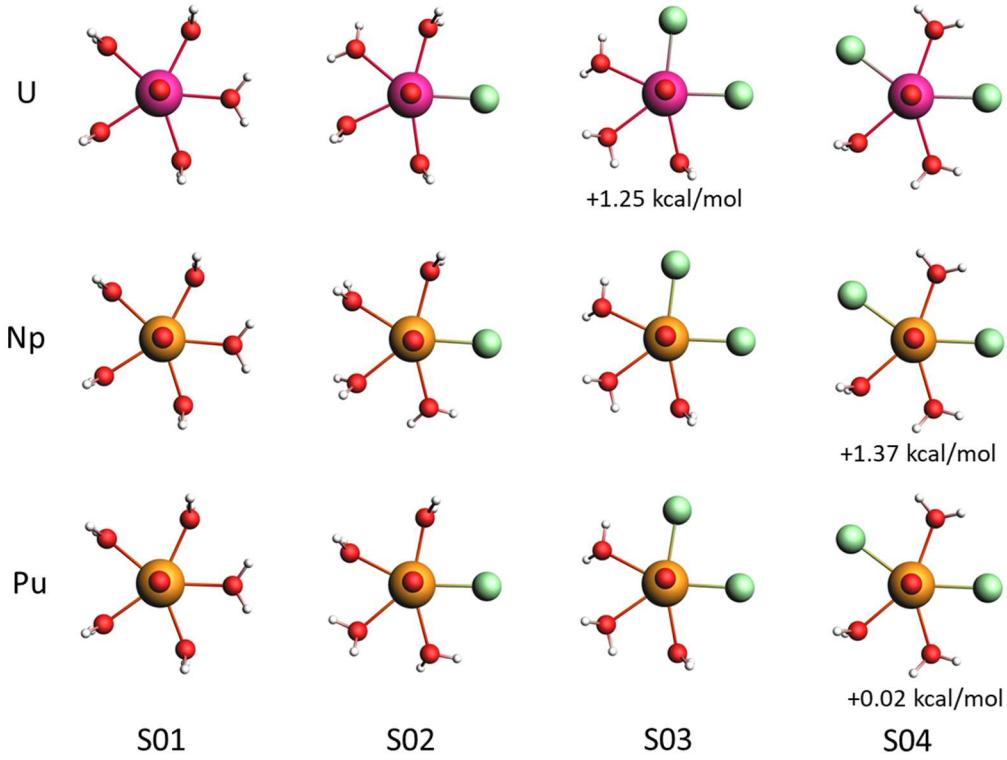

Figure 5.10 Selected aqueous actinide-chloride structures at 25°C/1 atm.

5.3.3. Vibrational Spectroscopy

A direct connection between the experimental studies and the calculated species was found in the calculation of the vibrational spectra for the molecular species identified to be in solution. The calculated IR and Raman active frequencies for the 4- and 5-coordinated species for the uranyl vibrations are summarized in Table 5.8.

Table 5.8 Calculated uranyl U=O Raman and IR peaks from aqueous uranyl chloride (cm^{-1}).

5-coordinate						4-coordinate					
# of Cl			25ºC	350ºC	500ºC	# of Cl			25ºC	350ºC	500ºC
0	S01	Raman	912	915	934	0	S09	Raman	912	915	933
		IR	959	965	1008			IR	959	965	1008
1	S02	Raman	882	883	895	1	S10	Raman	888	887	898
		IR	933	938	970			IR	937	940	972
2	S03	Raman	862	863	874	2	S11	Raman	862	863	870
		IR	914	918	949			IR	914	917	944
	S04	Raman	864	866	881		S12	Raman	865	865	873
		IR	916	922	957			IR	918	921	950
3	S05	Raman	851	850	862	3	S13	Raman	848	847	866
		IR	906	908	938			IR	901	903	942
	S06	Raman	850	852	866						
		IR	905	909	942						
4	S07	Raman	840	842	857	4	S14	Raman	833	833	847
		IR	897	901	935			IR	888	892	924

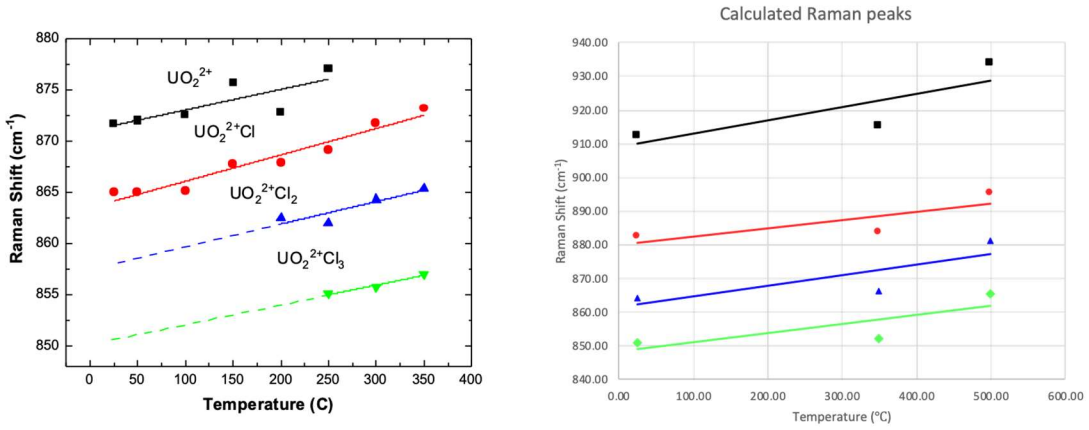

Figure 5.11 Calculated uranyl U=O and experimental Raman data in this work provided by collaborator

As Table 5.8 shows, there are two competing factors that change the uranyl U=O stretch: T and P as represented by the dielectric constants and the number of coordinated Cl^- anions. A decrease of the dielectric constant results in a shift of the Raman/IR peaks of the same compound to higher wave numbers as the U=O bonds become shorter (Tables 5.1 and 5.2). However, when the number of Cl increases, the Raman/IR peaks shift to lower wavenumbers as the uranyl U=O bonds become longer; the latter of these effect is dominant. This agrees well with experimental Raman shifts observed for uranyl U=O bonds, as seen in Figure 5.12. When the temperature is increased, additional peaks appear as higher coordination numbers of Cl coexist in solution. As discussed above (see Figure 5.4 at 350°C), the first three chlorine additions are at equilibrium between four- and five-coordination as the Gibbs free energy values are very close to 0. This suggests that the wide peak at 350°C (Figure 5.12) is a combination of the uranyl stretches of four- and five-coordinated complexes. On the other hand, although the pH values are quite low to avoid the hydrolysis of U(VI) under experimental conditions, at high temperatures, cations and anions associate as contact-ion pairs.[43, 44] Because of the absence of hydronium, the hydrolyzed species will be formed. Moreover Zanonato et al. found that UV/Vis absorption spectra supported the trend

that hydrolysis of U(VI) was enhanced at elevated temperatures.[45] The presence of hydroxide at high T/P also competes with Cl^- for coordination. Calculated Raman peaks of the hydrolyzed species are 843.80 and 842.38 cm^{-1} for $UO_2OH(H_2O)_2Cl$ and $UO_2OH(H_2O)_3Cl$, respectively. The stronger interaction of the U-OH bond makes the U=O bond even weaker and the Raman peaks shift to a lower area. The variety of the compounds present and the decrease of the dielectric constants will broaden the Raman peak at 350°C/200 atm and extend it into both higher and lower wave numbers. There is no peak for compounds with more than 3 Cl^- anions in the experimental Raman data, which also agrees well with the calculated thermodynamic results. The calculated Raman and IR results for NpO_2^{2+} and PuO_2^{2+} can be found in Tables A5.19 and A5.20, which show similar trends as for UO_2^{2+}.

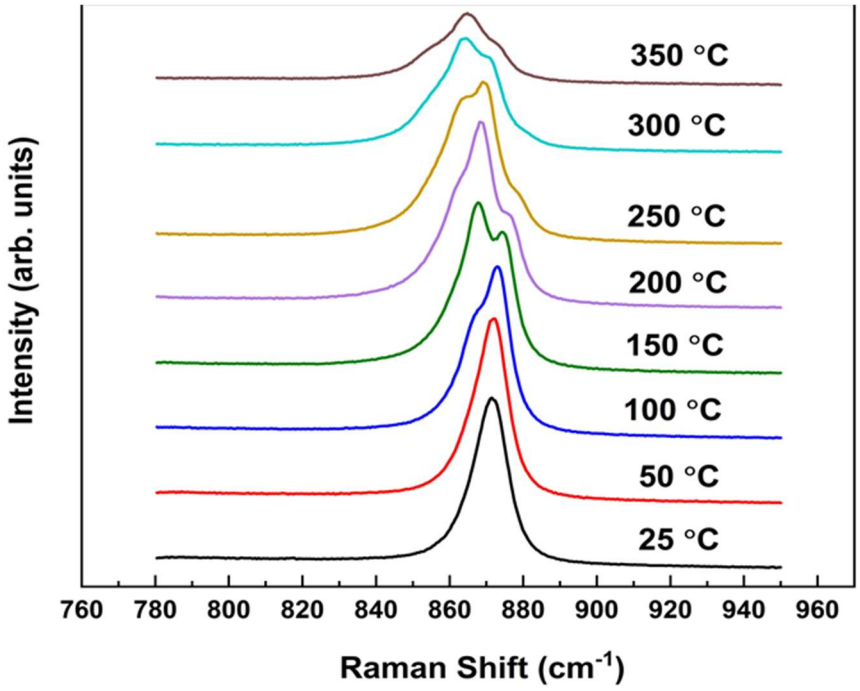

Figure 5.12 Experimental Raman data in this work provided by collaborator.

5.4. Conclusions

Building on and improving previous work, we have exhaustively examined the speciation of the aqueous uranyl chloride system using density functional theory and coupled cluster methods. In this work, dielectric constants that change as a function of pressure and temperature were used to successfully predict the properties of the aqueous AnO_2-Cl system at high pressure and temperature. Our computational thermodynamic and structural results match experimental EXAFS data at standard state conditions, giving confidence in the approach. These analyses are further extended to elevated temperatures and pressures that need to be considered in the nuclear fuel cycle, particularly within nuclear waste repositories. Including these relatively simple changes as well as a pressure correction and standard state correction in our calculations allows us to successfully reproduce experimental trends and accurately predict results for higher T/P, outside the experimentally observed range. Higher temperature and pressure make the coordination of chloride anions more favorable. The formation of $UO_2Cl_4^{2-}$ is thermodynamically unfavorable at all temperature examined here. If the temperature reaches 500℃, drastic changes of structure and corresponding properties can be expected. The Raman spectra of these compounds are affected by both increasing temperature and changing the number of coordinated chloride ions. An increased temperature increases the Raman shift of the uranyl U=O peak, as the uranyl U=O bonds become shorter for all species. When the number of Cl^- increases, the Raman peaks shift to lower frequency as the U=O bonds become longer. The change in the Raman spectrum from an additional chloride is greater than that due to temperature. NpO_2^{2+} and PuO_2^{2+} show similar trends as UO_2^{2+} but less favorable as the reaction Gibbs free energies are generally less negative than for the UO_2^{2+} system. This work helps us to better understand the behavior of AnO_2-Cl compounds at high T/P. It provides a convenient model to simulate the actinide aqueous system under extreme condition that

lack experimental data. This data could be crucial in nuclear waste storage as well as catastrophic nuclear incidents. It is worth to point out that, at higher temperatures, due to Boltzmann distributions, isomers have a greater probability of being found in higher energy states. This might also contribute to the wider peak observed from experiments.

5.5. References

1. Ahrland, S., ON THE COMPLEX CHEMISTRY OF THE URANYL ION. 6. THE COMPLEXITY OF URANYL CHLORIDE, BROMIDE AND NITRATE. *Acta Chemica Scandinavica* **1951,** *5* (9-10), 1271-1282.
2. Awasthi, S.; Sundaresan, M., Spectrophotometric & calorimetric study of uranyl cation/chloride anion system in aqueous solution. **1981**.
3. Davies, E.; Monk, C., Spectrophotometric studies of electrolytic dissociation. Part 4.—Some uranyl salts in water. *Transactions of the Faraday Society* **1957,** *53*, 442-449.
4. Choppin, G.; Du, M., *f*-Element complexation in brine solutions. *Radiochimica Acta* **1992,** *58* (1), 101-104.
5. Brown, P. L.; Wanner, H. *Predicted formation constants using the unified theory of metal ion complexation*; Nuclear Energy Agency: 1987.
6. Guillaumont, R.; Mompean, F. J., *Update on the chemical thermodynamics of uranium, neptunium, plutonium, americium and technetium*. Elsevier Amsterdam: 2003; Vol. 5.
7. Soderholm, L.; Skanthakumar, S.; Wilson, R. E., Structural correspondence between uranyl chloride complexes in solution and their stability constants. *The Journal of Physical Chemistry A* **2011,** *115* (19), 4959-4967.
8. Allen, P. G.; Bucher, J. J.; Shuh, D. K.; Edelstein, N. M.; Reich, T., Investigation of Aquo and Chloro Complexes of UO(2)(2+), NpO(2)(+), Np(4+), and Pu(3+) by X-ray Absorption Fine Structure Spectroscopy. *Inorg Chem* **1997,** *36* (21), 4676-4683.
9. Dargent, M.; Dubessy, J.; Truche, L.; Bazarkina, E. F.; Nguyen-Trung, C.; Robert, P., Experimental study of uranyl (VI) chloride complex formation in acidic LiCl aqueous solutions under hydrothermal conditions (T= 21 C–350 C, Psat) using Raman spectroscopy. *European Journal of Mineralogy* **2013,** *25* (5), 765-775.
10. Migdisov, A.; Boukhalfa, H.; Timofeev, A.; Runde, W.; Roback, R.; Williams-Jones, A., A spectroscopic study of uranyl speciation in chloride-bearing solutions at temperatures up to 250 C. *Geochimica et Cosmochimica Acta* **2018,** *222*, 130-145.
11. Timofeev, A.; Migdisov, A. A.; Williams-Jones, A. E.; Roback, R.; Nelson, A. T.; Xu, H., Uranium transport in acidic brines under reducing conditions. *Nature communications* **2018,** *9* (1), 1-7.
12. Baerends, E.; Ziegler, T.; Atkins, A.; Autschbach, J.; Bashford, D.; Baseggio, O.; Bérces, A.; Bickelhaupt, F.; Bo, C.; Boerritger, P., ADF2017, SCM, theoretical chemistry. *Vrije Universiteit* **2017**.
13. Te Velde, G. t.; Bickelhaupt, F. M.; Baerends, E. J.; Fonseca Guerra, C.; van Gisbergen, S. J.; Snijders, J. G.; Ziegler, T., Chemistry with ADF. *Journal of Computational Chemistry* **2001,** *22* (9), 931-967.

14. Lee, C.; Yang, W.; Parr, R. G., Development of the Colle-Salvetti correlation-energy formula into a functional of the electron density. *Physical Review B* **1988,** *37* (2), 785-789.
15. Becke, A. D., Density-functional exchange-energy approximation with correct asymptotic behavior. *Physical review A* **1988,** *38* (6), 3098.
16. Lenthe, E. v.; Baerends, E. J.; Snijders, J. G., Relativistic regular two-component Hamiltonians. *The Journal of Chemical Physics* **1993,** *99* (6), 4597-4610.
17. Lenthe, E. v.; Baerends, E. J.; Snijders, J. G., Relativistic total energy using regular approximations. *The Journal of Chemical Physics* **1994,** *101* (11), 9783-9792.
18. Lenthe, E. v.; Ehlers, A.; Baerends, E.-J., Geometry optimizations in the zero order regular approximation for relativistic effects. *The Journal of Chemical Physics* **1999,** *110* (18), 8943-8953.
19. Van Lenthe, E.; Baerends, E. J., Optimized Slater-type basis sets for the elements 1–118. *Journal of Computational Chemistry* **2003,** *24* (9), 1142-1156.
20. Drickamer, H. G.; Frank, C. W., *Electronic transitions and the high pressure chemistry and physics of solids*. Springer Science & Business Media: 2013.
21. Uematsu, M.; Frank, E. U., Static Dielectric Constant of Water and Steam. *Journal of Physical and Chemical Reference Data* **1980,** *9* (4), 1291-1306.
22. Hamelin, J.; Mehl, J. B.; Moldover, M. R., The Static Dielectric Constant of Liquid Water Between 274 and 418 K Near the Saturated Vapor Pressure. *International Journal of Thermophysics* **1998,** *19* (5), 1359-1380.
23. Pye, C. C.; Ziegler, T., An implementation of the conductor-like screening model of solvation within the Amsterdam density functional package. *Theoretical Chemistry Accounts* **1999,** *101* (6), 396-408.
24. Klamt, A., Conductor-like screening model for real solvents: a new approach to the quantitative calculation of solvation phenomena. *The Journal of Physical Chemistry* **1995,** *99* (7), 2224-2235.
25. Klamt, A.; Schüürmann, G., COSMO: a new approach to dielectric screening in solvents with explicit expressions for the screening energy and its gradient. *Journal of the Chemical Society, Perkin Transactions 2* **1993,** (5), 799-805.
26. Klamt, A.; Jonas, V., Treatment of the outlying charge in continuum solvation models. *The Journal of chemical physics* **1996,** *105* (22), 9972-9981.
27. Allinger, N. L.; Zhou, X.; Bergsma, J., Molecular mechanics parameters. *Journal of Molecular Structure: THEOCHEM* **1994,** *312* (1), 69-83.
28. Martin, R. L.; Hay, P. J.; Pratt, L. R., Hydrolysis of Ferric Ion in Water and Conformational Equilibrium. *The Journal of Physical Chemistry A* **1998,** *102* (20), 3565-3573.
29. Kelley, M. P.; Su, J.; Urban, M.; Luckey, M.; Batista, E. R.; Yang, P.; Shafer, J. C., On the Origin of Covalent Bonding in Heavy Actinides. *Journal of the American Chemical Society* **2017,** *139* (29), 9901-9908.
30. Deblonde, G. J.-P.; Kelley, M. P.; Su, J.; Batista, E. R.; Yang, P.; Booth, C. H.; Abergel, R. J., Spectroscopic and Computational Characterization of Diethylenetriaminepentaacetic Acid/Transplutonium Chelates: Evidencing Heterogeneity in the Heavy Actinide(III) Series. *Angewandte Chemie International Edition* **2018,** *57* (17), 4521-4526.
31. Kelley, M. P.; Deblonde, G. J. P.; Su, J.; Booth, C. H.; Abergel, R. J.; Batista, E. R.; Yang, P., Bond Covalency and Oxidation State of Actinide Ions Complexed with Therapeutic Chelating Agent 3,4,3-LI(1,2-HOPO). *Inorganic Chemistry* **2018,** *57* (9), 5352-5363.
32. Zhang, X.; Adelman, S.; Arko, B.; De Silva, C.; Su, J.; Kozimor, S.; Mocko, V.; Shafer, J.; Stein, B.; Schreckenbach, G., Advancing the Am Extractant Design through the Interplay

among Planarity, Preorganization, and Substitution Effects. *Inorganic Chemistry* **2022,** *61* (30), 11556-11570.
33. Paulechka, E.; Kazakov, A., Efficient DLPNO–CCSD(T)-Based Estimation of Formation Enthalpies for C-, H-, O-, and N-Containing Closed-Shell Compounds Validated Against Critically Evaluated Experimental Data. *The Journal of Physical Chemistry A* **2017,** *121* (22), 4379-4387.
34. Neese, F., Software update: the ORCA program system, version 4.0. *WIREs Computational Molecular Science* **2018,** *8* (1), e1327.
35. Weigend, F.; Ahlrichs, R., Balanced basis sets of split valence, triple zeta valence and quadruple zeta valence quality for H to Rn: Design and assessment of accuracy. *Physical Chemistry Chemical Physics* **2005,** *7* (18), 3297-3305.
36. Bühl, M.; Sieffert, N.; Golubnychiy, V.; Wipff, G., Density functional theory study of uranium (VI) aquo chloro complexes in aqueous solution. *The Journal of Physical Chemistry A* **2008,** *112* (11), 2428-2436.
37. Parmar, P.; Samuels, A.; Clark, A. E., Applications of polarizable continuum models to determine accurate solution-phase thermochemical values across a broad range of cation charge–the case of U (III–VI). *Journal of chemical theory and computation* **2015,** *11* (1), 55-63.
38. Schreckenbach, G.; Hay, P. J.; Martin, R. L., Density functional calculations on actinide compounds: Survey of recent progress and application to [UO2X4] 2−(X= F, Cl, OH) and AnF6 (An= U, Np, Pu). *Journal of computational chemistry* **1999,** *20* (1), 70-90.
39. Hay, P. J.; Martin, R. L.; Schreckenbach, G., Theoretical Studies of the Properties and Solution Chemistry of AnO22+ and AnO2+ Aquo Complexes for An = U, Np, and Pu. *The Journal of Physical Chemistry A* **2000,** *104* (26), 6259-6270.
40. Gutowski, K. E.; Dixon, D. A., Predicting the energy of the water exchange reaction and free energy of solvation for the uranyl ion in aqueous solution. *The Journal of Physical Chemistry A* **2006,** *110* (28), 8840-8856.
41. Clark, A. E.; Samuels, A.; Wisuri, K.; Landstrom, S.; Saul, T., Sensitivity of solvation environment to oxidation state and position in the early actinide period. *Inorganic chemistry* **2015,** *54* (13), 6216-6225.
42. Knope, K. E.; Soderholm, L., Solution and solid-state structural chemistry of actinide hydrates and their hydrolysis and condensation products. *Chemical Reviews* **2013,** *113* (2), 944-994.
43. Fulton, J. L.; Chen, Y.; Heald, S. M.; Balasubramanian, M., High-pressure, high-temperature X-ray absorption fine structure transmission cell for the study of aqueous ions with low absorption-edge energies. *Review of scientific instruments* **2004,** *75* (12), 5228-5231.
44. Simonet, V.; Calzavara, Y.; Hazemann, J.; Argoud, R.; Geaymond, O.; Raoux, D., X-ray absorption spectroscopy studies of ionic association in aqueous solutions of zinc bromide from normal to critical conditions. *The Journal of chemical physics* **2002,** *117* (6), 2771-2781.
45. Zanonato, P.; Di Bernardo, P.; Bismondo, A.; Liu, G.; Chen, X.; Rao, L., Hydrolysis of uranium (VI) at variable temperatures (10− 85 C). *Journal of the American Chemical Society* **2004,** *126* (17), 5515-5522.

Appendix 5.

5.1. Geometries and Properties

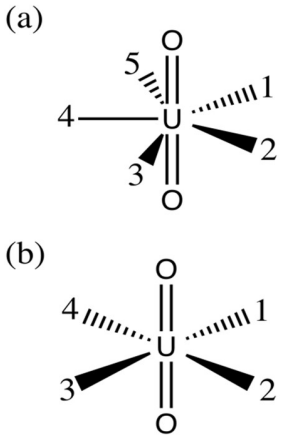

Figure A 5.1. Positions of ligands around the uranyl ion for (a) 5-coordinate species and (b) 4-coordinate species. For corresponding structures, see Table A 5.1.

Table A 5.1 Table A6.1. Calculated uranyl complexes. See Figure A 5.1 for position reference.

Name	Structure	CN	Number of Cl^-	Adjacent Cl^-	Cl^- Positions
S01	$[UO_2(H_2O)_5]^{2+}$	5	0	0	
S02	$[UO_2Cl(H_2O)_4]^{+}$	5	1	0	1
S03	$[UO_2(Cl)_2(H_2O)_3]^{0}$	5	2	2	1 2
S04	$[UO_2(Cl)_2(H_2O)_3]^{0}$	5	2	0	1 3
S05	$[UO_2(Cl)_3(H_2O)_2]^{-}$	5	3	3	1 2 3
S06	$[UO_2(Cl)_3(H_2O)_2]^{-}$	5	3	2	1 2 4
S07	$[UO_2(Cl)_4(H_2O)]^{2-}$	5	4	4	1 2 3 4
S08	$[UO_2(Cl)_5]^{3-}$	5	5	5	1 2 3 4 5
S09	$[UO_2(H_2O)_4]^{2+}$	4	0	0	
S10	$[UO_2Cl(H_2O)_3]^{+}$	4	1	0	1
S11	$[UO_2(Cl)_2(H_2O)_2]^{0}$	4	2	2	1 2
S12	$[UO_2(Cl)_2(H_2O)_2]^{0}$	4	2	0	1 3
S13	$[UO_2(Cl)_3(H_2O)]^{-}$	4	3	3	1 2 3
S14	$[UO_2(Cl)_4]^{2-}$	4	4	4	1 2 3 4

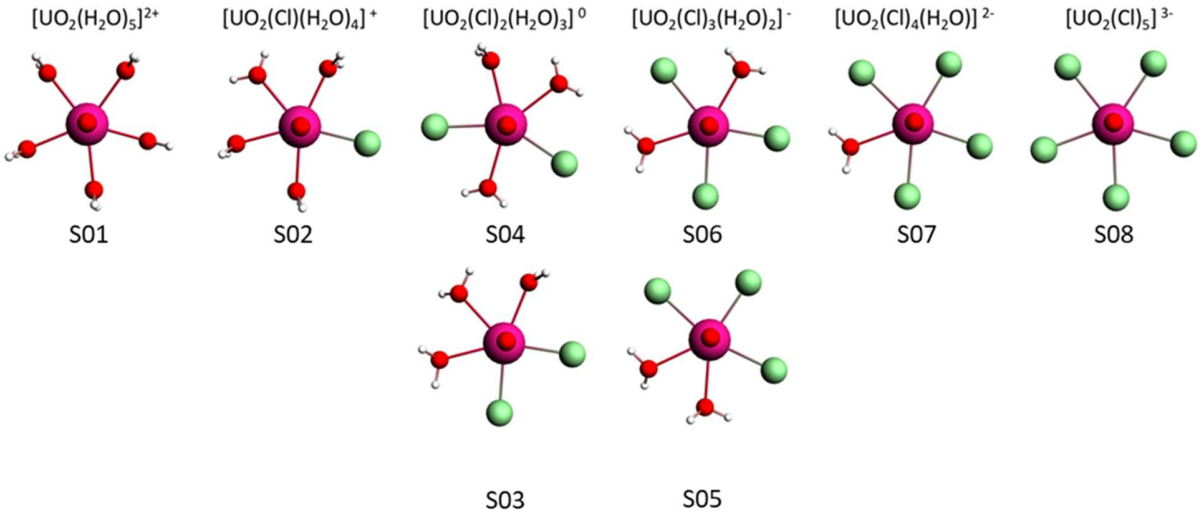

Figure A 5.2 Five coordinate aqueous uranyl-chloride structures; note the energy difference in isomers where the chlorine atoms are positioned adjacently or not are shown in Table A 5.2.

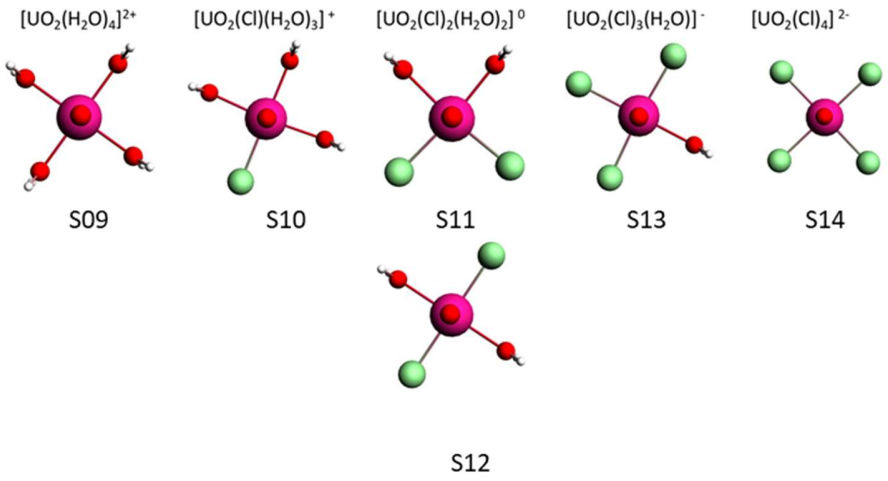

Figure A 5.3 Four coordinate aqueous uranyl-chloride structures; note the energy difference in isomers where the chlorine atoms are positioned adjacently or not are shown in Table A 5.2.

Table A 5.2 Energy terms for uranyl compounds: S03, S04, S05, S06, S11 and S12 at different temperature.

U		S03	S04	S05	S06	S11	S12
CCSD(T) [a]	298K	-30713.93	-30713.95	-31099.62	-31099.64	-30637.49	-30637.50
Solvation [b]		-43.14	-32.08	-75.26	-65.32	-41.83	-33.21
Gcorr [b]		22.36	19.88	7.94	6.81	7.66	6.75
Total [b]		-19273288.65	-19273289.90	-19515359.32	-19515360.32	-19225336.70	-19225333.75
CCSD(T) [a]	623K	-30713.93	-30713.95	-31099.62	-31099.63	-30637.49	-30637.50
Solvation [b]		-37.87	-26.21	-67.57	-60.22	-35.57	-30.36
Gcorr [b]		-20.05	-21.50	-33.65	-35.08	-31.93	-33.06
Total [b]		-19273326.97	-19273327.88	-19515394.84	-19515397.45	-19225371.90	-19225370.89
CCSD(T) [a]	773K	-30713.94	-30713.95	-31099.63	-31099.64	-30637.50	-30637.50
Solvation [b]		-9.30	-8.51	-22.87	-23.10	-10.03	-10.64
Gcorr [b]		-40.88	-43.06	-51.55	-55.52	-50.18	-51.39
Total [b]		-19273325.36	-19273333.37	-19515373.35	-19515382.90	-19225369.35	-19225370.32

[a] Energies are given in Hartree
[b] Energies are given in kcal/mol

Table A 5.3. Energy terms for neptunyl compounds: S03, S04, S05, S06, S11 and S12 at different temperature.

Np		S03	S04	S05	S06	S11	S12
CCSD(T) [a]	298K	-31583.89	-31583.91	-31969.58	-31969.60	-31507.46	-31507.47
Solvation [b]		-41.18	-30.36	-73.53	-64.04	-40.29	-31.03
Gcorr [b]		27.20	27.15	12.65	11.29	11.76	11.55
Total [b]		-19819191.60	-19819190.23	-20061262.13	-20061263.10	-19771241.36	-19771238.24
CCSD(T) [a]	623K	-31583.90	-31583.91	-31969.59	-31969.60	-31507.46	-31507.47
Solvation [b]		-35.24	-24.6	-65.99	-58.96	-35.33	-28.50
Gcorr [b]		-21.56	-19.02	-32.50	-35.06	-31.40	-33.32
Total [b]		-19819236.26	-19819233.27	-20061301.32	-20061304.81	-19771280.92	-19771280.86
CCSD(T) [a]	773K	-31583.91	-31583.92	-31969.59	-31969.60	-31507.47	-31507.47
Solvation [b]		-8.87	-8.05	-22.69	-22.67	-9.80	-9.79
Gcorr [b]		-38.08	-42.68	-50.98	-54.27	-49.19	-54.25
Total [b]		-19819231.62	-19819241.93	-20061281.38	-20061289.49	-19771277.90	-19771283.79

[a] Energies are given in Hartree
[b] Energies are given in kcal/mol

Table A 5.4. Energy terms for plutonyl compounds: S03, S04, S05, S06, S11 and S12 at different temperature.

Pu		S03	S04	S05	S06	S11	S12
CCSD(T) [a]	298K	-32473.35	-32473.37	-32859.04	-32859.04	-32396.91	-32396.92
Solvation [b]		-41.22	-29.61	-73.70	-64.02	-40.91	-30.05
Gcorr [b]		27.61	27.12	12.53	11.00	12.10	12.45
Total [b]		-20377332.65	-20377332.63	-20619403.55	-20619399.05	-20329381.99	-20329378.34
CCSD(T) [a]	623K	-32473.35	-32473.37	-32859.04	-32859.04	-32396.91	-32396.92
Solvation [b]		-35.64	-26.46	-66.04	-59.10	-35.77	-27.46
Gcorr [b]		-19.29	-18.73	-34.52	-34.76	-29.06	-29.79
Total [b]		-20377375.70	-20377376.03	-20619444.73	-20619440.19	-20329419.25	-20329418.23
CCSD(T) [a]	773K	-32473.36	-32473.37	-32859.04	-32859.06	-32396.92	-32396.92
Solvation [b]		-8.88	-7.73	-22.75	-22.70	-9.86	-9.46
Gcorr [b]		-42.37	-43.03	-50.71	-54.90	-47.90	-51.62
Total [b]		-20377378.32	-20377385.38	-20619416.22	-20619432.18	-20329418.27	-20329422.73

[a] Energies are given in Hartree
[b] Energies are given in kcal/mol

Table A 5.5 Hirshfeld charges for uranyl compounds: S03, S04, S05, S06, S11 and S12 at different temperatures.

Position			S03	S04	S05	S06	S11	S12
U			0.7852	0.7952	0.6653	0.6695	0.8263	0.8351
Cl	1		-0.3915	-0.3794	-0.4079	-0.4132	-0.3680	-0.3756
Cl	2	298K	-0.3723		-0.4082	-0.4134	-0.3679	
Cl	3			-0.3632	-0.4312			-0.3756
Cl	4					-0.3958		
U			0.7827	0.7934	0.6660	0.6684	0.8221	0.8287
Cl	1		-0.3807	-0.3557	-0.4008	-0.4073	-0.3565	-0.3677
Cl	2	623K	-0.3618		-0.4011	-0.4073	-0.3565	
Cl	3			-0.3542	-0.4195			-0.3678
Cl	4					-0.3934		
U			0.7790	0.7867	0.6774	0.6743	0.8028	0.7973
Cl	1		-0.2927	-0.3139	-0.3568	-0.3736	-0.2993	-0.3203
Cl	2	773K	-0.2876		-0.3568	-0.3733	-0.2993	
Cl	3			-0.3123	-0.3506			-0.3217
Cl	4					-0.3874		

Table A 5.6 Hirshfeld charges for neptunyl compounds: S03, S04, S05, S06, S11 and S12 at different temperatures.

Position			S03	S04	S05	S06	S11	S12
Np			0.7093	0.7233	0.5911	0.5988	0.7382	0.7429
Cl	1		-0.3800	-0.3757	-0.3992	-0.4002	-0.3575	-0.3594
Cl	2	298k	-0.3629		-0.3989	-0.4005	-0.3575	
Cl	3			-0.3549	-0.4213			-0.3594
Cl	4					-0.4068		
Np			0.7064	0.7203	0.5913	0.5994	0.7371	0.7393
Cl	1		-0.3659	-0.3475	-0.3905	-0.3952	-0.3477	-0.3522
Cl	2	623k	-0.3504		-0.3903	-0.3952	-0.3477	
Cl	3			-0.3457	-0.4092			-0.3521
Cl	4					-0.4042		
Np			0.7000	0.7145	0.6006	0.6056	0.7128	0.7095
Cl	1		-0.2812	-0.3056	-0.3500	-0.3618	-0.2863	-0.3053
Cl	2	773k	-0.2756		-0.3500	-0.3619	-0.2864	
Cl	3			-0.3029	-0.3375			-0.3053
Cl	4					-0.3869		

Table A 5.7 Hirshfeld charges for plutonyl compounds: S03, S04, S05, S06, S11 and S12 at different temperatures.

Position			S03	S04	S05	S06	S11	S12
Pu			0.8397	0.8502	0.7275	0.7347	0.8590	0.8581
Cl	1		-0.4099	-0.3933	-0.4266	-0.4351	-0.3942	-0.3869
Cl	2	298k	-0.3963		-0.4262	-0.4184	-0.3941	
Cl	3			-0.3823	-0.4555			-0.3869
Cl	4					-0.4353		
Pu			0.8353	0.8468	0.7268	0.734	0.8525	0.8533
Cl	1		-0.3951	-0.3854	-0.4178	-0.4284	-0.3818	-0.3793
Cl	2	623k	-0.3817		-0.4175	-0.4286	-0.3818	
Cl	3			-0.3735	-0.4409			-0.3793
Cl	4					-0.4191		
Pu			0.8276	0.8407	0.7325	0.7374	0.8348	0.8253
Cl	1		-0.3106	-0.3262	-0.3743	-0.3921	-0.3214	-0.3309
Cl	2	773k	-0.3061		-0.3743	-0.3920	-0.3215	
Cl	3			-0.3244	-0.3681			-0.3309
Cl	4					-0.4063		

Table A 5.8 Calculated neptunyl Np=O bond lengths (Å) dependence on temperature for five-coordinated structures.

# of Cl-	0	1	2		3		4	5
	S01	S02	S03	S04	S05	S06	S07	S08
25℃	1.739	1.749	1.755	1.753	1.759	1.757	1.762	1.761
350℃	1.737	1.748	1.755	1.753	1.759	1.757	1.762	1.761
500℃	1.732	1.747	1.754	1.750	1.758	1.756		1.759

Table A 5.9 Calculated neptunyl Np=O bond lengths (Å) dependence on temperature for four-coordinated structures.

# of Cl-	0	1	2		3	4
	S09	S10	S11	S12	S13	S14
25℃	1.737	1.746	1.756	1.756	1.762	1.766
350℃	1.736	1.748	1.756	1.756	1.761	1.766
500℃	1.730	1.746	1.757	1.756	1.757	1.764

Table A 5.10 Calculated Np-Cl bond lengths (Å) for for five-coordinated structures at different temperatures.

# of Cl-	1	2		3		4	5
	S02	S03	S04	S05	S06	S07	S08
25℃	2.657	2.673	2.704	2.690	2.714*	2.745*	
		2.688		2.751*	2.788	2.822*	2.853**
350℃	2.643	2.662	2.687	2.681	2.707*	2.738*	
		2.678		2.748*	2.804	2.833*	2.840**
500℃	2.589	2.633*	2.677	2.621	2.682*		2.878**
			2.686	2.774*	2.887		2.889**
							2.926

*Average bond length of two nearly equivalent Np-Cl bonds.
**Average bond length of four nearly equivalent Np-Cl bonds.

Table A 5.11 Calculated Np-Cl bond lengths (Å) for four-coordinated structures at different temperatures.

# of Cl-	1	2		3	4
	S10	S11	S12	S13	S14
25°C	2.630	2.641*	2.653*	2.660	
				2.677*	2.699**
350°C	2.599	2.633*	2.646*	2.660	
				2.678*	2.703**
500°C	2.552	2.590*	2.615*	2.632	
				2.657	
				2.722	2.725**

*Average bond length of two nearly equivalent Np-Cl bonds.
**Average bond length of four nearly equivalent Np-Cl bonds.

Table A 5.12 Calculated average Np-water bond lengths (Å) for five-coordinated structures at different temperatures.

# of Cl-	0	1	2		3		4
	S01	S02	S03	S04	S05	S06	S07
25°C	2.444	2.483	2.548	2.522	2.598	2.562	2.619
350°C	2.443	2.497	2.564	2.535	2.618	2.569	2.638
500°C	2.467	2.528	2.629	2.562	2.695	2.598	

Table A 5.13 Calculated average Np-water bond lengths (Å) for four-coordinated structures at different temperatures.

# of Cl-	0	1	2		3
	S09	S10	S11	S12	S13
25°C	2.369	2.394	2.423	2.411	2.443
350°C	2.373	2.403	2.436	2.418	2.451
500°C	2.398	2.444	2.516	2.479	2.593

Table A 5.14 Calculated uranyl Pu=O bond lengths (Å) dependence on temperature for five-coordinated structures.

# of Cl-	0	1	2		3		4	5
	S01	S02	S03	S04	S05	S06	S07	S08
25°C	1.721	1.730	1.736	1.736	1.741	1.740	1.744	1.745
350°C	1.721	1.730	1.737	1.737	1.741	1.741	1.744	1.745
500°C	1.716	1.734	1.737	1.734	1.741	1.739		1.744

Table A 5.15 Calculated uranyl Pu=O bond lengths (Å) dependence on temperature for four-coordinated structures.

# of Cl-	0	1	2		3	4
	S09	S10	S11	S12	S13	S14
25°C	1.720	1.730	1.738	1.738	1.744	1.748
350°C	1.719	1.730	1.739	1.739	1.744	1.748
500°C	1.714	1.731	1.740	1.740	1.740	1.747

Table A 5.16 Calculated Pu-Cl bond lengths (Å) for for five-coordinated structures at different temperatures.

# of Cl-	1	2		3		4	5
	S02	S03	S04	S05	S06	S07	S08
25℃	2.654	2.675	2.695	2.694	2.724*	2.747*	
		2.693	2.706	2.748*	2.762	2.820*	2.834**
350℃	2.643	2.661	2.686	2.679	2.717*	2.738*	
		2.681	2.697	2.749*	2.769	2.828*	2.835**
500℃	2.608	2.636	2.675*	2.662	2.688*		
				2.774*	2.849		2.890**

*Average bond length of two nearly equivalent Pu-Cl bonds.
**Average bond length of four nearly equivalent Pu-Cl bonds.

Table A 5.17 Calculated Pu-Cl bond lengths (Å) for for four-coordinated structures at different temperatures.

# of Cl-	1	2		3	4
	S10	S11	S12	S13	S14
25℃	2.614	2.645*	2.647*	2.670	
				2.674*	2.695**
350℃	2.599	2.631*	2.64*	2.664	
				2.670*	2.696**
500℃	2.542	2.594*	2.607*	2.632	
				2.652	
				2.710	2.718**

*Average bond length of two nearly equivalent Pu-Cl bonds.
**Average bond length of four nearly equivalent Pu-Cl bonds.

Table A 5.18 Calculated average Pu-water bond lengths (Å) for five-coordinated structures at different temperatures.

# of Cl-	0	1	2		3		4
	S01	S02	S03	S04	S05	S06	S07
25℃	2.433	2.480	2.538	2.516	2.590	2.550	2.612
350℃	2.431	2.486	2.545	2.518	2.598	2.558	2.617
500℃	2.452	2.522	2.612	2.554	2.674	2.589	

Table A 5.19 Calculated average Pu-water bond lengths (Å) for four-coordinated structures at different temperatures.

# of Cl-	0	1	2		3
	S09	S10	S11	S12	S13
25℃	2.354	2.380	2.402	2.398	2.417
350℃	2.356	2.382	2.410	2.400	2.422
500℃	2.379	2.429	2.492	2.459	2.575

5.2. Calculated Raman and IR spectrum

Table A 5.20 Calculated Np=O Raman and IR peaks from aqueous neptunyl chloride

5-coordinate						4-coordinate				
# of Cl			25ºC	350ºC	500ºC	# of Cl			25ºC	350ºC	500ºC
0	S01	Raman	913	916	933	0	S09	Raman	918	922	939
		IR	975	981	1019			IR	979	985	1025
1	S02	Raman	883	885	895	1	S10	Raman	889	887	898
		IR	948	953	981			IR	953	953	984
2	S03	Raman	862	864	874	2	S11	Raman	862	862	868
		IR	929	934	961			IR	927	929	953
	S04	Raman	866	867	881		S12	Raman	861	862	870
		IR	934	938	970			IR	928	931	959
3	S05	Raman	849	850	861	3	S13	Raman	844	845	861
		IR	919	923	949			IR	911	915	950
	S06	Raman	853	854	865						
		IR	922	926	954						
4	S07	Raman	839	841	847	4	S14	Raman	829	830	842
		IR	911	916	937			IR	898	902	932

Table A 5.21 Calculated Pu=O Raman and IR peaks from aqueous plutanyl chloride

5-coordinate						4-coordinate				
# of Cl			25ºC	350ºC	500ºC	# of Cl			25ºC	350ºC	500ºC
0	S01	Raman	906	907	923	0	S09	Raman	911	912	928
		IR	984	988	1023			IR	988	992	1027
1	S02	Raman	874	876	880	1	S10	Raman	877	876	884
		IR	958	963	988			IR	959	961	989
2	S03	Raman	853	851	863	2	S11	Raman	852	852	857
		IR	941	939	967			IR	937	939	961
	S04	Raman	855	855	869		S12	Raman	852	850	856
		IR	943	945	974			IR	937	939	962
3	S05	Raman	839	830	847	3	S13	Raman	833	834	850
		IR	929	934	954			IR	920	924	956
	S06	Raman	841	840	852						
		IR	930	932	958						
4	S07	Raman	827	828	835	4	S14	Raman	819	820	829
		IR	919	922	942			IR	909	912	937

Chapter 6. Reduction of Uranium(VI) at the Surface of Titanium Dioxide (TiO_2)

6.1. Introduction

Nuclear power provides a critical tool for meeting the demand of increasing energy supply and facing the challenge of climate change with its unparalleled energy density, while at the same time reducing greenhouse gas emissions. However, the world's amount of terrestrial uranium reserves is limited. The uranium ore resources may be exhausted within a century.[1-3] On the other hand, the uranium in the oceans is estimated to be about 4.5 billion tons.[4] Thus, the seawater uranium extraction became a focus of research over the past 60 years.[1, 5-7] Besides, the separation of U(VI) from waste water and at contaminated sites is also very important to prevent nuclear pollution due to highly mobile uranyl(VI). Therefore, efficient, economical, and environmentally friendly methods for extracting uranium from seawater and nuclear wastewater are needed. Compared to the traditional technologies, such as ionic exchange, ultrafiltration, adsorption, and evaporation, [8-14] controlling the oxidation states of uranium species is a potential way to efficiently separate uranium from aqueous solutions, namely, reducing the highly soluble U(VI) ion to insoluble U(IV) oxides.

The uranyl(VI) ion has been studied a lot in this thesis because it is the dominant form of uranium in the environment due to its high stability and solubility. The stability of the uranyl(VI) ion arises from the strongly covalent oxo groups with formally triple bonds. However, in an anaerobic environment, the one-electron $[U(VI)O_2]^{2+}$ to $[U(V)O_2]^{+}$ reduction can be achieved by minerals and microbes.[15] The less soluble U(V) can then disproportionate into U(VI) and U(IV) under the same conditions.[16] Interest in studying uranyl(V) compounds is increasing because of

the ability to bridge to other metals via more Lewis-basic oxo groups compared to *d*-block chemistry;[15, 17] for example, Chapter 2 in this thesis. The $[U(V)O_2]^+$ ion is also a key intermediate in uranyl(VI) photochemistry.[18] The $[U(VI)O_2]^{2+}$ photochemistry has many potential applications, such as metal ion sensing and biochemistry. [19-21] The photochemistry of $[U(VI)O_2]^{2+}$ is usually activated by exposing it to ultraviolet (UV) and near-UV light sources to generate an excited compound $[*UO_2]^{2+}$ and then form an $[U(V)O_2]^+$ intermediate with $5f^1$ electron configuration.[15] The $[U(V)O_2]^+$ intermediate contains an oxyl radical, O·, which has extreme reactivity. These two reaction paths are summarized in Scheme 6.1.[15]

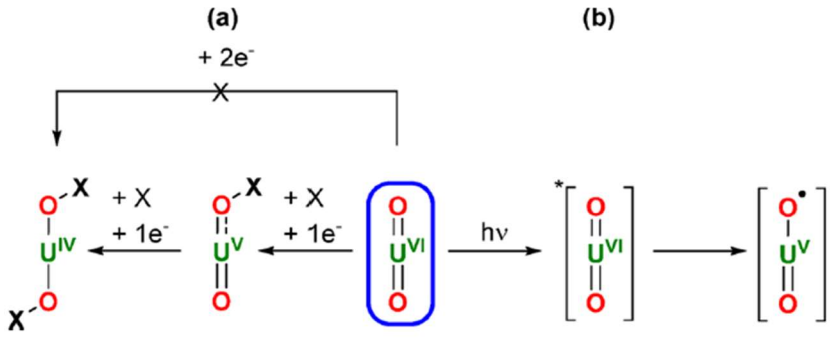

Scheme 6.1 (a) Thermal and (b) photochemical reductions of the uranyl ion. (Figure reproduced from reference 15)

However, without photocatalysts, direct photoreduction of U(VI) by UV light does not occur,[1] which has been confirmed by previous studies.[22, 23] The discovery of photocatalytic splitting of water on TiO_2 electrodes by Fujishima and Honda in 1972[24] is the beginning of a new era of heterogeneous photocatalysis. Because of its exceptional properties, chemical stability, nontoxicity, and low cost, TiO_2 has been widely used as photocatalysts until now.[25-29] The first reduction of uranyl on a TiO_2 surface under UV light was reported by Amadelli et al.[30] Many subsequent investigations of U(VI) photocatalytic reduction with UV-illuminated TiO_2 were carried out successfully by several researchers.[22, 23, 31-40] The TiO_2 provides a possible approach for

the photocatalytic reduction and extraction of U(VI) under different conditions. However, most mechanisms were proposed according to the experimental phenomena and aqueous uranium ions chemistry instead of direct evidence. [1] The mechanism behind U(VI) photocatalytic reduction still remains unclear.

The photocatalytic reduction of U(VI) was proposed via a two-electron reduction process[23, 33, 39, 41-44]:

$$U(VI) + 2e^- \rightarrow U(IV) \quad (6.1)$$

However, other researchers augured that the two electron-reduction is just the overall process of U(VI) reduction and a one-electron reduction process is the first step in the U(VI) photocatalytic reduction[31-34, 45-49]:

$$U(VI) + e^- \rightarrow U(V) \quad (6.2)$$

Then, further reduction can occur by either a second one-electron reduction[31, 32, 34, 46, 49]:

$$U(V) + e^- \rightarrow U(IV) \quad (6.3)$$

Or by U(V) disproportionation[16, 50, 51]:

$$2U(V) \rightarrow U(VI) + U(IV) \quad (6.4)$$

Another mechanism was also proposed where the U(VI) is reduced by $\cdot O_2^-$ radical[37, 52] or reductive organic radical intermediates[39], which are generated by oxidative ·OH from holes of photocatalytic processes.

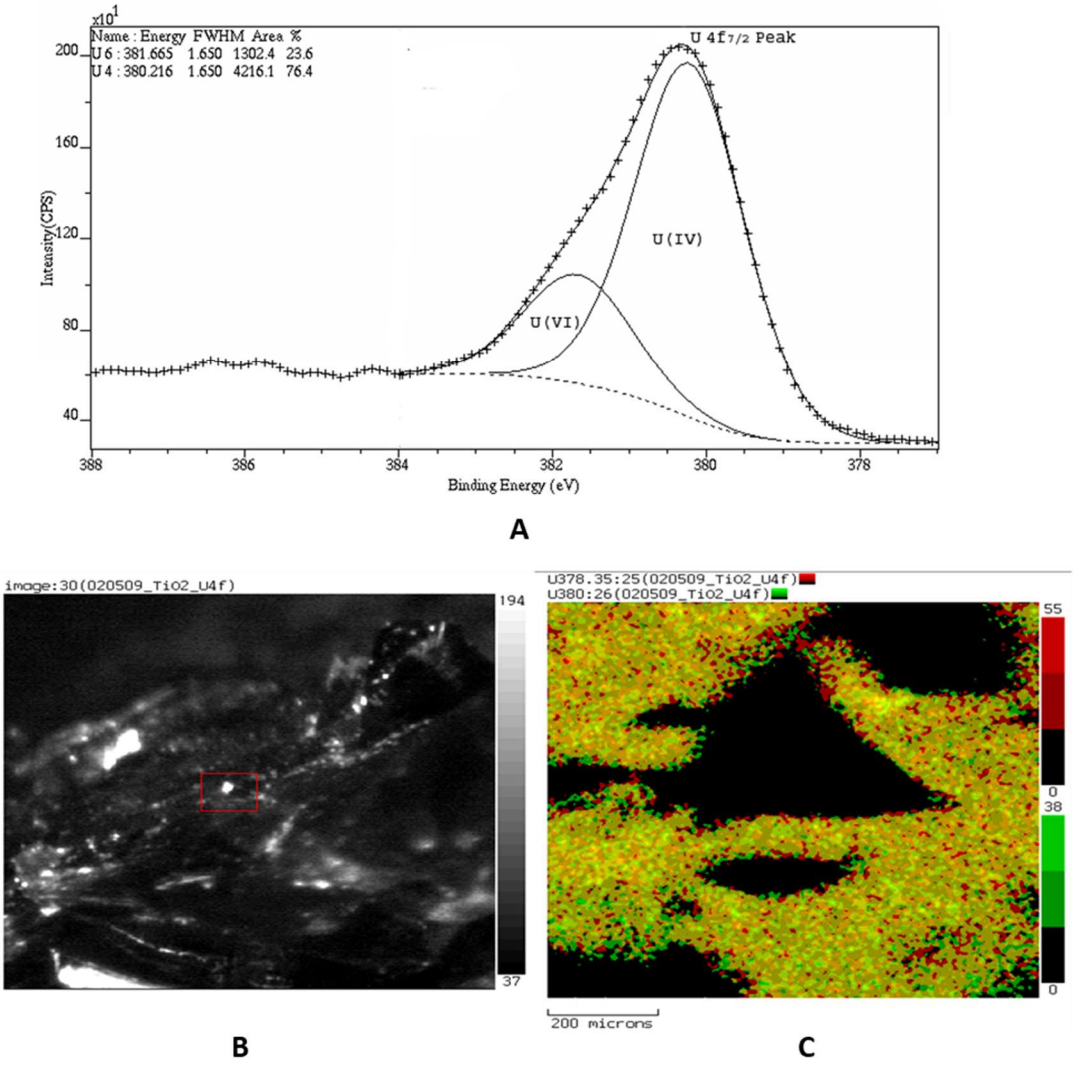

Figure 6.1 A) Uranium 4f XPS spectrum recorded from the surface of a rutile grain after exposure to 16.8 µM uranyl(VI) (unlabelled peaks are satellite peaks); B) Image of the analyzed rutile grain; the red square encompasses the analyzing spot. C) Elemental distribution map for the spot analyzed; red color shows U(IV) and green shows U(VI).[53]

In a natural environment, TiO_2 might be useful in subsurface environments as a passive reductant. Interestingly, there is some evidence showing that the reduction of the uranyl(VI) ion can occur without reducing minerals, organic compounds, microbes, or UV light, even in a dark environment. A recent imaging study using back-scattered electrons and high-resolution transmission electron microscopy revealed that the uranium contained in the Pozos conglomerate rock unit below the Nepal I uranium deposit, Mexico, is in the form of uraninite $U(IV)O_2$ in a dark

environment.[54] An unpublished study investigating the oxidation states of uranium sequestrated onto TiO_2 has been carried out by Fayek et al.[53] Contrary to the field conditions, no organic or other mineral species were present to facilitate reduction. XPS spectra (Figure 1) of a rutile grain (>175 μm) after being exposed to a 16.8 μM uranyl(VI) solution for 2 months in a laboratory system at room temperature show that both U(IV) and (UVI) were present at the surface, with reduced U(IV) being the dominant species (76.4 %, Figure 1A). Furthermore, U(IV) was found mainly distributed along the boundaries of the rutile grain, whereas U(VI) was distributed relatively evenly on the grain surface (Figure 1C). Similar results were obtained for anatase grains exposed to 4.2 mM uranyl(VI) for 3 months. Bonato et al.[34] reported that they found an XPS peak of U(IV) at the TiO_2 surface when TiO_2 nanotubes were exposed to a uranyl(VI) solution. Furthermore, their XPS spectra showed that 75±5% of the uranium on the anatase nanotubes was U(IV) in the darkness (which agreed very well with Fayek's value of 76.4% U(IV) on the rutile surface, Figure 1A); the presence of UV light only increased this to 89±5%. This may indicate that a process other than UV-induced photocatalytic reduction is primarily responsible for the observed U(VI) reduction on the TiO_2 surface. *We thus propose that the additional electrons which reduce U(VI) on the TiO_2 surface come from uranium decay*.

There are three kinds of radiation, α, β, and γ, occurring in uranium decay. The radiolysis of water due to ionizing radiation results in the production of electrons, H·, ·OH radicals[55] which may be captured by the TiO_2 surface and then further reduce U(VI). α radiation bombardment of the TiO_2 surface may also generate defect sites and bring TiO_2 into an excited state or form radicals for reducing U(VI). β radiation, in fact, is an electron beam that contains electrons to reduce U(VI) directly. In addition to ionizing water, γ radiation consists of packets of electromagnetic energy (photons) which can excite TiO_2 to generate e^- and hole+ like UV radiation. Suppose the e- and

hole+ model still is primarily responsible for the observed reduction. In that case, the reason why the presence of UV light only increased the reaction yield slightly may be that the γ radiation and the other radioactive decay processes already support a sufficient number of e^-/ $hole^+$ pairs.

TiO_2 nanoparticles play a critical role in a wide range of different technological applications. Different theoretical models for TiO_2 have been used to complement experiments. In the previous study of our group by Odoh et al.[45], uranyl complexes on clean stoichiometric and non-stoichiometric TiO_2 systems were modeled using periodic DFT calculations on a rutile (110) surface and molecular DFT calculations on an anatase cluster model respectively. The TiO_2 surface of periodic calculations was a rutile (110) slab containing 192 atoms and a surface hydroxyl or an oxygen vacancy defect induced in the periodic rutile (110) slab. Anatase nanoparticles were represented by a $Ti_{38}O_{76}$ cluster model which was about 12 Å × 16 Å in size. This theoretical study showed that, electronically, because the empty 5*f* states of the adsorbed uranyl complexes were below the Ti-3d conduction band, the charge-transfer mechanism, which is O-2p →Ti-3d → U-5f, is most likely responsible for the photoreduction of U(VI) on TiO_2 surfaces. This study showed that the electron which transfers from surface oxygen vacancies and hydroxyls defects, does not appear to be able to reduce U(VI) under dark conditions because the oxygen vacancy states have lower energy than the empty 5*f* states. However, the non-stoichiometric anatase cluster calculations showed that a small portion of the singly occupied molecular orbital (SOMO) is located on the uranyl moiety. However, this is most likely an artefact of the geometry optimization with the GGA functional.

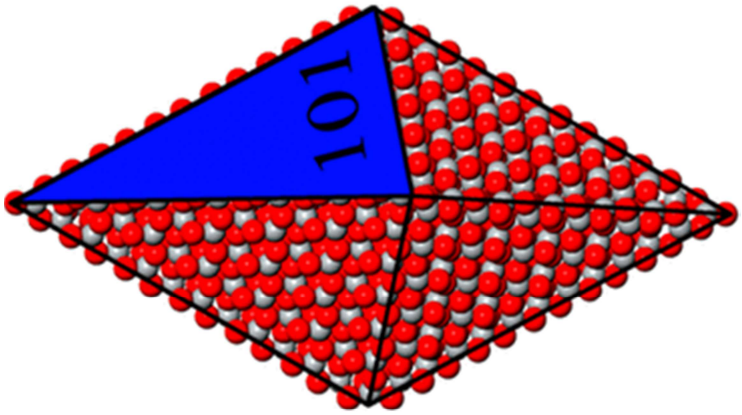

Scheme 6.2 Schematic representation of the octahedral TiO_2 anatase nanoparticles featuring (101) surfaces. (Figure reproduced from reference 56)

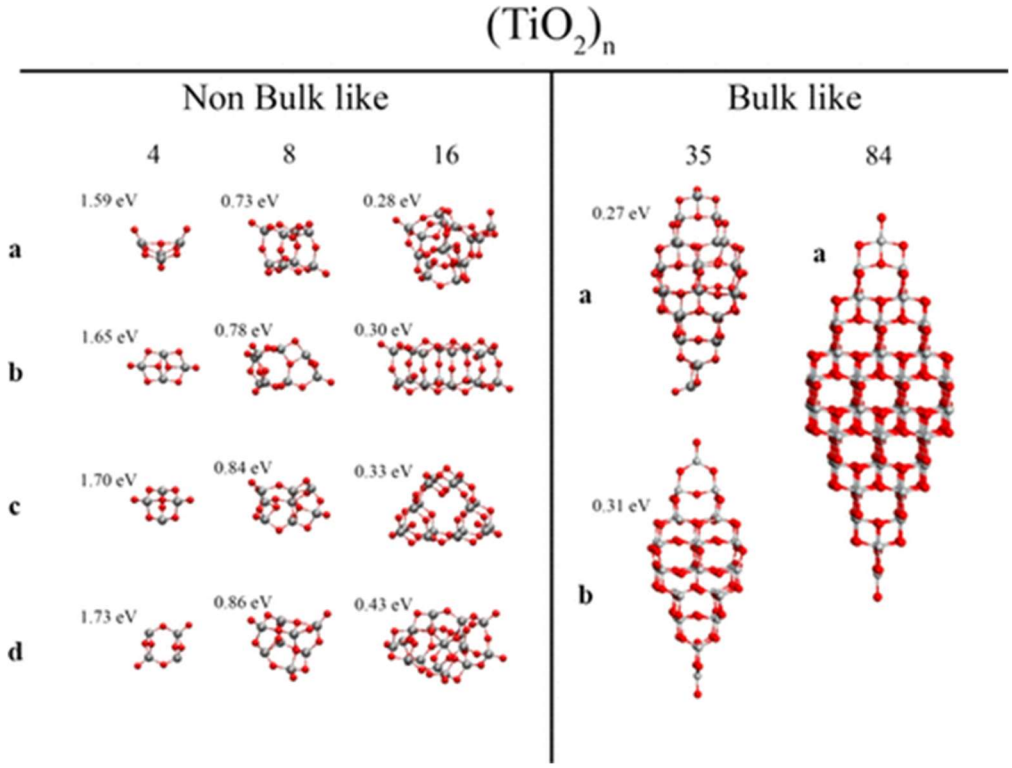

Figure 6.2 Optimized structures of the four isomers of $(TiO_2)_4$, $(TiO_2)_8$, and $(TiO_2)_{16}$ studied (left) and the bulk-cut structures for $(TiO_2)_{35}$ and $(TiO_2)_{84}$ (right). Relative total energies per TiO_2 unit are given relative to that of the $(TiO_2)_{84}$ nanoparticle. (Figure and figure caption taken directly from reference 57)

To further investigate the performance of TiO_2 anatase nanoparticles with an adsorbed uranyl moiety, an octahedral TiO_2 anatase nanoparticle cluster was introduced in the current study,

which exhibits the most stable (101) anatase surfaces, see Figure 6.2.[56] Lamiel-Garcia et al. studied the relative stability, atomic, and electronic structure of a series of stoichiometric TiO_2 anatase nanoparticles as a function of size and morphology using all electron relativistic density functional theory (DFT) with numerical atom-centered orbitals.[56, 57] Their calculations suggest that, when TiO_2 nanoparticles reach approximately 2–3 nm in diameter, the anatase-like crystallinity emerges, [57] as Figure 6.3 shows. Their results show that the electronic structure of TiO_2 clusters depends more on their geometry structure than on their size. They further extended the study to $(TiO_2)_n$ clusters with up to 1365 atoms, [56] which showed that the properties start to converge at n=35, see Figure 6.4. Thus, the $(TiO_2)_{35}$ cluster was selected in this study also due to the computational cost. This cluster offers both edges and surfaces, which is useful since Fayek et al. had found that U(IV) is mainly distributed along the boundaries, *vide supra*. Besides, the TiO_2 (101) surface contains amounts of Ti_{5c} (unsaturated 5-fold-coordinated Ti). The investigation of interactions between uranyl species and surface Ti atoms was not included in the previous study of our group by Odoh et al. [45] Because the presence of water may result in heavily hydroxylated nanoparticles, the solvent effect cannot be easily represented by implicit solvation models and needs further study on the appropriate surface and its potential effects on electronic structures. There are many studies about surface hydration for particles of anatase, however, most of them are on idealized 2-D periodic surfaces. Daniel et al. reported that nearly all H_2O molecules (96%) on anatase particles remained stable as associated $Ti–OH_2$ using of finite 3-D nanoparticles.[58] Therefore, because the nature of the bonding between uranium and anatase nanoparticles is the primary interest of this study, to avoid the interruptions from water molecules, a dry TiO_2 cluster model was applied in this study. However, the first water shell of uranyl was still included because the previous study by Odoh et al. [45] shows that the coordinated water will shift the energy of the empty 5*f* states. The defects by

oxygen vacancies are not included in this study because they are likely to be active sites for the adsorption of uranyl cations which would exclude them as electron donors for further electron transfer. What is more, they are also traps for photoexcited charged carriers, and there may be some competition between those sites and uranium center for trapping electrons. The work of Odoh et al.[45] also supports this by showing that oxygen vacancies states have lower energies than empty 5*f* orbitals. However, the surface defects by hydroxyl are investigated by replacing terminal oxygen atoms by hydroxyl groups. The adsorption positions of uranium are illustrated in **Scheme 6.2** as **Sites 1**, **2** and **3**, which relate to the (101) surface, short edge, and long edge adsorption site on the TiO_2 cluster.

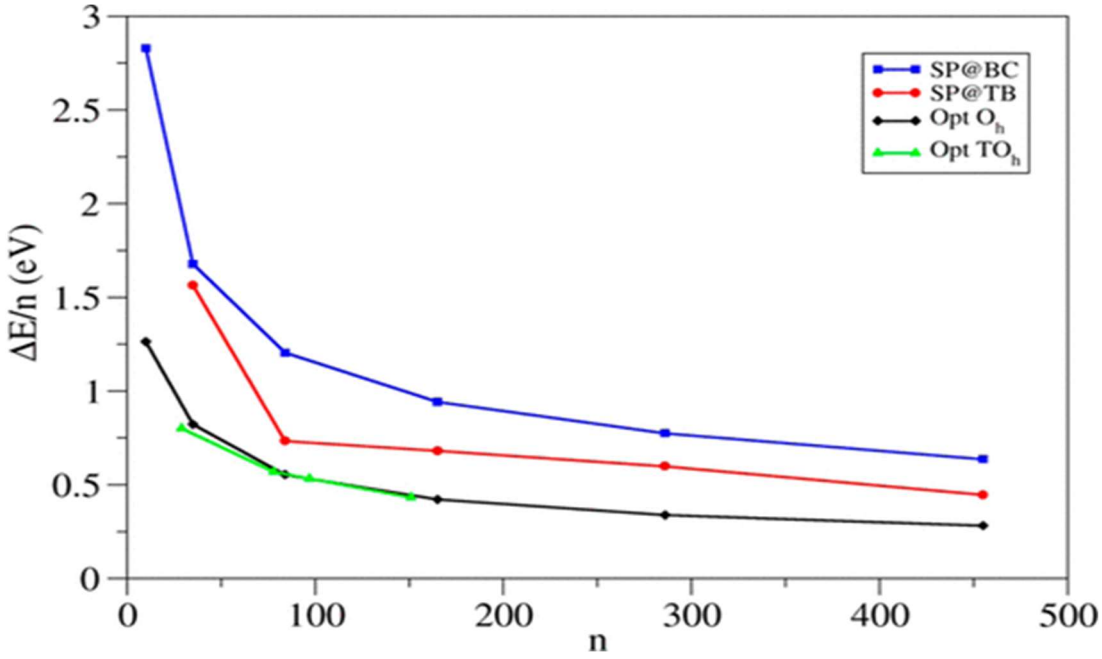

Figure 6.3 Energy per TiO_2 unit relative to anatase ($\Delta E/n$) for the different O_h and TO_h $(TiO_2)_n$ nanoparticles studied in the study of Lamiel-Garcia et al.[56] obtained from calculations using the PBE functional. For comparison, the values corresponding to the unrelaxed structure cut from bulk and to the tight-binding relaxed structures from Barnard et al. are also shown.[59] Blue squares correspond to single point calculations using the bulk cut structures (SP@BC), red dots correspond to single point calculations using the tight-binding relaxed structures (SP@TB), black diamonds correspond to the optimized octahedral (O_h) structures (Opt O_h), and green triangles correspond to the optimized truncated octahedral (TO_h) structures (Opt TO_h). (Figure and figure caption taken directly from reference 56.)

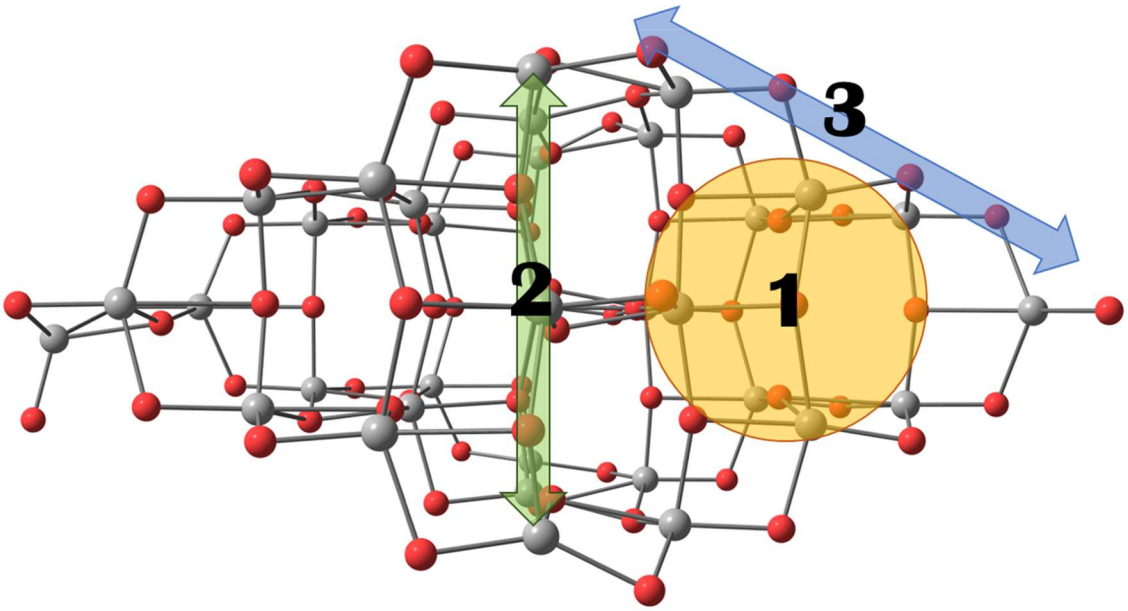

Scheme 6.3 Uranium adsorption positions on the $(TiO_2)_{35}$ cluster in this study. Yellow circle indicates (101) surface, and green and blue arrows indicate edges.

6.2. Computational details

Unless otherwise noted, all the electronic structure calculations presented in this chapter were carried out with the PBE0 functional[60, 61] and scalar ZORA using the ORCA program[62]. The SARC-ZORA-TZVP basis set[63, 64] was used for uranium, and the ZORA-def2-TZVP basis set[65] was used for the other light atoms.

To further understand the fundamental factors that drive bonding and separation, various analysis methods were used to analyze the bonding nature of the molecules. In particular, Hirshfeld charge analysis[66] was used to represent the charge rearrangement and distribution because it agrees well with conventional chemical intuition and was thus used in previous studies where it explained experimental results.[67, 68] Energy decomposition analysis (EDA)[69, 70] and its extension, the extended transition state method for energy decomposition analysis combined with the natural orbitals for chemical valence theory (ETS-NOCV)[71], provided rationalization of the ligand-metal

interactions using the MultiWFN package.[72] Note that the energies of NOCV orbitals in Multiwfn are not calculated in the strict way of the standard ETS-NOCV method as described in Chapter 1 because the F^{TS} in the ETS-NOCV analysis currently is not available in Multiwfn. Instead, in this chapter, Multiwfn generates the actual Fock matrix of the complex directly, based on the orbital energies and coefficients recorded in the input file via the $F = SCEC^{-1}$ relationship. Thus, the i^{th} NOCV orbital energy will be evaluated as $\langle \varphi i | \hat{F} | \varphi i \rangle$, where $\hat{F}$ is the Fock operator corresponding to the generated Fock matrix mentioned above. Hence, ΔE_{orb} is not exactly equal to the sum of energies of all NOCV orbitals or pairs given by Multiwfn.

6.3. Results and discussions

6.3.1. TiO_2 cluster

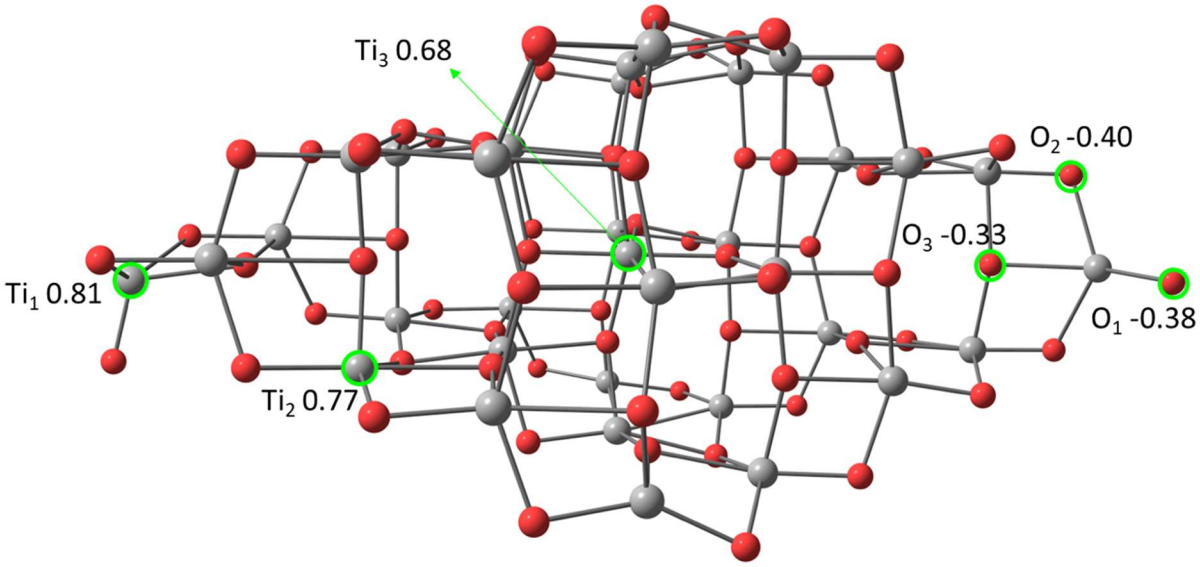

Figure 6.4 Optimized structure of the $(TiO_2)_{35}$ cluster and the Hirshfeld charges for unique atoms. Oxygen and titanium correspond to red and grey spheres respectively. $Ti_{1\text{-}3}$ and $O_{1\text{-}3}$ are labeled for easy identification, where Ti_1 is a terminal titanium atom, Ti_2 is a surface titanium atom, Ti_3 is a non-surface titanium atom in the center of the $(TiO_2)_{35}$ cluster, O_1 is is a terminal oxygen atom, O_2 is is a bridge oxygen atom, and O_3 is an oxygen atom with η-3 coordination.

Table 6.1 Calculated Mulliken, Hirshfeld, Voronoi deformation density (VDD), Löwdin, and Bader charges for the labeled atoms in Figure 6.4.

Atom	Mulliken	Löwdin	Hirshfeld	VDD	Bader
Ti_1	1.09	0.25	0.81	0.64	2.11
Ti_2	1.22	0.27	0.77	0.66	2.28
Ti_3	1.88	0.14	0.68	0.65	2.37
O_1	-0.37	-0.04	-0.38	-0.32	-0.86
O_2	-0.56	-0.12	-0.40	-0.33	-1.09
O_3	-0.69	-0.03	-0.33	-0.29	-1.17

Figure 6.5 shows the optimized $(TiO_2)_{35}$ cluster. The different types of Ti and O atoms are labeled with green circles. The atomic charges for these atoms are summarized in Table 1. The Mulliken charges[73] give the order in absolute terms as $Ti_1 \approx Ti_2 < Ti_3$ and $O_1 < O_2 < O_3$. The Mulliken atomic charge for Ti_3 is almost twice that of Ti_1. The situation is similar for O_3 and O_1. The Löwdin charges[74] are an improvement over Mulliken charges. They give the order (in absolute terms) as $Ti_1 \approx Ti_2 > Ti_3$ and $O_1 \approx O_3 < O_2$. The charge of Ti_3 is only half that of Ti_1 and Ti_2, and those of O_1 and O_3 are much smaller than the O_2 charge. The two methods considered so far, Mulliken population analysis and its improvements, are based on the wave function representation with basis functions. The half-half partitioning of the Mulliken population analysis usually yields unphysical charges. On the other hand, methods based on the electron density as a function in space are usually recommended because they yield chemically meaningful charges. The Hirshfeld [66]and VDD charges[75] provide very similar results. Though Bader charges[76] have occasionally been criticized,[75] they still show similar results as the Hirshfeld and VDD charges. The Hirshfeld, VDD, and Bader methods show that the atomic charges of Ti_{1-3} and O_{1-3} atoms are very close to each other. These confirm that the $(TiO_2)_{35}$ cluster is converged and stable.

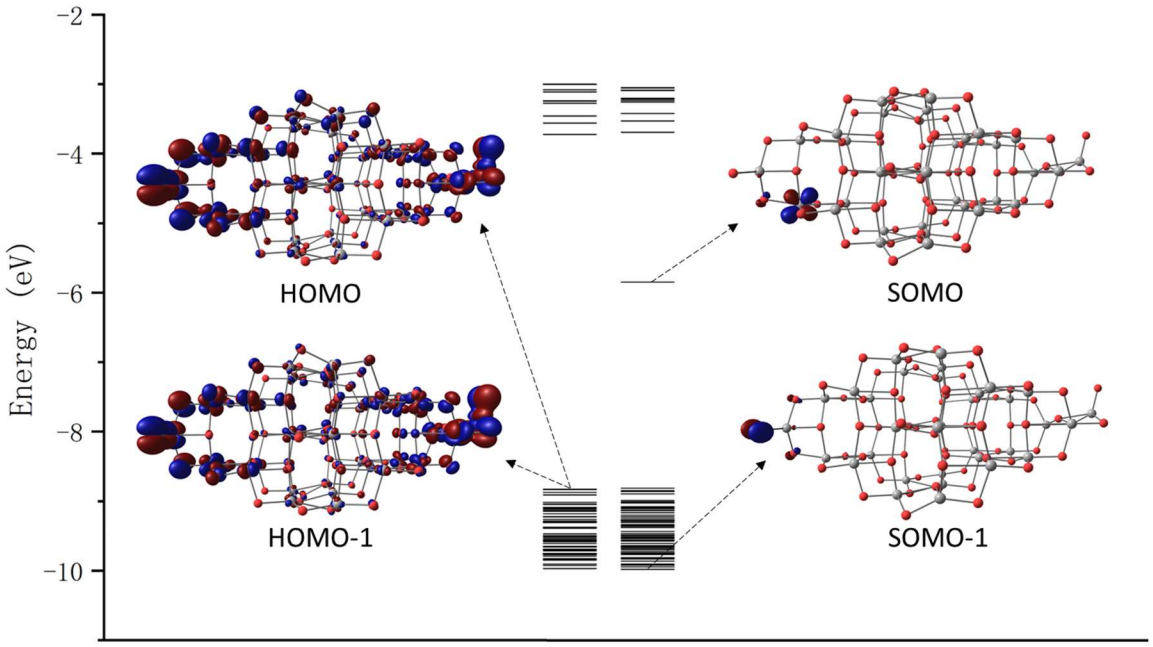

Figure 6.5 Electronic energy levels and MOs of the singlet (left) and triplet (right) states of the $(TiO_2)_{35}$ anatase cluster.

The calculated singlet-triplet gap of the $(TiO_2)_{35}$ anatase cluster is 66.4 kcal/mol. Figure 6.6 shows MO energy diagrams and selected MOs of the $(TiO_2)_{35}$ anatase cluster in the singlet and triplet states. The HOMO and HOMO-1 of the singlet state are two degenerate orbitals of O-2p character dominated by terminal Ti=O units. The HOMO and HOMO-1 indicate that the valence electrons in the terminal Ti=O bonds might firstly be excited to virtual orbitals of dominant Ti-3d character upon photoexcitation. The energy gap between HOMO and LUMO is about 4 eV, which is higher than the normal band gap of anatase TiO_2 of about 3.2 eV. Lamiel-Garcia et al. [56] suggested that this is due to PBE0 overestimating the band gaps of TiO_2 clusters. However, the work of Dette et al.[77] indicated that this can also be explained as the band gap of the oxygen terminated surface, see Figure 6.7. When an actinide compound is adsorbed on the surface of a

TiO_2 cluster, these excited electrons can be trapped in the actinide 5*f* orbitals. The SOMO and SOMO-1 orbitals of the triplet state of the $(TiO_2)_{35}$ anatase cluster relate to the hole on the terminal oxygen atom and an electron on a neighboring titanium atom which confirms that the terminal Ti=O bond will be broken first during photoexcitation. However, electronic transitions from the ground (singlet) state to the excited triplet states are spin forbidden. The transitions might still occur by intersystem crossing with the help of strong spin-orbit effect from the heavy actinide atoms. But it also indicates that the probability for the photoreduction pathway initiated by direct excitation into the lowest triplet states is low.

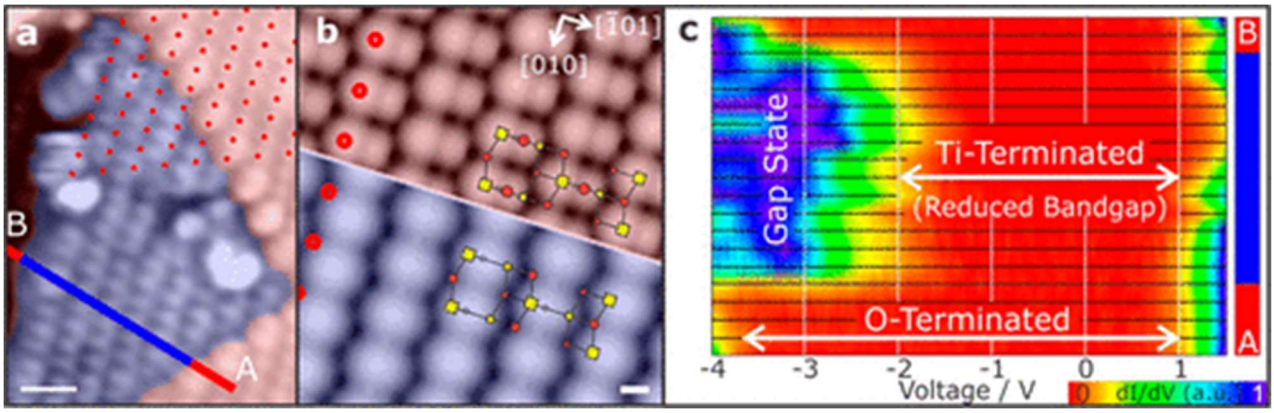

Figure 6.6 Electronic structure and topography of the Ti-terminated surface of TiO_2 anatase (101). (a) Atomic resolution STM image (V_s = 2.0 V, I = 0.1 nA) reveals a Ti-terminated patch (blue) embedded in an oxygen-terminated terrace (red). (b) DFT-calculated STM images of the oxygen- and titanium-terminated (101) surfaces for a positive bias voltage of 1 eV. The overlaid models indicate the atomic positions of the Ti (yellow rectangles) and O (red circles) atoms on the surface. The red dotted lines in (a) and (b) highlight the offset of the bright protrusions between the two different phases. (c) Top view of a waterfall plot of tunneling spectra taken on the line in (a). The variance in the CBM is an artifact due to the normalization of the differential conductance to 1 (see Supplementary Figure S4 in reference [77]). The spectra recorded at the O-terminated surface (red lines) reveal the common featureless bandgap of ~4 eV. The spectra on the blue line which are taken on the Ti-termination show a reduced bandgap (2 eV) due to the bandgap state at −3.3 V (scalebars: (a) 1 nm, (b) 2 Å). (Figure and figure caption taken directly from reference 77.)

6.3.2. Uranyl(VI) and (V) bonding

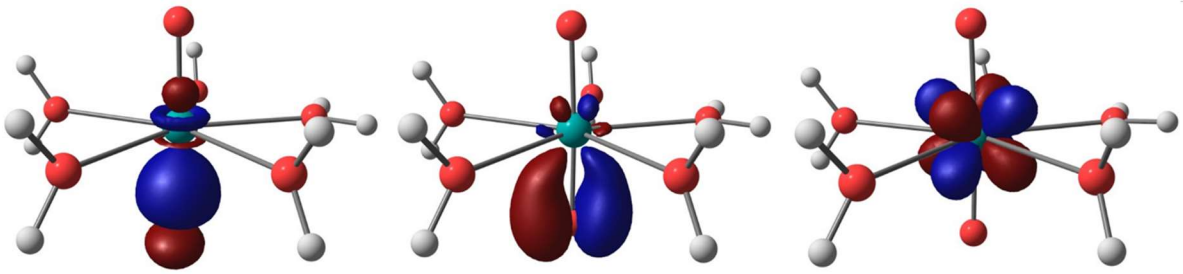

Figure 6.7 Selected localized bonding orbitals for uranyl(VI/V) U=O σ and π bonds and singly occupied f orbital of uranyl(V).

Table 6.2 The bond length (Å), Mayer bond order and bonding orbital composition of U=O bonds which illustrated in Figure 6.8.

	Bond length	Bond order	uranium contribution	
Uranyl(VI)	1.733	2.30	σ	35.0%
			π	25.9%
Uranyl(V)	1.791	2.27	σ	32.5%
			π	23.5%

Figure 6.8 illustrates the σ and π U=O bonds of uranyl(VI/V). On the axis of O=U=O, there are one σ and two π bonds. Table 6.2 shows the parameters of U=O bonds. The total Mayer bond order of the uranyl(VI) U=O bond is 2.30. The Mulliken spin population gives a spin of 1.1 on the uranium atom in uranyl(V). The single occupied orbital has pure *f* orbital character as Figure 6.8 shows. In uranyl(V), the U=O bonds are weakened with a longer bond length increasing by 0.058 Å comparing to uranyl(VI). The total bond order of U=O in urany(V) thus reduces to 2.27. As Table 6.2 shows, the localized σ U=O bonding orbital has larger uranium contributions than the π bonding orbital. Comparing to uranyl(VI), the contributions from uranium atom of the σ and π U=O bonds in uranyl(V) reduce from 35.0%/25.9% to 32.5%/23.5%.

6.3.3. Uranyl(VI) adsorption

Uranyl(VI) adsorption on Site 1

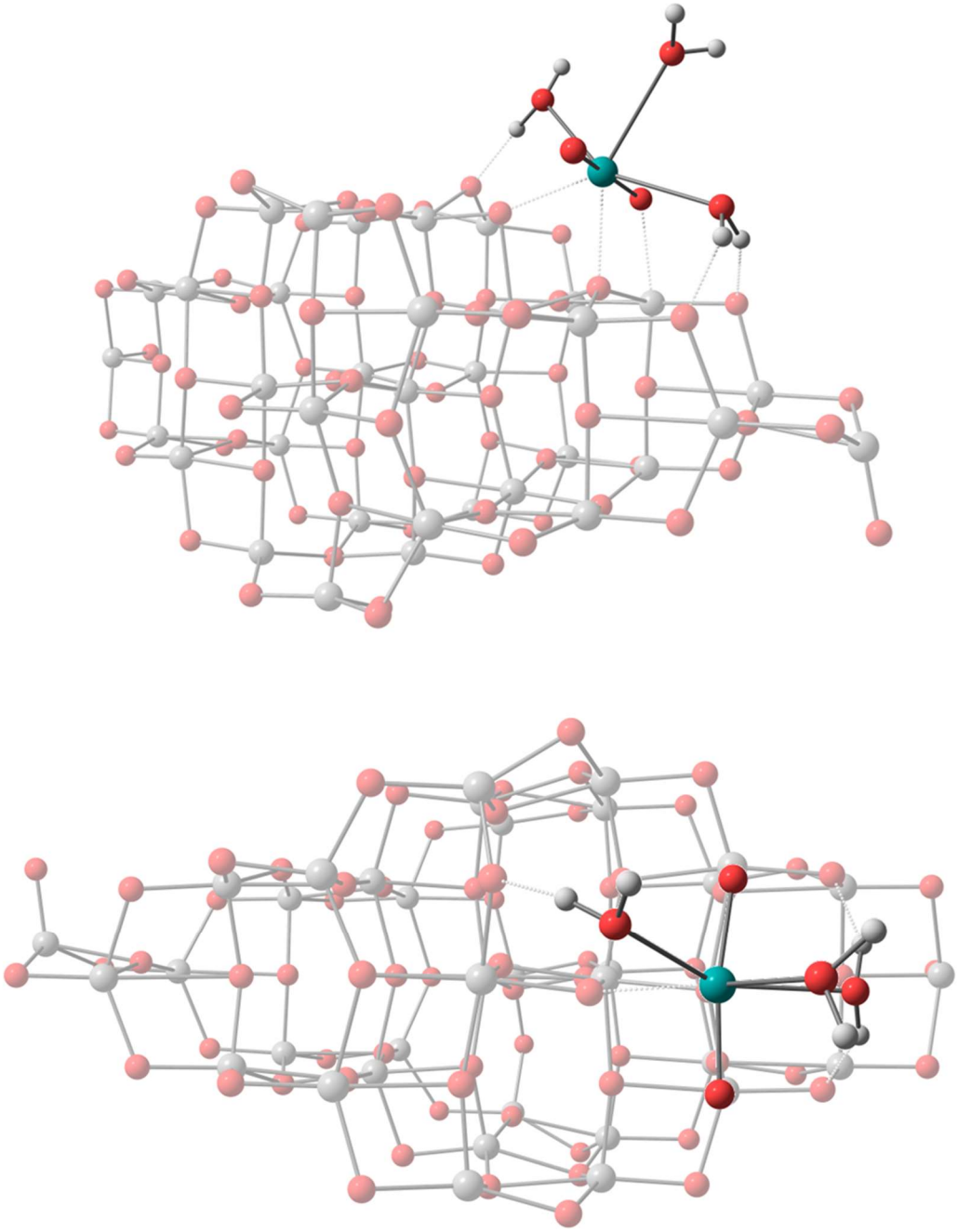

Figure 6.8 Side and top view of the optimized structure of uranyl(VI) adsorbed on **Site 1** of the $(TiO_2)_{35}$ cluster

Figure 6.8 shows the optimized structure when uranyl(VI) ion adsorbs on the **Site 1** position of the $(TiO_2)_{35}$ cluster (see Scheme 6.2). Selected geometry parameters are listed in Table 6.3. The uranium atom forms two U---O bonds with a bridge oxygen atom and an oxygen atom with η-3 coordination on the surface of TiO_2 cluster. The two bond lengths are 2.237Å and 2.256Å respectively. Their Mayer bond orders suggest that the bonding strengths are at the same level as uranyl water bonds (U-O_w in Table 6.3). The bond between uranyl oxygen and titanium (U=O---Ti) is slightly weaker than the U-O_w bonds. However, it significantly weakens the corresponding U=O bond, which has a bond order of 1.79 instead of 2.30 for the uranyl(VI) oxygen bonds in a free water cluster as listed in Table 6.2. On the other hand, although the other U=O bond is also slightly longer than in the free water cluster, the uranium contributions are almost the same as in the latter. The uranium center on the TiO_2 surface has similar equatorial 5-coordination structures as the free water cluster but with a weaker U=O bond. This indicates that it can be reduced to the oxidation state of V. The coordinated water molecules also form hydrogen bonds (bond order ~ 0.1) with TiO_2 surface oxygen atoms to strengthen the adsorption. The ETS-NOCV analysis gives similar results for the covalency of those bonds, see Figure 6.9. The U---O and U=O---Ti bonds contain both σ and π interactions. The degree of covalency of the uranium π interactions is at the same level as hydrogen bonds, which agrees with the results in Chapter 3.

Table 6.3 Selected bond lengths (Å), Mayer bond orders and bonding orbital compositions of localized U=O bonds for the **Site 1** structure illustrated in Figure 6.8. Where U=O, U---O, U=O---Ti, and U-O_w represent uranyl oxygen bonds, bonds between uranium and oxygen atoms of TiO_2 surface, bond between uranyl oxygen and titanium atom of TiO_2 surface, and uranyl water bonds.

	U=O		U---O		U=O---Ti	U-O_w		
Bond length	1.761	1.811	2.256	2.237	2.209	2.500	2.458	2.508
Bond order	2.18	1.79	0.44	0.60	0.29	0.44	0.61	0.41
uranium contributions	σ 34.8% π 23.9%	σ 20.6% π 18.6%						

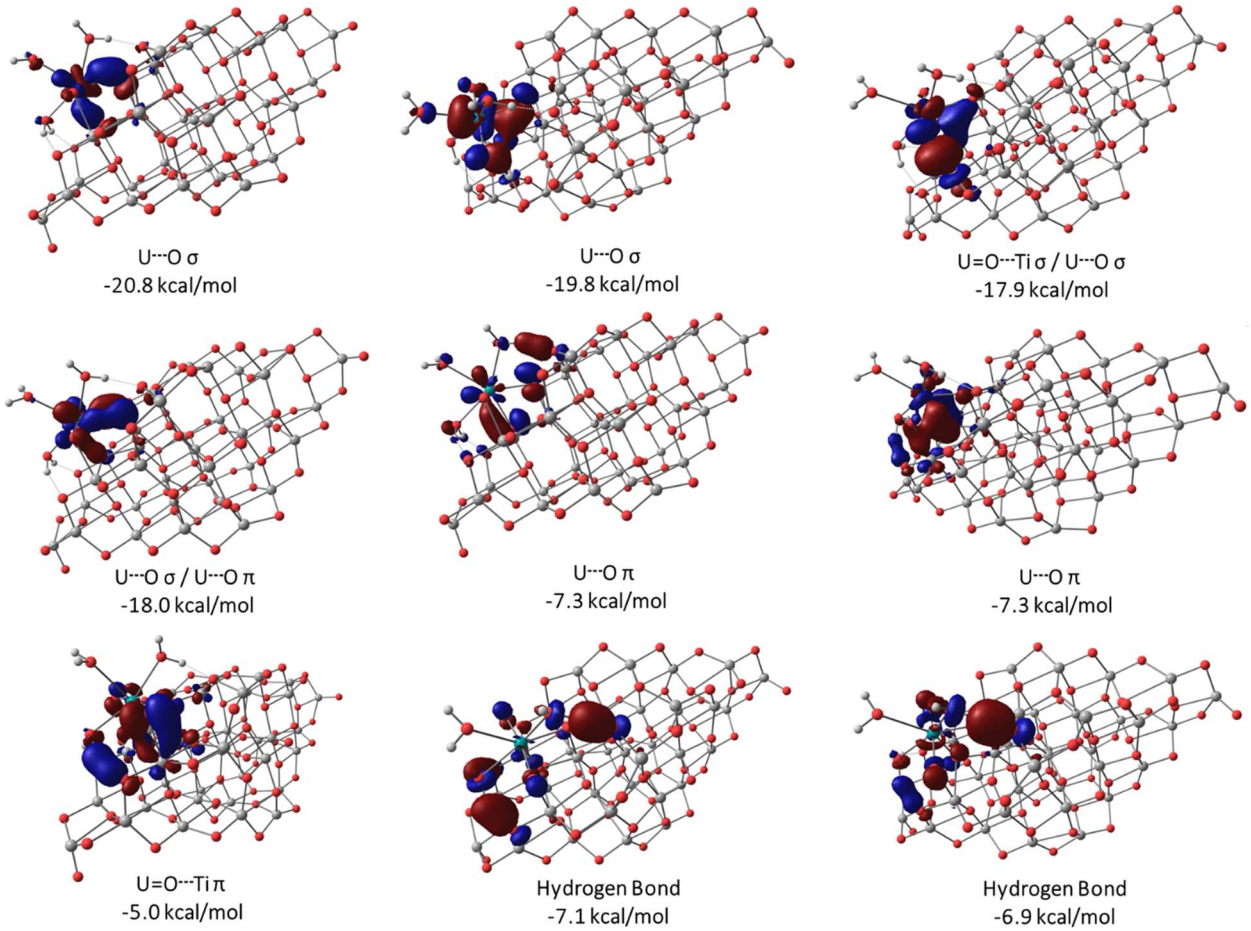

Figure 6.9 Selected important ETS-NOCV deformation density with energies for uranyl(VI) ion adsorption on **Site 1**. Electron density flow is from red to blue.

Uranyl(VI) adsorption on Site 2

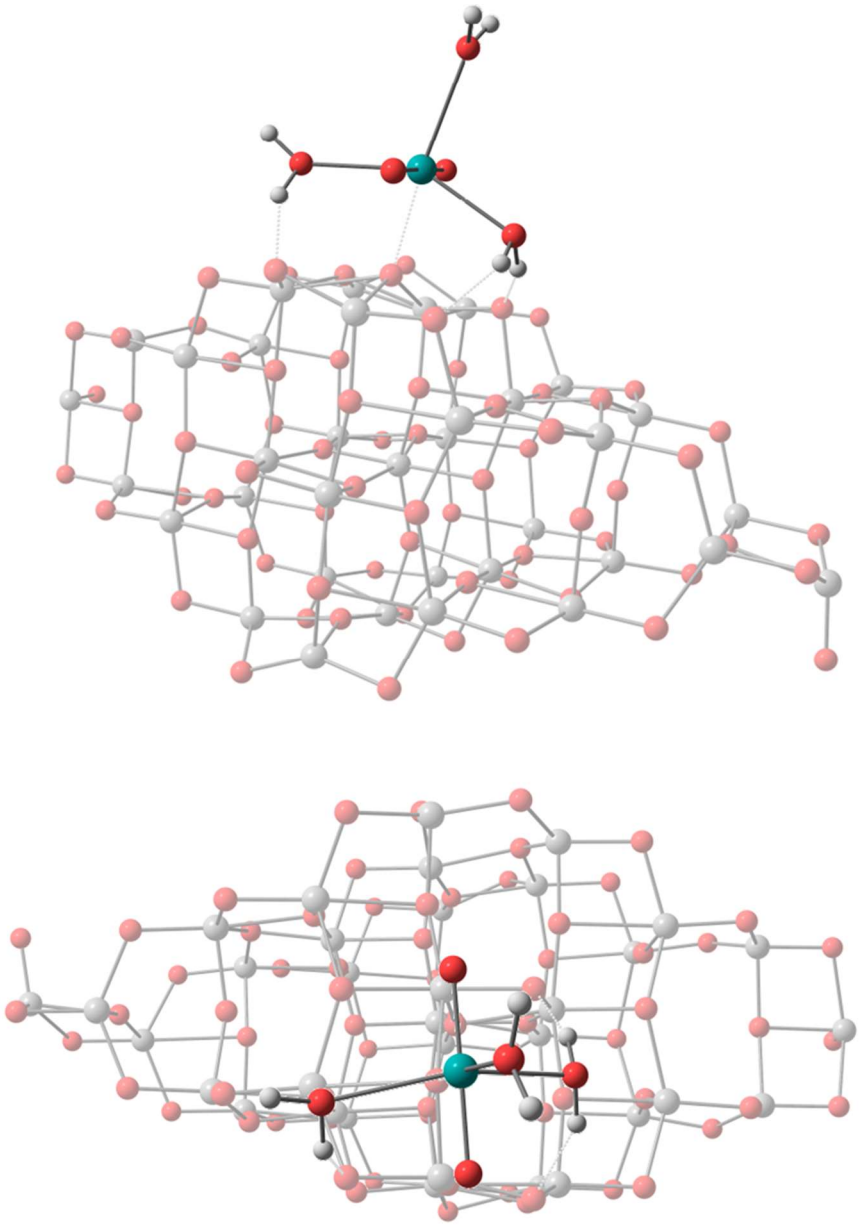

Figure 6.10 Side and top view of the optimized structure of uranyl(VI) adsorbed on **Site 2** of the $(TiO_2)_{35}$ cluster.

As Figure 6.10 shows, a η-1 coordination structure is formed when the uranyl(VI) ion adsorbs on the **Site 2** of the $(TiO_2)_{35}$ cluster. The bond order of the single U---O bond on **Site 2** is equal to the average of the two U---O bonds on **Site 1**. The two U=O bonds of uranyl(VI) are slightly longer than the U=O bonds in the free uranyl water cluster with bond orders of 2.18. The bond orders and uranium orbital compositions of these U=O bonds are the same as those of the uncoordinated U=O bond in the structure of **Site 1**. Because the uranyl(VI) on **Site 2** has only one U---O bond and three hydrogen bonds, the bonding between the uranyl(VI) moiety and the surface on **Site 2** is weaker than on **Site 1**.

Table 6.4 Selected bond lengths (Å), Mayer bond orders and bonding orbital compositions of localized U=O bonds for **Site 2** structure illustrated in Figure 6.10. Where U=O, U---O, U=O---Ti, and U-O_w represent uranyl oxygen bonds, bonds between uranium and oxygen atoms of TiO_2 surface, bond between uranyl oxygen and titanium atom of TiO_2 surface, and uranyl water bonds.

	U=O		U---O	U=O---Ti		U-Ow		
Bond length	1.754	1.758	2.202	3.016	2.746	2.467	2.331	2.472
Bond order	2.18	2.19	0.51	-	-	0.43	0.69	0.40
uranium contribution	σ 34.0% π 24.1%	σ 33.6% π 23.9%						

Uranyl(VI) adsorption on Site 3

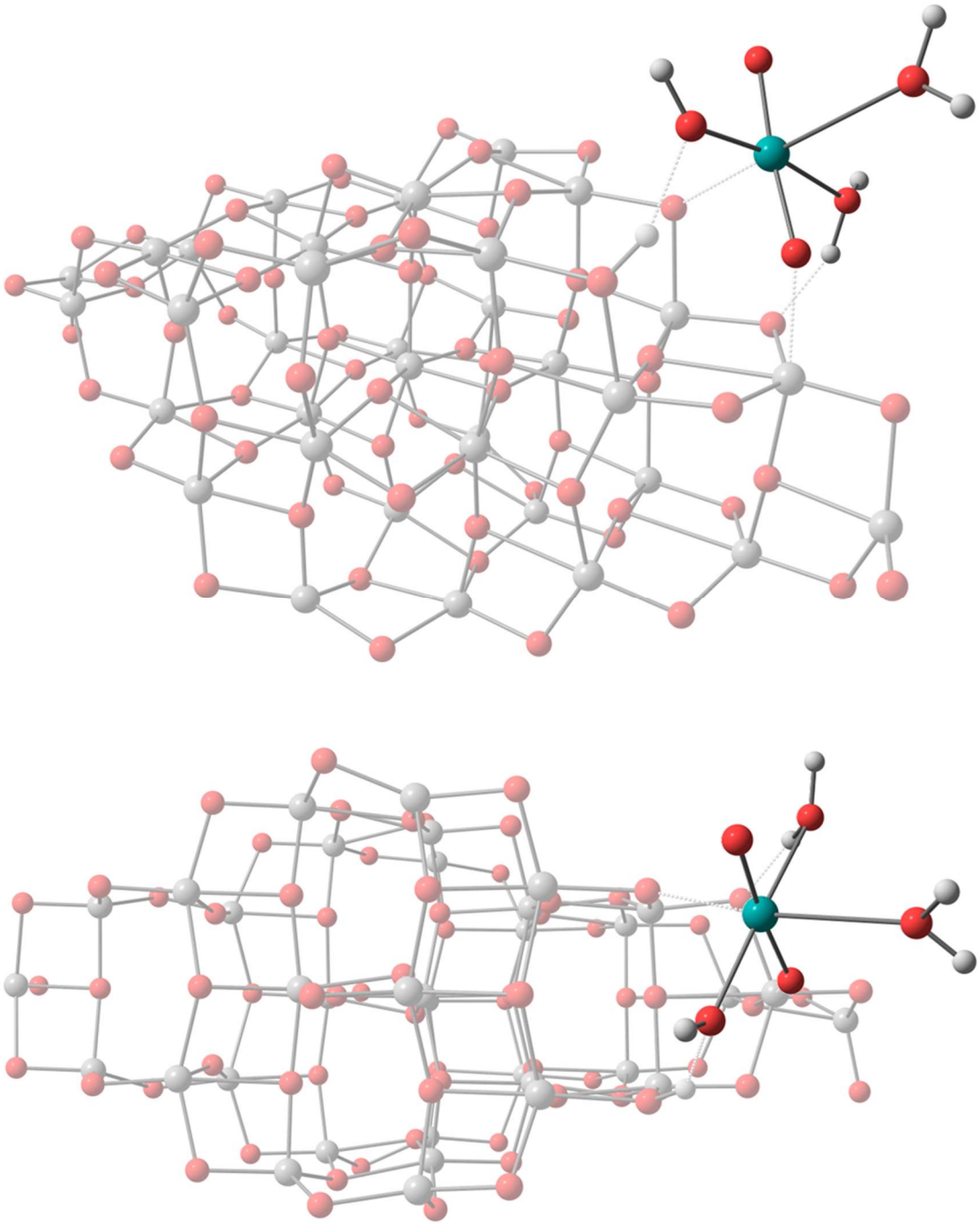

Figure 6.11 Side and top view of the optimized η-2 structure of uranyl(VI) adsorbed on **Site 3** of the $(TiO_2)_{35}$ cluster.

The adsorption of uranyl(VI) on **Site 3** of the dry $(TiO_2)_{35}$ cluster yields a deprotonation

structure, see Figure 6.11. One of the water hydrogens transfers to a bridge oxygen atom on the dry surface. However, the deprotonation does not occur in the geometry optimization with COSMO implicit water solvation model. Thus, this deprotonation structure is likely an artefact due to the strong interactions between the uranyl(VI) ion and the $(TiO_2)_{35}$ cluster in gas-phase. Furthermore, a η-3 structure was also located as Figure 6.12 shows. There is no deprotonation in this η-3 structure. The geometry parameters and bonding orbital compositions of localized U=O bonds for η-2* and η-3 structures are listed in Table 6.5. Note that the η-2* structure results from a constrained geometry optimization that sets the O-H bond length in water to a fixed value of 1.037Å to prevent deprotonation. The U=O bonds in both the η-2* and η-3 structures are very similar to each other. The uncoordinated U=O bonds in η-2* and η-3 are slightly longer than the U=O bonds in free uranyl(VI) as Table 6.2 shows. However, both uncoordinated U=O bonds in η-2* and η-3 structures have slightly higher uranium contributions. The sum of the bond orders for the uranium atoms in the η-2* and η-3 structures is 6.40 and 6.87 respectively, which indicates that the U(VI) η-2 structure may be easier to reduce to U(V) than the U(VI) in the η-3 structure.

Table 6.5 The selected bond lengths (Å), Mayer bond orders and bonding orbital compositions of localized U=O bonds for η-2 and η-3 **Site 3** structures. Where U=O, U---O, U=O---Ti, and U-O_w represent uranyl oxygen bonds, bonds between uranium and oxygen atoms of TiO_2 surface, bond between uranyl oxygen and titanium atom of TiO_2 surface, and uranyl water bonds.

		U=O		U---O		U=O---Ti		U-Ow	
η-2*	Bond length	1.747	1.793	2.165	-	2.218	2.340	2.461	2.388
	Bond order	2.27	1.82	0.56	-	0.24	0.56	0.43	0.53
	uranium contribution	σ 35.5%	σ 30.4%						
		π 24.9%	π 20.5%						
η-3	Bond length	1.748	1.807	2.536	2.286	2.147	2.536	2.479	2.437
	Bond order	2.28	1.77	0.54	0.59	0.31	0.47	0.41	0.50
	uranium contribution	σ 35.6%	σ 30.3%						
		π 24.9%	π 19.5%						

* Structure from constrained geometry optimization.

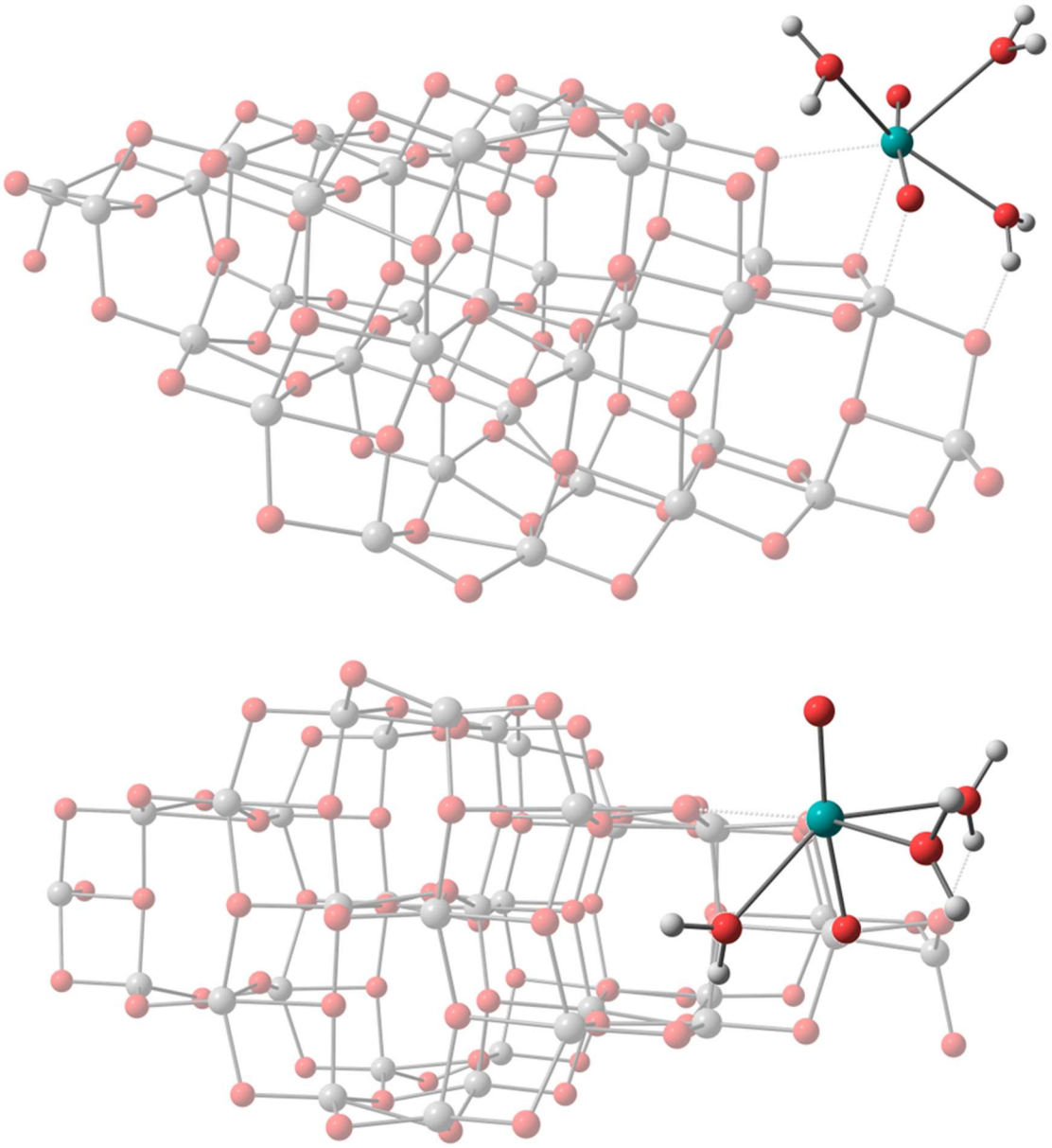

Figure 6.12 Side and top view of the optimized η-3 structure of uranyl(VI) adsorbed on **Site 3** of the $(TiO_2)_{35}$ cluster.

6.3.4. Uranyl(VI) reduction

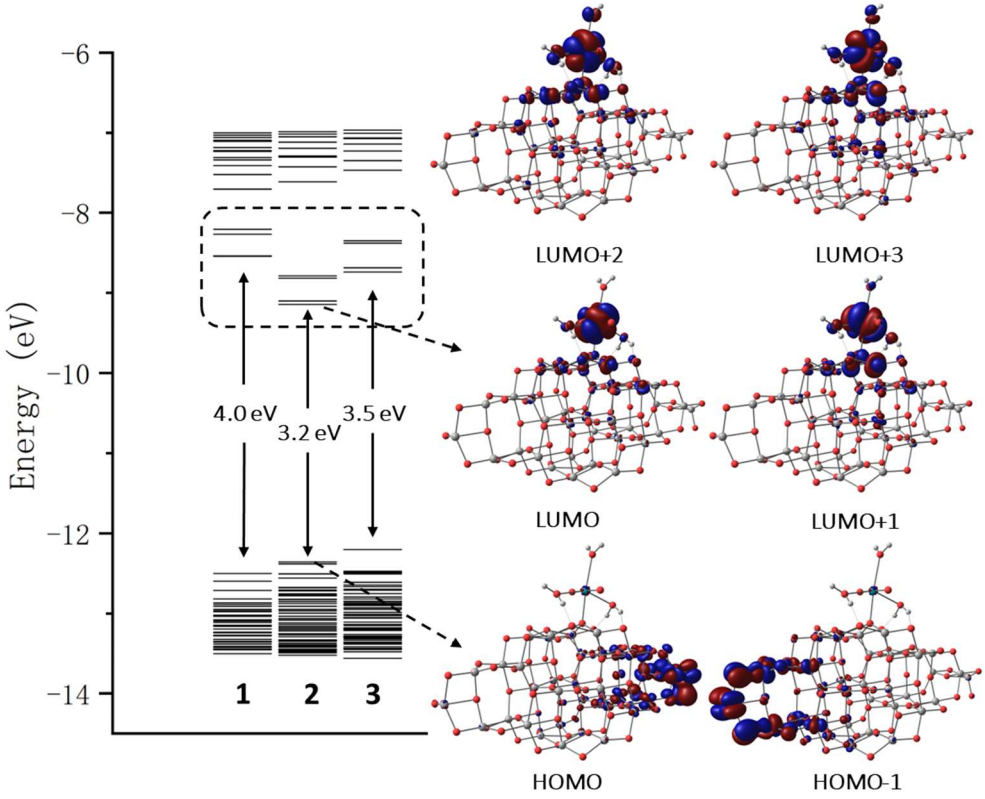

Figure 6.13 Electronic energy levels of the structures of **Sites 1**, **2**, and **3** uranyl(VI) adsorption on the $(TiO_2)_{35}$ anatase cluster. The MOs of **Site 2** adsorption are shown as examples. The η-2* structure was used here for **Site 3** adsorption.

The frontier orbitals for the singlet structures in section 6.3.2 are shown in Figure 6.13. The HOMOs are related to terminal Ti=O bonds, which agrees with the previous calculations on $(TiO_2)_{35}$ anatase cluster in section 6.3.1. The LUMOs, which are marked by a dash rectangle in Figure 6.13, are mostly pure empty uranium 5*f* orbitals. These 5*f* states are -0.8 eV, -1.5 eV, and -1.3 eV lower than the titanium empty 3*d* states, for the structures of **Sites 1**, **2**, and **3** uranyl(VI) adsorption, respectively. The bandgaps between the empty 5*f* states and the fully occupied states are 4.0 eV, 3.2 eV, and 3.5 eV, respectively, as Figure 6.13 shows. For the η-3 structure of **Site 3** uranyl(VI) adsorption, the empty 5*f* states are 0.9 eV lower than the titanium 3*d* states with a bandgap of 3.8 eV, which is similar to the η-2* structure. The positions of these empty 5*f* states

indicate that the adsorbed U(VI) can act as electron traps during the photocatalytic reaction. The electron is likely to be excited from a Ti=O bonding orbital to the empty uranium 5*f* orbitals. To investigate the one-electron reduction process in the U(VI) photocatalytic reduction (Equation 6.2), triplet state geometry optimization calculations were carried out based on the optimized singlet structures of **Sites 1**, **2**, and **3** uranyl(VI) adsorption in section 6.3.2.

Uranyl(VI) one-electron photocatalytic reduction adsorption on Site 1

The optimized triplet state structure of uranyl(V) adsorption on **Site 1** of the $(TiO_2)_{35}$ cluster is shown in Figure 6.14. The distance between uranyl(V) and TiO_2 cluster in triplet state is shorter than in singlet state as Table 6.5 shows. An additional U=O---Ti bond is generated with a bond length of 1.987 Å. Both of the U=O---Ti bonds have the same bond lengths and bond orders, which are much stronger than in the U(VI) compound. Thus, uranyl(V) forms a bridge structure on the $(TiO_2)_{35}$ cluster. The increased and decreased bond orders of U=O---Ti and U=O bonds indicate the reduction of uranium. Because of the shorter U=O---Ti and U---$O_{\eta\text{-}3}$ bonds, the U---O_{bridge} bond becomes longer. The U-O_w bonds also become longer due to the reduced formal charge on U(V).

Table 6.6 Selected bond lengths (Å), Mayer bond orders and bonding orbital compositions of localized U=O bonds for structures of uranyl(VI) and (V) **Site 1** adsorption. Where U=O, U---O, U=O---Ti, and U-O_w represent uranyl oxygen bonds, bonds between uranium and oxygen atoms of TiO_2 surface, bond between uranyl oxygen and titanium atom of TiO_2 surface, and uranyl water bonds.

		U=O		U---O		U=O---Ti		U-O_w		
U(VI)	Bond length	1.761	1.811	2.256	2.237	2.209	3.069	2.500	2.458	2.508
	Bond order	2.18	1.79	0.44	0.60	0.29	-	0.44	0.61	0.41
	uranium contribution	σ 34.8%	σ 20.6%							
		π 23.9%	π 18.6%							
U(V)	Bond length	1.926	1.921	2.216	2.287	1.995	1.987	2.535	2.461	2.564
	Bond order	1.48	1.48	0.48	0.49	0.63	0.62	0.40	0.59	0.40
	uranium contribution	σ 25.3%	σ 25.4%							
		π 15.5%	π 15.4%							

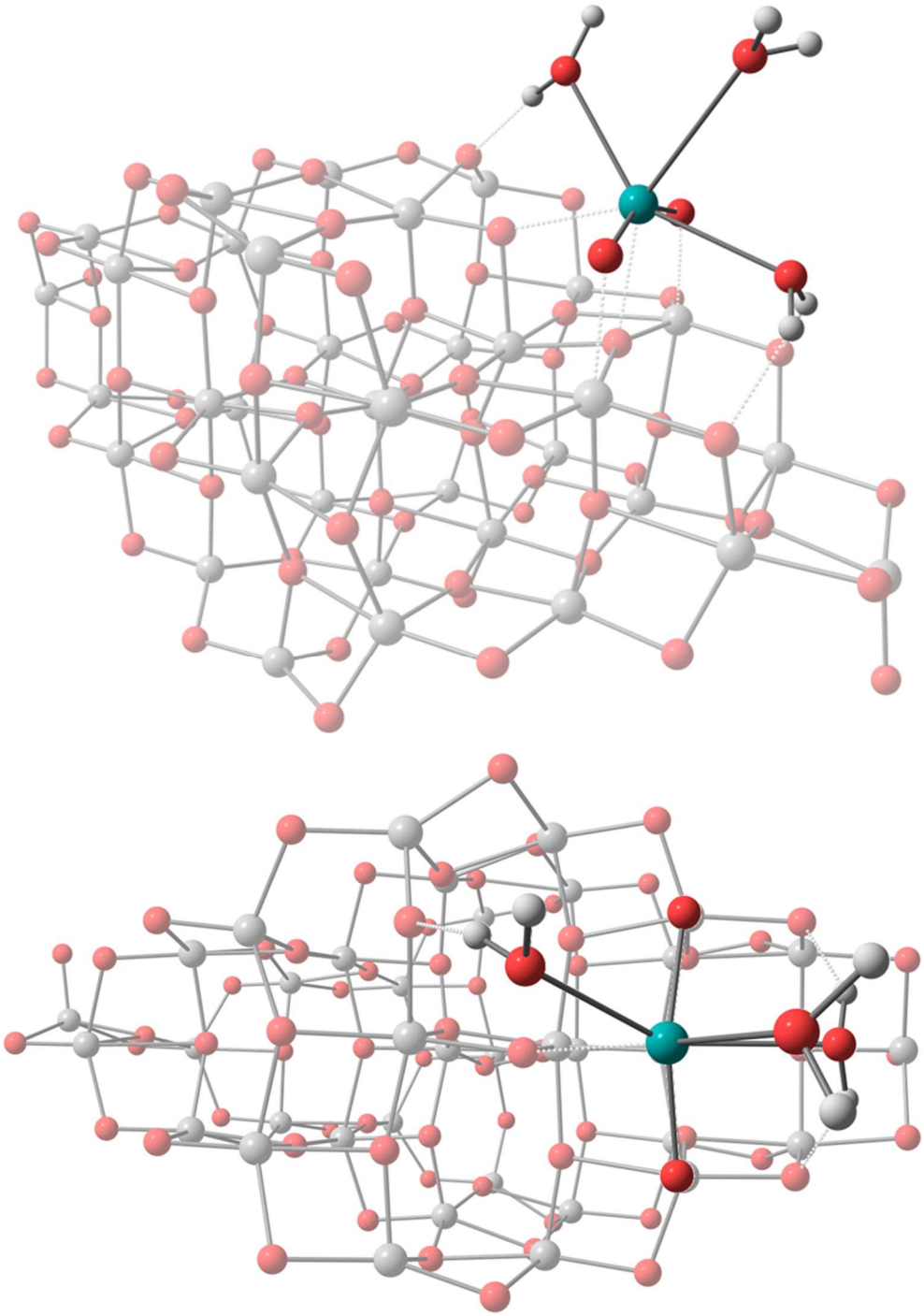

Figure 6.14 Side and top view of the optimized triplet state structure of uranyl(V) adsorption on **Site 1** of the $(TiO_2)_{35}$ cluster.

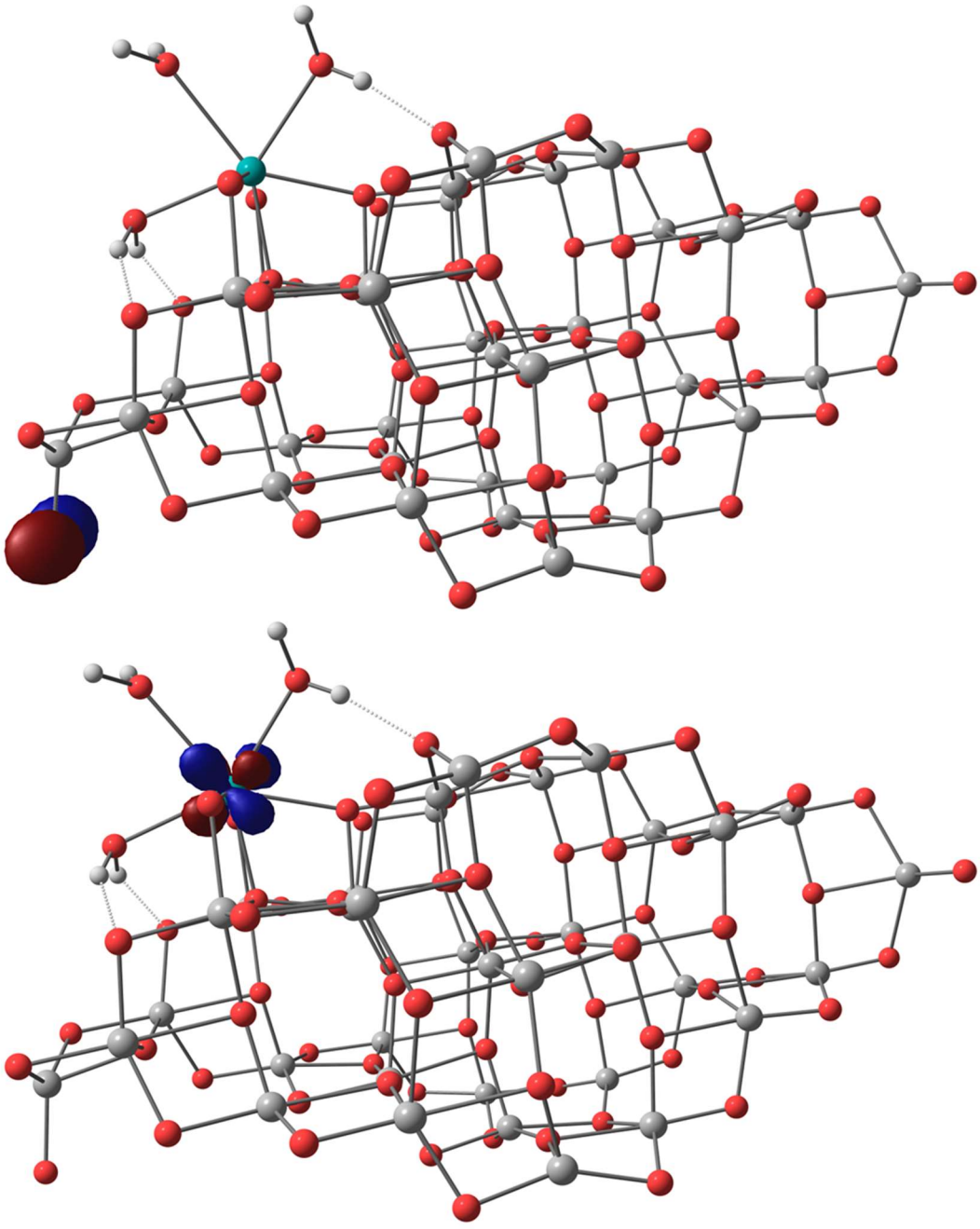

Figure 6.15 The localized singly occupied orbitals of the optimized triplet state structure of uranyl(V) adsorption on **Site 1** of the $(TiO_2)_{35}$ cluster.

The localized singly occupied orbitals of U(V) **Site 1** adsorption are shown in Figure 6.15. The two spins are located on a terminal oxygen atom and the uranium atom, respectively, which confirms that the oxidation state of uranium is V, and an electron was excited from the terminal Ti=O bond to uranyl. The stronger U=O---Ti bonds make the U=O bonds weaker. The lower bond orders and uranium contributions of the U=O bonds in Table 6.5 also support this oxidation state of uranium.

Uranyl(VI) one-electron photocatalytic reduction adsorption on Site 2

As Figure 6.16 shows, similar to **Site 1**, the triplet state optimization forms a uranyl bridge structure on S**ite 2** of the $(TiO_2)_{35}$ cluster. Table 6.6 summarizes geometry parameters and orbital contributions for this structure. However, the two U=O bonds are not as even as in the **Site 1** structure. The localized singly occupied orbitals are presented in Figure 6.17; they are similar to those of the **Site 1** structure, confirming the predicted oxidation state and electron charge transfer.

Table 6.7 Selected bond lengths (Å), Mayer bond orders and bonding orbital compositions of localized U=O bonds for structures of uranyl(VI) and (V) **Site 2** adsorption. Where U=O, U---O, U=O---Ti, and U-O_w represent uranyl oxygen bonds, bonds between uranium and oxygen atoms of TiO_2 surface, bond between uranyl oxygen and titanium atom of TiO_2 surface, and uranyl water bonds.

		U=O		U---O	U=O---Ti		U-Ow		
U(VI)	Bond length	1.754	1.758	2.202	3.016	2.746	2.467	2.331	2.472
	Bond order	2.18	2.19	0.51	-	-	0.43	0.69	0.40
	uranium contribution	σ 34.0%	σ 33.6%						
		π 24.1%	π 23.9%						
U(V)	Bond length	1.820	1.856	2.275	2.510	2.200	2.518	2.359	2.640
	Bond order	1.99	1.80	0.29	0.21	0.35	0.39	0.65	0.27
	uranium contribution	σ 29.6%	σ 27.0%						
		π 19.8%	π 17.7%						

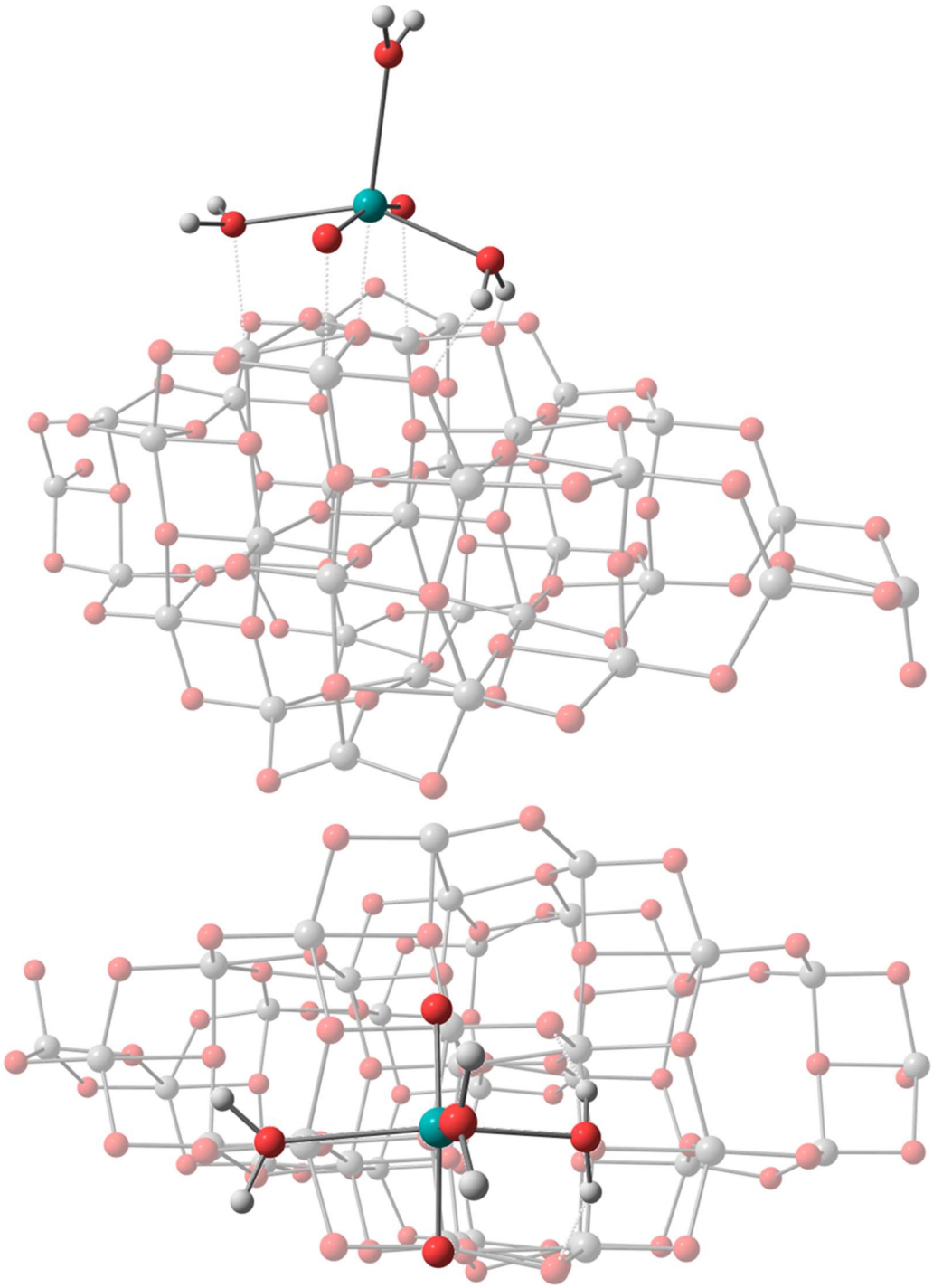

Figure 6.16 Side and top view of the optimized triplet state structure of uranyl(V) adsorption on **Site 2** of the $(TiO_2)_{35}$ cluster.

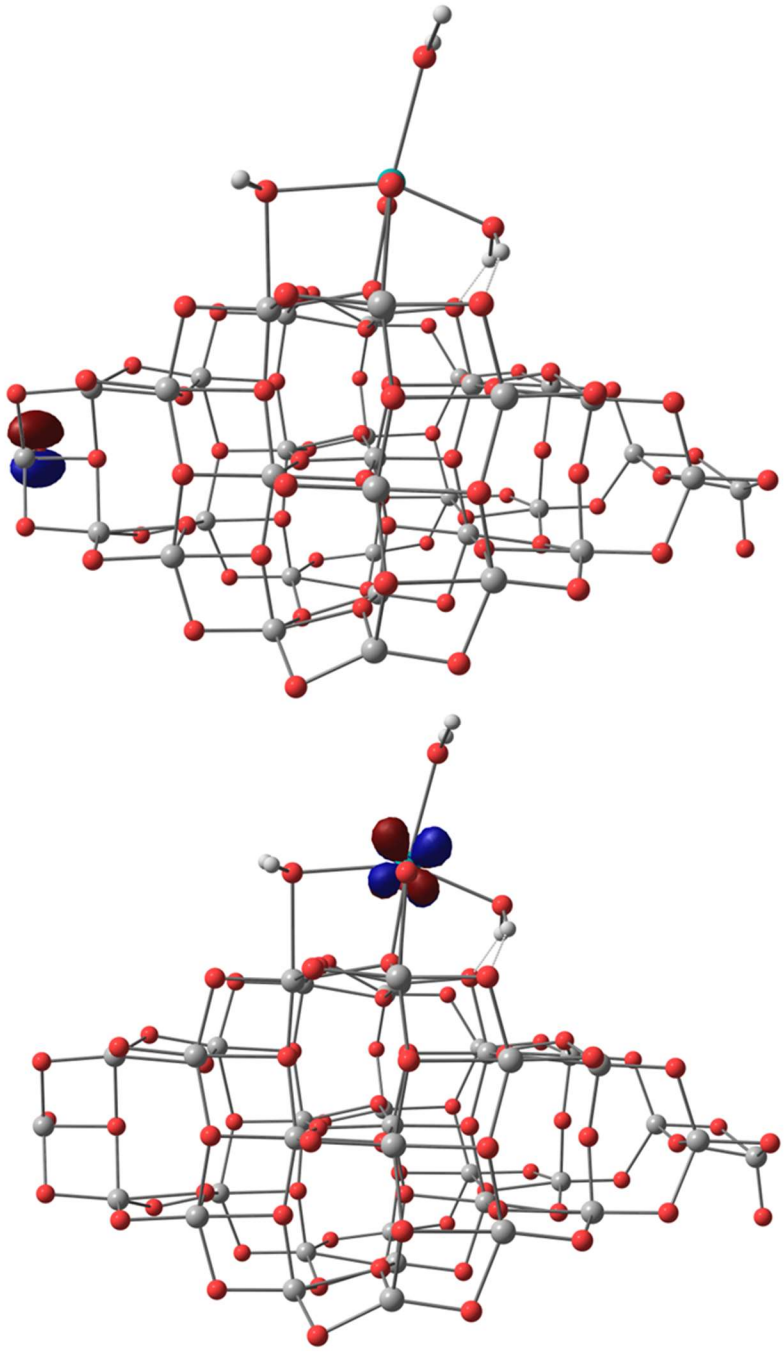

Figure 6.17 Localized single occupied orbitals of the optimized triplet state structure of uranyl(V) adsorption on **Site 2** of the $(TiO_2)_{35}$ cluster.

Uranyl(VI) one-electron photocatalytic reduction adsorption on Site 3

The triplet state calculation for **Site 3** also gives shorter distances between uranyl and TiO_2 cluster, as Table 6.7 shows. Note that the U(VI) data in Table 6.7 is from the η-2* structure. However, unlike for the singlet state, deprotonation did not occur in the optimization for the η-2 structure. Comparing to **Sites 1** and **2**, uranyl on the TiO_2 cluster does not form a bridge structure, see Figure 6.18. Instead, the uncoordinated U=O bond keeps the same bond length, bond order, and uranium contributions as in the free uranyl(VI) water cluster in section 6.3.2, which indicates that this U=O bond may have the same photocatalytic properties as the free uranyl(VI) water cluster. The localized singly occupied orbitals are illustrated in Figure 6.19. The locations of the two unpaired electrons support the prediction made at the beginning of this section. The triplet η-3 structure gives similar results as the η-2 structure but with a higher energy by 5 kcal/mol. When forcing the unpaired electron to locate on the uranium and oxygen atoms in the uncoordinated U=O bond in the η-3 structure, the energy is about 20 kcal/mol higher than the structure with spins on terminal Ti-O oxygen and uranium atoms. This indicates that the electron in the first reduction likely comes from the terminal Ti=O oxygen instead of uranyl U=O bond breaking.

Table 6.8 Selected bond lengths (Å), Mayer bond orders and bonding orbital compositions of localized U=O bonds for η-2 structures of uranyl(VI) and (V) **Site 3** adsorption. Where U=O, U---O, U=O---Ti, and U-O_w represent uranyl oxygen bonds, bonds between uranium and oxygen atoms of TiO_2 surface, bond between uranyl oxygen and titanium atom of TiO_2 surface, and uranyl water bonds.

		U=O		U---O	U=O---Ti		U-Ow	
U(VI)	Bond length	1.747	1.793	2.165	2.218	2.340	2.461	2.388
	Bond order	2.27	1.82	0.56	0.24	0.56	0.43	0.53
	uranium contribution	σ 35.5%	σ 30.4%					
		π 24.9%	π 20.5%					
U(V)	Bond length	1.774	1.937	2.325	1.914	2.484	2.443	2.405
	Bond order	2.30	1.32	0.43	0.69	0.40	0.45	0.47
	uranium contribution	σ 35.0%	σ 23.2.0%					
		π 24.2%	π 14.4%					

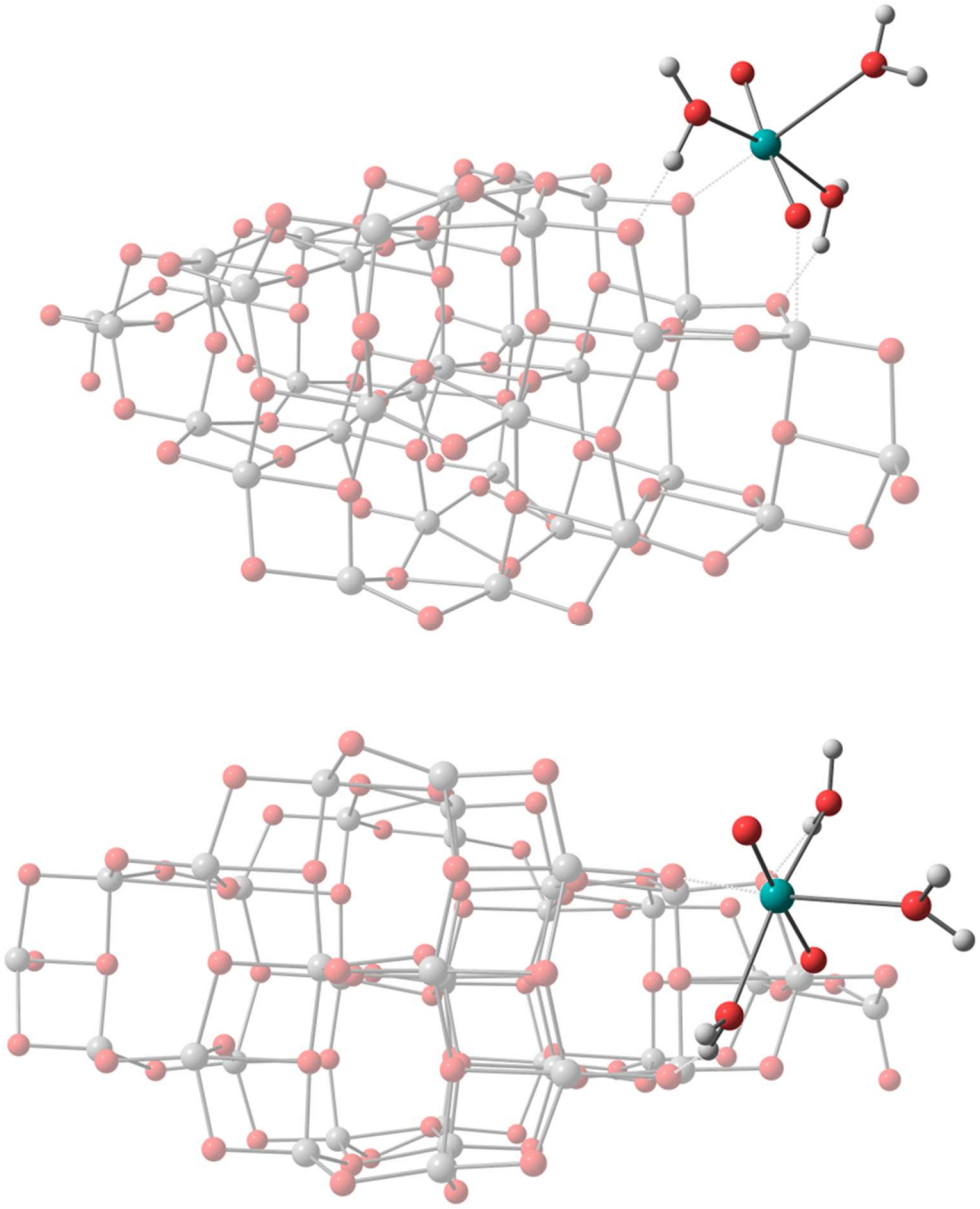

Figure 6.18 Side and top view of the optimized triplet state η-2 structure of uranyl(V) adsorption on **Site 3** of the $(TiO_2)_{35}$ cluster.

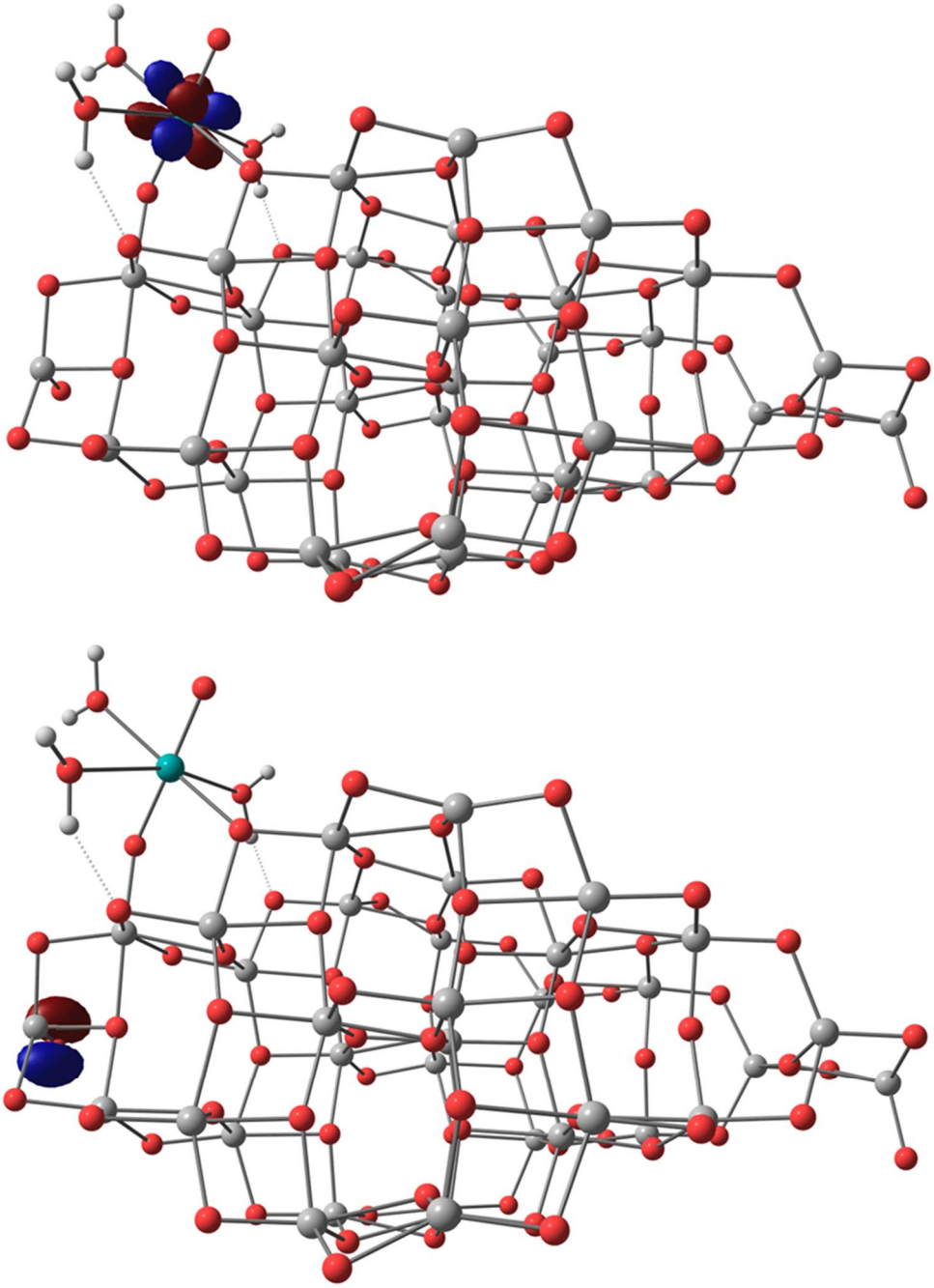

Figure 6.19 The localized singly occupied orbitals of the optimized triplet state η-2 structure of uranyl(V) adsorption on **Site 3** of the $(TiO_2)_{35}$ cluster.

Site 1 and Site 3 competition

Because uranyl(VI) on all three sites can be reduced to uranyl(V), additional calculations were carried out for comparing the capability for trapping an electron on **Site 1** and **Site 3**. As Figure 6.20 shows, two uranyl moieties are on the **Site 1** and **Site 3** positions of the same $(TiO_2)_{34}(TiO_2H)$ cluster. An additional hydrogen atom was added onto the terminal Ti=O oxygen atom to remove the oxygen radical and create a doublet state. The doublet state calculations show that the unpaired electron tends to stay on uranium of **Site 3**. Even starting with the initial structure of bridged uranyl(V) on **Site 1** in Figure 6.14, the final optimized structure is the same as in Figure 6.20. The **Site 1** represents the (101) face of the $(TiO_2)_{35}$ cluster, and **Site 3** is for the edge of the cluster. Since the U(V) can be further reduced to U(IV) by disproportionation or a second one-electron reduction, the doublet calculations that show a clear preference for **Site 3** explain why U(IV) was experimentally observed mainly distributed along the boundaries, see Figure 6.1.

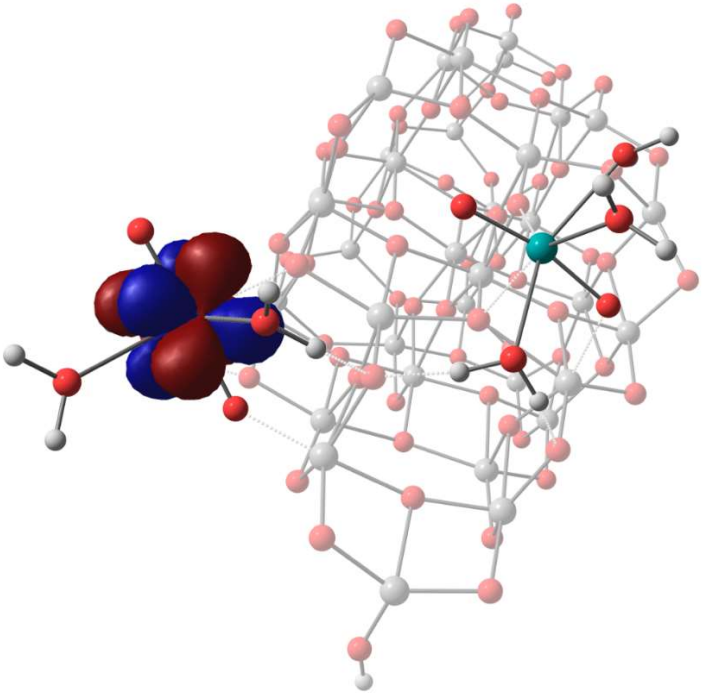

Figure 6.20 Localized singly occupied orbitals of the optimized doublet state structure of uranyl(V) adsorption on **Site 1** and **Site 3** of the $(TiO_2)_{34}(TiO_2H)$ cluster.

6.3.5. Electron transfer from defects to the uranyl ions

The additional hydrogen atom in the last part of section 6.3.4 actually introduces a surface defect on the structures by the hydroxyl group. As a result, the spin is on uranium, which is different from the previous study.[45] Thus, additional calculations for introducing a surface defect by hydroxyl group were carried out on the structures shown in Figures 6.14, 6.16, and 6.18, for **Sites 1**, **2** and **3**, respectively. The doublet state calculations show that, unlike the previous studies by Odoh et al.,[45] the unpaired electrons locate on the uranium atoms, see Figure 6.21 for an example. This might be due to the geometry effect, which is more important than size as Lamiel-Garcia et al. [1] pointed out. The anatase $(TiO_2)_{35}$ cluster used in this chapter is more like crystal particles than the clusters used in the previous studies by Odoh et al. [45] It might also be because of the difference between anatase and rutile, which needs to be further investigated.

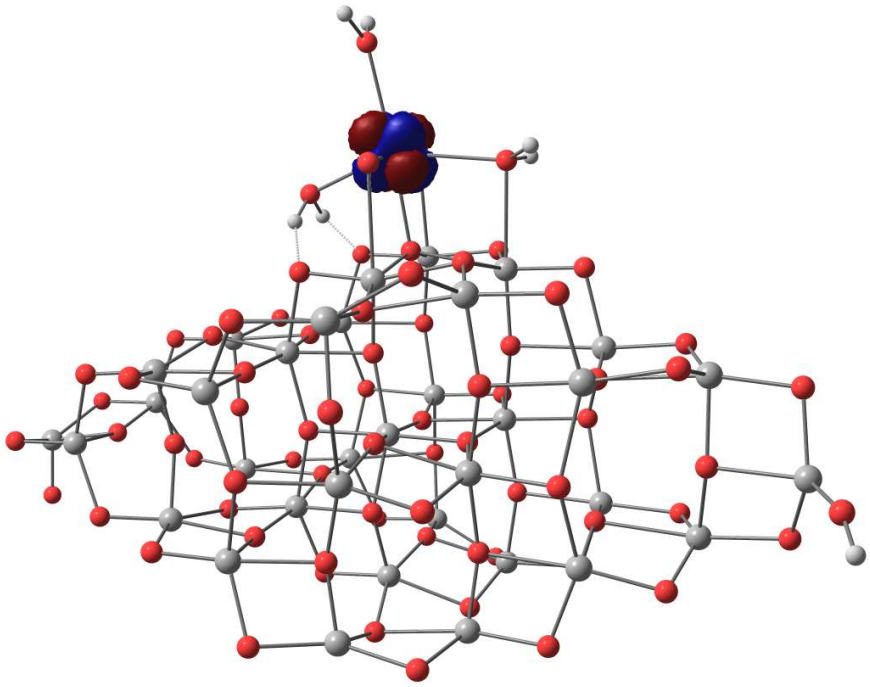

Figure 6.21 Localized singly occupied orbital of the optimized doublet state structure of uranyl(V) adsorption on **Site 2** of the $(TiO_2)_{34}(TiO_2H)$ cluster. **Sites 1** and **3** show very similar results.

6.3.6. Disproportionation reaction of the uranyl ions

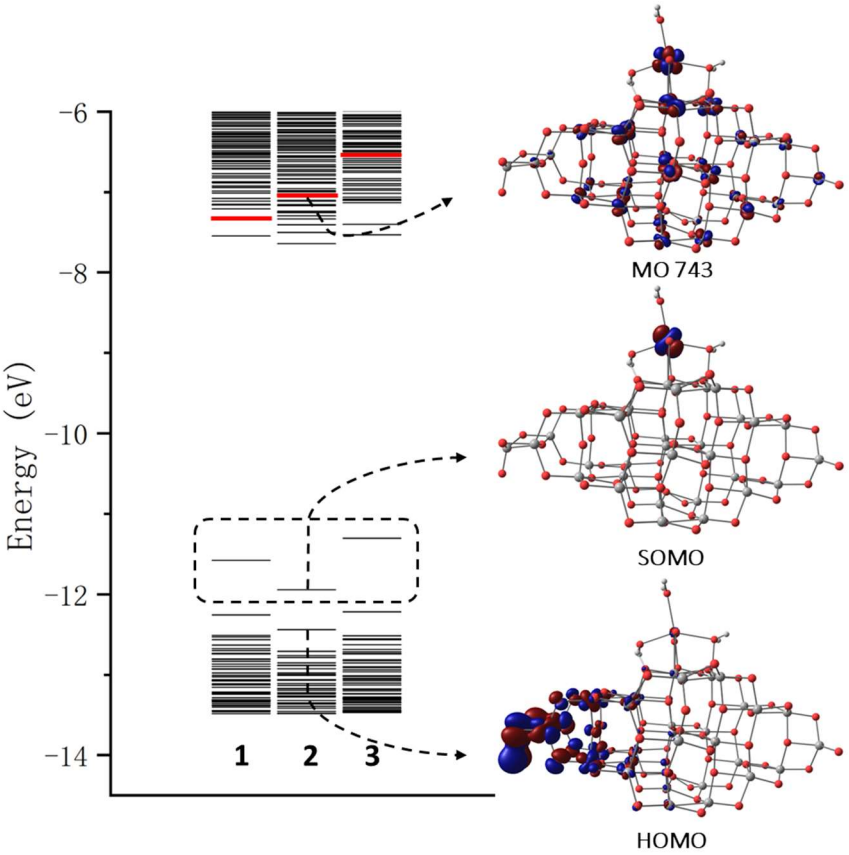

Figure 6.22 Electronic energy levels of the structures of **Sites 1**, **2**, and **3** uranyl(V) adsorption on the $(TiO_2)_{35}$ anatase cluster. The MOs of **Site 2** adsorption are shown as examples. The η-2 structure was used here for **Site 3** adsorption.

The frontier orbitals for the triplet structures in section 6.3.4 are shown in Figure 6.22. The HOMOs are related to the remaining terminal Ti=O bonds. The SOMOs for unpaired uranium 5*f* electrons are marked by a dash rectang;e in Figure 6.22. The MOs marked in red color are the lowest unoccupied orbitals contain significant 5*f* contributions. Comparing to the energy levels of the singlet state in section 6.3.4, the calculated empty 5*f* orbitals in the triplet state shift to significantly higher energies, which are already higher than some of the empty titanium 3*d* orbitals. This indicates that the U(IV) reduction via a second one-electron reduction (Equation 6.3) is unlikely to occur. Instead, the U(IV) likely stems from U(V) disproportionation (Equation 6.4).

A mechanism of U(V) disproportionation reaction in the absence of other redox reagents was proposed that involves a binuclear intermediate $[U(V)]_2O_4^{2+}$ followed by protonation, which fits the experimental rate data.[16, 50, 51] Steele and Taylor theoretically studied the inner-sphere disproportionation reaction mechanism of the pentavalent actinyl ions. [16] They pointed out that the electron transfer occurs after the first protonation. To investigate the U(V) disproportionation on the TiO_2 surface, in this study, Equations 6.2 and 6.4 can be rewritten as:

$$[U(VI)O_2]_2(TiO_2)_n^{4+} \xrightarrow{UV/\ radiation} [U(V)O_2]_2(TiO_2)_{n-2}(OTi\text{-}O\cdot)_2^{4+} \quad (6.5)$$

$$[U(V)O_2]_2(TiO_2)_{n-2}(OTi\text{-}O\cdot)_2^{4+} + 2H_2O \longrightarrow [U(V)O_2]_2(TiO_2)_{n-2}(OTi\text{-}OH)_2^{2+} + 2HO\cdot \quad (6.6)$$

$$[U(V)O_2]_2(TiO_2)n_{-2}(OTi\text{-}OH)_2^{2+} + H^+ \longrightarrow [OU(IV)OH][U(VI)O_2](TiO_2)_{n-2}(OTi\text{-}OH)_2^{3+} \quad (6.7)$$

The optimized triplet state structure and two localized singly occupied orbitals for the $[OU(IV)OH][U(VI)O_2](TiO_2)_{n-2}(OTi\text{-}OH)_2^{3+}$ cluster, which has both uranium atoms adsorbed on **Site 3**, are presented in Figure 6.23. The two unpaired 5*f* electrons locate on the O=U-OH moiety, which confirms the predicted oxidation state of IV. However, when the uranyls are adsorbed on **Sites 1** and **3** respectively, the electron transfer does not occur with protonation on **Site 1**, see structures **a** and **b** in Figure 6.24. The electron transfer from **Site 1** to **Site 3** only occurs when the protonation is on **Site 3** and **Site 1** has a non-bridge uranyl ion, which is like the singlet **Site 1** structure (structure **d** in Figure 6.25). On the other hand, if **Site 1** has a bridged structure (structure **c** in Figure 6.25), electron transfer cannot happen since the structure is similar to the U(V) structure. Although structures **c** and **d** have the same energies, breaking the O−Ti bond requires to overcome an additional energy barrier. This indicates that, after disproportionation, the U(IV) tends to appear on the edge instead of the surface of the TiO_2 nanoparticle, which also agrees with the experimental data in Figure 6.1 that U(IV) was found mainly distributed along the boundaries (edges).

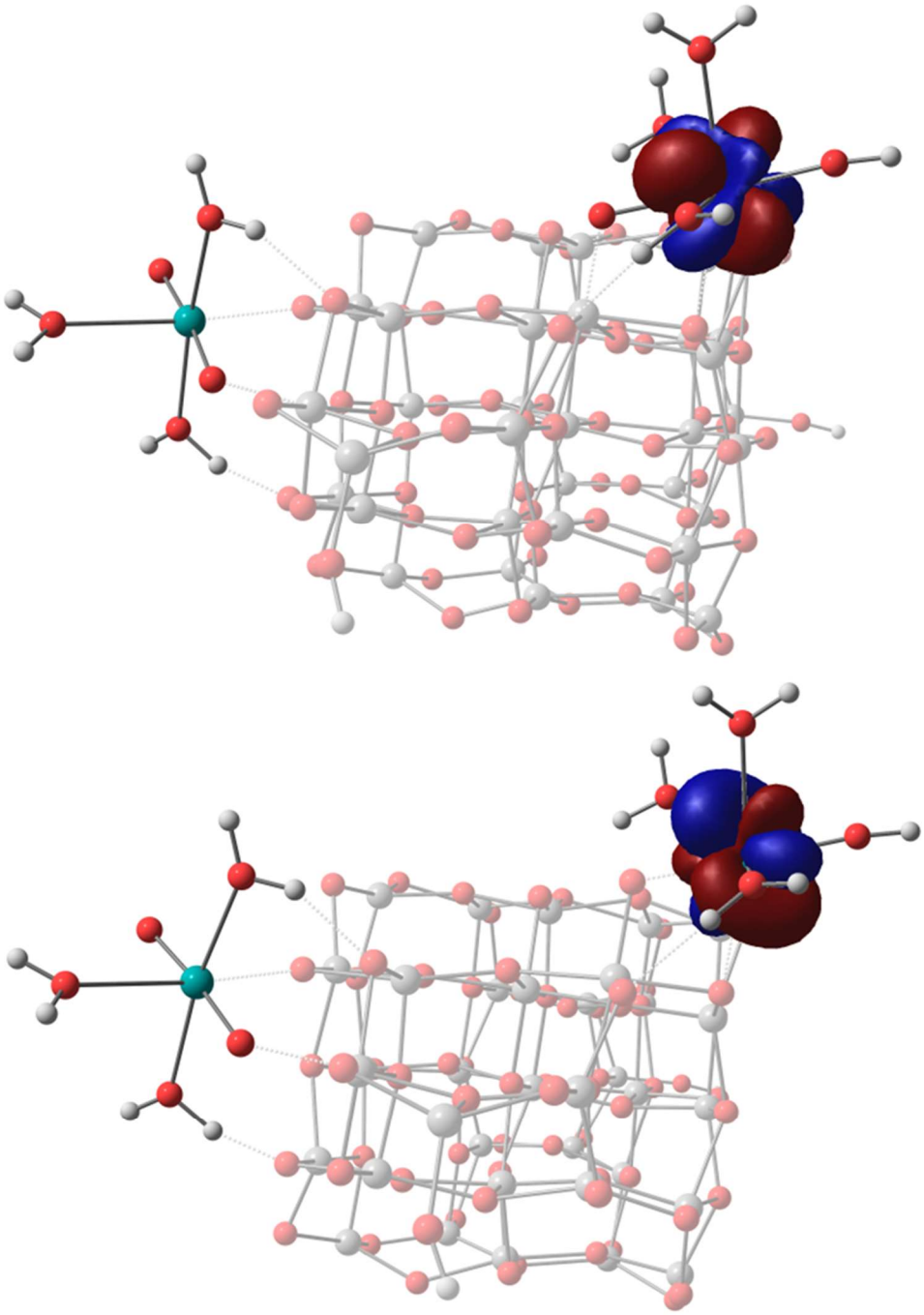

Figure 6.23 Localized singly occupied orbitals of the optimized triplet state structure of $[OU(IV)OH][U(VI)O_2](TiO_2)_{n-2}(OTi\text{-}OH)_2^{3+}$ cluster. Both uranium atoms are adsorbed on **Site 3** of the TiO_2 cluster.

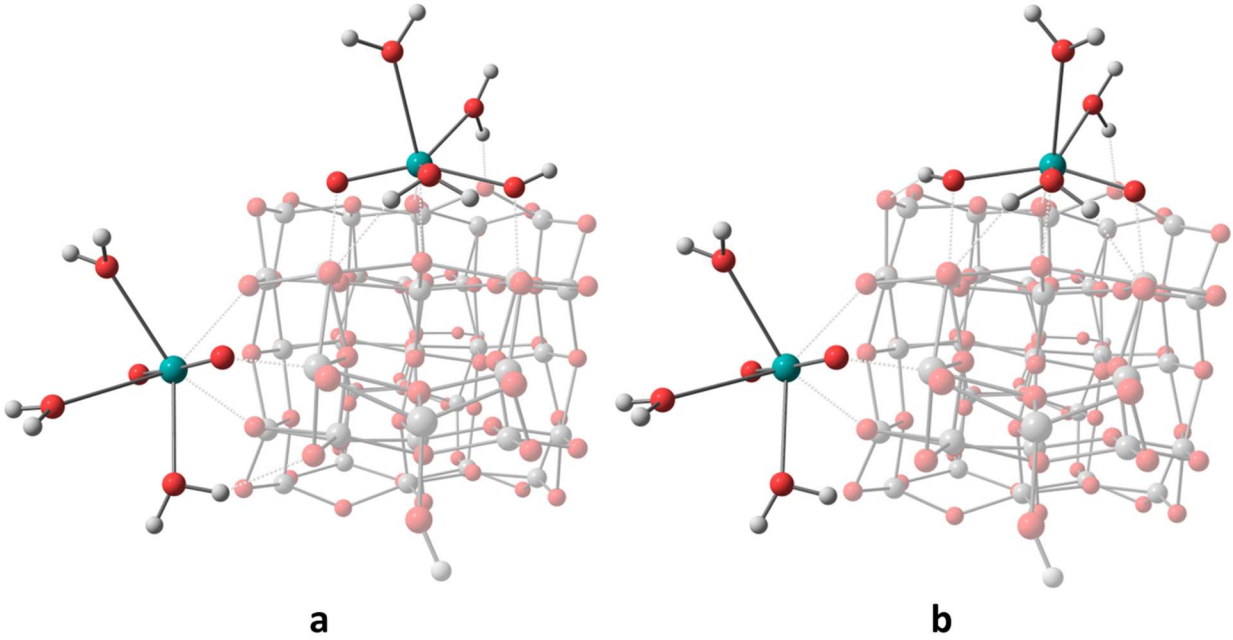

Figure 6.24 Optimized triplet state structures of $[OU(V)OH][U(V)O_2](TiO_2)_{33}(OTi\text{-}OH)_2^{3+}$ cluster. Uranyls are adsorbed on **Sites 1** and **3** of TiO_2 cluster. The two structures **a** and **b** show that protonation occurred on the two different uranyl oxygen atoms on **Site 1**.

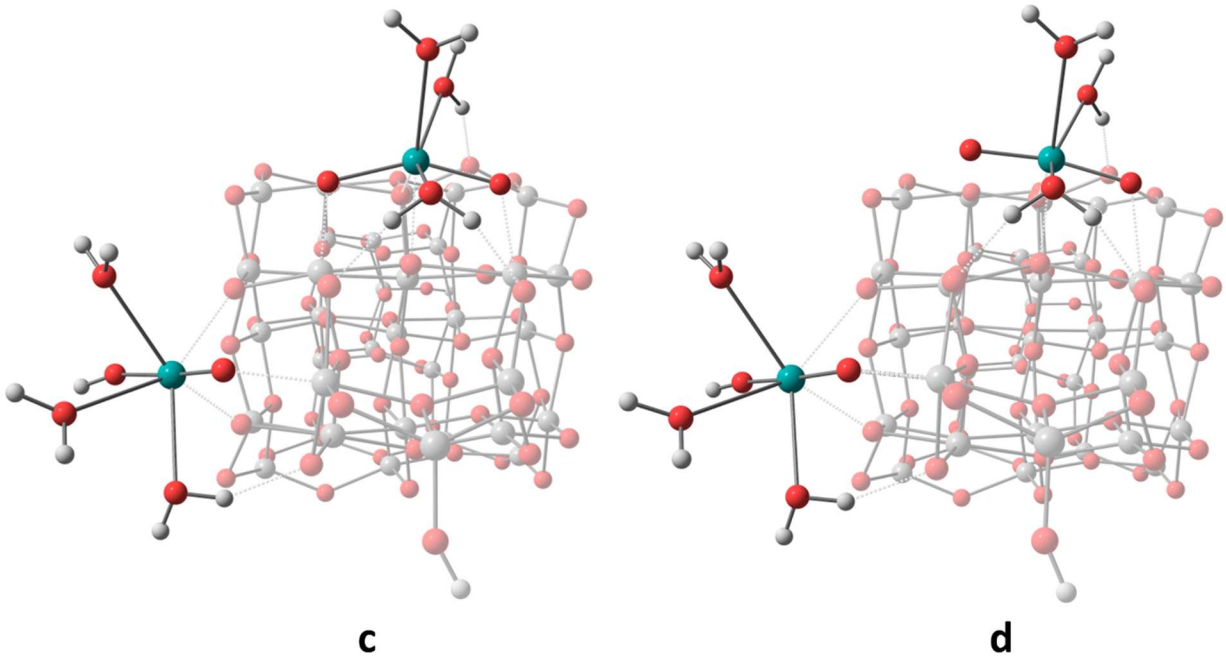

Figure 6.25 Optimized triplet state structures of **c** $[OU(V)OH][U(V)O_2](TiO_2)_{33}(OTi\text{-}OH)_2^{3+}$ and **d** $[OU(IV)OH][U(VI)O_2](TiO_2)_{33}(OTi\text{-}OH)_2^{3+}$ cluster. Uranyls are adsorbed on **Sites 1** and **3** of TiO_2 cluster. Protonation occurred on the terminal uranyl oxygen atoms on **Site 3**. The two structures **c** and **d** represent different geometries with and without bridge structure on **Sites 1**.

6.3.7. Uranyl(V) ion photoreduction

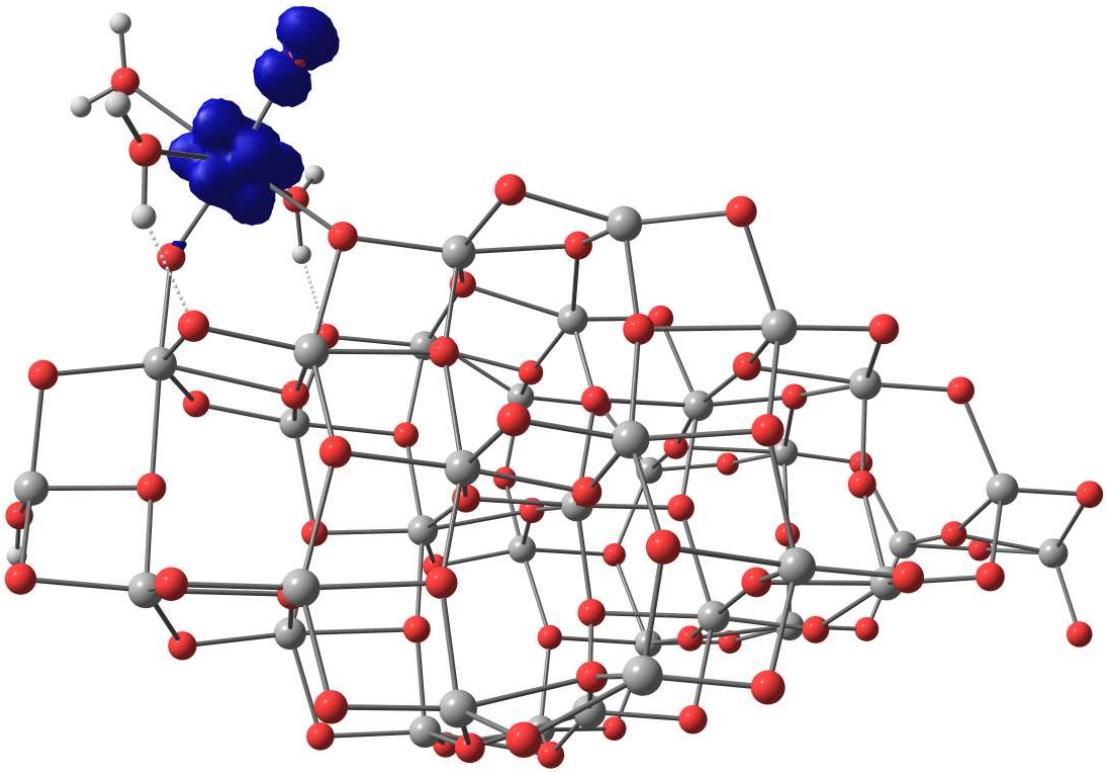

Figure 6.26 Spin density of the optimized quadruplet state structure of uranyl(IV) adsorption on **Site 3** of the $(TiO_2)_{34}(TiO_2H)$ cluster.

Although the energy level diagram Figure 6.22 in section 6.3.6 indicates that the second one-electron photoreduction is unlikely to occur, the U=O band may have the same photocatalytic properties as the free uranyl(VI) water cluster. The proposed mechanism is:

$$(O{=}U(V){-}O{-})(TiO_2)_n(OTi{-}OH)^{1+} \xrightarrow{UV/\,radiation} (\cdot O{-}U(IV){-}O{-})(TiO_2)_n(OTi{-}OH)^{1+} \quad (6.8)$$

$$(\cdot O{-}U(IV){-}O{-})(TiO_2)_n(OTi{-}OH)^{1+} + H_2O \longrightarrow (HO{-}U(IV){-}O{-})(TiO_2)_n(OTi{-}OH)^{1+} + HO\cdot \quad (6.9)$$

Hence, quadruplet state calculations on the geometry of the doublet state **Site 3** structures were carried out. The spin density of the optimized quadruplet state structure is shown in Figure 6.26. The spins are on the uranyl oxygen atom and the uranium atom with electron numbers of

0.66 and 2.32, respectively. The location of the unpaired electrons clearly confirms the oxidation state of IV and U=O bond breaking. When forcing two electrons to locate on the remaining Ti=O group, the energy of the structure is 0.6 kcal/mol higher. The radical on uranyl oxygen can further react with other molecules around to form stable a HO-U(IV)-O- moiety (Equation 6.9). This indicates that the reduction of U(V) can also be caused by the U=O bond breaking by UV light or radiation. Tables 6.5-6.7 show that the bond orders of the two uranyl(V) oxygen bonds are 1.48/1.48, 1.99/1.80, and 2.30/1.32, for **Site 1**, **2**, and **3**, respectively. Thus, the **Site 2** structure, which has uranyl adsorbed on the short edge, is between the **Site 1** and **Site 3**. Because of the bond orders and uranium contributions, the photoreduction on uranyl oxygen bond might still occur on the shorter U=O bond of the **Site 2** structure but needs to overcome the barrier for U=O---Ti bond breaking. On the other hand, for the **Site 1** structure, because the bond order of the uranyl oxygen bonds is close to single bonds, the uranyl oxygen bond photoreduction is unlikely to occur. The quadruplet state calculations on the geometries of the doublet state **Site 1** and **2** structures confirmed this prediction. Figure 6.27 shows the spin density of the optimized quadruplet state structure of uranyl(IV) adsorption on **Site 2**, which is very close to the spin density of **Site 3** shown in Figure 6.26. The electron numbers on uranium and uranyl oxygen of the U(IV) **Site 2** structure are 2.43 and 0.49, respectively. For the **Site 1** structure, the quadruplet state calculation only yielded a bond breaking on the remaining terminal Ti=O bond. Figure 6.28 clearly shows the unpaired $3d_z$ titanium and oxygen $2p$ electrons on the terminal Ti=O bond. The third electron is on the uranium atom, which means that the oxidation state of uranium is V instead of IV. The calculations for uranyl oxygen bond photoreduction suggest that, with this mechanism, the adsorption on edges still shows an advantage over the surface for U(IV) reduction. The **Site 3** (long edge) is more favorable than **Site 2** (short edge) for the uranyl oxygen bond photoreduction.

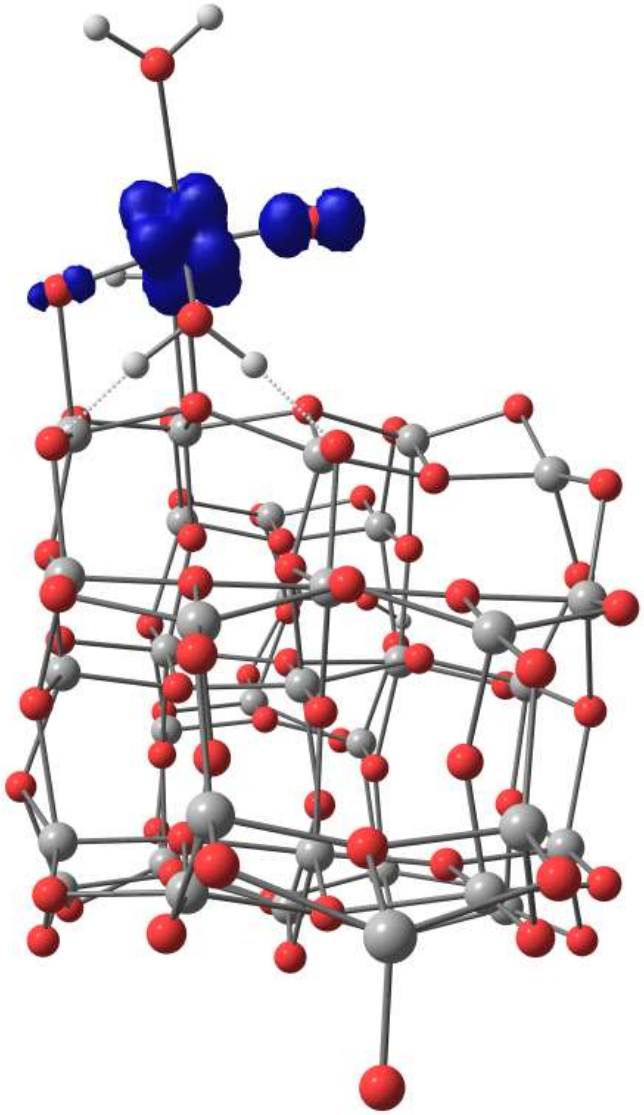

Figure 6.27 Spin density of the optimized quadruplet state structure of uranyl(IV) adsorption on **Site 2** of the $(TiO_2)_{34}(TiO_2H)$ cluster.

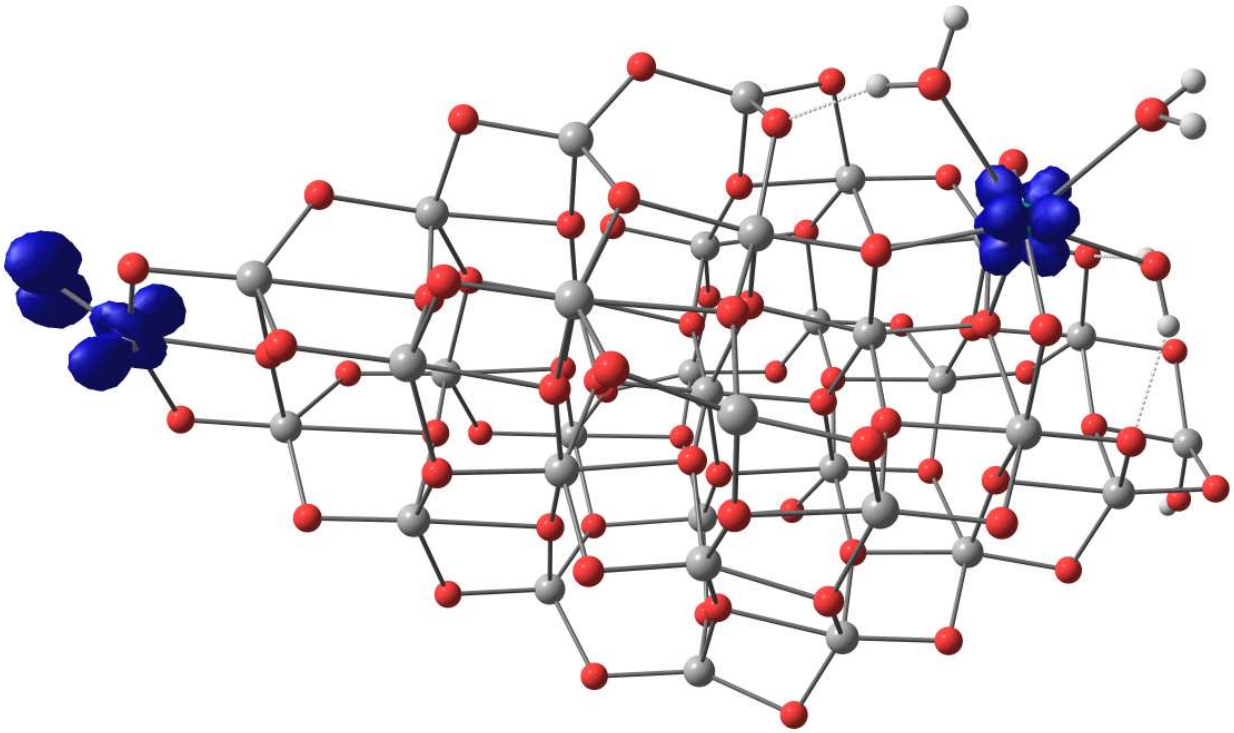

Figure 6.28 Spin density of the optimized quadruplet state structure of uranyl(V) adsorption on **Site 1** of the $(TiO_2)_{34}(TiO_2H)$ cluster.

6.3.8. Broken symmetry calculations for uranyl ion diradicals

Broken symmetry calculations were carried out on the triplet state structures of section 6.3.4. The fully broken symmetry geometry optimizations yielded exactly the same geometry structures and energies as in section 6.3.4. but with open-shell singlet biradical electronic structures. The unpaired electrons are at the same oxygen and uranium atoms as in section 6.3.4 but with a different spin. As mentioned in section 6.3.1, the electronic transitions from the ground (singlet) state to the excited triplet states are spin forbidden but might still occur by intersystem crossing with the help of strong spin-orbit effects from the heavy actinide atoms. However, in this way, the probability for the photoreduction pathway initiated by direct excitation into the lowest triplet states is low. The broken symmetry calculations indicate that the first one-electron U(VI) photoreduction does not need to go through a triplet state but can alternatively go through a stable

open-shell singlet state. This indicates that the uranium photoreduction efficiency will be much higher than expected.

6.4. Conclusion

To answer the questions about how uranium(VI) is reduced to uranium(IV) under dark environment without redox reagents, we propose that the photoreduction can be triggered by radiation from uranium decay. In this study, the reduction of uranium(VI) on the surface of a $(TiO_2)_{34}$ cluster was systemically investigated on **Sites 1**, **2**, and **3**, for the (101) surface, short edge, and long edge of the $(TiO_2)_{35}$ cluster, respectively (see Scheme 6.2). The calculations show that the reduction of U(VI) to U(V) is caused by one-electron transfer from the TiO_2 conduction band. This agrees with the previous studies.[45] In this study, the electron comes from terminal Ti=O bonds. The calculations also suggest that the electron tends to transfer to the **Site 3** position, which is related to the edge of the TiO_2 cluster. However, the energy state diagram shows that the second-electron transfer from photocatalytic reaction cannot occur due to the empty uranium 5*f* orbitals shifting to higher energies than the titanium 3*d* states. The calculations of disproportionation reactions show that the reactions are also likely to occur on the edges and that the reduced U(IV) will appear on the edges after reduction, and not on the faces of the cluster. In addition, the uranyl on **Site 3** (on the edge) still keeps a U=O bond, which is similar to the free uranyl water cluster. This U=O bond can be further broken by UV light or radiation to reduce U(V) to U(IV). Similar photoreduction can also occurr on **Site 2** with a weaker U=O bond. These results help to explain how the reduction can happen in dark environment without redox reagents and why the U(IV) is enriched near the boundaries. Lastly, the broken symmetry calculations indicate that the first one-electron reduction is more efficient than expected. As mentioned above, further investigation of the structure of hydroxylated TiO_2 clusters is also very important in future studies.

6.5. References

1. Li, P.; Wang, J.; Wang, Y.; Liang, J.; Pan, D.; Qiang, S.; Fan, Q., An overview and recent progress in the heterogeneous photocatalytic reduction of U(VI). *Journal of Photochemistry and Photobiology C: Photochemistry Reviews* **2019,** *41*, 100320.
2. Tsouris, C., Uranium extraction: fuel from seawater. *Nature Energy* **2017,** *2* (4), 1-3.
3. Liu, C.; Hsu, P.-C.; Xie, J.; Zhao, J.; Wu, T.; Wang, H.; Liu, W.; Zhang, J.; Chu, S.; Cui, Y., A half-wave rectified alternating current electrochemical method for uranium extraction from seawater. *Nature Energy* **2017,** *2* (4), 1-8.
4. Endrizzi, F.; Leggett, C. J.; Rao, L., Scientific basis for efficient extraction of uranium from seawater. I: understanding the chemical speciation of uranium under seawater conditions. *Industrial & Engineering Chemistry Research* **2016,** *55* (15), 4249-4256.
5. Abney, C. W.; Mayes, R. T.; Saito, T.; Dai, S., Materials for the recovery of uranium from seawater. *Chemical reviews* **2017,** *117* (23), 13935-14013.
6. Sun, Q.; Aguila, B.; Perman, J.; Ivanov, A. S.; Bryantsev, V. S.; Earl, L. D.; Abney, C. W.; Wojtas, L.; Ma, S., Bio-inspired nano-traps for uranium extraction from seawater and recovery from nuclear waste. *Nature communications* **2018,** *9* (1), 1-9.
7. Parker, B.; Zhang, Z.; Rao, L.; Arnold, J., An overview and recent progress in the chemistry of uranium extraction from seawater. *Dalton Transactions* **2018,** *47* (3), 639-644.
8. Behrends, T.; Van Cappellen, P., Competition between enzymatic and abiotic reduction of uranium (VI) under iron reducing conditions. *Chemical Geology* **2005,** *220* (3-4), 315-327.
9. Cantrell, K. J.; Kaplan, D. I.; Wietsma, T. W., Zero-valent iron for the in situ remediation of selected metals in groundwater. *Journal of Hazardous Materials* **1995,** *42* (2), 201-212.
10. Charlet, L.; Silvester, E.; Liger, E., N-compound reduction and actinide immobilisation in surficial fluids by Fe (II): the surface□ FeIIIOFeIIOH° species, as major reductant. *Chemical geology* **1998,** *151* (1-4), 85-93.
11. Noubactep, C.; Schöner, A.; Meinrath, G., Mechanism of uranium removal from the aqueous solution by elemental iron. *Journal of hazardous materials* **2006,** *132* (2-3), 202-212.
12. O'Loughlin, E. J.; Kelly, S. D.; Cook, R. E.; Csencsits, R.; Kemner, K. M., Reduction of Uranium(VI) by Mixed Iron(II)/Iron(III) Hydroxide (Green Rust): Formation of UO2 Nanoparticles. *Environmental Science & Technology* **2003,** *37* (4), 721-727.
13. Vaaramaa, K.; Lehto, J., Removal of metals and anions from drinking water by ion exchange. *Desalination* **2003,** *155* (2), 157-170.
14. Wang, X.; Chen, L.; Wang, L.; Fan, Q.; Pan, D.; Li, J.; Chi, F.; Xie, Y.; Yu, S.; Xiao, C., Synthesis of novel nanomaterials and their application in efficient removal of radionuclides. *Science China Chemistry* **2019,** *62*, 933-967.
15. Cowie, B. E.; Purkis, J. M.; Austin, J.; Love, J. B.; Arnold, P. L., Thermal and Photochemical Reduction and Functionalization Chemistry of the Uranyl Dication, [UVIO2]2+. *Chemical Reviews* **2019,** *119* (18), 10595-10637.
16. Steele, H.; Taylor, R. J., A Theoretical Study of the Inner-Sphere Disproportionation Reaction Mechanism of the Pentavalent Actinyl Ions. *Inorganic Chemistry* **2007,** *46* (16), 6311-6318.
17. Fortier, S.; Hayton, T. W., Oxo ligand functionalization in the uranyl ion (UO22+). *Coordination Chemistry Reviews* **2010,** *254* (3-4), 197-214.
18. Nagaishi, R.; Katsumura, Y.; Ishigure, K.; Aoyagi, H.; Yoshida, Z.; Kimura, T., Photoreduction of uranyl ion in aqueous solution. I. With ethanol in sulphuric acid solutions.

Journal of Photochemistry and Photobiology A: Chemistry **1996,** *96* (1), 45-50.
19. Li, Y.; Su, J.; Mitchell, E.; Zhang, G.; Li, J., Photocatalysis with visible-light-active uranyl complexes. *Science China Chemistry* **2013,** *56*, 1671-1681.
20. Natrajan, L. S., Developments in the photophysics and photochemistry of actinide ions and their coordination compounds. *Coordination Chemistry Reviews* **2012,** *256* (15-16), 1583-1603.
21. Baker, R. J., New reactivity of the uranyl (VI) ion. *Chemistry–A European Journal* **2012,** *18* (51), 16258-16271.
22. Wang, G.; Zhen, J.; Zhou, L.; Wu, F.; Deng, N., Adsorption and photocatalytic reduction of U(VI) in aqueous TiO2 suspensions enhanced with sodium formate. *Journal of Radioanalytical and Nuclear Chemistry* **2015,** *304* (2), 579-585.
23. Li, P.; Wang, J.; Wang, Y.; Liang, J.; He, B.; Pan, D.; Fan, Q.; Wang, X., Photoconversion of U(VI) by TiO2: An efficient strategy for seawater uranium extraction. *Chemical Engineering Journal* **2019,** *365*, 231-241.
24. Fujishima, A.; Honda, K., Electrochemical photolysis of water at a semiconductor electrode. *nature* **1972,** *238* (5358), 37-38.
25. Daghrir, R.; Drogui, P.; Robert, D., Modified TiO2 for environmental photocatalytic applications: a review. *Industrial & Engineering Chemistry Research* **2013,** *52* (10), 3581-3599.
26. Guan, X.; Du, J.; Meng, X.; Sun, Y.; Sun, B.; Hu, Q., Application of titanium dioxide in arsenic removal from water: a review. *Journal of Hazardous materials* **2012,** *215*, 1-16.
27. Henderson, M. A., A surface science perspective on TiO2 photocatalysis. *Surface Science Reports* **2011,** *66* (6-7), 185-297.
28. Cai, J.; Shen, J.; Zhang, X.; Ng, Y. H.; Huang, J.; Guo, W.; Lin, C.; Lai, Y., Light-driven sustainable hydrogen production utilizing TiO2 nanostructures: a review. *Small Methods* **2019,** *3* (1), 1800184.
29. Fang, W.; Xing, M.; Zhang, J., Modifications on reduced titanium dioxide photocatalysts: A review. *Journal of Photochemistry and Photobiology C: Photochemistry Reviews* **2017,** *32*, 21-39.
30. Amadelli, R.; Maldotti, A.; Sostero, S.; Carassiti, V., Photodeposition of uranium oxides onto TiO2 from aqueous uranyl solutions. *Journal of the Chemical Society, Faraday Transactions* **1991,** *87* (19), 3267-3273.
31. Chen, J.; Ollis, D. F.; Rulkens, W. H.; Bruning, H., Photocatalyzed deposition and concentration of soluble uranium(VI) from TiO2 suspensions. *Colloids and Surfaces A: Physicochemical and Engineering Aspects* **1999,** *151* (1), 339-349.
32. Selli, E.; Eliet, V.; Spini, M. R.; Bidoglio, G., Effects of humic acids on the photoinduced reduction of U (VI) in the presence of semiconducting TiO2 particles. *Environmental science & technology* **2000,** *34* (17), 3742-3748.
33. Evans, C. J.; Nicholson, G. P.; Faith, D. A.; Kan, M. J., Photochemical removal of uranium from a phosphate waste solution. *Green chemistry* **2004,** *6* (4), 196-197.
34. Bonato, M.; Allen, G.; Scott, T., Reduction of U (VI) to U (IV) on the surface of TiO2 anatase nanotubes. *Micro Nano Lett* **2008,** *3* (2), 57.
35. Bonato, M.; Ragnarsdottir, K.; Allen, G., Removal of uranium (VI), lead (II) at the surface of TiO 2 nanotubes studied by X-ray photoelectron spectroscopy. *Water, Air, & Soil Pollution* **2012,** *223*, 3845-3857.
36. Zhang, L.; Li, H.; Li, L.; Deng, J.; Deng, W.; Zhao, Y., Photocatalytic Reduction of Uranyl Ions over Anatase and Rutile Nanostructured TiO2. *Chemistry Letters* **2013,** *42* (7), 689-690.

37. Kim, Y. K.; Lee, S.; Ryu, J.; Park, H., Solar conversion of seawater uranium (VI) using TiO2 electrodes. *Applied Catalysis B: Environmental* **2015,** *163*, 584-590.
38. Meichtry, J. M.; Levy, I. K.; Mohamed, H. H.; Dillert, R.; Bahnemann, D. W.; Litter, M. I., Mechanistic Features of the TiO2 Heterogeneous Photocatalysis of Arsenic and Uranyl Nitrate in Aqueous Suspensions Studied by the Stopped-Flow Technique. *ChemPhysChem* **2016,** *17* (6), 885-892.
39. He, H.; Zong, M.; Dong, F.; Yang, P.; Ke, G.; Liu, M.; Nie, X.; Ren, W.; Bian, L., Simultaneous removal and recovery of uranium from aqueous solution using TiO 2 photoelectrochemical reduction method. *Journal of Radioanalytical and Nuclear Chemistry* **2017,** *313*, 59-67.
40. Li, P.; Wang, J.; Peng, T.; Wang, Y.; Liang, J.; Pan, D.; Fan, Q., Heterostructure of anatase-rutile aggregates boosting the photoreduction of U (VI). *Applied Surface Science* **2019,** *483*, 670-676.
41. Guo, Y.; Li, L.; Li, Y.; Li, Z.; Wang, X.; Wang, G., Adsorption and photocatalytic reduction activity of uranium (VI) on zinc oxide/rectorite composite enhanced with methanol as sacrificial organics. *Journal of Radioanalytical and Nuclear Chemistry* **2016,** *310*, 883-890.
42. Li, Z.-J.; Huang, Z.-W.; Guo, W.-L.; Wang, L.; Zheng, L.-R.; Chai, Z.-F.; Shi, W.-Q., Enhanced photocatalytic removal of uranium (VI) from aqueous solution by magnetic TiO2/Fe3O4 and its graphene composite. *Environmental science & technology* **2017,** *51* (10), 5666-5674.
43. Zhang, Y.; Zong, S.; Cheng, C.; Shi, J.; Guo, P.; Guan, X.; Luo, B.; Shen, S.; Guo, L., Rapid high-temperature treatment on graphitic carbon nitride for excellent photocatalytic H2-evolution performance. *Applied Catalysis B: Environmental* **2018,** *233*, 80-87.
44. Guo, Y.; Guo, Y.; Wang, X.; Li, P.; Kong, L.; Wang, G.; Li, X.; Liu, Y., Enhanced photocatalytic reduction activity of uranium (vi) from aqueous solution using the Fe 2 O 3–graphene oxide nanocomposite. *Dalton Transactions* **2017,** *46* (43), 14762-14770.
45. Odoh, S. O.; Pan, Q. J.; Shamov, G. A.; Wang, F.; Fayek, M.; Schreckenbach, G., Theoretical study of the reduction of uranium (VI) aquo complexes on titania particles and by alcohols. *Chemistry–A European Journal* **2012,** *18* (23), 7117-7127.
46. Salomone, V. N.; Meichtry, J. M.; Zampieri, G.; Litter, M. I., New insights in the heterogeneous photocatalytic removal of U (VI) in aqueous solution in the presence of 2-propanol. *Chemical Engineering Journal* **2015,** *261*, 27-35.
47. Lee, S.; Kang, U.; Piao, G.; Kim, S.; Han, D. S.; Park, H., Homogeneous photoconversion of seawater uranium using copper and iron mixed-oxide semiconductor electrodes. *Applied Catalysis B: Environmental* **2017,** *207*, 35-41.
48. Miyake, C.; Nakase, T.; Sano, Y., EPR study of uranium (V) species in photo-and electrolytic reduction processes of UO2 (NO3) 2-2TBP. *Journal of Nuclear Science and Technology* **1993,** *30* (12), 1256-1260.
49. Litter, M. I., Last advances on TiO2-photocatalytic removal of chromium, uranium and arsenic. *Current opinion in green and sustainable chemistry* **2017,** *6*, 150-158.
50. Newton, T. W.; Baker, F. B., A Uranium(V)-Uranium(VI) Complex and Its Effect on the Uranium (V) Disproportionation Rate. *Inorganic Chemistry* **1965,** *4* (8), 1166-1170.
51. Ekstrom, A., Kinetics and mechanism of the disproportionation of uranium(V). *Inorganic Chemistry* **1974,** *13* (9), 2237-2241.
52. Hu, L.; Yan, X.-W.; Zhang, X.-J.; Shan, D., Integration of adsorption and reduction for uranium uptake based on SrTiO3/TiO2 electrospun nanofibers. *Applied Surface Science* **2018,** *428*,

819-824.
53. Fayek., M., Personal communication.
54. Calas, G.; Angiboust, S.; Fayek, M.; Camacho, A.; Allard, T.; Agrinier, P., Epithermal uranium deposits in a volcanogenic context: the example of Nopal 1 deposit, Sierra de Pena Blanca, Mexico. *AGU Fall Meeting Abstracts* **2009**.
55. Le Caër, S., Water Radiolysis: Influence of Oxide Surfaces on H2 Production under Ionizing Radiation. *Water* **2011,** *3* (1), 235-253.
56. Lamiel-Garcia, O.; Ko, K. C.; Lee, J. Y.; Bromley, S. T.; Illas, F., When Anatase Nanoparticles Become Bulklike: Properties of Realistic TiO2 Nanoparticles in the 1–6 nm Size Range from All Electron Relativistic Density Functional Theory Based Calculations. *Journal of Chemical Theory and Computation* **2017,** *13* (4), 1785-1793.
57. Cho, D.; Ko, K. C.; Lamiel-García, O.; Bromley, S. T.; Lee, J. Y.; Illas, F., Effect of Size and Structure on the Ground-State and Excited-State Electronic Structure of TiO2 Nanoparticles. *Journal of Chemical Theory and Computation* **2016,** *12* (8), 3751-3763.
58. Hummer, D. R.; Kubicki, J. D.; Kent, P. R. C.; Heaney, P. J., Single-Site and Monolayer Surface Hydration Energy of Anatase and Rutile Nanoparticles Using Density Functional Theory. *The Journal of Physical Chemistry C* **2013,** *117* (49), 26084-26090.
59. Barnard, A. S.; Erdin, S.; Lin, Y.; Zapol, P.; Halley, J. W., Modeling the structure and electronic properties of $\mathrm{Ti}{\mathrm{O}}_{2}$ nanoparticles. *Physical Review B* **2006,** *73* (20), 205405.
60. Perdew, J. P.; Ernzerhof, M.; Burke, K., Rationale for mixing exact exchange with density functional approximations. *The Journal of chemical physics* **1996,** *105* (22), 9982-9985.
61. Adamo, C.; Barone, V., Toward reliable density functional methods without adjustable parameters: The PBE0 model. *The Journal of chemical physics* **1999,** *110* (13), 6158-6170.
62. Neese, F., Software update: the ORCA program system, version 4.0. *WIREs Computational Molecular Science* **2018,** *8* (1), e1327.
63. Pantazis, D. A.; Neese, F., All-Electron Scalar Relativistic Basis Sets for the Actinides. *Journal of Chemical Theory and Computation* **2011,** *7* (3), 677-684.
64. Pantazis, D. A.; Neese, F., All-Electron Scalar Relativistic Basis Sets for the Lanthanides. *Journal of Chemical Theory and Computation* **2009,** *5* (9), 2229-2238.
65. Weigend, F.; Ahlrichs, R., Balanced basis sets of split valence, triple zeta valence and quadruple zeta valence quality for H to Rn: Design and assessment of accuracy. *Physical Chemistry Chemical Physics* **2005,** *7* (18), 3297-3305.
66. Hirshfeld, F. L., Bonded-atom fragments for describing molecular charge densities. *Theoretica chimica acta* **1977,** *44* (2), 129-138.
67. Zegke, M.; Zhang, X.; Pidchenko, I.; Hlina, J. A.; Lord, R. M.; Purkis, J.; Nichol, G. S.; Magnani, N.; Schreckenbach, G.; Vitova, T.; Love, J. B.; Arnold, P. L., Differential uranyl(v) oxo-group bonding between the uranium and metal cations from groups 1, 2, 4, and 12; a high energy resolution X-ray absorption, computational, and synthetic study. *Chemical Science* **2019,** *10* (42), 9740-9751.
68. Arnold, P. L.; Dutkiewicz, M. S.; Zegke, M.; Walter, O.; Apostolidis, C.; Hollis, E.; Pécharman, A. F.; Magnani, N.; Griveau, J. C.; Colineau, E., Subtle interactions and electron transfer between UIII, NpIII, or PuIII and uranyl mediated by the oxo group. *Angewandte Chemie* **2016,** *128* (41), 12989-12993.
69. Ziegler, T.; Rauk, A., A theoretical study of the ethylene-metal bond in complexes between copper(1+), silver(1+), gold(1+), platinum(0) or platinum(2+) and ethylene, based on the Hartree-

Fock-Slater transition-state method. *Inorganic Chemistry* **1979,** *18* (6), 1558-1565.
70. Ziegler, T.; Rauk, A., Carbon monoxide, carbon monosulfide, molecular nitrogen, phosphorus trifluoride, and methyl isocyanide as .sigma. donors and .pi. acceptors. A theoretical study by the Hartree-Fock-Slater transition-state method. *Inorganic Chemistry* **1979,** *18* (7), 1755-1759.
71. Mitoraj, M. P.; Michalak, A.; Ziegler, T., A Combined Charge and Energy Decomposition Scheme for Bond Analysis. *Journal of Chemical Theory and Computation* **2009,** *5* (4), 962-975.
72. Lu, T.; Chen, F., Multiwfn: A multifunctional wavefunction analyzer. *Journal of Computational Chemistry* **2012,** *33* (5), 580-592.
73. Mulliken, R. S., Electronic population analysis on LCAO–MO molecular wave functions. I. *The Journal of Chemical Physics* **1955,** *23* (10), 1833-1840.
74. Löwdin, P. O., On the non-orthogonality problem connected with the use of atomic wave functions in the theory of molecules and crystals. *The Journal of Chemical Physics* **1950,** *18* (3), 365-375.
75. Fonseca Guerra, C.; Handgraaf, J.-W.; Baerends, E. J.; Bickelhaupt, F. M., Voronoi deformation density (VDD) charges: Assessment of the Mulliken, Bader, Hirshfeld, Weinhold, and VDD methods for charge analysis. *Journal of Computational Chemistry* **2004,** *25* (2), 189-210.
76. Bader, R. F. W.; Bader, R. F., *Atoms in Molecules: A Quantum Theory*. Clarendon Press: 1990.
77. Dette, C.; Pérez-Osorio, M. A.; Kley, C. S.; Punke, P.; Patrick, C. E.; Jacobson, P.; Giustino, F.; Jung, S. J.; Kern, K., TiO2 Anatase with a Bandgap in the Visible Region. *Nano Letters* **2014,** *14* (11), 6533-6538.

Chapter 7. Summary and Future Studies

7.1. Summary

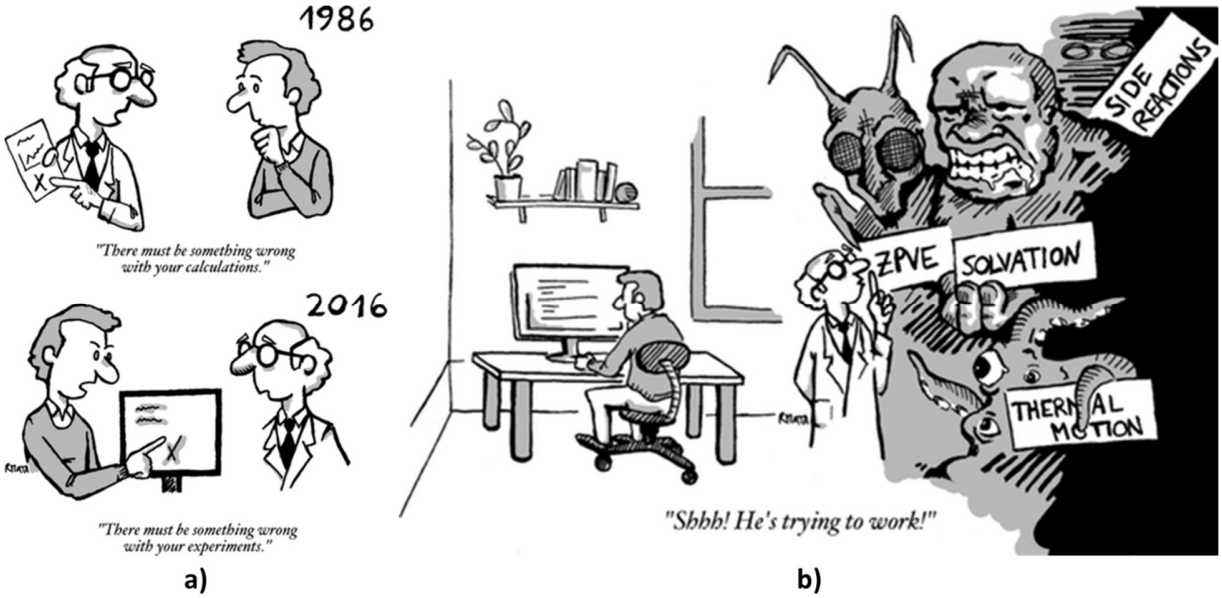

Figure 7.1 a) The change of paradigm. b) Complexity in different chemical systems that needs to be overcome. The figures are from ref 1.

There were 17,000 transistors in total in the integrated circuit of the Apollo Guidance Computer. However, nowadays, the A16 Bionic chip in the iPhone 14 Pro features 16 billion transistors, which surpasses the performance of the most advanced computing clusters decades ago. With the remarkable development of computing hardware, accompanied by significantly improved new methods and algorithms, it has become possible to model larger systems with higher accuracy. Thus, theoretical calculations play an essential role in the modern chemical research. Those achievements changed the relation between theory and experiment in chemistry research. As Figure 7.1 a) shows, quite a few researchers share the point of view that quantum chemical calculations can stand on equal footing with experimental methods rather than serve as a supplement to just interpret the results from latter. In spite of that, it is still a challenge to bring

theory and experiment together due to the complexity of the chemical environments in the real world. Theoreticians must consider many factors in the calculations to simulate reality as depicted in Figure 7.1 b), which usually is a nightmare. Nevertheless, one should not only worry about the mismatch between calculations and experiments, but also should be cautious when they agree well without good reasons. ***Thus, it requires a synergy of quantum chemists and experimentalists to deal with those challenges by carefully designing experimental and computational approaches that deal with the fewest possible factors. This is especially true for actinide chemistry.***

The overall aim of this thesis is to further understand the bonding in actinide chemistry by using computational methods. However, the ***scarcity of experimental data*** is particularly significant for 5*f* block elements. Not to mention that much of the existing data stems from studies conducted several decades ago. The accuracy and reliability of the data should be subject to questioning. Therefore, in this thesis we closely collaborated with experimental groups to verify the theoretical results with new experimental data. ***In this context, high-level theoretical calculations have become a cornerstone of contemporary actinide research. Conversely, sound experimental data is crucial for building accurate theoretical models and obtaining reliable calculation results.***

Hence, various research projects are presented in this thesis, from small actinide systems consisting of actinyl water clusters to large TiO_2 complexes. Each project also aimed to overcome different computational challenges, for example, the difficulty in calculating open-shell actinides, especially the convergence problems for the calculations on the fragments in bonding analysis. A great amount of information arises from all the challenges overcome. Therefore, in this chapter, the main findings of this thesis as well as future studies are summarized. It is worth to point out that although the summary in this chapter is for computational actinide chemistry, the conclusion

will also apply to, for example, main group chemistry in similar situations. The ***logic*** behind these projects in this thesis is to explore the arrows in the schematic representation in Figure 7.2, specifically, the "**Chemical Environment**", "**Dirac Equation**", and "**Bonding Analysis Tools**" axes of the diagram.

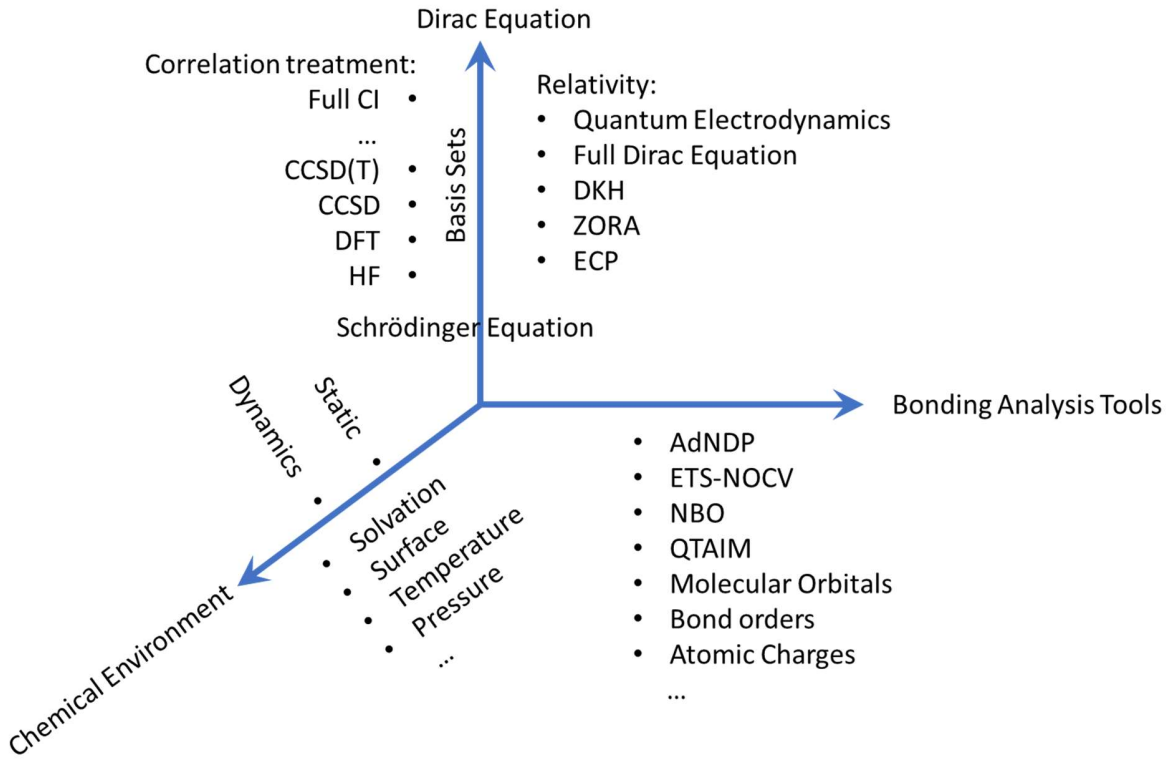

Figure 7.2 Schematic representation of three levels of approximation required in computational actinide chemistry in this thesis

The first arrow, "**Chemical Environment**", is mentioned in Figure 7.1 as well. Despite the relatively rare occurrence of gas-phase reactions and solid-phase synthesis, most chemical reactions take place in solution. Therefore, the handling of solutions is crucial for simulating both homogeneous and heterogeneous reactions. Since many, if not most, of these reactions happen in aqueous environments, the treatment of water in the calculations is of importance to comprehend

these reactions. Despite the very simple appearance of the water molecule, the structure of water in condensed phase at a molecular level is still not fully understood from either experiment or theory, due to the complexity of the H-bond network.[2] Nevertheless, handling either implicit or explicit solvation models is a challenge in calculations, for example, the accompanying technical issues such as numerical noise during geometry optimization or frequency calculations. For "**Solvation**", the models used in the projects span the range from gas-phase simulation (no solvation, Chapter 2) to the combination of the explicit and implicit solvation models (Chapters 3 and 4), and then even to high temperature and pressure conditions (Chapter 5). Although in Chapter 6 the implicit solvation model was not used due to the complexity of the TiO_2 surface, the explicit solvent molecules (water) around uranyl were still included. In Chapter 2, the actinyl ions are buried inside the "Pacman" ligand. Therefore, the gas-phase calculations are totally acceptable. For smaller actinide compounds, previous experimental and theoretical studies suggest that the first solvation shell is crucial.[3] Thus, a combination of explicit and implicit solvation models was utilized in this thesis. However, it is worth noting that the default values of the atomic sphere radii for actinides in many implicit solvation models of different programs are not adequately optimized. In Chapters 3 - 5, these heavy metals are well buried inside of the first solvation shell or ligands and do not have direct contact with the solvation cavity. Hence, the radii settings for them do not affect the calculation results. Despite the need to understand the aqueous chemistry of systems relevant to the nuclear fuel cycle under non-standard state conditions, most thermodynamic measurements of actinide systems have been performed at room temperature and atmospheric pressure. Also, most implicit solvation models are optimized at standard temperature (298.15K) and pressure (1 atm). In Chapter 5, ***dielectric constants*** that change as a function of pressure and temperature were used to successfully predict the properties of the aqueous AnO_2-Cl system at

high pressure and temperature. This provides a cost-effective modeling approach without very expensive *ab initio* dynamics calculations to simulate actinide aqueous system under extreme conditions, which usually lack experimental data. The equation relating the separation factor (SF) for actinides over lanthanides (An/Ln) to the Gibbs free energy difference of extraction ($\Delta\Delta G_{ext}$) can be given by:

$$SF_{(An/Ln)} = \sim \exp(-\Delta\Delta G_{ext}/RT) \tag{7.1}$$

where R is the gas constant and T is temperature. Because the $\Delta\Delta G_{ext}$ is usually very small (several kcal/mol), when applying the implicit solvation model in the calculations, we include various thermodynamic corrections to obtain accurate energies, such as the density correction and the standard state correction. This is another reason why only the first solvation shell is introduced, as it helps to minimize the interference of the varied structures of explicit water molecules in geometry optimization, which is usually much larger compared to $\Delta\Delta G_{ext}$. In Chapter 6, the simulation of the TiO_2 nanoparticle was conducted using a cluster model that includes both ***edges and surfaces***. In contrast to previous studies carried out by our group, this specific cluster model yielded significantly different results compared to previous regular periodic calculations. The results in Chapter 6 align well with experimental observations. However, we did not use either explicit or implicit models directly on the TiO_2 surface/cluster. This is because the interactions between water and TiO_2 nanoparticles are complicated. As discussed above, solvation models are of utmost importance in computational actinide chemistry, particularly when assessing the separation capability of ligands. ***The treatment of solvation adds another level of complexity to the calculations.*** However, as mentioned at the beginning of this chapter, collaboration between theoreticians and experimentalists is crucial. By adopting an alternative approach that involves obtaining gas-phase data from experimental sources, we can utilize purer data for understanding

the bonding natures with gas-phase calculations. This can help mitigate errors arising from the use of solvation models, especially for actinides/lanthanides ions.

Nonetheless, there is one factor that cannot be eliminated from the experimental side, and that is the fundamental "**Schrödinger Equation**" or its relativistic extension "**Dirac Equation**", which is the second arrow in Figure 7.2. When it comes to actinides, solving this equation faces a distinct challenge due to the significant influence of "**Relativity**". Due to the challenges of implementation and the relatively small research community, we often find ourselves "dancing with shackles on". For example, in this thesis, we have to stick to the scalar ZORA or ECP methods. Not only because, from the previous experience, the structural and electronic properties as well as the chemistry of actinide species are predicted by using scalar ZORA/ECP using DFT at a sufficiently accurate level.[4, 5] But also many tools are not implemented for higher levels of relativity calculations in Figure 7.2 yet, for example, those including ***spin-orbit effects***. The all-electrons scalar ZORA method generally gives more accurate results than the ECP method, especially for the large-core ECPs. More importantly, the core electrons are needed for calculating the properties such as X-ray spectroscopy, which is a powerful experimental tool[6] for investigating actinide bonds. Thus, the all-electrons scalar ZORA method is used in most of the chapters in this thesis. The "**Correlation Energy**" in quantum chemistry is small compared to the total energy. However, the treatment of it, see left hand side of the arrow in Figure 7.2, is very important to predict the chemical properties like reaction energies. The reaction free energy differences in actinide chemistry, for example, the ligand An/Ln exchange reactions as shown in equation 7.l, are usually very small because of the similar chemical properties. Therefore, besides solvation energies as mentioned earlier, we need to consider as much correlation energy as possible in order to achieve accurate results. The pure GGA functions, such as PBE, were used a lot in the previous

studies in our group because of their efficiency. However, from the early chapters in this thesis, the drawbacks of using the pure GGA functionals are revealed. The pure GGA functionals generally give longer bond lengths compared to experimental data. Moreover, the pure GGA functional in Chapter 3 underestimated the bonding energies for actinides comparing to lanthanides. The $\Delta\Delta G_{ext}$ at the PBE level gave an oppose trend compared to experimental data and computational results after applying high level single-point corrections. Thus, in Chapters 5 and 6, hybrid GGA functionals, such as B3LYP and PBE0, were used instead of the pure GGA PBE functional. From previous experience and unpublished benchmark work, the hybrid GGAs B3LYP and PBE0 perform similarly. In Chapter 5, the B3LYP method successfully predicts the U=O bond lengths in solution with good agreement with experimental data. In Chapter 6, the PBE0 functional was used to test the performance of hybrid GGA for a much larger system. One of the reasons is that the pure GGA PBE functional gives a too small HOMO-LUMO gap for the TiO_2 cluster. As a direct result, the calculations of the triplet state of TiO_2-UO_2 complexes cannot converge. Thus, from the studies of small and large systems in this thesis, using the hybrid GGA with scalar ZORA Hamiltonian is generally recommend for studying the ground states of early actinide systems. To get better accuracy of energies, single point energy corrections, such as double hybrid GGAs or even DLPNO-CCSD(T), on the structure obtained from hybrid GGA calculations is an effective way and usually needed. The ""**Basis Sets**" at the ZORA level are also limited. So far, the only available basis sets that include actinides are SARC basis sets for both ZORA and DKH in the ORCA code, which was used for high level single point energy calculations, while for lanthanides newer SARC2 basis sets are available which are easier to converge in the calculations. The SDD ECP is usually recommended for the heavy elements like actinides and lanthanides.[7] The only missing correlation correction in this thesis are "**Multi-Reference Effects**". Previous studies have

shown that single-reference methods such as DFT can provide reasonable descriptions of the electronic properties as well as structural and vibrational properties of the ground states of the open-shell actinide systems.[4] The TiO_2 system in Chapter 6 is our first attempt to deal with excited states, although we have somewhat "cheated" by employing the triplet ground state (T_1) instead of actual excitation calculations. But the T_1 state does serve as the final state for subsequent photochemical reactions. However, it becomes crucial to take into account the multi-reference character and spin-orbit effects in electronic excited state calculations, especially when simulating X-ray spectra, which is a valuable tool for investigate chemical bonds.

The next arrow in Figure 7.2 represents "**Bonding Analysis Tools**". It is important to note that many traditional chemical concepts are not directly observable at the quantum mechanical level. Hence, various methods in computational chemistry have been developed to reconstruct these concepts. Unlike for the second arrow, there is not clear hierarchical system for those methods. Each of the different theoretical tools for bonding analysis has its own set of limitations. Thus, it is crucial to employ multiple methods in parallel to corroborate the findings. For example, in Chapter 2, the experimental data of "Pacman" complexes were utilized to validate and assess various theoretical tools. The results indicate that Hirshfeld charges typically exhibit better performance than the widely used Mulliken charges, which is consistent with the findings discussed in Chapters 3-6. Also, in Chapter 2, spin density has been proven to be highly useful for validating the oxidation state. This has been widely applied in Chapter 6 to elucidate the reduction of uranyl ions on the TiO_2 surface in a dark environment. Molecular orbitals and QTAIM are two commonly used tools for discussing various properties in quantum chemistry. However, molecular orbitals are often delocalized, and the specific properties of interest can be distributed among multiple orbitals. This can not only complicate but also potentially mislead the discussion and

analysis process. On the other hand, the BCP in QTAIM only offers information at a single point in space, which may not be sufficient for comprehensive investigation of the bonding nature. On the contrary, the ETS-NOCV method provides more comprehensive information about bonding compared to MOs and QTAIM. Specifically, ETS-NOCV can offer insights into both the shapes and energies of orbitals involved in bonding. Thus, it was used intensely for actinide covalent bonding analysis in Chapter 3 and later chapters. Nevertheless, all the tools gave the same trend in the study. The ETS-NOCV analysis in Chapter 3 shows the importance of π interactions between extractants and actinide/lanthanide. However, the ETS-NOCV approach is still based on MOs. Thus, when multiple bonding sites exist in a molecule with symmetry, it is hard to investigate a single bond individually. Therefore, in Chapter 5, the AdNDP method was successfully introduced. Unlike NBO, the determination of AdNDP orbitals relies on the user's chemical intuition, which allows for the possibility of obtaining different AdNDP patterns through different search processes. However, from another perspective, this also is the flexibility of the AdNDP method. Hence, many other methods, such as the ETS-NOCV, and multicenter bond order, were also used to validate the generated AdNDP results. The AdNDP results show that π interactions are strongly affected by the local symmetry of rings in the extractants. Based on the AdNDP results, a new extractant was designed, which gives the best performance in this thesis for Am^{3+}/Eu^{3+} separation computationally. Lastly, it should be noted that the majority of these tools are only implemented at the scalar relativistic and single-reference level.

Overall, the work in this thesis used actinyls, especially uranyl, as a model system to investigate the bonding nature of actinide bonds successfully. On the other hand, a new TiO_2 cluster was introduced due to its crystal-like structure and the presence of both edges and surfaces. This

cluster exhibits great potential for simulating mineral systems. We propose that photoreduction can also be triggered by radiation from uranium decay.

Various theoretical tools were tested to simulate and understand the bonding nature of actinide complexes. To ensure reliable results, it is generally recommended to follow the guidelines indicated by the three arrows in Figure 7.2. Although, the relativistic DFT calculations are found to be suitable for investigating actinide chemistry in various environmental phases, high-level calculations for energy corrections are needed for correct reaction energies, especially for actinide/lanthanide exchange reactions. However, the significance of multi-reference character and spin-orbit effects remains untested for systems involving elements with more *f* electrons, such as Np, Pu, or Am. The solvation effects need to be considered carefully depending on the systems. The different theoretical tools for bonding analysis all have their own limitations. Thus, it is important to use multiple methods simultaneously to verify the results. Many useful methods, such as ETS-NOCV and QTAIM, were examined in this thesis and exhibited good application potential. The analysis suggests that π interaction between ligands and actinides could play a crucial role in separation, although direct evidence from experimental measurements, such as X-ray spectroscopy, is still awaited to confirm this. However, these tools were typically implemented in single-reference methods using scalar relativistic Hamiltonians. When multi-reference character and spin-orbit effects become significant, the reliability of these tools becomes questionable. I hope future researchers find the results useful and interesting and can use them as the foundation for their work.

7.2. Future Studies

Possible directions for future research, and the work that could not be included due to technical constraints or time constraints in this thesis, are summarized in the following:

Chapters 2: There is evidence that the hydrogen bonds in the lower pocket of "Pacman" compounds are related to the redox potential of the coordinated uranyl. A full investigation is desirable because the redox potential is an important factor for the behavior of uranyl in those "Pacman" compounds. Due to the increased Lewis basicity of $U^{V}O_2^{+}$ compared to $U^{VI}O_2^{2+}$, uranyl(V) complexes may also be employed to model the behavior of highly radioactive neptunium ions NpO_2^{2+}, which are present in nuclear waste. Furthermore, multi-reference characters are important for lower oxidation states of early actinides. Determining this effect is useful for the actinide chemistry community. However, the multi-reference calculations are usually too expensive for 5*f* block compounds. One approach is to calculate the multi-reference character for a single actinyl ion, and then apply the resulting energy corrections to regular DFT calculations of larger complexes. Another approach is the ab initio charge transfer multiplet ligand field method.[8] However, this approach is still in the development stage for actinides and requires collaborative efforts from both experimentalists and theoreticians to further advance its application.

Chapters 3 and 4: It would be intriguing to directly examine the predictions from calculations through further experimental investigations. As discussed earlier, ideally, the gas-phase X-ray spectrum measurement will be used in the validation. Furthermore, uranyl has proven to be a cost-effective screening model for identifying potential ligand candidates. These ligand candidates can be generated on a large scale through the utilization of artificial intelligence (AI). Also, the proposed models and methods, such as ETS-NOCV and AdNDP, can be used in other similar compounds or for validating new methods in the future. However, these tools require expensive quantum chemistry calculations and must be carried out manually. It would be highly beneficial if an AI model could be trained to directly predict the electronic structure from geometric

structures, as it would eliminate the need for expensive quantum chemistry calculations and manual intervention.

Chapters 5: In high temperature and pressure conditions, the hydroxide compounds are likely to form, which might also be the reason for the observed shift of the Raman spectrum. Some calculations have already been carried out using regular DFT but need further investigation. Preliminary ab initio molecular dynamics calculations show that, at high-temperature, the Cl anions will take hydrogen atoms from coordinated water from uranyl to form HCl and uranyl hydroxide compounds. The mechanism still needs a systematic study.

Chapter 6: The new crystal-like TiO_2 cluster model showed the importance of edges and corners for reactivity. The new hypothesis is that this can also apply to simulations of surface reaction (heterogeneous catalysis) for mineral and metal systems more generally. For example, the uranyl-TiO_2 system can be extended to other members of the actinide series, such as Np, Pu, Am, etc. On the other hand, other mineral surfaces, such as montmorillonite, magnetite, kaolinite, etc., can also be simulated similarly. Further investigation of the structure of the hydroxylated TiO_2 cluster is also very important for including solvation effects. In this study, the position of the uranyl moiety has been chosen manually. It will also be interesting to do dynamics simulations for how uranyl adsorbs on the surface using machine learning force fields.

Additionally, the implementation of analysis tools at higher levels of relativistic effects and multi-reference methods is necessary.

7.3. References

1. Mata, R. A.; Suhm, M. A., Benchmarking Quantum Chemical Methods: Are We Heading in the Right Direction? *Angewandte Chemie International Edition* **2017,** *56* (37), 11011-11018.
2. Chen, M.; Ko, H.-Y.; Remsing, R. C.; Calegari Andrade, M. F.; Santra, B.; Sun, Z.; Selloni, A.; Car, R.; Klein, M. L.; Perdew, J. P.; Wu, X., Ab initio theory and modeling of water. *Proceedings of the National Academy of Sciences* **2017,** *114* (41), 10846-10851.
3. Spencer, S.; Gagliardi, L.; Handy, N. C.; Ioannou, A. G.; Skylaris, C.-K.; Willetts, A.; Simper, A. M., Hydration of UO22+ and PuO22+. *The Journal of Physical Chemistry A* **1999,** *103* (12), 1831-1837.
4. Clavaguéra-Sarrio, C.; Vallet, V.; Maynau, D.; Marsden, C. J., Can density functional methods be used for open-shell actinide molecules? Comparison with multiconfigurational spin-orbit studies. *The Journal of Chemical Physics* **2004,** *121* (11), 5312-5321.
5. Shamov, G. A.; Schreckenbach, G.; Vo, T. N., A Comparative Relativistic DFT and Ab Initio Study on the Structure and Thermodynamics of the Oxofluorides of Uranium(IV), (V) and (VI). *Chemistry – A European Journal* **2007,** *13* (17), 4932-4947.
6. Vitova, T.; Pidchenko, I.; Fellhauer, D.; Bagus, P. S.; Joly, Y.; Pruessmann, T.; Bahl, S.; Gonzalez-Robles, E.; Rothe, J.; Altmaier, M.; Denecke, M. A.; Geckeis, H., The role of the 5f valence orbitals of early actinides in chemical bonding. *Nature Communications* **2017,** *8* (1), 16053.
7. Shamov, G. A.; Schreckenbach, G., Density Functional Studies of Actinyl Aquo Complexes Studied Using Small-Core Effective Core Potentials and a Scalar Four-Component Relativistic Method. *The Journal of Physical Chemistry A* **2006,** *110* (43), 12072-12072.
8. Haverkort, M. W., Quanty for core level spectroscopy - excitons, resonances and band excitations in time and frequency domain. *Journal of Physics: Conference Series* **2016,** *712* (1), 012001.